MONITORING CORROSION OF REBAR EMBEDDED IN MORTAR
USING GUIDED ULTRASONIC WAVES

BY

BENJAMIN LEE ERVIN

B.S., University of Illinois at Urbana-Champaign, 2001
M.S., University of Illinois at Urbana-Champaign, 2003

DISSERTATION

Submitted in partial fulfillment of the requirements
for the degree of Doctor of Philosophy in Systems and Entrepreneurial Engineering
in the Graduate College of the
University of Illinois at Urbana-Champaign, 2007

Urbana, Illinois

UMI Number: 3290229

INFORMATION TO USERS

The quality of this reproduction is dependent upon the quality of the copy submitted. Broken or indistinct print, colored or poor quality illustrations and photographs, print bleed-through, substandard margins, and improper alignment can adversely affect reproduction.

In the unlikely event that the author did not send a complete manuscript and there are missing pages, these will be noted. Also, if unauthorized copyright material had to be removed, a note will indicate the deletion.

UMI®

UMI Microform 3290229

Copyright 2008 by ProQuest Information and Learning Company.

All rights reserved. This microform edition is protected against unauthorized copying under Title 17, United States Code.

ProQuest Information and Learning Company
300 North Zeeb Road
P.O. Box 1346
Ann Arbor, MI 48106-1346

CERTIFICATE OF COMMITTEE APPROVAL

University of Illinois at Urbana-Champaign
Graduate College

August 28, 2007

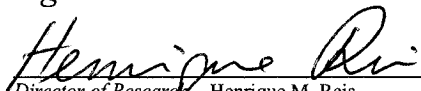*We hereby recommend that the thesis by:*

BENJAMIN LEE ERVIN

Entitled:

**MONITORING CORROSION OF REBAR EMBEDDED IN MORTAR
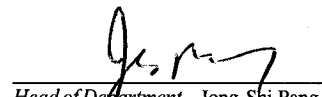USING GUIDED ULTRASONIC WAVES**

Be accepted in partial fulfillment of the requirements for the degree of:
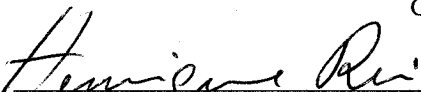
Doctor of Philosophy

Signatures:

_____
Director of Research - Henrique M. Reis
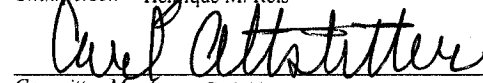
_____
Head of Department - Jong-Shi Pang

Committee on Final Examination*
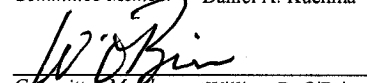
_____
Chairperson - Henrique M. Reis

_____
Committee Member - Daniel A. Kuchma

_____
Committee Member - Carl Altstetter

_____
Committee Member - William D. O'Brien

_____
Committee Member - Jennifer T. Bernhard

_____
Committee Member - John S. Popovics

* Required for doctoral degree but not for master's degree

ABSTRACT

This thesis investigates the use of guided mechanical waves for monitoring uniform and localized corrosion in steel reinforcing bars embedded in concrete. The main forms of structural deterioration from uniform corrosion in reinforced concrete are the destruction of the bond between steel and concrete, the loss of steel cross-sectional area, and the loss of concrete cross-sectional area from cracking and spalling. Localized corrosion, or pitting, leads to severe loss of steel cross-sectional area, creating a high risk of bar tensile failure and unintended transfer of loads to the surrounding concrete.

Reinforcing bars were used to guide the waves, rather than bulk concrete, allowing for longer inspection distances due to lower material absorption, scattering, and divergence. Guided mechanical waves in low frequency ranges (50 - 200 kHz) and higher frequency ranges (2 – 8 MHz) were monitored in reinforced mortar specimens undergoing accelerated uniform corrosion. The frequency ranges chosen contain wave modes with varying amounts of interaction, i.e. displacement profile, at the material interface. Lower frequency modes were shown to be sensitive to the accumulation of corrosion product and the level of bond between the surrounding mortar and rebar. This allows for the onset of corrosion and bond deterioration to be monitored. Higher frequency modes were shown to be sensitive to changes in the bar profile surface, allowing for the loss of cross-sectional area to be monitored. Guided mechanical waves in the higher frequency range were also used to monitor reinforced mortar specimens undergoing accelerated localized corrosion. The high frequency modes were also sensitive to the localized attack. Also promising was the unique frequency spectrum response for both uniform and localized corrosion, allowing the two corrosion types to be differentiated from through-transmission evaluation. The isolated effects of the reinforcing ribs, simulated debonding, simulated pitting, water surrounding, and mortar surrounding were also investigated using guided mechanical waves.

Results are presented and discussed within the framework of a corrosion process degradation model and service life. A thorough review and discussion of the corrosion process, modeling the propagation of corrosion, nondestructive methods for monitoring corrosion in reinforced concrete, and guided mechanical waves have also been presented.

To my wonderful family: Steven, Leslie, Stefanie, Jonathon, and Natallie

ACKNOWLEDGMENTS

TABLE OF CONTENTS

CHAPTER 1:

INTRODUCTION TO CORROSION OF REINFORCED CONCRETE

Reinforced concrete (RC) makes up a large part of the U.S. and international infrastructure. For instance, over half of the bridge inventory in the U.S. is reinforced concrete [1]. From bridges to buildings, the ease of formability, cost, fire resistance, durability, and aesthetics makes concrete a valuable construction material. In many cases, reinforced concrete is designed to withstand harsh environments for well over one hundred years. Normally, concrete reinforced with steel is a rather splendid combination. One can think of the combination as a composite material, where the concrete is the matrix and the steel is the reinforcement. Both materials have similar thermal expansion coefficients allowing for its use in a wide range of temperatures. The high tensile strength of the steel reinforcement makes up for the weak tensile strength of the concrete. Concrete also provides a high alkaline environment for the steel, helping to protect it from corrosion.

However, corrosion does occur and it is currently one of the primary durability concerns for reinforced concrete structures [2]. Corrosion leads to infrastructure problems associated with aesthetics, serviceability, and safety. Infrastructures in almost all geographic locations are considered vulnerable to corrosion. Corrosion of reinforced concrete is complicated, costly, and the frequency of its occurrence has increased with time. One of the major complications in addressing the problem of corrosion is that so many different sciences must be employed to completely define the process such as electrochemistry, chemistry, mechanics, and physics to name a few. It is not always clear what approach is best to address the problem.

To begin discussion on this topic, general descriptions of several aspects of the problem will be given. A description of the service life of an RC structure with respect to corrosion, structural implications, methods to offset the effects, real examples of in service deterioration, and cost estimates will be given. The objective of the current report will be outlined, along with assumptions, description of experiments, and a summary of how the report has been organized.

1.1   CORROSION PROCESS MODEL FOR REINFORCED CONCRETE

To effectively deal with corrosion in RC structures, one must try to understand the entire process. Tuutti [3] set forth a model for the corrosion process in RC structures. Figure 1.1 is a close derivative of the original model [4-6].

1
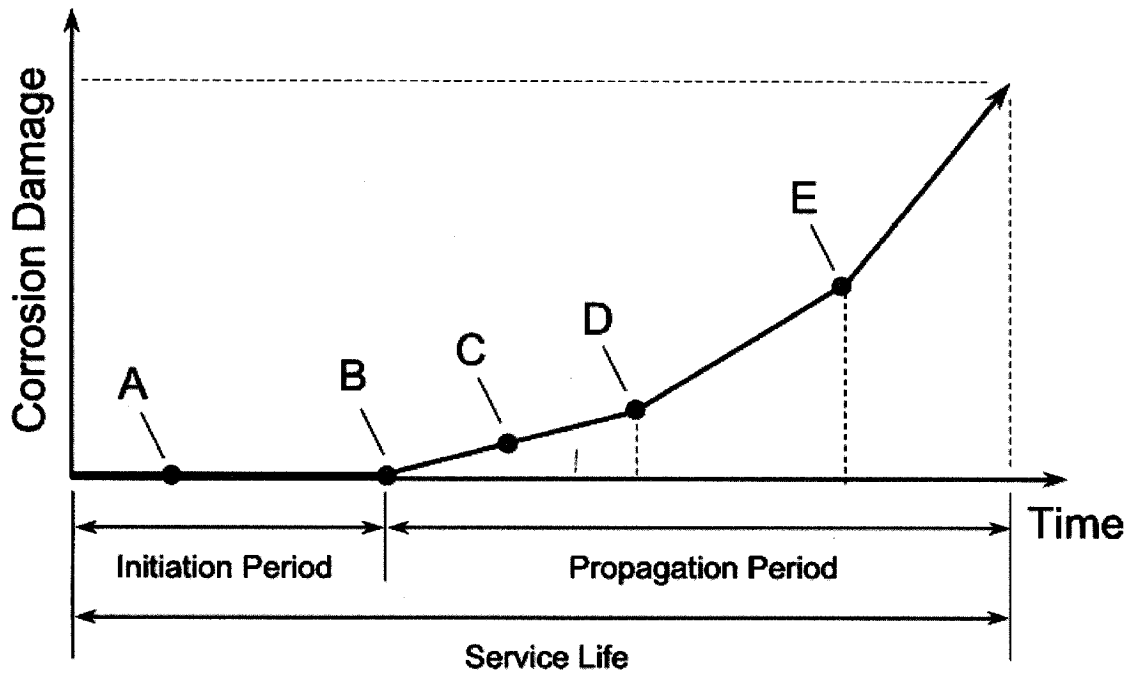
Figure 1.1: Corrosion process model for reinforced concrete. Points A, B, C, D and E are located in different stages of the corrosion process and are illustrated in Figure 1.2. Point A is after deleterious substances have started to ingress but before reaching reinforcement depth. Point B is immediately after corrosion initiation. Point C is after the initial corrosion product accumulation but prior to cracking. Point D indicates that cracking is beginning while point E indicates more substantial cracking and possible spalling.

Corrosion damage in Figure 1.1 can be thought of as the amount of metallic mass loss from the corrosion reaction, but a similar model could be given for many different condition parameters (e.g., aesthetics, cracks, deflection, spalling, flexural capacity, shear capacity, and compressional capacity). The model defines two periods during the corrosion process: initiation and propagation.

When bare steel is initially exposed to oxygen and water, it forms a very thin (1 μm) dense layer of either metal oxide or hydroxide on its surface [7]. This film, referred to as the passive layer, protects the steel while it is contained in the proper environment. The initiation period is the amount of time that the passive layer on the embedded steel is protected by the surrounding concrete. The initiation period begins when the structure is built or rehabilitated and it is assumed that the passive layer has been formed on the surface of the steel. The concrete provides a highly alkaline environment to protect the passive layer. The length of the initiation period is determined by the amount of time that deleterious substances (e.g., chlorides and carbon dioxide) take to ingress through the concrete pore structure and/or cracks and reach a critical threshold at the reinforcement depth. Both chlorides and carbon dioxide can eventually destroy the passive layer and lead to the initiation of corrosion. In Figure 1.1, point A reflects a moment during the ingress of the deleterious substances prior to reaching the reinforcement depth, with an illustration of this process in Figure 1.2.

2
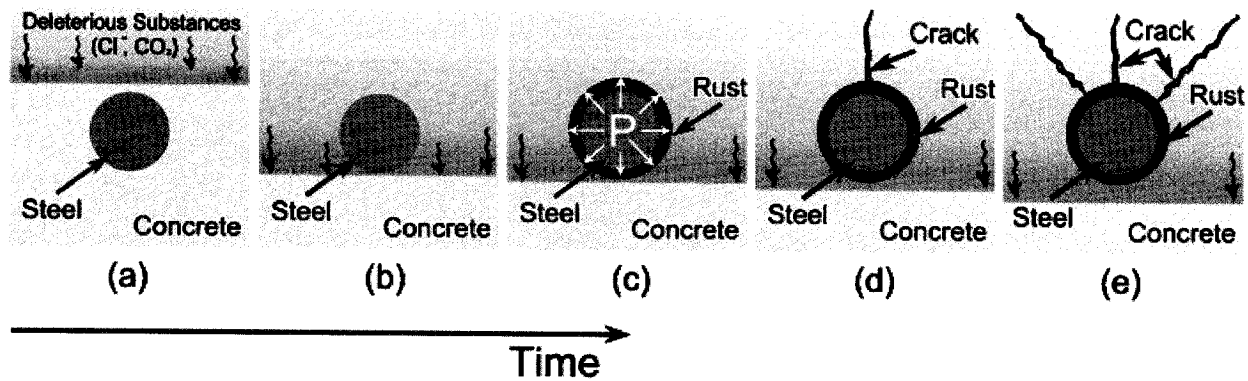
Figure 1.2: Progressive stages of corrosion process in RC structure. Points A, B, C, D and E are located in different stages of the corrosion process model shown in Figure 1.1.

Chlorides are present from deicing salts deposited during the winter months in certain regions, exposure to seawater, and/or admixtures (e.g., set accelerators) present at the time of concrete mixing. In the northern United States, deicing salt usage increased from less than one million tons per year in 1950 to approximately 15 million tons per year forty years later [8]. Carbonation takes place from a reaction between the concrete and carbon dioxide present in the atmosphere. There are four mechanisms allowing for fluids and ions (dissolved in fluid) to move through the concrete: capillary suction, permeation, diffusion, and migration [9]. The ingress of chlorides and carbon dioxide are usually considered to take place by a diffusion process through the pore system of the concrete. If cracks are present, there are direct pathways for chlorides, water, and oxygen to reach the reinforcement. Once the chlorides or carbonation has reached the reinforcement depth and destroyed the passive layer, both oxygen and water must be present in order for the steel to corrode. For instance, reinforced concrete that is in a splash zone of sea water (a few feet above sea level) usually corrodes at a higher rate than a section that is completely submerged in sea water due to the availability of oxygen. Figure 1.3 shows the conditions for corrosion of steel in concrete.
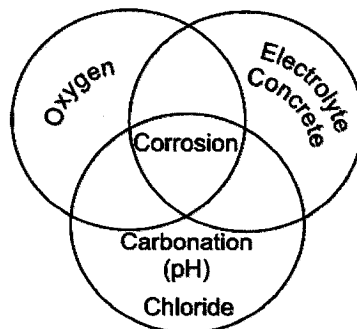
Figure 1.3: Conditions for corrosion of steel in concrete (extracted from [10]).

It should be noted that the type of corrosion depends on whether carbon dioxide or chlorides are present and by the amount that ingresses. Carbon dioxide and a high concentration of chlorides usually remove

3

the passive layer more uniformly which leads to uniform corrosion (i.e. general or homogeneous), while a lower concentration of chlorides remove the passive layer in select locations which leads to localized (i.e. pitting) corrosion. Cracks connecting the concrete cover to the depth of reinforcement, usually caused by other sources of deterioration (e.g., shrinkage, overloading, freezing/thawing, and settling), will lead to more localized corrosion as well. Once the passive layer has been destroyed (point B), the initiation period is over and the propagation period begins.

The propagation period tracks the progression of reinforcement corrosion over its service life. Point C from Figure 1.1 is an example of corrosion product accumulation after the breakdown of the passive layer. It is illustrated in Figure 1.2. Corrosion products are more voluminous than iron, generally two (black rust) to six (red rust) times the volume. The surrounding concrete confines the amount of volume expansion, creating hoop stresses from the pressure. Cracks are created (point D) in the concrete from the hoop stress. The cracks degrade the ability of the surrounding concrete to confine the corrosion product and subsequently reduce the interfacial bond. The crack patterns created are dependent on the reinforcement location, the ratio of the depth of cover to the reinforcement diameter, and the type of corrosion [11]. Multiple cracks (point E) can eventually lead to concrete section loss (spalling). The end of the propagation period is determined by how service life is defined for the particular structure (e.g., crack width limit, deflection limit, and excessive spalling). Notice in Figure 1.1 that the rate of deterioration increases as more pathways are generated from the surface of the concrete to the reinforcement depth.

1.2 STRUCTURAL IMPLICATIONS OF CORROSION IN REINFORCED CONCRETE

Localized corrosion accentuates the loss of bar cross-sectional area in one location, creating high stress concentrations. This results in a loss of ductility and load bearing capacity of the structure. Localized corrosion does not necessarily cause damage to the surrounding concrete, making detection of the damage particularly difficult using traditional nondestructive evaluation methods.

The main contributing factors to structural damage in RC infrastructure from uniform corrosion are:
- Loss of the steel cross-sectional area during the corrosion reaction
- Cracking and spalling of the concrete from corrosion product accumulation
- Destruction of bond between the steel and concrete from corrosion product accumulation

4

Studies have been conducted to assess the depreciation of structural design parameters such as flexural strength, shear strength, yield strength, ultimate strength, bond strength, ductility, and fatigue strength. Those studies will be discussed further in Chapter 2.

1.3 EFFORTS TO COMBAT CORROSION IN REINFORCED CONCRETE

To counteract the destructive corrosion process, standard practices for reinforced concrete design have been improved over the last 25 years. The quality of the concrete cover with respect to mix design, placement, compaction, depth, sealants, and curing practices will tremendously delay the ingress of deleterious substances. Carbon fiber-reinforced polymer wraps [12] and electrochemical chloride removal systems [13] have been used to protect and restore reinforced concrete in corrosive environments. Protection of the reinforcement by polymer/metallic coatings [14] and/or cathodic protection [15] have also been effectively used. Ultimately, however, these practices generally only *delay* the onset of corrosion rather than prevent the process entirely. Monitoring the corrosion process over time is still necessary to ensure serviceability and safety requirements. Furthering the need for monitoring is the industry goal to push service design lives of reinforced concrete structures well over one hundred years.

1.4 EXAMPLES OF CORROSION IN REINFORCED CONCRETE

There are numerous examples of corroding reinforced concrete structures with only a few recent incidents highlighted in this section. One very publicized example was Wrigley Field in Chicago, IL. The baseball park had several large chunks of concrete fall off (spalling) into the seating area in 2004 after being in use for over 90 years. The cause of the falling concrete was most likely from corrosion of the steel reinforcement initiated from chloride ingress and possible carbonation. Figure 1.4 shows the predominant reasons for the spalling of concrete.
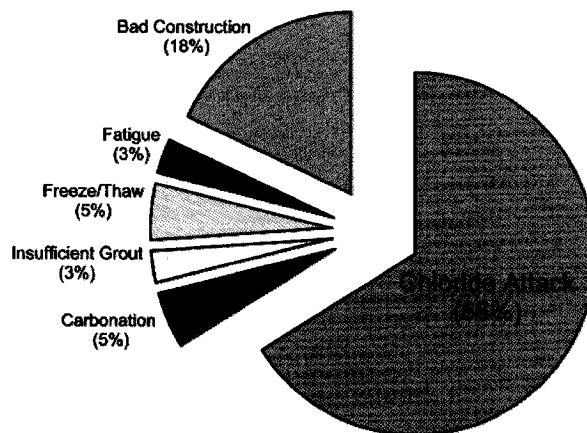
Figure 1.4: Common reasons for spalling in reinforced concrete structures (extracted from [16]).

5

Clearly, corrosion of the reinforcement is the predominate reason for spalling in concrete structures. In 2005, a 60-ton bridge spanning 53 feet in length over Interstate 70 in Pittsburgh, PA. collapsed onto the highway [17]. Figure 1.5(a) is a picture of the collapsed bridge.
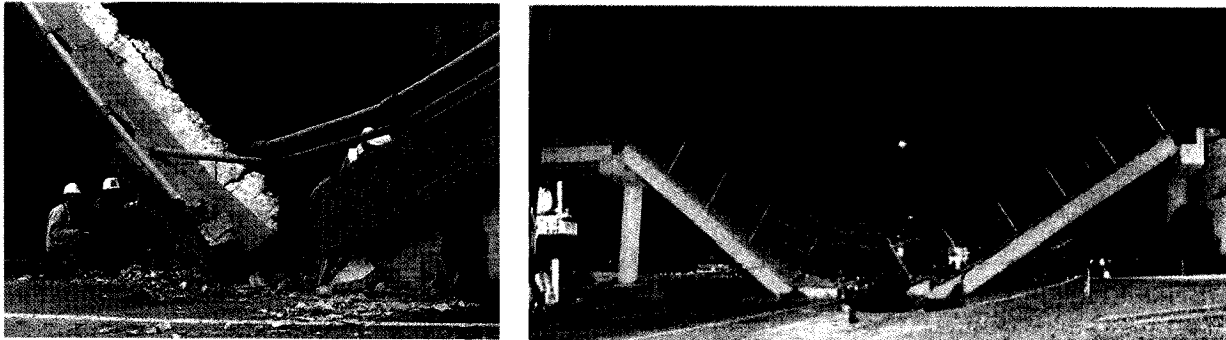
Figure 1.5: Structural collapse of a reinforced concrete **(a)** bridge onto highway I-70 in Pittsburgh, Pa (extracted from [17]) and **(b)** pedestrian walkway onto highway U.S. 29 in Charlotte, N.C. (extracted from [18]).

The collapse was attributed to two factors, corrosion of the bridge and a history of being hit by trucks. The corrosion of the bridge was caused by 45 years of depositing deicing salts on the structure. In 2000, a pedestrian bridge at the Motor Speedway in Charlotte, N.C. collapsed. A picture of the collapsed pedestrian bridge is shown in Figure 1.5(b). The collapse was attributed to high amounts of calcium chloride (used as a set-accelerating admixture) in the grout mix, causing the steel strands to corrode. Over 100 pedestrians were injured in the collapse. There are numerous other examples, such as those shown in Figure 1.6, of aesthetic and serviceability problems in current structures.

Figure 1.6: Rust staining and cracking in RC structures from corrosion (extracted from [19]).

1.5 COST OF CORROSION IN REINFORCED CONCRETE

The annual cost associated with metallic corrosion in the United States alone has been estimated at $276 billion, making up 3% of the GDP (Gross Domestic Product) [20]. Of these costs, 16.4% ($22.6 billion) are estimated for the infrastructure. Highway bridges are considered to make up 37% ($8.33 billion) of the infrastructure, with the majority being reinforced concrete. If indirect costs to users (delays, inconvenience, lost productivity) are taken into account, the cost can be over ten times as much per year.

6

Taking direct and indirect costs into account and assuming that half of the highway bridge inventory is reinforced concrete, the cost of the problem is estimated at nearly $46 billion annually. To make matters worse, the federal government has gradually reduced investment in public works. Due to the large cost associated with the problem and the lack of funding, many have called for innovative testing methods to be developed in order to help alleviate the situation [21].

1.6   OBJECTIVE OF INVESTIGATION

Ultimately, the public demands RC structures that are functional, cost-effective, reliable, and safe. Therefore, regardless of whether better materials, design practices, and corrosion inhibiting systems are being used, inspection of RC structural health must be undertaken. To date, numerous on-site non-destructive and semi-destructive testing methods exist and are discussed further in Appendix A. However, many of the methods are time-consuming procedures that require the structure to be temporarily shut down. The closure will create indirect costs associated with the use of the method. Direct costs associated with the methods use is the human task force sent out to inspect the structure and the equipment involved. Most of the methods rely very heavily on the inspector's expertise to visually assess damage and their knowledge of the equipment (if any) used to inspect the structure. For some structures, the demand of having an inspector on-site poses safety risks (e.g., heavy traffic areas). Other methods that can avoid on-site inspections (e.g., ground penetrating radar from a moving vehicle) are generally structure specific, allowing for inspection of only certain parts of a structure (e.g., bridge deck).

Therefore, a demand exists for smart structural health monitoring systems. The current research is aimed towards the development of an embeddable corrosion monitoring systems for RC structures. Embeddable sensors, in conjunction with artificial intelligence systems (e.g., neural networks, case-based reasoning, and fuzzy logic) for the processing and interpretation of data, would allow for continuous updates of structural health and real-time decision-making capabilities to ensure serviceability and safety requirements. Since the corrosion process occurs in multiple stages (discussed in more detail in Chapters 2 and 3), it is doubtful that one particular method or technique can monitor the entire process. Within recent years, several embeddable sensors for detection and monitoring of corrosion in reinforced concrete have been or are currently being developed. A need still exists for an embeddable sensing method that will allow for a more direct assessment of the condition (e.g., steel cross-sectional loss and bond loss) of the reinforcing steel.

Towards the development of such a methodology, a guided mechanical wave approach has been undertaken. An ultrasonic approach was chosen because of the relative feasibility of using an embedded

7

ultrasonic network for monitoring corrosion in real structures. Guided mechanical waves were chosen because of the cylindrical geometry of the rebar, the lower attenuation of wave propagation in steel compared to concrete, and the possibility of analyzing guided wave behavior in certain frequency ranges to distinguish between the loss of bar cross-sectional area and changes in interface conditions. A system of wireless embedded sensors for ultrasonic wave transmission and reception are envisioned. Figure 1.7 shows a sensor mounted onto the side of a reinforcing bar, within a bridge.
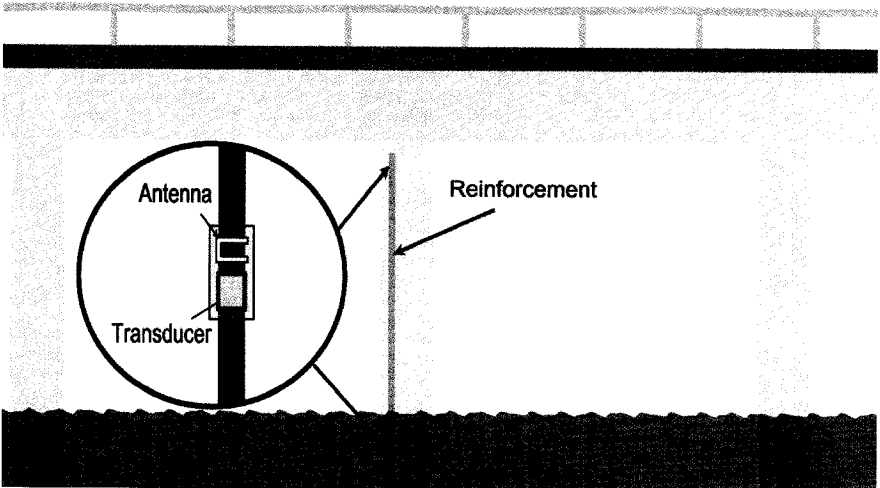
Figure 1.7: Idealized wireless embedded sensor for in-situ ultrasonic corrosion monitoring system.

The possibility exists for utilizing the same ultrasonic network to monitor the time of set [22] and other durability issues besides corrosion such as freeze-thaw attack, overloading, cracking, and earthquake damage. For the testing reported, waves were propagated along exposed rebar ends under different types of environmental and deterioration conditions. Figure 1.8 is an example of how specimens were tested.
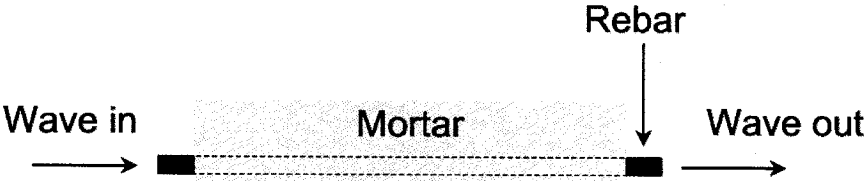
Figure 1.8: Guided mechanical wave propagating along rebar embedded in mortar.

One disadvantage of guided mechanical waves for monitoring corrosion in reinforced concrete is the limitation of inspection range for certain modes and frequencies. Unlike guided wave propagation in metal pipelines in air, wave energy in steel bars embedded in mortar is lost (i.e. attenuated) at high rates due to leakage into the surrounding mortar. Generally, different modes have attenuation minima that have a minimal amount of wave energy lost due to leakage and material absorption. However, once corrosion begins to occur the corrosion product accumulation will actually cause an increase in bond

(discussed in more detail in Chapter 2) and subsequently lead to more energy leaking into the surrounding mortar. Irregularities in the bar profile surface from corrosion can cause more attenuation from reflections, scattering, and mode conversions. Figure 1.9 is an illustration of wave energy leaking out into the surrounding mortar.
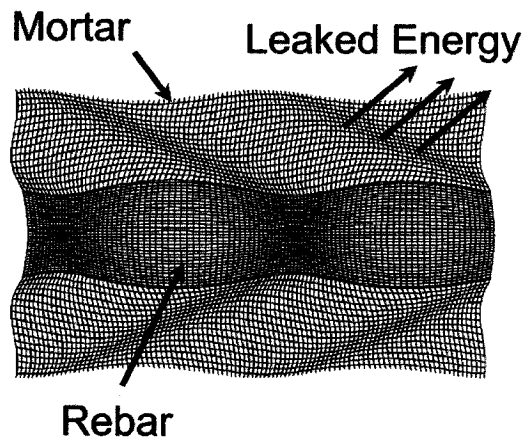
Figure 1.9: Wave energy leaked from rebar into the surrounding mortar. Image was generated with the aid of Disperse software.

Further complicating the analysis of guided wave behavior is the presence of water in the mortar, the unknown angle and depth of bar profile irregularities during testing, the change in pressure at the rebar/mortar interface, and the constantly changing confinement strength provided by the surrounding mortar. For an in-situ monitoring system using guided mechanical waves to be realized, the effects of these factors must be isolated and better understood. This report intends to begin shedding light on many of these issues.

1.7   ASSUMPTIONS FOR THIS INVESTIGATION

To date, the use of guided mechanical waves for continuous monitoring of actual corroding reinforced concrete specimens has not been reported. Since the experimental results detailed in this report are one of many steps towards an actual in-situ monitoring system, a few simplifying assumptions were made.

- Mortar was used for testing rather than concrete. Concrete is the combination of cement, water, small aggregate (e.g., sand), and large aggregate (e.g., rocks). To create mortar, the same combination of materials was used as with concrete but without the large aggregate. The omission was made to reduce variability from large aggregate placement and interaction along the specimen. Mortar was used, as opposed to a cement paste (cement, water), because the mechanical behavior is closer to concrete.

- In this report, reinforcement refers to ribbed cylindrical reinforcing bars (rebar) with solid cross-section. Although reinforcing strands (tendons) are used in industry for prestressed reinforced

9

concrete, they are not explored within this report. In 2003, the FHWA reported that prestressed concrete (i.e. concrete using strands for reinforcement) makes up the majority of all new and replaced bridges in the United States at 38.7%. However, normal concrete is a close second, with 35.7% of the market. Reinforcing strands have typically one center strand with six outer strands wrapped around the center strand. Figure 1.10 is a photograph of both a rebar and a seven-wire strand specimen.

Figure 1.10: Photograph of rebar (left) and seven-wire strand (right). Rebar was monitored in this report.

Small diameter tendons have been investigated in previous work [23] for monitoring wire breaks from corrosion. It was reported that the tendons would have limited inspection potential due to the attenuative effects of curvature and leakage. Opportunity might still exist for embeddable sensors attached to strands to overcome these issues. However, the report noted that there was much more promise with inspecting larger diameter rebar and grouted bolts.

- Corrosion is accelerated using impressed current. The corrosion process can take several years to occur naturally. To allow for several guided wave tests, the corrosion process was substantially accelerated.

- Mortar specimens were tested with no external loading, temperature changes, or wet/dry cycling. The mortar specimens used had a relatively small cross-sectional area to allow for a rapid corrosion reaction. The effects of external loading and other environmental factors are critical to the use of guided mechanical systems for an in-situ monitoring system. However, the effects were not explored within this report.

1.8 DESCRIPTION OF EXPERIMENTAL INVESTIGATION

To explore guided mechanical waves as a viable method for monitoring corrosion of reinforced concrete, several experiments have been designed. Material properties of the mortar were first investigated. Compression tests were conducted on dry and wet mortar cylindrical specimens to ascertain the static modulus of elasticity and Poisson's ratio. The effect of reinforcing ribs on wave propagation was investigated by testing rebar with different rib patterns and comparing the results to those obtained for a

10

solid steel bar. Guided wave experiments with an embedded steel bar in water and mortar were conducted to find the attenuation characteristics for different modes and frequencies. Since water is present in the corrosion process and likely to fill cracks and voids adjacent to rebar, its effect on guided wave characteristics was investigated.

Since the process of corrosion in actual structures is a complicated interaction between several variables, simulated corrosion experiments were then conducted to isolate certain effects. Rebar specimens with corrosion damage along their length were tested in air. Bond was inhibited between the rebar and mortar over specific lengths, with different guided wave modes and frequencies tested for monitoring capabilities. A rebar specimen in air was monitored while being cut in half to determine the effect on the guided waves. A set of reinforced mortar specimens with seeded local defects were used to test the feasibility of monitoring pitting corrosion. The effect of moisture at the rebar level was investigated by wetting dry reinforced mortar specimens while monitoring.

Actual corrosion tests were then conducted on reinforced mortar specimens. Corrosion was accelerated using impressed current. In order to find a relationship between the theoretical amount of mass loss and the actual amount of mass loss from corrosion, several specimens were corroded to various levels and then the bar was extracted and weighed. Once the actual amount of mass loss was known for a certain level of accelerated uniform corrosion, continuous monitoring of reinforced mortar beams was conducted using various modes and frequency sweeps. Continuous monitoring of localized corrosion in reinforced mortar beams was also conducted for higher frequency modes.

1.9 OVERVIEW OF ENTIRE REPORT

Chapter 2 provides a description of concrete and its hydration products, a review of electrochemistry and Pourbaix diagrams, and the chemical and electrochemical reactions that take place during the ingress of deleterious substances and the propagation of the corrosion reaction. Efforts to model the corrosion process, specifically the propagation period, are described in Chapter 3. Details on the modeling of corrosion pressure at the steel/concrete interface are given, with a solution for the geometry of specimens used in this report. The theoretical results from the model of corrosion pressure are used to compare to the experimental results from guided mechanical wave testing. The derivation of guided mechanical wave solutions for the system with mode selection is provided in Chapter 4. Chapter 5 provides a literature review of previous research on monitoring reinforced concrete with guided mechanical waves. Chapter 6 is a full description of the experimental setup and results from guided wave testing. Chapter 7 provides conclusions from the experimental investigation and suggestion for the direction of future work.

11

The Appendices provide a review of nondestructive testing and evaluation (NDT & E) methods for corrosion monitoring, modeling efforts for the initiation period and service life of corroding reinforced concrete structures, and wave propagation in solid bulk materials. Brief descriptions are also provided on Pourbaix diagrams, Fick's 2nd law of diffusion, cylindrical coordinates, vector and tensor notation, and Bessel functions.

CHAPTER 2:

CORROSION PROCESS FOR REINFORCED CONCRETE

The purpose of this chapter is to physically describe the entire corrosion process in reinforced concrete and how it affects the structural performance of RC structures. The discussion will begin with a description of the hydration of concrete and subsequent hydration products. An overview of the electrochemical nature of metals is provided, with specific emphasis on iron. The different mechanisms for the initiation and propagation periods of the corrosion process will then be discussed. The different mechanisms initiating corrosion are discussed first, with the chemical and electrochemical equations for the propagation period given next. Discussion of the different types of metallic corrosion is provided. The structural implications are given at the end.

2.1   DESCRIPTION OF CONCRETE HYDRATION PRODUCTS

Concrete affects the corrosion process by providing a highly alkaline environment for creation of a passive layer on the surface of the steel and acting as a barrier for the ingress of deleterious substances. In order to understand how concrete affects these two aspects of the process, one must understand the chemistry. The chemistry related to concrete hydration is rather involved and complex. Therefore, this section shall only try to briefly summarize the components of the process that will affect corrosion of the reinforcement surrounded by concrete. Concrete is a composite material consisting of cement, water, small aggregate (e.g. sand), and large aggregate (e.g. rocks). The type of cement that is typically used is Portland cement, consisting of the components shown in Table 2.1.

Table 2.1: Main components of Portland cement (extracted from [9] and [24]).

Component	Chemical Formula	Shorthand Notation	Weight Percentage
Tricalcium silicate	$3CaO \cdot SiO_2$	C_3S	$45 - 60\%$
Dicalcium silicate	$2CaO \cdot SiO_2$	C_2S	$5 - 30\%$
Tricalcium aluminate	$3CaO \cdot Al_2O_3$	C_3A	$6 - 15\%$
Tetracalcium ferroaluminate	$4CaO \cdot Al_2O_3 \cdot Fe_2O_3$	C_4AF	$6 - 8\%$
Gypsum	$CaSO_4 \cdot 2H_2O$	$C\bar{S}$	$3 - 5\%$

Reactions with water are referred to as hydration reactions and the products are referred to as hydration products. When only cement and water are mixed to create a paste, the components in Table 2.1 will combine with water to create hydration products. The two calcium silicates (C_3S and C_2S) will produce calcium silicate hydrate and calcium hydroxide:

$$2C_3S + 6H_2O \rightarrow C_3S_2H_3 + 3Ca(OH)_2 \quad\quad\quad (2.1)$$

$$2C_2S + 4H_2O \rightarrow C_3S_2H_3 + Ca(OH)_2 \quad\quad\quad (2.2)$$

13

Calcium hydroxide (also referred to as portlandite), $Ca(OH)_2$, are hexagonal crystals that occupy 20 – 25% of the paste volume [24]. The calcium hydroxide can create a pore liquid with a pH of up to 13.5, helping to protect the steel from corrosion (refer to Section 2.2.1).

After hydration, the cement paste will have interconnected pores varying in sizes throughout its matrix. The three types of pores are macropores, capillary pores, and gel pores. Gel pores are the result of interlayer spacing with the calcium silicate hydrate $(C_3S_2H_3)$ [9]. The gel pores are roughly 28% of the gel volume and are in the size range of nanometers. Capillary pores are the result of areas not filled with hydration products. They are much larger than gel pores, generally ranging in size from 10 to 50 nm, and in some cases reaching as high as a few micrometers. Powers [25] proposed an equation to solve for the volume of capillary pores in a cement paste:

$$V_{cp} = (w/c - 0.36h) \dotfill (2.3)$$

where w/c is the water-to-cement ratio and h is the degree of hydration. The macropores are the result of trapped (or entrained) air bubbles and are on the size of a few millimeters. The macropores and capillary pores play a critical role with respect to the ingress of deleterious substances discussed later. Figure 2.1 is a sketch of the microstructure of concrete.
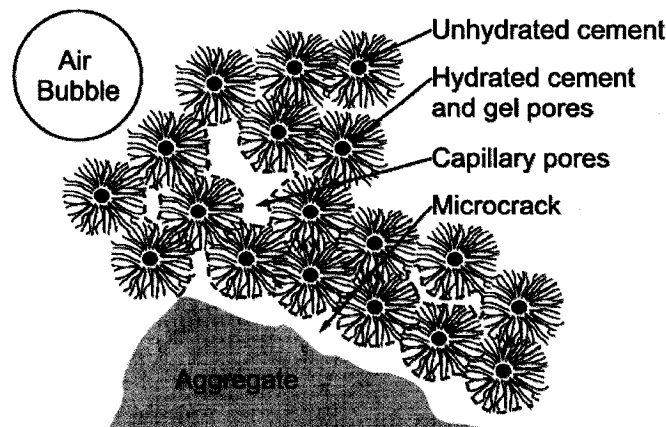
Figure 2.1: Microstructure of concrete (extracted from [26]).

When rebar is embedded in fresh concrete, an interfacial transition zone (ITZ) develops between the two materials. It is comprised mainly of portlandite and is approximately 50 μm thick [27,28]. The ITZ is less stiff, more porous, and more heterogeneous than the bulk concrete. The ITZ stiffness has even been reported as larger on the top of a bar compared to below the bar due to internal bleeding and settlement of particles during the placement of the concrete [28]. The difference in stiffness and higher porosity may explain some of the discrepancies in predictions from modeling and experimental results discussed later.

14

The ITZ will also act as a porous zone for the deposit of corrosion products, allowing for some accumulation before a dramatic increase occurs in the concrete hoop stresses.

2.2 DESCRIPTION OF ELECTROCHEMICAL NATURE OF METALS

Corrosion typically occurs between two dissimilar conducting metals where electrons are transferred from the metal with a lower electrode potential (anode) to the metal with a higher electrode potential (cathode). This type of corrosion reaction is termed galvanic corrosion. A classic example of galvanic corrosion is illustrated in a galvanic cell, or a voltaic cell. Below in Figure 2.2, a galvanic cell setup is illustrated.
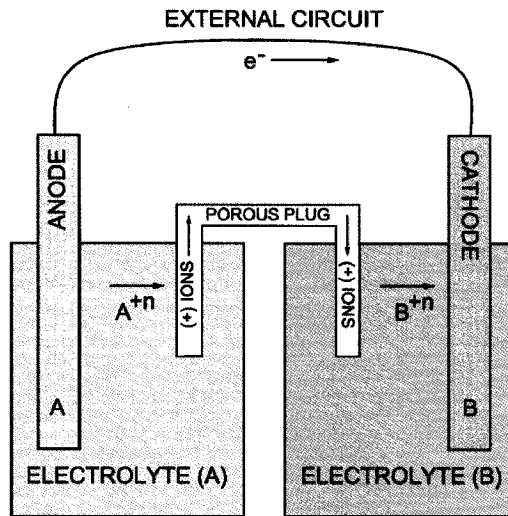
Figure 2.2: Galvanic cell.

The anode, material A, is connected to the cathode, material B, via an external circuit. The anode and cathode has been placed in electrolytes containing positive ions of the respective material. A porous plug connects both solutions to allow transfer of positive ions, maintaining electrical neutrality. If electrical neutrality is not maintained, the reaction would stop due to the buildup of such a large charge. The following reaction occurs at the anode (oxidation reaction) and cathode (reduction reaction):

$$A \rightarrow A^{+n} + ne^- \text{ (anodic reaction)} \dotfill (2.4)$$

$$B^{+n} + ne^- \rightarrow B \text{ (cathodic reaction)} \dotfill (2.5)$$
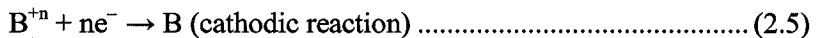
where n represents the number of ions and electrons involved. The electrons given off by the anode, travel through the external circuit to the cathode. The anode is considered corroding due to the release of electrons. This process is termed an oxidation reaction. The cathode has a collection of reaction products forming at its surface. This process is termed a reduction reaction. The formation of products on the cathode protects the material from corrosion.

15

Assuming a constant temperature and pressure, there must be a decrease in free energy for the chemical reaction to take place from left to right [29]. This change in energy is related to the conversion of the reactants to the products. It is typically measured from the heat given off (exothermic) or the heat taken away (endothermic) from the environment. Take for instance a typical generic chemical reaction:

$$n_a A + n_b B = n_c C + n_d D \dotfill (2.6)$$
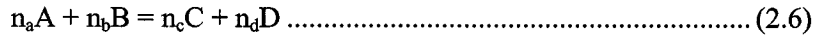
where A and B are the reactants, C and D are the products, and each n represents the number of moles involved for each respective material. For this reaction to occur (reactants to products) the associated change in free energy (ΔG) must be less than zero. The change in free energy is found by using the following equation:

$$\Delta G = \Delta G^\circ + RT \cdot \ln \frac{[C]^{n_c}[D]^{n_d}}{[A]^{n_a}[B]^{n_b}} \dotfill (2.7)$$

where ΔG° is a thermodynamic constant experimentally found for each respective reaction, R is a gas constant, T is the temperature at which the reaction occurs (in Kelvins), and the brackets circumscribing the reactants and products refer to the concentration of each material. The concentration of the material is in molarity, which is the amount of moles of species per liter of solution. A mole represents 6.023×10^{23} atoms. A state of equilibrium exists if the change in free energy is zero. The possible occurrence of this chemical reaction can be estimated if the thermodynamic constant, respective reactant concentrations, and the environment can be relatively well estimated. For the particular case of corrosion, one is dealing with an electrochemical reaction. The generic electrochemical reaction shown below will be used for this discussion:

$$n_a A + n_b B + ze^- = n_c C + n_d D \dotfill (2.8)$$
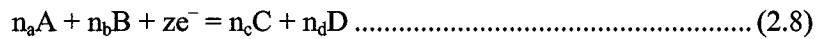
where the same idea applies from the chemical reaction, except that free electrons are involved and the number of which is designated by 'z'. In order for this reaction to occur from left to right (reactants to products) the electrode potential must be less than the value of electrode potential at equilibrium. The following equation, called the Nernst equation, now describes the electrode potential at equilibrium for the case of the generic electrochemical reaction:

$$E_{eq} = E^\circ + \frac{RT}{zF} \cdot \ln \frac{[A]^{n_a}[B]^{n_b}}{[C]^{n_c}[D]^{n_d}} = E^\circ + \frac{RT}{zF} \cdot 2.303 \cdot \log \frac{[A]^{n_a}[B]^{n_b}}{[C]^{n_c}[D]^{n_d}} \dotfill (2.9)$$

16

where F is Faraday's constant and E° refers to the standard electrode potential for the reaction (relative to the thermodynamic constant for the chemical reaction). Faraday's constant is equal to 96,500 Coulomb/mole. This represents the amount of charge contained in 1 mole of electrons. An estimate can be made as to whether this electrochemical reaction will occur if the standard electrode potential, reactant concentrations, and the environment can be reasonably estimated. The Nernst equation determines if the corrosion reaction is thermodynamically possible. However, it does not determine the rate of the reaction. When a potential is applied to the cell and E deviates from E_{eq}, the concentrations of ions will change to regain equilibrium [30]. During the time it takes to regain equilibrium, electrons flow in the external circuit shown in Figure 2.2. At equilibrium the rate of transfer is equal in both directions and is termed the exchange current density, i_o. Each material has an i_o value, which is dependent on how catalytic the material is and the surface characteristics. Faraday's law provides a relationship between the current and the amount of mass (grams) reacted:

$$m = \frac{Ita}{zF} \quad\dotfill\quad (2.10)$$

where I is the current (amps), t is time (in seconds), and a is the atomic weight of the reactant (grams). One could rewrite this as a rate for the electrochemical reaction:

$$\dot{j}_r = \frac{ia}{zF} \quad\dotfill\quad (2.11)$$

where i is the current density (amps/area). Current density, rather than current, indicates the rate of the corrosion reaction and is proportional to the rate of loss of anode material per unit area of anode [31].

The difference between the cell potential, V, and the equilibrium potential, E_{eq}, is defined as the overvoltage, η. When $\eta \neq 0$, the cell is considered polarized. An overvoltage can control the direction and rate of the reaction. Two different types of polarization exist: activation and concentration [32]. Activation polarization arises from a free energy barrier (i.e. electrical double layer or Helmholtz layer) at the electrode/electrolyte interface. Essentially water molecules at the interface interact more strongly with the electrode than the metal ions in solution [30]. In order for the reaction to occur, the free energy barrier must be surmounted. Ultimately, the anodic and cathodic overpotentials from activation polarization can be written as a function of the anodic and cathodic current densities [31]:

$$\eta_a = \beta_a \cdot \log\left(\frac{i_a}{i_o}\right) \quad\dotfill\quad (2.12)$$

17

$$\eta_c = \beta_c \cdot \log\left(\frac{i_c}{i_o}\right) \quad\dotfill (2.13)$$

where $\beta_a = 2.3RT/\alpha_t zF$, $\beta_c = 2.3RT/(1-\alpha_t)zF$, and α_t is a transfer coefficient (i.e. fitting parameter) with idealized behavior equal to ½. The relationship between η and i is of the form $\eta \propto \log i$ and is referred to as Tafel behavior [30]. Concentration polarization is the result of high currents either depleting the adjacent solution at the cathode of the dissolved species or not allowing the transport of soluble oxidation products away from the anodic surface [31]. The overvoltage can be written as a function of the current density:

$$\eta = \frac{2.3RT}{zF} \cdot \log\left(1 - \frac{i_o}{i_L}\right) \quad\dotfill (2.14)$$

where i_L is the limiting current density. The limiting corrosion density can be calculated based on an expression for the rate of ion diffusion through an idealized diffusion layer near the electrode [7]. The overvoltage from activation and concentration polarization can be added together to give the total overvoltage.

2.2.1   POURBAIX DIAGRAMS

Pourbaix diagrams are electrochemical phase diagrams for metals, originally proposed by Pourbaix and associates for use with iron in water. However, Pourbaix diagrams have been constructed for most other metals. They aid in understanding what type of environmental conditions allow corrosion to occur. Depending on the particular electrode potential and pH, various electrochemical reactions are thermodynamically possible. The diagram indicates which type of ion or solid is present at equilibrium. The diagram does not shed light into the kinetics of the reaction. In other words, the diagram will allow for a determination of whether corrosion is possible but not a determination of the rate of the reaction. The diagram is much more sensitive to increased temperature than pressure [33]. The Pourbaix diagram does not convey the effect of strong reducing environments (e.g. chlorides and sulfides), the effects of which will be discussed later. Pourbaix diagrams for iron have been provided (Figures 2.3 and 2.4) with more information on how they were constructed provided in Appendix B.
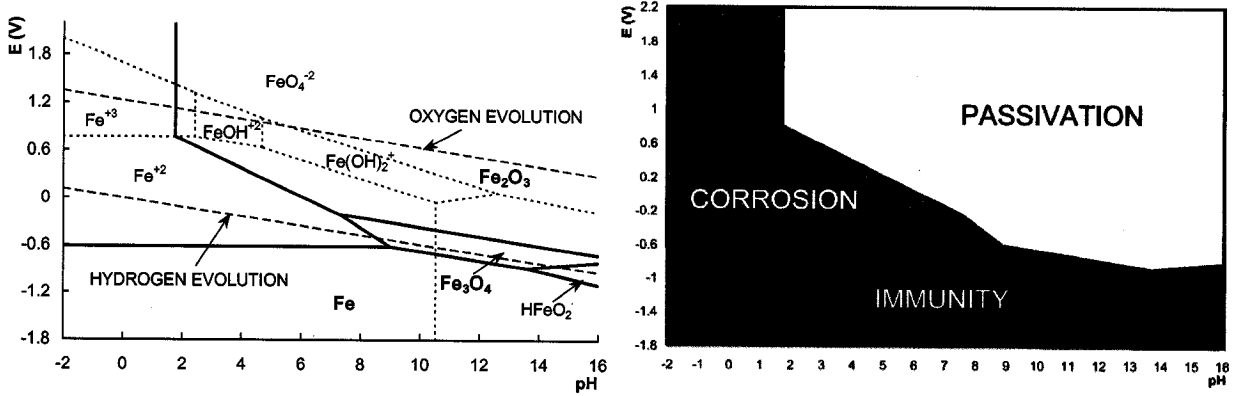
Figure 2.3: Pourbaix diagram for iron in water (T = 25°C, p = 1 atm, solids considered: Fe, Fe_3O_4 and Fe_2O_3).
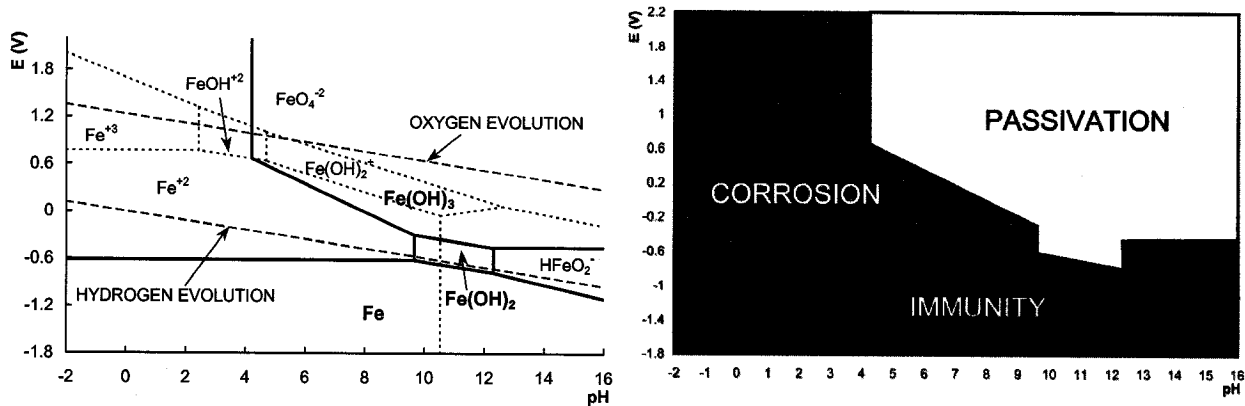
Figure 2.4: Pourbaix diagram for iron in water (T = 25°C, p = 1 atm, solids considered: Fe, $Fe(OH)_2$ and $Fe(OH)_3$).

One notices in Figures 2.3 and 2.4 there are solid, dashed, and dotted lines on the diagram. The solid lines represent areas of solid substances (solid names bolded). The dashed lines pertain to the stability of water. Water is unstable above and below the dashed lines marked "oxygen evolution" and "hydrogen evolution", respectively. In between the two dashed lines, water is thermodynamically stable for 25°C and 1 atm of pressure. The dotted lines represent areas where ions are present. One can assume that the solids are more stable than the ions. The ions in areas of solids are shown to give the reader an idea of how many types of reactions can occur. Two different Pourbaix diagrams are provided for iron based on assumptions of what type of solid substances will form. Table 2.2 lists some of the different solid corrosion products that can form from corroding iron. The mass (α) and volume (α_1) ratios for the corrosion products with respect to iron are also listed.

19

Table 2.2: Various corrosion products resulting from corrosion of iron (extracted from [34]).

	FeO	Fe$_3$O$_4$	Fe$_2$O$_3$	Fe(OH)$_2$	Fe(OH)$_3$	Fe(OH)$_3\cdot$3H$_2$O
Name	Ferrous Oxide	Magnetite	Haematite	Ferrous Hydroxide	Ferric Hydroxide	Hydrated Ferric Hydroxide
Color	Black	Black	Red-Brown	White	Red-Brown	Red-Brown
α	0.777	0.724	0.699	0.622	0.523	0.347
α_1	1.80	2.00	2.20	3.75	4.20	6.40

The region labeled immunity is the best protection against corrosion. In this region, corrosion is thermodynamically impossible. The next best region is passivity. In the region marked passivity, a passive layer forms on the steel surface composed of the solid substance indicated in the diagram. The third region is corrosion, meaning that the steel is in an active state. In this region, the iron has a strong tendency to break down into ions. For iron in water, corrosion refers to uniform (i.e. general) corrosion.

2.3 DESCRIPTION OF CORROSION PROCESS IN REINFORCED CONCRETE

A description of the corrosion process stages is now outlined. Even though models of the corrosion process are covered in more depth in Chapter 3, the classical representation (described by [3]) of the process is used in this chapter for illustrative purposes (Figure 2.5).
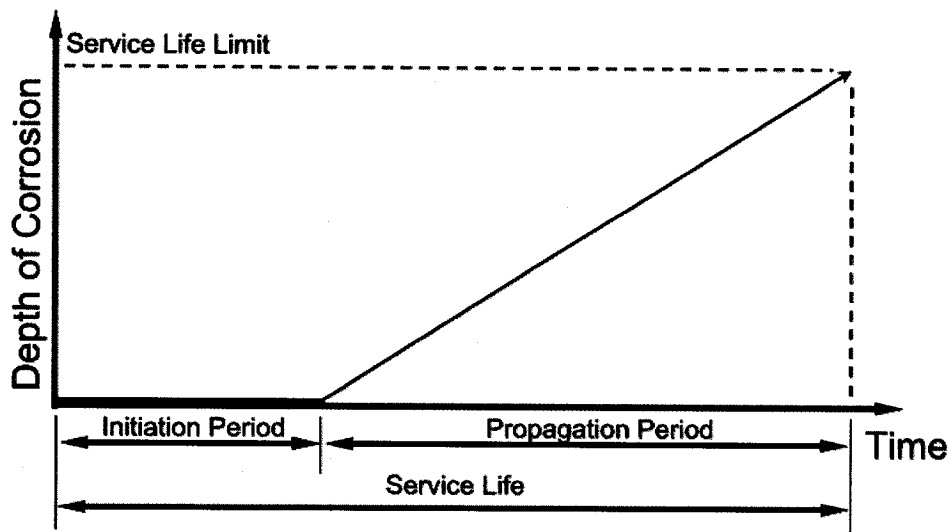
Figure 2.5: Classical corrosion process model (extracted from [3]).

There are two distinct periods described for the corrosion process in reinforced concrete, the initiation period and the propagation period. The initiation period begins with the initial construction, repair, and/or rehabilitation of the structure. It is assumed that a protective passive layer is uniformly created along the length of reinforcement. The end of the initiation period is marked by the destruction of this passive layer (depassivation) with the subsequent initiation of corrosion. How permeable or damaged (i.e. cracked and spalled) the concrete is determines the ability of fluids to penetrate the concrete and initiate corrosion.

20

Assuming the passive film is destroyed and that oxygen and water are available, reinforcement corrosion begins. This marks the end of the initiation period and the beginning of the propagation period. The propagation period starts with the initiation of corrosion and ends with whatever definition of service life is in place for the structure (e.g., aesthetics or flexural failure). The primary substances responsible for the destruction of the passive layer are the ingress of carbon dioxide (CO_2) and/or chlorides. The interaction of these two substances will be discussed later since both could be present at the same time. The initiation period is the time that these deleterious substances take to ingress (shown in Figure 2.6) to the reinforcement depth.
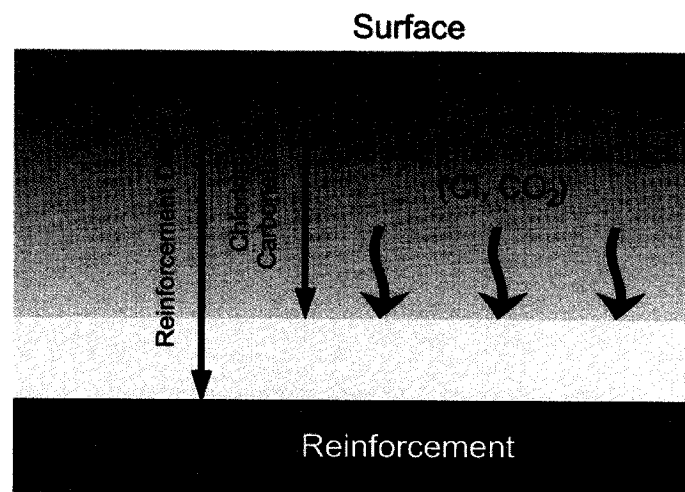
Figure 2.6: Ingress of deleterious substances in concrete.

The passive layer can also be destroyed by a lack of oxygen (fully submerged and/or buried RC structures), resulting from the limiting cathodic current density becoming insufficient [29]. To model the length of time for the initiation period of the structure, one must model the ingress of CO_2 and chlorides in concrete.

2.3.1 INITIATION PERIOD IN CONCRETE

There are four mechanisms allowing for fluids and ions (dissolved in fluid) to move through the concrete: capillary suction, permeation, diffusion, and migration [9]. Each will be briefly described with special emphasis on diffusion since this is usually assumed as the main mechanism of ingress for real structures.

Capillary suction is from the capillary action from long slender (small diameter) spaces called capillary pores in the cement paste (see Figure 2.1). Capillary action describes the physical effect of a fluids interaction with the walls of a narrow tube or passageway (water "climbs" up the walls). Water behaves as bulk water and menisci are created as the pores are filled and emptied [24]. How much capillary

21

suction takes place in concrete is dependent on the surface tension, viscosity, and density of the liquid as well as the size of the pores [9].

Permeability is a quantitative measure of the ability of a porous media to conduct fluid flow. Permeation is the physical act of fluids flowing through the porous media, resulting from a pressure gradient in the concrete. The rate (dq/dt, units of kg/m^3) at which the fluid will penetrate is calculated using Darcy's Law:

$$\frac{dq}{dt} = \frac{K \cdot \Delta P \cdot A}{L \cdot \mu} \quad\text{.. (2.15)}$$

where K is the intrinsic permeability of concrete (m^2), ΔP is the difference in pressure (Pa), A is the transverse area (m^2), L is the thickness of the concrete specimen (m), and μ is the viscosity of the fluid (N·s/m^2). This not only describes the ingress of chlorides and carbonation, it can also take into account the amount of corrosion product that permeates away from the reaction site from pressure buildup at the material interface.

Diffusion is the process by which matter is transported from one part of a system to another as a result of random molecular motions [35]. A relevant example of diffusion is helium trapped within a balloon. Over time the balloon will get smaller due to helium atoms diffusing through the balloon membrane. Differences in the concentration of the diffusing matter will drive the transport. For the diffusion of chlorides and carbon dioxide through concrete, the process is more complicated due to the porous nature of the concrete. Fick's 1st law characterizes diffusion in a steady state condition:

$$F = -D \cdot \nabla C \text{ (three-dimensional)} \quad\text{... (2.16)}$$

$$F = -D\frac{\partial C}{\partial x} \text{ (one-dimensional)} \quad\text{... (2.17)}$$

The variable F represents the diffusion flux, D is the coefficient of diffusivity, C is the concentration, and ∇ represents the gradient (refer to Appendix H). Flux is the amount of diffusing matter that flows through a unit area per unit time. Fick's 1st law defines how fast particles pass through a given area, assuming steady state diffusion (concentration within the diffusion volume does not change with respect to time). Non-steady state diffusion occurs when the concentration changes within the diffusion volume with respect to time. Fick's 2nd law (refer to Appendix D) can be used to define the chloride level when non-steady state diffusion occurs:

22

$$C(x,t) = C_o \left[1 - erf \left(\frac{x}{2\sqrt{tD}} \right) \right] \quad \text{...(2.18)}$$

where C_o is the surface chloride ion concentration, x is the depth, t is the time, D is assumed a constant coefficient of diffusivity, and:

$$erf(z) = \frac{2}{\sqrt{\pi}} \int_0^z e^{-t^2} dt \quad \text{..(2.19)}$$

Tables of calculated erf values exist to allow for quick calculation using this closed form solution.

Migration is the transport of ions in a solution from an electric field [9]. In order to accelerate corrosion in laboratory studies, impressed current has been used to transport the chloride ions to the reinforcement. During corrosion initiated from the ingress of chlorides, an electric field can be created from the accumulation of chloride ions.

2.3.1.1 INGRESS OF CARBON DIOXIDE IN CONCRETE

Carbonation of concrete is the result of a chemical reaction involving carbon dioxide (CO_2) from the atmosphere and calcium hydroxide ($Ca(OH)_2$) from the concrete (refer to Section 2.1). The reaction is a multiple step process starting with calcium hydroxide dissolving [36]:

$$Ca(OH)_2 \rightarrow Ca^{+2} + 2OH^- \quad \text{..(2.20)}$$

and the carbon dioxide dissolving in the concrete pore water:

$$H_2O + CO_2 \rightarrow HCO_3^- + H^+ \quad \text{...(2.21)}$$

$$HCO_3^- \rightarrow CO_3^{-2} + H^+ \quad \text{..(2.22)}$$
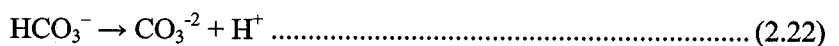
Calcium carbonate (carbonation product) is finally produced from the combination of the products of the previous equations:

$$Ca^{+2} + 2OH^- + 2H^+ + CO_3^{-2} \rightarrow CaCO_3 + 2H_2O \quad \text{.......................(2.23)}$$

The total reaction is more generally written in the literature:

$$CO_2 + Ca(OH)_2 \xrightarrow{H_2O} CaCO_3 + H_2O \quad \text{...(2.24)}$$

23
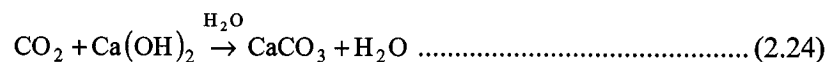
As carbon dioxide reacts with the calcium hydroxide, the pH of the concrete decreases from around 13 to below 9. The carbon dioxide proceeds in steps, eventually penetrating to the depth of reinforcement. Referring to the Pourbaix diagrams in Figures 2.3 and 2.4, pH levels below 9 indicate that corrosion is thermodynamically possible. The environment, the pore structure of the concrete, and the presence of water in the pores will determine the rate at which carbon dioxide will react and further ingress. Diffusion of carbon dioxide in air is much faster than in water (10^4 time faster in air) [29]. However, the carbonation reaction will not occur if water is not present. Therefore, partially water filled pores in concrete is the quickest route for the carbonation reaction to proceed.

2.3.1.2 INGRESS OF CHLORIDES IN CONCRETE

As mentioned previously, chlorides are present from deicing salts, exposure to seawater, admixtures, and ground salinity. The sum of the chlorides that enter the concrete are referred to as the total chlorides. A portion of the total chlorides will react chemically with components of the cement paste and become chemically bound or will become physically adsorbed to the cement gel or physically trapped in gel or capillary pores [37]. These chlorides are referred to as bound chlorides. The portion of the total chlorides not bound are referred to as free chlorides. Free chlorides are responsible for acting as a reaction catalyst [38]. Corrosion is typically thought to occur once a critical free chloride threshold has been breached. Figure 2.7 illustrates the electrochemical behavior of steel immersed in a chloride free solution and a solution containing chloride.
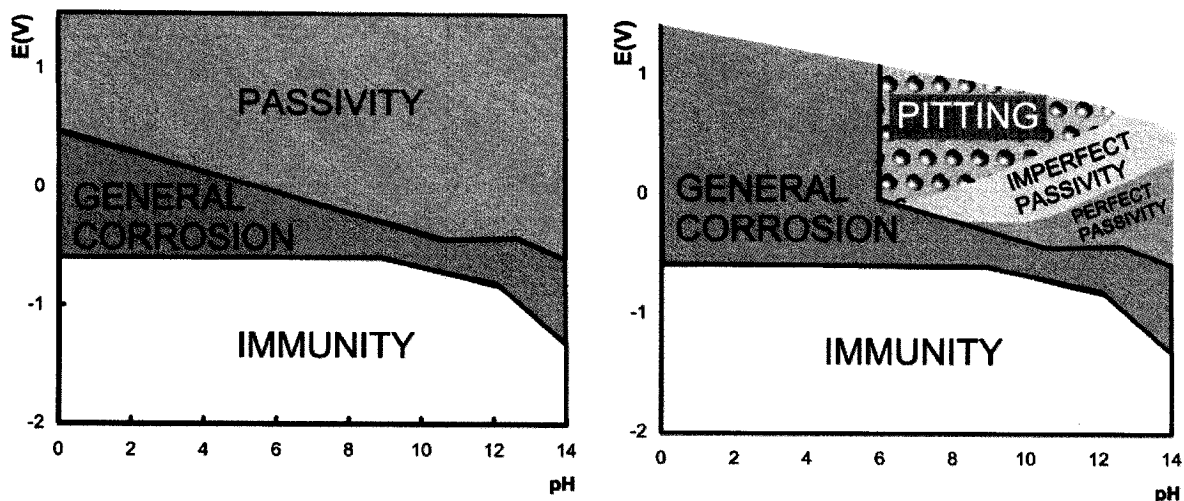
Figure 2.7: Behavior of iron in solutions containing (a) no chloride (left) and (b) containing chloride (355 ppm). Experimental conditions for immunity, general corrosion, perfect and imperfect passivity, and pitting are shown (extracted from [39]).

Protection that is considered perfect or imperfect depends on whether or not the passive film perfectly shields the metal from contact with the solution [39]. Imperfect passivity allows corrosion to affect weak

points in the passive film and therefore is localized in nature. The effect of chloride is pronounced from the diagrams. The region of passivity is significantly decreased in the presence of chloride, with the appearance of a pitting region for a pH range of 6 to 10. For even lower pH values, the region of general corrosion has been further increased. Free chlorides have the unique ability to be reused over and over as a reaction catalyst. The ferrous ions react with chloride to create ferrous chloride [38]:

$$Fe^{2+} + 2Cl^- \rightarrow FeCl_2 \quad \text{..} (2.25)$$
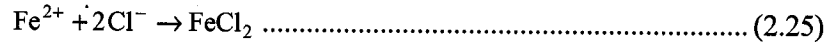
The ferrous chloride can react with water to create ferrous hydroxide and free chlorides:

$$FeCl_2 + 2H_2O \rightarrow Fe(OH)_2 + 2Cl^- \quad \text{..} (2.26)$$

or react with oxygen and water to create magnetite, hydrogen ions, and free chlorides:

$$6FeCl_2 + O_2 + 6H_2O \rightarrow 2Fe_3O_4 + 12H^+ + 12Cl^- \quad \text{......................} (2.27)$$
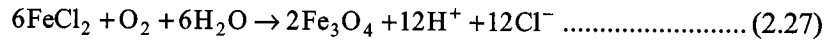
Figure 2.8 shows how both the chloride concentration and pH play a critical role in determining the likelihood of corrosion initiation.
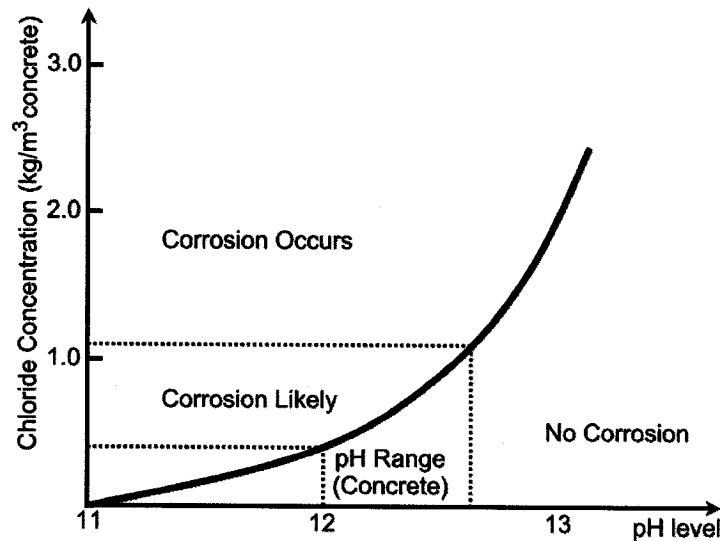
Figure 2.8: Critical chloride concentration threshold as a function of pH level (extracted from [24]).

2.3.1.3 INTERACTION OF CARBON DIOXIDE AND CHLORIDES IN CONCRETE

When the carbonation reaction lowers the pH, some hydration products with bound chlorides (e.g. Friedel's salt) will breakdown. This chemical effect raises the chloride concentration in the concrete. However, the carbonation reaction will also reduce the total porosity of the concrete [40]. This physical effect will slow down the diffusion of the chlorides in the concrete. The physical effect has been shown

to be the dominant effect [41]. The mix design will play a critical role in determining the overall interaction effects between carbon dioxide and chloride ingress.

2.3.2 PROPAGATION PERIOD FOR CORROSION OF REINFORCEMENT IN CONCRETE

Unlike galvanic corrosion, corrosion in reinforced concrete does not usually have two dissimilar metals fueling the corrosion process. The corrosion in reinforced concrete usually takes place within the same bar of steel, however there must still be an anode and a cathode in order for corrosion to occur. The anode and cathode are created due to heterogeneities in the steel such as grain structure, composition, impurity levels, and different amounts of residual strain [24,42]. These are typically a reflection of how the reinforcement was created during the casting process, loading scenario, and age of the material. The concrete also creates heterogeneities due to its inherent nature. Different concentrations of oxygen and water will exist along the bar. The pH level, compaction, cracks, w/c ratio, and void size will vary along the steel and concrete interface. Other causes are air bubbles trapped in the mix, bleeding, and mechanical degradation of the interface between the steel and concrete [27]. Three conditions typically exist to allow corrosion in reinforced concrete [43]:

1. A difference in voltage potential between points on the steel surface or surrounding material
2. The concrete must be conductive to form the electrolyte (i.e. close the circuit)
3. The concrete must have electrical contact with the steel

A sketch of the process is shown in Figure 2.9.

Figure 2.9: Corrosion reactions in reinforced concrete.

It should be noted that the entire electrochemical process at the interface is very complicated. The explanation given here is a simplified view including the critical components. To start, it is assumed that the pH has been sufficiently lowered and/or a critical chloride concentration at bar level has been reached
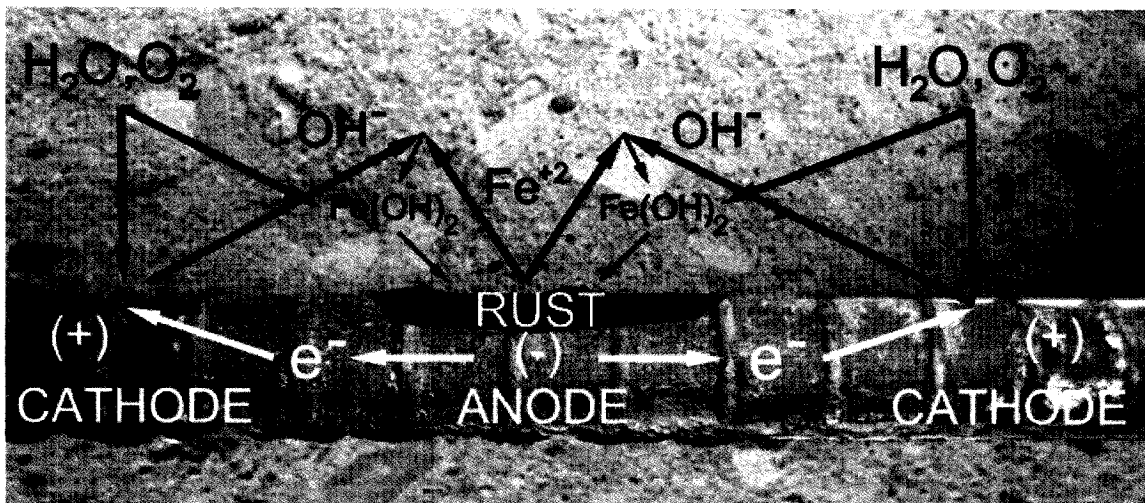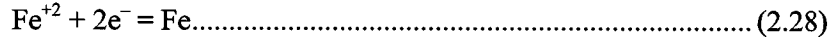
to initiate corrosion. The Nernst equation will be used with the electrochemical equations involved to derive the potential. The corrosion process begins with the dissolution of iron in the pore water:

$$Fe^{+2} + 2e^- = Fe \dotfill (2.28)$$

The ferrous ion Fe^{+2} is a green color. The standard half-cell potential for this oxidation reaction (E° = 0.440 v) is measured versus the standard hydrogen electrode (SHE) and was found from reference [31]. The electrons freed from the electrochemical reaction travel through the steel to the site of the cathode. At the cathodic site, the electrons transferred from the anode combine with water and oxygen to form hydroxyl ions:

$$2H_2O + O_2 + 4e^- \rightarrow 4OH^- \dotfill (2.29)$$
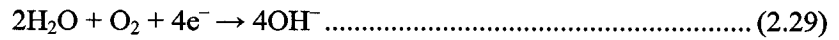
The standard half-cell potential for this reduction reaction (E° = 0.401 v) is measured versus the standard hydrogen electrode (SHE) and was found from reference [31]. The entire cell reaction can be written:

$$2Fe + 2H_2O + O_2 \rightarrow 4OH^- + 2Fe^{+2} \dotfill (2.30)$$
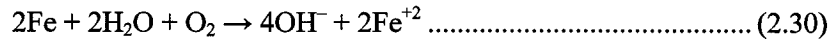
The standard potential for this reaction is calculated by adding the anodic and cathodic standard half-cell potentials together (E° = 0.841 v). Using the Nernst equation the electrode potential can be found for the cell reaction (assuming a temperature of 25° C):

$$E_{eq} = E^{\circ} - \frac{RT}{ZF} \cdot \ln\frac{[C]^{n_c}[D]^{n_d}}{[A]^{n_a}[B]^{n_b}} = 0.841 - \frac{\left(8.314 \, \text{J/}_{\circ K}\right)\left(298°\,K\right)}{(4)\left(96{,}500 \, \text{Coulomb/}_{mole}\right)}(2.303)\log\left(\frac{[OH^-]^4[Fe^{+2}]^2}{[Fe]^2[H_2O]^2[O_2]}\right) \dotfill (2.31)$$

$$= 0.841 - (0.01478)\log\left(\frac{[OH^-]^4[Fe^{+2}]^2}{[Fe]^2[H_2O]^2[O_2]}\right)$$

The molarity of the water is equal to one because it is the solvent in the cathodic reaction (O_2 dissolved in water). The molarity of the iron is equal to one because it is a pure metal. Also, a substitution can be made for the hydroxide concentration in the form $\log[OH^-]$ = pH − 14. One can now rewrite the equation:

$$E_{eq} = 1.669 - (0.0591)pH - (0.0296)\log[Fe^{+2}] + (0.0148)\log[O_2] \dotfill (2.32)$$

After the creation of the hydroxyl ions, they travel towards the anodic site in the pore solution in the concrete. The ferrous ions then combine with the hydroxyl ions at a location between the anodic and cathodic sites to create ferrous hydroxide:

$$Fe^{+2} + 2OH^- \rightarrow Fe(OH)_2 \dotfill (2.33)$$

27

The ferrous hydroxide combines with oxygen and water to create ferric hydroxide:

$$4Fe(OH)_2 + O_2 + 2H_2O \rightarrow 4Fe(OH)_3 \dots\dots\dots\dots (2.34)$$
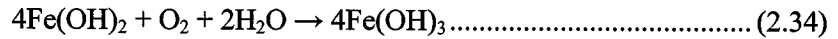
The ferric hydroxide can be further converted to hydrated haematite:

$$4Fe(OH)_3 \rightarrow 2Fe_2O_3 \cdot H_2O + 4H_2O \dots\dots\dots\dots (2.35)$$
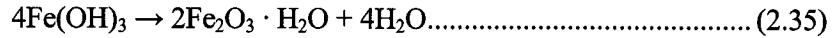
Since the molarity of Fe^{+2} will equal that of $Fe(OH)_2$, relationships can be formed. Bazant rewrote the concentration of $[Fe^{+2}]$ in terms of mass concentrations (grams per cubic meter of concrete) of $Fe(OH)_2$ and the capillary water (electrolyte) involved in the anodic reaction using the symbols u_f and $u_w{}^A$, respectively [7]:

$$\left[Fe^{+2}\right] = \frac{1}{u_w{}^A} \times \frac{1,000g}{1\,liter} \times u_f \times \frac{1\,mole\,Fe}{1\,mole\,Fe(OH)_2} \times \frac{1\,mole\,Fe(OH)_2}{88.87g} = (11.255)\frac{u_f}{u_w{}^A} \dots (2.36)$$

The concentration of $[O_2]$ was rewritten in terms of mass concentrations (grams per cubic meter of concrete) of O_2 and the capillary water (electrolyte) involved in the cathodic reaction using the symbols $u_o{}^C$ and $u_w{}^C$, respectively:

$$[O_2] = \frac{1}{u_w{}^C} \times \frac{1,000g}{1\,liter} \times u_o \times \frac{1\,mole\,O_2}{32g} = (31.250)\frac{u_o{}^C}{u_w{}^C} \dots\dots (2.37)$$

Bazant assumed that the pH would stay around 12.5 due to the large amount of $Ca(OH)_2$. Plugging pH = 12.5 into the equation and the rewritten concentrations of Fe^{+2} and O_2, one arrives at the formulation for the electrode potential:

$$E_{eq} = 0.9213 + (0.0148)\log u_o{}^C + (0.0296)\log u_w{}^A - (0.0148)\log u_w{}^C - (0.0296)\log u_f \dots\dots (2.38)$$

As pointed out previously [7], the potential is still dependent on the supply of oxygen at the anode because of the u_f term. The standard potential for this reaction is $E^\circ = 0.841$ v. Therefore, a small concentration of oxygen or a large concentration of ferrous ions at the anode could affect the electric potential difference enough to bring the reaction into equilibrium conditions (i.e. stopping corrosion).

Some consider activation polarization to be the controlling factor with reinforcing bar corrosion [32], while others consider concentration polarization to be the controlling factor [7]. Bazant argued that the diffusion of oxygen in concrete is a very slow process, while surmounting the free energy barrier under

28

anodic polarization takes place much quicker [7]. Lack of oxygen at the cathode or abundance of ferrous ions at the anode could cause concentration polarization to determine the rate.

2.4 TYPES OF CORROSION IN METALS

The intrinsic modes of corrosion occur in a material despite the geometry of the surrounding environment [33]. The modes of corrosion are commonly referred to as general, intergranular, pitting, stress corrosion (transgranular, intergranular) and fatigue. Figure 2.10 shows the different modes of metallic corrosion.
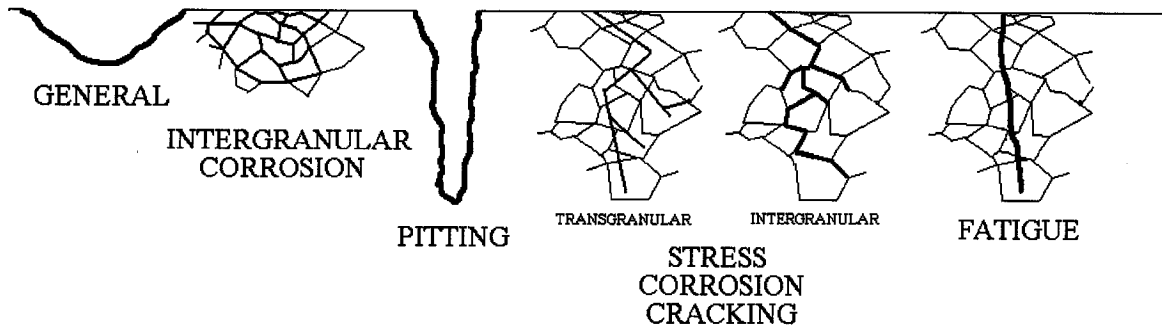
Figure 2.10: Intrinsic modes of corrosion (extracted from [33]).

General corrosion is typically due to a widespread acidic environment. It causes the largest amount of material loss. It is termed microcell corrosion, because the anodic and cathodic reactions are immediately adjacent to one another and mixed [9,44]. Intergranular corrosion takes place along grain boundaries, does not necessitate the application of any kind of stress to take place, and is typically a problem with welds. Pitting corrosion is considered to be localized corrosion, arising due to a large concentration of an acidic environment in a very specific location. It is difficult to detect, but catastrophic under certain circumstances (e.g. post-tensioned ducts). It is termed macrocell corrosion, because there is a local anode and a large cathode. Macrocell corrosion can take place within the same bar or between separate bars, such as a top rebar exposed to chlorides and a bottom rebar that is still passivated. Due to the current flowing from the anodic area towards the cathodic areas, some ferrous ions migrate away from the corrosion site [9]. This could lead to macrocell corrosion having less corrosion product accumulation at the anodic site, possibly preventing cracking. The prevention of cracking keeps the surrounding concrete in good health but prevents early detection of pitting corrosion through visual inspection of surface cracks. Stress corrosion cracking is caused by stress in the metal and the environment (i.e. temperature, pH level). Transgranular stress corrosion cracking takes place through the grains. Intergranular stress corrosion cracking takes place along the grains. Fatigue corrosion is caused by the dual action of cyclical stresses and a corrosive environment. The endurance limit of a material can be severely depreciated by a corrosive environment.

29

For reinforced concrete, the two modes of corrosion that are most common are general and pitting. Using special alloys and/or careful placement of welds can prevent intergranular corrosion [45]. Stress corrosion can usually be avoided by proper design of structural loads. In a typical scenario, the critical level for stress corrosion is well above the stress condition. Fatigue corrosion is a problem in certain situations, but for typical structural applications, the cyclical loading and environment is not conducive to fatigue corrosion. Carbonation attack, high chloride concentrations, and/or other acidic gases lead to general corrosion because the passive layer is destroyed along the whole surface of the steel [9]. This is caused by the lowering of the pH of the pore water at the depth of the reinforcement [29]. Chloride attack is considered localized (pitting) corrosion because there are smaller areas of attack (anodic site) surrounded by larger non-corroding areas (cathodic sites). The situation is accentuated in cases where cracks are present in the structure. When the positive iron ions are located within the pit, it draws even more negative chloride ions into the pit. This excess amount of chloride ions makes it difficult for the pit to form a protective film. The iron ions also start to hydrolyze according to the reaction:

$$Fe^{+2} + H_2O \rightarrow FeOH^+ + H^+ \quad\quad\quad (2.39)$$

which makes the pit environment even more acidic (lower pH) and harder to passivate. Even in cases where the surrounding environment is at a high pH, the localized pit could be at a much lower pH due to drawing in more chlorides and the metal hydrolyzing. Looking at the Pourbaix diagrams (Figures 2.3 and 2.4), as the pH is lowered it makes passivation more difficult and corrosion more likely. Figure 2.11 is considered a representation of differential aeration, showing the pitting of steel.
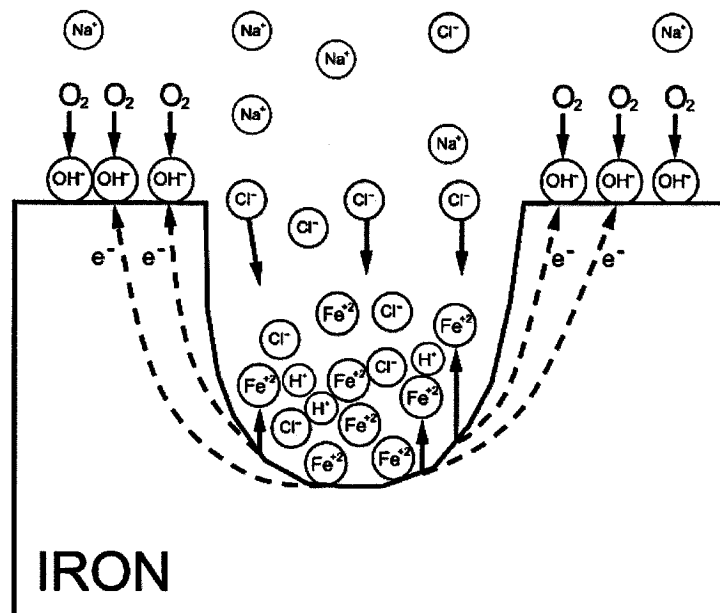

Figure 2.11: Pitting of steel from differential aeration (extracted from [46]).

Notice that the walls of the pit and surface of the steel become the large cathodic site, while the bottom of the pit becomes the local anode increasing the depth further.

2.5 STRUCTURAL RESPONSE OF CORRODED REINFORCED CONCRETE

Pitting corrosion will not usually cause concrete cracking due to the localized nature of the attack, the less expansive form of oxidation products from the corrosion reaction, and the macrocell reaction causing corrosion products to migrate away from the corrosion site [9,47]. There is obviously a reduction in steel cross-sectional area at the location of pitting corrosion, but even more damaging is the stress concentration that is created from the abrupt discontinuity. Researchers have found that the maximum penetration of pitting corrosion is equivalent to four to eight times the average general penetration [48]. The average strain over the undamaged portion of the bar is smaller than the local strain in the pit. This results in the bar breaking at an average strain smaller than the ultimate strain of a healthy bar [49]. While there is some increase in strength due to the hardening of the undamaged steel at the localized corrosion site, ductility is severely impaired with the bar eventually becoming brittle. Researchers simulated pits on rebar specimens and conducted tensile tests [47]. The ductility of bars with 5% and 50% section loss at the simulated pit location was reduced by 30-40% and by approximately 80%, respectively.

The main forms of degradation to the structural performance of reinforced concrete from uniform corrosion is the cross-sectional loss of the reinforcement, the cracking of the concrete matrix, and the bond loss between the steel and concrete interface. The cracking of the concrete matrix can result in section loss (e.g. spalling). Figure 1.2 illustrates the progression of the corrosion process. When iron dissolves into ferrous ions, the cross-sectional area of the reinforcement is effectively reduced. The ferrous ions are eventually converted to rust, which is considered to be a granular material. Granular materials (e.g. sand) have only compressional properties. Rust is more voluminous than iron in almost all forms (refer to Table 2.2). When the rust replaces the iron, pressure immediately starts to accumulate at the steel and concrete interface from the confinement of the surrounding concrete. The pressure accumulates even if some aqueous rust products diffuse into the concrete matrix or fill surrounding pores. The pressure will cause the concrete and the steel to deform elastically. The stiffness of the concrete is much less than the steel and therefore it will deform more substantially. Hoop stresses are created in the concrete that eventually causes rupture (i.e. cracking). As more rust product accumulates, the cracks propagate further. Cracking, spalling, and rust staining are usually the earliest indications of corrosion in the concrete. The crack provides an exit channel for aqueous rust products to leak out and cause staining (refer to Figure 1.6). Cracking occurs at small percentages of steel mass loss, usually around a rust

31

thickness of 0.1-0.2 mm [11]. This is a good indication that bond deterioration occurs much earlier during uniform corrosion than significant loss of cross-sectional area in the steel [50]. Cracking of the concrete decreases the confinement level of the surrounding concrete, reducing the amount of bond between the steel and concrete. The rust product between the two interfaces can act as a lubricant (especially when hydrated), further reducing the bond between steel and concrete. The loss of reinforcing rib area also reduces mechanical interlock at the interface.

Studies have been conducted to assess the depreciation of structural design parameters from uniform corrosion damage [2,51-55]. While not all of the studies conducted testing in the same manner, an appreciation can be gained for the level of structural degradation caused by corrosion. In one study [53], corrosion resulting in a 10% reduction of steel mass embedded in a concrete beam reduced its flexural strength capacity by 75%. In another study [55], corrosion resulting in a 10% reduction of the steel mass embedded in a concrete slab reduced both the yield and the ultimate load by 20%, but the fatigue strength capacity by up to 75%. The large reduction in capacity, from a comparatively small loss in cross-sectional area, was caused by corrosion induced longitudinal splitting cracks that extended through to supports and significantly reduced anchorage capacity. In a third study [51], corrosion resulting in a 9% reduction in steel mass embedded in a concrete beam increased the mid span deflection by 1.5 times. With regards to ultimate strength, a reduction in steel mass loss of 4%, 11%, and 17.5% had a relative depreciation of 1.6%, 10.4%, and 20% compared to an uncorroded specimen, respectively [54].

Bond strength is discussed with the most detail since it has major implications towards guided wave behavior discussed later. Bond strength for varying degrees of uniform corrosion follows a trend similar to what is shown in Figure 2.12. Note that this discussion excludes the effects of stirrups. Stirrups are U-shaped bars that pass around the tension steel and are hooked at the top for anchorage in the compression zone [56]. They are primarily used to increase the shear capacity and ductility of a reinforced concrete member. The characters shown in Figure 2.12 correspond to the stages shown in Figure 1.2. In most cases, bond strength increases initially up to an apex (point D). This initial region is sometimes referred to as the pre-cracking stage. The initial increase in bond strength is attributed to a couple of factors. As the corrosion product begins to accumulate between the steel and concrete, the pressure increases. This pressure increases the reactionary confinement and the mechanical interlocking of concrete around the bar [52]. Also, as the steel corrodes the roughness of the surface increases, creating more friction between the two interfaces. Bond failure in pullout tests conducted on specimens at corrosion levels below the apex is usually caused by the crushing of the concrete keys adjacent to the ribs without any splitting of the concrete [52].

32
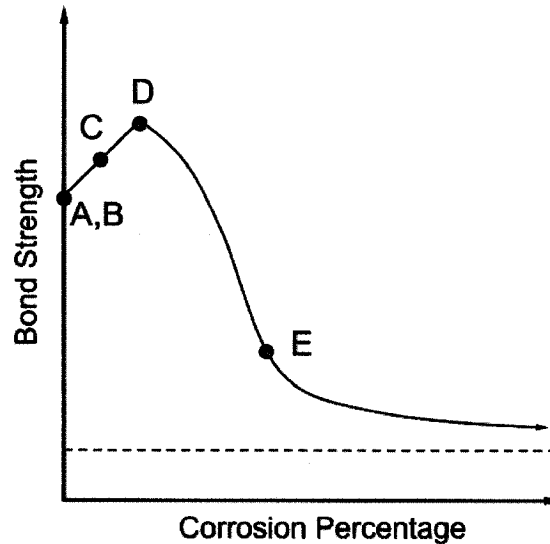
Figure 2.12: Bond strength as a function of corrosion percentage.

The region between points D and E is sometimes referred to as the cracking stage. It is not clear from existing published literature as to whether cracking always initiates before the apex. However, cracks seem to have more of a critical role in the type of bond failure after the apex. At the beginning of the cracking stage, the reinforcing ribs have not been depreciated to negligible levels. When the bar is pulled, the ribs create horizontal bearing stresses and hoop stresses in the concrete. The hoop stresses widen the present cracks, causing less confinement of the reinforcement. Bond failure occurs due to the splitting of the specimen along the cracks [52].

The region after E is sometimes referred to as the post-cracking stage. The ribs are becoming more appreciably degraded and the behavior is more similar to a plain bar. The corrosion product between the steel and concrete can act as a lubricant, further reducing the bond strength. Cracks and the rib profile deterioration have saturated to levels where further progression will not contribute to loss of bond.

Bond strength of embedded reinforcement has been measured experimentally for varying percentages of general corrosion using accelerated corrosion techniques [2,53,54,57]. Figures 2.13(a) and 2.13(b) show the results from two experimental studies. All points were normalized with respect to the pullout specimens without corrosion.

33
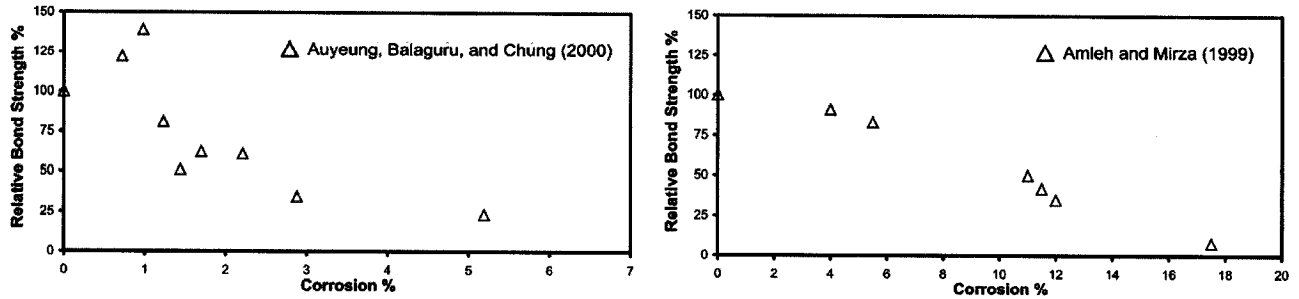
Figure 2.13: Pullout test results **(a)** (extracted from [57]) and **(b)** (extracted from [54]).

Figure 2.13(a) shows experimental points with increasing bond levels for low levels of corrosion (<1%). However, quickly after reaching the apex the bond strength begins to depreciate. A saturation level of bond strength occurs for higher levels of corrosion. Figure 2.13(b) does not have any data points with bond levels higher than the specimen tested without corrosion. However, no pullout specimens were tested in the region most likely to produce this type of behavior. For higher corrosion levels, the bond strength is reduced significantly. Figure 2.14 shows experimental results for pullout specimens with different diameters.
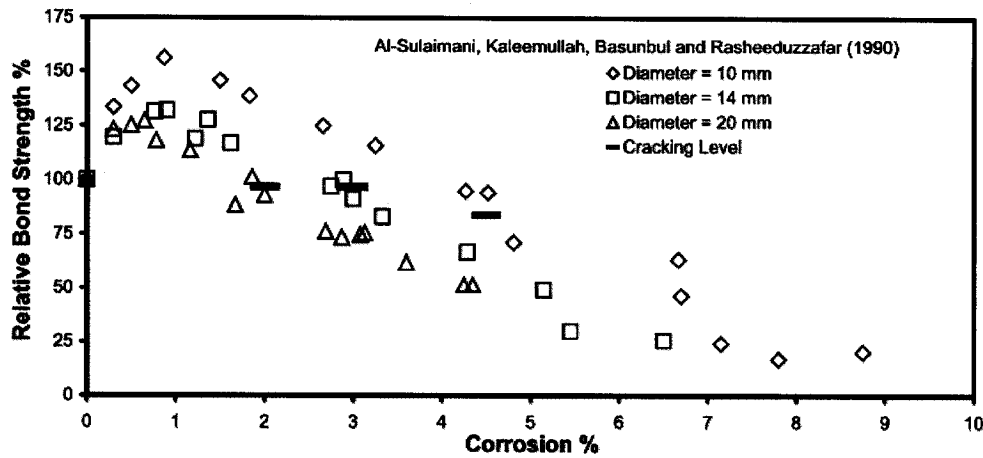
Figure 2.14: Pullout tests for varying rebar diameters (data extracted from [2]).

The bond strength initially increases for all of the pullout specimens with different diameters. Each reach an apex and then the bond strength decreases with further corrosion. Notice that observable surface cracking occurred at a corrosion level after the apex and changed for the different diameters. Figure 2.15 plots bond strength and surface cracking results for the same type of experimental specimens. Surface cracking was measured with a microscope.

34
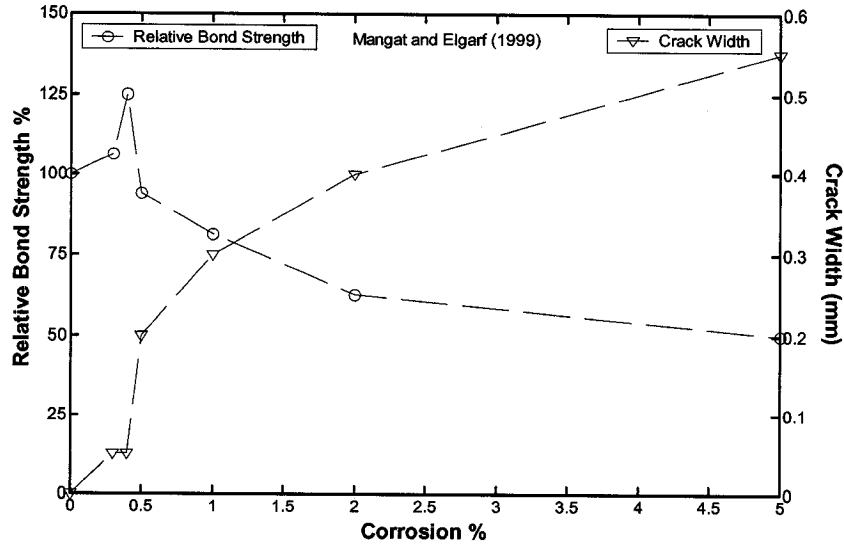
Figure 2.15: Measured bond strength and crack widths from pullout tests (data extracted from [53]).

The surface cracking occurred before the apex for this particular specimen set. This implies that cracking was initiated and propagated to the surface almost immediately after corrosion products started to accumulate. There is a sharp jump in the crack width after the apex is reached. As the crack width gets wider, the bond strength keeps depreciating due to the loss of confinement.

2.6   SUMMARY

This chapter has provided a brief introduction to the hydration products of concrete, the electrochemical nature of iron corrosion, an outline of the initiation and propagation periods for the corrosion process, a description of the types of metallic corrosion, and the structural response of the reinforced concrete undergoing corrosion attack. The main purpose was to introduce all of the terminology that is used in later sections, along with bringing the reader up to speed in the multifaceted areas involved in understanding corrosion in reinforced concrete. The next chapter will go into more depth as to how the propagation period has been and will be modeled within this report.

CHAPTER 3:

CORROSION PROCESS MODELING FOR REINFORCED CONCRETE

There has been an extensive effort to model the entire corrosion process in reinforced concrete. The capability of modeling the entire corrosion process for specific structures with different loading scenarios, environmental conditions, corrosion inhibiting systems, and design (e.g., w/c ratio, cover depth, admixtures, bar diameter, and stirrups) is enticing. A major difficulty lies in the acquisition of data for validation of the models with a combination of different service conditions. If the models could be validated, the opportunity would allow for service life estimates of the structure, making rehabilitation and maintenance scheduling much more efficient. It would also allow for life cycle cost estimates, affording the designer to take durability into account from the outset. With respect to the ultrasonic monitoring system that is the focus of this report, one could plan for the integration of the system during the construction of the structure. Using the models discussed, the life cycle cost could be estimated with the structural health monitoring system embedded. This would help determine what type of structure would be best suited for the system, the optimal location, and other nondestructive test methods to be coupled with the system. For the purposes of this report, modeling is used to relate the deterioration process from corrosion to the results of the guided mechanical waves monitored.

A rather comprehensive review of service life models has been presented elsewhere [58]. More general equations that can be used to model the process for most scenarios up to service life limits are now discussed. The modeling efforts will be branched into two categories: initiation and propagation models. By modeling the ingress of chlorides and carbon dioxide, the time to corrosion initiation can be estimated. By modeling the electrochemical reactions involved, the rate of rust product accumulation and cross-sectional loss can be estimated. The time to initiate concrete cracking from the rust product accumulation rate can be estimated using a mechanics of materials approach. The progression of concrete cracking can be modeled with the use of mechanics of materials or fracture mechanics. Modeling of the initiation period for both carbon dioxide and chloride ingress is presented in Appendix C. Modeling the propagation period is presented within this chapter. Discussions of various service limits, along with probabilistic service life models, are provided in Appendix E.

In the past, greater emphasis was placed on modeling the initiation period than the propagation period [59]. This is most likely a result of how long (in years) the initiation period usually is with respect to the propagation period. Liang et al. used several initiation and propagation models from recent literature and found the initiation period is on average six and a half times longer than the propagation period [58]. For some models, the propagation period is considered a fixed value because it is so short compared to the

initiation period [60]. In other cases, some have reported that when RC structures are exposed to marine environment (especially in the presence of load-induced cracks) the initiation time is relatively short in terms of the overall service life [59]. Nevertheless, the propagation period is an extremely important region because of its direct impact on structural health and determining long-term viability of the RC structure. It is the current focus of the modeling detailed in this chapter and the monitoring effort detailed in this report.

3.1 RATE OF REACTION

The rate of the electrochemical reaction will ultimately determine the characteristics of the propagation period. Using the Nernst equation, the potentials of the electrochemical reactions can be written. A model of the resistance between the anodic and cathodic sites can then be formulated. Using Ohm's law, one can solve for the corrosion current. The corrosion current can be converted directly to mass loss (using Faraday's Law) and will dictate the rate at which the propagation period progresses. The model shown in Figure 2.5 assumes a constant corrosion rate once corrosion has been initiated. For this to occur, the temperature and pressure would have to be constant with adequate amounts of water and oxygen for the reaction to proceed. While water is generally abundant, oxygen can play a critical role in determining the corrosion rate (especially in water immersed structures). It is also likely that once corrosion products start to accumulate, the corrosion rate will slow due to corrosion product buildup at the anodic site along with a change in the area ratio between the anodic and cathodic sites [61,62]. Therefore, the corrosion rate is highly variable over the lifetime of the RC structure.

Assuming that the corrosion current can be reasonably estimated, the amount of rust that would have to accumulate to cause cracking of the concrete can be solved. Solutions have been provided in the literature using a mechanics of materials formulation and more extensive finite element analysis (FEA) models. Once cracking has occurred, a model using mechanics of materials or fracture mechanics can be created along with an FEA model. There have been empirical formulas derived for the time leading up to and after the initiation of concrete cracking as well. The driving force behind the initial cracking and more extensive damage after cracking is still the electrochemical reactions. However, it is most likely that the resistance and potential will drastically change after progressive damage occurs. Bazant wrote the corrosion current densities as the following [63]:

$$i^A = \frac{E_{eq}}{a_b A^2 R} \quad \text{..(3.1)}$$

$$i^C = \frac{E_{eq}}{a_b C^2 R} \quad \text{..(3.2)}$$

37

where a_b is the steel bar surface per unit area, A^2 is the anodic area, C^2 is the cathodic area, and R is the total ohmic resistance of the circuit. Bazant assumed effective cross-sections and simple paths for the electrical current between the cathode and anode for the cases of large-scale and small-scale corrosion to estimate the total ohmic resistance of the circuit. The potential E_{eq} can be solved from Equation 2.38 in Chapter 2. Bazant's formulation of corrosion current is based off of an idealized representation of the electrochemical nature of the process [63]. There are several unknowns within the equations that change over time. Many have simply assumed constant corrosion rates based on averages of experimental findings. The linear polarization resistance (LPR) method, detailed in Appendix A, has been used to find the corrosion rate in-situ. Others have formulated empirical relationships for the corrosion current based on experimental evidence [61]. Vu & Stewart assumed that when oxygen availability dictates the corrosion rate, factors such as concrete quality (w/c ratio), cover, and the environmental conditions (i.e. temperature, relative humidity) determine the rate [61]. These factors will determine how quickly oxygen can diffuse into the concrete and fuel the reaction. They used the following empirical relationship to model the corrosion rate at initiation, assuming a relative humidity of 75% and a temperature of 20°C:

$$i^A(1) = \frac{37.8(1 - \text{w}/_\text{c})^{-1.64}}{\text{cover}} \left(\mu A / cm^2 \right) \quad \text{...................................... (3.3)}$$

To model the corrosion rate after initiation, experimental data from [64] was used to form an empirical formula:

$$i^A(t_P) = i^A(1) \cdot 0.85 t_P^{-0.29} \quad \text{... (3.4)}$$

where t_P is the time elapsed since initiation of corrosion. When water availability dictates the corrosion rate, the electrical resistivity of the concrete is the critical issue [61]. Hansen and Saouma simulated the electrochemical process as a mass transfer using finite element code and were able to model the effects of activation polarization [32].

Referring to Equation 2.11, the rate of rust (e.g. $Fe(OH)_3$) formation per unit area can be written:

$$j_r = \frac{106.87}{2(96,500)} \cdot i^A = (0.0005537) \cdot i^A \quad \text{... (3.5)}$$

The amount of rust mass per unit length that has accumulated is calculated with the following equation:

38

$$M_r = j_r \cdot t = \frac{a}{zF} \cdot i^A \cdot t = \frac{106.87}{2(96,500)} \cdot i^A \cdot t = (0.0005537) \cdot i^A \cdot t \quad\quad\quad (3.6)$$

If uniform corrosion is assumed, the change in diameter is calculated as:

$$\Delta D = 0.0232 \cdot t \cdot i^A \quad\quad\quad (3.7)$$

with the change in millimeters, t in years, and the corrosion current density in $\mu A/cm^2$. The rate of increase in the thickness (and the weight) of the layer of corrosion products at the surface of the metal can be affected by the thickness of the layer. The increase in layer thickness can slow the diffusion process of iron atoms through the oxide layer. This can lead to concentration polarization and a reduction in the corrosion current density. Three common trends between the weight gain of an oxidation layer as a function of time are shown in Figure 3.1:
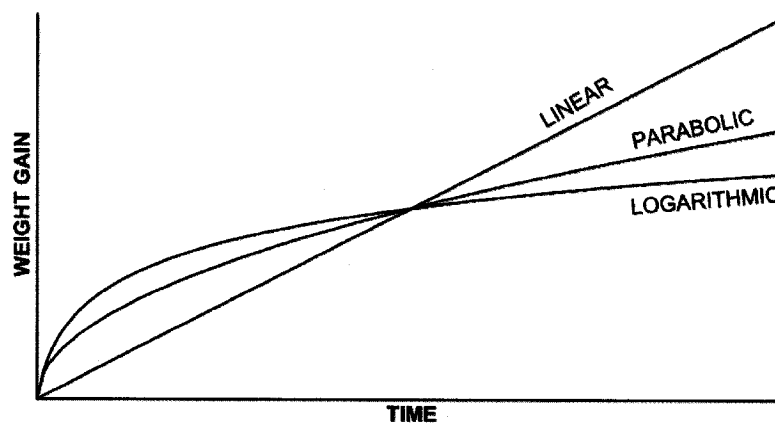
Figure 3.1: Common trends in weight gain as a function of time for the oxide layer (extracted from [31]).

Linear proportionality between weight and time usually occurs when the layer thickness is rather low. It can also occur from microcracking of the oxide layer or porosity leading to direct pathways to the surface of the steel [31]. Many times a linear rate will transition to a parabolic rate during corrosion. Equation 3.5 assumes the linear rate law for the production of rust. The logarithmic rate law generally occurs from very thin oxide layers and is thought to involve electric fields across the layer. Parabolic rates result from diffusion of iron atoms through the oxide layer as the controlling mechanism. The parabolic rate law usually defines relatively thick oxide layers. The following equation defines how the rate is affected by the weight accumulation:

$$j_r = \frac{dM_r}{dt} = \frac{\beta}{M_r} \quad\quad\quad (3.8)$$

39

where β is a function of the corrosion current. Pantazopoulou & Papoulia [65] fit Equation 3.8 to data from a previous study [64]. A linear relationship between β and i^4 (also referred to as i_{cor}) was assumed, yielding $\beta = (3.328 \times 10^{-10})\pi D_i i_{cor}$ [65]. D_i is the initial diameter of the bar in meters, while i_{cor} is in units of A/m^2. One can integrate and arrive at a relationship between the weight and time:

$$M_r^2 = 2\beta t = k_p t \qquad (3.9)$$

where t is in seconds, k_p is the parabolic rate constant, and M_r is in kg/m. For more information on the diffusion process through the oxide layer and the parabolic rate constant consult [31,66]. Generally, to find the parabolic rate constant for a material (assuming constant temperature) one can plot the square of the mass loss as a function of the corrosion time with the slope of the function the parabolic rate constant, k_p.

3.2 PROPAGATION MODELS (PRE-CRACKING OF CONCRETE COVER)

Relationships have been derived between the amount of rust mass accumulated (M_r) and the duration of time during the propagation period (t_p). Corrosion products will be generically referred to as rust products in this chapter for convenience. Rust is more voluminous than steel (refer to Table 2.2). Therefore, internal pressure is created as rust accumulates between the steel and concrete interfaces. The amount of volume the rust can occupy prior to cracking of the concrete varies depending on which particular model is used. A brief review of some analytical and finite element models is now discussed.

Imagine a bar of steel embedded in a bulk surrounding of concrete to a cover depth $R_o - R_i$, illustrated in Figure 3.2. Now assume that the bulk surrounding of concrete is translated to a thick walled cylinder of concrete, also shown in Figure 3.2.

40
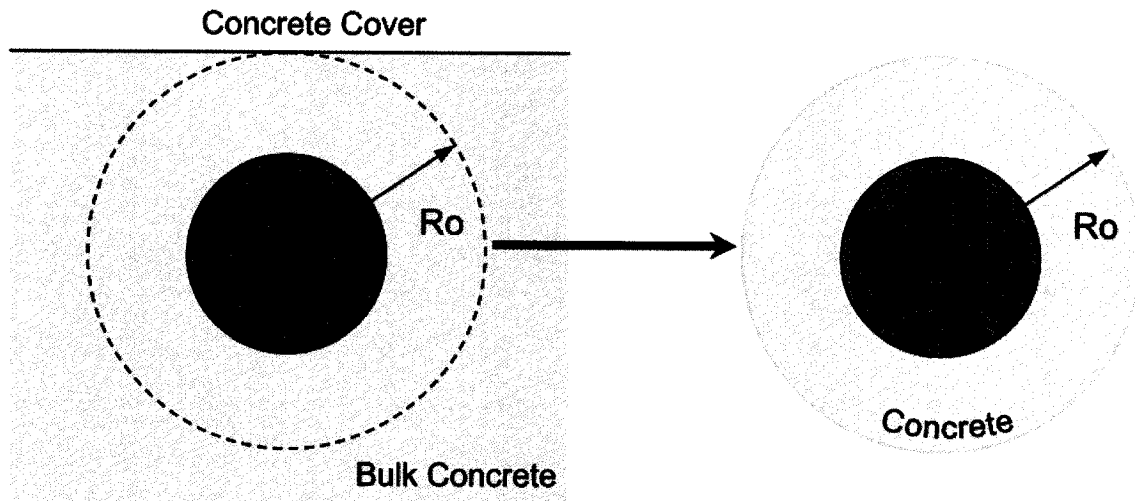
Figure 3.2: Translation of steel in bulk concrete medium to a thick walled concrete cylinder.

Figure 3.3 is an illustration of some propagation period models prior to the cracking of the concrete cover. Figure 3.3(a) shows the translated thick walled cylinder assumed at the beginning of each model with initial steel radius R_i and outer concrete radius R_o.
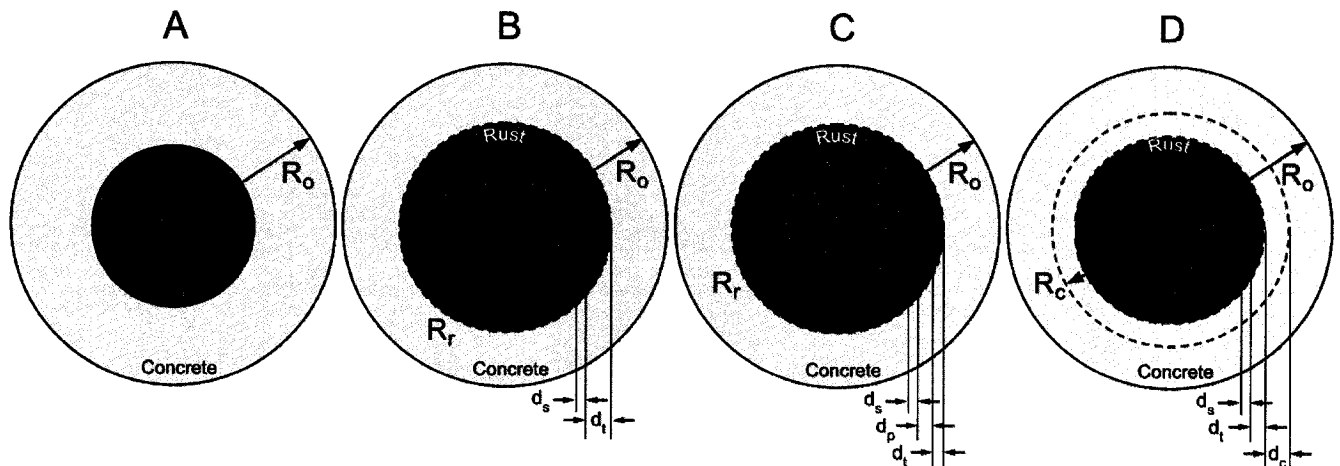
Figure 3.3: (a) Healthy concrete prior to corrosion. The other figures detail rust accumulation using the (b) Bazant [7,63], (c) Liu & Weyers [62], and (d) Pantazopoulou & Papoulia [65] models, respectively.

3.2.1   BAZANT MODEL

Figure 3.3(b) shows the Bazant corrosion model. The radius of steel after corrosion has occurred is R_s, while the radius of the rust front is R_r. Notice that $R_s < R_i < R_r$. The rust radius R_r can be assumed greater than R_i because all of the rust products in consideration are more voluminous than steel (refer to Table 2.2). The rust front will displace the concrete in the radial direction by d_t, equal to the difference between R_r and R_i. The distance between the initial radius, R_i, and the radius after corrosion, R_s, is d_s. The total thickness of the rust layer is equal to $d_r = d_t + d_s$, because the steel converted to rust will free up volume. The amount of volume that is available to the rust using the Bazant model is the following:

41

$$V_r = \left(\pi R_r^2 - \pi R_s^2\right) = \left(\pi(R_s + d_r)^2 - \pi R_s^2\right) = 2\pi(R_i - d_s)d_r = 2\pi(R_i - d_s)(d_s + d_t) \quad \text{...............} (3.10)$$

Assuming this volume is available for rust accumulation, the time to cover cracking can be estimated. Bazant translated the problem to a pressurized thick walled cylinder shown in Figure 3.4. The internal pressure p_i on the inside surface of the cylinder simulates the pressure from the rust product accumulation (p_{cor}). In reality, the steel and rust product deforms from internal pressure as well. However, the stiffness of the steel is significantly larger than concrete and the rust layer is very thin so both are neglected.
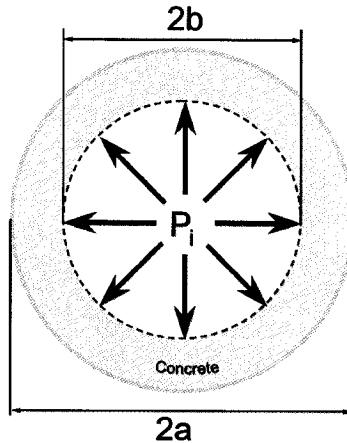
Figure 3.4: Translation of rust accumulation between the steel and concrete interfaces to a pressurized thick walled cylinder. The internal pressure p_i is considered the corrosion pressure p_{cor}.

The elastic response of the thick-walled cylinder is the following [67]:

$$d_t = \Delta R_i = p_i \cdot \delta_{pp} = p_i \cdot \frac{b}{E}\left[\frac{a^2 + b^2}{a^2 - b^2} + \upsilon\right] \quad \text{...............................} (3.11)$$

where p_i is the pressure, δ_{pp} is the flexibility (inverse of stiffness), υ is Poisson's ratio, and E is the modulus of elasticity. Bazant assumed the response of reinforced concrete (δ_{pp}) would be somewhere between the response of a pressurized hole in an infinite surrounding of concrete (δ_{pp}^0 where $a = R_o \to \infty$, $b = R_i$) and a pressurized thick walled cylinder (δ_{pp}^1 where $a = R_o$, $b = R_i$):

$$\delta_{pp}^0 < \delta_{pp} < \delta_{pp}^1 \quad \text{..} (3.12)$$

Assuming that the outer radius of the thick walled cylinder becomes infinitely large, δ_{pp}^0 is the following:

$$\delta_{pp}^0 = \frac{R_i}{E_{ef}}(1 + \upsilon) \quad \text{...} (3.13)$$

42

The effective elastic modulus of concrete, E_{ef}, has been used in place of the elastic modulus, E, to account for creep (i.e. viscoelasticity) in the model. The effective elastic modulus can be written $E_{ef} = E/(1+\phi_{cr})$ where ϕ_{cr} is the creep coefficient (around 2). δ_{pp}^1 is the following:

$$\delta_{pp}^1 = \frac{R_i}{E_{ef}}\left[\frac{R_o^2 + R_i^2}{R_o^2 - R_i^2} + \upsilon\right] \quad\dotfill\quad (3.14)$$

Bazant assumed an average of the two:

$$\delta_{pp} = \frac{1}{2}\left[\delta_{pp}^0 + \delta_{pp}^1\right] \quad\dotfill\quad (3.15)$$

The flexibility of the concrete surrounding a corroding bar is affected by other corroding bars that are in close proximity. Bazant solved for the change in flexibility assuming that 's' is the distance from the center of one bar to the center of an adjacent bar:

$$\Delta\delta = \frac{16R_i^3}{s^2 E_{ef}} \quad\dotfill\quad (3.16)$$

When other corroding bars are near, Equation 3.15 is added to Equation 3.16 to calculate the flexibility:

$$\delta_{pp} = \frac{R_i}{E_{ef}}\left[\frac{R_o^2 + R_i^2}{2\left(R_o^2 - R_i^2\right)} + \frac{16R_i^2}{s^2} + \upsilon + \frac{1}{2}\right] \quad\dotfill\quad (3.17)$$

Plugging the flexibility into Equation 3.11 and assuming p_i is equal to p_{cor}:

$$d_t = \frac{p_{cor} \cdot R_i}{E_{ef}}\left(\frac{R_o^2 + R_i^2}{2\left(R_o^2 - R_i^2\right)} + \frac{16R_i^2}{s^2} + \upsilon + \frac{1}{2}\right) \quad\dotfill\quad (3.18)$$

Bazant solved for the corrosion pressure, p_{cor}, for two cases of cracking; inclined planar cracks and cover peeling. Figure 3.5 shows the different cracking cases:

43
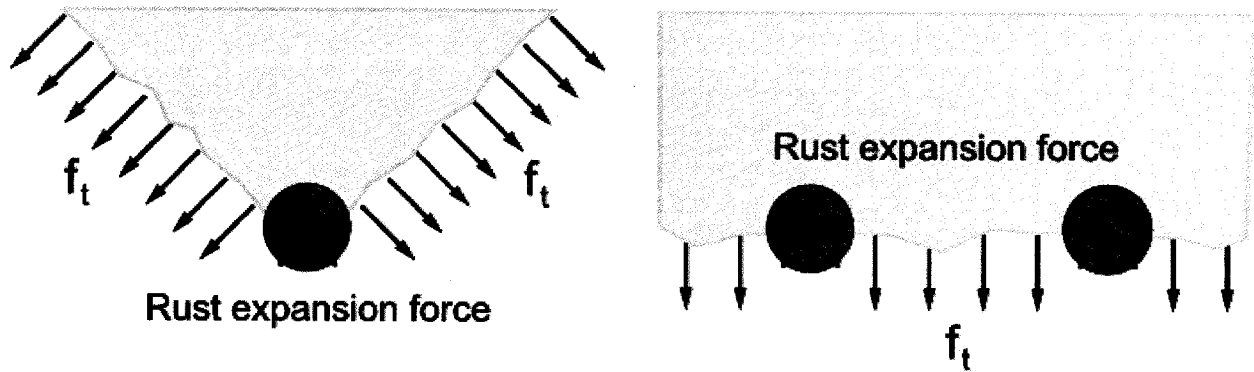
Figure 3.5: Inclined cracking (left) and cover peeling (right) due to rust expansion force (extracted from [63]). The label f_t refers to the tensile strength of concrete.

The left diagram in Figure 3.5 shows inclined cracking. Inclined planar cracks were assumed to occur when the spacing between two adjacent bars is large (e.g. $s > 12R_o$). The right diagram in Figure 3.5 shows cover peeling, assumed when bar spacing is relatively close. To solve for the critical rust thickness for inclined cracking, the forces are summed in the y-direction and the concrete is assumed fully plastic at failure ($\sigma_\theta = f_t$ at every layer, where f_t is the tensile strength of concrete). The force created in the y-direction from the pressure p_i is the following (θ is considered the angle from vertical direction):

$$F_y = \int_{-\pi/2}^{\pi/2} R_i \cdot p_{cor} \cdot \cos\theta \cdot d\theta = 2p_{cor} R_i \quad \text{...} (3.19)$$

The force created in the y-direction from the concrete is the following (assuming cracking angle is 45° from horizontal):

$$F_y = 2(R_o - R_i)f_t \quad \text{...} (3.20)$$

Setting the two equations equal to each other and solving for p_{cor}:

$$p_{cor} = \frac{(R_o - R_i)f_t}{R_i} \quad \text{...} (3.21)$$

Plugging Equation 3.21 into Equation 3.18, one arrives at the critical d_t value for inclined cracks:

$$d_t = \frac{(R_o - R_i)f_t}{E_{ef}} \left(\frac{R_o^2 + R_i^2}{2(R_o^2 - R_i^2)} + \frac{16R_i^2}{s^2} + \upsilon + \frac{1}{2} \right) \quad \text{...................} (3.22)$$

For cover peeling, the bars are spaced closer together. If the forces are summed in the y-direction for cover peeling, one arrives at:

44

$$(s - 2R_i)f_t = 2p_{cor}R_i \quad \text{...} \quad (3.23)$$

Solving for p_{cor}:

$$p_{cor} = \frac{(s - 2R_i)f_t}{2R_i} \quad \text{...} \quad (3.24)$$

Plugging into Equation 3.18, one arrives at the following critical d_t value for cover peeling:

$$d_t = \frac{(s - 2R_i)f_t}{2E_{ef}} \left(\frac{R_o^2 + R_i^2}{2(R_o^2 - R_i^2)} + \frac{16R_i^2}{s^2} + \upsilon + \tfrac{1}{2} \right) \quad \text{.....................} \quad (3.25)$$

Equation 3.10 solves for the volume of rust using the Bazant model, with d_s, d_t, and R_i needed. The initial radius R_i is known, d_t is calculated from Equations 3.22 or 3.25, leaving d_s to be calculated. The volume of rust is created from the following volume of steel:

$$V_s = \pi(R_i - d_s)d_s \quad \text{...} \quad (3.26)$$

This volume of steel is converted to a mass by multiplying by the density of steel:

$$M_s = V_s \cdot \rho_s \quad \text{...} \quad (3.27)$$

A conversion from the mass of steel to rust is given by the following:

$$M_s = M_r \cdot \alpha \quad \text{...} \quad (3.28)$$

where α is the ratio of atomic weights between steel and the particular type of rust assumed in the model (provided in Table 2.2). Therefore:

$$M_r = \frac{\pi(R_i - d_s)d_s \cdot \rho_s}{\alpha} \quad \text{...} \quad (3.29)$$

The amount of rust created is the volume of rust multiplied by the density:

$$M_r = V_r \cdot \rho_r \quad \text{...} \quad (3.30)$$

This can be rearranged in terms of V_r and set equal to Equation 3.10 to solve for d_s:

45

$$d_s = \frac{2d_t}{\left(\dfrac{n}{\alpha} - 2\right)} \quad\text{..} (3.31)$$

Once both d_t and d_s are calculated, V_r will yield the critical volume of rust to cause cracking. To calculate the amount of time for this to happen, one must assume a rate law. Bazant assumed a linear rate law. Equation 3.30 was rearranged in terms of V_r and Equation 3.6 was plugged in for M_r. The equation was rearranged in terms of t and the critical time to cracking is the following:

$$t = \frac{2\pi \cdot j_r \cdot \rho_s}{n}(R_i - d_s)(d_s + d_t) \quad\text{..} (3.32)$$

3.2.2 LIU & WEYERS MODEL

Liu & Weyers added the effects of a porous zone at the steel and concrete interface [62,64]. Effectively, the porous zone is extra space for rust product to deposit before pressure starts to build (refer to Section 2.1). The pores are considered evenly distributed around the steel and concrete interface, with an average depth. It is accounted for by making a composite thickness (d_p) based on the volume of interconnected pores at the interface distributed in a uniform layer. Figure 3.3(c) shows the Liu & Weyers model. This extra accumulation of rust in the pores is not accounted for in the Bazant model. After the porous zone volume is filled, the corrosion product accumulation starts to create hoop stresses in the concrete. This will proceed as described in the Bazant model. The volume of the rust product is the following:

$$V_r = \left(\pi R_r^2 - \pi R_s^2\right) = \left(\pi (R_s + d_r)^2 - \pi R_s^2\right) = 2\pi (R_i - d_s)d_r = 2\pi (R_i - d_s)(d_s + d_p + d_t) \quad\text{.................} (3.33)$$

To solve for d_t, one can use Equation 3.22 or 3.25 as in the Bazant model. To solve for d_s, multiply the volume of rust (V_r) in the Liu & Weyer model by rust density and set it equal to Equation 3.29:

$$M_r = \frac{\pi (R_i - d_s)d_s \cdot \rho_s}{\alpha} = \frac{2\pi \rho_s}{n}(R_i - d_s)(d_s + d_p + d_t) \quad\text{...............} (3.34)$$

$$d_s = \frac{2(d_t + d_p)}{\left(\dfrac{n}{\alpha} - 2\right)} \quad\text{...} (3.35)$$

Petra-Lazar provided Equation 3.36 to calculate the pore band thickness [68]. The thickness is:

$$d_p = t_{in} \cdot p_m \quad\text{..} (3.36)$$

46

where t_{in} is the thickness of the rebar/mortar interface (reported as 40 μm) and p_m is the porosity of the mortar. The porosity of the mortar was estimated to be half of the porosity of the cement paste and is calculated as:

$$p_m = \frac{1}{2}\left(1 - \frac{1 + 1.31\alpha_h}{1 + 3.2\,{}^w\!/_c}\right) \dotfill (3.37)$$

where α_h is the degree of hydration and w/c is the water to cement ratio. Liu & Weyers used a value of 12.5 μm for the pore band thickness.

Liu & Weyers used the parabolic rate law, accounting for the slowed rate of rust production due to the accumulation of the oxide layer at the steel surface. Using the same procedure for finding the critical volume of rust as described with the Bazant model, but assuming a parabolic rate law, the following is the time to cracking using the Liu & Weyers model:

$$t = \frac{1}{k_p}\left(\frac{2\pi\rho_s}{n}(R_i - d_s)(d_s + d_p + d_t)\right)^2 \dotfill (3.38)$$

3.2.3 PANTAZOPOULOU & PAPOULIA MODEL

Pantazopoulou & Papoulia [65] modeled the problem using a smeared crack approach. Smeared refers to the crack being distributed around the entire cross-section. The strain field is dealt with rather than modeling crack characteristics (e.g., number of cracks, size, location, and pattern). For more discussion on smeared cracks and the differences between it and a discrete crack, refer to [69]. The Bazant and Liu & Weyer models assumed instantaneous cover cracking when the tensile strength of the concrete is breached. Pantazopoulou & Papoulia assume the concrete cover maintains some residual strength, even after its tensile strength is breached at the inner surface. Instead of the cover cracking instantaneously, a crack front was modeled that propagates toward the outside surface. As more rust product accumulates, the crack width increases and the residual strength decreases. Another feature was that corrosion products move away from the reaction site, depositing into the concrete cracks (similar to the porous zone). Figure 3.3(d) shows the cracked layer of concrete (radius = R_c) surrounding the passive layer. The volume of rust deposited in the cracks is dependent on the crack length. The volume of each individual crack is assumed one half of the crack width opening (w) multiplied by the length (triangular in shape):

$$V_{crack} = \frac{1}{2}\cdot w \cdot (R_c - R_r) \dotfill (3.39)$$

47

The total amount of crack width openings is calculated as the difference in circumference between the original bar radius and the rust front:

$$\sum w = 2\pi(R_r - R_i) \quad \text{...(3.40)}$$

Therefore, the volume of rust assumed to deposit in the cracks is:

$$V_{cracks} = \pi(R_r - R_i)(R_c - R_r) \quad \text{...(3.41)}$$

The volume of rust created from the corrosion reaction is:

$$V_r = \left(\pi(R_r)^2 - \pi(R_s)^2\right) + V_{cracks} = \left(\pi(R_r)^2 - \pi(R_s)^2\right) + \pi(R_r - R_i)(R_c - R_r) \quad \text{..............(3.42)}$$

If one substitutes in $R_r = R_s + d_r$, where d_r is the thickness of the rust layer, the volume of rust created in the corrosion reaction can be rewritten as:

$$V_r = \pi d_r(2R_s + d_r) + \pi(R_r - R_i)(R_c - R_r) \quad \text{.................................(3.43)}$$

The volume of steel lost to the corrosion reaction can be written:

$$\Delta V_s = \pi R_i^2 - \pi R_s^2 = \pi(R_s + d_s)^2 - \pi R_s^2 = \pi d_s\left(2R_s + d_s^2\right) \quad \text{........(3.44)}$$

This can be written in terms of the volume of rust created:

$$V_r = n \cdot \Delta V_s = \pi d_s\left(2R_s + d_s^2\right) \quad \text{...(3.45)}$$

The crack propagation distance and the corrosion thickness can be equated by setting Equation 3.43 equal to Equation 3.45 and rearranging in terms of d_r:

$$d_r = \frac{n\left(2R_i d_s - d_s^2\right) + d_s(R_c - R_i + d_s)}{(R_c + R_i)} \quad \text{.....................................(3.46)}$$

The radial displacement d_t (also referred to as $u_r|_{r=Ri}$) caused by rust accumulation is equal to $R_r - R_i = d_r - d_s$. This can be written as:

$$u_r\big|_{r=R_i} = R_r - R_i = d_r - d_s = \frac{(n-1)\left(2R_i d_s - d_s^2\right)}{(R_c + R_i)} \quad \text{.......................(3.47)}$$

Assuming once again the pressure analogy used in previous models, the solution for hoop stresses in a thick-walled cylinder under internal pressure p_i, as shown in Figure 3.4, is the following:

$$\sigma_\theta(r) = p_i \cdot \frac{\left(R_o/r\right)^2 + 1}{\left(R_o/R_i\right)^2 - 1} \quad\quad\quad\quad\quad\quad\quad\quad\quad\quad\quad\quad\quad\quad\quad\quad\quad\quad\quad (3.48)$$

As in previous models, the stiffness of the steel and rust are neglected. In the Bazant and Liu & Weyers models, the entire cross-section was assumed to go into a fully plastic state. In the current model, the hoop stress in the elastic uncracked outer ring ($R_c \leq r \leq R_o$), as shown in Figure 3.3(d), is assumed equal to the tensile strength of the concrete at the crack tip ($r = R_c$) only. The hoop stress distribution is then:

$$\sigma_\theta(r = R_c) = p_i \cdot \frac{\left(R_o/R_c\right)^2 + 1}{\left(R_o/R_i\right)^2 - 1} = f_t \quad\quad\quad\quad\quad\quad\quad\quad\quad\quad\quad\quad\quad (3.49)$$

$$\frac{p_i}{\left(R_o/R_i\right)^2 - 1} = \frac{f_t}{\left(R_o/R_c\right)^2 + 1} \quad\quad\quad\quad\quad\quad\quad\quad\quad\quad\quad\quad\quad (3.50)$$

Plugging back into Equation 3.48:

$$\sigma_\theta(r) = f_t \cdot \frac{\left(R_o/r\right)^2 + 1}{\left(R_o/R_c\right)^2 + 1} \quad\quad\quad\quad\quad\quad\quad\quad\quad\quad\quad\quad\quad\quad\quad (3.51)$$

A visualization of the hoop stress field over the elastic uncracked outer ring is shown in Figure 3.6.
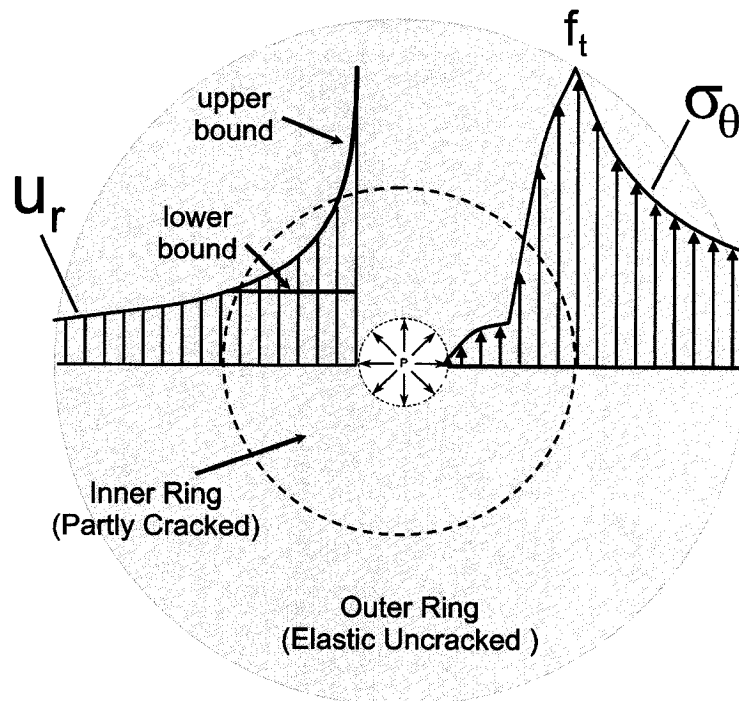
Figure 3.6: Hoop stress and radial displacement distribution in cracked thick-walled cylinder. The partly cracked inner ring has a softening behavior dependent on the hoop strain. The crack front layer has a hoop stress equal to the tensile strength of the concrete f_t.

Neglecting Poisson's ratio, the hoop strain ε_θ and radial displacement u(r) for the elastic uncracked outer ring can be written:

$$\varepsilon_\theta(r) = \frac{\sigma_\theta(r)}{E} \qquad\qquad (3.52)$$

$$u(r) = r \cdot \varepsilon_\theta(r) = r \cdot \varepsilon_{ct} \cdot \frac{\left(R_o/r\right)^2 + 1}{\left(R_o/R_c\right)^2 + 1} = r \cdot \frac{f_t}{E} \cdot \frac{\left(R_o/r\right)^2 + 1}{\left(R_o/R_c\right)^2 + 1} \qquad (3.53)$$

Note that ε_{ct} refers to the critical tensile hoop strain to cause cracking at a layer and is equal to f_t/E. The assumption has been made, presently and in previous models, that the radial displacement distribution for the elastic uncracked outer ring (Equation 3.53) is also valid for the cracked inner ring [70,71]. The radial displacement distribution is shown in Figure 3.6. The assumption is an upper bound on the radial displacement distribution with the lower bound being a constant radial displacement distribution equal to the displacement at the crack tip layer. As pointed out by [70], the true radial displacement distribution for the cracked inner ring lies somewhere between these two bounds. The elastic hoop stress distribution used for the uncracked outer ring is not considered valid for the cracked inner ring (see Figure 3.6). The hoop stress equations for the cracked inner ring are dependent on the hoop strains, with the complete

50

solution detailed shortly. Using Equation 3.53 to solve for the radial displacement at the inner wall ($r = R_i$) of the thick-walled cylinder:

$$u_r\big|_{r=R_i} = R_i \cdot \frac{f_t}{E} \cdot \frac{\left(R_o/R_i\right)^2 + 1}{\left(R_o/R_c\right)^2 + 1} \quad\text{...} (3.54)$$

A relationship between the steel bar thickness loss from corrosion and the propagation distance of the crack layer can now be formed by setting Equation 3.47 equal to Equation 3.54:

$$\frac{(n-1)\left(2R_i d_s - d_s^2\right)}{R_c + R_i} = \frac{f_t}{E} \cdot R_i \cdot \frac{\left(R_o/R_i\right)^2 + 1}{\left(R_o/R_c\right)^2 + 1} \quad\text{.............................} (3.55)$$

Using Equation 3.55 allows for an estimate of either R_c or d_s by assuming a value for the other. If one assumes $R_c = R_o$, the critical d_s value for cracking to reach the concrete cover can be solved. To find the time for this to occur one must calculate the amount of steel involved in a thickness loss of d_s:

$$V_s = 2\pi\left(R_i - d_s\right)d_s \quad\text{..} (3.56)$$

Converting this volume of steel to a volume of rust:

$$V_r = n \cdot V_s \quad\text{...} (3.57)$$

and then converting the volume of rust to a weight:

$$W_r = \rho_r \cdot V_r \quad\text{...} (3.58)$$

one can now use either the linear or parabolic rate law to calculate the amount of time to accumulate the critical amount of rust.

Once d_s and R_c have been solved, the corrosion pressure p_{cor} can be calculated. Figure 3.7(a) shows the pressure due to the outer uncracked ring and the corrosion pressure. Figure 3.7(b) shows the translation to forces over a small volume element of the cracked ring.
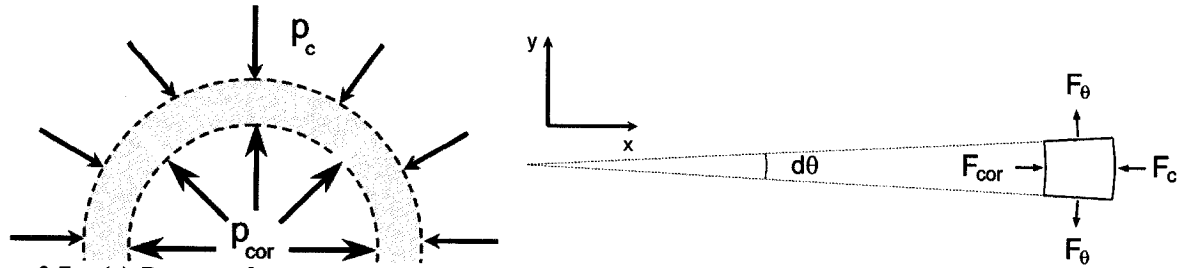
51

Figure 3.7: **(a)** Pressure from corrosion product accumulation is shown along with the pressure from the outer uncracked ring with **(b)** a translation to forces for a small volume element in the cracked ring.

To solve for the force from corrosion pressure:

$$F_{cor} = p_{cor} \cdot R_i \cdot d\theta \cdot dl \quad\text{...}\text{(3.59)}$$

where dl is the length of the small volume segment. To solve for the force from the elastic uncracked outer ring pressure p_c:

$$F_c = p_c \cdot R_c \cdot d\theta \cdot dl \quad\text{...}\text{(3.60)}$$

The force in the x-direction from the hoop stress is the following:

$$F_\theta = d\theta \cdot \int_{R_i}^{R_c} \sigma_\theta (r) \cdot dr \cdot dl \quad\text{...}\text{(3.61)}$$

Summing the forces in the x-direction:

$$p_{cor} \cdot R_i = p_c \cdot R_c + \int_{R_i}^{R_c} \sigma_\theta (r) dr \quad\text{...}\text{(3.62)}$$

The pressure from the elastic uncracked outer ring (p_c) must now be solved. In order to do this, the forces are summed in the x-direction:

$$p_c \cdot R_c = \int_{R_c}^{R_o} \sigma_\theta (r) dr \quad\text{...}\text{(3.63)}$$

Using Equation 3.51 for hoop stress and integrating, the pressure from the elastic uncracked outer ring can be solved:

$$p_c = f_t \cdot \frac{R_o^2 - R_c^2}{R_o^2 + R_c^2} \quad\text{..}\text{(3.64)}$$

Equation 3.62 can now be rewritten:

52

$$p_{cor} \cdot R_i = R_c \cdot f_t \cdot \frac{R_o^2 - R_c^2}{R_o^2 + R_c^2} + \int_{R_i}^{R_c} \sigma_\theta(r) dr \quad \dots\dots\dots\dots\dots\dots\dots (3.65)$$

The hoop stress in the cracked ring is now needed. A tension-softening model was used to describe the mechanical behavior of the cracked ring. The tension-softening model allows for some residual strength after the concrete has reached its critical tensile strain. There have been a variety of different tension-softening curves proposed (e.g., linear, bilinear, and exponential), with a bilinear curve used for this derivation. The equations for hoop stress in the cracked region are dependent on the hoop strain and are shown in Table 3.1. The value of strains ε_1 and ε_u are 0.0003 and 0.002 respectively, with the determination of these values detailed in [65]. Figure 3.8 shows the assumed stress-strain behavior of the concrete:

Table 3.1: Relationship between average hoop stress and strain using tension-softening model.

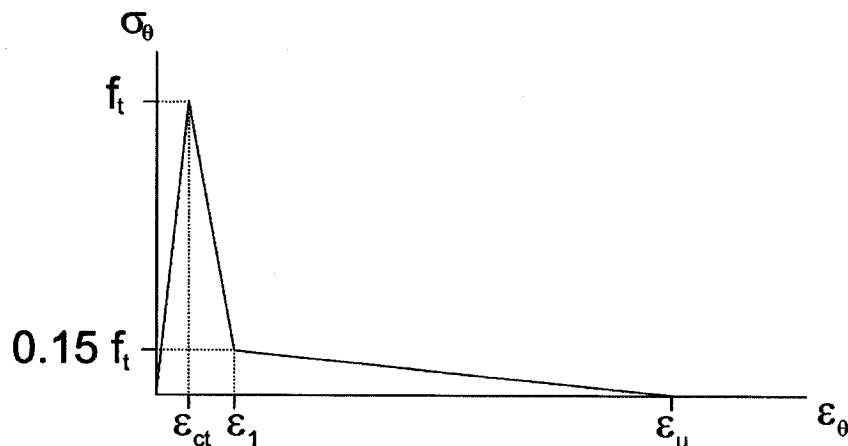| $\varepsilon_\theta(r) \leq \varepsilon_{ct}$	$\varepsilon_{ct} < \varepsilon_\theta(r) \leq \varepsilon_1$	$\varepsilon_1 < \varepsilon_\theta(r) \leq \varepsilon_u$	$\varepsilon_u < \varepsilon_\theta(r)$
$\sigma_\theta = \sigma_{\theta 1} = E \cdot \varepsilon_\theta(r)$	$\sigma_\theta = \sigma_{\theta 2} = f_t \cdot \left[1 - 0.85 \cdot \frac{\varepsilon_\theta(r) - \varepsilon_{ct}}{\varepsilon_1 - \varepsilon_{ct}}\right]$	$\sigma_\theta = \sigma_{\theta 3} = 0.15 \cdot f_t \cdot \frac{\varepsilon_u - \varepsilon_\theta(r)}{\varepsilon_u - \varepsilon_1}$	$\sigma_\theta = \sigma_{\theta 4} = 0$

Figure 3.8: Average stress-strain relationship for cracked concrete (extracted from [65]).

To solve for the corrosion pressure, the proper hoop stress equations must be inserted into Equation 3.65 and integrated. Wang & Liu solved for the equations explicitly, with their solutions provided here [71]. The hoop stress solutions are divided into two regions: prior to cracking reaching the concrete cover and after. Before cracks reach the concrete cover, [71] rearranged Equation 3.53 in terms of r and plugged in ε_1 and ε_u separately to solve for the radial distances (named RR1 and RRu respectively) where those hoop strains would be reached:

53

$$RR1 = \frac{R_o}{\varepsilon_1 \cdot \frac{E}{f_t}\left[\left(\frac{R_o}{R_c}\right)^2 + 1\right] - 1} \quad\text{...} (3.66)$$

$$RRU = \frac{R_o}{\varepsilon_u \cdot \frac{E}{f_t}\left[\left(\frac{R_o}{R_c}\right)^2 + 1\right] - 1} \quad\text{...} (3.67)$$

This assumes the upper bound elastic displacement distribution defined earlier, even in locations where the hoop strain at the inner wall has breached ε_u. Table 3.2 provides the conditions with the corresponding solution for the integral of hoop stress prior to cracks reaching the concrete cover ($\varepsilon_{\theta o} < \varepsilon_{ct}$). The hoop strain $\varepsilon_{\theta o}$ refers to the hoop strain at the outer radius of the thick walled cylinder.

Table 3.2: Hoop stress integral equations after crack initiation but prior to surface cracks ($\varepsilon_{\theta o} < \varepsilon_{ct}$) [71].

#	Condition:	$I = \int_{R_r}^{R_c}\sigma_\theta(r)\,dr =$	Solution:
1	$\varepsilon_{ct} < \varepsilon_{\theta o} \le \varepsilon_1$	$\int_{R_r}^{R_c}\sigma_{\theta 2}(r)\,dr$	$f_t\left[\dfrac{\varepsilon_1 - 0.15\varepsilon_{ct}}{\varepsilon_1 - \varepsilon_{ct}}\cdot(R_c - R_r) - \dfrac{0.85f_t}{(\varepsilon_1 - \varepsilon_{ct})E}\cdot\dfrac{1}{\left(\frac{R_o}{R_c}\right)^2 + 1}\cdot\left(\dfrac{R_o^2}{R_i} - \dfrac{R_o^2}{R_c} + R_c - R_i\right)\right]$
2	$\varepsilon_1 < \varepsilon_{\theta o} \le \varepsilon_u$	$\int_{R_r}^{RR1}\sigma_{\theta 3}(r)\,dr + \int_{RR1}^{R_c}\sigma_{\theta 2}(r)\,dr$	$\dfrac{0.15f_t}{\varepsilon_u - \varepsilon_1}\left[\varepsilon_u(RR1 - R_i) - \dfrac{f_t}{E}\cdot\dfrac{1}{\left(\frac{R_o}{R_c}\right)^2 + 1}\cdot\left(\dfrac{R_o^2}{R_i} - \dfrac{R_o^2}{RR1} + RR1 - R_i\right)\right] +$ $f_t\left[\dfrac{\varepsilon_1 - 0.15\varepsilon_{ct}}{\varepsilon_1 - \varepsilon_{ct}}(R_c - RR1) - \dfrac{0.85f_t}{(\varepsilon_1 - \varepsilon_{ct})E}\cdot\dfrac{1}{\left(\frac{R_o}{R_c}\right)^2 + 1}\cdot\left(\dfrac{R_o^2}{RR1} - \dfrac{R_o^2}{R_c} + R_c - RR1\right)\right]$
3	$\varepsilon_u \le \varepsilon_{\theta o}$	$\int_{RRU}^{RR1}\sigma_{\theta 3}(r)\,dr + \int_{RR1}^{R_c}\sigma_{\theta 2}(r)\,dr$	$\dfrac{0.15f_t}{\varepsilon_u - \varepsilon_1}\left[\varepsilon_u(RR1 - R_i) - \dfrac{f_t}{E}\cdot\dfrac{1}{\left(\frac{R_o}{R_c}\right)^2 + 1}\cdot\left(\dfrac{R_o^2}{RRU} - \dfrac{R_o^2}{RR1} + RR1 - RRU\right)\right] +$ $f_t\left[\dfrac{\varepsilon_1 - 0.15\varepsilon_{ct}}{\varepsilon_1 - \varepsilon_{ct}}(R_c - RR1) - \dfrac{0.85f_t}{(\varepsilon_1 - \varepsilon_{ct})E}\cdot\dfrac{1}{\left(\frac{R_o}{R_c}\right)^2 + 1}\cdot\left(\dfrac{R_o^2}{RR1} - \dfrac{R_o^2}{R_c} + R_c - RR1\right)\right]$

Bhargava et al. [34] solved analytically for three different variations of this model. The first, referred to as M3, assumed that the cracked concrete retains its original strength. The second, referred to as M4, assumed that the cracked concrete has zero strength post-cracking. The third, referred to as M5, assumed the linear softening model as described earlier. M3 and M4 were considered upper and lower bounds on

54

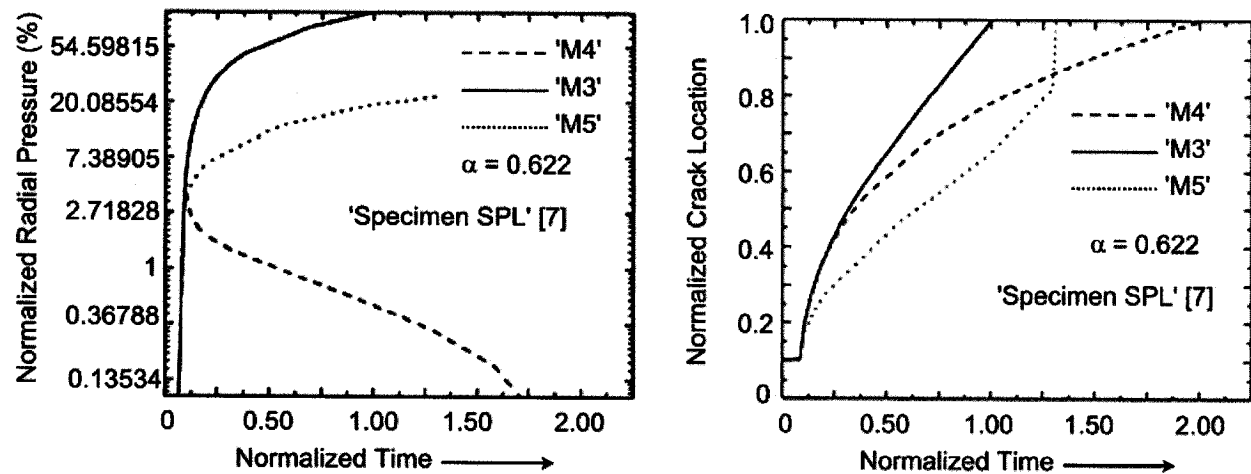the residual strength of the concrete. The results of the three models are shown in Figures 3.9(a) and 3.9(b).

Figure 3.9: (a) Normalized radial pressure and **(b)** normalized crack location as a function of normalized time (both images extracted from [34]).

In Figure 3.9(a), the corrosion pressure climbs rapidly once corrosion products start to accumulate and continues to climb until fracture (except for M4). The tension-softening model (M5) is clearly bounded by the other two models (M3 & M4). The models only predict corrosion pressure up to when the crack reaches the concrete cover. In Figure 3.9(b), the crack length can be tracked as a function of time, allowing for the time to cover cracking to be estimated. Figure 3.10 shows the models with experimental results. The corrosion pressure has been normalized with respect to the tensile strength of the concrete and the corrosion penetration depth has been normalized with respect to the radius.
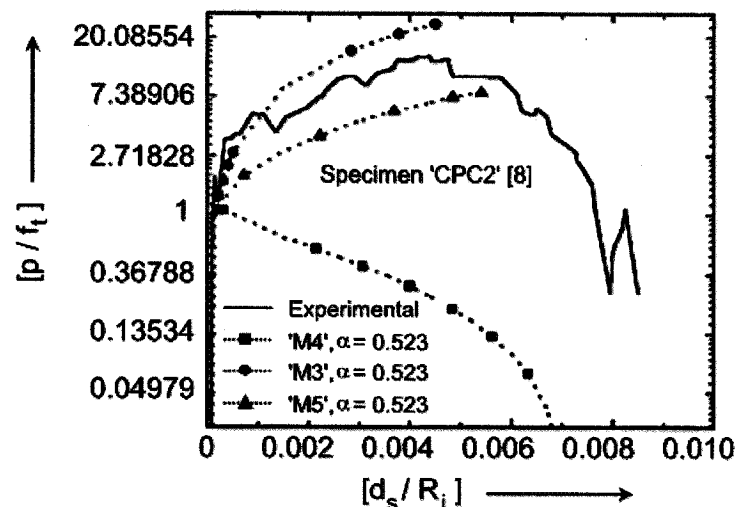

Figure 3.10: Normalized pressure (w.r.t. tensile strength) as a function of the normalized corrosion penetration depth (w.r.t. initial radius) (extracted from [34]).

55

The corrosion pressure increases substantially after a small amount of penetration depth due to the voluminous rust product. It reaches a maximum value of corrosion pressure when the crack had propagated almost 90% of the distance to the concrete cover. The experimental data shows a substantial drop off in corrosion pressure after the crack has reached the concrete cover.

3.2.4 SUWITO & XI MODEL

Suwito and Xi used a tension-softening model to track the progression of smeared cracking to the concrete cover [72]. The cracking is initiated by the interface pressure reaching the tensile strength of the concrete. A porous zone was assumed to exist at the concrete surface. Permeation of rust at the interface was also taken into account from the pressure buildup using Darcy's Law. The pressure at the interface will cause rust product to deposit within the concrete matrix. The relationship between the rust concentration and the pressure distribution was given as:

$$\frac{\partial C_{rust}}{\partial t} = \nabla\left(\frac{\kappa_{rust}}{\eta_{rust}} \nabla P_{rust} \right) \quad\quad\quad (3.68)$$

where C_{rust} is the concentration of rust, κ_{rust} is the permeability of rust in the porous concrete, η_{rust} is the viscosity of rust, and P_{rust} is the pressure distribution from the rust product accumulation. The concentration C_{rust} is set equal to $\beta \cdot P_{rust}$, where β is the state function for the concrete and is determined by the amount of rust saturation. The volume of rust that permeates into the concrete matrix from the pressure buildup in the model is calculated:

$$V_{permeate} = \int_{R_i}^{R_o} 2\pi \cdot r \cdot C_{rust}\, dr \quad\quad\quad (3.69)$$

The volume of rust that permeates away from the corrosion site can be added to the available volume for rust deposits for the particular model used. This will slow down the rate at which concrete cracking will occur. Suwito & Xi solved for the corrosion pressure as a function of time using an iterative numerical method. Figure 3.11 shows the interface pressure as a function of time.
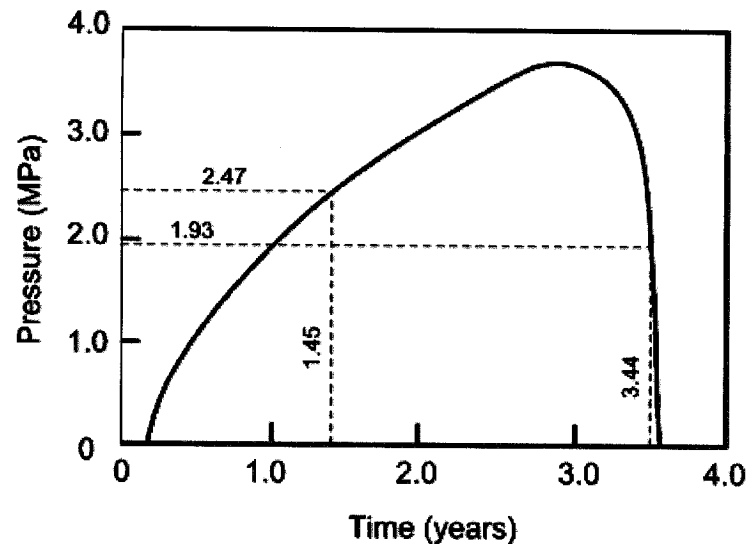
Figure 3.11: Corrosion pressure as a function of time using a tension-softening model that takes into account permeation of rust into the concrete and a porous zone layer (extracted from [72]).

The pressure builds after corrosion is initiated but not as rapidly as in previous models. As the crack starts to approach the concrete cover, pressure drops off quite rapidly. The strength of the concrete was assumed negligible in Figure 3.11 once the crack has reached the cover.

3.2.5 LEUNG MODEL

Leung developed an analytical solution describing the relationship between the propagation of assumed cracks in a reinforced concrete specimen and the thickness of the corrosion product [73]. The assumed cracking pattern was two cracks, each on opposite sides of the bar. In the corrosion model, the displacement of the steel form the corrosion pressure was taken into account. However, the loss of bar thickness from corrosion was not taken into account in the model. It was assumed the bar was embedded in an infinite surrounding of concrete. Fracture mechanics was used in order to derive stress intensity factors for the model. A lower bound and upper bound solution was derived. The lower bound solution (case I) was assumed to have no friction between the steel and concrete interface (free sliding), allowing for no constraints on the crack opening. The upper bound solution (case II) was assumed to have a perfect bond between the steel and concrete, allowing for no crack opening at the interface. Figure 3.12 illustrates the two situations.
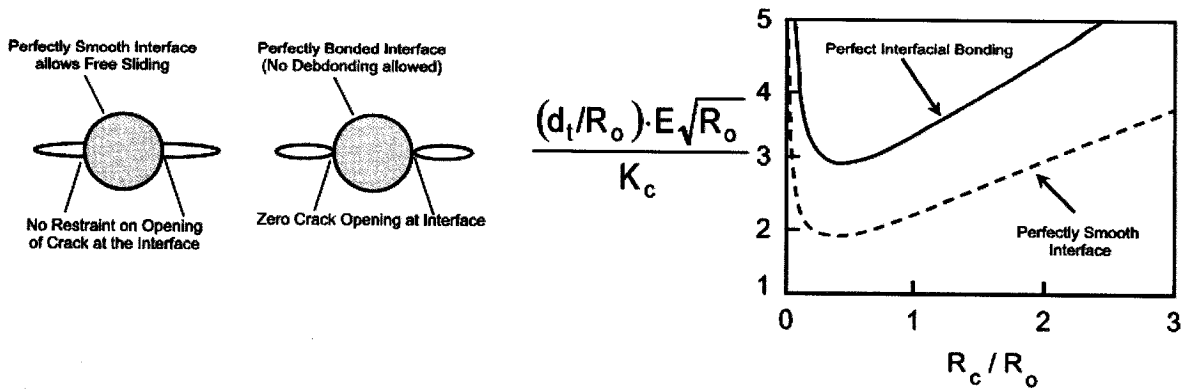
57

Figure 3.12: The **(a)** lower bound (free sliding) picture, **(b)** upper bound (no debonding) picture, and **(c)** solutions for both the lower and upper bound (extracted from [73]).

Leung used a previous derived solution for case I and derived case II, arriving at the solutions shown in Figure 3.12. K_c is the critical stress intensity factor for concrete. The real cracking behavior should lie somewhere between these two bounds. The solution shows that for crack sizes that are very small, the volume of corrosion products needed to propagate the crack further is substantial. However, the larger the initial crack size is, the less corrosion products necessary to further propagate the crack. As soon as the corrosion product reaches a critical value for a particular initial crack size, the crack will jump over to the rising portion of the same curve at the corresponding corrosion product thickness level. The results are of interest because it shows how quickly large cracks can form once a certain level of corrosion products have accumulated.

3.3   PROPAGATION MODELS (POST-CRACKING OF CONCRETE COVER)

Models have now been discussed that attempt to describe the corrosion pressure and crack propagation prior to the crack reaching the surface of the concrete. Discussion is now provided on models that describe the mechanical behavior of the concrete once cracking has propagated completely through the concrete cover.

3.3.1   LI, LAWANWISUT, & ZHENG MODEL

Li, Lawanwisut, & Zheng developed an analytical solution for the crack width opening at the surface [74]. The crack width w_c at the surface is given as:

$$w_c = 2\pi R_o \left[\varepsilon_\theta (R_o) - \varepsilon_{ct} \right] \quad\quad\quad\quad\quad\quad\quad\quad\quad (3.70)$$

where ε_θ is the hoop strain at the cover surface and ε_{ct} is the elastic hoop strain at fracture. One can calculate the hoop strain with the following equation:

$$\varepsilon_\theta (R_o) = \frac{2\,d_t/R_o}{(1-\upsilon)\left(R_r/R_o\right)^{\sqrt{\alpha_r}} + (1+\upsilon)\left(R_o/R_r\right)^{\sqrt{\alpha_r}}} \quad\text{.........................} (3.71)$$

where α_r is the tangential stiffness reduction factor (<1). Equation 3.70 can be rewritten:

$$w_c = \frac{4\pi d_t}{(1-\upsilon)\left(R_r/R_o\right)^{\sqrt{\alpha_r}} + (1+\upsilon)\left(R_o/R_r\right)^{\sqrt{\alpha_r}}} - \frac{2\pi R_o f_t}{E_{ef}} \quad\text{.................} (3.72)$$

Verification of the applicability of the equation was conducted by comparing the numerical solutions of the equation with experimental results [75]. Figure 3.13 plots the analytical solution along with the experimental points.
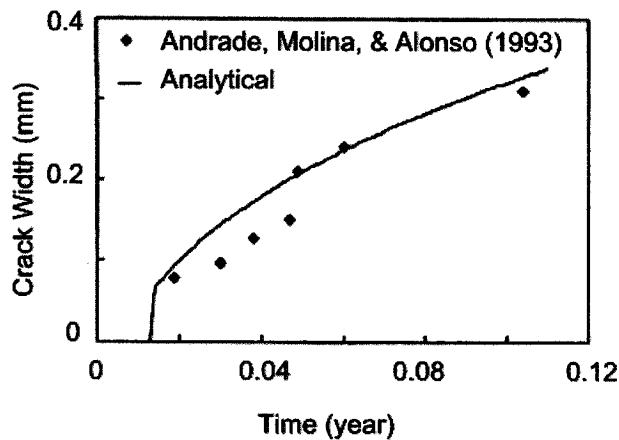

Figure 3.13: Analytical solution for crack width at the concrete cover surface caused by corrosion of reinforcement. Experimental data [75] was plotted for verification of the model (extracted from [76]).

3.3.2 VU, STEWART, & MULLARD MODEL

Vu, Stewart, and Mullard developed an empirical formula for use in calculating the time to reach a critical crack width [77]. Two parameters were determined as being critical for estimating the time to reach a critical crack width once surface cracking has initiated: water-to-cement ratio (w/c) and the depth of the concrete cover (R_o). The 'concrete quality' was quantitatively described as $R_o(w/c)^{-1}$. They accelerated corrosion in the reinforced concrete specimens galvanostatically ($i^A_{exp} = 100\ \mu A/cm^2$), monitoring the time for a surface crack to appear and different crack widths to be reached. The following empirical relationship between the time (in hours) to reach a critical crack width and the concrete quality was found:

$$t_{cr}\,(\text{experiment}) = A\left(\frac{R_o}{w/c}\right)^{B} \quad\text{..} (3.73)$$

59

The value of constants A and B are determined for particular critical crack width limit and are provided in Table 3.3. The coefficient of correlation is listed as well to provide an indication of the linear relationship between the concrete quality and the time since cracking initiated at the surface.

Table 3.3: Empirical constants for time to critical crack width limit equation (extracted from [77]).

Critical crack width (mm)	Constants		Coefficient of Correlation
w_{cr}	A	B	R
0.3	65	0.45	0.89
0.5	225	0.29	0.60
1.0	700	0.23	0.45

The correlation between the concrete quality and the time since the initiation of cracking decreases as the crack width increases. Since the corrosion current density in a real structure will most likely not be 100 $\mu A/cm^2$, an equation for extrapolation of the time to reach a critical crack width is created:

$$t_{cr}\left(\exp\right) = k_R \cdot \frac{i^A_{exp}}{i^A_{real}} \cdot t_{cr}\left(\text{experiment}\right) \quad\quad (3.74)$$

The correction factor k_R is used to account for discrepancies between the mechanical response of concrete from different loading rates (i.e. sensitivity to corrosion rate). This will be discussed further in Chapter 6 with regards to the experimental results presented in this document. For corrosion current densities below 200 $\mu A/cm^2$, k_R can be estimated from experimental data:

$$k_R \approx 0.95\left[e^{\left(-0.3\cdot\frac{i^A_{exp}}{i^A_{real}}\right)} - \frac{1}{2,500}\cdot\frac{i^A_{exp}}{i^A_{real}} + 0.3\right] \quad\quad (3.75)$$

3.3.3 WANG & LIU MODEL

Wang & Liu continued the modeling effort of [65] once surface cracks were created. Once cracks reach the concrete cover, Equation 3.65 changes because there is no longer an uncracked outer ring. The equilibrium equation is now:

$$p_{cor}\cdot R_r = \int_{R_r}^{R_c} \sigma_\theta\left(r\right)dr \quad\quad (3.76)$$

The radial displacement distribution (Equation 3.53) will also change. There is no longer a crack tip layer radius (R_c) so the outer cover radius (R_o) is used for a substitution. Also, the critical tensile hoop strain,

written f_t/E in Equation 3.53, was changed to the average hoop strain at the concrete cover ($\varepsilon_{\theta o}$). The elastic radial displacement distribution, assumed over the entire cylinder that is now completely cracked, is the following:

$$u(r) = r \cdot \varepsilon_\theta (r) = r \cdot \varepsilon_{\theta o} \cdot \frac{\left(R_o/r \right)^2 + 1}{2} \quad\text{.. (3.77)}$$

Assuming $R_o = R_c$ for Equation 3.47 as well, the radial displacement at the inner wall ($r = R_i$) from corrosion product accumulation is now written:

$$u_r\big|_{r=R_i} = R_r - R_i = d_r - d_s = \frac{(n-1)\left(2R_i d_s - d_s^2\right)}{\left(R_o + R_i\right)} \quad\text{.................... (3.78)}$$

This assumes that the volume created by the cracks for rust products to deposit stay triangular in shape. While this is not entirely accurate, it is a reasonable assumption. Setting Equation 3.77 equal to Equation 3.78 at $r = R_c$ yields a relationship between the steel bar thickness loss from corrosion and the average hoop strain at the concrete cover once cracks have reached the cover:

$$\frac{(n-1)\left(2R_i d_s - d_s^2\right)}{\left(R_o + R_i\right)} = R_i \cdot \varepsilon_{\theta o} \cdot \frac{\left(R_o/R_i \right)^2 + 1}{2} \quad\text{................................ (3.79)}$$

The average hoop strain at the concrete cover is used to determine which tension softening equation to use to calculate hoop stress. Again, the radial distances RR1 and RRu where the hoop strains reach ε_1 and ε_u respectively are written for convenience. The radial distance RR1 is written again by using Equation 3.51 and now assuming $R_o = R_c$.

$$RR1 = \frac{R_o}{\sqrt{2\,\varepsilon_1/\varepsilon_{\theta o} - 1}} \quad\text{.. (3.80)}$$

Wang & Liu assume a lower bound radial displacement distribution (as shown in Figure 3.6) once ε_u has been breached at a location. The displacement at the initial radius ($u_r\big|_{r=Ri}$) is assumed to have the same displacement as the location of the layer at a hoop strain equal to ε_u ($u_r\big|_{r=RRu}$). Using Equation 3.77:

$$RRu = \frac{u_r\big|_{r=R_i}}{\varepsilon_u} \quad\text{.. (3.81)}$$

61

This assumption is not entirely compatible with Equation 3.79 because it was assumed an elastic distribution was valid over the entire cross-section in order to calculate $\varepsilon_{\theta o}$. However, the assumption affects the overall solution marginally and is kept to maintain a consistent model to [71]. Table 3.4 provides the conditions with the corresponding solution for the integral of hoop stress.

Table 3.4: Hoop stress integral equations after cracking reaches the concrete cover ($\varepsilon_{ct} < \varepsilon_{\theta o}$) [71].

#	Condition:	$I = \int_{R_r}^{R_c} \sigma_\theta (r)\, dr =$	Solution:
1	$\varepsilon_{\theta o} \leq \varepsilon_1 < \varepsilon_u < \varepsilon_{\theta i}$	$\int_{RRu}^{RR1} \sigma_{\theta 3}(r)\, dr + \int_{RR1}^{R_o} \sigma_{\theta 2}(r)\, dr$	$\int_{RRu}^{RR1} \sigma_{\theta 3}(r)\, dr = \dfrac{0.15 f_t}{\varepsilon_u - \varepsilon_1}\left[\varepsilon_u (RR1 - RRu) - \dfrac{\varepsilon_{\theta o}}{2}\left(\dfrac{R_o^2}{RRu} - \dfrac{R_o^2}{RR1} + RR1 - RRu\right)\right]$ $\int_{RR1}^{R_o} \sigma_{\theta 2}(r)\, dr = f_t\left[\dfrac{\varepsilon_1 - 0.15\varepsilon_{ct}}{\varepsilon_1 - \varepsilon_{ct}}\cdot (R_o - RR1) - \dfrac{0.85}{(\varepsilon_1 - \varepsilon_{ct})}\cdot \dfrac{\varepsilon_{\theta o}}{2}\dfrac{R_o^2 - RR1^2}{RR1}\right]$
2	$\varepsilon_1 < \varepsilon_{\theta o} \leq \varepsilon_u < \varepsilon_{\theta i}$	$\int_{RRu}^{R_o} \sigma_{\theta 3}(r)\, dr$	$\int_{RRu}^{R_o} \sigma_{\theta 3}(r)\, dr = \dfrac{0.15 f_t}{\varepsilon_u - \varepsilon_1}\left[\varepsilon_u (R_o - RRu) - \dfrac{\varepsilon_{\theta o}}{2}\left(\dfrac{R_o^2 - RRu^2}{RRu}\right)\right]$
3	$\varepsilon_u < \varepsilon_{\theta o} \leq \varepsilon_{\theta i}$	$\int_{R_r}^{R_o} \sigma_{\theta 4}(r)\, dr$	$\int_{R_r}^{R_o} \sigma_{\theta 4}(r)\, dr = 0$
4	$\varepsilon_1 < \varepsilon_{\theta o} < \varepsilon_{\theta i} \leq \varepsilon_u$	$\int_{R_i}^{R_o} \sigma_{\theta 3}(r)\, dr$	$\int_{R_i}^{R_o} \sigma_{\theta 3}(r)\, dr = \dfrac{0.15 f_t}{\varepsilon_u - \varepsilon_1}\left[\varepsilon_u (R_o - R_i) - \dfrac{\varepsilon_{\theta o}}{2}\left(\dfrac{R_o^2 - R_i^2}{R_i}\right)\right]$
5	$\varepsilon_{\theta o} < \varepsilon_1 < \varepsilon_{\theta i} \leq \varepsilon_u$	$\int_{R_i}^{RR1} \sigma_{\theta 3}(r)\, dr + \int_{RR1}^{R_o} \sigma_{\theta 2}(r)\, dr$	$\int_{R_i}^{RR1} \sigma_{\theta 3}(r)\, dr = \dfrac{0.15 f_t}{\varepsilon_u - \varepsilon_1}\left[\varepsilon_u (RR1 - R_i) - \dfrac{\varepsilon_{\theta o}}{2}\left(\dfrac{R_o^2}{R_i} - \dfrac{R_o^2}{RR1} + RR1 - R_i\right)\right]$ $\int_{RR1}^{R_o} \sigma_{\theta 2}(r)\, dr = f_t\left[\dfrac{\varepsilon_1 - 0.15\varepsilon_{ct}}{\varepsilon_1 - \varepsilon_{ct}}\cdot (R_o - RR1) - \dfrac{0.85}{(\varepsilon_1 - \varepsilon_{ct})}\cdot \dfrac{\varepsilon_{\theta o}}{2}\dfrac{R_o^2 - RR1^2}{RR1}\right]$
6	$\varepsilon_{\theta o} < \varepsilon_{\theta i} \leq \varepsilon_1$	$\int_{R_i}^{R_o} \sigma_{\theta 2}(r)\, dr$	$\int_{R_i}^{R_o} \sigma_{\theta 2}(r)\, dr = f_t\left[\dfrac{\varepsilon_1 - 0.15\varepsilon_{ct}}{\varepsilon_1 - \varepsilon_{ct}}\cdot (R_o - R_i) - \dfrac{0.85}{(\varepsilon_1 - \varepsilon_{ct})}\cdot \dfrac{\varepsilon_{\theta o}}{2}\dfrac{R_o^2 - R_i^2}{R_i}\right]$

Pantazopoulou & Papoulia solved the boundary value problem using a finite difference scheme [65]. A linear rate law (Faraday's Law) and a parabolic rate law (referred to as 'Liu & Weyers (1998)' in their analysis) were used. The problem was solved with no rust product accumulating in the cracks and then with the cracks completely filled with rust product for both rate laws. The solutions are shown in Figures 3.14 and 3.15 ($i_{cor} = 0.018$ A/m^2, $\alpha = 0.622$), respectively.
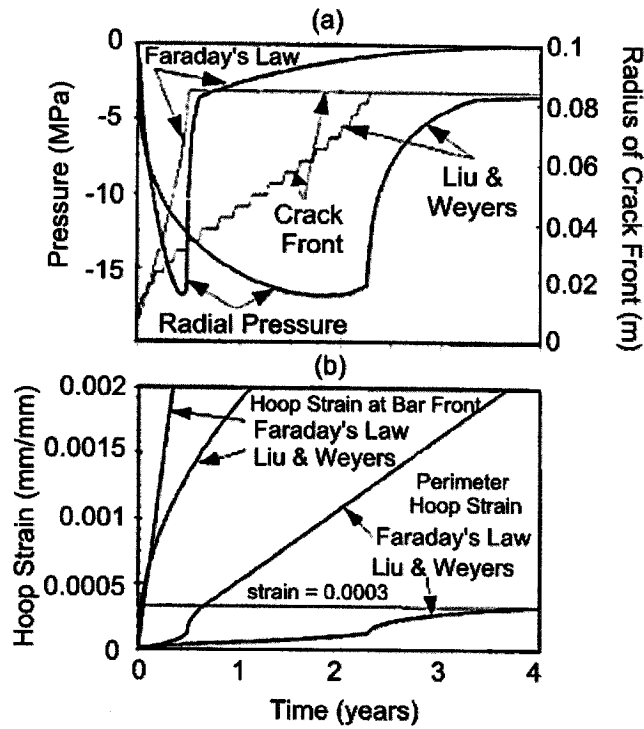
Figure 3.14: **(a)** Pressure and **(b)** hoop strain for no rust product accumulating in cracks as a function of time (extracted from [65]).
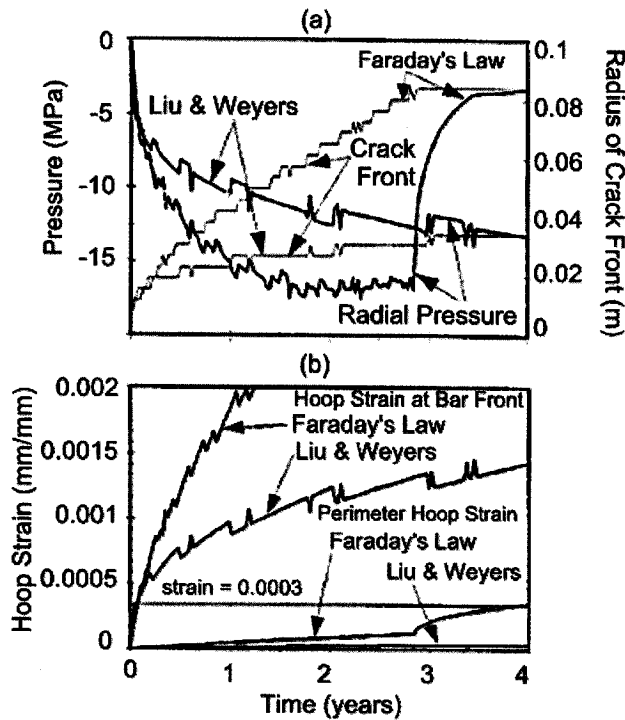

Figure 3.15: **(a)** Pressure and **(b)** hoop strain with rust product accumulating in cracks as a function of time (extracted from [65]).

63

Figures 3.14 and 3.15 show the corrosion pressure at the steel/concrete interface. The corrosion pressure builds until cracking occurs for both the linear and parabolic rate laws. However, the parabolic rate law takes significantly longer to rupture than with the linear rate law. For Figure 3.15, the rust product fills the cracks completely and a parabolic rate law is assumed. The time to cover cracking is significantly delayed. Realistically, there are probably partially filled cracks with rust product accumulating initially at a linear rate and later at a parabolic rate. Notice that when the crack front reaches the surface, there is a substantial drop off in corrosion pressure for both rate laws.

3.4   FINITE ELEMENT MODELS

A brief review of previous work on finite element models towards reinforced concrete corrosion is now provided.

3.4.1   OHTSU & YOSIMURA MODEL

Ohtsu and Yosimura used a pressure vessel to model the volume increase from creation of corrosion products [78]. From the boundary conditions, equations for the stress state and displacement were formulated due to the pressure at the hole. The displacements were used to solve for the stress intensity factor K_I at the location of proposed cracks. When K_I exceeded the critical stress intensity factor, K_{IC}, for concrete, the crack would propagate further. Figure 3.16 shows the boundary element model (BEM) used.
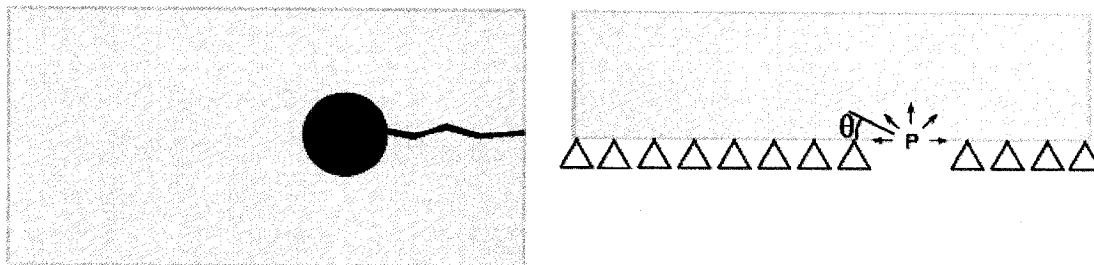
Figure 3.16: Boundary element model (extracted from [78]).

To model the propagation of the crack tip, displacement constraints are released at the node located at the crack tip. Two different pressure distributions were modeled, uniform and vertical. The vertical pressure distribution is simply the uniform pressure distribution without any horizontal contribution. The vertical pressure distribution was modeled to investigate cases where cracking around the reinforcement destroys the contact between the steel and concrete partially. The results for uniform pressure applied at the hole, with the generation of a surface crack (extending from rebar to concrete cover), are shown in Figure 3.17(a).
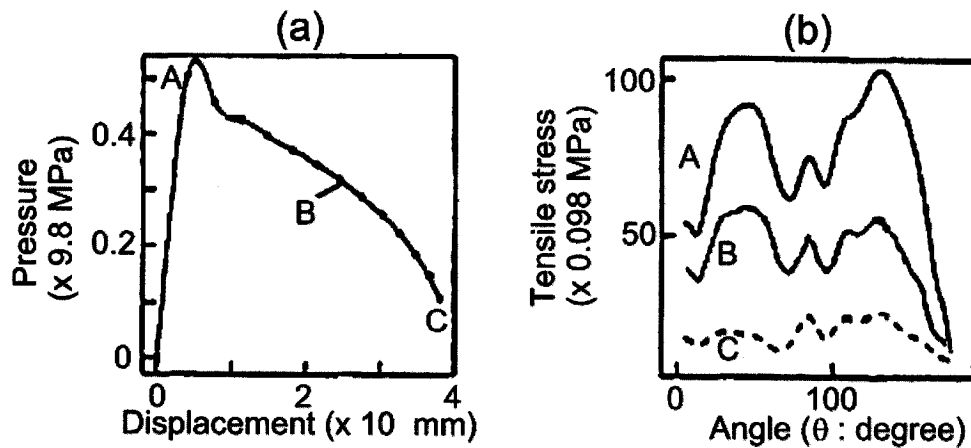
64

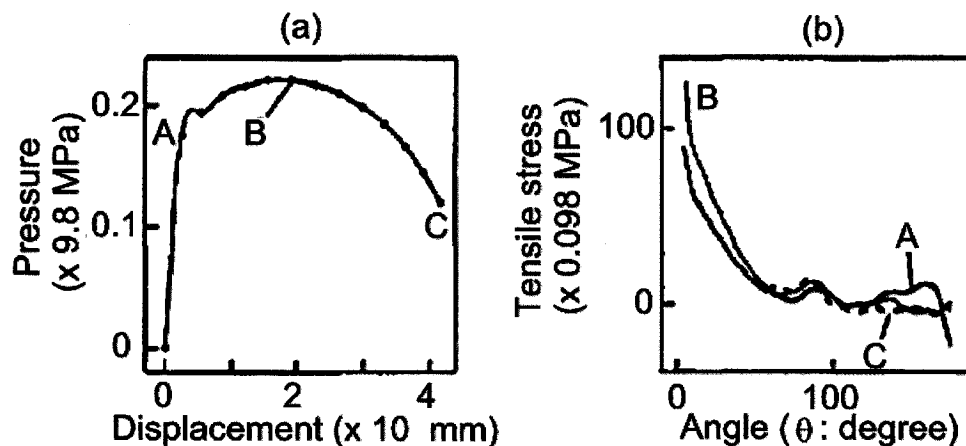**Figure 3.17:** **(a)** Pressure as a function of displacement and **(b)** tensile stress as a function of angle for a uniform pressure distribution (extracted from [78]).

The pressure shown is at the top of the hole. Point A marks the initiation of the surface crack. The tensile stresses in the concrete are shown in Figure 3.17(b). Notice that there are large stresses at 45° and 135°. These large stresses could explain the initiation of alternative cracks. The results for a vertical pressure distribution with the generation of a surface crack are shown in Figure 3.18(a).

Figure 3.18: **(a)** Pressure as a function of displacement and **(b)** tensile stress as a function of angle for a vertical pressure distribution (extracted from [78]).

After the crack is initiated at point A, the pressure continues to climb. At point B, the pressure finally starts to decrease. It appears as though an alternative crack at 0° could be created. This type of modeling is of interest because it allows one to understand better the different crack distributions that arise during corrosion of reinforced concrete. Since completely uniform corrosion is never realized in real structures, the various pressure distributions help to explain some of the different cracking behavior.

65

3.4.2 PADOVAN & JAE MODEL

Padovan and Jae used finite element analysis to model crack propagation caused by the rust product accumulation [79]. In the model, a global mesh was created with a moveable template mesh assigned to each crack tip to more accurately calculate the crack tip behavior (i.e. stress intensity factor, crack direction, and growth). To calculate the stress state within the moveable template, the load and deflection data along the boundaries are found by interpolation of the global field. The global field is determined from the displacement caused by the growing oxide layer. A slowed rust accumulation rate relative to rust thickness was assumed via an empirical relationship (similar to the parabolic rate law). The tensile fracture strength of concrete was used as the criteria for the initiation of cracking and determined the direction of the crack as time progressed. The case of all rebar uniformly corroding in a column (column 1), corner rebar uniformly corroding in a column (column 2), and all rebar uniformly corroding in a slab are shown in Figure 3.19(a).

(a)   (b)
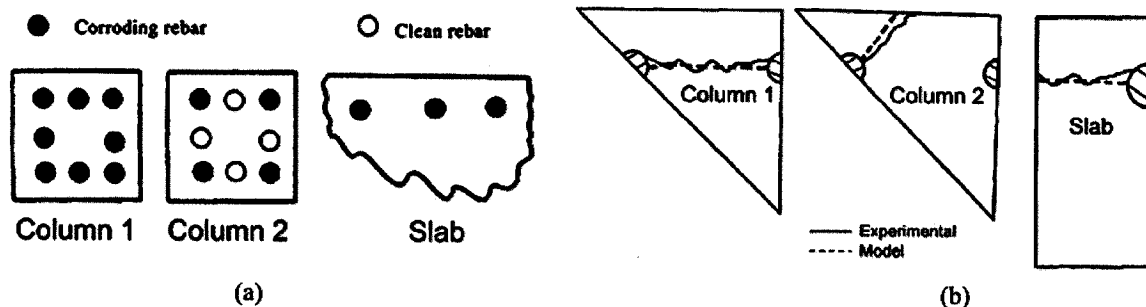
Figure 3.19: (a) Rebar uniformly corroding in a column (column 1), corner rebar uniformly corroding in a column (column 2), and all rebar uniformly corroding in a slab. (b) Experimental and finite element results. All figures extracted from [79].

Figure 3.19(b) shows the comparison of the crack trajectory using the model, compared to the crack trajectory of experimental corrosion specimens for column 1, column 2, and the slab. Cracks from both corroding rebar connect, creating cover peeling in column 1. In column 2, the cracks from the corroding rebar in the corner lead to the corner cracking off. In the slab, the cracks of the corroding rebar link up together and create cover peeling. The experimental cracks are more jagged than the model cracks and this was attributed to the non-homogeneous aggregate to cement material property transitions and that real concrete will most likely have stronger local properties. It should be noted that a non-uniform buildup of corrosion product was solved using the finite element program for the case of the slab. The corrosion product buildup was fastest on the side of the rebar closest to the surface of the slab. Cracking concentrated itself between the rebar and the surface but eventually the cracks between the non-uniformly corroding rebar linked up and again caused cover peeling.

66

3.4.3 LUNDGREN MODEL

Lundgren developed a corrosion model, coupled with a model of the bond mechanism between steel and concrete, to predict the bond strength using three-dimensional finite element analysis [80]. To calculate the critical deformation at the concrete interface to cause cover cracking, the stiffness of the reinforcement and rust layer, along with the deformation of the bond layer, are all taken into account. The stiffness of the rust is treated like a granular material, meaning that the stiffness increases with the stress level [80]. Lundgren estimates the relationship between stress and strain for rust as the following:

$$\sigma_n = K_{cor} \cdot \varepsilon_{cor}{}^p \quad\text{.. (3.82)}$$

where K_{cor} = 14 GPa and p = 7. The relationship was found from the experimental data shown in Figure 3.20(a).
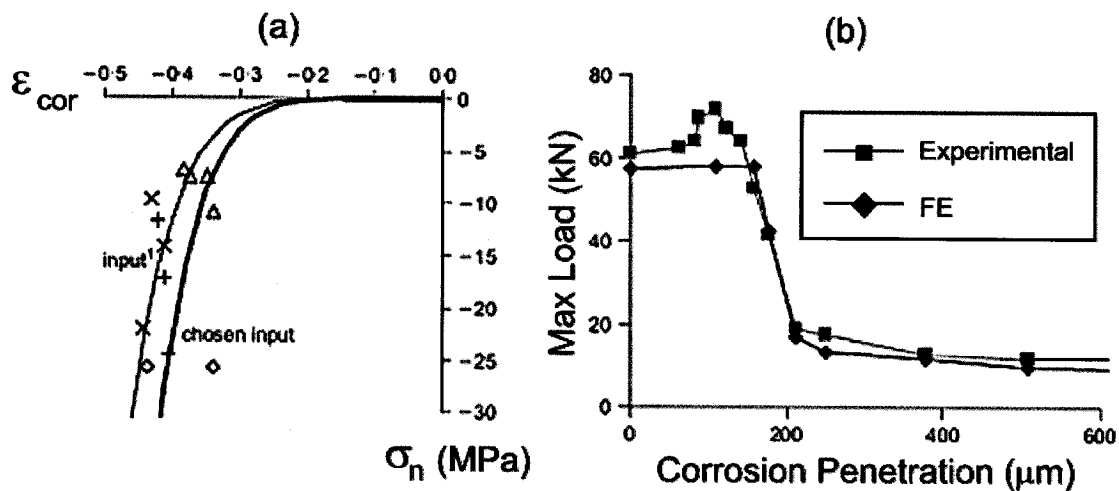
Figure 3.20: **(a)** The normal stress as a function of strain in the rust layer and **(b)** maximum load as a function of corrosion penetration for experimental and finite element results. Both plots extracted from [80].

Figure 3.20(b) is one example of using the FEA model to predict the maximum load during pullout tests of actual specimens. The experimental results were gathered by [52]. One can see that the finite element analysis reasonably predicts the maximum load during pullout tests.

3.4.4 MOLINA, ALONSO, & ANDRADE MODEL

Molina et al. [75,81] created a finite element model to simulate cracking. The material properties of the corrosion layer were assumed to be almost equal to that of water, due to the possibility of aqueous corrosion products. A smeared crack with tension softening of the cracked concrete was assumed. Figure 3.21 shows the solution provided from finite element analysis.
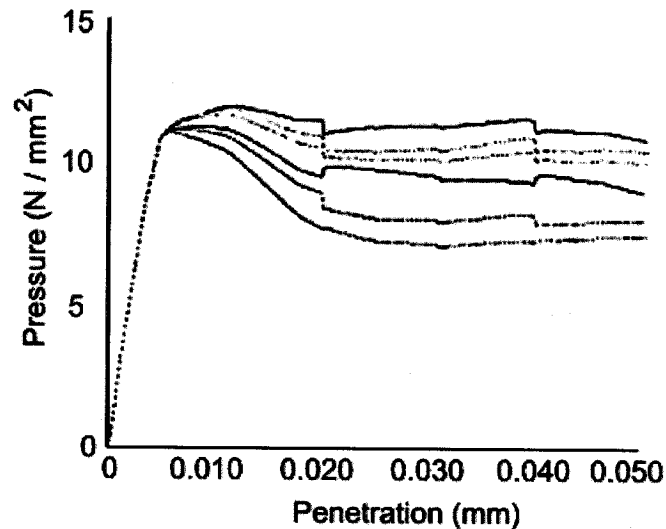
Figure 3.21: Finite element analysis solution for pressure at the rebar interface at six different elements (extracted from [81]).

Molina et al. assumed that the corrosion current was 100% efficient in dissolving iron atoms in the corrosion process, while noting that more work needed to be done in order to verify the true relationship. The pressure at the rebar interface is shown as increasing initially but then hitting a plateau. The specimen maintains pressure at the interface despite substantial cracking using this model.

3.5 SUMMARY

Examples of models used for the entire corrosion propagation period have now been discussed. Obviously, no model will ever capture the entire process completely due to the enormous amount of complexity, uncertainty, and interaction between different parameters. However, many simple models do a decent job of illustrating the major trends of the experimental data. The modeling allows for design changes to be explored, maintenance and rehabilitation efforts to be planned, and life cycle cost analysis to be conducted when used in a probabilistic manner.

For the purposes of this report, corrosion pressure has been solved as a function of corrosion percentage (i.e. percentage mass loss) for a reinforced mortar cylindrical specimen using a few of the analytical models discussed. The diameter of the rebar is 0.472" (11.99 mm) and the outer diameter of the concrete is 4" (101.6 mm). The mortar had a modulus of elasticity of 24.1 GPa and a tensile strength of $f_t = 3$ MPa. The corrosion product was considered twice the volume of steel ($n = 2$). Figure 3.22 shows the corrosion pressure solution as a function of corrosion percentage for the analytical models.
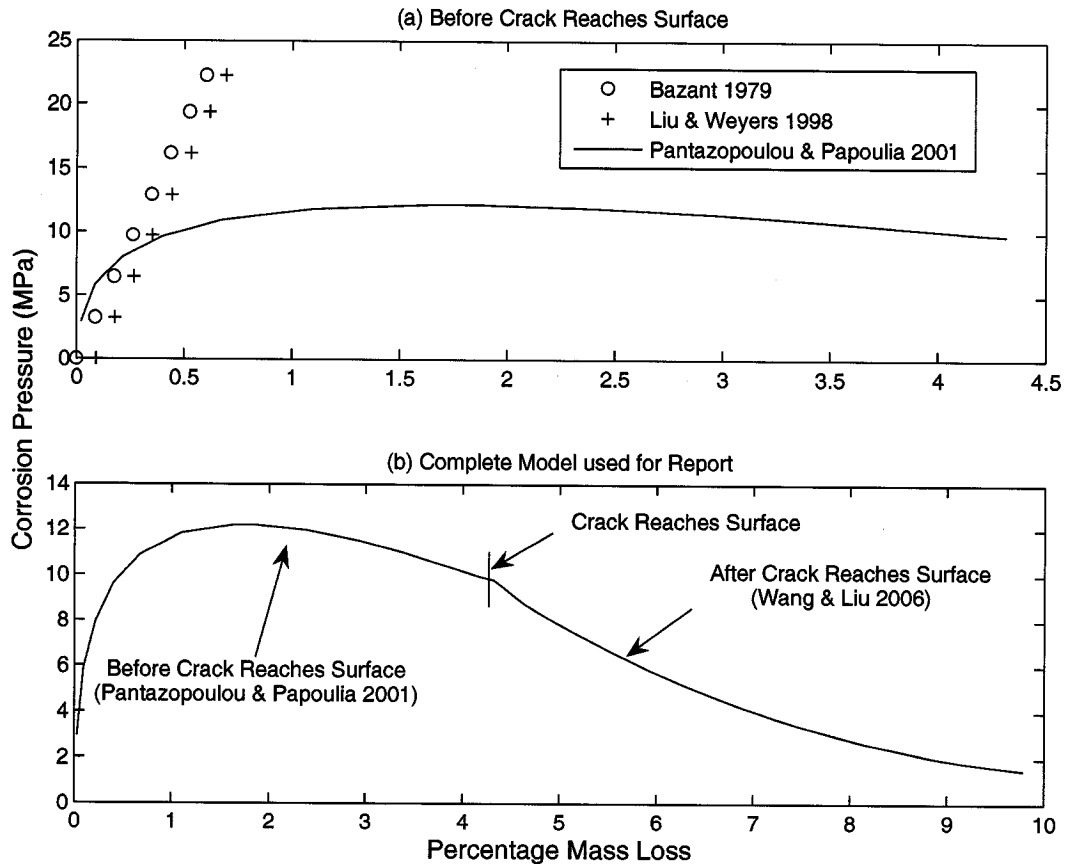
68

Figure 3.22: **(a)** Corrosion pressure as a function of corrosion percentage for a reinforced concrete cylindrical specimen prior to the crack reaching the concrete cover for three different models. **(b)** Pantazopoulou & Papoulia model conjoined with the Wang & Liu model (i.e. complete model), which was used to compare to guided wave results in Chapter 6.

Both the Bazant and Liu & Weyers model have a linear increase in pressure prior to the crack reaching the concrete cover. The Liu & Weyers model has a slight delay since corrosion products are assumed deposited in the porous zone. The Pantazopoulou & Papoulia model has a steep initial increase in pressure but then bows over as the rust is deposited in the propagating crack and the tension softening behavior begins. The Pantazopoulou & Papoulia model is conjoined with the Wang & Liu model in Figure 3.22 (bottom). Notice that once the crack reaches the surface, the interface pressure steadily decreases in value and then reaches a plateau. The conjoined model will be used for later analysis of guided wave experimental results.

As discussed in Section 3.4.3, the corrosion product is a granular material. As such the material properties are dependent on the confinement level. The corrosion pressure model shown in Figure 3.22 predicts that pressure increases at the mortar interface, causing an increase in the confinement of the

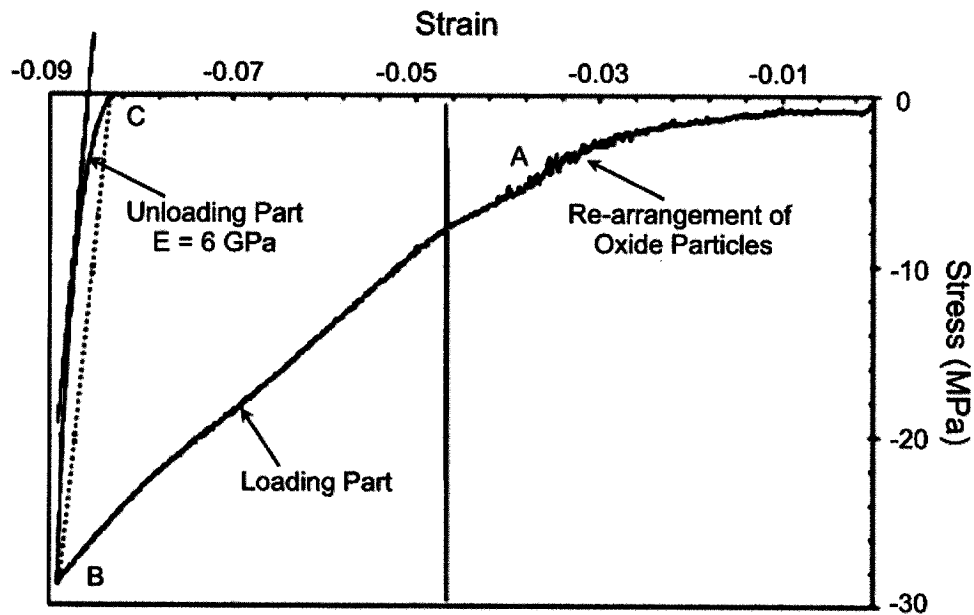corrosion product. Figure 3.23 shows a stress-strain curve for a compression test conducted on a dried iron oxide:

Figure 3.23: Compression test on a dried iron oxide (extracted from [82]).

Non-linear behavior is observed from point 0 to A, attributed to the rearrangement of the particles [82]. There is a linear response from point A to B during loading, but a non-linear response during the unloading (B-C). A permanent strain was present in the granular material after unloading. The tangent modulus was measured from the unloading portion of the curve for different stress-states (provided in Table 3.5).

Table 3.5: Tangent modulus from unloading portion of stress-strain curve for stress-states (extracted from [82]).

Stress (MPa)	E (GPa)
-28	7
-20	6
-10	4.38
-5	1.26

Therefore, the material properties of the corrosion product layer will change during the corrosion process. Adding to this complexity is the formation of several different types of corrosion products and the change in material properties due to being aqueous or dry. The effect of changing the material properties is studied in a parametric study contained in Chapter 4. The implications of the material properties change on guided wave testing are also discussed in Chapters 6 and 7.

70

CHAPTER 4:

GUIDED MECHANICAL WAVES IN A CYLINDER

A description of the theoretical framework for guided mechanical waves in a cylinder is described within this chapter. While the following presentation of guided mechanical wave theory is based on several derivations [83-88], the main source of information follows the derivation provided by [89]. The discussion will begin with the use of the 'equation of motion'. Appendix F has been provided to explain the derivation of the 'equation of motion' and wave propagation within bulk materials. For discussion of other waveguide geometries (e.g., plates and pipes) please refer to [85,89,90]. After the presentation of the theory, solutions to the layered system (i.e. rebar embedded in mortar) used in this report are provided and discussed. The selection process used to choose the guided waves to monitor corrosion in reinforced concrete is explained. A parametric study has been included to discuss the changes in guided wave behavior from several aspects associated with corrosion, geometry, and material property changes. The utility of guided mechanical waves for a wide-range of industrial inspection applications has been discussed previously [91].

There are a few assumptions for this particular presentation that must be addressed prior to beginning discussion of the model. It is assumed that:

1. continuous sinusoidal waves are propagated
2. waves propagate through homogeneous isotropic materials
3. the cylinder has infinite length
4. the bar is a solid cylinder

These assumptions do not invalidate the solutions of the model towards use in comparison to the experimental work. Previous authors [92-94] have shown that the propagation of pulses applies to the theory as well. Steel is considered a homogeneous isotropic material, while mortar (or concrete) is generally considered a heterogeneous viscoelastic material. However, the effects are limited and the solution is considered adequate, as it has been used in other investigations with success [23,95-100]. Previous studies [101] have shown that the finite length has a negligible role in determining wave behavior when the diameter-to-length ratio for the bar is below 0.4. The diameter-to-length ratio used in the current study is well below this value for all tests. Beard [95] has shown that the wave mode features are largely unaffected by the presence of ribs, provided the ratio of the wavelength to the surface characteristic dimension of the ribs is large. Strong scattering effects were described for longitudinal modes (>600 kHz) propagating in rebar 7/8" (22.2 mm) in diameter [102]. There was particular sensitivity to diagonal rib patterns compared to an orthogonal axisymmetric rib pattern. The presence of

71

ribs is thought to affect the behavior of the guided waves in certain frequency ranges used in the experimental investigation used in this study. At 2.5 MHz, the ratio of the wavelength to the width of the rib for the lowest attenuated longitudinal mode is approximately 3 (compared to a ratio of 82 at 80 kHz). However, at even higher frequencies wave energy becomes more concentrated at the center of the bar. This concentration of energy should create less sensitivity to the effects of the ribs. Experimental results are provided in Chapter 6 illustrating the effect of the ribs on guided wave behavior.

4.1 THEORY

Wave propagation within a bounded configuration, such as a cylindrical bar, is considered a guided wave. The cylindrical bar is considered the waveguide. Energy flows mainly along the direction of the guiding configuration [103]. Guided waves are combinations of compressional and shear waves that continually interact with the boundaries to form a composite wave [96]. Therefore, the geometry and boundary conditions of the waveguide affect the characteristics of the propagating wave.

For a cylindrical bar in a vacuum, the only boundary condition that must be met is that the outer surface is traction free (zero stress). The displacement profile at the outer surface has no imposed boundary conditions. The boundary conditions for stress at the outer radius ($r = a$) are listed below for a cylindrical bar in a vacuum:

$$\sigma_{rr}\big|_{r=a} = 0 \quad\text{.. (4.1)}$$

$$\tau_{rz}\big|_{r=a} = 0 \quad\text{.. (4.2)}$$

$$\tau_{r\theta}\big|_{r=a} = 0 \quad\text{.. (4.3)}$$

For a review of stress terms within a cylindrical coordinate system please refer to Appendix G. For a multilayered waveguide (e.g., rebar embedded in mortar), the derivation is similar to a solid cylindrical bar in a vacuum; however stress *and* displacement boundary conditions must now be met at the layer interfaces ($r = a$):

$$u_r\big|_{r=a^+} = u_r\big|_{r=a^-} \quad\text{.. (4.4)}$$

$$u_\theta\big|_{r=a^+} = u_\theta\big|_{r=a^-} \quad\text{.. (4.5)}$$

$$u_z\big|_{r=a^+} = u_z\big|_{r=a^-} \quad\text{.. (4.6)}$$

$$\sigma_{rr}\big|_{r=a^+} = \sigma_{rr}\big|_{r=a^-} \quad\text{.. (4.7)}$$

$$\tau_{rz}\big|_{r=a^+} = \tau_{rz}\big|_{r=a^-} \quad\text{.. (4.8)}$$

$$\tau_{r\theta}\big|_{r=a^+} = \tau_{r\theta}\big|_{r=a^-} \quad\text{.. (4.9)}$$

72

Waveguides affect two different wave characteristics: velocity and attenuation. In a bulk substance, the velocity of a waveform is generally considered constant and independent of frequency. However, the wave velocity in a waveguide becomes dependent on the frequency (i.e. dispersive). In a bulk substance and a waveguide, attenuation of the waveform is caused by material absorption. However, in multilayered waveguides (e.g. rebar embedded in mortar) wave energy can also leak out into the surrounding material. To determine how a cylindrical waveguide will specifically affect waveform characteristics one must start with the equation of motion:

$$\rho \frac{\partial^2 s}{\partial t^2} = (\lambda + 2\mu)\nabla\nabla \bullet s - \mu\nabla\times\nabla\times s \quad\text{...} (4.10)$$

where ρ is the density of the material, λ and μ are Lamé's constants, and s is the displacement vector. For further information on the derivation of the equation of motion refer to Appendix F. The equation of motion is written in terms of vector operators (refer to Appendix H) where different coordinate systems can be transferred. Therefore, a cylindrical coordinate system (refer to Appendix G) is used, writing the displacement vector as:

$$s = u_r i_r + u_\theta i_\theta + u_z i_z \quad\text{...} (4.11)$$

Much like the derivation provided in Appendix F, where the original displacement of a point in space for rectangular coordinates is given as (u_x, u_y, u_z), it is now given in cylindrical coordinates as (u_r, u_θ, u_z). If the displacement vector (written in cylindrical coordinates) is inserted into the equation of motion, one arrives at the following set of equations:

$$\rho\frac{\partial^2 u_r}{\partial t^2} = (\lambda+2\mu)\left(\frac{\partial^2 u_r}{\partial r^2}+\frac{1}{r}\frac{\partial u_r}{\partial r}-\frac{u_r}{r^2}+\frac{\partial^2 u_z}{\partial z\partial r}+\frac{\partial^2 u_\theta}{\partial r\partial\theta}-\frac{1}{r^2}\frac{\partial u_\theta}{\partial\theta}\right)-\mu\left(\frac{1}{r^2}\frac{\partial u_\theta}{\partial\theta}+\frac{1}{r}\frac{\partial^2 u_\theta}{\partial\theta\partial r}-\frac{1}{r^2}\frac{\partial^2 u_r}{\partial\theta^2}-\frac{\partial^2 u_r}{\partial z^2}+\frac{\partial^2 u_z}{\partial z\partial r}\right)\text{.................} (4.12)$$

$$\rho\frac{\partial^2 u_\theta}{\partial t^2} = (\lambda+2\mu)\left(\frac{1}{r^2}\frac{\partial u_r}{\partial\theta}+\frac{1}{r}\frac{\partial^2 u_r}{\partial\theta\partial r}+\frac{1}{r^2}\frac{\partial^2 u_\theta}{\partial\theta^2}+\frac{1}{r}\frac{\partial^2 u_z}{\partial\theta\partial z}\right)-\mu\left(\frac{1}{r}\frac{\partial^2 u_z}{\partial z\partial\theta}-\frac{\partial^2 u_\theta}{\partial z^2}+\frac{1}{r^2}u_\theta-\frac{1}{r}\frac{\partial u_\theta}{\partial r}-\frac{\partial^2 u_\theta}{\partial r^2}-\frac{1}{r^2}\frac{\partial u_r}{\partial\theta}-\frac{1}{r}\frac{\partial^2 u_r}{\partial r\partial\theta}\right)\text{....} (4.13)$$

$$\rho\frac{\partial^2 u_z}{\partial t^2} = (\lambda+2\mu)\left(\frac{1}{r}\frac{\partial u_r}{\partial z}+\frac{\partial^2 u_r}{\partial z\partial r}+\frac{1}{r}\frac{\partial^2 u_\theta}{\partial z\partial\theta}+\frac{\partial^2 u_z}{\partial z^2}\right)-\mu\left(\frac{1}{r}\frac{\partial u_r}{\partial z}+\frac{\partial^2 u_r}{\partial r\partial z}-\frac{1}{r}\frac{\partial u_z}{\partial r}-\frac{\partial^2 u_z}{\partial r^2}-\frac{1}{r^2}\frac{\partial^2 u_z}{\partial\theta^2}+\frac{1}{r}\frac{\partial^2 u_\theta}{\partial\theta\partial z}\right)\text{.....................} (4.14)$$

Using Helmholtz decomposition, the displacement vector is rewritten in terms of an irrotational and rotational part:

$$s = u_r i_r + u_\theta i_\theta + u_z i_z = \nabla\Phi + \nabla\times H \quad\text{...} (4.15)$$

73

where Φ is the scalar potential (irrotational) and $\mathbf{H} = H_r \mathbf{i_r} + H_\theta \mathbf{i_\theta} + H_z \mathbf{i_z}$ is the vector potential (rotational). The following stipulation is given for the vector potential:

$$\nabla \cdot \mathbf{H} = F(\mathbf{r},t) = 0 \dotfill (4.16)$$

where $\mathbf{r}$ is the position vector and t is the time. Assuming that the divergence of the vector potential is zero eliminates the possibility of sources or sinks of energy in the region, making the field solenoidal [89]. This allows for the unique determination of three components of the displacement vector $\mathbf{u}$ from the four components of the two potentials Φ and $\mathbf{H}$ [89]. The displacement vector can be rewritten in terms of the potentials Φ and $\mathbf{H}$:

$$\mathbf{s} = \left(\frac{\partial \Phi}{\partial r} + \frac{1}{r} \frac{\partial H_z}{\partial \theta} - \frac{\partial H_\theta}{\partial z} \right) \mathbf{i_r} + \left(\frac{1}{r} \frac{\partial \Phi}{\partial \theta} + \frac{\partial H_r}{\partial z} - \frac{\partial H_z}{\partial r} \right) \mathbf{i_\theta} + \left(\frac{\partial \Phi}{\partial z} + \frac{1}{r} \left(\frac{\partial}{\partial r}(rH_\theta) - \frac{\partial H_r}{\partial \theta} \right) \right) \mathbf{i_z} \dotfill (4.17)$$

The equation of motion can be rewritten in terms of the potentials Φ and $\mathbf{H}$ as well:

$$\nabla^2 \Phi = \left(\frac{1}{c_d^2} \right) \frac{\partial^2 \Phi}{\partial t^2} = \frac{\partial^2 \Phi}{\partial r^2} + \frac{1}{r} \frac{\partial \Phi}{\partial r} + \frac{1}{r^2} \frac{\partial^2 \Phi}{\partial \theta^2} + \frac{\partial^2 \Phi}{\partial z^2} \dotfill (4.18)$$

$$\nabla^2 \mathbf{H} = \left(\frac{1}{c_s^2} \right) \frac{\partial^2 \mathbf{H}}{\partial t^2} = \left(\nabla^2 H_r - \frac{H_r}{r^2} - \frac{2}{r^2} \frac{\partial H_\theta}{\partial \theta} \right) \mathbf{i_r} + \left(\nabla^2 H_\theta - \frac{H_\theta}{r^2} + \frac{2}{r^2} \frac{\partial H_r}{\partial \theta} \right) \mathbf{i_\theta} + \nabla^2 H_z \mathbf{i_z} \dotfill (4.19)$$

where c_d and c_s are the bulk dilatational (i.e. compressional) and shear wave speeds, respectively. Potentials must now be found that satisfy the wave equation by assuming a general form and modifying later. One can assume potentials with harmonic motion and r, θ, and z dependence. Since the wave propagates in the z-direction (along the cylinder axis) and does not change except due to harmonic motion and attenuation, the following form has been assumed:

$$\Phi = f(r)g_\phi(\theta)e^{i(kz-\omega t)} \dotfill (4.20)$$

$$H_r = -h_r(r)g_r(\theta)e^{i(kz-\omega t)} \dotfill (4.21)$$

$$H_\theta = -i(h_\theta(r)g_\theta(\theta)e^{i(kz-\omega t)}) \dotfill (4.22)$$

$$H_z = -i(h_z(r)g_z(\theta)e^{i(kz-\omega t)}) \dotfill (4.23)$$

where k is the wavenumber ($k = \omega/c_p$), ω is the angular frequency ($\omega = 2\pi f$), f is the frequency, c_p is the phase velocity, z is the axial distance, and t is the time. This form states that there is an unknown r and θ-dependence. The θ-dependence, assuming it exists, must be sinusoidal so the same solution exists at θ and $\theta + 2\pi$. Phase angles have been added to the potential equations to make terms drop out later. They

74

do not affect the final solution because they are compensated for by the coefficients of the functions themselves [89]. Plugging the general form of the scalar potential Φ and vector potential $\mathbf{H}$ into the equation of motion, the following differential equations are found:

$$\frac{\partial^2 f}{\partial r^2} + \frac{1}{r}\frac{\partial f}{\partial r} + \left(\alpha^2 - \frac{Q}{r^2}\right)f = 0 \quad\text{(4.24)}$$

$$\frac{\partial^2 h_r}{\partial r^2} + \frac{1}{r}\frac{\partial h_r}{\partial r} + \left(\beta^2 - \frac{(R+1)}{r^2}\right)h_r - i\frac{2}{r^2}\frac{1}{g_r}\frac{\partial g_\theta}{\partial \theta}h_\theta = 0 \quad\text{(4.25)}$$

$$\frac{\partial^2 h_\theta}{\partial r^2} + \frac{1}{r}\frac{\partial h_\theta}{\partial r} + \left(\beta^2 - \frac{(S+1)}{r^2}\right)h_\theta - i\frac{2}{r^2}\frac{1}{g_\theta}\frac{\partial g_r}{\partial \theta}h_r = 0 \quad\text{(4.26)}$$

$$\frac{\partial^2 h_z}{\partial r^2} + \frac{1}{r}\frac{\partial h_z}{\partial r} + \left(\beta^2 - \frac{T}{r^2}\right)h_z = 0 \quad\text{(4.27)}$$

where:

$$Q = -\frac{1}{g_\phi}\frac{\partial^2 g_\phi}{\partial \theta^2} \quad\text{(4.28)}$$

$$R = -\frac{1}{g_r}\frac{\partial^2 g_r}{\partial \theta^2} \quad\text{(4.29)}$$

$$S = -\frac{1}{g_\theta}\frac{\partial^2 g_\theta}{\partial \theta^2} \quad\text{(4.30)}$$

$$T = -\frac{1}{g_z}\frac{\partial^2 g_z}{\partial \theta^2} \quad\text{(4.31)}$$

and:

$$\alpha^2 = \frac{\omega^2}{c_d^{\,2}} - k^2 = \omega^2\left(\frac{1}{c_d^{\,2}} - \frac{1}{c_p^{\,2}}\right) \quad\text{(4.32)}$$

$$\beta^2 = \frac{\omega^2}{c_s^{\,2}} - k^2 = \omega^2\left(\frac{1}{c_s^{\,2}} - \frac{1}{c_p^{\,2}}\right) \quad\text{(4.33)}$$

The equations are very similar in form to that of the Bessel equation (refer to Appendix I). Looking at the differential equations resulting from the scalar wave equation and the third component of the vector wave equation, the equations would match with the Bessel equation if $Q = T = n^2$. Setting $Q = T = n^2$:

$$Q = -\frac{1}{g_\phi}\frac{\partial^2 g_\phi}{\partial \theta^2} = n^2 \quad\text{(4.34)}$$

75

$$T = -\frac{1}{g_z}\frac{\partial^2 g_z}{\partial \theta^2} = n^2 \quad \text{...} \quad (4.35)$$

then one possible solution for $g_\phi(\theta)$ and $g_z(\theta)$ is the following:

$$g_\phi(\theta) = g_z(\theta) = \cos(n\theta) + i\sin(n\theta) = e^{i(n\theta)} \quad \text{...................................} \quad (4.36)$$

In order for the same solution to exist at θ and $\theta + 2\pi$, 'n' must be an integer. Using the equation for θ-dependence shown above, the solution for the r-dependence in the scalar potential and the third component of the vector potential is the following:

$$f(r) = AZ_n(\alpha r) + BW_n(\alpha r) \quad \text{...} \quad (4.37)$$

$$h_z(r) = A_3 Z_n(\beta r) + B_3 W_n(\beta r) \quad \text{...} \quad (4.38)$$

where Z and W represent Bessel functions with the particular combination depending on whether α and β (Eqns. 4.32 & 4.33) are real, imaginary, or complex. The symbols A and B represent integration constants and are discussed shortly. Appendix I provides a brief overview of the different Bessel functions that are used, with an explanation of the recurrence parameter γ. Table 4.1 gives the conditional statements for the use of different Bessel functions:

Table 4.1: Conditional statements for the use of different Bessel functions.

		If $c_p > c_d$	If $c_d > c_p > c_s$	If $c_s > c_p$
Finite layer		$\gamma_1 = 1$	$\gamma_1 = -1$	$\gamma_1 = -1$
		$\gamma_2 = 1$	$\gamma_2 = 1$	$\gamma_2 = -1$
		$Z_n(\alpha r) = J_n(\alpha r)$	$Z_n(\alpha r) = I_n(\alpha r)$	$Z_n(\alpha r) = I_n(\alpha r)$
		$W_n(\alpha r) = Y_n(\alpha r)$	$W_n(\alpha r) = K_n(\alpha r)$	$W_n(\alpha r) = K_n(\alpha r)$
		$Z_n(\beta r) = J_n(\beta r)$	$Z_n(\beta r) = J_n(\beta r)$	$Z_n(\beta r) = I_n(\beta r)$
		$W_n(\beta r) = Y_n(\beta r)$	$W_n(\beta r) = Y_n(\beta r)$	$W_n(\beta r) = K_n(\beta r)$
Surrounding	Infinite layer	$\gamma_1 = 1$	$\gamma_1 = 1$	$\gamma_1 = 1$
		$\gamma_2 = 1$	$\gamma_2 = 1$	$\gamma_2 = 1$
		$W_n(\alpha r) = H_n^1(\alpha r)$	$W_n(\alpha r) = H_n^1(\alpha r)$	$W_n(\alpha r) = H_n^1(\alpha r)$
		$W_n(\beta r) = H_n^1(\beta r)$	$W_n(\beta r) = H_n^1(\beta r)$	$W_n(\beta r) = H_n^1(\beta r)$

The first and second components of the vector potential have a dependence on both g_r and g_θ and h_r and h_θ. The two components are grouped together and solved simultaneously. If one uses the same form for the θ-dependence as with g_ϕ and g_z, then subtracting the second equation from the first results in:

$$\left\{\frac{\partial^2}{\partial r^2} + \frac{1}{r}\frac{\partial}{\partial r} + \beta^2 - \frac{(n+1)^2}{r^2}\right\}(h_r - h_\theta) = 0 \quad \text{................................} (4.39)$$

where:

$$h_r - h_\theta = 2A_1 Z_{n+1}(\beta r) + 2B_1 W_{n+1}(\beta r) \quad \text{..} (4.40)$$

Adding the first component to the second component results in:

$$\left\{\frac{\partial^2}{\partial r^2} + \frac{1}{r}\frac{\partial}{\partial r} + \beta^2 - \frac{(n-1)^2}{r^2}\right\}(h_r + h_\theta) = 0 \quad \text{................................} (4.41)$$

where:

$$h_r + h_\theta = 2A_2 Z_{n-1}(\beta r) + 2B_2 W_{n-1}(\beta r) \quad \text{..} (4.42)$$

Since there are only six boundary conditions at each interface layer that must be met (u_r, u_{rz}, $u_{r\theta}$, σ_{rr}, τ_{rz}, $\tau_{r\theta}$) and there are eight integration constants (A, A_1, A_2, A_3, B, B_1, B_2, B_3), two of the integration constants can be eliminated. This is a property known as gauge invariance, meaning that the actual field is unaffected by changes in the potential solution (as long as the wave equations are satisfied) [104]. The integration constants A_2 and B_2 will be set to zero, resulting in $h_r(r) = -h_\theta(r)$. The form for the r-dependence in the case of the first and second components of the vector potential are shown below:

$$h_r = A_1 Z_{n+1}(\beta r) + B_1 W_{n+1}(\beta r) \quad \text{..} (4.43)$$

$$h_\theta = -(A_1 Z_{n+1}(\beta r) + B_1 W_{n+1}(\beta r)) \quad \text{................................} (4.44)$$

The general forms for the scalar and vector potentials are shown below:

$$\Phi = (A Z_n(\alpha r) + B W_n(\alpha r))e^{i(n\theta + kz - \omega t)} \quad \text{..} (4.45)$$

$$H_r = -(A_1 Z_{n+1}(\beta r) + B_1 W_{n+1}(\beta r))e^{i(n\theta + kz - \omega t)} \quad \text{................................} (4.46)$$

$$H_\theta = -i(A_1 Z_{n+1}(\beta r) + B_1 W_{n+1}(\beta r))e^{i(n\theta + kz - \omega t)} \quad \text{................................} (4.47)$$

$$H_z = -i(A_3 Z_n(\beta r) + B_3 W_n(\beta r))e^{i(n\theta + kz - \omega t)} \quad \text{................................} (4.48)$$

Now that the scalar and vector potentials have been rewritten in terms of Bessel functions, partial wave amplitudes are discussed. The partial wave amplitudes are the partial bulk wave contributions that interact to make a composite guided wave. The partial wave amplitudes are the integration constants: A,

A_1, A_3, B, B_1, B_3. The partial wave amplitudes represented by 'A', 'A1', and 'A3' are inward (-) propagating waveforms that are referred to as 'L-', 'SV-', and 'SH-', respectively. The partial wave amplitudes represented by 'B', 'B1', and 'B3' are outward (+) propagating waveforms and are referred to as 'L+', 'SV+', and 'SH+', respectively. 'L', 'SV', and 'SH' represent the bulk compressional, shear vertical, and shear horizontal components, respectively. The naming convention was created for plates, but was carried over to cylinders by previous authors [89]. All of the terms are contained in Table 4.2 for clarity.

Table 4.2: Naming convention for integration constants.

Integration Constant	A	B	A_1	B_1	A_3	B_3
Partial Wave	L-	L+	SV-	SV+	SH-	SH+

An illustration has been provided in Figure 4.1 to better explain what is meant by inward and outward propagating waves within cylindrical layers.
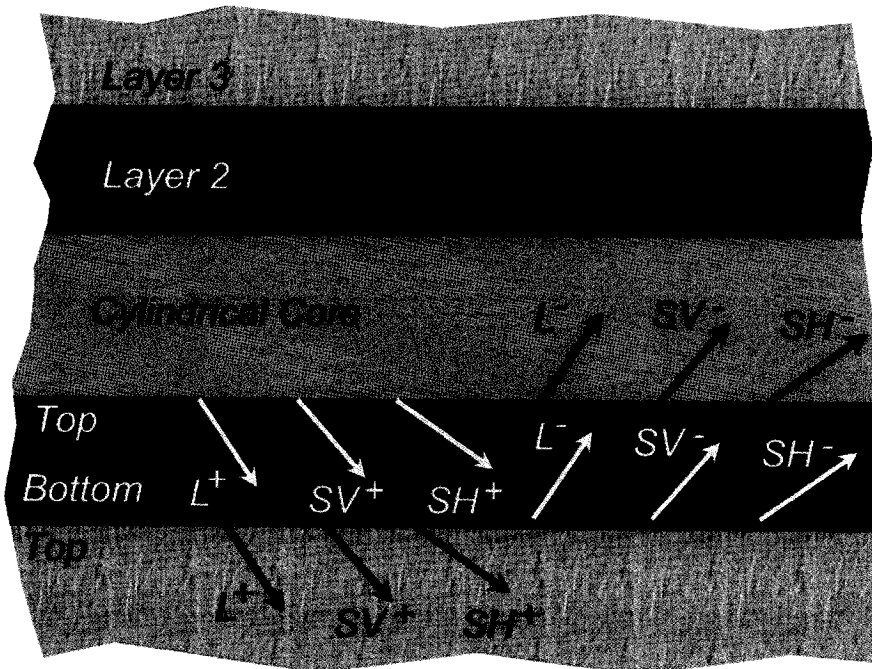
Figure 4.1: Inward and outward propagating waves in a multilayered cylinder (extracted from [89]).

Bessel functions represented by 'Z' in the equations are inward propagating waveforms, while those represented with 'W' are outward propagating waveforms. The cylindrical core only has inward (-) propagating waveforms. The core is modeled as a semi-infinite half-space. The outward (+) propagating waves not shown in the core are represented by the inward propagating waves from the other half of the core [89]. Semi-infinite surrounding layers (e.g. layer 3 in Figure 4.1) will have only outward (+)

78

propagating waves since no waves are reflected inward. The final forms of the boundary conditions are now written. Shortcuts for the derivatives of Z and W terms are found in Appendix I. The three displacements are written:

$$u_r = \frac{\partial \Phi}{\partial r} + \frac{1}{r}\frac{\partial H_z}{\partial \theta} - \frac{\partial H_\theta}{\partial z} = \left(\frac{\partial f}{\partial r} + \frac{n}{r}h_z + kh_r\right)e^{i(n\theta+kz-\omega t)}$$

$$= \frac{1}{r^2}\begin{pmatrix} A\left(nrZ_n(\alpha r) - r^2\gamma_1\alpha Z_{n+1}(\alpha r)\right) + B\left(nrW_n(\alpha r) - r^2\alpha W_{n+1}(\alpha r)\right) + \\ A_1 r^2 kZ_{n+1}(\beta r) + B_1 r^2 kW_{n+1}(\beta r) + A_3 nrZ_n(\beta r) + B_3 nrW_n(\beta r) \end{pmatrix}e^{i(n\theta+kz-\omega t)} \quad \text{...........................(4.49)}$$

$$u_\theta = \frac{1}{r}\frac{\partial \Phi}{\partial \theta} + \frac{\partial H_r}{\partial z} - \frac{\partial H_z}{\partial r} = i\left(\frac{n}{r}f + \frac{\partial h_z}{\partial r} - kh_r\right)e^{i(n\theta+kz-\omega t)}$$

$$= i\frac{1}{r^2}\begin{pmatrix} AnrZ_n(\alpha r) + BnrW_n(\alpha r) - A_1 r^2 kZ_{n+1}(\beta r) - \\ B_1 r^2 kW_{n+1}(\beta r) + A_3\left(nrZ_n(\beta r) - r^2\gamma_2\beta Z_{n+1}(\beta r)\right) + B_3\left(nrW_n(\beta r) - r^2\beta W_{n+1}(\beta r)\right) \end{pmatrix}e^{i(n\theta+kz-\omega t)} \quad \text{...............(4.50)}$$

$$u_z = \frac{\partial \Phi}{\partial z} + \frac{H_\theta}{r} + \frac{\partial H_\theta}{\partial r} - \frac{1}{r}\frac{\partial H_r}{\partial \theta} = i\left(kf + \frac{(n+1)}{r}h_r + \frac{\partial h_r}{\partial r}\right)e^{i(n\theta+kz-\omega t)}$$

$$= i\frac{1}{r^2}\left(Ar^2 kZ_n(\alpha r) + Br^2 kW_n(\alpha r) + A_1 r^2\beta Z_n(\beta r) + B_1 r^2\gamma_2\beta W_n(\beta r)\right)e^{i(n\theta+kz-\omega t)} \quad \text{.........................(4.51)}$$

The three stress boundary conditions can now be written. By plugging the original differential equation back into the stress formulas, the recurrence relationships and parameters can be used.

$$\sigma_{rr} = \lambda\Delta + 2\mu\frac{\partial u_r}{\partial r} = \lambda\nabla^2\Phi + 2\mu\frac{\partial}{\partial r}\left(\left(\frac{\partial f}{\partial r} + \frac{n}{r}h_z + kh_r\right)e^{i(n\theta+kz-\omega t)}\right)$$

$$= \frac{\lambda}{c_d^2}\cdot\frac{\partial^2\Phi}{\partial t^2} + 2\mu\left(\frac{\partial^2 f}{\partial r^2} + k\frac{\partial h_r}{\partial r} + \frac{n}{r}\frac{\partial h_z}{\partial r} - \frac{n}{r^2}h_z\right)e^{i(n\theta+kz-\omega t)}$$

$$= \mu\left(-\frac{\lambda}{\mu}\left(\alpha^2 + k^2\right)f + 2\frac{\partial^2 f}{\partial r^2} + 2k\frac{\partial h_r}{\partial r} - 2\frac{n}{r^2}h_z + \frac{2n}{r}\frac{\partial h_z}{\partial r}\right)e^{i(n\theta+kz-\omega t)}$$

$$= \frac{\mu}{r^2}\begin{pmatrix} A\left(\left(\left(k^2-\beta^2\right)r^2 + 2n(n-1)\right)Z_n(\alpha r) + 2\gamma_1\alpha r Z_{n+1}(\alpha r)\right) + B\left(\left(\left(k^2-\beta^2\right)r^2 + 2n(n-1)\right)W_n(\alpha r) + 2\alpha r W_{n+1}(\alpha r)\right) + \\ A_1\left(2k\beta r^2 Z_n(\beta r) - 2kr(n+1)Z_{n+1}(\beta r)\right) + B_1\left(2k\gamma_2\beta r^2 W_n(\beta r) - 2kr(n+1)W_{n+1}(\beta r)\right) + \\ A_3\left(2n(n-1)Z_n(\beta r) - 2n\gamma_2\beta r Z_{n+1}(\beta r)\right) + B_3\left(2n(n-1)W_n(\beta r) - 2n\beta r W_{n+1}(\beta r)\right) \end{pmatrix}e^{i(n\theta+kz-\omega t)} \quad \text{..(4.52)}$$

$$\tau_{r\theta} = \mu\gamma_{r\theta} = \mu\left(\frac{1}{r}\frac{\partial u_r}{\partial \theta} + r\frac{\partial}{\partial r}\left(\frac{u_\theta}{r}\right)\right)$$

$$= \mu\left(i\frac{n}{r}\left(\frac{\partial f}{\partial r} + \frac{n}{r}h_z + kh_r\right) - i\frac{1}{r}\left(\frac{n}{r}f + \frac{\partial h_z}{\partial r} - kh_r\right) + i\frac{\partial}{\partial r}\left(\frac{n}{r}f + \frac{\partial h_z}{\partial r} - kh_r\right)\right)e^{i(n\theta+kz-\omega t)}$$

$$= -i\frac{\mu}{r^2}\left(2nf - 2nr\frac{\partial f}{\partial r} - (n+1)rkh_r + kr^2\frac{\partial h_r}{\partial r} + r\frac{\partial h_z}{\partial r} - n^2 h_z - r^2\frac{\partial^2 h_z}{\partial r^2}\right)e^{i(n\theta+kz-\omega t)}$$

$$= -i\frac{\mu}{r^2}\begin{pmatrix} A\left(2n(1-n)Z_n(\alpha r) + 2nr\gamma_1\alpha Z_{n+1}(\alpha r)\right) + B\left(2n(1-n)W_n(\alpha r) + 2nr\alpha W_{n+1}(\alpha r)\right) + \\ A_1\left(kr^2\gamma_2\beta Z_n(\beta r) - 2(n+1)rkZ_{n+1}(\beta r)\right) + B_1\left(kr^2\beta W_n(\beta r) - 2(n+1)rkW_{n+1}(\beta r)\right) + \\ A_3\left(\left(2n(1-n) + \beta^2 r^2\right)Z_n(\beta r) - 2r\gamma_2\beta Z_{n+1}(\beta r)\right) + B_3\left(\left(2n(1-n) + \beta^2 r^2\right)W_n(\beta r) - 2r\beta W_{n+1}(\beta r)\right) \end{pmatrix}e^{i(n\theta+kz-\omega t)} \quad \text{.....(4.53)}$$

79

$$\tau_{rz} = \mu\gamma_{rz} = \mu\left(\frac{\partial u_r}{\partial z} + \frac{\partial u_z}{\partial r}\right) = i\mu\left(2k\frac{\partial f}{\partial r} + \frac{nk}{r}h_z + \left(k^2 - \frac{(n+1)}{r^2}\right)h_r + \frac{(n+1)}{r}\frac{\partial h_r}{\partial r} + \frac{\partial^2 h_r}{\partial r^2}\right)\cos(n\theta)e^{i(kz-\omega t)}$$

$$= i\frac{\mu}{r^2}\left\{\begin{array}{l} A\left(2knrZ_n(\alpha r) - 2\gamma_1 k\alpha r^2 Z_{n+1}(\alpha r)\right) + B\left(2knrW_n(\alpha r) - 2k\alpha r^2 W_{n+1}(\alpha r)\right) + \\ A_1\left(\beta nrZ_n(\beta r) + r^2\left(k^2 - \beta^2\right)Z_{n+1}(\beta r)\right) + B_1\left(\beta nr\gamma_2 W_n(\beta r) + r^2\left(k^2 - \beta^2\right)W_{n+1}(\beta r)\right) + \\ A_3\left(nkrZ_n(\beta r)\right) + B_3\left(nkrW_n(\beta r)\right) \end{array}\right\}\cos(n\theta)e^{i(kz-\omega t)} \quad\ldots\ldots (4.54)$$

The displacements and stresses are all multiplied by r^2 to avoid dividing by the radius, eliminate the common term, and be consistent with previous derivations. The displacements and stresses are organized into the partial wave amplitude contributions to each boundary condition [89]:

	L+(B)	L−(A)	SV+(B_1)	SV−(A_1)	SH+(B_3)	SH−(A_3)
u_z	$D(1,1)$	$D(1,2)$	$D(1,3)$	$D(1,4)$	$D(1,5)$	$D(1,6)$
u_r	$D(2,1)$	$D(2,2)$	$D(2,3)$	$D(2,4)$	$D(2,5)$	$D(2,6)$
u_θ	$D(3,1)$	$D(3,2)$	$D(3,3)$	$D(3,4)$	$D(3,5)$	$D(3,6)$
σ_{rr}	$D(4,1)$	$D(4,2)$	$D(4,3)$	$D(4,4)$	$D(4,5)$	$D(4,6)$
τ_{rz}	$D(5,1)$	$D(5,2)$	$D(5,3)$	$D(5,4)$	$D(5,5)$	$D(5,6)$
$\tau_{r\theta}$	$D(6,1)$	$D(6,2)$	$D(6,3)$	$D(6,4)$	$D(6,5)$	$D(6,6)$

$D(1,1) = i\left(r^2 k W_n(\alpha r)\right)$

$D(1,2) = i\left(r^2 k Z_n(\alpha r)\right)$

$D(1,3) = i\left(r^2 \gamma_2 \beta W_n(\beta r)\right)$

$D(1,4) = i\left(r^2 \beta Z_n(\beta r)\right)$

$D(1,5) = 0$

$D(1,6) = 0$

$D(2,1) = nrW_n(\alpha r) - r^2\alpha W_{n+1}(\alpha r)$

$D(2,2) = nrZ_n(\alpha r) - r^2\gamma_1\alpha Z_{n+1}(\alpha r)$

$D(2,3) = r^2 k W_{n+1}(\beta r)$

$D(2,4) = r^2 k Z_{n+1}(\beta r)$

$D(2,5) = nrW_n(\beta r)$

$D(2,6) = nrZ_n(\beta r)$

$D(3,1) = i\left(nrW_n(\alpha r)\right)$

$D(3,2) = i\left(nrZ_n(\alpha r)\right)$

$D(3,3) = -i\left(r^2 k W_{n+1}(\beta r)\right)$

$D(3,4) = -i\left(r^2 k Z_{n+1}(\beta r)\right)$

$D(3,5) = i\left(nrW_n(\beta r)r^2 - \beta W_{n+1}(\beta r)\right)$

$D(3,6) = i\left(nrZ_n(\beta r) - r^2\gamma_2\beta Z_{n+1}(\beta r)\right)$

$D(4,1) = \mu\left(\left(\left(k^2 - \beta^2\right)r^2 + 2n(n-1)\right)W_n(\alpha r) + 2\alpha r W_{n+1}(\alpha r)\right)$

$D(4,2) = \mu\left(\left(\left(k^2 - \beta^2\right)r^2 + 2n(n-1)\right)Z_n(\alpha r) + 2\gamma_1\alpha r Z_{n+1}(\alpha r)\right)$

$D(4,3) = \mu\left(2\gamma_2 k\beta r^2 W_n(\beta r) - 2kr(n+1)W_{n+1}(\beta r)\right)$

$D(4,4) = \mu\left(2k\beta r^2 Z_n(\beta r) - 2kr(n+1)Z_{n+1}(\beta r)\right)$

$D(4,5) = \mu\left(2n(n-1)W_n(\beta r) - 2n\beta r W_{n+1}(\beta r)\right)$

$D(4,6) = \mu\left(2n(n-1)Z_n(\beta r) - 2n\gamma_2\beta r Z_{n+1}(\beta r)\right)$

$D(5,1) = i\mu\left(2knrW_n(\alpha r) - 2k\alpha r^2 W_{n+1}(\alpha r)\right)$

$D(5,2) = i\mu\left(2knrZ_n(\alpha r) - 2\gamma_1 k\alpha r^2 Z_{n+1}(\alpha r)\right)$

$D(5,3) = i\mu\left(\gamma_2\beta nrW_n(\beta r) + r^2\left(k^2 - \beta^2\right)W_{n+1}(\beta r)\right)$

$D(5,4) = i\mu\left(\beta nrZ_n(\beta r) + r^2\left(k^2 - \beta^2\right)Z_{n+1}(\beta r)\right)$

$D(5,5) = i\mu\left(nkrW_n(\beta r)\right)$

$D(5,6) = i\mu\left(nkrZ_n(\beta r)\right)$

$D(6,1) = i\mu\left(2n(n-1)W_n(\alpha r) - 2nr\alpha W_{n+1}(\alpha r)\right)$

$D(6,2) = i\mu\left(2n(n-1)Z_n(\alpha r) - 2\gamma_1 nr\alpha Z_{n+1}(\alpha r)\right)$

$D(6,3) = i\mu\left(-kr^2\gamma_2\beta W_n(\beta r) + 2(n+1)rkW_{n+1}(\beta r)\right)$

$D(6,4) = i\mu\left(-kr^2\beta Z_n(\beta r) + 2(n+1)rkZ_{n+1}(\beta r)\right)$

$D(6,5) = i\mu\left(\left(2n(n-1) - \beta^2 r^2\right)W_n(\beta r) + 2r\beta W_{n+1}(\beta r)\right)$

$D(6,6) = i\mu\left(\left(2n(n-1) - \beta^2 r^2\right)Z_n(\beta r) + 2\gamma_2 r\beta Z_{n+1}(\beta r)\right)$

Now that partial wave amplitudes have been defined for a cylindrical layer, the boundary conditions are used at the layer interfaces to construct a matrix. The method used here, the global matrix method, follows that of previous derivations [89]. Shown below is the global matrix, [G], for a four cylindrical layer system. One can see that each row correlates to a displacement or stress that must be continuous

across the layer interfaces. Layer 1 has only inward propagating waves and layer 4 has only outward propagating waves.

	LAYER 1 (HALF-SPACE)			LAYER 2						LAYER 3						LAYER 4 (HALF-SPACE)		
	L^-	SV^-	SH^-	L^+	L^-	SV^+	SV^-	SH^+	SH^-	L^+	L^-	SV^+	SV^-	SH^+	SH^-	L^+	SV^+	SH^+
u_z	D_{12}	D_{14}	D_{16}	$-D_{11}$	$-D_{12}$	$-D_{13}$	$-D_{14}$	$-D_{15}$	$-D_{16}$									
u_r	D_{22}	D_{24}	D_{26}	$-D_{21}$	$-D_{22}$	$-D_{23}$	$-D_{24}$	$-D_{25}$	$-D_{26}$									
u_θ	D_{32}	D_{34}	D_{36}	$-D_{31}$	$-D_{32}$	$-D_{33}$	$-D_{34}$	$-D_{35}$	$-D_{36}$									
σ_{rr}	D_{42}	D_{44}	D_{46}	$-D_{41}$	$-D_{42}$	$-D_{43}$	$-D_{44}$	$-D_{45}$	$-D_{46}$									
τ_{rz}	D_{52}	D_{54}	D_{56}	$-D_{51}$	$-D_{52}$	$-D_{53}$	$-D_{54}$	$-D_{55}$	$-D_{56}$									
$\tau_{r\theta}$	D_{62}	D_{64}	D_{66}	$-D_{61}$	$-D_{62}$	$-D_{63}$	$-D_{64}$	$-D_{65}$	$-D_{66}$									
u_z				D_{11}	D_{12}	D_{13}	D_{14}	D_{15}	D_{16}	$-D_{11}$	$-D_{12}$	$-D_{13}$	$-D_{14}$	$-D_{15}$	$-D_{16}$			
u_r				D_{21}	D_{22}	D_{23}	D_{24}	D_{25}	D_{26}	$-D_{21}$	$-D_{22}$	$-D_{23}$	$-D_{24}$	$-D_{25}$	$-D_{26}$			
u_θ				D_{31}	D_{32}	D_{33}	D_{34}	D_{35}	D_{36}	$-D_{31}$	$-D_{32}$	$-D_{33}$	$-D_{34}$	$-D_{35}$	$-D_{36}$			
σ_{rr}				D_{41}	D_{42}	D_{43}	D_{44}	D_{45}	D_{46}	$-D_{41}$	$-D_{42}$	$-D_{43}$	$-D_{44}$	$-D_{45}$	$-D_{46}$			
τ_{rz}				D_{51}	D_{52}	D_{53}	D_{54}	D_{55}	D_{56}	$-D_{51}$	$-D_{52}$	$-D_{53}$	$-D_{54}$	$-D_{55}$	$-D_{56}$			
$\tau_{r\theta}$				D_{61}	D_{62}	D_{63}	D_{64}	D_{65}	D_{66}	$-D_{61}$	$-D_{62}$	$-D_{63}$	$-D_{64}$	$-D_{65}$	$-D_{66}$			
u_z										D_{11}	D_{12}	D_{13}	D_{14}	D_{15}	D_{16}	$-D_{11}$	$-D_{13}$	$-D_{15}$
u_r										D_{21}	D_{22}	D_{23}	D_{24}	D_{25}	D_{26}	$-D_{21}$	$-D_{23}$	$-D_{25}$
u_θ										D_{31}	D_{32}	D_{33}	D_{34}	D_{35}	D_{36}	$-D_{31}$	$-D_{33}$	$-D_{35}$
σ_{rr}										D_{41}	D_{42}	D_{43}	D_{44}	D_{45}	D_{46}	$-D_{41}$	$-D_{43}$	$-D_{45}$
τ_{rz}										D_{51}	D_{52}	D_{53}	D_{54}	D_{55}	D_{56}	$-D_{51}$	$-D_{53}$	$-D_{55}$
$\tau_{r\theta}$										D_{61}	D_{62}	D_{63}	D_{64}	D_{65}	D_{66}	$-D_{61}$	$-D_{63}$	$-D_{65}$

(Interface 1:2, Interface 2:3, Interface 3:4)

In order to satisfy all boundary conditions simultaneously, the global matrix is multiplied by a vector of the partial wave amplitudes:

$$[G]\{A\} = 0 \tag{4.55}$$

This equation is satisfied when:

$$\det[G] = 0 \tag{4.56}$$

4.1.1 ATTENUATION

Attenuation is the loss of waveform amplitude, typically represented in units of dB/m or Np/m (1 Neper = 8.7 decibels). There are many different causes of waveform amplitude loss, with those accounted for in the model discussed below:

1) **Absorption mechanisms** – combined effect of attenuation due to intrinsic mechanisms and those due to imperfections. An example of an intrinsic mechanism is thermal effects. Application of strain can create an effective temperature change of phonon modes, leading to a redistribution of their populations by the phonon-phonon interaction [105]. Energy is dissipated due to the phase lag that is created. Imperfections in the material (e.g. voids and misoriented grains) reduce the amplitude of the wave by causing scattering and reflections. For more information on scattering refer to [106-108].

81

2) **Leakage** – Energy may radiate (i.e. leak) from an embedded material into the surrounding medium.

For an unbounded infinite medium, the attenuation is considered dependent only on the material absorption of wave energy in the medium. For a guided wave in a layered system, wave energy is lost due to material absorption and leakage into the surrounding material. The bulk material properties in the model are altered to account for material absorption (refer to Appendix F). The total attenuation caused by material absorption and leakage is calculated in the model by using a complex wavenumber:

$$k = k_{real} + i k_{imag} \qquad \qquad \qquad (4.57)$$

The real wavenumber, k_{real}, describes the harmonic propagation of the waveform while the imaginary wavenumber, k_{imag}, describes the exponential decay of the wave. The potential functions have the form:

$$\Phi = Amplitude \cdot e^{i(k_{real}z - \omega t)} e^{-k_{imag}z} = Amplitude \cdot e^{i(kz - \omega t)} \qquad \qquad (4.58)$$

When solving for the global matrix system, a solution will contain the frequency (f), phase velocity (c_p), and the attenuation (k_{imag}). Figure 4.2 shows a slice of a solution plane for solving the determinant of the global matrix. The frequency was held constant at 2.53 MHz while the phase velocity and attenuation values were swept. The contour plot beneath the three-dimensional surface reveals the minima (solutions) for longitudinal propagation.
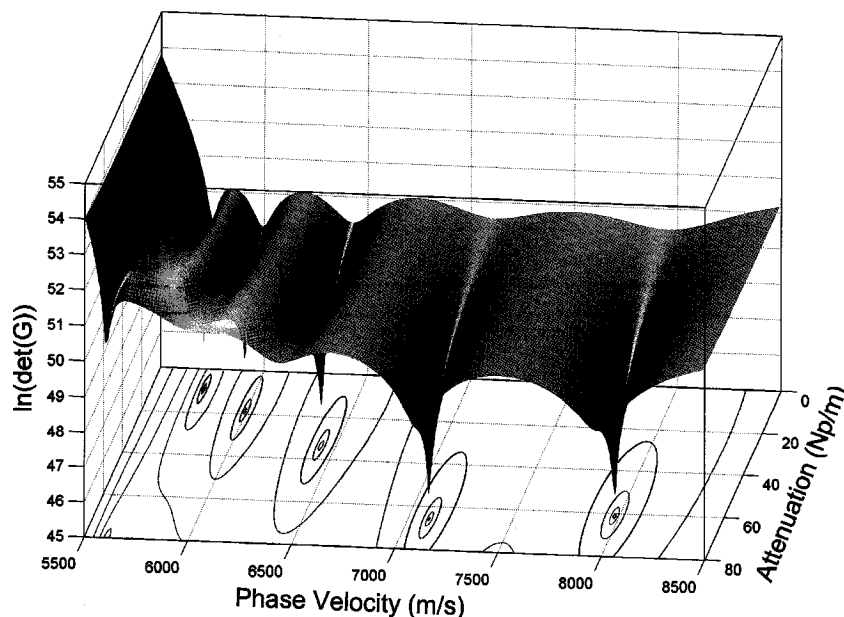
Figure 4.2: Three-dimensional slice of solution plane for the determinant of the global matrix. The frequency was held constant at 2.53 MHz, while the phase velocity and attenuation values were swept. The contour plot reveals the minima (solutions) for longitudinal propagation.

82

4.1.2 PHASE, GROUP AND ENERGY VELOCITY

The rate at which individual wave crests travel within a wave packet is termed the phase velocity (c_p). For a non-dispersive bulk medium, crests within the wave packet will travel at the same velocity as the wave packet itself. For a dispersive medium, the wave packet travel at a different velocity than the crests. This can be thought of as a bullet ricocheting down a hard-walled corridor [109]. The bullet travels with a particular speed that makes an angle with the longitudinal axis of the corridor. The speed of the bullet in the direction of the longitudinal axis of the corridor is different than the speed of the bullet in the direction at an angle to the axis. For a dispersive medium without attenuation, the velocity of the wave packet can be calculated from the derivative of the dispersion curve and is termed the group velocity:

$$c_g = \frac{\partial \omega}{\partial k} \quad \text{...............(4.59)}$$

For a dispersive medium with attenuation, the derivative of the dispersion curve will not accurately calculate the velocity of the packet in all regions. Therefore, the velocity of the mode energy in the axial direction will be calculated. This is termed the energy velocity and is calculated in the following manner:

$$c_e = \frac{\int_S \int_T (P_z) \, dT \, dS}{\int_S \int_T (TED) \, dT \, dS} \quad \text{...............(4.60)}$$

where P_z is the power flow density in the axial direction, S is the cross-section perpendicular to the direction of propagation, T is the time period of the wave, and TED is the total energy density [89,100]. Power is the amount of work per unit time. Power flow density is the amount of power that travels through a given cross-section. To calculate the power flow density, the dot product of the velocity vector (calculated from the derivative of displacements with respect to time) and the stress tensor is calculated. The dot product will yield the Poynting vector:

$$P = c \cdot \sigma = \begin{bmatrix} c_r & c_\theta & c_z \end{bmatrix} \cdot \begin{bmatrix} \sigma_{rr} & \sigma_{r\theta} & \sigma_{rz} \\ \sigma_{\theta r} & \sigma_{\theta\theta} & \sigma_{\theta z} \\ \sigma_{zr} & \sigma_{z\theta} & \sigma_{zz} \end{bmatrix} = P_r i_r + P_\theta i_\theta + P_z i_z$$

$$= (c_r \sigma_{rr} + c_\theta \sigma_{\theta r} + c_z \sigma_{zr}) i_r + (c_r \sigma_{r\theta} + c_\theta \sigma_{\theta\theta} + c_z \sigma_{z\theta}) i_\theta + (c_r \sigma_{rz} + c_\theta \sigma_{\theta z} + c_z \sigma_{zz}) i_z \quad \text{.........(4.61)}$$

The equation for power flow density assumes that real values are used. The expression for power flow density must be halved if complex values are used. Power flow in the axial direction is the following:

$$P_z = c_r \sigma_{rz} + c_\theta \sigma_{\theta z} + c_z \sigma_{zz} \quad \text{...............(4.62)}$$

To find the total energy density (TED), both the potential and kinetic energy densities must be summed. The potential energy density is the strain energy density (also referred to as the strain energy per unit volume). The strain energy density (SED) can be calculated with the following equation:

$$SED = \tfrac{1}{2}\varepsilon \cdot \sigma = \tfrac{1}{2}\{\sigma_{rr}\varepsilon_{rr} + \sigma_{\theta\theta}\varepsilon_{\theta\theta} + \sigma_{zz}\varepsilon_{zz} + \sigma_{rz}\varepsilon_{rz} + \sigma_{r\theta}\varepsilon_{r\theta} + \sigma_{\theta z}\varepsilon_{\theta z}\} \quad\quad (4.63)$$

The equation for strain energy density assumes that real values are used. The expression for strain energy density must be halved if complex values are used. The kinetic energy density (KED) is calculated from the following expression:

$$KED = \tfrac{1}{2}\rho\{\dot{c} \cdot \dot{c}\} = \tfrac{\rho}{2}\left\{\left(\frac{\partial u_r}{\partial t}\right)^2 + \left(\frac{\partial u_\theta}{\partial t}\right)^2 + \left(\frac{\partial u_z}{\partial t}\right)^2\right\} \quad\quad (4.64)$$

Again, the expression for kinetic energy density assumes that real values are used. The expression for kinetic energy density must be halved if complex values are used. The total energy density (TED) is calculated as the summation of kinetic energy density (KED) and strain energy density (SED):

$$TED = KED + SED \quad\quad (4.65)$$

4.2   SPECIFIC TYPES OF WAVE PROPAGATION

There are three types of wave propagation in cylindrical waveguides: longitudinal, torsional, and flexural. Longitudinal propagation has only radial and axial displacement. Torsional propagation has only angular displacements. Flexural propagation has radial, axial, and angular displacements. Longitudinal, torsional, and flexural waveforms are represented by the notation L(n,m), T(n,m), and F(n,m), respectively. The characters 'n' and 'm' represent the circumferential order and the sequential order of the mode, respectively. The circumferential order 'n' determines the number of displacement cycles around the bar outer diameter, varying as a function of $\cos(n\theta)$ [95]. Longitudinal and torsional propagation have circumferential displacements of zero (i.e. no angular motion, n = 0). Flexural propagation can have circumferential displacements of n = 1, 2, 3, etc. There are an infinite number of modes for each type of propagation.

Wave propagation within this report has been broken up into two types of propagation: wave motion independent of the angle 'θ' (n = 0) and wave motion dependent on the angle 'θ' (n = 1, 2, 3, etc.). Two specific waveguide configurations are considered for all types of propagation. The first is propagation through a cylindrical bar in a vacuum. This is applicable to reinforcing steel completely debonded from concrete. The second is propagation through a cylindrical bar embedded in an infinite medium. This is

applicable to reinforcing steel immersed in water or embedded in mortar. Other waveguide system examples are considered once mode selection has occurred.

Material properties are necessary to model the guided wave behavior in the layered cylindrical system. The elastic modulus and Poisson's ratio of the mortar were measured from compression tests, while the elastic modulus of the steel was measured from a tension test. The density and Poisson's ratio of the steel were taken from standard reference values [110]. The material absorption coefficients for both steel and mortar were taken from reported values [96]. The material properties for water and air were taken from standard reference values [89]. All the material properties used for modeling guided wave behavior in this paper are given in Table 4.3.

Table 4.3: Material properties used in this report.

Material	Elastic Modulus	Density	Poisson's Ratio	Compressional Velocity	Shear Velocity	Compressional Absorp. Coeff.	Shear Absorp. Coeff.
Units	(GPa)	(kg/m^3)	------	(m/s)	(m/s)	Neper / λ	Neper / λ
Symbol	E	ρ	υ	c_d	c_s	α_d	α_s
Steel	208	7,700	0.29	5,954	3,238	0.003	0.008
Dry Mortar	19.9	2,066	0.192	3,256	2,010.1	0.05	0.12
Wet Mortar	24.1	2,170	0.229	3,588	2,125	0.05	0.12
Water	------	1,000	------	1,478	------	------	------
Air	------	1.205	------	344	------	------	------

4.2.1 WAVE PROPAGATION WITH MOTION INDEPENDENT OF 'θ'

Wave motion independent of the angle 'θ' has a circumferential order equal to zero (n = 0). There are two different types of wave motion in cylindrical bars independent of the angle 'θ' that will be discussed. The first is longitudinal propagation and the second is torsional propagation. These two types of waves are discussed after the general equations for wave motion independent of 'θ' have been written. The displacement and stress components are shown below to help illustrate the behavior:

$$u_r = \frac{1}{r^2}\left(-Ar^2\gamma_1\alpha Z_1(\alpha r) - Br^2\alpha W_1(\alpha r) + A_1 r^2 k Z_1(\beta r) + B_1 r^2 k W_1(\beta r)\right)e^{i(kz-\omega t)} \quad\text{...............} (4.66)$$

$$u_\theta = -i\frac{1}{r^2}\left(A_1 r^2 k Z_1(\beta r) + B_1 r^2 k W_1(\beta r) + A_3 r^2 \gamma_2 \beta Z_1(\beta r) + B_3 r^2 \beta W_1(\beta r)\right)e^{i(kz-\omega t)} \quad\text{...........} (4.67)$$

$$u_z = i\frac{1}{r^2}\left(Ar^2 k Z_0(\alpha r) + Br^2 k W_0(\alpha r) + A_1 r^2 \beta Z_0(\beta r) + B_1 r^2 \gamma_2 \beta W_0(\beta r)\right)e^{i(kz-\omega t)} \quad\text{...............} (4.68)$$

The following is the material layer matrix for zero circumferential order (n = 0):

	$L+(B)$	$L-(A)$	$SV+(B_1)$	$SV-(A_1)$	$SH+(B_3)$	$SH-(A_3)$
u_z	$D(1,1)$	$D(1,2)$	$D(1,3)$	$D(1,4)$	0	0
u_r	$D(2,1)$	$D(2,2)$	$D(2,3)$	$D(2,4)$	0	0
u_θ	0	0	$D(3,3)$	$D(3,4)$	$D(3,5)$	$D(3,6)$
σ_{rr}	$D(4,1)$	$D(4,2)$	$D(4,3)$	$D(4,4)$	0	0
τ_{rz}	$D(5,1)$	$D(5,2)$	$D(5,3)$	$D(5,4)$	0	0
$\tau_{r\theta}$	0	0	$D(6,3)$	$D(6,4)$	$D(6,5)$	$D(6,6)$

$$D(1,1) = i\left(r^2 k W_0(\alpha r)\right)$$
$$D(1,2) = i\left(r^2 k Z_0(\alpha r)\right)$$
$$D(1,3) = i\left(r^2 \gamma_2 \beta W_0(\beta r)\right)$$
$$D(1,4) = i\left(r^2 \beta Z_0(\beta r)\right)$$
$$D(1,5) = 0$$
$$D(1,6) = 0$$

$$D(2,1) = -r^2 \alpha W_1(\alpha r)$$
$$D(2,2) = -r^2 \gamma_1 \alpha Z_1(\alpha r)$$
$$D(2,3) = r^2 k W_1(\beta r)$$
$$D(2,4) = r^2 k Z_1(\beta r)$$
$$D(2,5) = 0$$
$$D(2,6) = 0$$

$$D(3,1) = 0$$
$$D(3,2) = 0$$
$$D(3,3) = -i\left(r^2 k W_1(\beta r)\right)$$
$$D(3,4) = -i\left(r^2 k Z_1(\beta r)\right)$$
$$D(3,5) = i\left(-r^2 \beta W_1(\beta r)\right)$$
$$D(3,6) = i\left(-r^2 \gamma_2 \beta Z_1(\beta r)\right)$$

$$D(4,1) = \mu\left(\left(\left(k^2 - \beta^2\right)r^2\right)W_0(\alpha r) + 2\alpha r W_1(\alpha r)\right)$$
$$D(4,2) = \mu\left(\left(\left(k^2 - \beta^2\right)r^2\right)Z_0(\alpha r) + 2\gamma_1 \alpha r Z_1(\alpha r)\right)$$
$$D(4,3) = \mu\left(2\gamma_2 k\beta r^2 W_n(\beta r) - 2krW_1(\beta r)\right)$$
$$D(4,4) = \mu\left(2k\beta r^2 Z_0(\beta r) - 2krZ_1(\beta r)\right)$$
$$D(4,5) = 0$$
$$D(4,6) = 0$$

$$D(5,1) = i\mu\left(-2k\alpha r^2 W_1(\alpha r)\right)$$
$$D(5,2) = i\mu\left(-2\gamma_1 k\alpha r^2 Z_1(\alpha r)\right)$$
$$D(5,3) = i\mu\left(r^2\left(k^2 - \beta^2\right)W_1(\beta r)\right)$$
$$D(5,4) = i\mu\left(r^2\left(k^2 - \beta^2\right)Z_1(\beta r)\right)$$
$$D(5,5) = 0$$
$$D(5,6) = 0$$

$$D(6,1) = 0$$
$$D(6,2) = 0$$
$$D(6,3) = i\mu\left(-kr^2 \gamma_2 \beta W_0(\beta r) + 2rkW_1(\beta r)\right)$$
$$D(6,4) = i\mu\left(-kr^2 \beta Z_0(\beta r) + 2rkZ_1(\beta r)\right)$$
$$D(6,5) = i\mu\left(\left(\beta^2 r^2\right)W_0(\beta r) + 2r\beta W_1(\beta r)\right)$$
$$D(6,6) = i\mu\left(\left(\beta^2 r^2\right)Z_0(\beta r) + 2\gamma_2 r\beta Z_1(\beta r)\right)$$

This material layer matrix can now be configured into a global matrix to match the waveguide configurations mentioned previously.

Wave Propagation Independent of 'θ' for a Cylindrical Bar in a Vacuum

It will be assumed that there are no outward propagating waves, only inward propagating waves, since the waves do not propagate in a vacuum. This is a result of the impedance mismatch between the two mediums. In this case, the displacement terms are not needed for boundary conditions since the cylindrical bar is not constrained. Therefore, all of the stress terms equal zero at the outer circumference of the cylinder ($r = a$). Below is the global matrix condensed to fit this case:

	L-(A)	SV-(A$_1$)	SH-(A$_3$)
σ_{rr}	$\mathbf{D}(4,2)$	$\mathbf{D}(4,4)$	0
τ_{rz}	$\mathbf{D}(5,2)$	$\mathbf{D}(5,4)$	0
$\tau_{r\theta}$	0	$\mathbf{D}(6,4)$	$\mathbf{D}(6,6)$

The determinant of this 3 x 3 matrix is the following:

$$\mathbf{D}(4,2)\cdot\begin{vmatrix}\mathbf{D}(5,4) & 0 \\ \mathbf{D}(6,4) & \mathbf{D}(6,6)\end{vmatrix} - \mathbf{D}(4,4)\cdot\begin{vmatrix}\mathbf{D}(5,2) & 0 \\ 0 & \mathbf{D}(6,6)\end{vmatrix}$$
$$= \mathbf{D}(6,6)\cdot[\mathbf{D}(4,2)\cdot\mathbf{D}(5,4) - \mathbf{D}(4,4)\cdot\mathbf{D}(5,2)].$$

These equations will have no solution unless the determinant of the system is zero [111]. When the determinant of a matrix is zero, the matrix is said to be singular. For the determinant of the 3 x 3 matrix to be zero, the determinant of the upper left 2 x 2 matrix must equal zero and/or $\mathbf{D}(6,6)$ must be equal to zero. Either or both of these would ensure a solution to wave motion independent of the angle 'θ' for a cylindrical bar in a vacuum.

Wave Propagation Independent of 'θ' for a Cylindrical Bar Surrounded by an Infinite Medium

It is assumed that there are only outward propagating waves in the surrounding infinite medium, and only inward propagating waves for the cylindrical bar. This is a result of the infinite surrounding reflecting no waves back towards the cylinder. Therefore, waves that leak from the cylindrical bar are assumed to never return. In this case, the displacement and stress terms are needed for boundary conditions since the isotropic cylinder is constrained by the surrounding medium. The displacement and stress terms in the cylinder will equal the displacement and stress terms in the surrounding medium at the outer circumference of the cylinder (r = a). Below is the global matrix for this case:

	L-$_{cyl}$	SV-$_{cyl}$	SH-$_{cyl}$	L+$_{inf}$	SV+$_{inf}$	SH+$_{inf}$
u_z	$\mathbf{D}(1,2)$	$\mathbf{D}(1,4)$	0	$-\mathbf{D}(1,1)$	$-\mathbf{D}(1,3)$	0
u_r	$\mathbf{D}(2,2)$	$\mathbf{D}(2,4)$	0	$-\mathbf{D}(2,1)$	$-\mathbf{D}(2,3)$	0
u_θ	0	$\mathbf{D}(3,4)$	$\mathbf{D}(3,6)$	0	$-\mathbf{D}(3,3)$	$-\mathbf{D}(3,5)$
σ_{rr}	$\mathbf{D}(4,2)$	$\mathbf{D}(4,4)$	0	$-\mathbf{D}(4,1)$	$-\mathbf{D}(4,3)$	0
τ_{rz}	$\mathbf{D}(5,2)$	$\mathbf{D}(5,4)$	0	$-\mathbf{D}(5,1)$	$-\mathbf{D}(5,3)$	0
$\tau_{r\theta}$	0	$\mathbf{D}(6,4)$	$\mathbf{D}(6,6)$	0	$-\mathbf{D}(6,3)$	$-\mathbf{D}(6,5)$

For the determinant to be zero, the determinant of either of the two matrices below must equal zero:

87

	$L-_{cyl}$	$SV-_{cyl}$	$L+_{inf}$	$SV+_{inf}$
u_z	$D(1,2)$	$D(1,4)$	$-D(1,1)$	$-D(1,3)$
u_r	$D(2,2)$	$D(2,4)$	$-D(2,1)$	$-D(2,3)$
σ_{rr}	$D(4,2)$	$D(4,4)$	$-D(4,1)$	$-D(4,3)$
τ_{rz}	$D(5,2)$	$D(5,4)$	$-D(5,1)$	$-D(5,3)$

	$SH-_{cyl}$	$SH+_{inf}$
u_θ	$D(3,6)$	$-D(3,5)$
$\tau_{r\theta}$	$D(6,6)$	$-D(6,5)$

Longitudinal Propagation

This type of propagation is axially symmetric, with displacements occurring only in the radial and axial directions. Therefore, the angular displacement is equal to zero ($u_\theta = 0$). In other words, the stresses and displacements occurring at an arbitrary radial boundary from the center of the cylinder are the same around the circumference. Knowing this allows the global matrices for motion independent of 'θ' to be reduced for the case of longitudinal propagation.

Case I: Longitudinal Propagation for a Cylindrical Bar in a Vacuum

For longitudinal propagation, only the stress components σ_{rr} and τ_{rz} are needed for boundary conditions. The stresses yield no components from the potential H_z ($D(4,6) = D(5,6) = 0$). Therefore, the determinant of the upper left 2 x 2 matrix describes longitudinal propagation for a cylindrical bar in a vacuum.

	$L-(A)$	$SV-(A_1)$
σ_{rr}	$D(4,2)$	$D(4,4)$
τ_{rz}	$D(5,2)$	$D(5,4)$

The two stress components are set equal to zero at the outer circumference ($r = a$) and a solution matrix is constructed:

$$\begin{bmatrix} \left(\left(k^2-\beta^2\right)a^2\right)Z_0(\alpha a)+2\gamma_1\alpha aZ_1(\alpha a) & 2k\beta a^2 Z_0(\beta a)-2kaZ_1(\beta a) \\ -2\gamma_1 k\alpha a^2 Z_1(\alpha a) & a^2\left(k^2-\beta^2\right)Z_1(\beta a) \end{bmatrix}\begin{bmatrix} A \\ A_1 \end{bmatrix}=\begin{bmatrix} 0 \\ 0 \end{bmatrix}$$

The determinant of the matrix is shown below:

$$\frac{2\alpha}{a}\gamma_1\left(\beta^2+k^2\right)Z_1(\alpha a)Z_1(\beta a)-\left(\beta^2-k^2\right)^2 Z_0(\alpha a)Z_1(\beta a)-\left(4k^2\alpha\beta\gamma_1\right)Z_0(\beta a)Z_1(\alpha a)=0 \quad \ldots\ldots\ldots\ldots (4.69)$$

88

This is referred to as the 'Pochhammer' frequency equation for longitudinal modes [84] or the 'characteristic equation' [101]. Pochhammer [112] first derived the equation followed by a later independent derivation by Chree [113]. The solutions to this equation define longitudinal propagation for the case of a cylindrical bar in a vacuum. Since the material properties of steel are given in Table 4.3, the only unknowns are then the frequency, phase velocity, and attenuation (assuming a specified radius). The displacements are now derived. Since $H_r = 0$ and $H_z = 0$, the following are the displacements:

$$u_r = \frac{\partial \Phi}{\partial r} - \frac{\partial H_\theta}{\partial z} = \left(-A\gamma_1 \alpha Z_1(\alpha r) + A_1 k Z_1(\beta r)\right)e^{i(kz-\omega t)} = A_1\left(-\frac{A}{A_1}\gamma_1 \alpha Z_1(\alpha r) + k Z_1(\beta r)\right)e^{i(kz-\omega t)} \quad\text{..........(4.70)}$$

$$u_\theta = 0 \quad\text{..(4.71)}$$

$$u_z = \frac{\partial \Phi}{\partial z} + \frac{H_\theta}{r} + \frac{\partial H_\theta}{\partial r} = i\left(A k Z_0(\alpha r) + A_1 \beta Z_0(\beta r)\right)e^{i(kz-\omega t)} = A_1\left(\frac{A}{A_1} k Z_0(\alpha r) + \beta Z_0(\beta r)\right)e^{i(kz-\omega t)} \quad\text{..........(4.72)}$$

where A/A_1 is found by the stress boundary conditions from above:

$$\frac{A}{A_1} = \frac{\left(k^2 - \beta^2\right)Z_1(\beta r)}{2\gamma_1 k\alpha Z_1(\alpha r)} \quad\text{..(4.73)}$$

Case II: Longitudinal Propagation for a Cylindrical Bar surrounded by an Infinite Medium

The first matrix is solved for longitudinal propagation. Again, the potential H_z does not contribute to either the displacements (u_z, u_r) or the stresses (σ_{rr}, τ_{rz}) for the boundary conditions.

	L_{cyl}^-	SV_{cyl}^-	L_{inf}^+	SV_{inf}^+
u_z	$D(1,2)$	$D(1,4)$	$-D(1,1)$	$-D(1,3)$
u_r	$D(2,2)$	$D(2,4)$	$-D(2,1)$	$-D(2,3)$
σ_{rr}	$D(4,2)$	$D(4,4)$	$-D(4,1)$	$-D(4,3)$
τ_{rz}	$D(5,2)$	$D(5,4)$	$-D(5,1)$	$-D(5,3)$

Therefore, the determinant of the first matrix is set equal to zero to solve for longitudinal propagation for the general case of an isotropic cylinder embedded in an infinite isotropic medium. Using the material properties from Table 4.3, with the displacement and stress component equations, a solution can be found. Figure 4.3 shows phase velocity as a function of frequency for longitudinal modes up to 11 MHz. The solution is for rebar 0.472" (11.99 mm) in diameter embedded in an infinite surrounding of dry mortar.
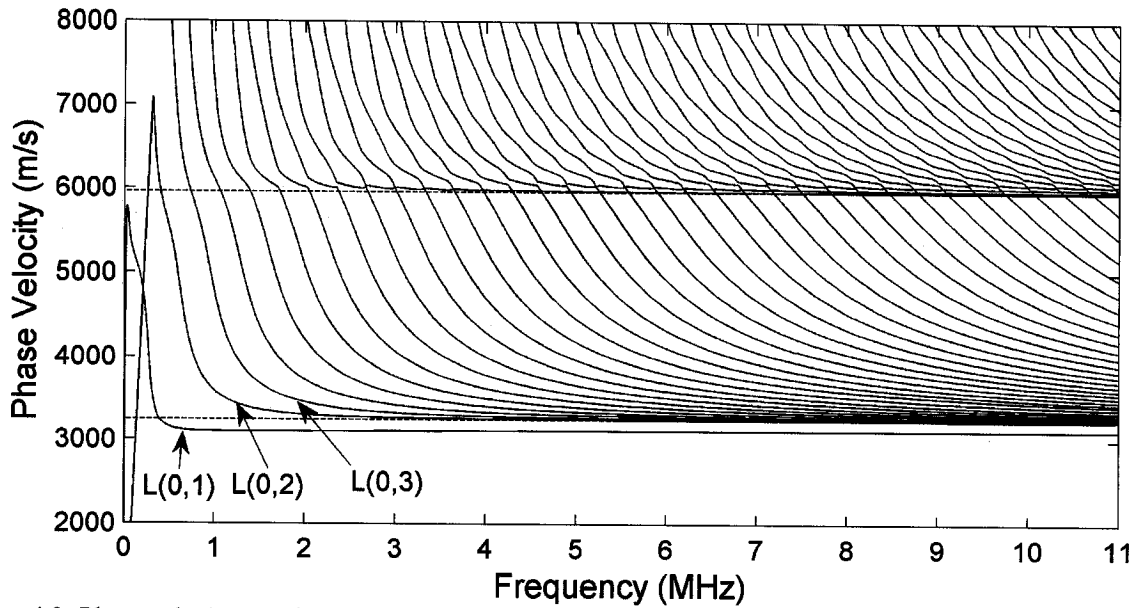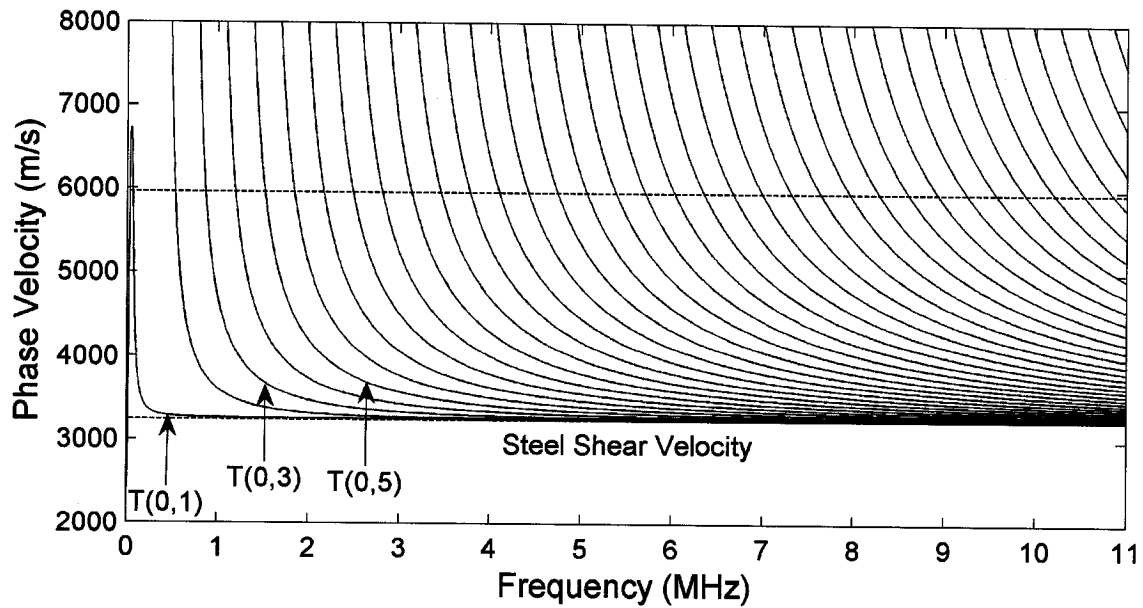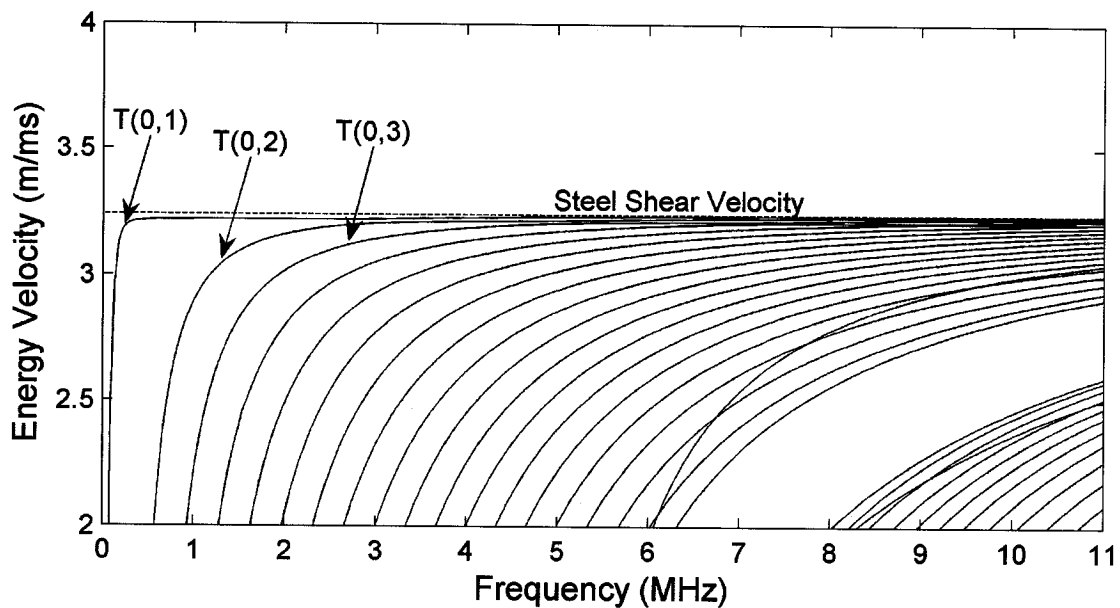
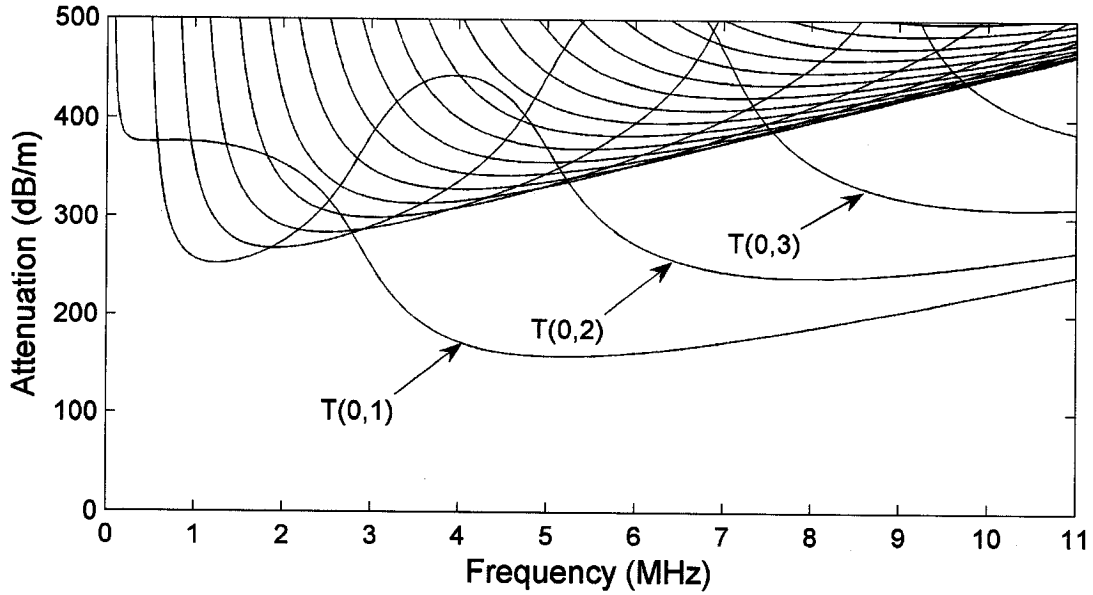**Figure 4.3:** Phase velocity as a function of frequency for longitudinal modes of propagation in a 0.472" (11.99 mm) diameter plain steel bar embedded in an infinite surrounding of dry mortar. Dashed lines indicate the bulk compressional velocity (top line) and shear velocity (bottom line) in steel.

Modes that exist at a frequency of zero are considered fundamental modes. The curve labeled L(0,1) is a fundamental mode. The fundamental longitudinal mode is referred to as the "Young's Modulus" mode [87]. Figure 4.4 shows energy velocity as a function of frequency for the longitudinal modes up to 11 MHz.
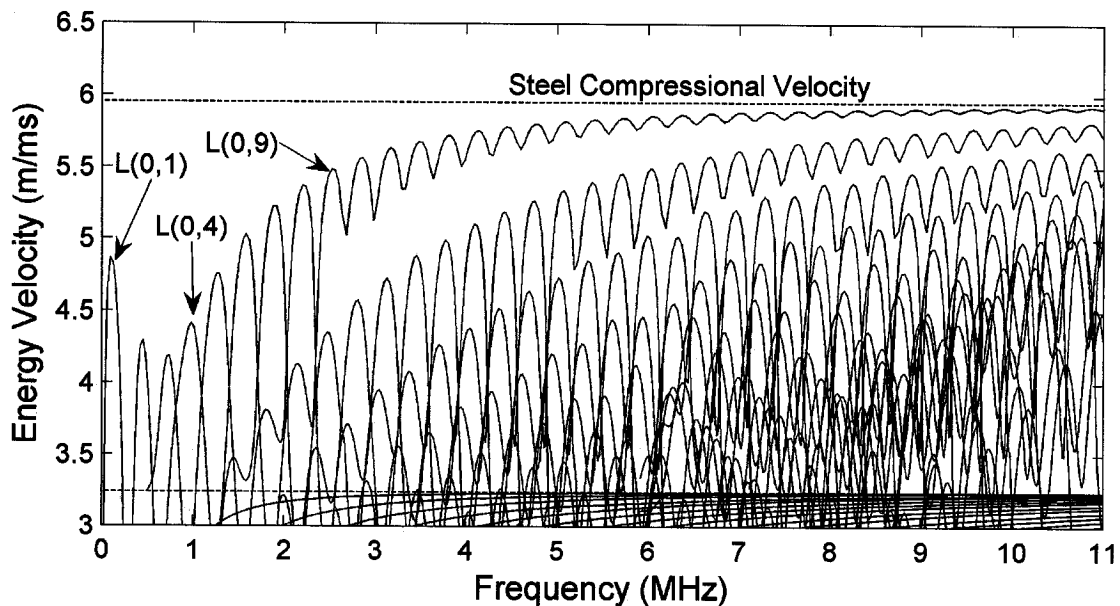
Figure 4.4: Energy velocity as a function of frequency for longitudinal modes of propagation in a 0.472" (11.99 mm) diameter plain steel bar embedded in an infinite surrounding of dry mortar. Dashed lines indicate the bulk compressional velocity (top line) and shear velocity (bottom line) in steel.

90

Figure 4.5 shows attenuation as a function of frequency for longitudinal modes up to 11 MHz.
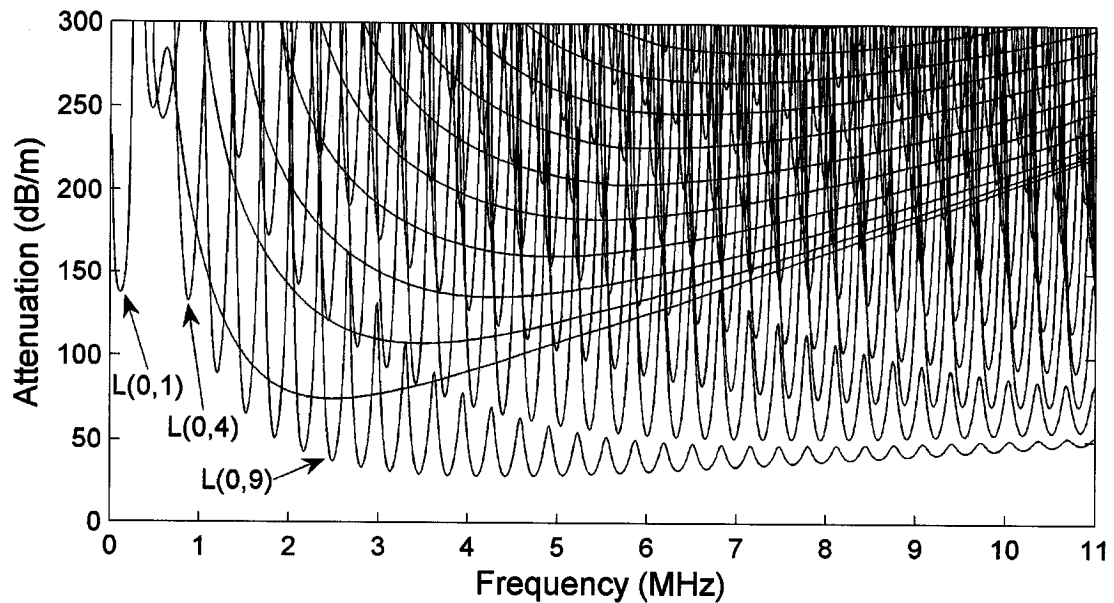
Figure 4.5: Attenuation as a function of frequency for longitudinal modes of propagation in a 0.472" (11.99 mm) diameter plain steel bar embedded in an infinite surrounding of dry mortar.

Torsional Propagation

Torsional propagation has no displacements in the radial or axial directions. It is specified that $u_\theta \neq 0$ and is independent of the angle θ (n = 0). This implies that the only non-zero potential is H_z. In other words, only amplitude coefficients A_3 and B_3 have values.

Case I: Torsional Propagation in a Cylindrical Bar in a Vacuum

The second choice for solving the global matrix for this waveguide configuration was setting **D(6,6)** equal to zero at the outer circumference (r = a) of the cylinder. Since H_z is the only non-zero potential term for torsional propagation, the only stress component that is needed for a boundary condition is $\tau_{r\theta}$:

$$\tau_{r\theta} = 2\beta a \gamma_2 Z_1(\beta a) - \beta^2 a^2 Z_0(\beta a) = 0 \quad\text{...} (4.74)$$

This could also be rewritten [87]:

$$\frac{Z_o(\beta a)}{Z_1(\beta a)} = \frac{2\gamma_2}{\beta a} \quad\text{...} (4.75)$$

When **D(6,6)** is set equal to zero, it implies that **D(6,4)** is also equal to zero. This makes sense because **D(6,4)** is a term from the potentials H_r and H_θ which are assumed to be zero in the case of torsional

91

propagation. However, substituting n = 0 into this term does not automatically yield a product of zero. Therefore, the term is checked below by plugging in r = a and solving:

$$\frac{Z_0(\beta a)}{Z_1(\beta a)} = \frac{2}{\beta a} \quad\ldots\ldots\ldots\ldots\ldots\ldots\ldots\ldots\ldots\ldots\ldots\ldots\ldots\ldots\ldots\ldots\ldots\ldots\ldots\ldots\ldots\ldots (4.76)$$

The term is almost identical to that of $D(6,6)$ set equal to zero, except that the recurrence parameter γ_2 is not included. However, it may be ascertained that no roots exist for $\beta^2 < 0$, therefore the phase velocity of the torsional wave is always greater than or equal to the bulk shear velocity of the material [83]. This implies that the recurrence parameter γ_2 is always equal to one (refer to Table 4.1). Therefore, the two equations are identical and $D(6,4)$ is indeed zero at the outer circumference.

The first mode of propagation corresponds to $\beta = 0$. When $\beta = 0$ (assuming no material absorption), the phase velocity equals the shear velocity of the material (i.e. $c_p = c_s$) at all frequencies. It is therefore non-dispersive in nature. The second mode, and all those after, corresponds to the product of βa solving equation 4.75. The first three roots (2nd, 3rd, and 4th torsional modes) are [84]:

$$\beta_1 a = 5.136, \ \beta_2 a = 8.417, \ \beta_3 a = 11.62,\ldots$$

Case II: Torsional Propagation in a Cylindrical Bar surrounded by an Infinite Medium

The global matrix for this case was broken down into two separate matrices that must be satisfied. The second matrix defines torsional propagation for this waveguide configuration. It is shown below:

$$
\begin{array}{ccc}
 & SH -_{cyl} & SH +_{cyl} \\
u_\theta & D(3,6) & -D(3,5) \\
\tau_{r\theta} & D(6,6) & -D(6,5)
\end{array}
$$

Solving the determinant and setting it equal to zero:

$$\beta_{cyl}\beta_{inf}\left(\begin{array}{c}2\gamma_2\left(\mu_{cyl}-\mu_{inf}\right)W_1\left(\beta_{inf}a\right)Z_1\left(\beta_{cyl}a\right)+ \\ a\left(-\mu_{cyl}W_1\left(\beta_{inf}a\right)Z_0\left(\beta_{cyl}a\right)+\gamma_2\mu_{inf}W_0\left(\beta_{inf}a\right)Z_1\left(\beta_{cyl}a\right)\right)\end{array}\right)=0 \quad\ldots\ldots\ldots\ldots\ldots (4.77)$$

Figure 4.6 shows phase velocity as a function of frequency for torsional modes up to 11 MHz. The solution is for rebar 0.472" (11.99 mm) in diameter embedded in an infinite surrounding of dry mortar.
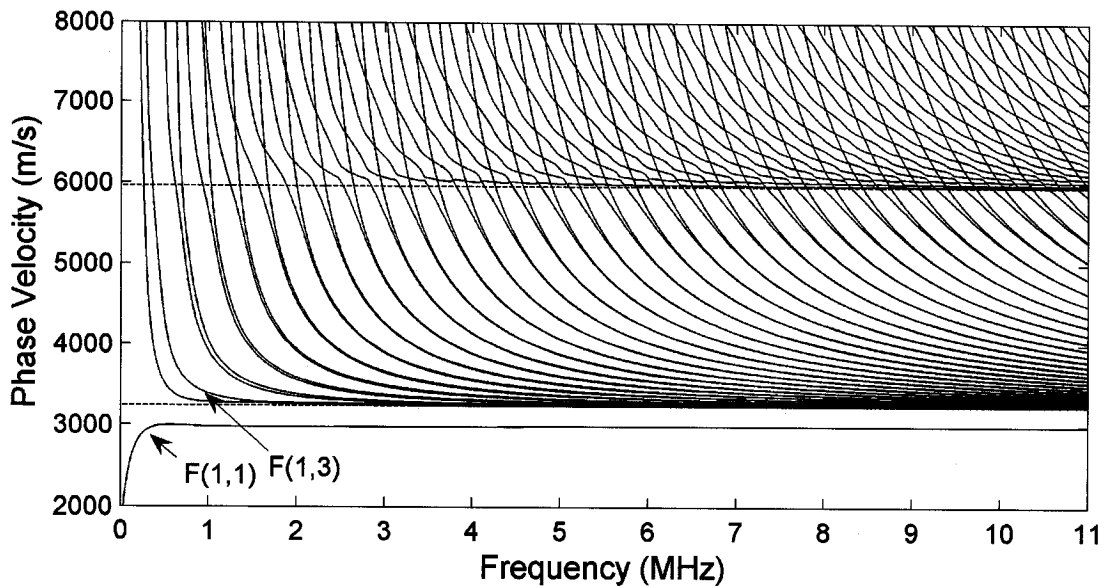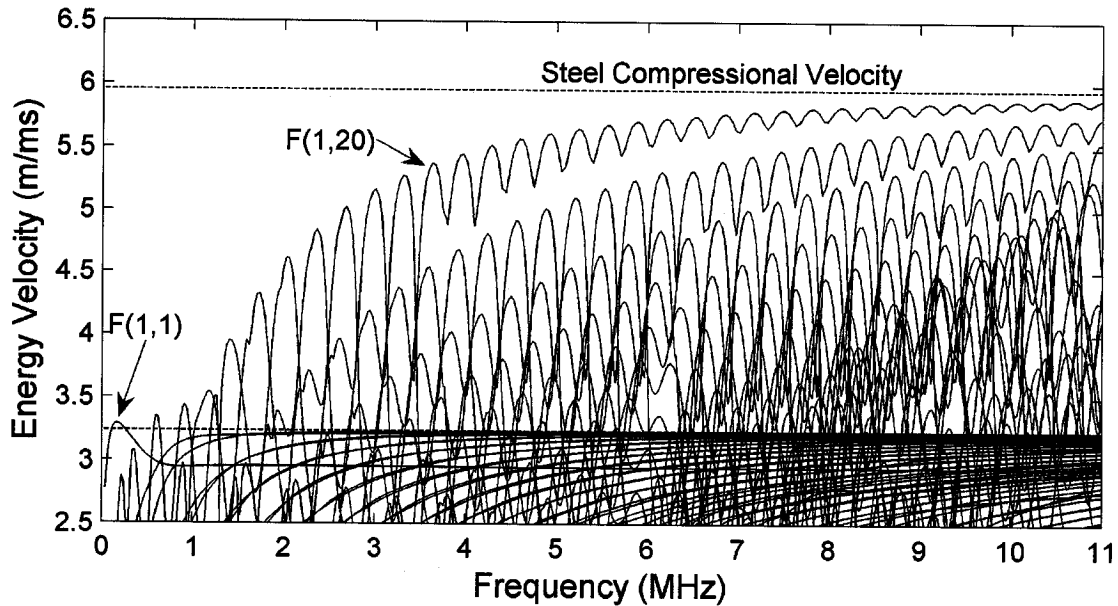
92

Figure 4.6: Phase velocity as a function of frequency for torsional modes of propagation in a 0.472" (11.99 mm) diameter plain steel bar embedded in an infinite surrounding of dry mortar. The dashed line indicates the bulk shear velocity in steel.

Figure 4.7 shows energy velocity as a function of frequency for torsional modes up to 11 MHz.

Figure 4.7: Energy velocity as a function of frequency for torsional modes of propagation in a 0.472" (11.99 mm) diameter plain steel bar embedded in an infinite surrounding of dry mortar. The dashed line indicates the bulk shear velocity in steel.

Figure 4.8 shows attenuation as a function of frequency for torsional modes up to 11 MHz.
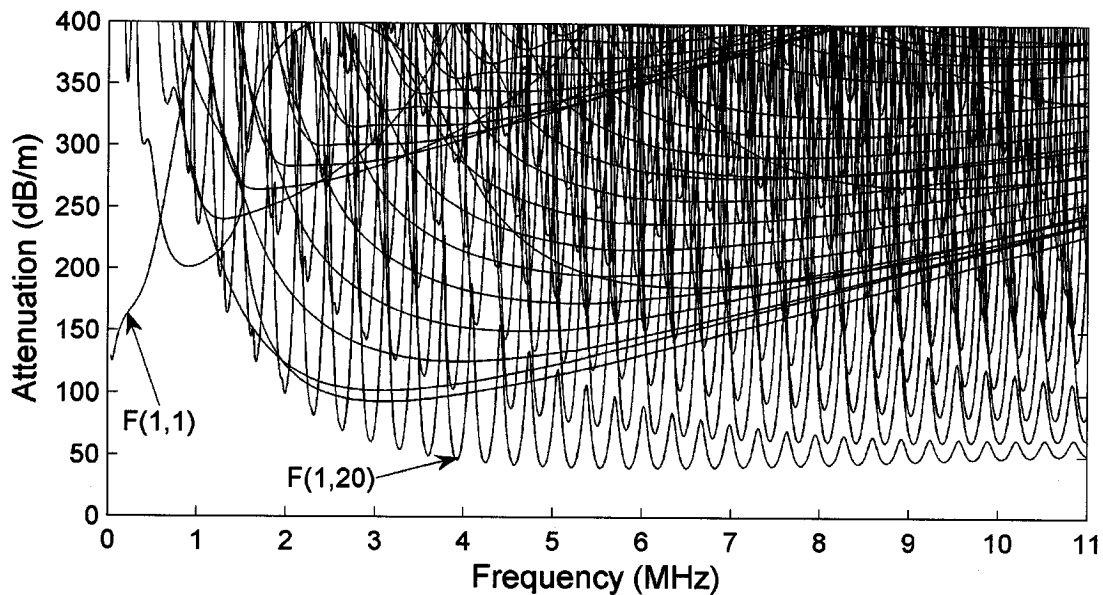
93

Figure 4.8: Attenuation as a function of frequency for torsional modes of propagation in a 0.472" (11.99 mm) diameter plain steel bar embedded in an infinite surrounding of dry mortar.

4.2.2 WAVE PROPAGATION WITH MOTION DEPENDENT ON 'θ'

Wave propagation that is dependent on the angle 'θ' has a circumferential order, 'n', equal to one or greater ('n' must be an integer). The type of wave motion is generally named flexural propagation. A circumferential order equal to one (n = 1) will be assumed, while more complicated types of flexural propagation (i.e. n greater than 1) are not solved for in this report. Flexural modes with a circumferential order greater than one have rather high attenuation in the layered system and are considered impractical for testing. Flexural waves with circumferential order equal to one, considered the lowest ordered family of flexural waves, are discussed after the general equations for wave motion dependent on 'θ' have been written. The displacement and stress components are shown below to help illustrate the behavior:

$$D(1,1) = i\left(r^2 k W_1(\alpha r)\right)$$

$$D(1,2) = i\left(r^2 k Z_1(\alpha r)\right)$$

$$D(1,3) = i\left(r^2 \gamma_2 \beta W_1(\beta r)\right)$$

$$D(1,4) = i\left(r^2 \beta Z_1(\beta r)\right)$$

$$D(1,5) = 0$$

$$D(1,6) = 0$$

$$D(2,1) = r W_1(\alpha r) - r^2 \alpha W_2(\alpha r)$$

$$D(2,2) = r Z_1(\alpha r) - r^2 \gamma_1 \alpha Z_2(\alpha r)$$

$$D(2,3) = r^2 k W_2(\beta r)$$

$$D(2,4) = r^2 k Z_2(\beta r)$$

$$D(2,5) = r W_1(\beta r)$$

$$D(2,6) = r Z_1(\beta r)$$

$$D(3,1) = i\left(r W_1(\alpha r)\right)$$

$$D(3,2) = i\left(r Z_1(\alpha r)\right)$$

$$D(3,3) = -i\left(r^2 k W_2(\beta r)\right)$$

$$D(3,4) = -i\left(r^2 k Z_2(\beta r)\right)$$

$$D(3,5) = i\left(r W_1(\beta r) - r^2 \beta W_2(\beta r)\right)$$

$$D(3,6) = i\left(r Z_1(\beta r) - r^2 \gamma_2 \beta Z_2(\beta r)\right)$$

$$D(4,1) = \mu\left(\left(k^2 - \beta^2\right) r^2 W_1(\alpha r) + 2\alpha r W_2(\alpha r)\right)$$

$$D(4,2) = \mu\left(\left(k^2 - \beta^2\right) r^2 Z_1(\alpha r) + 2\gamma_1 \alpha r Z_2(\alpha r)\right)$$

$$D(4,3) = \mu\left(2\gamma_2 k\beta r^2 W_1(\beta r) - 4 k r W_2(\beta r)\right)$$

$$D(4,4) = \mu\left(2 k\beta r^2 Z_1(\beta r) - 4 k r Z_2(\beta r)\right)$$

$$D(4,5) = \mu\left(-2\beta r W_2(\beta r)\right)$$

$$D(4,6) = \mu\left(-2\gamma_2 \beta r Z_2(\beta r)\right)$$

$$D(5,1) = i\mu\left(2 k r W_1(\alpha r) - 2 k\alpha r^2 W_2(\alpha r)\right)$$

$$D(5,2) = i\mu\left(2 k r Z_1(\alpha r) - 2\gamma_1 k\alpha r^2 Z_2(\alpha r)\right)$$

$$D(5,3) = i\mu\left(\gamma_2 \beta r W_1(\beta r) + r^2\left(k^2 - \beta^2\right) W_2(\beta r)\right)$$

$$D(5,4) = i\mu\left(\beta r Z_1(\beta r) + r^2\left(k^2 - \beta^2\right) Z_2(\beta r)\right)$$

$$D(5,5) = i\mu\left(k r W_1(\beta r)\right)$$

$$D(5,6) = i\mu\left(k r Z_1(\beta r)\right)$$

94

$$D(6,1) = i\mu(-2r\alpha W_2(\alpha r))$$

$$D(6,2) = i\mu(-2\gamma_1 r\alpha Z_2(\alpha r))$$

$$D(6,3) = i\mu(-kr^2\gamma_2\beta W_1(\beta r) + 4rkW_2(\beta r))$$

$$D(6,4) = i\mu(-kr^2\beta Z_1(\beta r) + 4rkZ_2(\beta r))$$

$$D(6,5) = i\mu(-\beta^2 r^2 W_1(\beta r) + 2r\beta W_2(\beta r))$$

$$D(6,6) = i\mu(-\beta^2 r^2 Z_1(\beta r) + 2\gamma_2 r\beta Z_2(\beta r))$$

Flexural Propagation (n = 1)

In the derivation of longitudinal and torsional propagation, one and then two of the displacement equations (u_r, u_θ, u_z) were equal to zero, respectively. For flexural propagation, all of the displacement equations are assumed to exist and are dependent on the angle 'θ'. For the lowest family of flexural propagation (n = 1), the displacement at the top and bottom of the cylinder is 180° out of phase. The displacement equations are shown below:

$$u_r = \frac{1}{r^2}\left(\begin{array}{l} A(rZ_1(\alpha r) - r^2\gamma_1\alpha Z_2(\alpha r)) + B(rW_1(\alpha r) - r^2\alpha W_2(\alpha r)) + \\ A_1 r^2 kZ_2(\beta r) + B_1 r^2 kW_2(\beta r) + A_3 rZ_1(\beta r) + B_3 rW_1(\beta r) \end{array} \right) \cos(\theta)e^{i(kz-\omega t)} \quad \ldots\ldots\ldots(4.78)$$

$$u_\theta = -\frac{1}{r^2}\left(\begin{array}{l} ArZ_1(\alpha r) + BrW_1(\alpha r) - A_1 r^2 kZ_2(\beta r) - B_1 r^2 kW_2(\beta r) + \\ A_3(rZ_1(\beta r) - r^2\gamma_2\beta Z_2(\beta r)) + B_3(rW_1(\beta r) - r^2\beta W_2(\beta r)) \end{array} \right) \sin(\theta)e^{i(kz-\omega t)} \quad \ldots\ldots\ldots(4.79)$$

$$u_z = i\frac{1}{r^2}(Ar^2 kZ_1(\alpha r) + Br^2 kW_1(\alpha r) + A_1 r^2\beta Z_1(\beta r) + B_1 r^2\gamma_2\beta W_1(\beta r))\cos(\theta)e^{i(kz-\omega t)} \quad \ldots\ldots(4.80)$$

Case I: Flexural Propagation for a Cylindrical Bar in a Vacuum

The determinant of the general 3 x 3 material layer matrix shown below is solved for flexural (n = 1) propagation.

	L – (A)	SV – (A_1)	SH – (A_3)
σ_{rr}	D(4,2)	D(4,4)	D(4,6)
τ_{rz}	D(5,2)	D(5,4)	D(5,6)
$\tau_{r\theta}$	D(6,2)	D(6,4)	D(6,6)

Case II: Flexural Propagation for a Cylindrical Bar Surrounded by an Infinite Medium

The determinant of the entire global matrix will be solved for flexural propagation.

95

$$\begin{bmatrix} \mathbf{D}_{12} & \mathbf{D}_{14} & \mathbf{D}_{16} & -\mathbf{D}_{11} & -\mathbf{D}_{13} & -\mathbf{D}_{15} \\ \mathbf{D}_{22} & \mathbf{D}_{24} & \mathbf{D}_{26} & -\mathbf{D}_{21} & -\mathbf{D}_{23} & -\mathbf{D}_{25} \\ \mathbf{D}_{32} & \mathbf{D}_{34} & \mathbf{D}_{36} & -\mathbf{D}_{31} & -\mathbf{D}_{33} & -\mathbf{D}_{35} \\ \mathbf{D}_{42} & \mathbf{D}_{44} & \mathbf{D}_{46} & -\mathbf{D}_{41} & -\mathbf{D}_{43} & -\mathbf{D}_{45} \\ \mathbf{D}_{52} & \mathbf{D}_{54} & \mathbf{D}_{56} & -\mathbf{D}_{51} & -\mathbf{D}_{53} & -\mathbf{D}_{55} \\ \mathbf{D}_{62} & \mathbf{D}_{64} & \mathbf{D}_{66} & -\mathbf{D}_{61} & -\mathbf{D}_{63} & -\mathbf{D}_{65} \end{bmatrix} \begin{bmatrix} A \\ A_1 \\ A_3 \\ B \\ B_1 \\ B_3 \end{bmatrix} = \begin{bmatrix} 0 \\ 0 \\ 0 \\ 0 \\ 0 \\ 0 \end{bmatrix}$$

(where the first three columns correspond to the **Cylinder (Half-Space)** and the last three columns correspond to the **Infinite Medium (Half-Space)**)

Figure 4.9 shows phase velocity as a function of frequency for flexural modes (n = 1) up to 11 MHz. The solution is for rebar 0.472" (11.99 mm) in diameter embedded in an infinite surrounding of dry mortar.

Figure 4.9: Phase velocity as a function of frequency for flexural modes of propagation in a 0.472" (11.99 mm) diameter plain steel bar embedded in an infinite surrounding of dry mortar. Dashed lines indicate the bulk compressional velocity (top line) and shear velocity (bottom line) in steel.

Figures 4.10 and 4.11 show the energy velocity and attenuation as a function of frequency for flexural modes (n = 1) up to 11 MHz, respectively.

96

Figure 4.10: Energy velocity as a function of frequency for flexural modes of propagation in a 0.472" (11.99 mm) diameter plain steel bar embedded in an infinite surrounding of dry mortar. Dashed lines indicate the bulk compressional velocity (top line) and shear velocity (bottom line) in steel.

Figure 4.11: Attenuation as a function of frequency for flexural modes of propagation in a 0.472" (11.99 mm) diameter plain steel bar embedded in an infinite surrounding of dry mortar.

4.2.3 MULTILAYERED SYSTEM

Since smaller specimen sizes will be used for the experimental investigation contained within this report, the longitudinal and flexural modes for a steel bar in a cylindrical mortar layer 1.76" (4.48 cm) thick within an infinite surrounding of air are plotted in Figure 4.12.

97
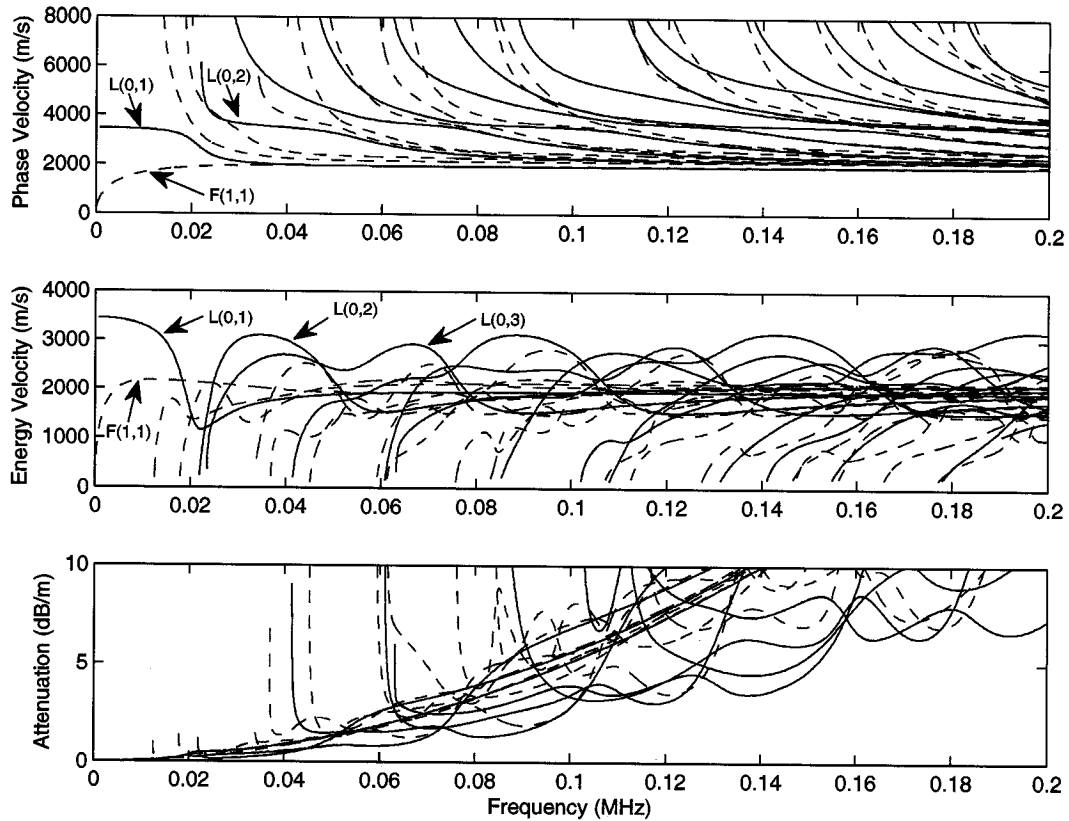
Figure 4.12: Dispersion curves for guided wave propagation in a reinforced cylindrical mortar beam. The system consists of a solid steel cylinder 0.472" (11.99 mm) in diameter embedded in a 1.76" (4.48 cm) thick cylindrical layer of mortar with an infinite surrounding of air on the outside.

4.3 MODE SELECTION

Notice in Figures 4.5, 4.8, and 4.11 there are dips in the attenuation for the family of modes. Previous authors have discussed attenuation dips [96,99]. Typically, one thinks of higher frequency waveforms as being more attenuated than lower frequencies due to material absorption. This is usually the case for wave propagation in a bulk medium. However, for a layered waveguide system, leakage plays a critical role. Frequency regions with the lowest attenuating modes are those with displacement profiles centered in the middle of the bar to avoid leakage but at a low enough frequency to avoid substantial material absorption. The objective of this report is to find guided wave modes capable of monitoring corrosion in reinforced concrete. Therefore, modes are needed that are sensitive to different elements of the corrosion process but can be utilized over realistic propagation distances. Only the lowest attenuating and most easily distinguished modes are considered for this investigation. The L(0,1), F(1,1), and L(0,9) modes are chosen for the experimental investigation. Figure 4.13 illustrates the strain energy density profile for the three modes at specific frequencies for a 0.472" (11.99 mm) diameter steel bar embedded in an infinite surrounding of dry mortar.

98
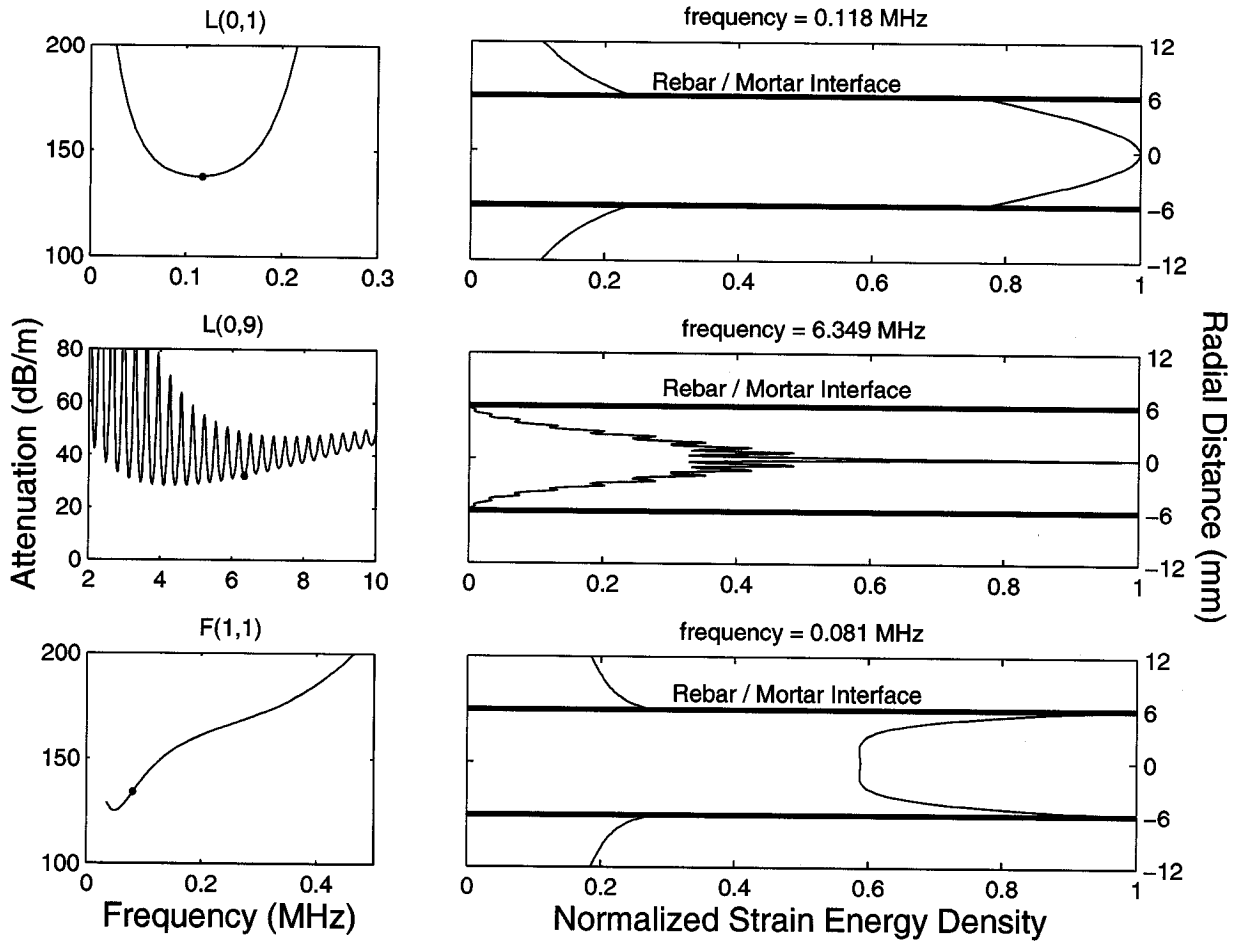
Figure 4.13: Strain energy density profiles for the L(0,1), F(1,1), and L(0,9) modes in rebar 0.472" (11.99 mm) in diameter embedded in an infinite surrounding of dry mortar. The location of the frequencies on the attenuation curve are shown on the left.

The locations of the frequencies on the attenuation solution are shown on the left in Figure 4.13. Both the L(0,1) and F(1,1) modes have significant energy at the rebar/mortar interface, resulting in leakage. Because the frequencies are so low, the amount of signal loss due to material absorption is negligible. Therefore, these two modes were selected for investigation to assess interfacial damage between the steel and mortar. The modes should be distinguishable from each other in the same frequency region because their energy velocities are substantially different. Figure 4.14 shows the L(0,1) and F(1,1) energy velocities together.
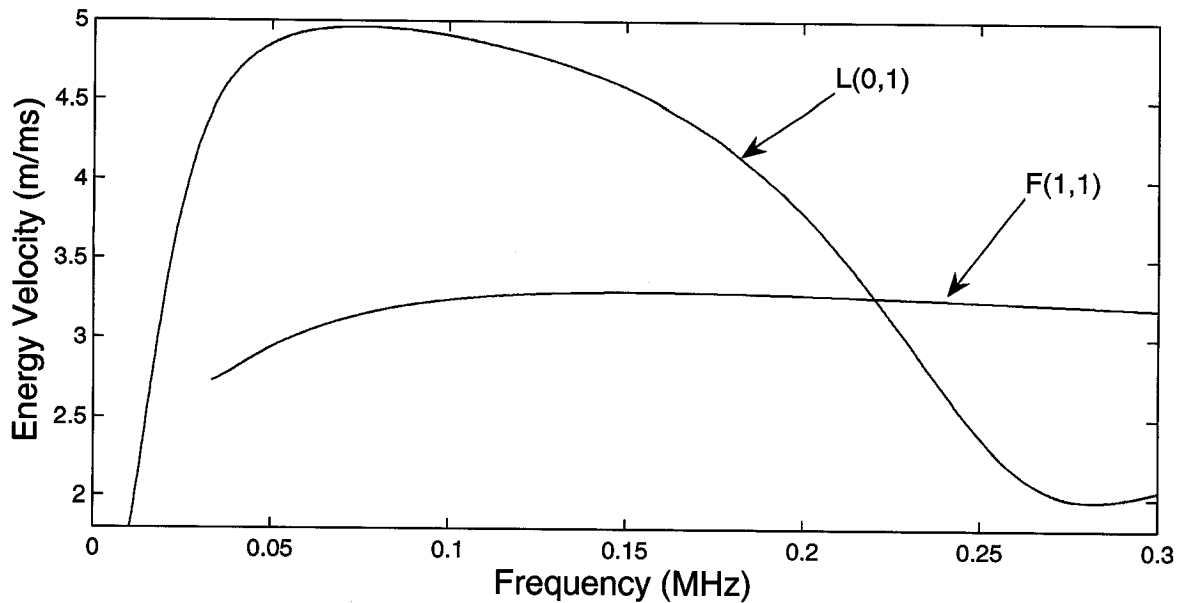
Figure 4.14: Energy velocity as a function of frequency for the L(0,1) and F(1,1) modes in rebar 0.472" (11.99 mm) in diameter embedded in an infinite surrounding of mortar.

The L(0,9) mode was chosen because it is the lowest attenuating mode in the entire system. Notice in Figure 4.13 that the strain energy is concentrated in the center of the rebar. This prevents excessive leakage. Before material absorption becomes prohibitively high at higher frequencies, the mode reaches the global attenuation minimum of 28.37 dB/m at 4.416 MHz. The L(0,9) mode crosses over other modes around the bulk compressional velocity of steel. This behavior was discussed in previous literature [99]. Note that there are other higher order longitudinal modes, as well as flexural modes, that behave in this manner. However, the L(0,9) is the fastest and lowest attenuating mode in the system. Figure 4.15 plots the phase velocity for the L(0,8), L(0,9), L(0,10), and L(0,11) modes to illustrate the mode-crossing behavior. Due to the L(0,9) being the fastest propagating mode, it will be easily distinguished from all other modes in this frequency range.

100
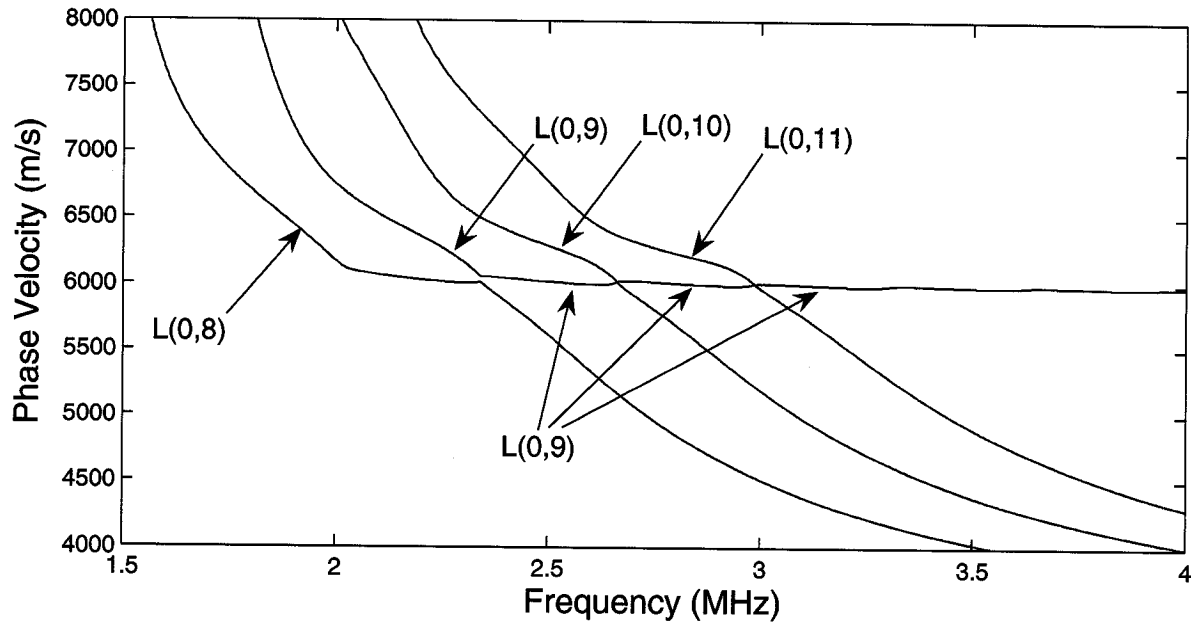
Figure 4.15: Phase velocity of L(0,8), L(0,9), L(0,10), and L(0,11) modes as a function of frequency. Notice that the L(0,9) mode crosses over the other modes.

4.4 SENSITIVITY ANALYSIS

Sensitivity analysis is now conducted for the three modes chosen for investigation. Of interest is how guided wave behavior is affected by the geometry of the guiding configuration, the presence of different interface conditions surrounding the bar (e.g. water and air), and the material properties of the mortar, steel, and rust. The effects of material property changes in the mortar are examined first. Figure 4.16 illustrates the individual effect of a 20% change in the mortar elastic modulus (E), the mortar density (ρ), and the mortar material absorption coefficients (α_d, α_s).

101
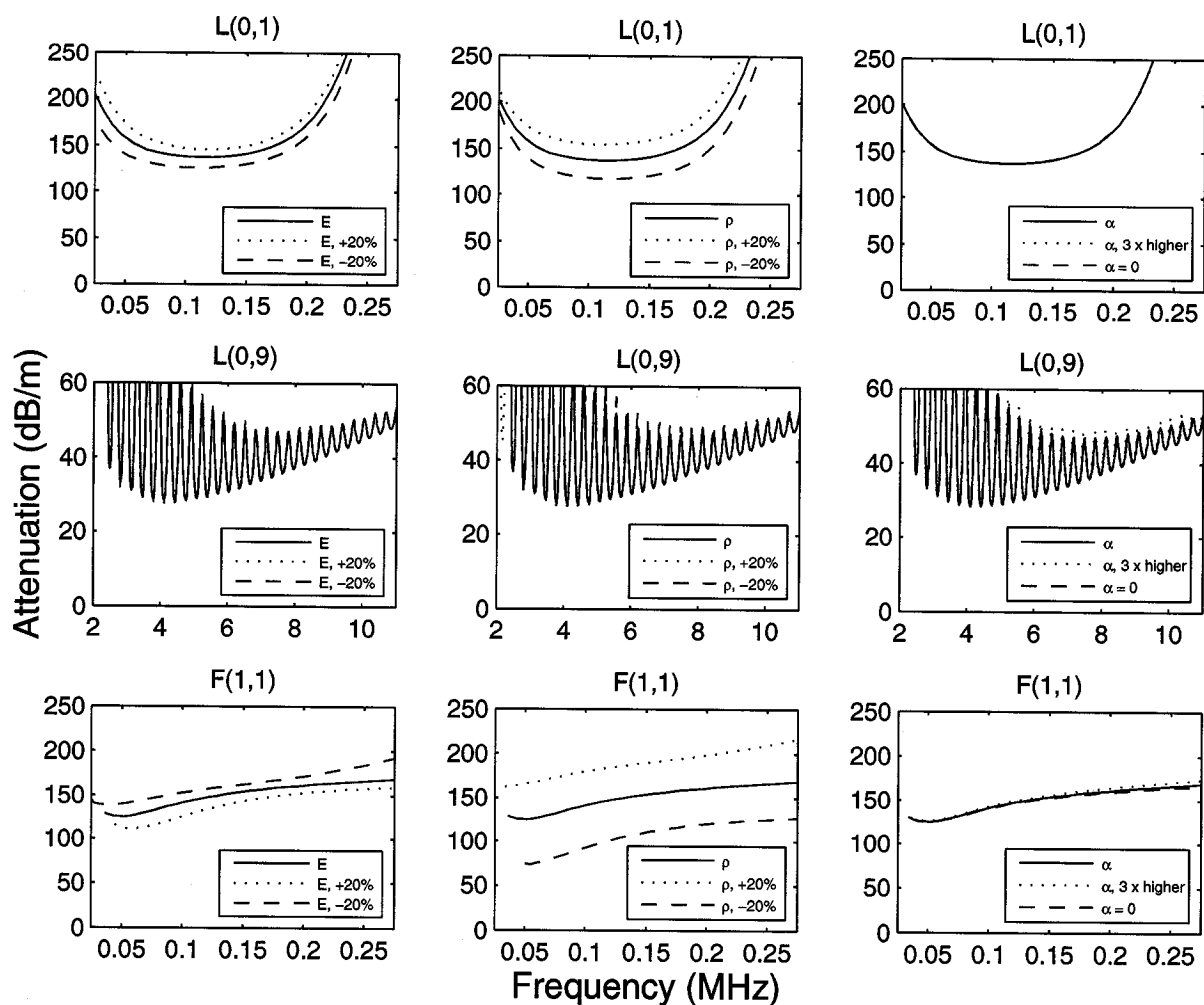
Figure 4.16: Attenuation as a function of frequency for rebar surrounded by mortar. Sensitivity analysis was conducted on mortar material properties (E, ρ, α_d, α_s).

The L(0,9) mode is virtually unaffected by changes in the mortar material properties. The energy profile of the L(0,9) mode is centered in the middle of the bar, making the mode less sensitive to the surrounding mortar. All three modes have no sensitivity to the mortar material absorption coefficient. The L(0,1) and F(1,1) modes have such a low frequency that material absorption is negligible. The L(0,1) and F(1,1) modes are sensitive to the changes in E and ρ, with the most sensitivity to the density. For the F(1,1) mode, an increase in the mortar stiffness will actually decrease the amount of attenuation. The opposite is true for the L(0,1) mode. As the mortar cracks from the corrosion product accumulation, there should be a decrease in the overall stiffness. The lower frequency modes might be able to detect these changes. For both the L(0,1) and F(1,1) modes, a more dense mortar mix will lead to significantly more attenuation. However, concrete/mortar mixes used on-site have variability with respect to the hardened material properties. This could play a critical role in determining the applicability of the lower frequency modes. The lack of sensitivity of the L(0,9) mode to mortar material properties makes it a particularly attractive

102

option for in-situ condition monitoring. Figure 4.17 displays the energy velocity of the three modes as the mortar material properties are changed.
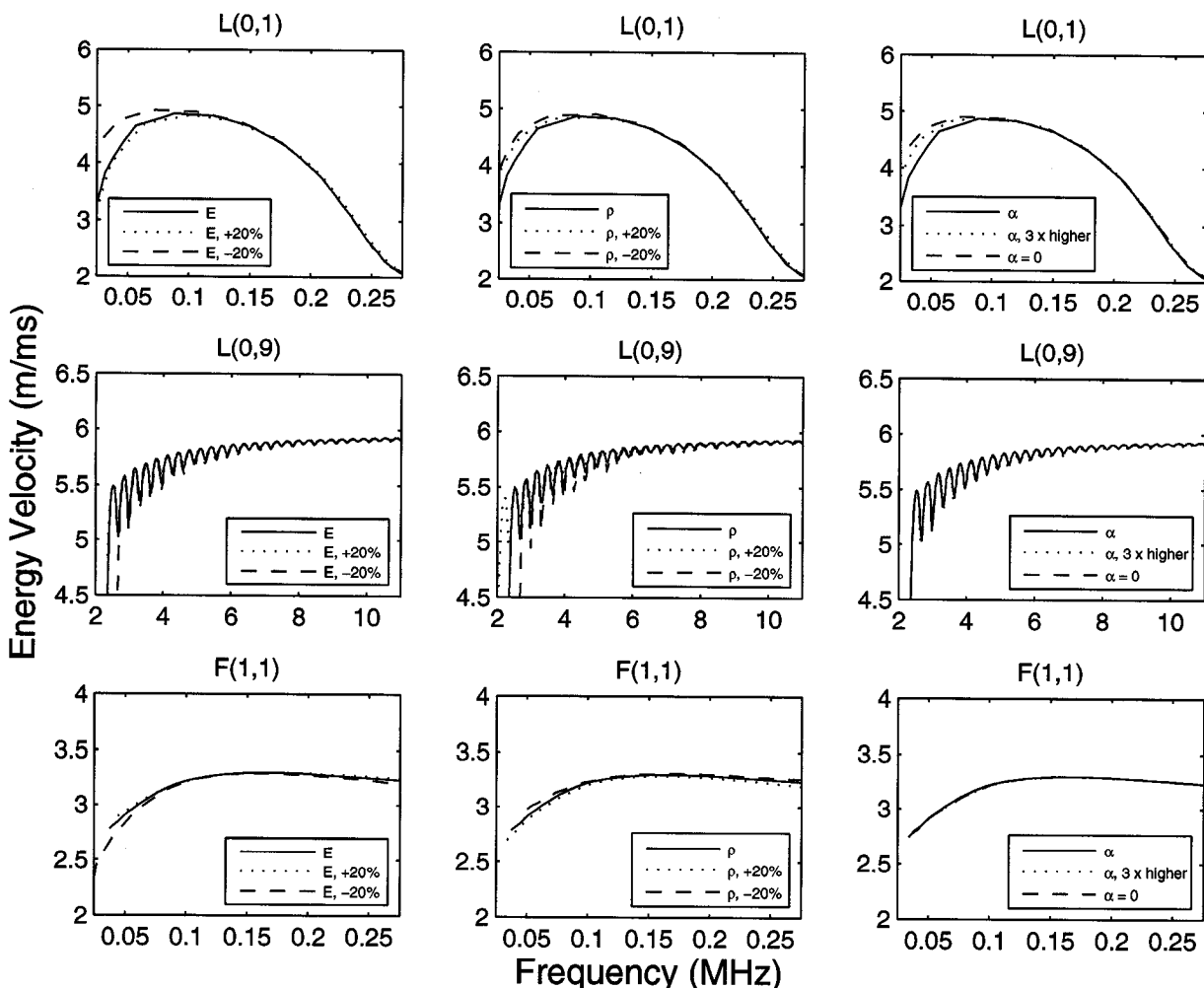
Figure 4.17: Energy velocity as a function of frequency for rebar surrounded by mortar. Sensitivity analysis was conducted on mortar material properties (E, ρ, α_d, α_s).

There is some discrepancy for the changes in the L(0,1) behavior at very low frequencies but overall the mortar material properties do not dictate the wave packet velocity. This is a positive feature in the sense that variability in mix designs used on-site should not dictate the mode velocity. However, tracking velocity changes from the depreciation of the mortar stiffness may be less prone to error than tracking attenuation changes. Figure 4.18 shows the attenuation of the modes for a change in rebar material properties.

103
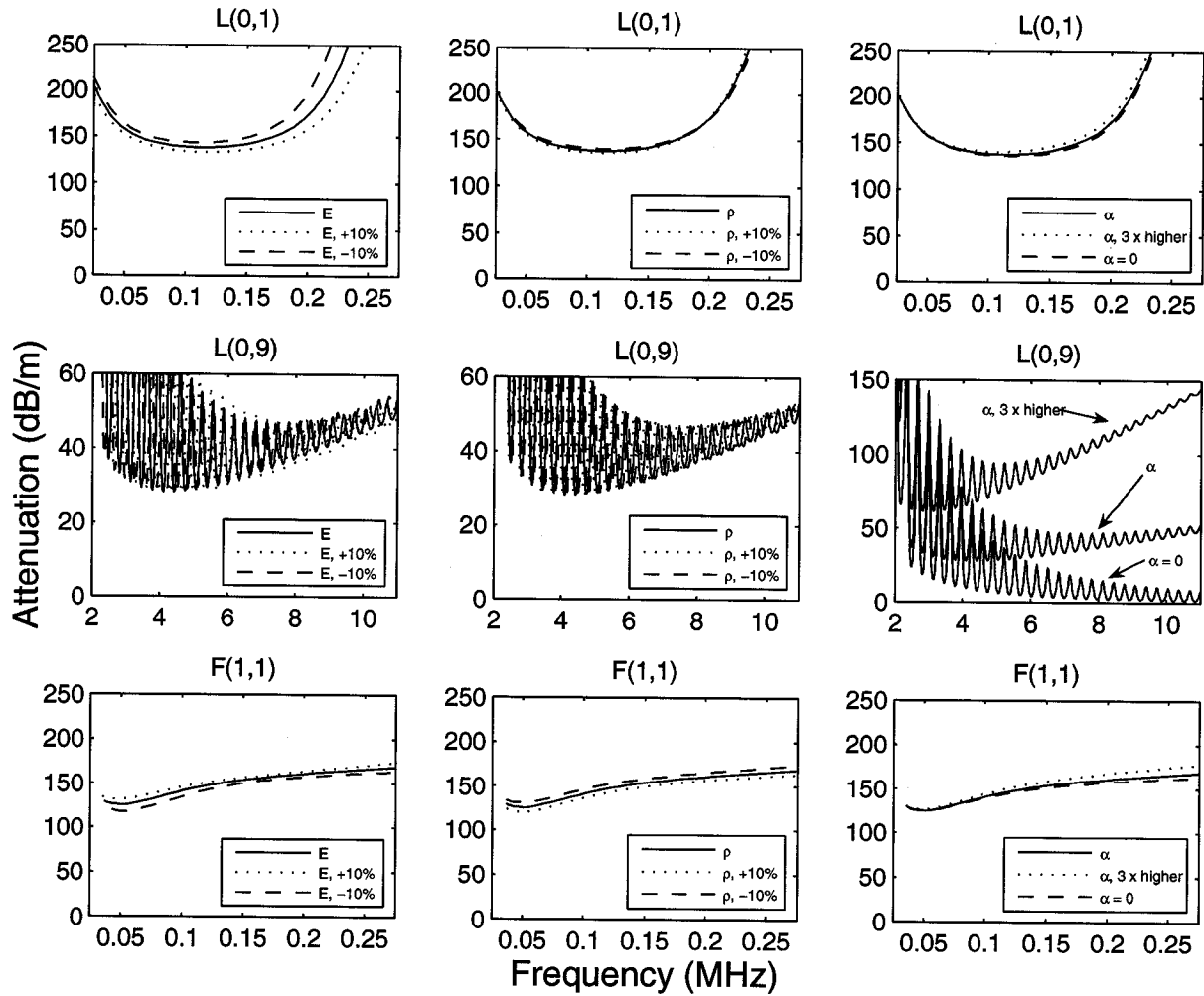
Figure 4.18: Attenuation as a function of frequency for rebar surrounded by mortar. Sensitivity analysis was conducted on rebar material properties (E, ρ, α_d, α_s).

The L(0,9) mode is the most sensitive to the change in rebar material properties. The change in elastic modulus and density causes the frequencies at which attenuation dips occur to shift slightly. The L(0,9) mode has very high sensitivity to the rebar material absorption coefficients. Since this mode is centered and attenuates primarily due to material absorption, this ultimately controls the amount of attenuation, particularly at the highest frequency range. Notice that when the steel material absorption coefficient is set to zero the L(0,9) mode has virtually zero attenuation at the higher frequencies. This confirms that leakage does not affect the behavior at higher frequency attenuation dips for the L(0,9) mode. Figure 4.19 shows energy velocity for the modes as the rebar material properties are changed.
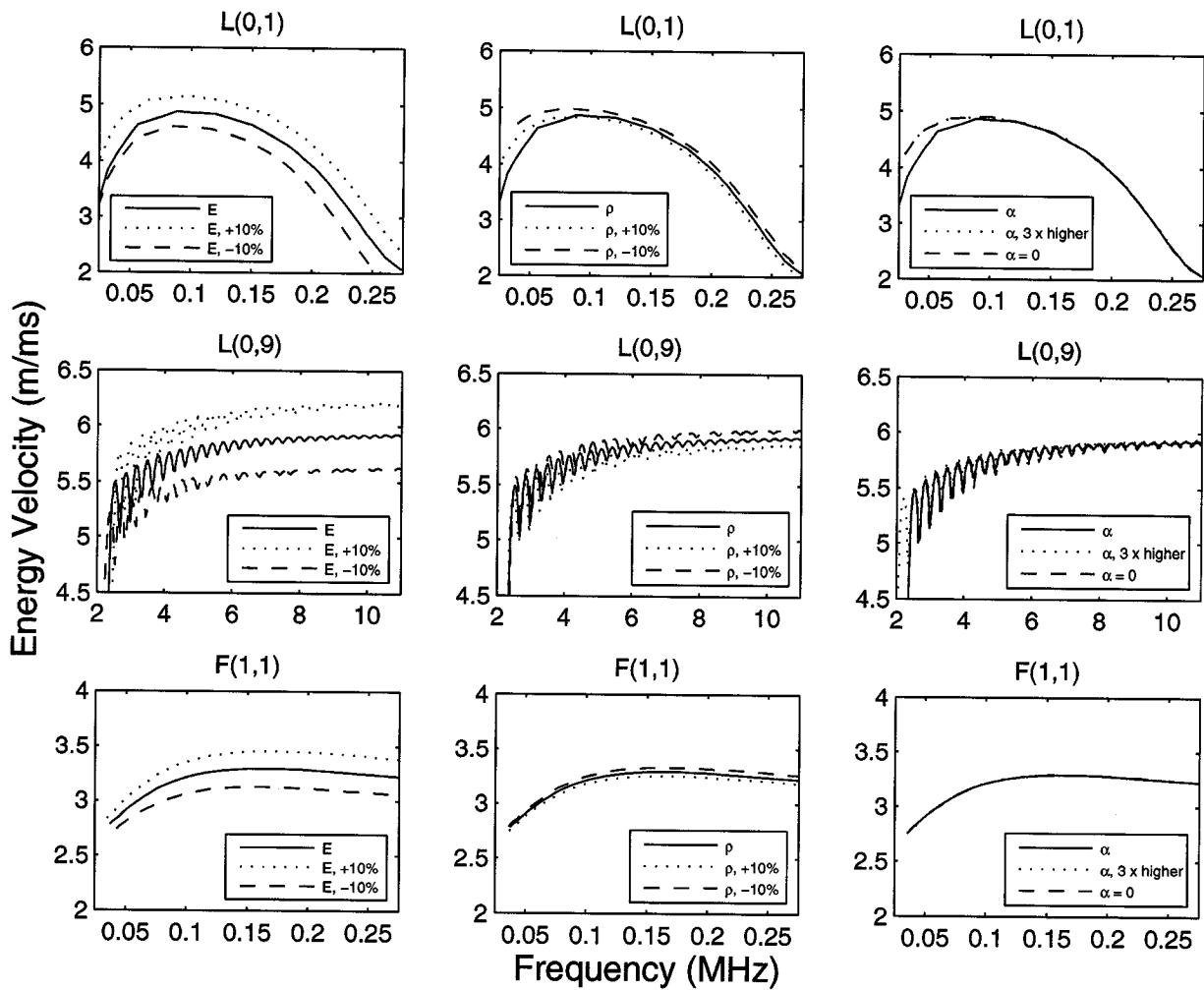
Figure 4.19: Energy velocity as a function of frequency for rebar surrounded by mortar. Sensitivity analysis was conducted on rebar material properties (E, ρ, α).

The change in the steel elastic modulus has a strong effect on the energy velocity for all three modes. As the steel elastic modulus increases and/or density decreases, the velocity increases. Figure 4.20 shows the effect of interface changes on the attenuation of all three modes.

105
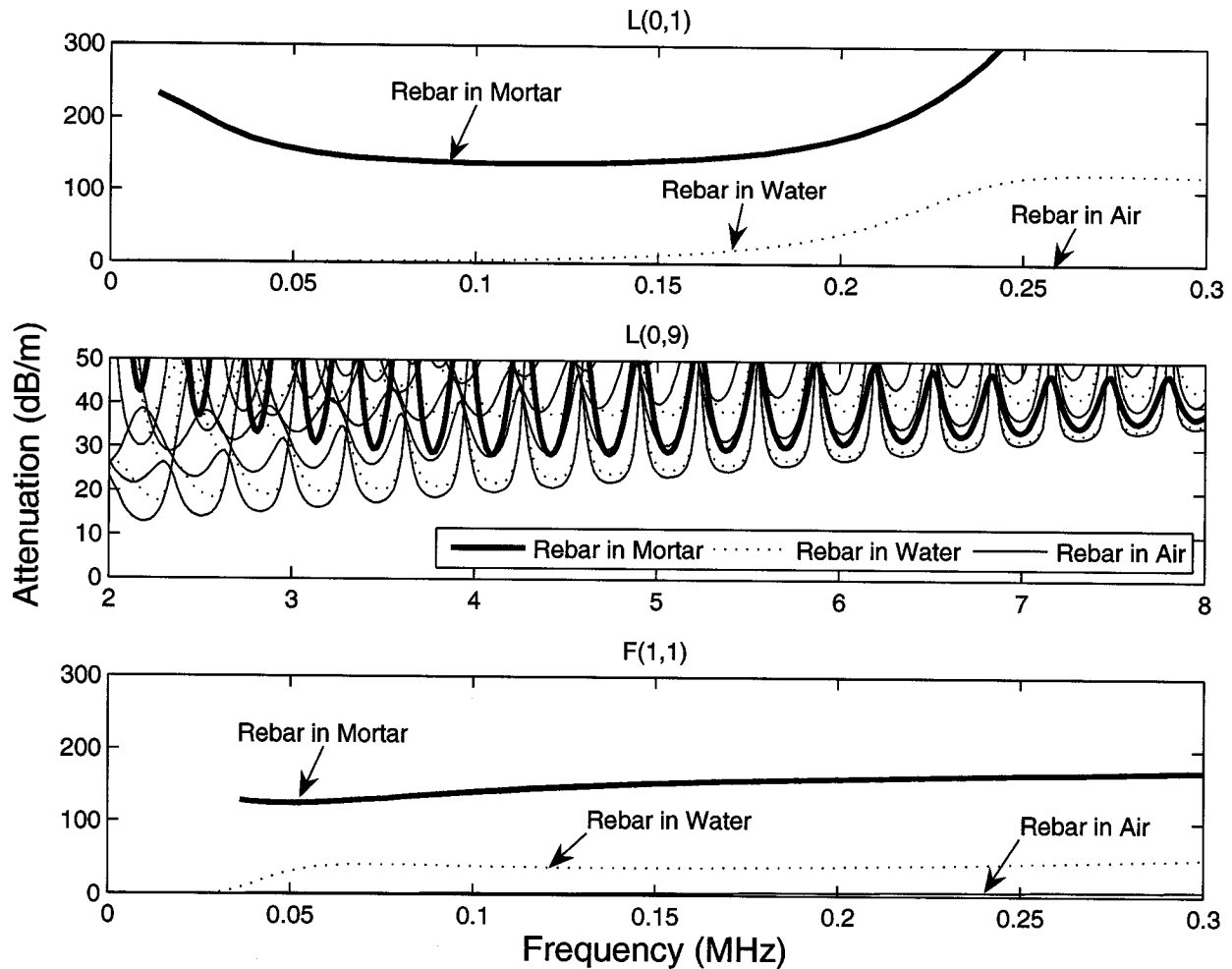
Figure 4.20: Attenuation as a function of frequency for rebar surrounded by mortar, water, and air.

Water will be present in the corrosion reaction. Air could be present at the interface due to debonding, porosity, and poor compaction. In reality, the bar could have partial mortar, water, and air interfaces at any given time. The attenuation will most likely be somewhere between these bounds. The L(0,1) and F(1,1) modes should have sensitivity to debonding because of how large the difference is between a mortar and air surrounding. The difference in attenuation between a mortar and water surrounding is greater for the L(0,1) mode than the F(1,1) mode. In other words, water may play a role in the applicability of the F(1,1) mode to monitor debonding. The L(0,9) mode has decreasing sensitivity to the interfacial conditions as the frequency increases. While the material absorption increases, the lack of sensitivity to the surrounding interfaces decreases. Figure 4.21 shows the effect of interfacial changes on the energy velocity of the modes.
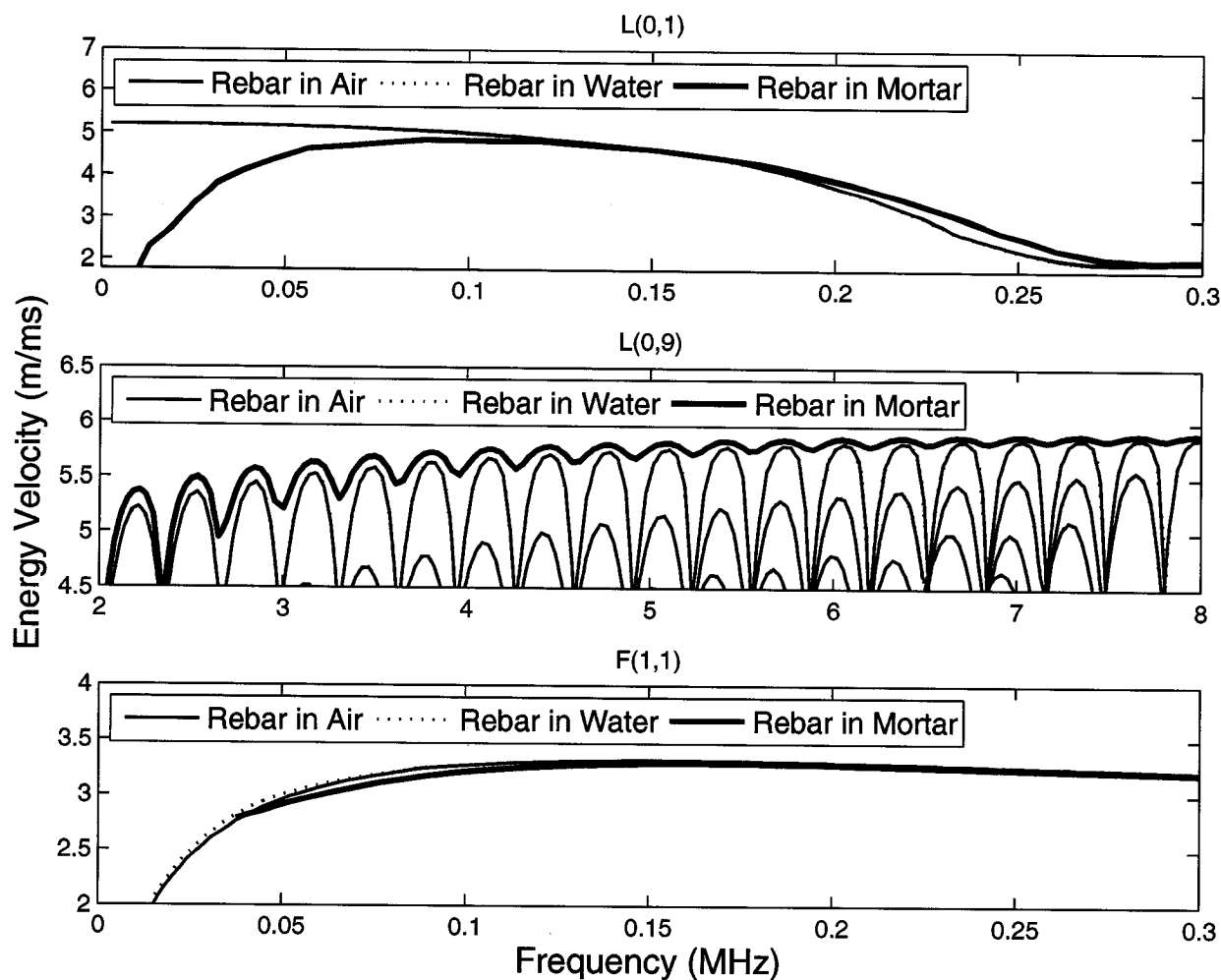
Figure 4.21: Energy velocity as a function of frequency for rebar surrounded by mortar, water, and air.

The L(0,1) has a velocity difference only at the lowest frequencies. The F(1,1) mode shows relatively no change in velocity for the three conditions. An interesting feature of the L(0,9) mode is that there is no significant drop off in the velocity between velocity peaks. Notice that for the bar in air and/or water, when the frequency moves to the left or right of a velocity peak, the velocity drops off rapidly. However, this does not occur for the bar in mortar. Figure 4.22 shows the effect of the surrounding mortar becoming wet (i.e. material property change) on the attenuation characteristics of the three modes.
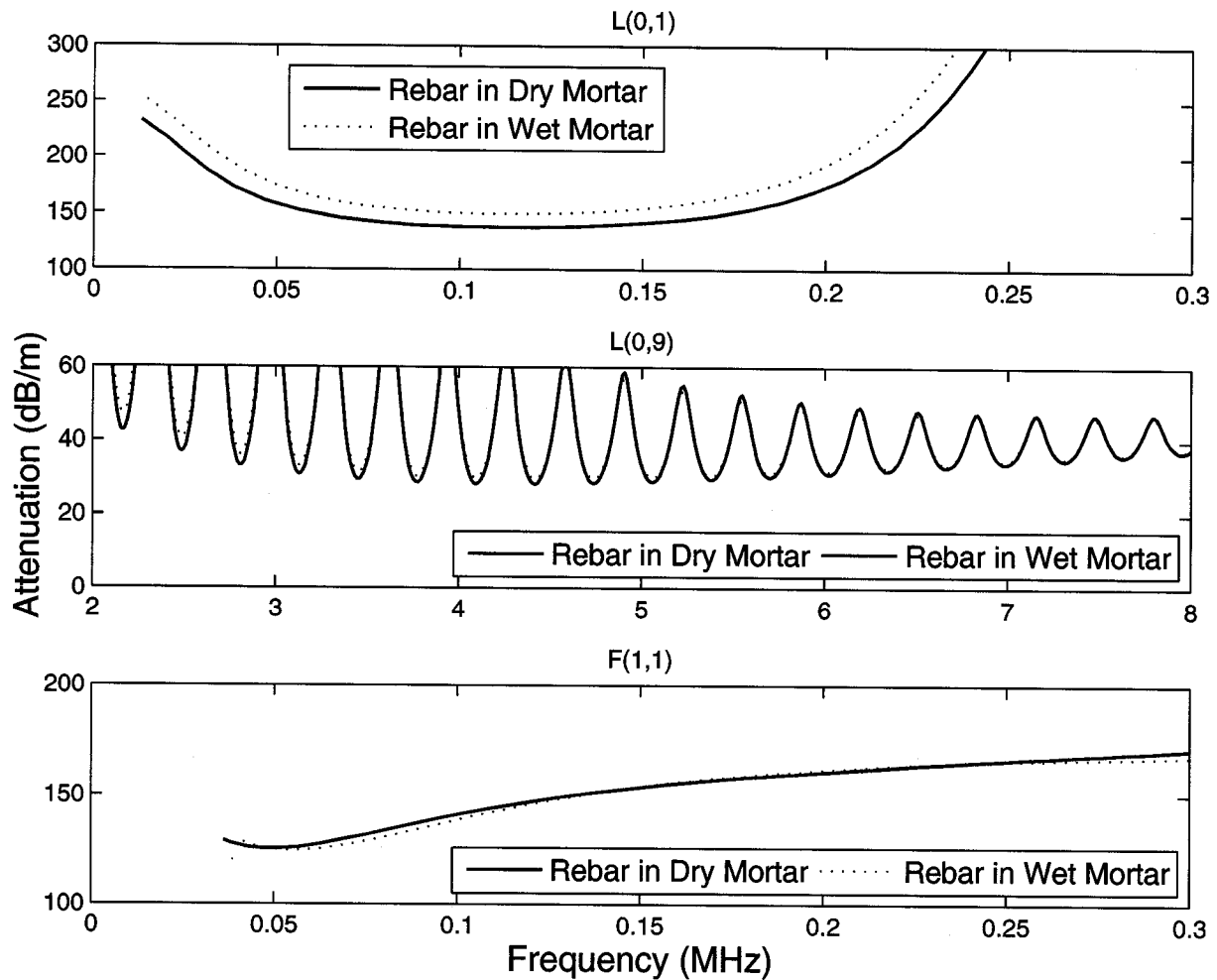
Figure 4.22: Attenuation as a function of frequency for rebar surrounded by dry mortar and wet mortar.

There is an increase in attenuation for the L(0,1) mode as the mortar is wetted, while the L(0,9) remains the same. The F(1,1) mode has a very slight decrease in attenuation as the mortar is wetted. It seems that the wetting of the mortar based on the change of the mortar material properties will most affect the L(0,1) mode attenuation characteristics. Figure 4.23 shows the effect of the surrounding mortar becoming wet on the energy velocity of the three modes.

108
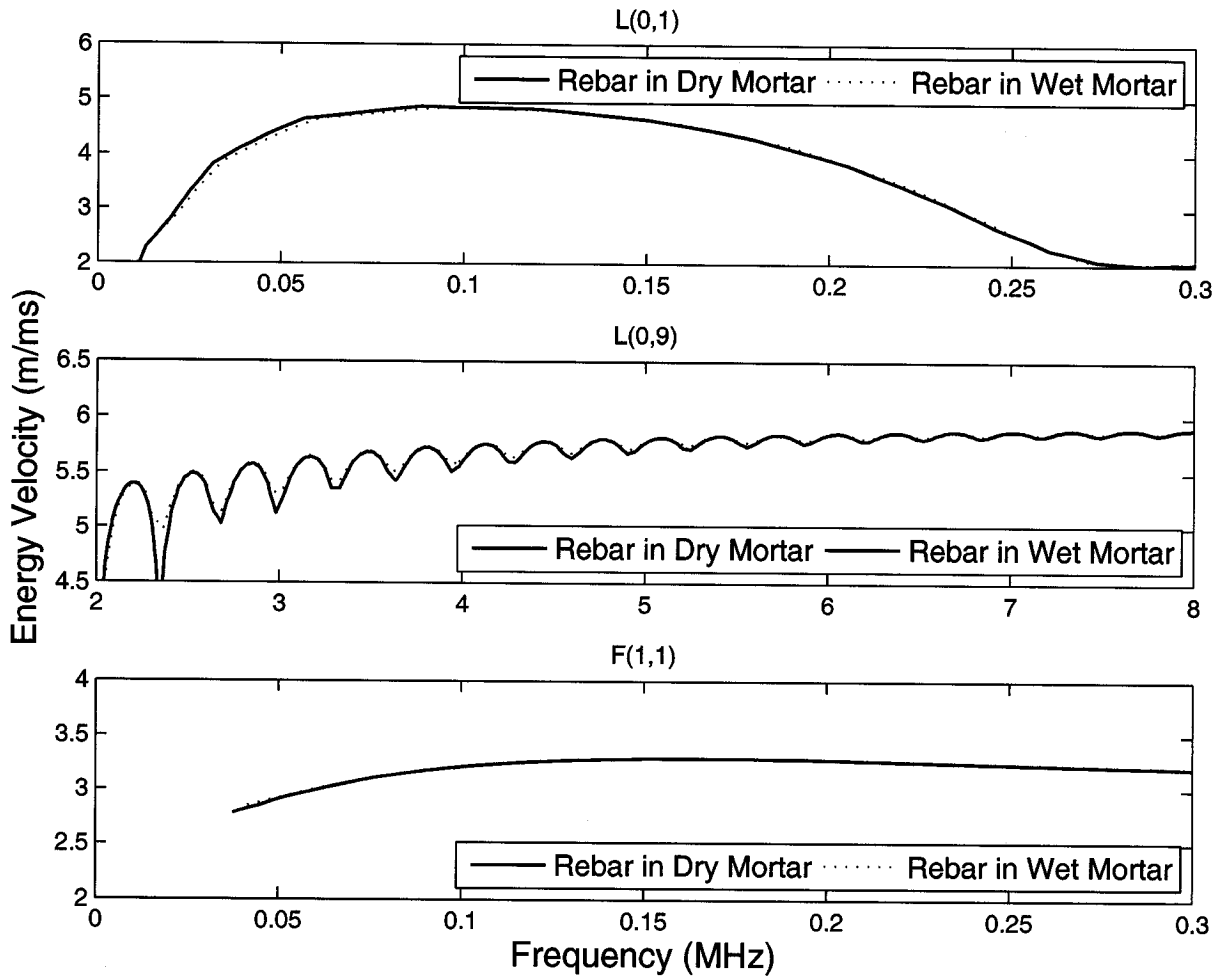
Figure 4.23: Energy velocity as a function of frequency for rebar surrounded by dry mortar and wet mortar.

All three modes have negligible changes in the energy velocity from the change in the mortar material properties from wetting. Figure 4.24 shows the effect of changing the radius of a bar in air (models cross-sectional loss from corrosion) on the attenuation of the three modes.
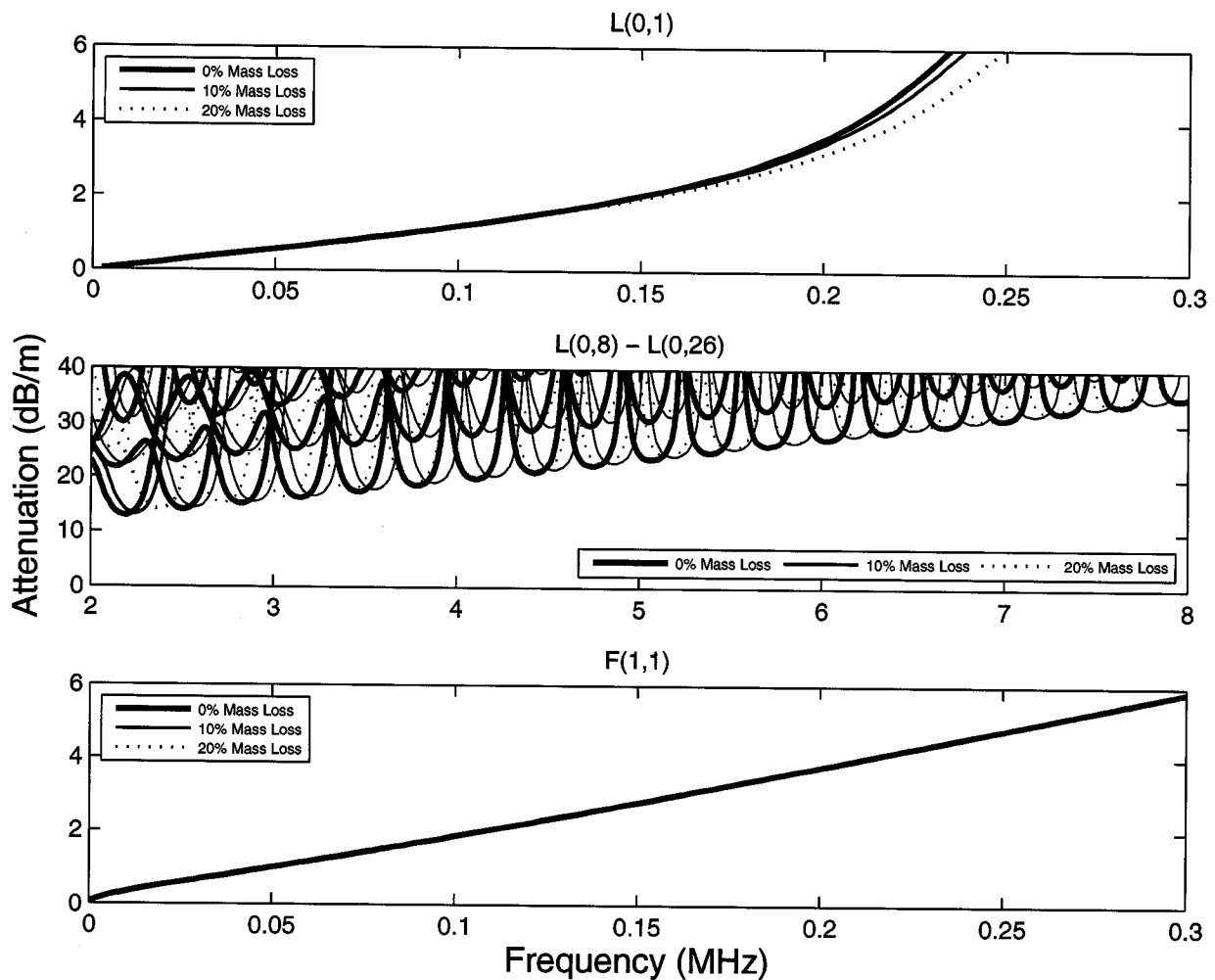
Figure 4.24: Attenuation as a function of frequency for rebar in air with varying cross-sectional areas.

The L(0,1) mode is minimally affected at frequencies above 200 kHz, while the F(1,1) mode is not affected by the diameter loss. Since this is a bar in air, the L(0,9) mode does not display mode-crossing behavior. Therefore, each attenuation dip is a separate mode. While the magnitude of attenuation stays the same, the location of the attenuation dip shifts for the high frequency modes. In realistic cases of uniform corrosion, the diameter along the length of the bar may vary substantially and be best represented by a statistical distribution. Therefore, attenuation dips may occur at several frequency locations. Figure 4.25 shows the effect of the diameter change on the energy velocity for the modes.
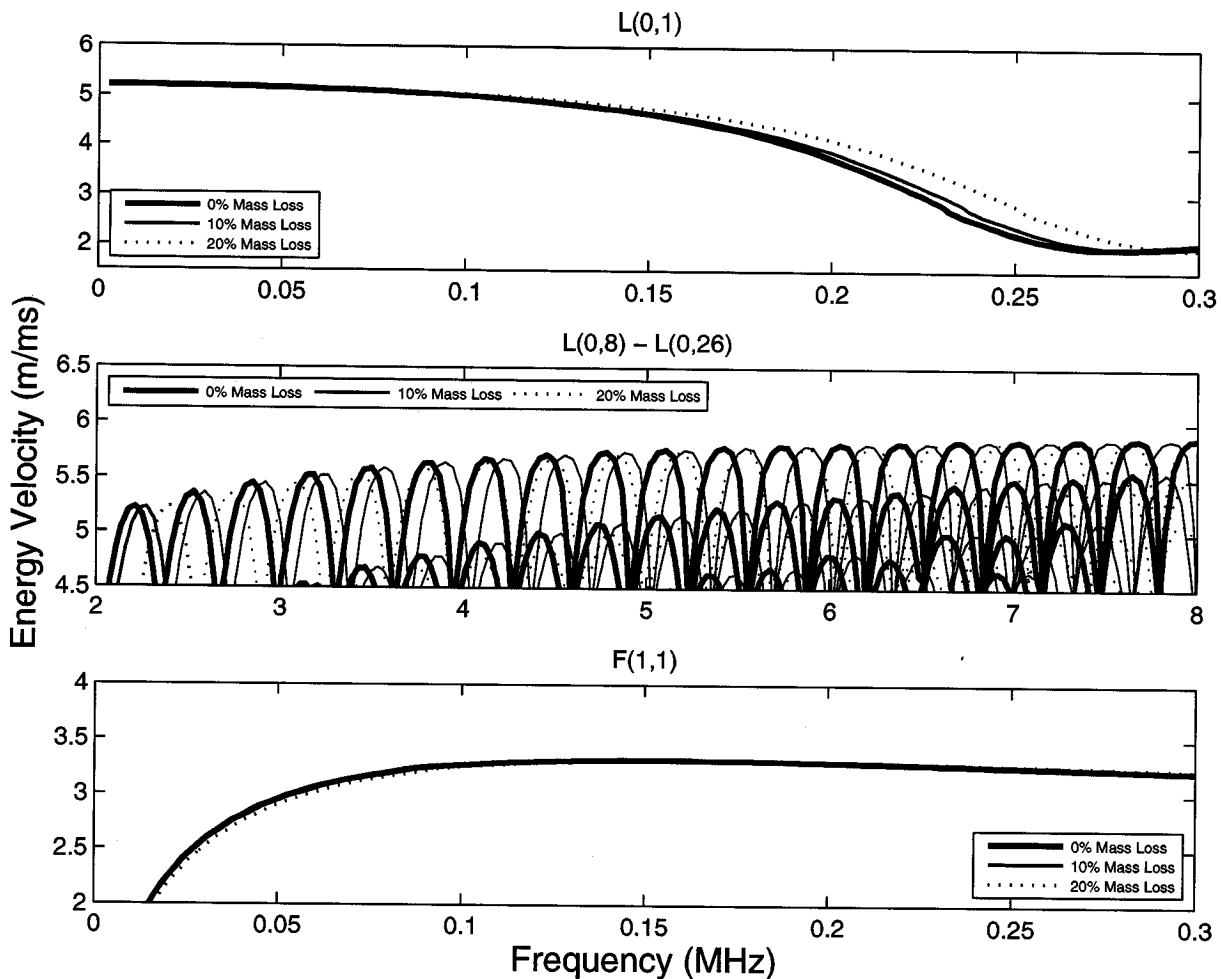
Figure 4.25: Energy velocity as a function of frequency for rebar in air with varying cross-sectional areas.

The L(0,1) has some velocity increase in the 200-275 kHz range for decreases in the bar diameter. The F(1,1) is virtually unaffected by the change in diameter. For the high frequency longitudinal modes, it seems that a frequency shift in the location of the peaks may signal cross-sectional loss. Figure 4.26 shows the effect of increasing the corrosion product elastic modulus on the attenuation characteristics of the modes. The thickness of the corrosion product layer was 0.00288" (0.07305 mm), while the bar remained 0.472" (11.99 mm) in diameter with an infinite surrounding of wet mortar.

111
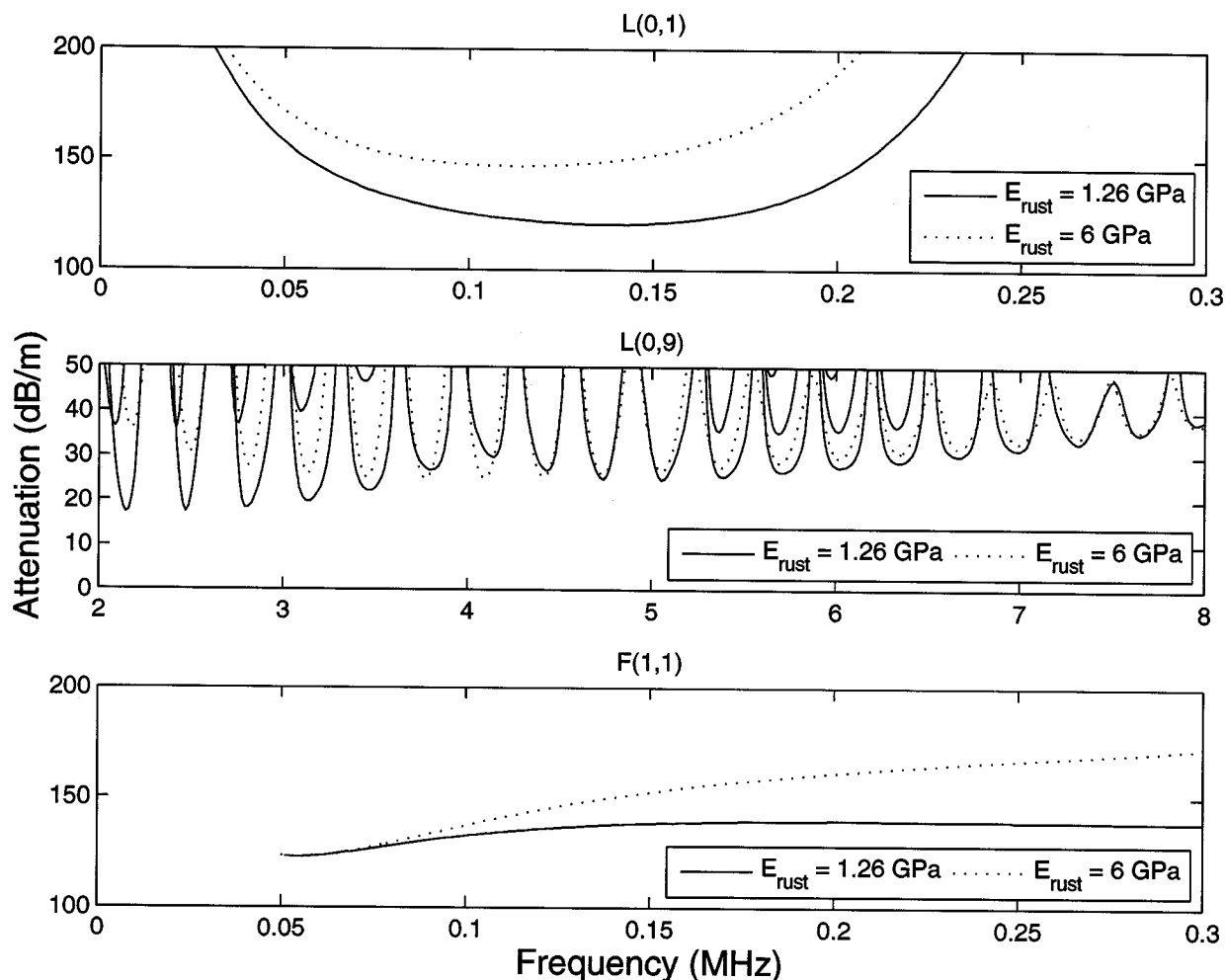
Figure 4.26: Attenuation as a function of frequency for changes in the elastic modulus of the corrosion product located between the steel and mortar. The corrosion product layer was assumed to be 0.00288" (0.07305 mm) thick, which corresponds to approximately 1.87% mass loss using the complete model (combination of Pantazopoulou & Papoulia model with Wang & Liu model) discussed at the end of Chapter 3.

As the elastic modulus of the corrosion product increases, there is an increase in the attenuation of the modes in most locations. For the L(0,9) mode, notice that for a few attenuation dips the attenuation actually decreases as the elastic modulus of the corrosion product increases. The effect on the L(0,9) is minimal except for the lowest frequencies shown. For the F(1,1) mode, the effect is fairly minimal at frequencies below 100 kHz. Figure 4.27 shows the effect of increasing the corrosion product elastic modulus on the energy velocity characteristics of the modes.

112
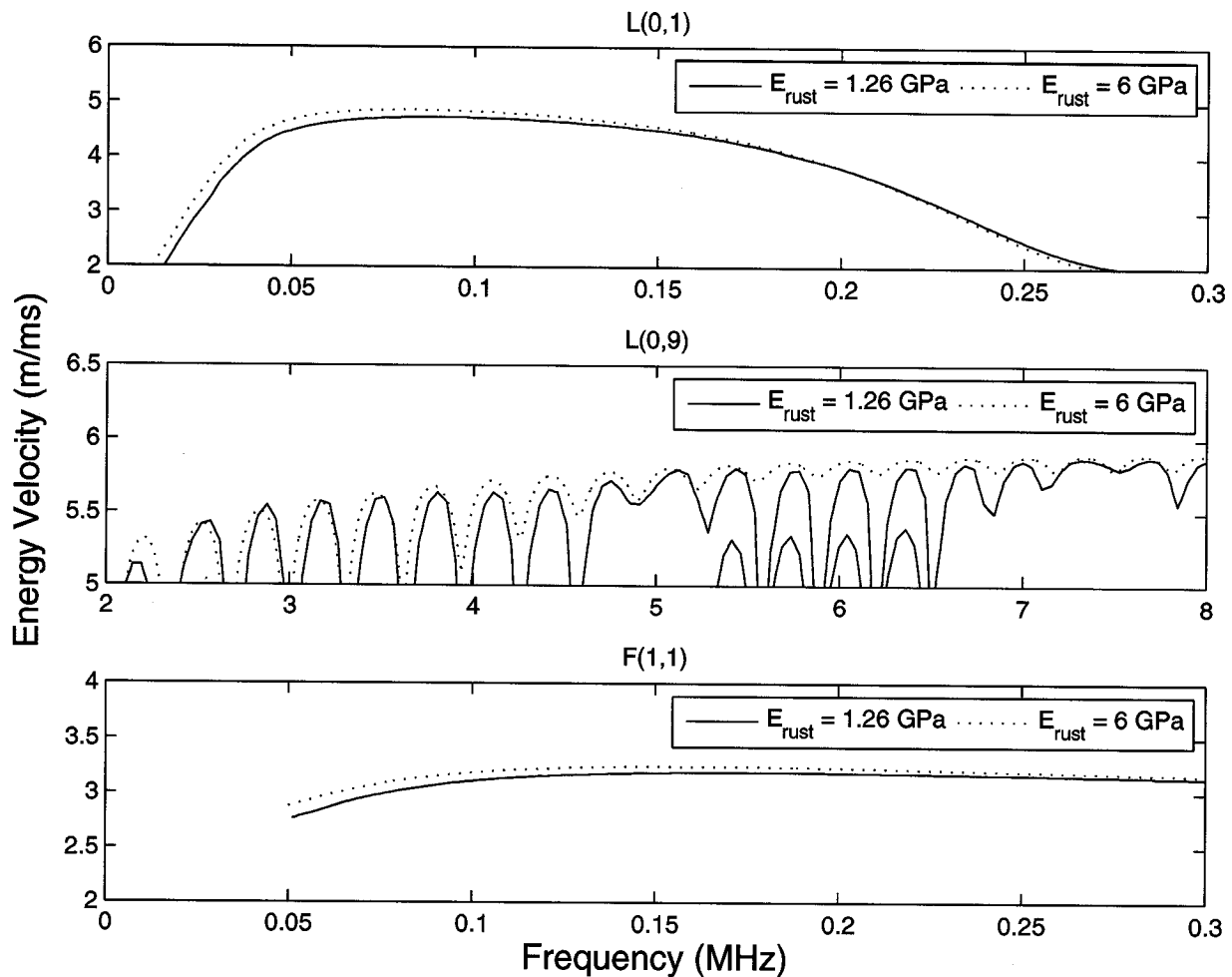
Figure 4.27: Energy velocity as a function of frequency for changes in the elastic modulus of the corrosion product located between the steel and mortar. The corrosion product layer was assumed to be 0.00288" (0.07305 mm) thick, which corresponds to approximately 1.87% mass loss using the complete model (combination of Pantazopoulou & Papoulia model with Wang & Liu model) discussed at the end of Chapter 3.

There is a very slight increase in the energy velocity as the rust elastic modulus increases for all of the modes. Figure 4.28 shows how a change in bar diameter embedded in mortar would affect the attenuation of the modes.

113
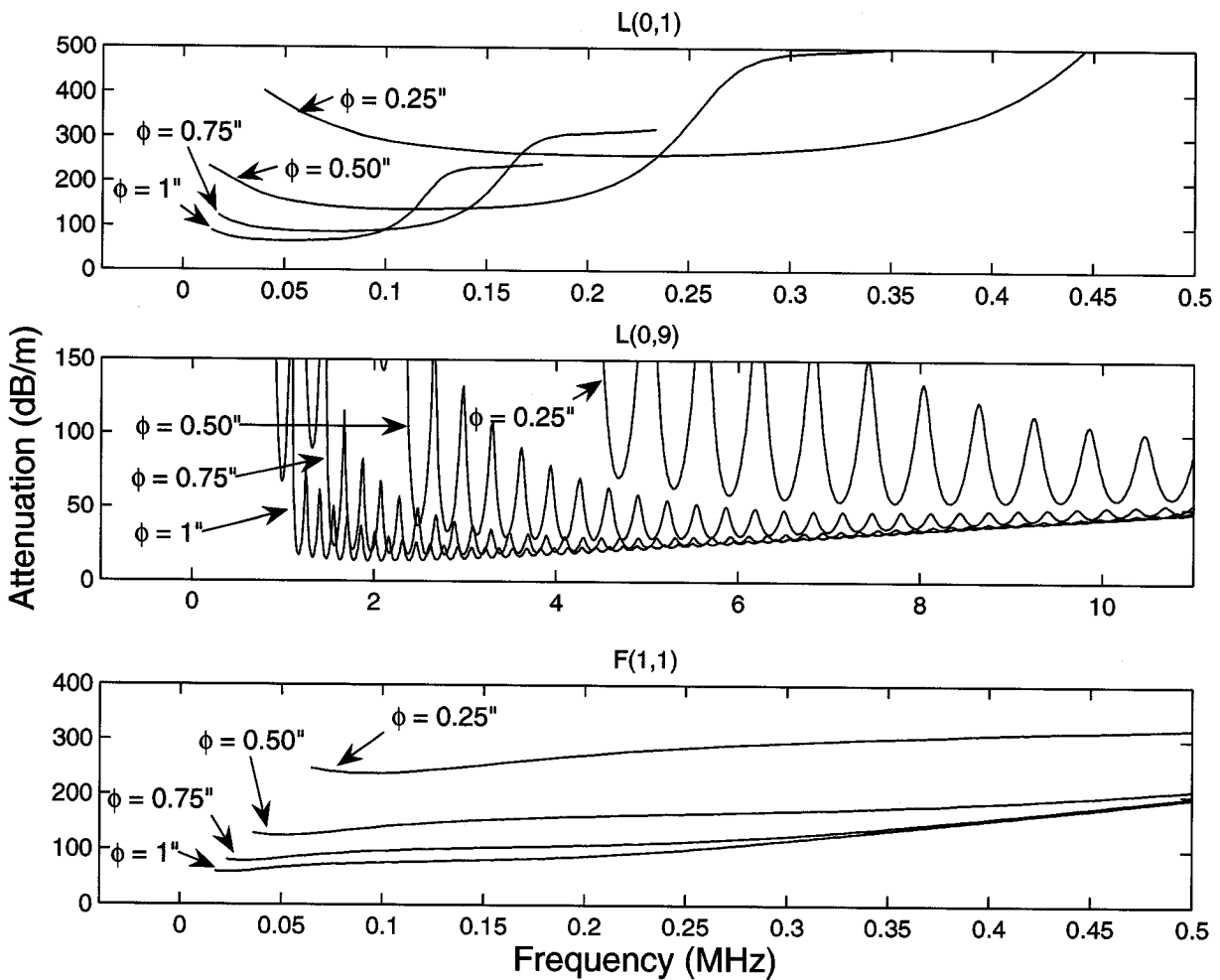
Figure 4.28: Attenuation as a function of frequency for rebar surrounded by mortar. Sensitivity analysis was conducted on the rebar diameter.

In all three cases, as the embedded bar diameter becomes larger the attenuation curve shifts downward and to the left. The distance between sensors will be dependent on the diameter of the embedded bar examined. It should be noted that 100% bond between the steel and mortar is assumed and therefore this is a conservative estimate of the attenuation. Figure 4.29 shows the energy velocity for all three modes as the diameter of the embedded bar is changed.
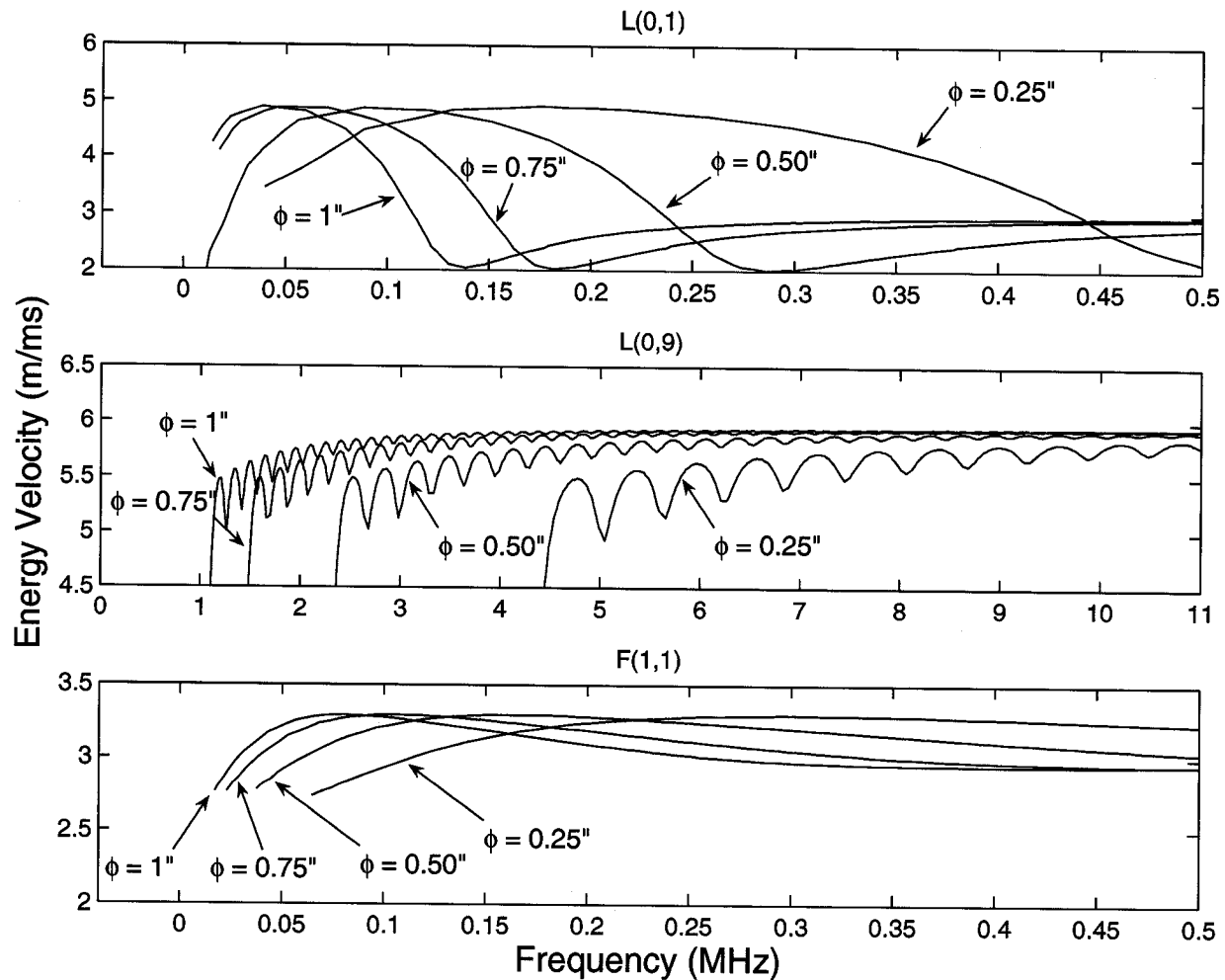
Figure 4.29: Energy velocity as a function of frequency for rebar surrounded by mortar. Sensitivity analysis was conducted on the rebar diameter.

As the diameter of the bar decreases, the energy velocity curve is stretched somewhat to the right. Similar shaped energy velocity curves should be expected, but at shifted frequencies, when different diameter bars are used.

4.4   SUMMARY

The theory of guided mechanical waves in cylinders has been presented, with longitudinal, torsional, and flexural solutions derived for the cylindrical system studied in this report. The L(0,1) and F(1,1) modes were chosen to use for guided wave testing because they were easily distinguishable, their attenuation levels were not prohibitively high, and their theoretical displacement profile suggested the modes would be sensitive to the corrosion product accumulation and debonding. The L(0,9) mode was chosen to use for testing because it too was easily distinguishable, the attenuation was the lowest for the cylindrical system, and the theoretical displacement profile suggested the mode would be mainly sensitive to the

115

changes in the bar profile. It was anticipated that an in-situ guided wave monitoring system would invoke several different modes and frequencies to arrive at a more detailed assessment of corrosion damage. Sensitivity analysis modeled and discussed the effect of changes in the mortar material properties, steel material properties, interfacial mediums, bar diameter, and corrosion product material properties.

CHAPTER 5:

PREVIOUS WORK TOWARDS MONITORING REINFORCED CONCRETE USING GUIDED MECHANICAL WAVES

This chapter provides a brief overview of previous research pertaining to guided mechanical waves used to monitor reinforced concrete (or mortar/grout). While not all of the research reported focused specifically on monitoring corrosion, the test results are applicable to this report due to the similarity in damage mechanisms. Studies have been conducted to assess the bond level between steel and concrete, the location and type of discontinuity in the bar, attenuation from the surrounding concrete, and the effects of loading conditions and other interfaces such as corrosion products, anchorage (i.e. stirrups), and ribs.

5.1   BOND LEVEL

Wu & Chang created a set of reinforced concrete beam specimens with various bond levels and tested using guided mechanical waves at lower frequencies [114]. The diameter of the steel rebar was ¾" (19.05 mm) and the specimen size was 4" x 4" x 20" (10.16 cm x 10.16 cm x 50.8 cm). Figure 5.1 provides an illustration of the reinforced concrete specimen.
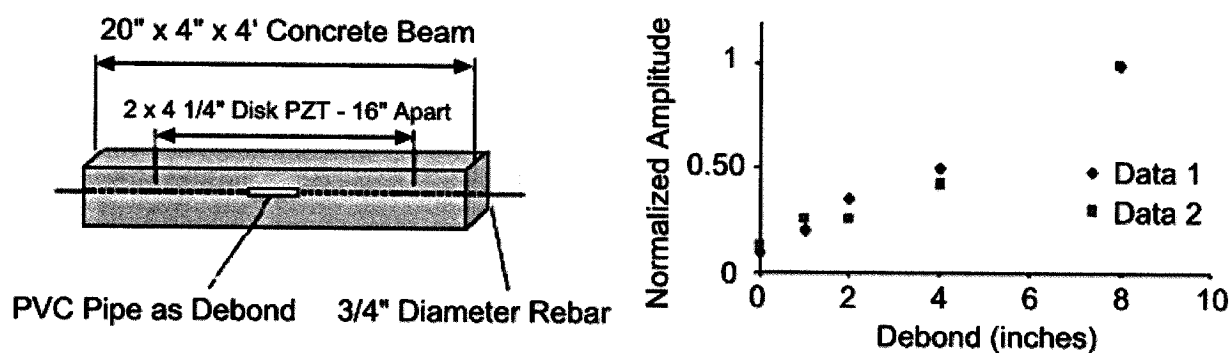
Figure 5.1: Reinforced concrete beam specimen with debonding (left). Normalized amplitude of the guided wave as a function of delamination length is also shown (right). The specimen was tested with 5-cycle tonebursts around 90 kHz. Both pictures extracted from [114].

Transducers were attached to the steel rebar via silver epoxy in a through-transmission arrangement (see Figure 6.4) and then embedded into concrete. The transducers were spaced 16" (40.64 cm) apart. Specimens simulating 0%, 6.25%, 12.5%, 25%, and 50% debonding were created. Bond was inhibited between the steel and concrete by surrounding the rebar with PVC pipe for the necessary length prior to embedment. Longitudinal modes were invoked using 5-cycle tonebursts, primarily around 90 kHz. Figure 5.1 provides the results of the guided mechanical wave testing. The results indicated that the

117

received waveform was less attenuated as the amount of debonding increased. However, there was no significant change in the waveform arrival time reported.

He et al. created a set of reinforced concrete cylinder specimens with various bond levels and tested using guided mechanical waves at higher frequencies [115]. The diameter of the steel rebar and concrete cylinder was ¾" (19.05 mm) and 4" (10.16 cm), respectively. The reinforced concrete specimen was 3' (0.914 m) long. Figure 5.2 provides an illustration of the reinforced concrete specimen.
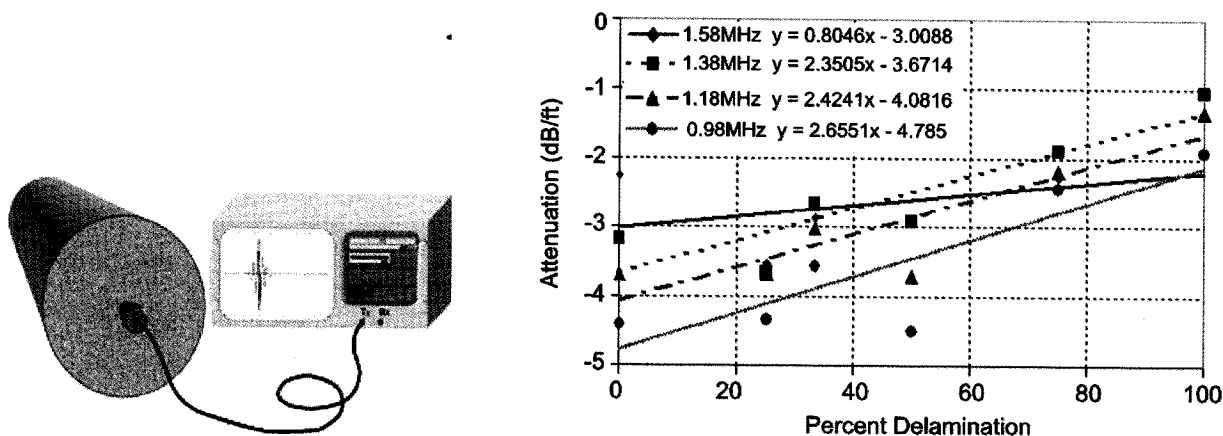
Figure 5.2: Reinforced concrete cylinder specimen (left). Attenuation as a function of delamination (right) is provided from the guided wave testing at different frequencies using toneburst excitations. Both pictures extracted from [115].

Frequencies were tested between 1-2 MHz using toneburst excitations. The transducer was attached to the exposed end of the rebar in a pulse-echo arrangement. Specimens simulating 0%, 25%, 33%, 50%, 75%, and 100% debonding were created. Bond was inhibited between the steel and concrete by surrounding the rebar with HDPE for the necessary length prior to embedment. Figure 5.2 provides the results of the guided mechanical wave testing. The results indicated that the received waveform is less attenuated as the amount of debonding increased for all frequencies. However, the lowest frequencies tested showed more sensitivity to the change in bond.

Na, Kundu, & Ehsani created a set of reinforced concrete beam specimens with various bond levels and tested using guided mechanical waves at low and high frequencies [97]. The diameter of the steel bar was 0.9" (22.86 mm) and the specimen size was 5" x 5" x 24" (12.7 cm x 12.7 cm x 60.96 cm). Frequencies were tested at 1 MHz (flexural) and 150 kHz (longitudinal) using toneburst excitations. Transducers were attached to the exposed ends of the rebar, setup in a through-transmission arrangement. Specimens simulating 0%, 25%, 50%, and 75% debonding were created. Bond was inhibited between the steel and concrete by surrounding the rebar with PVC pipe for the necessary length prior to embedment. The

118

results of lower and higher frequencies indicated that the received waveform is less attenuated as the amount of debonding increased. Specimens were tested with lengths of debonding in different locations along the bar. The results indicated that the location was not discernible. In other words, the amount of bond loss, rather than the location, was the critical factor in determining the guided wave characteristics.

5.2 CORROSION PRODUCT

Gaydecki et al embedded a 0.275" (7 mm) steel wire into a concrete mix with 4% calcium chloride solution added to induce corrosion [116]. The reinforced concrete specimen was cylindrical, with an outer diameter of 5.91" (150 mm) and a length of 3.28' (1 m). The steel wire was exposed on either end of the concrete to allow for transducer coupling. Figure 5.3 provides a picture of the specimen with transducers attached at the ends.
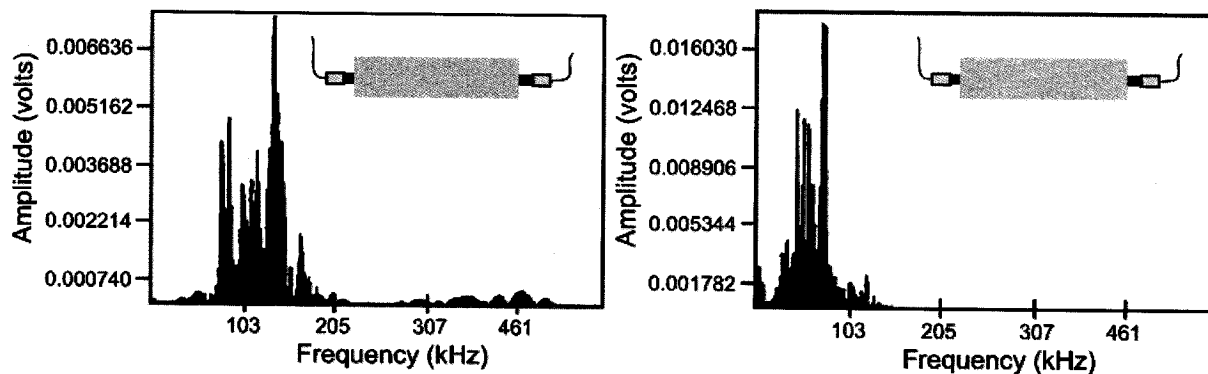
Figure 5.3: Shown are the frequency domains for a reinforced cylindrical concrete specimen with 4% calcium chloride solution added before (left) and after (right) slight corrosion has occurred. Both pictures extracted from [116].

A longitudinal wave was invoked, using a single pulse, after the concrete had initially cured using a transducer with a resonance of 200 kHz. Six months later, after slight corrosion had occurred (confirmed after breaking open), another wave was sent into the specimen. Figure 5.3 provides the frequency domain results for before and after slight corrosion. Notice that the higher frequency content was most affected by the corrosion product accumulation. This was attributed to the corrosion pressure creating better acoustic coupling at the interface between the steel and concrete, thereby allowing more energy leakage.

Miller, Hauser, & Kundu corroded rebar specimens to different levels using impressed current and then embedded the bars into concrete [102]. The diameter of the steel rebar was 7/8" (22.23 mm) and the specimen size was 5" x 5" x 24" (12.7 cm x 12.7 cm x 60.96 cm). Toneburst pulses were invoked at 1 MHz. The results indicate that the wave is more attenuated as corrosion level increases. This was attributed to better bonding between the corroded steel surface and concrete, allowing more energy leakage.

119

5.3   PITTING CORROSION

Previous research on pitting corrosion has included modeling to determine the feasibility of using guided mechanical waves. Pavlakovic modeled a guided mechanical wave in a steel bar with a square notch of varying depth embedded in grout to find reflection and transmission coefficients [100]. The steel bar radius was 0.04" (1 mm), with the radius of the surrounding grout at 1.3" (32 mm). A 6-cycle Gaussian windowed toneburst at 0.75 MHz was used to excite the L(0,1) mode. Figure 5.4 contains the reflection and transmission coefficient results for an embedded bar and a free bar with varying square notch depths.
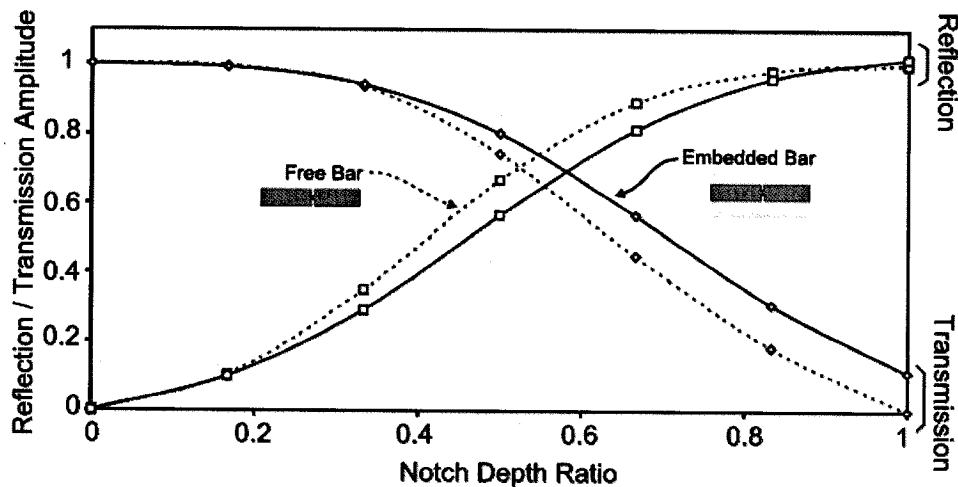
Figure 5.4: Reflection and transmission coefficients at 0.70 MHz for a free and grout embedded steel bar with 0.04" (1 mm) radius with varying square notch depths (extracted from [100]). A 6-cycle Gaussian windowed toneburst at 0.75 MHz was used to generate the L(0,1) mode.

The reflection and transmission coefficients for a free and embedded bar are very similar. An interesting result is that when the bar is embedded, and the square notch cuts completely through the diameter of the bar, there is still transmitted energy. The reason is that the grout carries some of the energy around the notch present in the steel bar. Different orientations of discontinuities were also examined. A 45° notch and the leading edge of a corrosion patch were modeled. Figure 5.5(a) shows the reflection and transmission coefficients for a diagonal notch cut into the steel bar.

120
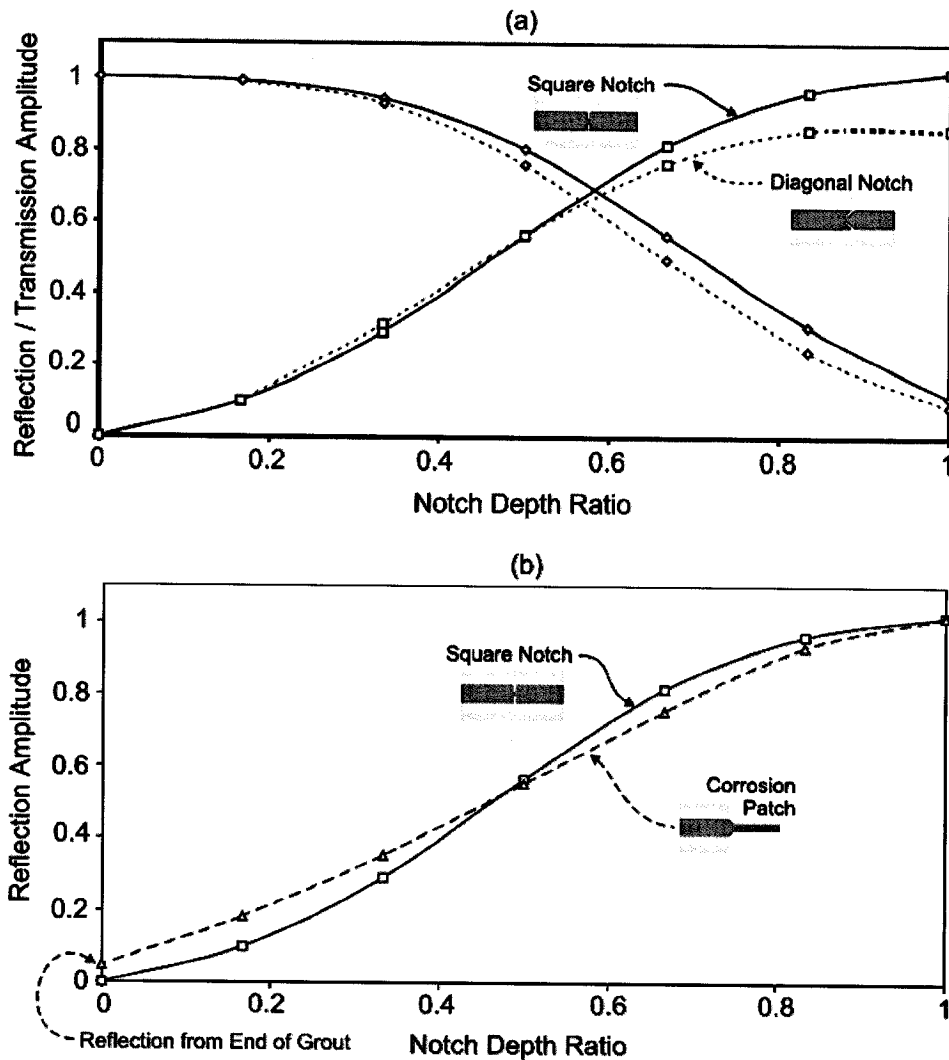
Figure 5.5: Reflection and transmission coefficients at 0.70 MHz for a grout embedded steel bar with 0.04" (1 mm) radius with varying **(a)** diagonal and **(b)** leading edge corrosion patch notch depths. A 6-cycle Gaussian windowed toneburst at 0.75 MHz was used to generate the L(0,1) mode. Both pictures extracted from [100].

The diagonal notch deviates from the square notch solutions for larger notch depths because the diagonal notch reflects energy into the surrounding grout. Figure 5.5(b) shows the reflection amplitude for the leading edge of a corrosion patch. The corrosion patch solution has close agreement with the square notch solution. A higher frequency guided wave was also invoked in a free steel bar with varying square notch depths using the model. Figure 5.6 shows the results of invoking the L(0,4) mode at a 6 MHz-mm product in a free steel bar with varying square notch depths.
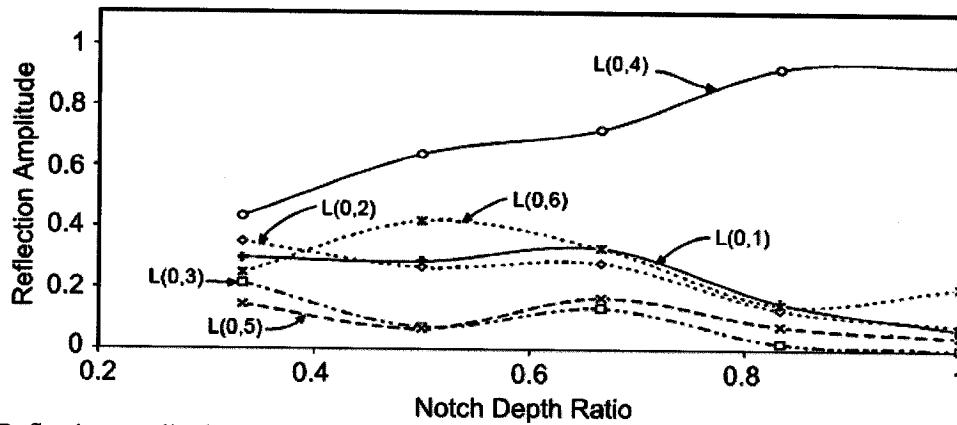
Figure 5.6: Reflection amplitude as a function of square notch depth ratio for a free steel bar with an invoked L(0,4) mode at a 6 MHz-mm product (extracted from [100]). The other modes are created via mode conversion at the notch.

The results show that most of the L(0,4) waveform is reflected at the square notch. Even though other modes are created via mode conversion at the square notch, the high attenuation of the other modes in that frequency range will filter them out prior to reception.

Experimental testing has been conducted on strand specimens with seeded defects [117,118]. A saw cut (defect A) was made on an outer wire in a seven-wire strand specimen to a depth of 0.12" (3 mm), which is slightly larger than the radius of the outer wire. Figure 5.7 shows the experimental setup of the wire with defect A and transducers (top) and the captured through-transmission waveform (bottom) for the wire with and without the defect.
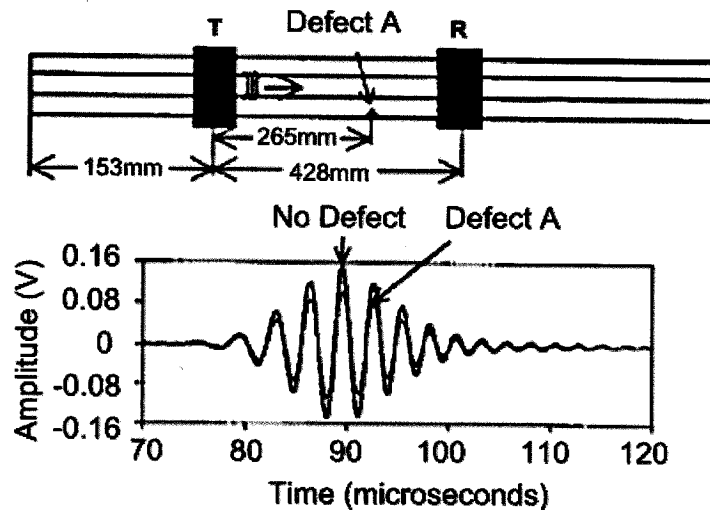
Figure 5.7: Experimental setup of a wire with a 0.12" (3 mm) deep saw cut in a seven-wire strand specimen and transducers (top) along with the captured through-transmission waveform (bottom) for the wire with and without the defect (extracted from [118]). The frequency of the invoked waveform was not reported.

122

A 32% decrease in transmitted waveform amplitude was measured, with only a 7% decrease in strand cross-sectional area. It should be noted that there was increased sensitivity in the experiment to the outer helical wires due to the use of magnetostrictive transducers. Another experiment was conducted on a specimen with two helical wires cut (defect B) to a depth of 0.08" (2 mm) with the specimen loaded to 45% of UTS (ultimate tensile stress). Figure 5.8 shows the experimental setup with defects and transducers (top) and the experimental results (bottom).
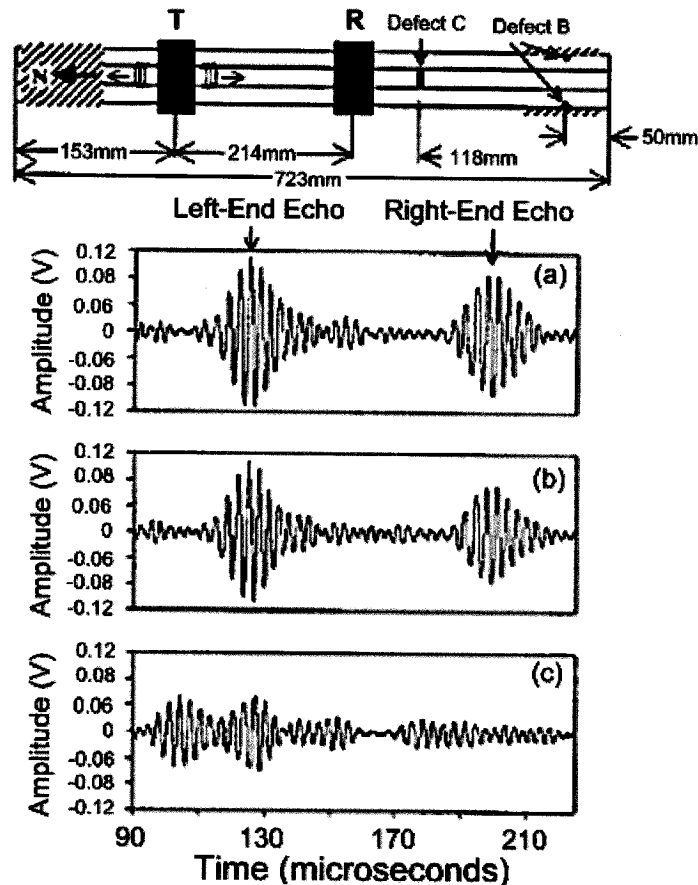
Figure 5.8: Experimental setup for testing the waveform response of a seven-wire strand specimen to various defects. The specimen was tested (a) before any defects (healthy), (b) after two helical wires were cut to 0.08" (2 mm) depth, and (c) after another helical wire was cut completely (extracted from [118]). The frequency of the invoked waveform was not reported.

Figure 5.8(a) is the waveform captured from the left and right end of the strand specimen before any defects were made. The signal received directly from the transmitter was not shown. Figure 5.8(b) shows the waveform results after two wires were cut (defect B). The right end reflection was affected as expected. The amplitude was reduced by 23% of the original waveform. Figure 5.8(c) shows the addition of a complete wire cut (defect C) to another helical wire. The right end reflection is no longer visible and there is destructive interference between the left end reflection and the reflection from defect C.

123

Seven-wire strands with seeded defects were embedded in grout and tested using a pulse-echo configuration for varying distances [100]. The seven-wire strands had a center wire of 0.22" (5.5 mm) with six wires of slightly smaller diameter spiraled around the center wire. The input signal was a 25-cycle Hanning windowed toneburst centered at 4.75 MHz. The seeded defects were complete fractures at 45° from strand axis. Experiments were conducted with the complete fracture occurring at 19.7" (500 mm), 39.4" (1000 mm), 59.1" (1500 mm), and 78.7" (2000 mm) from the sending transducer. Reflections were obtained at all distances except for 78.7" (2 m). Figure 5.9 shows the time domain captured from the center wire of a grout embedded seven-wire strand of diameter 0.63" (15.9 mm) [95]. The invoked signal was a 100-cycle toneburst centered at 6.18 MHz, with the center wire length at 11.8" (300 mm).
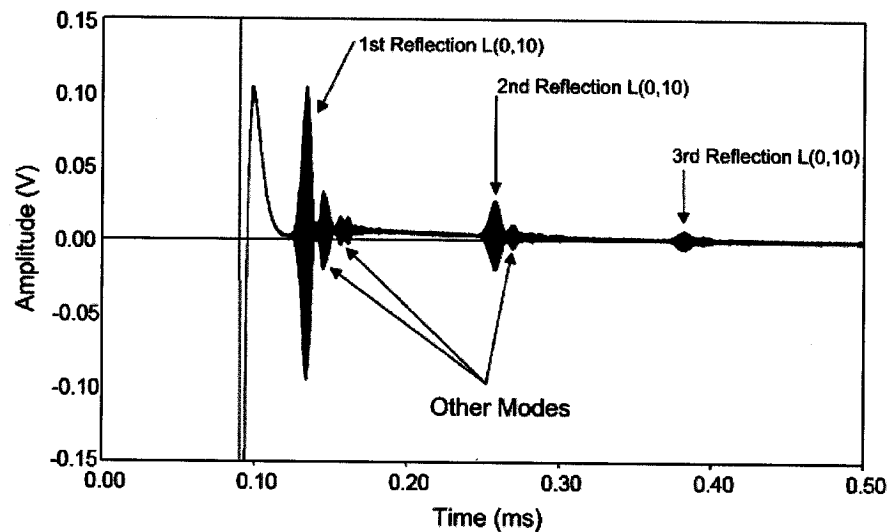
Figure 5.9: Reflections from the end of a center wire with diameter 0.22" (5.5 mm) from a grout embedded strand of diameter 0.63" (15.9 mm). The input signal was a 100-cycle toneburst centered at 6.18 MHz, with the center wire length at 11.8" (300 mm) (extracted from [95]).

The reflections from the end of the center wire are clearly visible. Results from testing the outer helical wires of seven-wire strands are not as promising. Figure 5.10 shows the pulse-echo reflection from a seven-wire strand specimen with five wires cut (including center wire) and three wires cut (not including center wire), respectively [100].

124
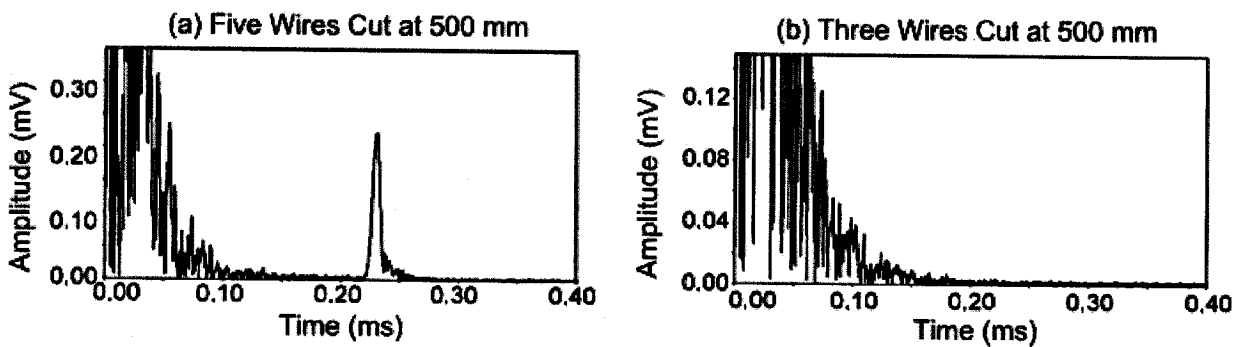
Figure 5.10: Pulse-echo reflections from grout embedded seven-wire strand specimen with **(a)** five wires (including center wire) and **(b)** three wires (not including center wire) being cut (extracted from [100]).

The results suggest that most of the guided wave energy is carried by the center wire. For example, in one study the attenuation was measured at 20 dB/m and 60 dB/m in the center and outer wire respectively of a 0.60" (15.2 mm) diameter seven-wire strand for the L(0,8) mode [95]. The primary reason is that the curvature of the surrounding wires affects the attenuation of the guided mechanical wave [95]. Another reason is that the center wire is not completely bonded to the surrounding helical wires and therefore does not leak as much energy into the grout. Lower frequencies lacking sensitivity to the curvature effects were not investigated due to concern with receivable bulk wave reflections from grouting duct walls. It was thought that larger diameter rebar and grouted steel anchors would have more potential for guided wave testing than small diameter grouted tendons [95].

An experimental investigation was undertaken to find reflection coefficients as a function of the end angle of a cylindrical bar [95]. Figure 5.11 provides the reflection coefficients for a 0.79" (20 mm) diameter free steel bar with varying end angle invoked at a lower frequency range using a 10-cycle toneburst. The lower frequencies appear to lack sensitivity to the angle of the cylindrical bar end. Figure 5.11(b) is the waveform loss (in decibels) for higher frequencies reflected off of varying end angles in a 0.86" (21.7 mm) diameter rock bolt embedded in mortar. For only slight end angles (~10°) there is waveform loss of over 40 decibels for the frequencies tested. The results show that higher frequency modes with low system attenuation are limited in effectiveness for pulse-echo testing due to their sensitivity to the angle of discontinuity formed by pitting corrosion.

125
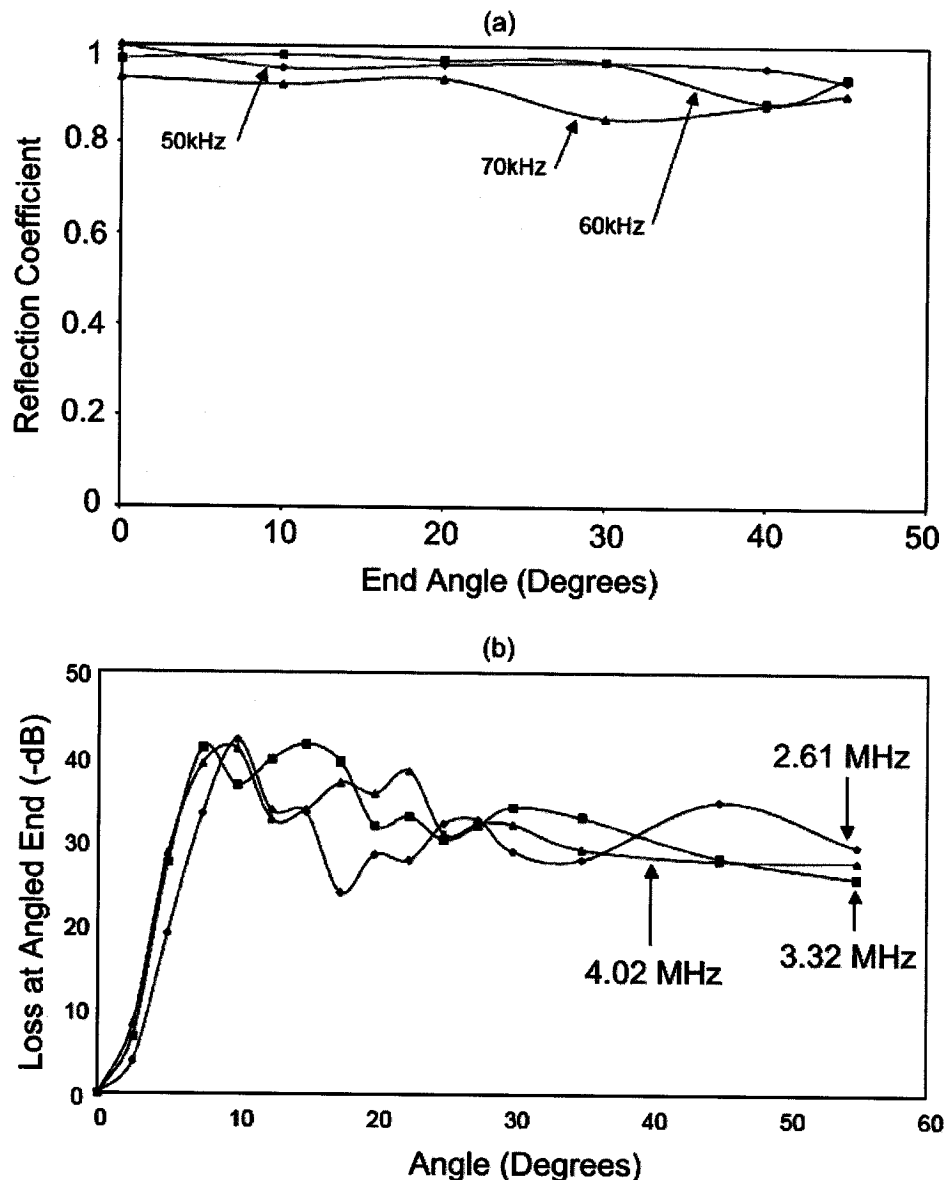
Figure 5.11: Reflection coefficients as a function of varying end angle using **(a)** 10-cycle toneburst lower frequencies in a 0.79" (20 mm) diameter free steel bar. The loss in decibels is provided as a function of end angle for **(b)** higher frequencies in a 0.86" (21.7 mm) diameter rock bolt embedded in mortar. Both pictures extracted from [95].

End reflections from rock bolts embedded in concrete have been captured using a pulse-echo configuration. The rock bolt is essentially a steel bar with mixing ribs on the side and threads on the end. It was installed by casting a hole in a mortar/concrete block, filling the hole with plastic capsules containing epoxy resin and a hardening agent, and then inserting the rock bolt into the hole while spinning it to puncture and mix the content of the plastic capsules. The invoked frequencies were 20 kHz, 30 kHz, 35 kHz, 40 kHz, 50 kHz, and 60 kHz. Each frequency was invoked with a 6-cycle toneburst in a rock bolt with a 0.86" (21.7 mm) diameter embedded in a mortar/concrete block for a length of 6.56' (2 m) [95]. The results indicate that an end reflection was detectable at every frequency except for 20 kHz. No

126

reflection was thought to occur at an invoked frequency of 20 kHz due to transducer ringing and reverberations in the free end of the bolt [95]. Discontinuities in solid rebar 0.32" (8 mm) in diameter were simulated by creating 0.08" (2 mm) and 0.16" (4 mm) deep saw cuts and then casting in grout [100]. A pulse-echo experimental setup was used to detect the saw cut, located 17.7" (450 mm) away from transmission site, with a 50-cycle Hanning windowed toneburst centered at 3.75 MHz invoked. The results of the experiment are shown in Figure 5.12.
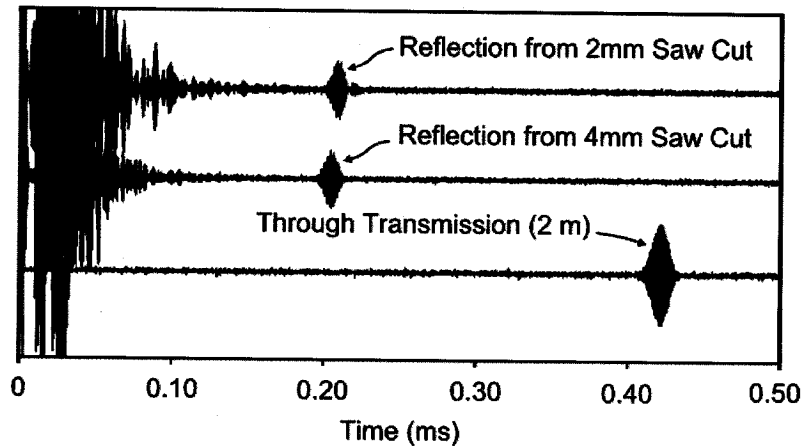
Figure 5.12: Pulse echo time domain response for a 0.08" (2 mm) and 0.16" (4 mm) saw cut in an 0.32" (8 mm) diameter steel bar, along with a through-transmission time domain response (extracted from [100]). A 50-cycle Hanning windowed toneburst centered at 3.75 MHz was invoked.

The reflections from both saw cut specimens are clearly detectable. Another study machined a neck into the side of a rock bolt specimen 0.86" (21.7 mm) in diameter and 7.87' (2.4 m) in length embedded in concrete [95]. Figure 5.13 shows the captured time domain response for the specimen.
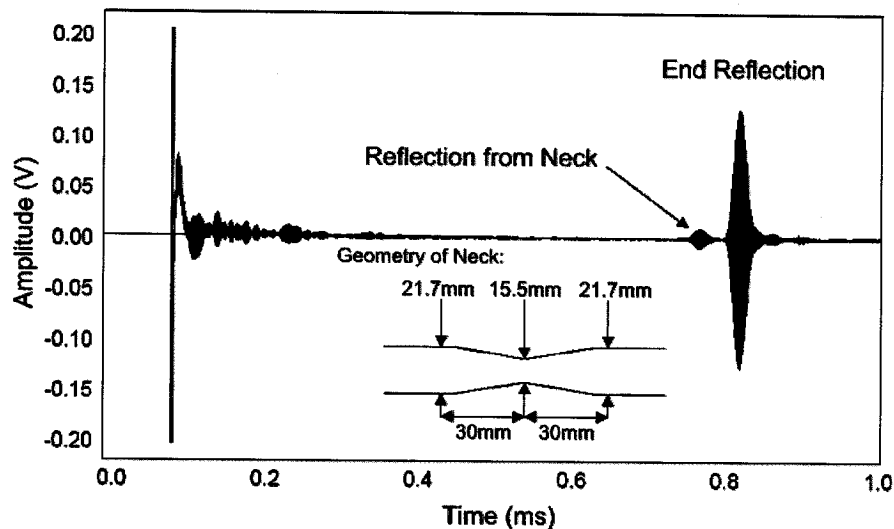
Figure 5.13: Pulse-echo reflection from a machined neck on a 0.86" (21.7 mm) diameter rock bolt 7.87' (2.4 m) in length embedded in concrete (extracted from [95]). A 100-cycle toneburst centered at 3.86 MHz was invoked.

127

The reflection from the neck is much smaller than the end reflection of the rock bolt but is still clearly detectable. Correlations between stress wave features of a guided mechanical wave and the location and degree of pitting have been found in the field as well. Researchers have used guided mechanical waves to inspect anchor rods embedded in earth for section loss [119]. A pulse-echo configuration was used to invoke the L(0,1) mode at 0.5 MHz and capture returning reflected waveforms from in-situ corroded anchor rods.

Higher frequencies were also tested for a rock bolt embedded in a mortar cylinder. Figures 5.14(a) and 5.14(b) show captured waveform reflections in a 7.87' (2.4 m) rock bolt with 0.85" (21.7 mm) diameter embedded in a concrete block using a pulse-echo arrangement with a flat end and an angled end, respectively [95]. The invoked waveform was a 200-cycle toneburst centered at 2.8 MHz.
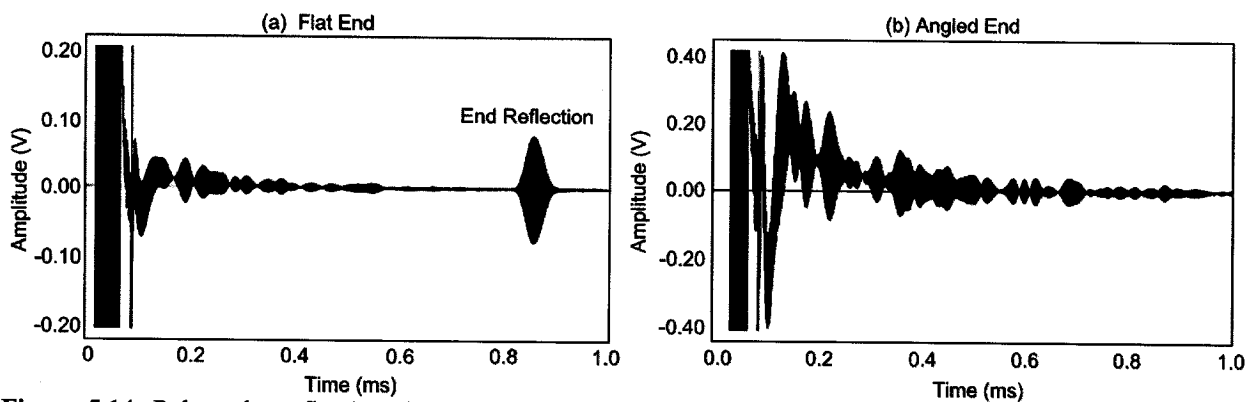
Figure 5.14: Pulse-echo reflections in a 7.87' (2.4 m) rock bolt with 0.85" (21.7 mm) diameter embedded in a concrete test block with a **(a)** flat end and **(b)** angled end (extracted from [95]). The waveform invoked was a 200-cycle toneburst centered at 2.8 MHz.

The results confirm that there is significant loss for higher frequency modes when the end is angled. Since pits will not always form perpendicular to the bar axis, the potential of using higher frequency guided mechanical waves for detection and monitoring of pitting corrosion in pulse-echo mode seems limited.

It seems that using guided mechanical waves for detection of pitting corrosion in tendons is limited. The effect of the curvature of the helical wires and the small diameter make inspection distances of even modest size difficult. Lower frequency techniques may be employed in a through-transmission setup, as long as reflections from leaked waves bouncing off of the grouting duct walls do not interfere. Anchor rods and larger diameter rebar have potential for pitting corrosion detection using lower frequencies since strong reflections are found at variable pit angles. Higher frequencies, with attenuation dips for the layered system, suffer from large reflection loss at even slight end angles.

128

5.4   ATTENUATION MEASUREMENT

Beard embedded different diameter plain steel bars 1.08' (0.33 m) in length into grout [95]. The grout size was 3.94" x 3.94" x 11.81" (0.1 m x 0.1 m x 0.3 m). The embedment length was short enough that multiple reflections from the end of the bar could be detected and compared to each other for attenuation measurements. Figure 5.15 is a picture of the specimen.
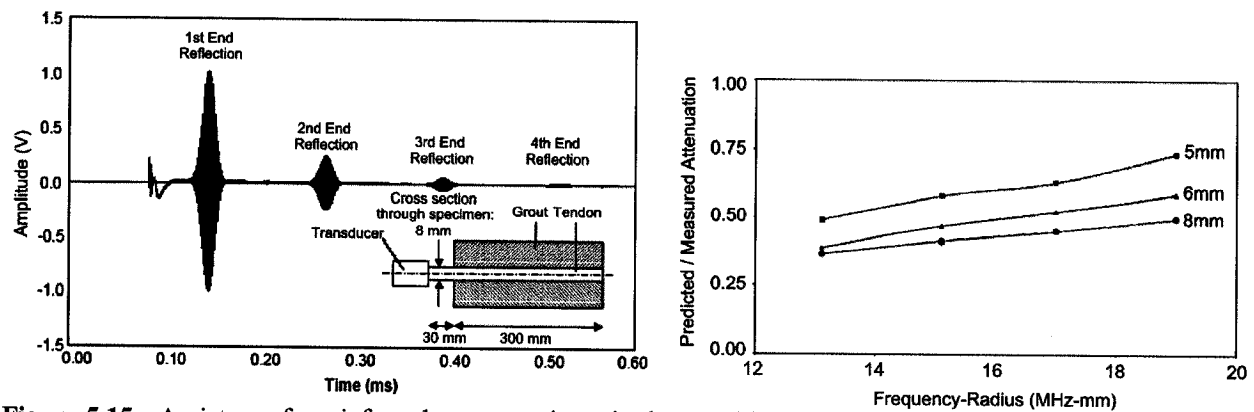
Figure 5.15: A picture of a reinforced grout specimen is shown with multiple end reflections captured in a pulse-echo arrangement (left). The multiple echoes are compared in order to measure the attenuation in the reinforced system. The results of the measured attenuation are normalized with respect to predicted analytical attenuation values for each frequency tested (right). Both pictures were extracted from [95].

Multiple frequencies were invoked for the different bar diameters using a 100-cycle toneburst. All modes of propagation were longitudinal. It was assumed that losses from reflections off of the back wall of the steel bar were less than +/- 5%. Figure 5.15 provides the results from the guided wave testing. The predicted values for attenuation (as discussed in Chapter 4) are used to normalize the measured values. Notice that in every case the predicted values overestimate the amount of attenuation. In fact, the measured attenuation values were closer to the predicted attenuation values for a free bar. The difference in predicted and measured attenuation values was attributed to two main factors. The first is that the material damping constants are most likely imprecise due to the difficulty in accurate measurements. The second factor is that the interface conditions between the steel and grout are not completely known (i.e. bond is most likely less than perfect). It was concluded that the predicted attenuation measurements were not completely reliable and should be used as an upper bound for determining maximum inspection ranges.

5.5   ANCHORS

Na, Kundu, & Ehsani tested reinforced concrete specimens with and without stirrups surrounding the reinforcing bars [97]. Frequencies were tested at 1 MHz (flexural) and 150 kHz (longitudinal) using toneburst excitations. Transducers were attached to the exposed ends of the rebar, setup in a through-

129

transmission arrangement. It was concluded that specimens without stirrups had stronger waveform amplitudes than specimens with stirrups.

5.6   RIBS

Beard tested a smooth bar and a rock bolt to examine whether the surface features affected wave propagation [95]. The rock bolt tested had threads and mixing ribs along segments of the 7.87' (2.4 m) length. The smooth bar tested was 5.91' (1.8 m) in length. Both bars had a diameter of 0.79" (20 mm) and were excited with a 10-cycle Gaussian windowed toneburst at 50 kHz. There were no reflections from surface features and the wave amplitude was relatively unaffected. The results indicated that wave propagation is largely unaffected by the presence of surface features when the ratio of the wavelength to the surface feature dimensions is large.

Miller et al. described strong scattering effects for longitudinal modes (>600 kHz) propagating in rebar 7/8" (22.2 mm) in diameter [102]. There was particular sensitivity to diagonal rib patterns compared to an orthogonal axisymmetric rib pattern. Similar filtering of frequency ranges has been studied for guided waves in plates with corrugated patterns [120]. Frequency ranges that were filtered out were referred to as stop bands, while frequencies that still effectively propagated in the corrugated plate were referred to as pass bands.

5.7   LOADING

Wu & Chang investigated the effect of applying load on rebar would have on the guided wave characteristics [114]. The diameter of the rebar was 3/4" (19.05 mm) and the length was 26" (66.04 cm). A tapered notch was created in the middle of the bar length to ensure that yielding would occur at that location. Figure 5.16 provides an illustration of the rebar specimen.

The transducers were attached to the sides of the rebar in a through-transmission setup. There was spacing between the transducers of 16" (40.64 cm). Longitudinal modes were invoked using 5-cycle tonebursts, primarily around 90 kHz. Figure 5.16 provides the results of the guided wave testing. The results indicate that the applied load does not affect the wave amplitude for the frequency range and mode tested. However, the time of arrival of the waveforms did change once yielding occurred due to the rapid increase in length.

130
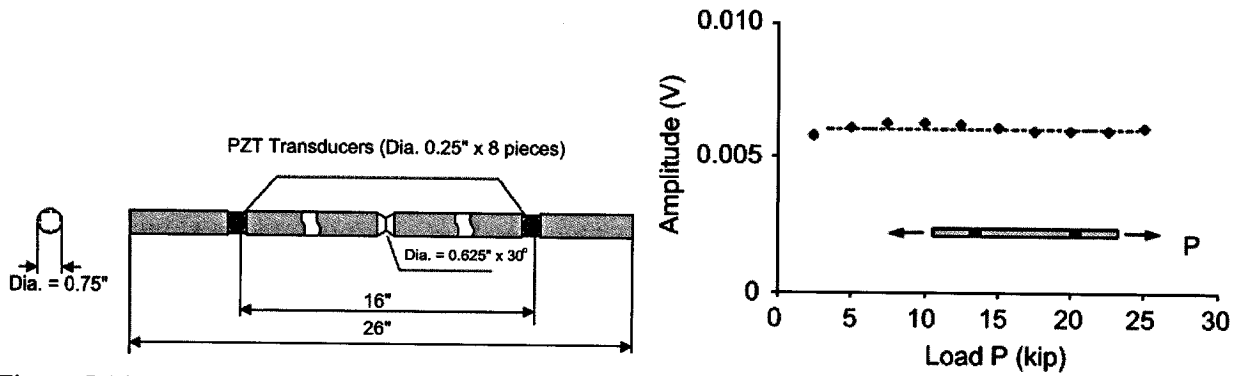
Figure 5.16: Picture of a rebar specimen tested using guided mechanical waves while tensile load was applied (left). The guided wave amplitude as a function of applied tensile load is also given (right). The specimen was tested with a 5-cycle toneburst around 90 kHz. Both pictures extracted from [114].

5.8 BENDING

Wu & Chang investigated how guided wave characteristics are affected by bending. The reinforced concrete specimen was subjected to a four-point bending test while monitored with guided waves [114]. The diameter of the rebar was ½" (12.7 mm) and the specimen size was 4" x 4" x 24" (10.16 cm x 10.16 cm x 60.96 cm). Figure 5.17 provides an illustration of the reinforced concrete specimen and the location of the applied loads during four-point bending.
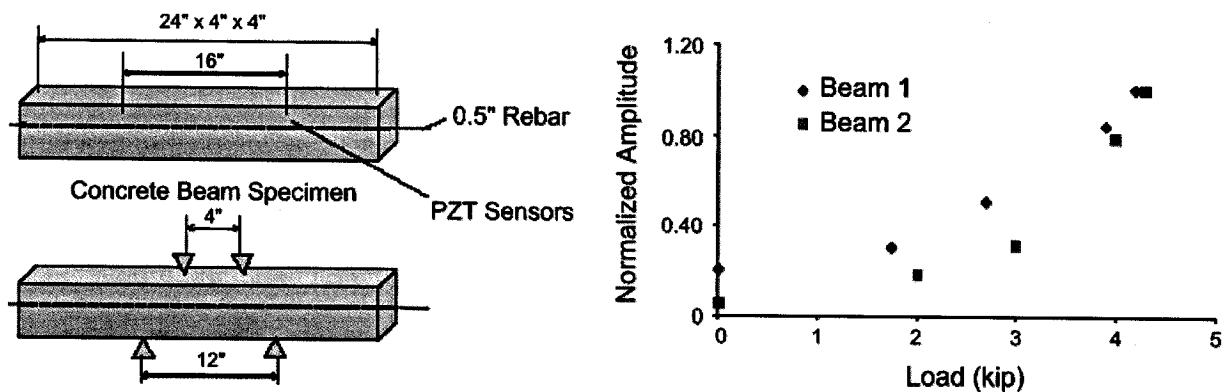
Figure 5.17: Picture of a reinforced concrete beam specimen tested using guided mechanical waves during a four-point bending test (left). The normalized amplitude of the guided wave as a function of the applied four-point bending load is also shown (right). The specimen was tested with a 5-cycle toneburst around 90 kHz. Both pictures extracted from [114].

The transducers were attached to the sides of the rebar in a through-transmission setup. There was spacing between the transducers of 16" (40.64 cm). Longitudinal modes were invoked using 5-cycle tonebursts, primarily around 90 kHz. Figure 5.17 provides the results of the guided wave testing. The four-point bending test created a crack that was perpendicular to the axis of the reinforced mortar specimen in the tension zone. The crack extended up towards the neutral axis during the test. The results indicate that as the applied loads and cracking of the surrounding concrete matrix increased, the amplitude

131

of the waveform increased. Notice that the load increases in a rapid fashion after 3 kips of applied load. This was attributed to the crack reaching the bar and causing more significant delaminations.

5.9   SUMMARY

The testing described here has all focused on using the reinforcing bar (e.g., rebar, anchor, and strand) to guide mechanical waves through surrounding mediums such as concrete and air. The results of testing to date show that both low and mid-range frequency modes are less attenuated as debonding occurs. Testing on the corrosion products alone have shown that they increase the bond between the steel and mortar and caused greater waveform attenuation through leakage. Low and high frequency longitudinal waves were shown to have strong reflection coefficients from discontinuities that were perpendicular to the axis of the bar. However, the high frequency longitudinal waveforms were shown to be heavily attenuated at discontinuity angles of 10° or greater from a completely perpendicular discontinuity. This is unfortunate since the high frequency longitudinal modes are the lowest attenuating and fastest propagating modes in the system, making them the obvious first choice for pulse-echo testing. While low frequencies were shown to have strong reflection coefficients from different end angles, they are more heavily attenuated from leaking into the system. Through-transmission testing may be the only way of monitoring bar damage from corrosion. Previous work has shown that wire cuts were detectable from signal strength loss in a through-transmission setup. Another interesting result of previous testing is that the low frequency guided waves gained signal strength as the specimen was subjected to a bending test. The results imply that the low frequency modes will be sensitive to crack damage and mortar stiffness changes that occur from rust product accumulation. There has been no found published experimental work using guided mechanical waves to monitor reinforced concrete undergoing corrosion.

132

CHAPTER 6:

EXPERIMENTAL INVESTIGATION

A description of all materials, equipment, and experiments conducted are contained within this chapter.

6.1 MATERIALS

Mortar, steel, water, and air were used for experimental testing. A brief review of the mortar mix and the type of steel rebar used is provided. Material properties are given in Table 4.3.

6.1.1 MORTAR MIX

Mortar is the combination of cement, sand, and water. Concrete is the combination of cement, sand, large aggregate (e.g. rocks), and water. Cement paste is the combination of cement and water. Mortar was used in this investigation to avoid possible wave interaction with large aggregates, but still keep the material properties as close to concrete as possible. Throughout all experimental testing and modeling presented in this report, the same mortar mix was used. The mortar mix had the following weight proportions of sand, Type I cement, and water: 2.11:1:0.45. The fine aggregate used was in the wet condition. The water used in the mix was taken from a drinking faucet. In general, water safe enough to drink is sufficient for making concrete (or mortar) mixes.

Portland cement and sand were first added to a concrete mixer and mixed in a dry state for approximately 1 minute. Water was then added to the mixer and stopped after 2 minutes of mixing. The batch was manually stirred using a shovel for 1 minute and then mixed for another two minutes. The mortar mix was then ready to be placed in formwork using plastic scoops. When placed, the mortar was consolidated by steel rodding to ensure that mortar was located underneath the rebar and distributed as evenly as possible. The tops of the specimens were then finished with a trowel. All specimens were air-cured for at least 96 hours before form removal.

Compression testing, adhering to ASTM C 469-94, was conducted on mortar specimens air-cured for 28 days to attain material properties [121]. Compression testing was conducted on four dry and wet mortar specimens. Wet specimens were submerged in water for four days prior to compression testing. The mortar material absorption coefficients were taken from reported values [96]. The material properties obtained from compression testing are given in Table 4.3.

133

6.1.2   STEEL BARS

Three types of steel bars were used in the current experimental investigation. The first type of bar was a solid cylinder ½" (12.7 mm) in diameter. The solid cylinder is shown in Figure 6.1 on the far left.
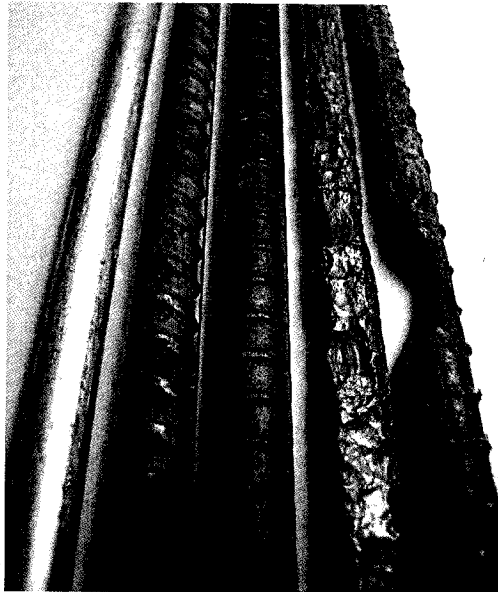
Figure 6.1: Photograph (starting on left) of a solid steel bar, rebar with an angled rib pattern, rebar with an orthogonal axisymmetric rib pattern, rebar under uniform corrosion (approximately 25% mass loss), and rebar under localized corrosion.

The second and third type of bar are both referred to as deformed rebar. The term "deformed" means that the bars have protrusions and are generally used for reinforced concrete construction. The deformations on the outside of the rebar are commonly referred to as ridges, lugs, protrusions, or ribs. The protrusions are used to anchor the rebar in the concrete and inhibit the amount of longitudinal movement of the rebar with respect to the surrounding mortar or concrete. The second type of bar has an angled rib pattern, while the third type of bar has an orthogonal axisymmetric rib pattern. The orthogonal axisymmetric rib pattern is referred to as an orthogonal rib pattern throughout this report. Figure 6.1 shows both the angled rib pattern rebar (second from left) and the orthogonal rib pattern rebar (middle).

The size of the rebar diameter is referred to in numbers. Each bar number is based on the number of eighths of an inch in the diameter. A #4 rebar refers to an average diameter of 4/8". All rebar used in this investigation were #4 bars, with a measured base (i.e. core) diameter of 0.472" (11.99 mm). The base diameter (shown in Figure 6.2) is the diameter of the rebar without the ribs.

134

$$\phi = 0.472"$$
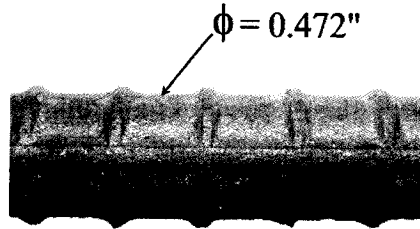
Figure 6.2: Photograph of rebar base diameter.

The elastic modulus of the rebar was measured from a tension test. The density and Poisson's ratio of the rebar were taken from standard reference values [110]. The values are given in Table 4.3.

6.2 EQUIPMENT FOR DATA COLLECTION

A description of the equipment used to collect waveforms during guided wave testing is now provided. Figures 6.3 and 6.4 are schematic diagrams of the experimental setup used to generate low and high frequency waveforms during testing, respectively.
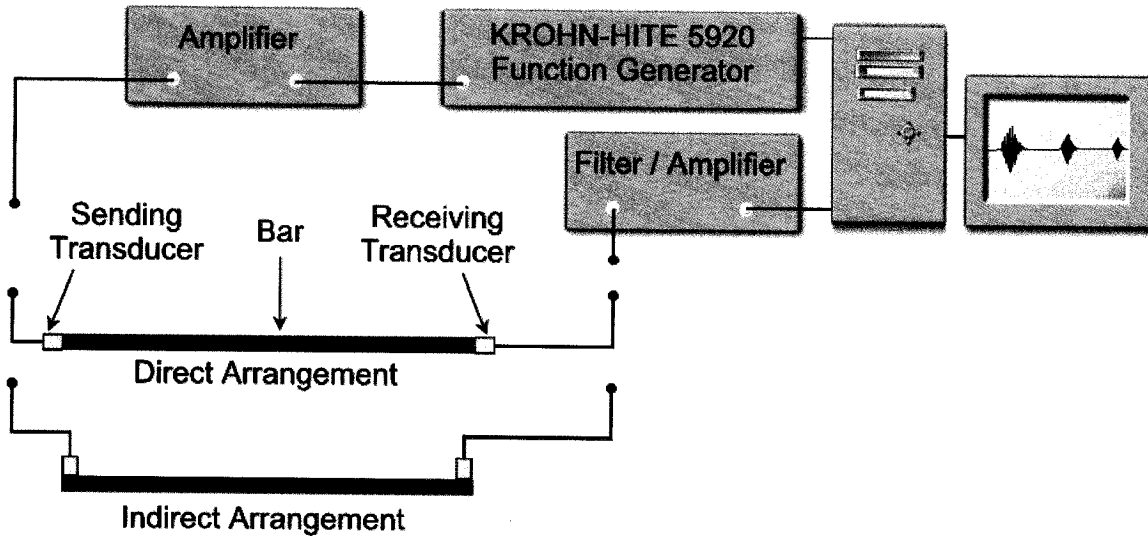
Figure 6.3: Schematic diagram of ultrasonic through-transmission experimental setup for low frequency testing. Both direct and indirect transducer arrangements are shown.

135
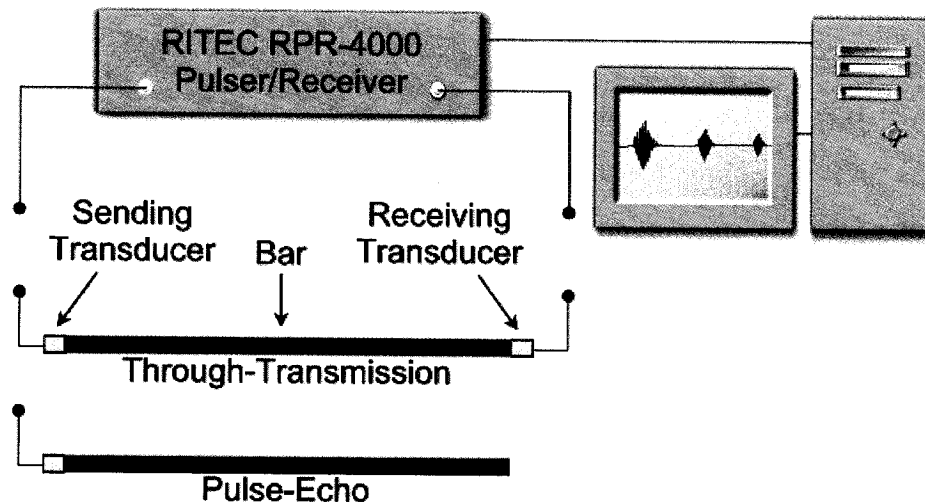
Figure 6.4: Schematic diagram of the ultrasonic experimental setup for high frequency testing. Both through-transmission and pulse-echo arrangements are shown.

Figure 6.3 shows an experimental setup for generating low frequency waveforms. All low frequency testing presented in this report was conducted in a through-transmission (i.e. pitch-catch) mode. A Krohn-Hite (model 5920) function generator was used to generate all low frequency waveforms. The frequency output by the function generator was adjusted externally by the use of an HP-IB interface card. The waveforms created by the function generator were sent to a Krohn-Hite wideband amplifier (model 7602M) for amplification to 200 Volts peak-to-peak. The signal was then sent from the power amplifier to a transducer coupled at the end of a bar.

Longitudinal waves have been invoked with transducers on the end of cylindrical steel bars [85,96] and by the use of an angled transducer on the side [97]. In this study, a compressional transducer was coupled onto the end face of the exposed reinforcement (direct transducer arrangement as shown in Figure 6.3) to invoke (sending transducer) and to detect (receiving transducer) longitudinal waveforms. Similarly, a compressional transducer was coupled perpendicular to the rebar (indirect transducer arrangement as shown in Figure 6.3) to invoke and to detect flexural waveforms.

After transmission of the wave through the bar, the receiving transducer sent the waveform to a filter/amplifier unit. The signal was then amplified and filtered using a band pass Butterworth filter before being digitized and stored in a computer for further processing. The type of transducers used for all low frequency testing were Digital Wave piezoelectric contact compressional transducers (refer to Appendix J).

136

Figure 6.4 shows an experimental setup for generating high frequency waveforms. High frequency testing presented in this report was conducted using both a through-transmission and pulse-echo configuration. A Ritec pulser/receiver unit (model RPR-4000) was used to generate all high frequency waveforms. The signal was sent from the pulser/receiver to a piezoelectric transducer. In pulse-echo mode, the sending transducer would begin receiving after transmission of the waveform. In through-transmission mode, a separate piezoelectric transducer received the transient waveform. The type of transducers used for all high frequency testing were Panametrics piezoelectric contact compressional transducers (refer to Appendix J). Received signals were filtered and amplified before being digitized and stored in a computer for processing.

6.3   MODE SENSITIVITY TO RIBS, WATER, AND MORTAR

To procure a system for in-situ monitoring of concrete structures, the effect of the reinforcing ribs, water, and the mortar needs to be better understood. Guided wave testing of different rib patterns and surroundings are presented in this section.

6.3.1   MODE SENSITIVITY TO REINFORCING RIBS

The effect of the ribs was demonstrated by ultrasonically testing a solid bar (i.e. no ribs), a rebar with an orthogonal rib pattern, and a rebar with an angled rib pattern (see Figure 6.1). A direct transducer arrangement was first tested using Digital Wave transducers (model B-1025). A 500 kHz single cycle pulse was transmitted. The highpass and lowpass filters were set at 5 kHz and 1 MHz, respectively. Figures 6.5-6.7 show the received time domain, frequency domain, and spectrogram (refer to Appendix K for more information) for the solid bar, a rebar with an orthogonal rib pattern, and a rebar with an angled rib pattern, respectively. The longitudinal (solid lines) and flexural (dashed lines) modes that exist within the testing range are also shown. The energy velocity curves were converted to time-of-arrival curves by dividing the propagation distance by the energy velocity. It should be noted that the y-scale for the frequency domain refers to the amplitude of the normalized power spectrum.

The solid bar had a large portion of the received frequency content above 500 kHz, while both deformed bars had almost none. The L(0,1), L(0,3), and L(0,4) modes were clearly excited from the solid bar test, with the behavior following the theoretical dispersion curves. The L(0,1) and L(0,3) modes were excited in the deformed bars, however there appears to be some scattering of the L(0,3) mode and portions of the L(0,1) mode (late arriving content shown below the dispersion curve in the spectrogram). The low frequency behavior (<200 kHz) for all three bars appears to be similar. At low frequencies, the ribs do not affect the modes because the wavelength is so large relative to the characteristic dimension of the rib.
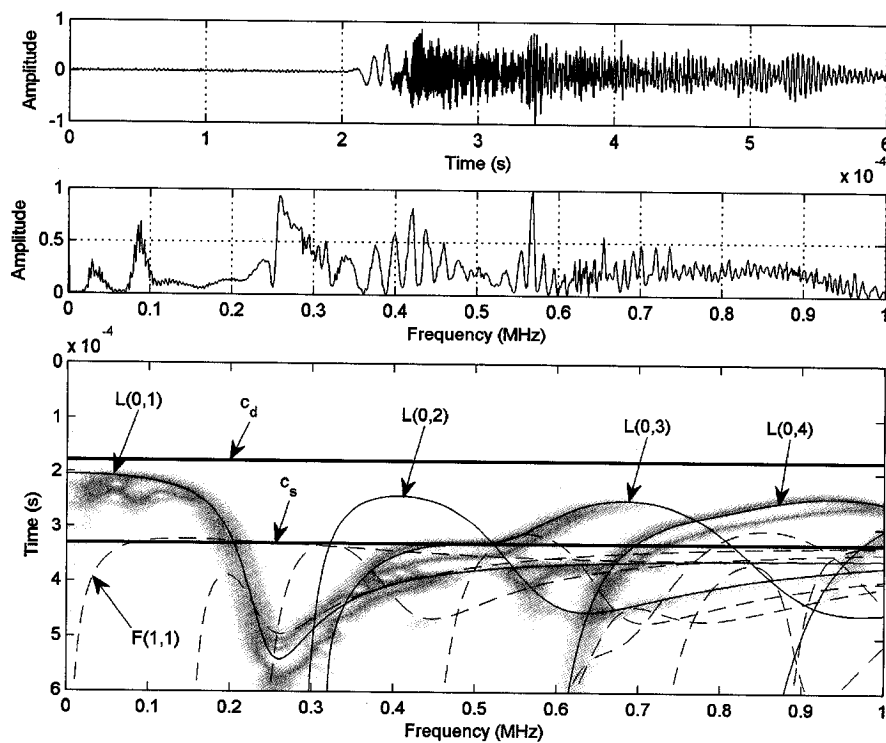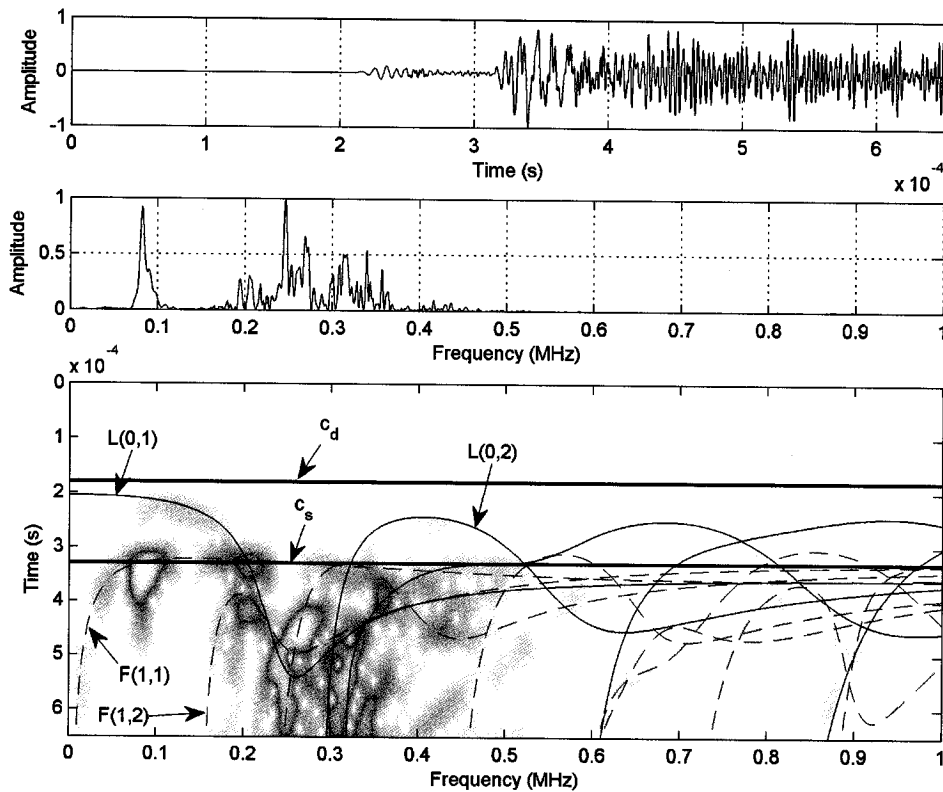
Figure 6.5: A 500 kHz single cycle pulse transmitted (direct arrangement) through a solid bar 42" (1.067 m) in length and ½" (12.7 mm) in diameter. The gain was 46 dB.
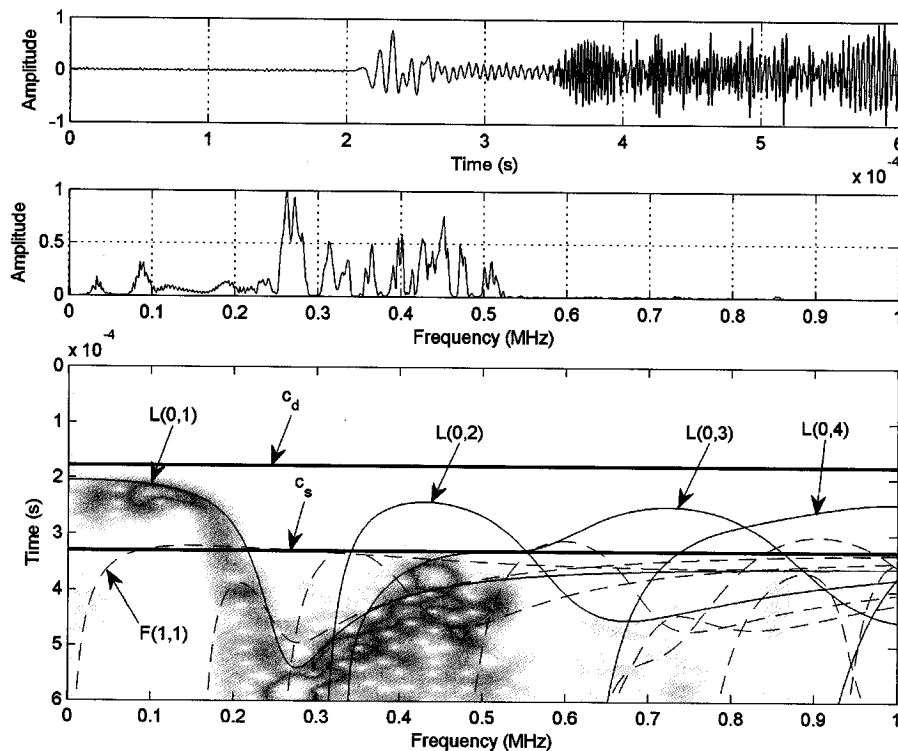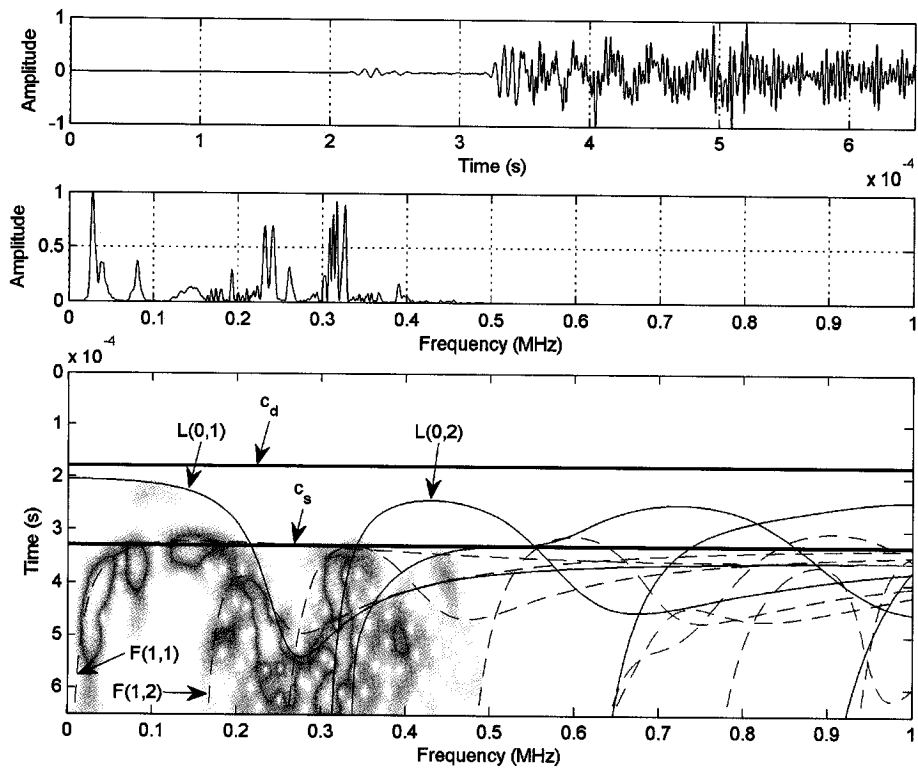

Figure 6.6: A 500 kHz single cycle pulse transmitted (direct arrangement) through a rebar (orthogonal rib pattern) 42" (1.067 m) in length and 0.472" (11.99 mm) in base diameter. The gain was 44.4 dB.
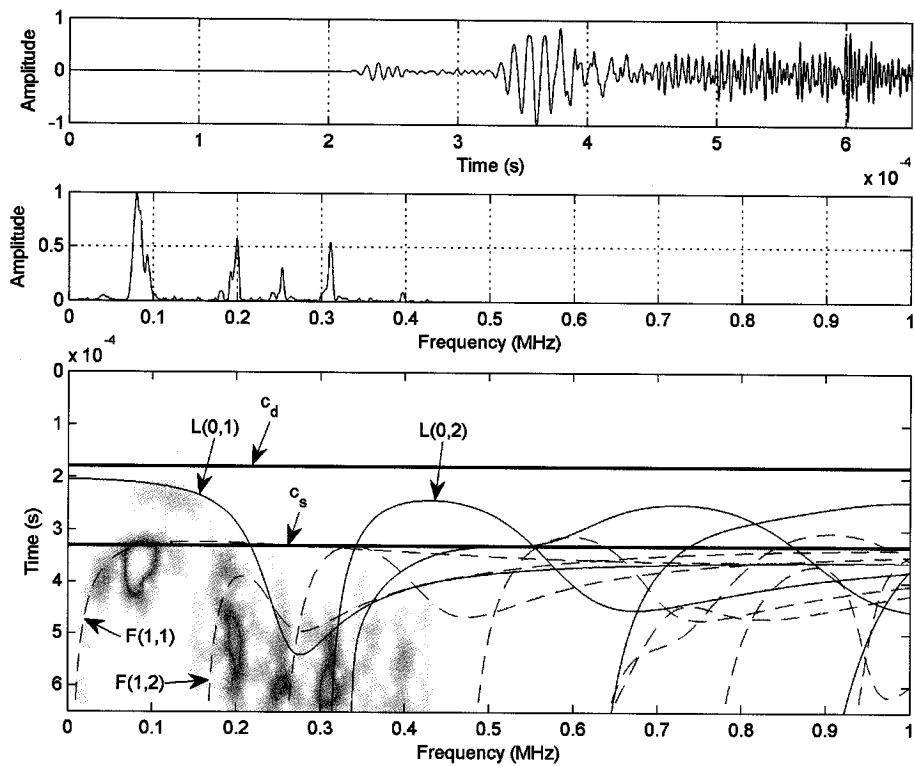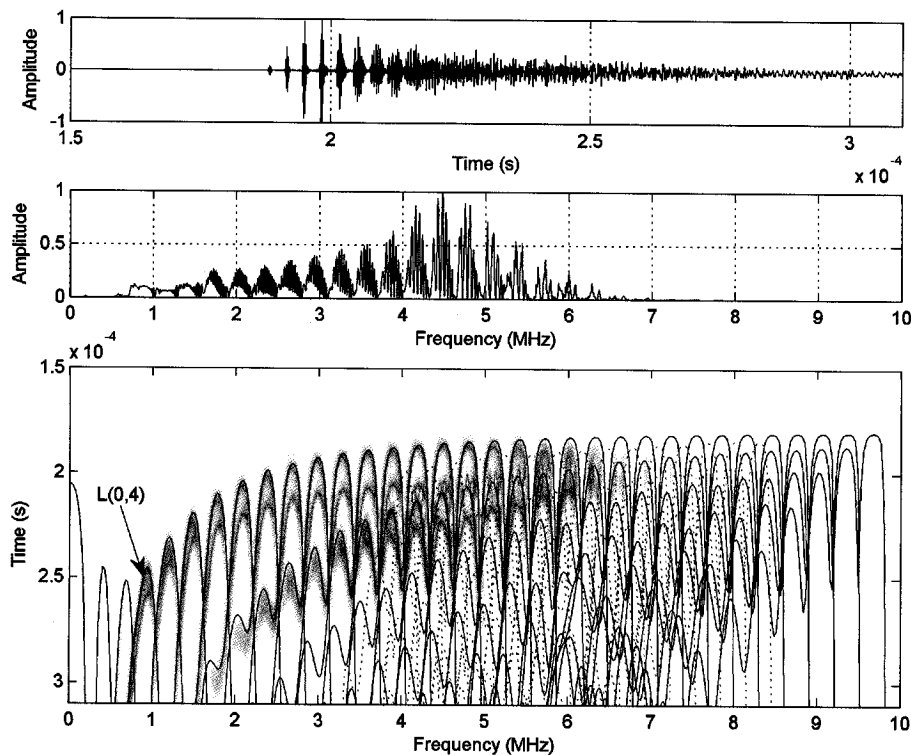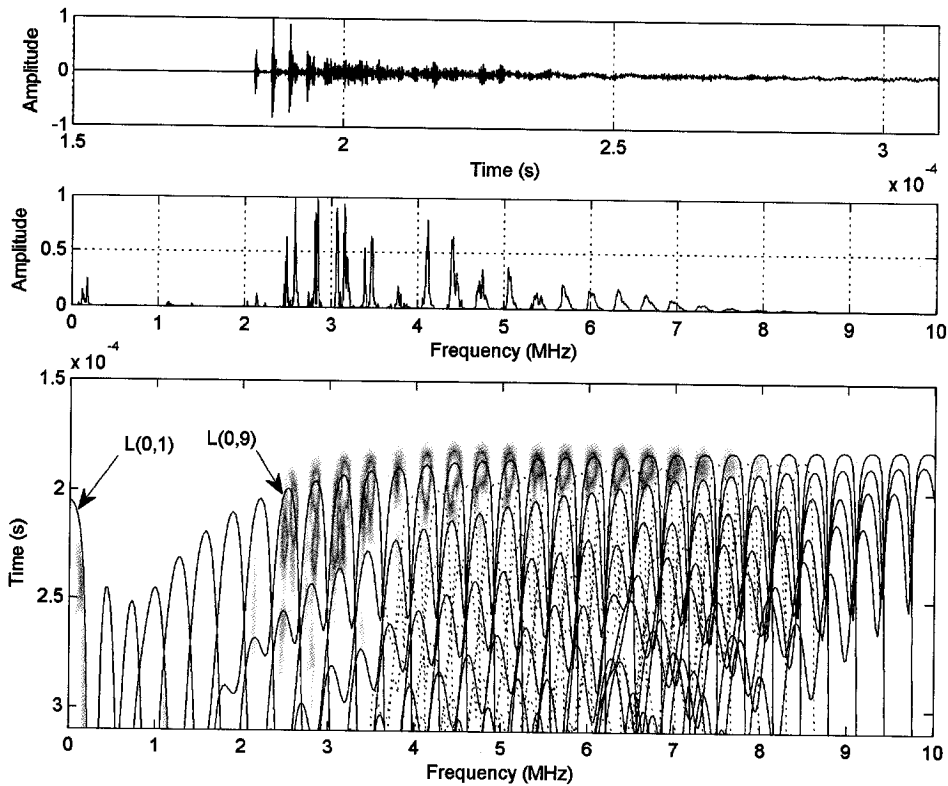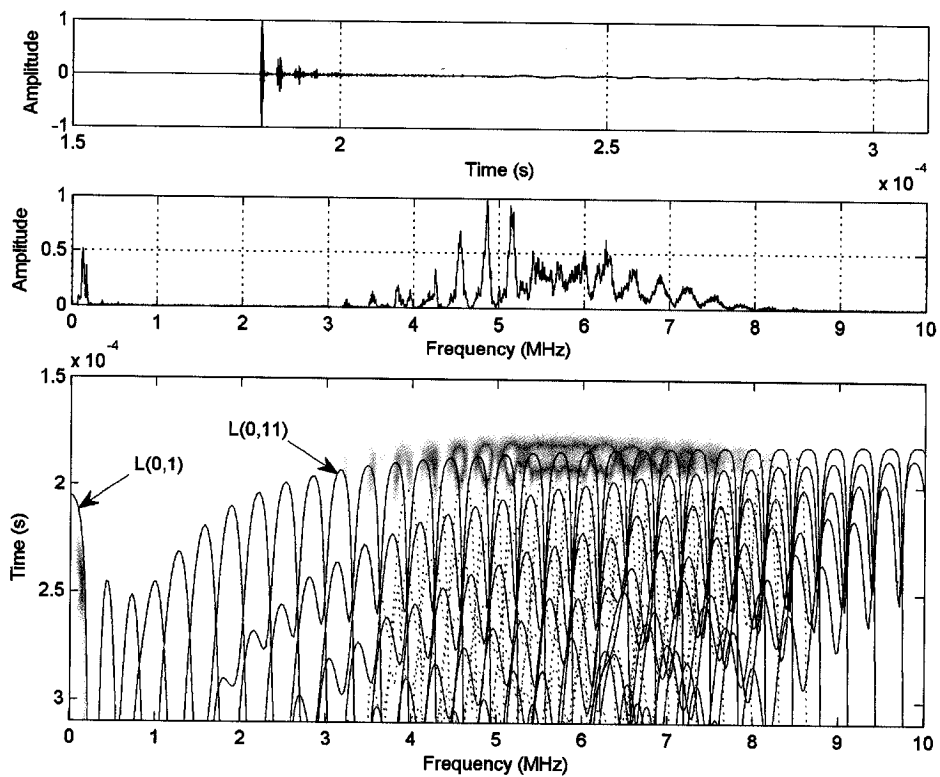
138
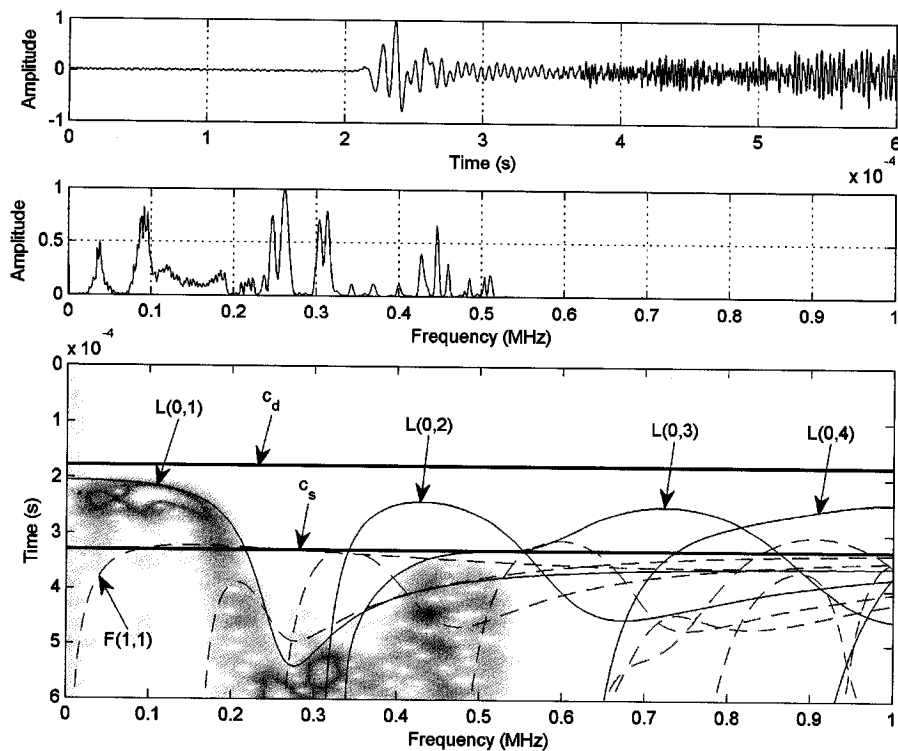
Figure 6.7: A 500 kHz single cycle pulse transmitted (direct arrangement) through a rebar (angled rib pattern) 42" (1.067 m) in length and 0.472" (11.99 mm) in base diameter. The gain was 44.4 dB.

There appears to be a frequency cutoff point for the deformed bars above 500 kHz. The modes within this frequency range have larger amounts of displacement at the bar outer circumference, but the wavelength is not as large compared to the characteristic dimension of the rib. Similar filtering of frequency ranges has been studied for guided waves in plates with corrugated patterns [120]. Frequency ranges that were filtered out were referred to as stop bands, while frequencies that still effectively propagated in the corrugated plate were referred to as pass bands. The ribs might have a beneficial effect of filtering out modes that are overly sensitive to interface conditions. These modes could cause confusion, making it difficult to distinguish between actual deterioration and other conditions (e.g., ingress of water, rib pattern, different concrete material properties, and bars in the near vicinity). There is, however, a need for the theoretical prediction of dispersion curves for guided waves in cylinders with corrugated deformation patterns.

An indirect transducer arrangement was then tested using Digital Wave transducers (model B-1025). A 250 kHz single cycle pulse was transmitted. The highpass and lowpass filters were set at 5 kHz and 1 MHz. The gain was the same level for all three bars. Figures 6.8-6.10 show the received time domain, frequency domain, and spectrogram for the solid bar, a rebar with an orthogonal rib pattern, and a rebar with an angled rib pattern. The longitudinal (solid lines) and flexural (dashed lines) modes that exist

139

within the testing range are also shown. The F(1,1) and L(0,1) modes were excited in each bar. The F(1,1) mode was the strongest invoked mode. All three bars had a strong response around 80 kHz for the F(1,1) mode. The response in the solid bar does not follow the dispersion curves as closely as the direct arrangement results. This is expected because the wave energy is transmitted into the bar perpendicular to the axis initially, causing scattering and reflections at the outset. There is observable scattering in the response for all three bars. The rebar with an orthogonal rib pattern had a similar response as the solid bar, but with more received energy in the lower frequencies. There is no observable wave energy received above 500 kHz. The first three flexural modes are invoked, with a strong F(1,1) response. The rebar with an angled rib pattern had the weakest overall response.

Figure 6.8: A 250 kHz single cycle pulse transmitted (indirect arrangement) through a solid bar 42" (1.067 m) in length and ½" (12.7 mm) in diameter.

140

Figure 6.9: A 250 kHz single cycle pulse transmitted (indirect arrangement) through a rebar (orthogonal pattern) 42" (1.067 m) in length and 0.472" (11.99 mm) in diameter.

Figure 6.10: A 250 kHz single cycle pulse transmitted (indirect arrangement) through a rebar (angled pattern) 42" (1.067 m) in length and 0.472" (11.99 mm) in diameter.

141

Higher frequencies were then tested on the three bars using Panametrics 5 MHz contact compressional transducers (model V110). A single cycle 5 MHz pulse was transmitted. The highpass and lowpass filters were set at 200 kHz and 10 MHz, respectively. Figures 6.11-6.13 show the received time domain, frequency domain, and spectrogram results for the solid bar, rebar with an orthogonal rib pattern, and rebar with an angled rib pattern. The solid and dotted lines are longitudinal and flexural modes, respectively.

The solid bar matches the predicted dispersion behavior very closely. There is a strong frequency response between 500 kHz and 7 MHz. It should be pointed out again that the diameter of the solid bar is 0.028" (0.71 mm) larger than the base diameter of the rebar specimens and may have very slight differences in material properties. These differences will shift the frequency locations of the attenuation minima slightly. However, the overall shape of the curve should look the same if the ribs have no influence. The frequency domain for the solid bar displays wider 'hills' at the frequency amplitude peaks compared to the rebar. Guided wave propagation at frequencies with less than negligible displacement profiles at the outer diameter of the bar (rib location) might result in the mode being scattered and/or reflected.

Figure 6.11: A 5 MHz single cycle pulse transmitted (direct arrangement) through a solid bar 42" (1.067 m) in length and ½" (12.7 mm) in diameter. The gain level was 48 dB.

142

Figure 6.12: A 5 MHz single cycle pulse transmitted (direct arrangement) through rebar (orthogonal ribs) 42" (1.067 m) in length and 0.472" (11.99 mm) in diameter. The gain was 58 dB.
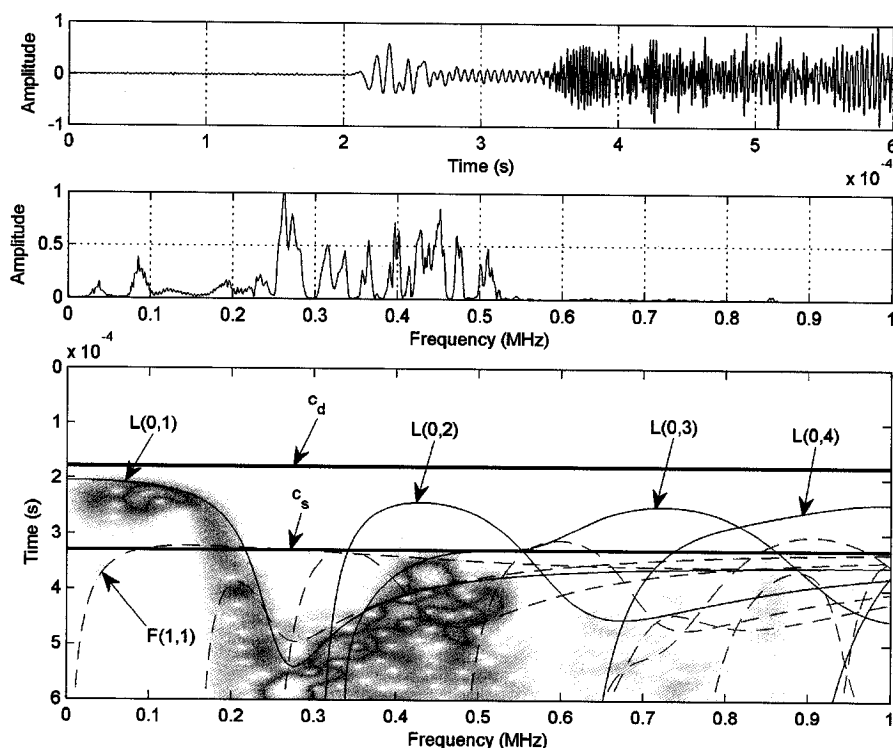

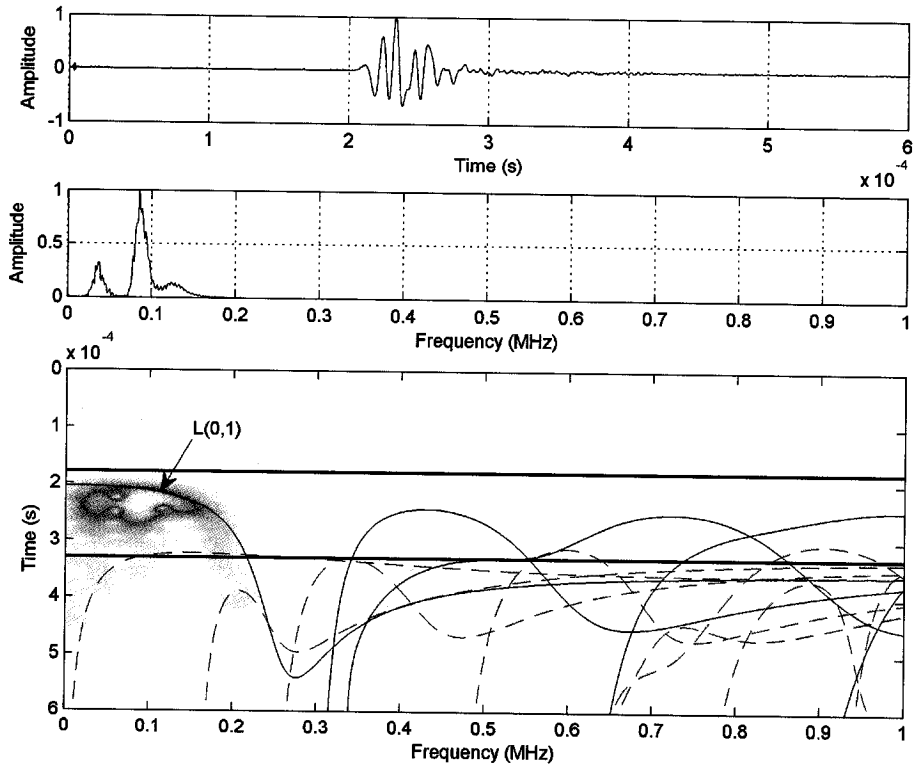**Figure 6.13:** A 5 MHz single cycle pulse transmitted (direct arrangement) through rebar (angled ribs) 42" (1.067 m) in length and 0.472" (11.99 mm) in diameter. The gain was 58 dB.

The deformed bars do not have a strong response for modes below the L(0,9) mode, with the exception of the L(0,1) mode. The L(0,1) mode has a large wavelength in comparison to the rib characteristic dimension, making it less sensitive to the effect of the ribs. The deformed bars have strong responses for modes between L(0,11) and L(0,26) for this test. Attenuation in the highest frequency region is mainly from material absorption due to the wave energy being centered in the bar. This would explain why the higher frequencies are affected less by the ribs in the frequency range studied. For the rebar (orthogonal rib pattern), the modes match closely to the predicted values at the velocity peaks. However, as the frequency moves to either side of the velocity peak, the response is not nearly as strong as with the solid bar. The displacement structure changes for frequencies on either side of the velocity peak. The rebar with an angled rib pattern does not follow the predicted dispersion curves as well. Despite both deformed bars having nearly the same base diameter, it appears the dispersion curves should be shifted slightly. This could be caused by slight differences in the density, diameter, material absorption, or elastic modulus. Despite the slight shift, it seems that the behavior would not follow the predicted curves as well as the other two bars. The best response is at the predicted velocity peaks, similar to the behavior of the other deformed bar. Notice that there is substantial frequency content between the frequency peaks. More discussion on this type of behavior is provided in later sections.

6.3.2 MODE SENSITIVITY TO WATER

A guided wave experiment was conducted to compare waveforms propagating through rebar before and after immersion in water. Water is capable of ingressing into the mortar and being present at the rebar interface. For all water tests, the rebar used had an orthogonal rib pattern, was 42" (1.067 m) in length, and had a 0.472" (11.99 mm) base diameter. The experimental setup is shown in Figure 6.14.
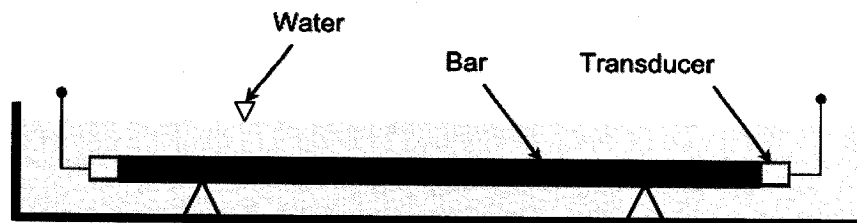
Figure 6.14: Rebar immersed in water (direct transducer arrangement shown).

Lower frequencies were first tested using a direct and indirect transducer arrangement. Digital Wave transducers (model B-1025) were used. A 500 kHz single cycle pulse was transmitted using the direct arrangement, while an 80 kHz single cycle pulse was used for the indirect arrangement. A signal was first transmitted for the rebar in air. The rebar was then immersed in water and another signal was transmitted and received. Figures 6.15 and 6.16 provide the time domain, frequency domain, and spectrogram retrieved using a direct transducer arrangement for the 500 kHz single cycle signal before and after

144

immersion in water, respectively. Figures 6.17 and 6.18 provide the time domain, frequency domain, and spectrogram retrieved using an indirect transducer arrangement for the 80 kHz single cycle signal before and after immersion in water, respectively. For both direct and indirect testing, the gain levels were the same before and after immersion in water and the highpass and lowpass filters were set at 5 kHz and 1 MHz, respectively.

Comparing the results before and after water immersion, the L(0,2) and portions of the L(0,1) response are severely attenuated. The low frequency response of the L(0,1) mode was still strong after immersion in water. Most of the displacement at the bar circumference in this region is in the axial direction, rather than radial. Therefore, there was less leakage into the water. The lowest frequency response for flexural propagation was relatively insensitive to the water. The F(1,1) mode has a phase velocity lower than the bulk compressional velocity of water at frequencies below 28.4 kHz. Therefore, the mode will not leak into the surrounding water in this frequency range.

Figure 6.15: A 500 kHz single cycle pulse transmitted (direct arrangement) through a rebar in air. The rebar (orthogonal ribs) was 42" (1.067 m) in length, with a 0.472" (11.99 mm) diameter.

145

Figure 6.16: A 500 kHz single cycle pulse transmitted (direct arrangement) through a rebar (orthogonal ribs) immersed in water. The rebar was 42" (1.067 m) in length, with a 0.472" (11.99 mm) diameter.
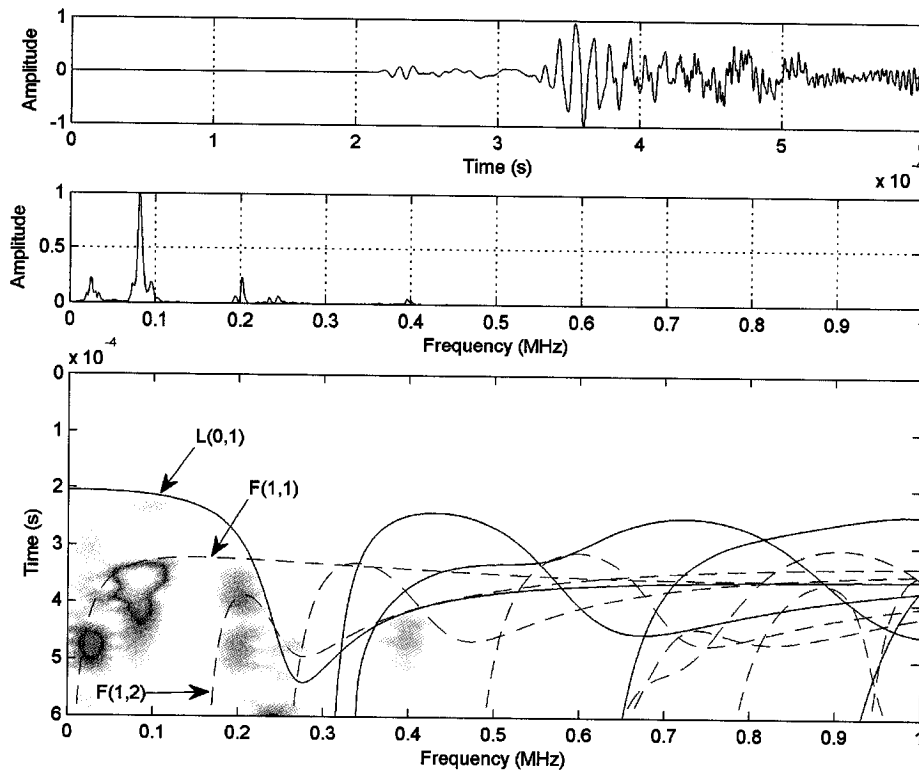
Figure 6.17: An 80 kHz single cycle pulse transmitted (indirect arrangement) through a rebar (orthogonal ribs) prior to being immersed in water. The rebar was 42" (1.067 m) in length, with a 0.472" (11.99 mm) diameter.

146
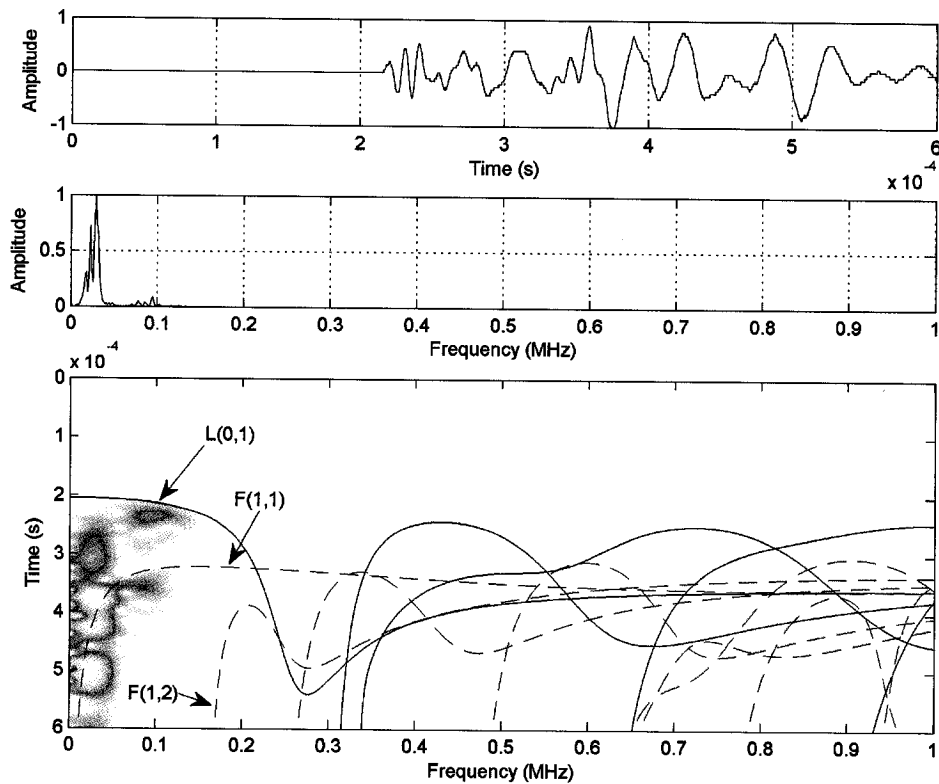
Figure 6.18: An 80 kHz single cycle pulse transmitted (indirect arrangement) through a rebar (orthogonal ribs) immersed in water. The rebar was 42" (1.067 m) in length, with a 0.472" (11.99 mm) diameter.

The change in the amplitude of the frequency response was calculated for waveforms before and after water immersion and converted to a decibel scale. The following equation was used to calculate the relative attenuation in decibels from the change in frequency amplitudes:

$$\text{Attenuation} = 20 \cdot \log\left(\frac{A_o}{A_1}\right) \qquad \qquad (6.1)$$

where A_o is the initial amplitude at a particular frequency prior to water immersion and A_1 is the amplitude of the same frequency after water immersion. The L(0,1) and F(1,1) theoretical attenuation curves for a 0.472" (11.99 mm) diameter steel bar immersed in water with experimental points are shown in Figure 6.19. The relative attenuation measurements for the low frequency water testing were considered absolute attenuation measurements due to the extremely low attenuation values for rebar in air in this frequency range.

147
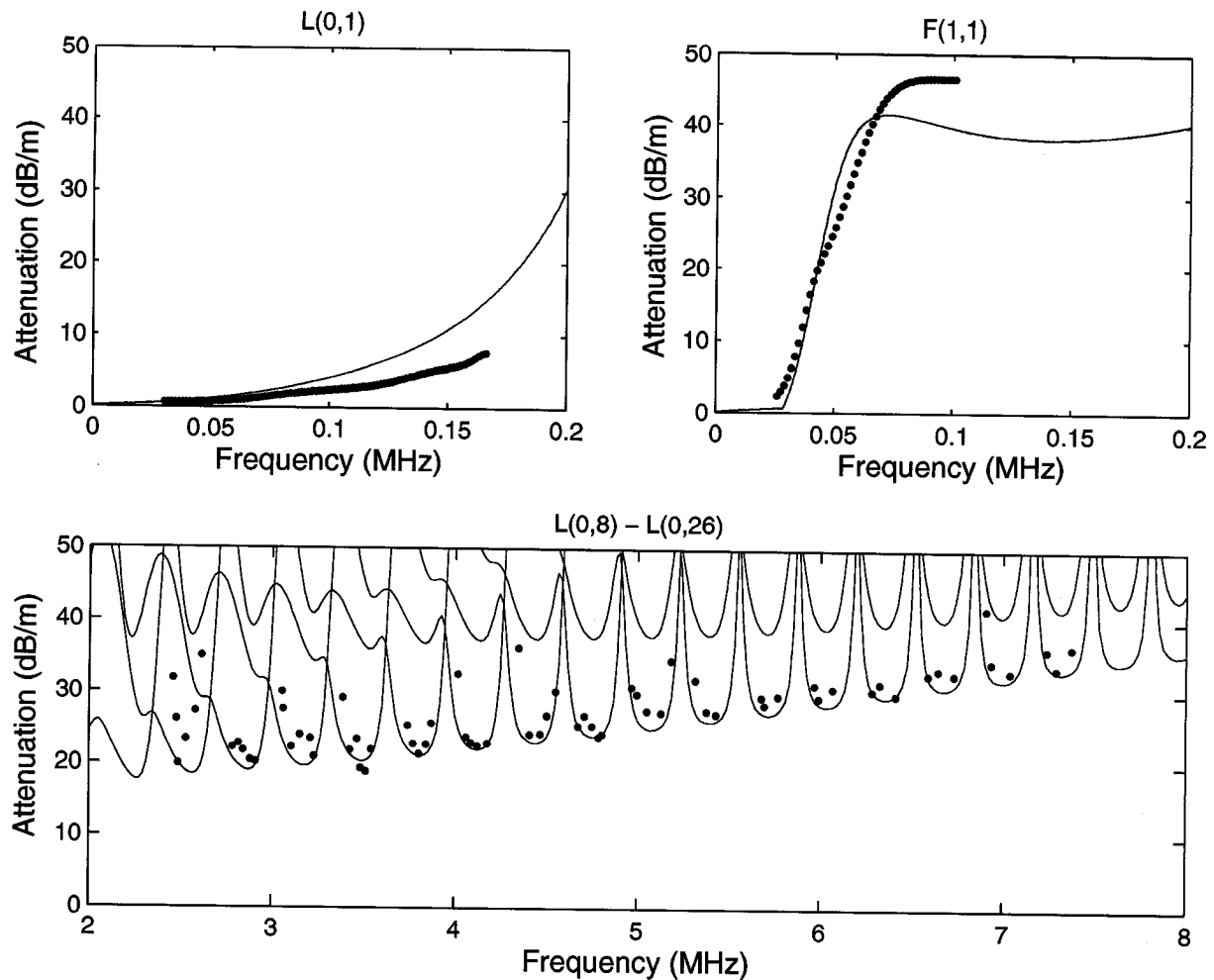
Figure 6.19: Comparison of the L(0,1) (upper left), F(1,1) (upper right), and higher order longitudinal modes (bottom) predicted attenuation curves to experimental points for a solid bar 0.472" (11.99 mm) in diameter immersed in water.

There is rather close agreement between the theoretical attenuation curves and the experimental data. While the attenuation increases over the tested frequency range for the L(0,1) mode, it is much less sensitive to the water in comparison to the F(1,1) mode.

High frequency testing was then conducted using 5 MHz Panametrics contact compressional transducers (model V110). A 5 MHz single cycle pulse was transmitted in a direct arrangement for a rebar in air. The rebar was then immersed in water and another signal was transmitted and received. Figures 6.20 and 6.21 provide the time domain, frequency domain, and spectrogram for testing before and after water immersion. Gain levels were the same before and after immersion in water. The highpass and lowpass filters were set at 200 kHz and 10 MHz, respectively. The solid and dotted lines are longitudinal and flexural modes, respectively.

148
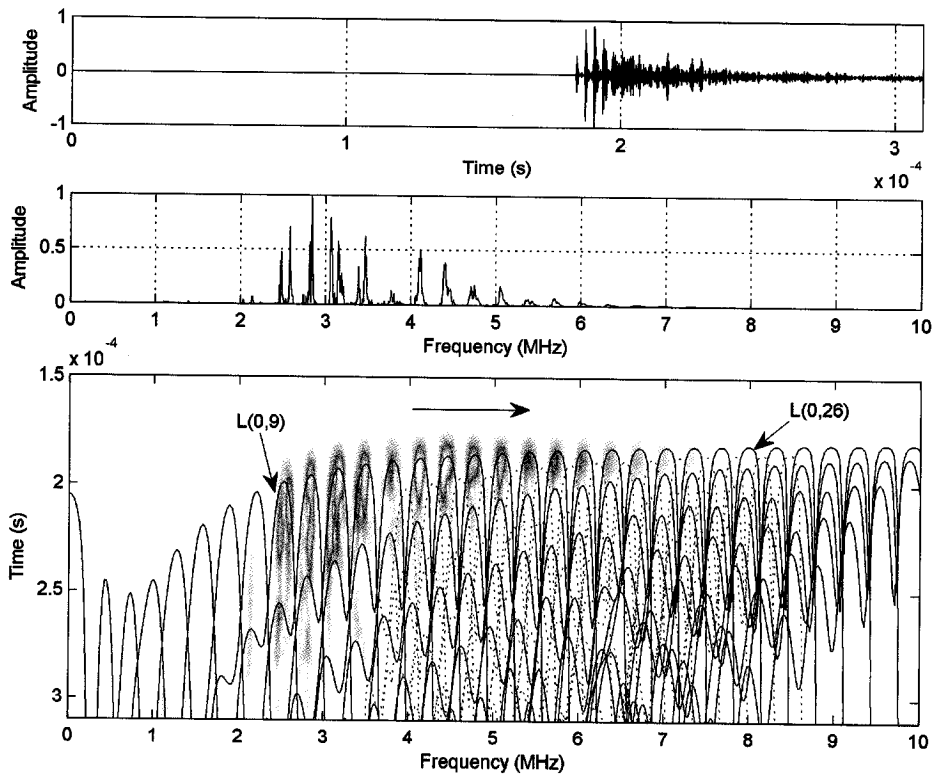
Figure 6.20: A 5 MHz single cycle pulse transmitted (direct arrangement) through rebar (orthogonal ribs) 42" (1.067 m) in length and 0.472" (11.99 mm) in diameter prior to being immersed in water.
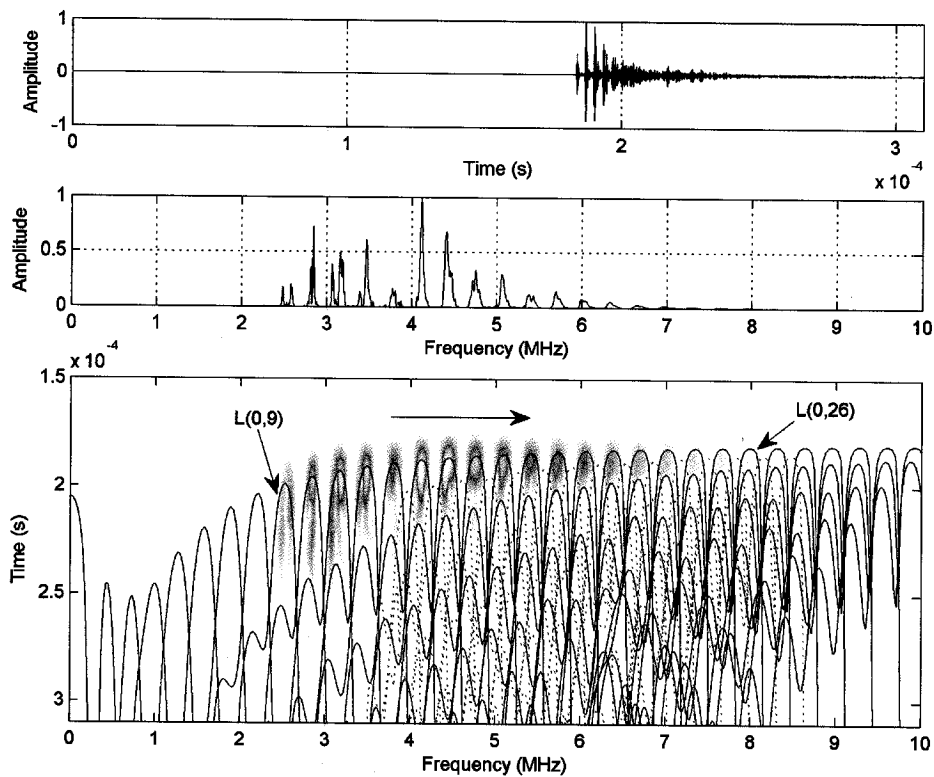
Figure 6.21: A 5 MHz single cycle pulse transmitted (direct arrangement) through rebar (orthogonal ribs) 42" (1.067 m) in length and 0.472" (11.99 mm) in diameter after being immersed in water.

149

The results indicate that as the frequency decreases, the water has more of an attenuative effect. The highest frequencies are only slightly affected by water immersion. This characteristic of the higher frequencies makes it particularly desirable for in-situ monitoring systems since it is not overly sensitive to a water surrounding. The signals before and after immersion in water were then compared and relative attenuation was quantified. Theoretical attenuation values for rebar in air were added to the experimental relative attenuation values from immersion in water, with the results shown in Figure 6.19. The quantitative attenuation measurement confirms the observations from the frequency domain. The higher frequencies are relatively insensitive to a surrounding of water due to the negligible displacement structure at the bar circumference (as predicted from Figure 4.20).

6.3.3 MODE SENSITIVITY TO MORTAR

A guided wave experiment was conducted to compare waveforms propagating through rebar before and after being embedded in mortar. Wooden formwork was created with inside dimensions of 8" x 7.5" x 6.5" (20.3 cm x 19.1 cm x 16.5 cm). Holes were drilled through the wooden form so that rebar could span the length of the longest dimension. A rebar (orthogonal rib pattern) with a 0.472" (11.99 mm) diameter and 60" (1.524 m) in length was centered through the holes. Digital Wave transducers (model B-1025) were attached in a direct and indirect arrangement. The experimental setup is shown in Figure 6.22.
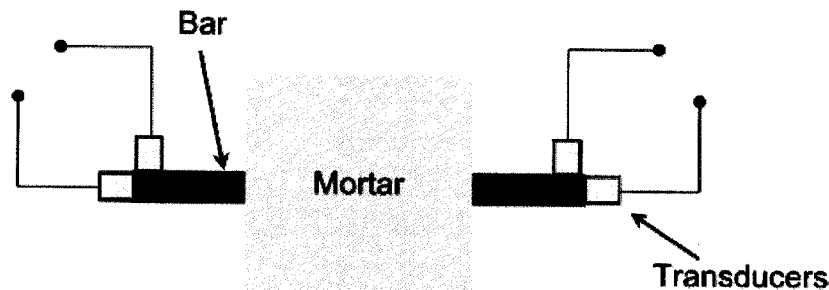
Figure 6.22: Rebar embedded in mortar with a direct and indirect through-transmission transducer arrangement.

The purpose of the test is to measure the amount of waveform energy leaked into the surrounding mortar. A baseline measurement will be taken when the rebar is in air (i.e. prior to the mortar being poured around the bar). A 250 kHz single cycle pulse was transmitted for both the direct and indirect transducer arrangements. After the mortar is poured and has had sufficient time to hydrate (i.e. 28 days) another waveform measurement will be taken. Material absorption is present before and after the mortar is poured so the effects should not be noticeable. Since this is a through-transmission arrangement (i.e. transducers on opposite sides), there is no loss due to reflections off of the ends of the bars, as with pulse-

150

echo. However, some waveform energy may be reflected from the mortar entry point, as shown in Figure 6.23.
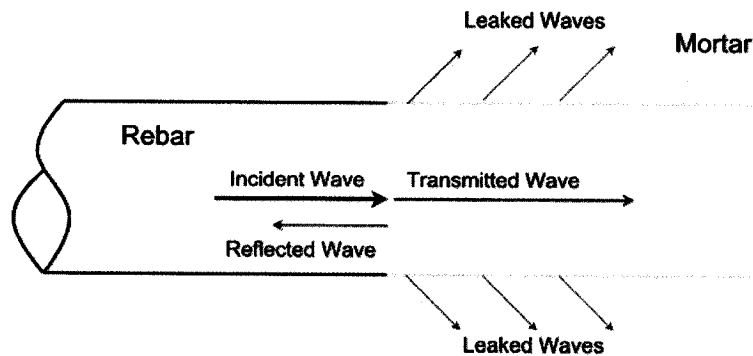

Figure 6.23: Transmission and reflection of incident waveform at mortar entry point.

Vogt et al. investigated entry point reflections for the L(0,1) mode in a cylindrical bar partly embedded in an epoxy resin [122]. The results showed that the reflection coefficient is dependent on the frequency-radius product. Scattering and reflections of the incident wave at the mortar interface occur at the bar circumference. Modes with substantial displacement and energy profiles at the outer diameter of the bar will have more sensitivity (i.e. higher reflection coefficient). However, also critical is the ratio of the circumference of the bar to the bar cross-sectional area. This was found to relate the ratio of the scattered wave to the total power of the incident mode [122]. While the L(0,1) and F(1,1) have large displacement profiles at the bar circumference, the bar size used for testing increases the frequency-radius product and thus reduced the amount of loss due to entry point reflection.

Figures 6.24 and 6.25 provide the time domain, frequency domain, and spectrogram retrieved using a direct transducer arrangement for the 250 kHz single cycle pulse before and after being embedded in mortar, respectively. Figures 6.26 and 6.27 provide the time domain, frequency domain, and spectrogram retrieved using an indirect transducer arrangement for the 250 kHz single cycle pulse before and after being embedded in mortar, respectively. For both direct and indirect tests, the highpass and lowpass filters were set at 20 kHz and 300 kHz, respectively. The solid and dashed lines are longitudinal and flexural modes, respectively.

The 250 kHz single cycle pulse transmitted in a direct transducer arrangement shows signs of attenuation, with the highest frequencies invoked being the most affected. It appears as though the F(1,1) mode is received around 100 kHz for testing conducted after hydration of the mortar. A second reflection is visible for the bar in air, arriving shortly after 900 μs. After the hydration of the mortar, this reflection

151

can no longer be seen. Notice that the frequencies around 50 kHz appear slowed after hydration of the mortar. The energy velocity decreases in this frequency range for the L(0,1) mode (refer to Figure 4.21). The 250 kHz single cycle pulses transmitted in an indirect transducer arrangement are also attenuated, with the higher frequencies showing the most sensitivity. Notice that the lowest frequencies for the F(1,1) mode seem to be affected as well. The F(1,1) mode has a phase velocity lower than the bulk compressional and shear velocity of mortar at frequencies below 34.9 kHz. Therefore, the mode should not leak into the surrounding mortar in this frequency range. It is thought that the signal loss may result from the entry point reflection.
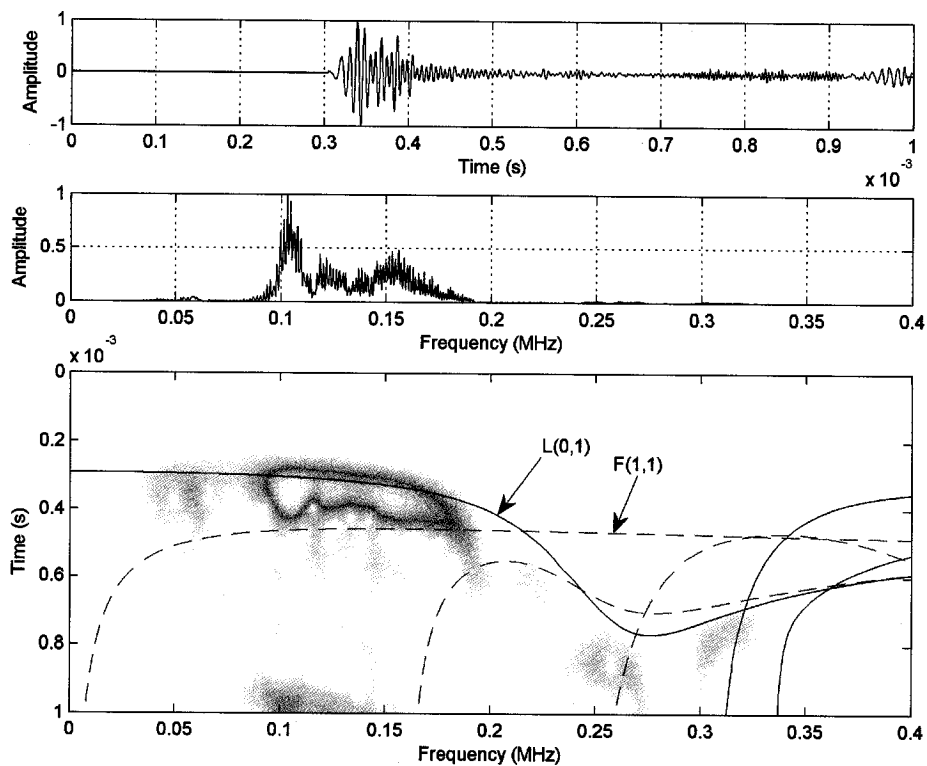
Figure 6.24: A 250 kHz single cycle pulse transmitted (direct arrangement) through rebar (orthogonal ribs) prior to mortar being poured into the formwork. The gain was 10 dB.

152
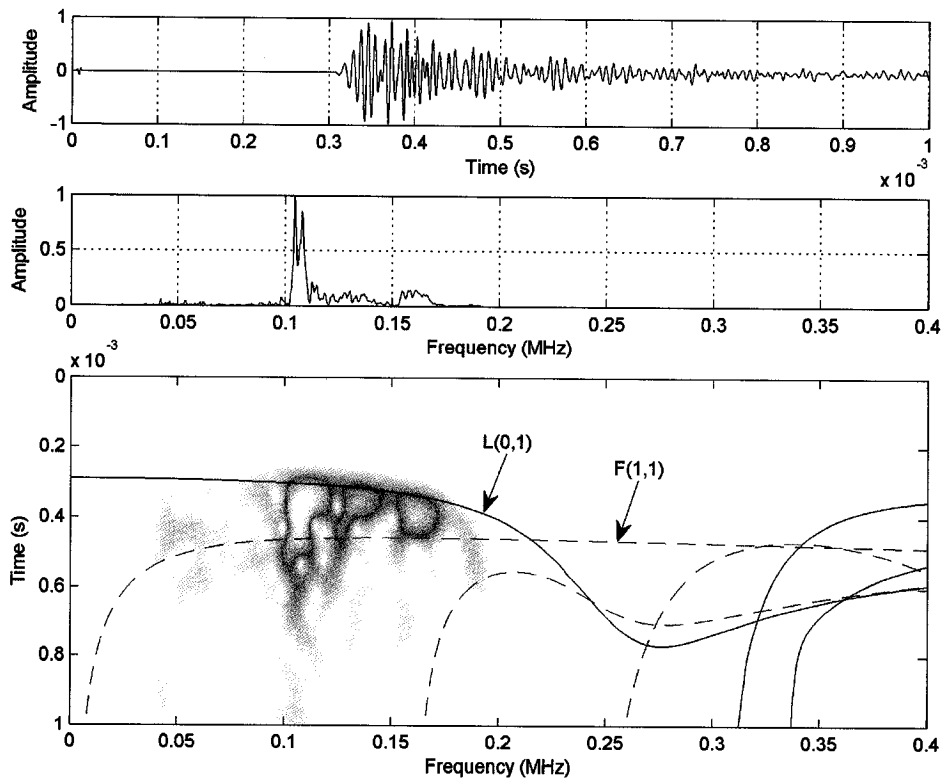
Figure 6.25: A 250 kHz single cycle pulse transmitted (direct arrangement) through rebar (orthogonal ribs) after the mortar is poured into the formwork and allowed to hydrate for 30 days. The gain was 30 dB.
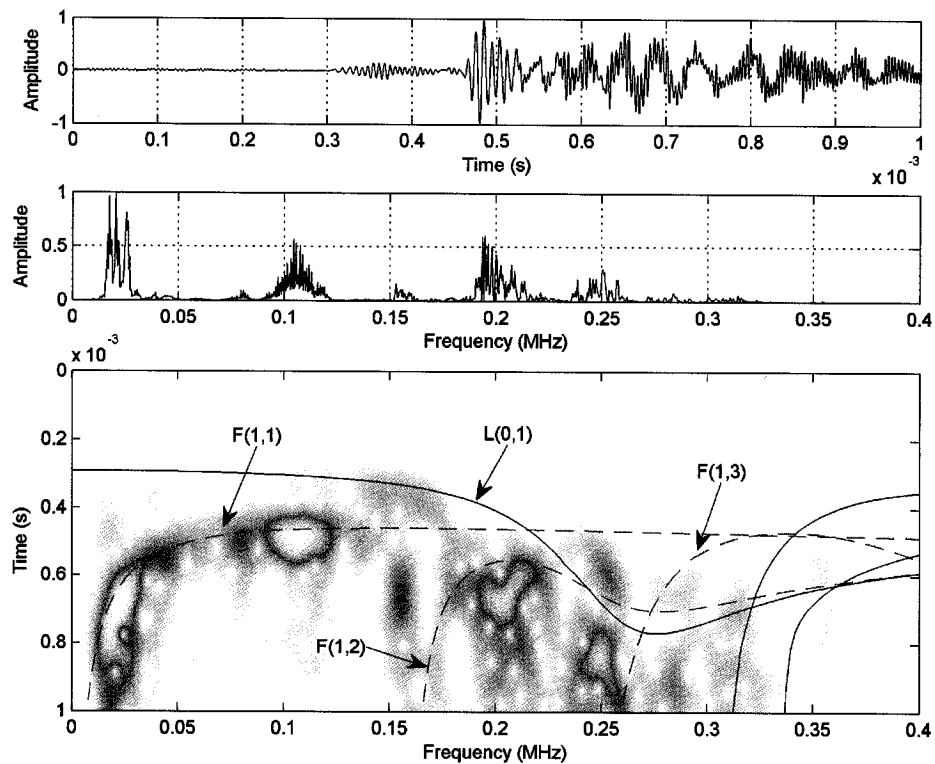
Figure 6.26: 250 kHz single cycle pulse transmitted (indirect arrangement) through rebar (orthogonal ribs) prior to the mortar being poured into the formwork. The gain was 50 dB.

153
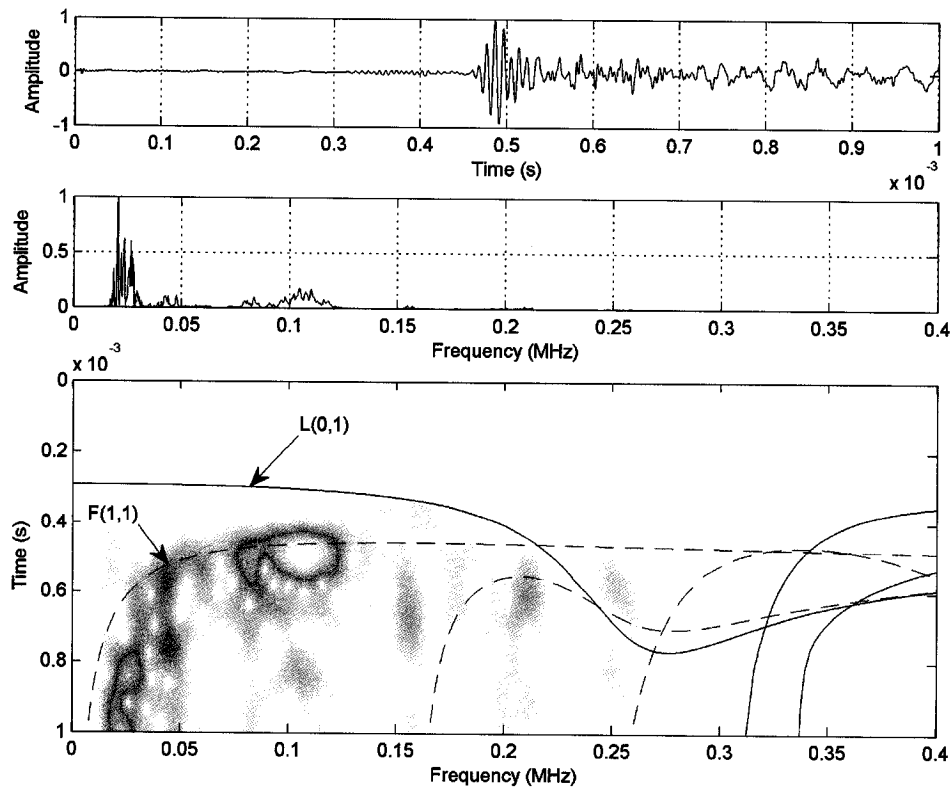
Figure 6.27: A 250 kHz single cycle pulse transmitted (indirect arrangement) through rebar (orthogonal ribs) after the mortar is poured into the formwork and allowed to hydrate for 30 days. The gain was 60 dB.

In order to more easily assess the attenuation of the system at specific frequencies, tonebursts were used. A 20-cycle toneburst was invoked, with a bandpass filter of +/- 5 kHz of the input frequency. A frequency sweep from 20 to 200 kHz, in 10 kHz increments, was used as the input frequency. Before mortar was placed in the wooden formwork, a frequency sweep was conducted for both the direct and indirect transducer arrangement. Most frequencies invoked, using both the direct and indirect arrangements, had a clear distinguishable waveform received on the other end. Next, the mortar was placed and compacted in the wooden formwork. After twenty-eight days of hydration, another frequency sweep was conducted. Now only certain frequencies invoked had a clear distinguishable received waveform. The change in received signal energy for these waveforms was calculated and converted to a decibel scale in the same manner described in Section 6.3.2. Figure 6.28 provides the L(0,1) and F(1,1) theoretical attenuation curves for a 0.472" (11.99 mm) diameter steel bar embedded in an infinite surrounding of mortar, along with the experimental points from the direct and indirect transducer arrangements, respectively.
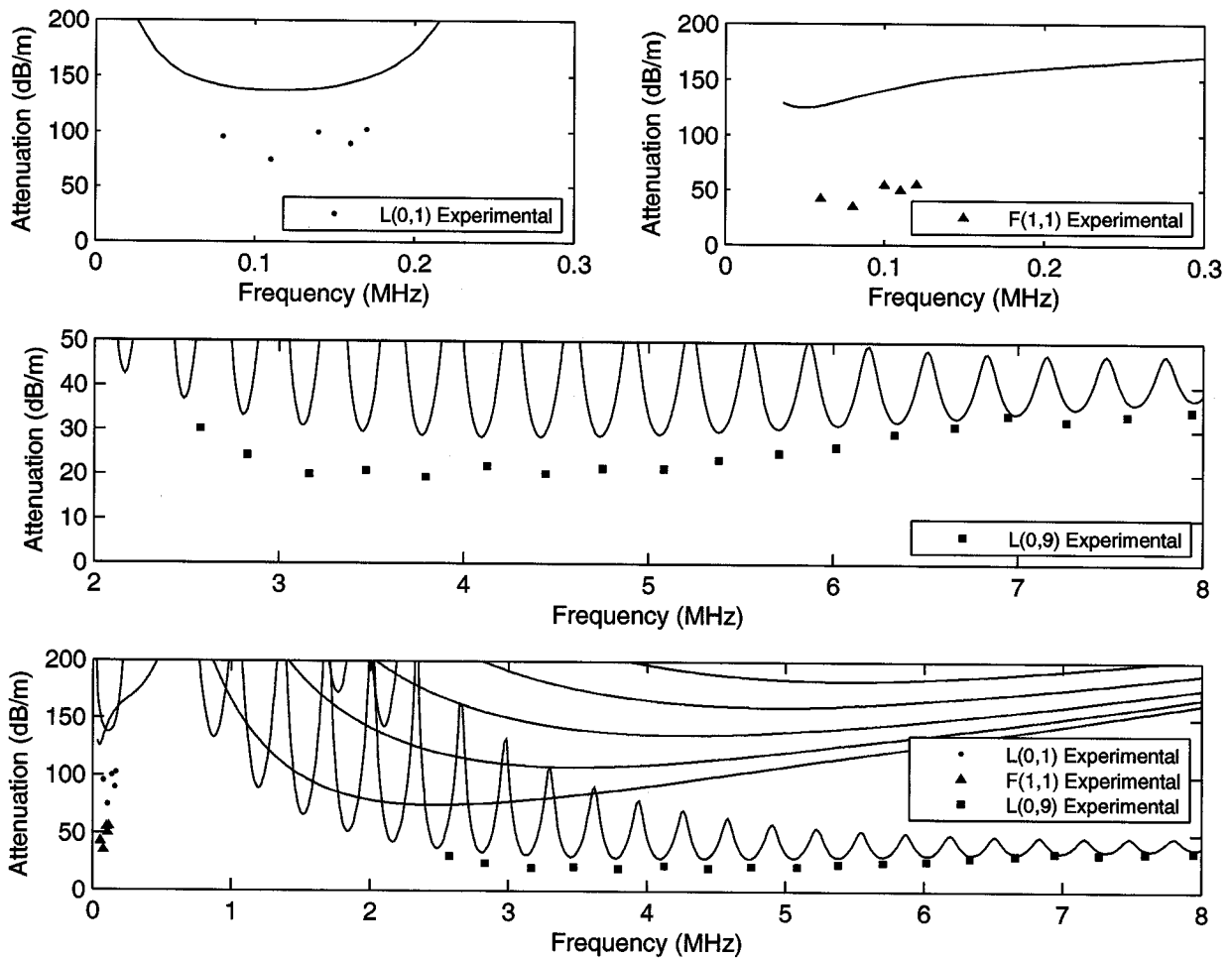
Figure 6.28: Theoretical attenuation curves plotted with experimental attenuation data points for the L(0,1) mode (top left), F(1,1) mode (top right), L(0,9) mode (middle), and all of the modes together (bottom).

The shape of the experimental points generally agrees with the shape of the theoretical curves, however both theoretical curves overestimated the amount of attenuation in the system. Others have observed similar overestimation of attenuation and have concluded that the error is caused by less than perfect bond between the steel and mortar [95]. Another source of error could arise from the difference in mechanical properties of the interfacial transition zone between the steel and mortar (refer to Section 2.1) as compared to the bulk mechanical properties of the mortar mix. The 50 - 200 kHz frequency range tested is particularly sensitive to bond, as the main mechanism of attenuation is leakage rather than material absorption. There is little published data for non-axisymmetric modes leaking into solid materials and therefore there may be some discrepancy [89].

A guided wave test was conducted to validate the L(0,9) theoretical attenuation curves predicted for a steel bar embedded in mortar. The entry point reflection was considered negligible for the L(0,9) mode because the frequency-radius product was even higher than before and the displacement profile is

155

concentrated in the center of the bar. A rebar (orthogonal rib pattern) with a 0.472" (11.99 mm) diameter and a length of 14.88" (37.78 cm) was centered through the holes of the same wooden formwork used for the low frequency testing in this section. The transducers were Panametrics contact compressional (model V110), attached in a direct arrangement. A total of 18 frequencies were tested using both single cycle pulses and 100-cycle tonebursts: 2.59, 2.85, 3.16, 3.47, 3.80, 4.12, 4.41, 4.76, 5.08, 5.39, 5.71, 6.04, 6.34, 6.69, 6.98, 7.32, 7.64, and 7.98 MHz. An initial waveform was taken before the mortar was poured into the formwork (i.e. rebar in air). Another waveform is taken after the mortar has been poured into the formwork and allowed to hydrate for 28 days. The frequency domain for the received 5.08 MHz single cycle pulse before and after the presence of mortar is shown in Figure 6.29.
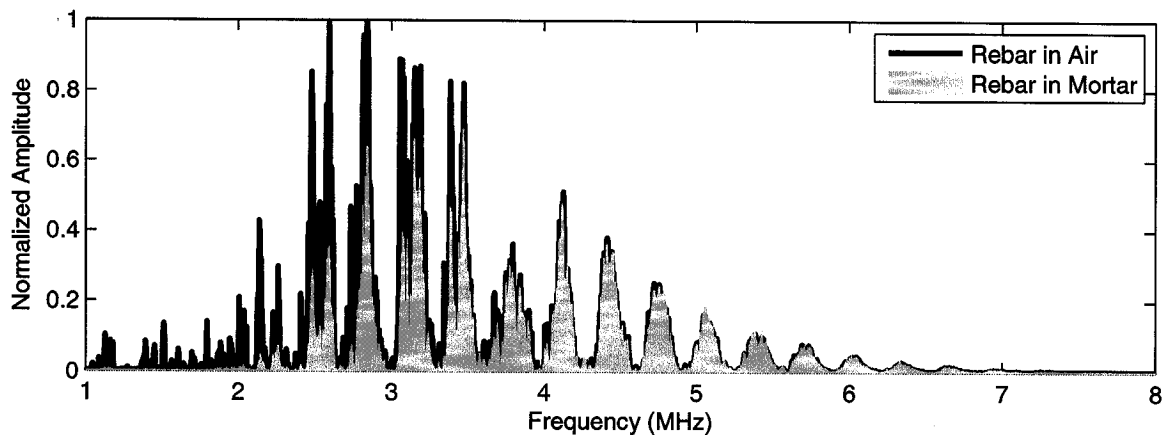
Figure 6.29: A 5.08 single cycle pulse received before and after the presence of mortar. The gain levels were the same for both signals. The highpass and lowpass filters were set at 2 and 10 MHz, respectively.

The lowest frequencies within the tested range were the only frequencies affected by the presence of the mortar. At frequencies higher than 4 MHz, the signal was virtually unaffected. The differences in signal strength were calculated by comparison of the peak amplitudes in the time and frequency domains for the 100-cycle tonebursts. Figure 6.28 shows the attenuation of the signal from the presence of mortar. The relative change in attenuation in decibels calculated from the experimental data was added to the theoretical attenuation value predicted for a bar in air. The experiment yielded results very similar to the theoretical predictions for attenuation levels from mortar. The higher frequencies in the tested range were virtually unaffected by the change in surrounding (as predicted from Figure 4.20).

6.4 MODE SENSITIVTY TO DIFFERENT CORROSION EFFECTS

As stated earlier, the main forms of deterioration from uniform corrosion is the loss of steel cross-sectional area, the destruction of bond between the steel and concrete, and the loss of concrete cross-sectional area. To test the loss of steel cross-sectional area, several rebar specimens were corroded to different levels of mass loss and tested using guided waves. To test the effect of bond loss and concrete

156

spalling, reinforced specimens were created with inhibited bond over different lengths. To test the effect of severe localized corrosion, reinforced mortar specimens were created with different types of seeded defects simulating discontinuities.

6.4.1 EFFECT OF BAR PROFILE CHANGE

Rebar specimens (orthogonal rib pattern) extracted from reinforced mortar accelerated corrosion testing (presented in Section 6.5), were used to evaluate the influence of the bar profile changes on guided wave behavior. Low frequencies were evaluated using a 250 kHz single cycle pulse in a direct and indirect transducer arrangement. Digital Wave (model B-1025) compressional transducers were used. A total of five corroded bars (orthogonal rib pattern) were tested, each with a total length of 42" (1.067 m) and an original base diameter of 0.472" (11.99 mm). Four of the bars were corroded uniformly over the middle 36" (0.9144 m) of the length to a percentage mass loss of 1.8%, 4.2%, 9%, and 14.1%. The fifth specimen had undergone mainly uniform corrosion until a localized pit formed extending almost 50% through the bar depth over a length of 1" (2.54 cm). The total percentage mass loss for the specimen was 13.3%. The results of the low frequency direct transducer arrangement testing are shown in Figures 6.30-6.34. The highpass and lowpass filters were set at 5 kHz and 1 MHz, respectively.

Since the transducers had to be coupled to each bar individually, quantitative comparisons are prone to error. However, the same gain level was used for each test, with similar signal strengths for the low frequency tests. Frequencies below 100 kHz were relatively unaffected for the rebar specimens with only uniform corrosion. Above 100 kHz, there is a low signal strength for specimens with 4% mass loss or higher. The specimen with localized corrosion showed lower signal strength for the entire frequency range examined. The lowest frequencies are thought to have reflected off of the discontinuity formed along the length.
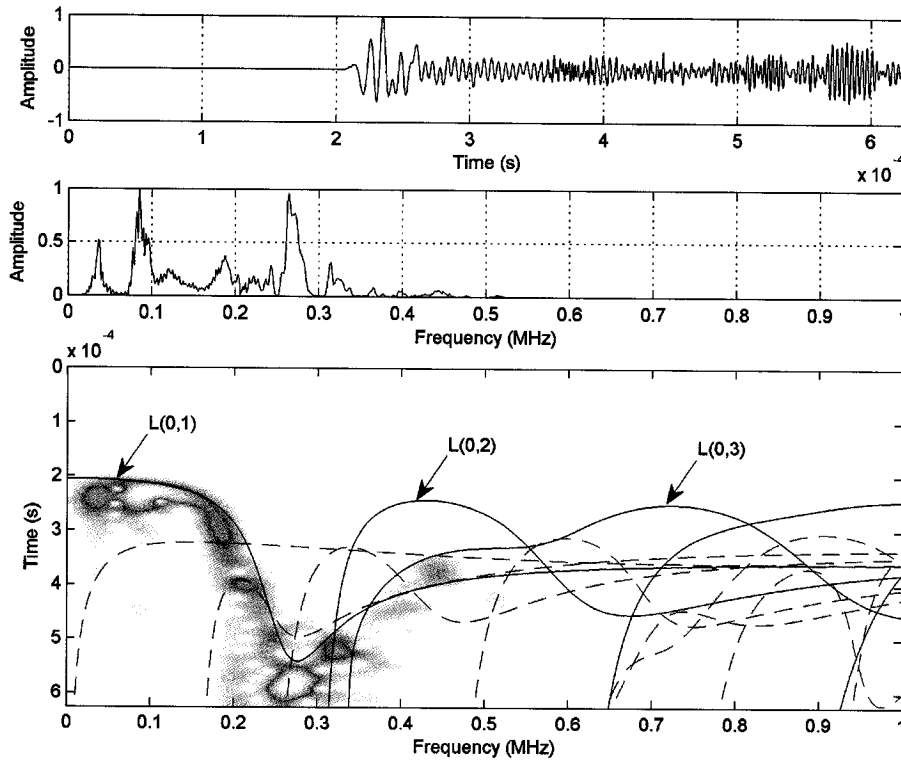
157

Figure 6.30: A 250 kHz single cycle pulse transmitted (direct arrangement) through corroded rebar (extracted from accelerated corrosion tests) in air with 1.8% uniform mass loss.
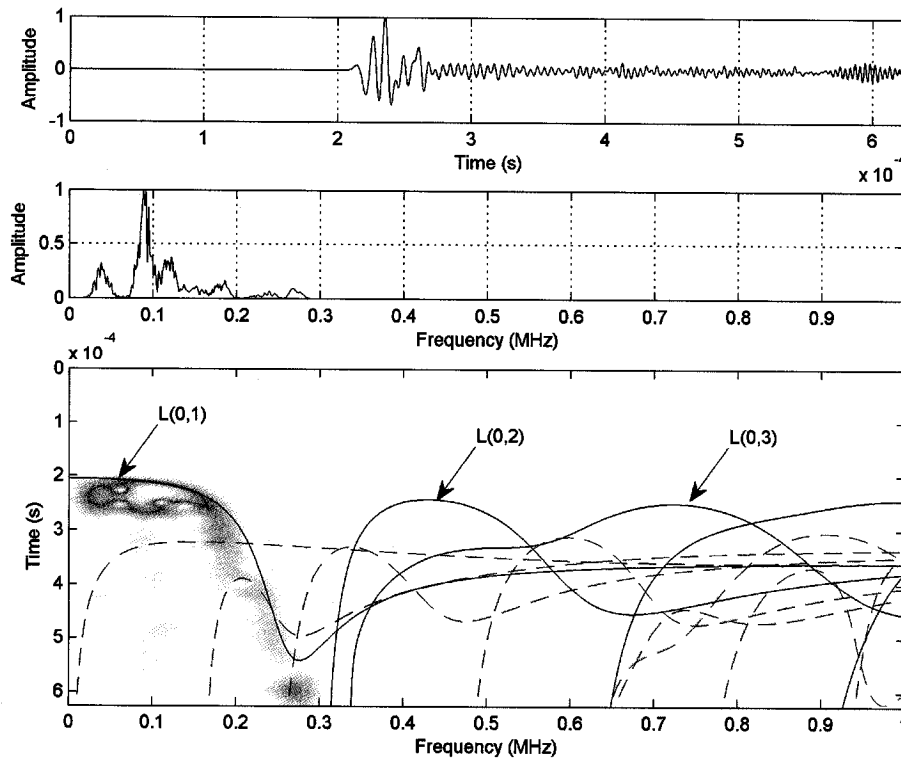

Figure 6.31: A 250 kHz single cycle pulse transmitted (direct arrangement) through corroded rebar (extracted from accelerated corrosion tests) in air with 4.2% uniform mass loss.
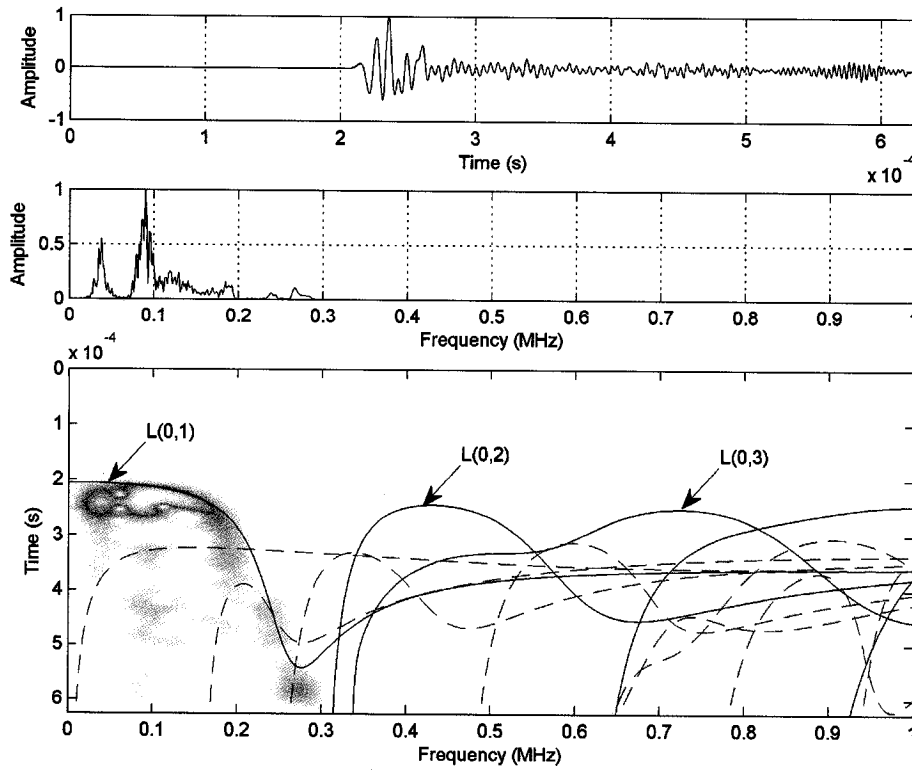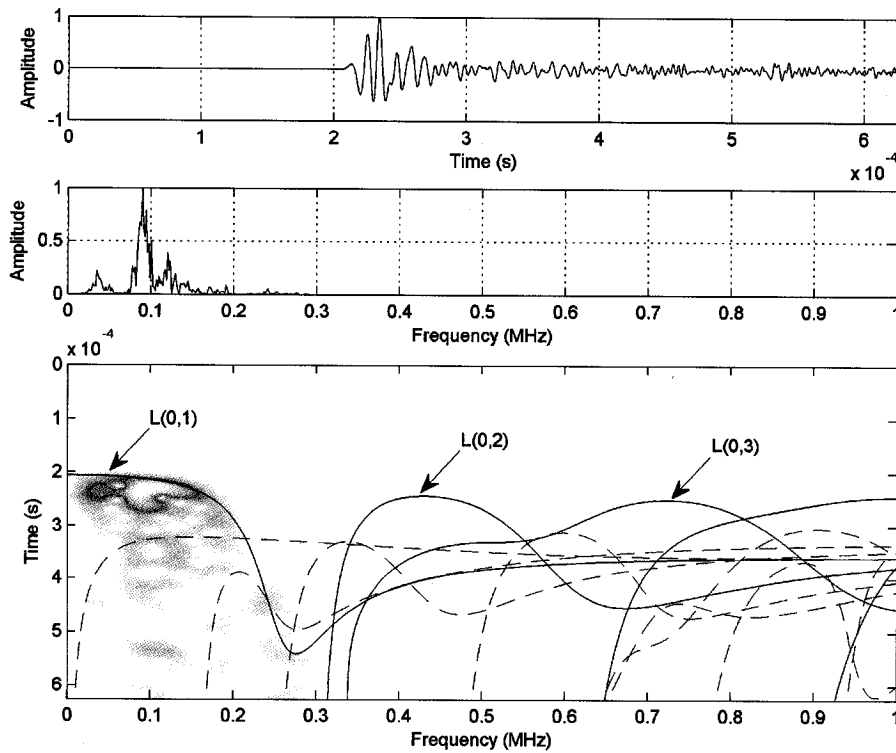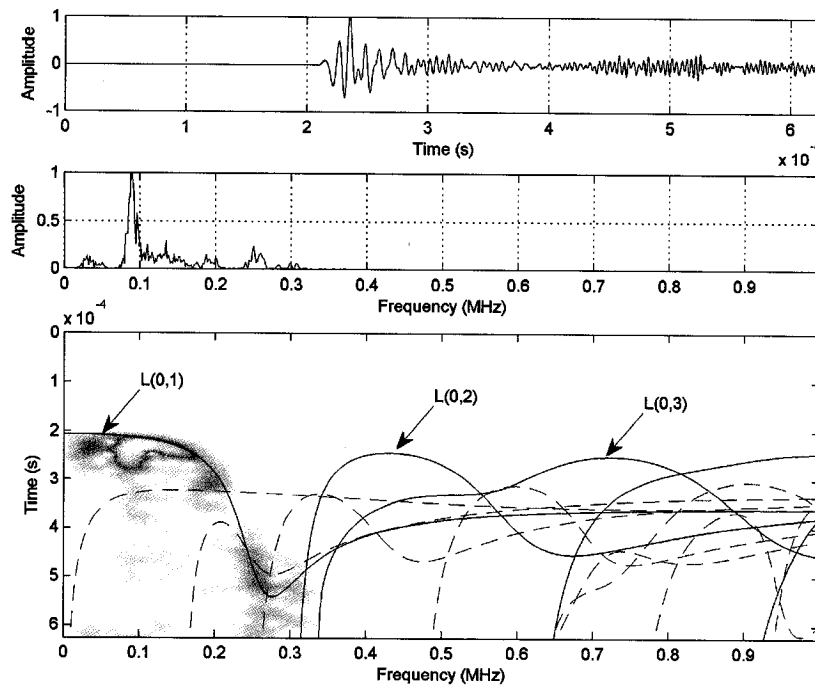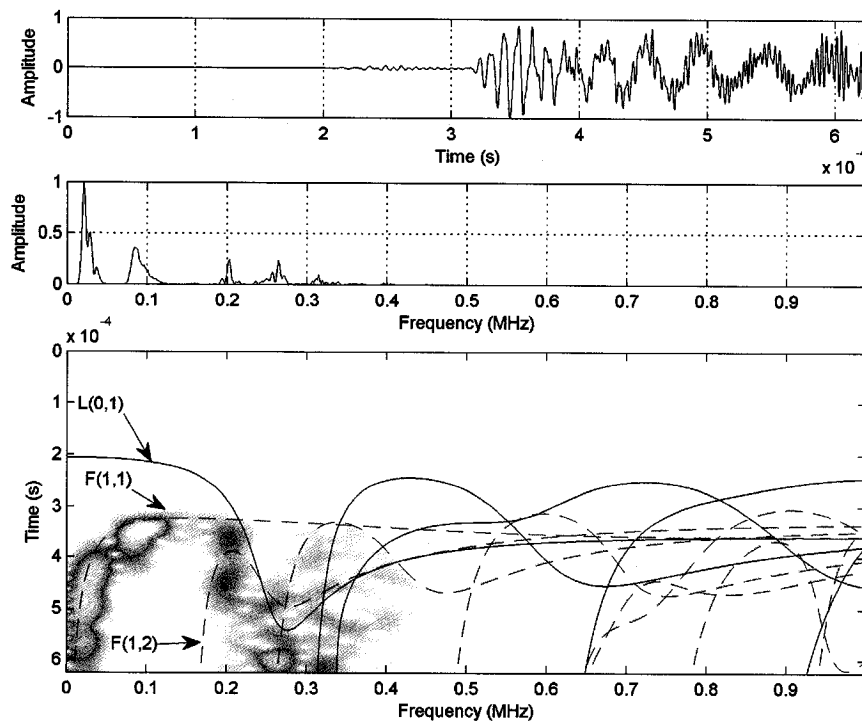
158

Figure 6.32: A 250 kHz single cycle pulse transmitted (direct arrangement) through corroded rebar (extracted from accelerated corrosion tests) in air with 9% uniform mass loss.

Figure 6.33: A 250 kHz single cycle pulse transmitted (direct arrangement) through corroded rebar (extracted from accelerated corrosion tests) in air with 14.1% uniform mass loss.
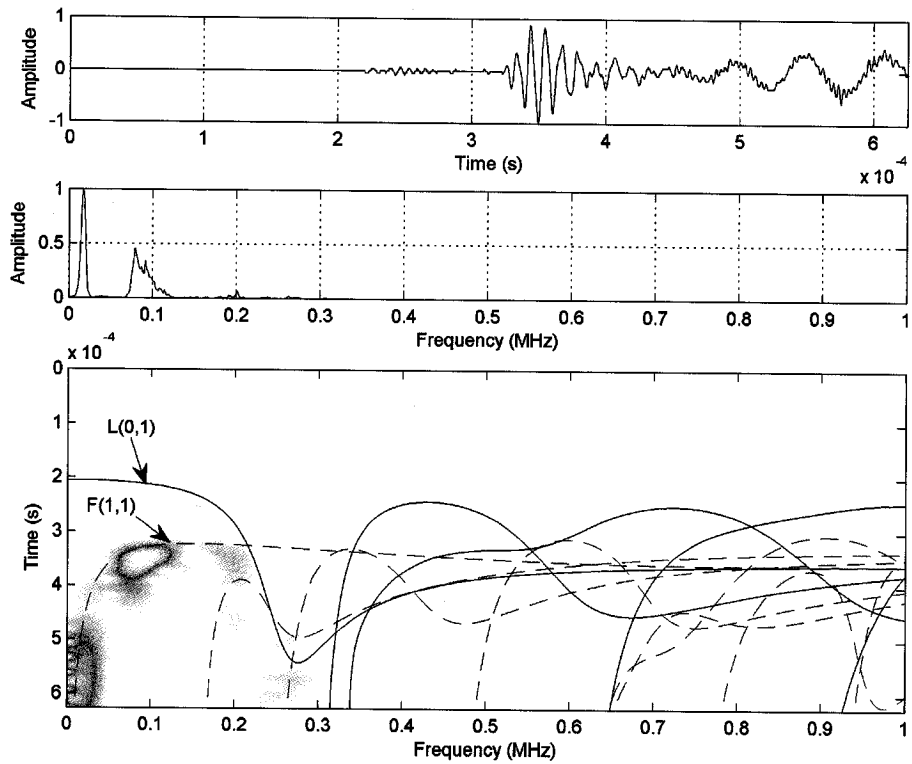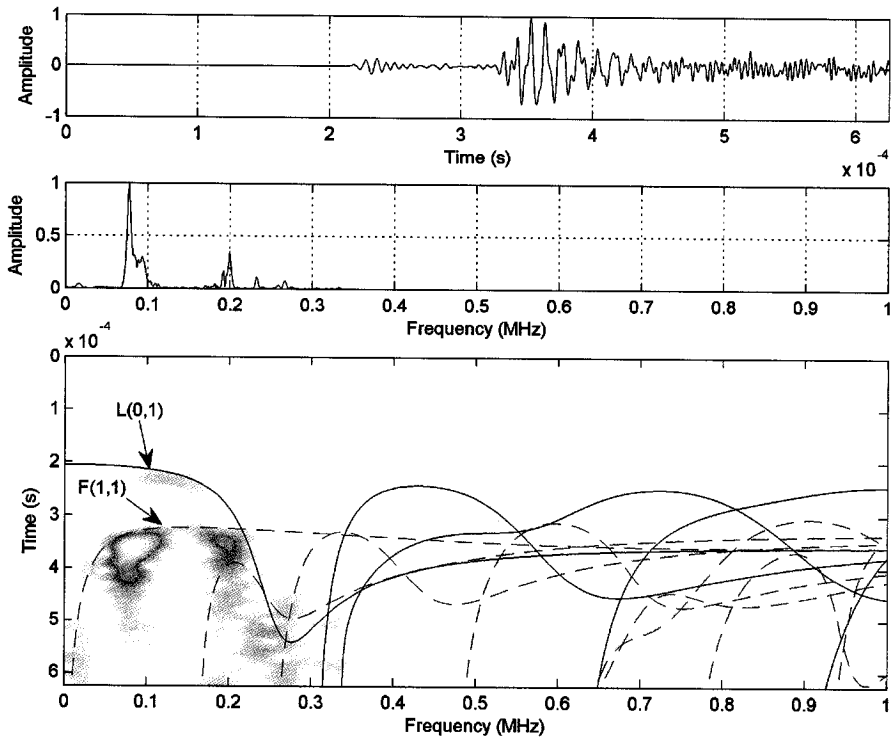
159

Figure 6.34: A 250 kHz single cycle pulse transmitted (direct arrangement) through corroded rebar (extracted from accelerated corrosion tests) in air with 13.3% uniform and localized mass loss.

The results of the low frequency indirect transducer arrangement testing are shown in Figures 6.35-6.39. The highpass and lowpass filters were set at 5 kHz and 1 MHz, respectively.

Figure 6.35: A 250 kHz single cycle pulse transmitted (indirect arrangement) through corroded rebar (extracted from accelerated corrosion tests) in air with 1.8% uniform mass loss.
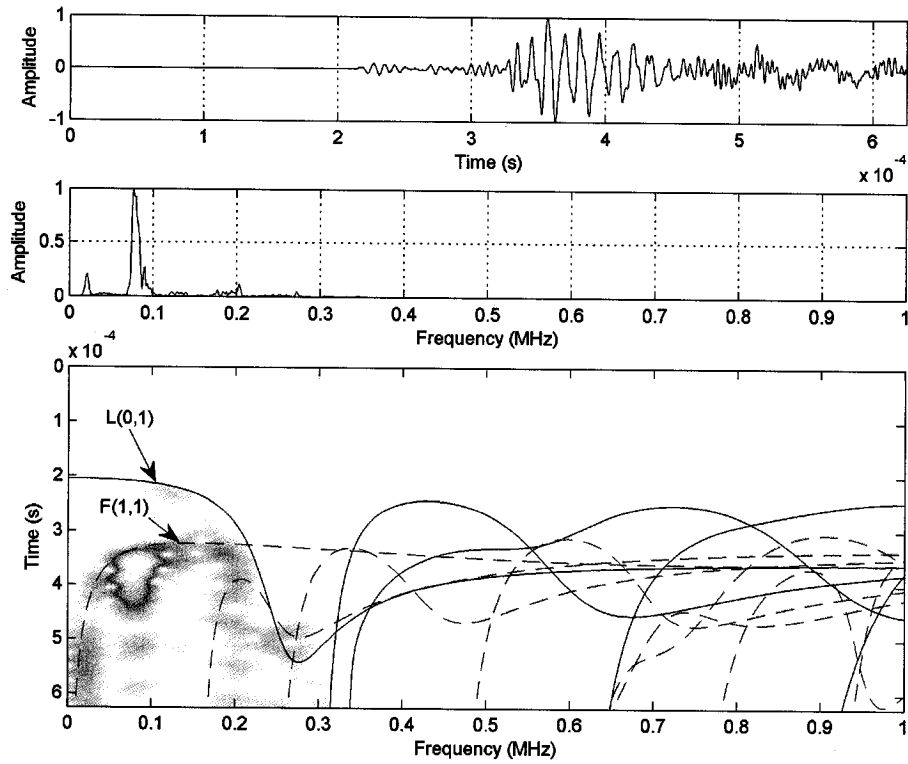
160

Figure 6.36: A 250 kHz single cycle pulse transmitted (indirect arrangement) through corroded rebar (extracted from accelerated corrosion tests) in air with 4.2% uniform mass loss.

Figure 6.37: A 250 kHz single cycle pulse transmitted (indirect arrangement) through corroded rebar (extracted from accelerated corrosion tests) in air with 9% uniform mass loss.

Figure 6.38: A 250 kHz single cycle pulse transmitted (indirect arrangement) through corroded rebar (extracted from accelerated corrosion tests) in air with 14.1% uniform mass loss.
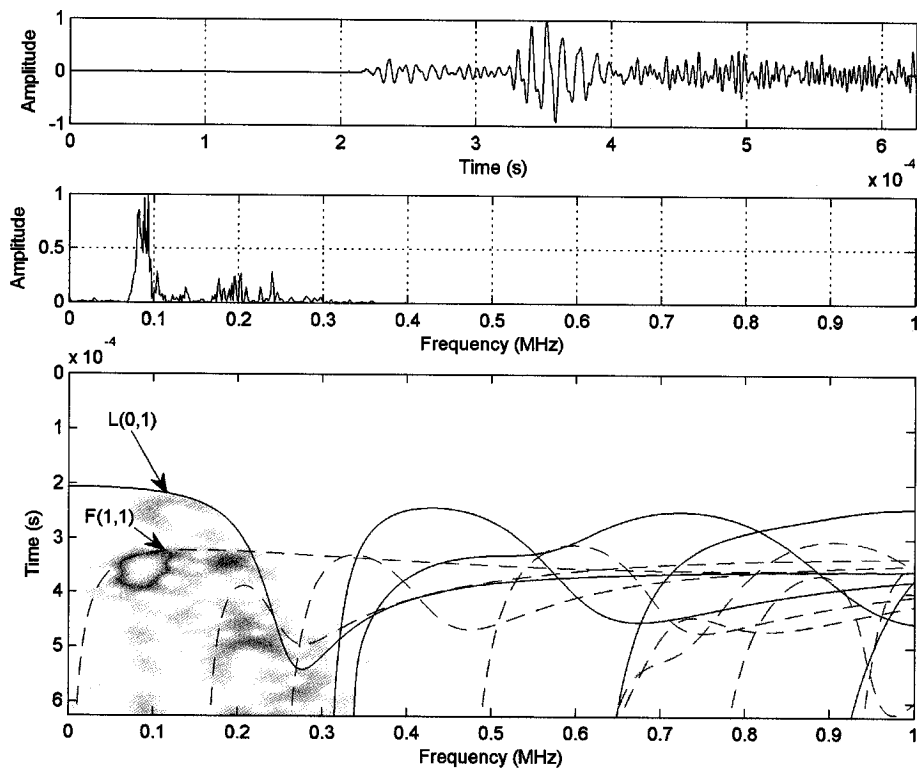

Figure 6.39: A 250 kHz single cycle pulse transmitted (indirect arrangement) through corroded rebar (extracted from accelerated corrosion tests) in air with 13.3% uniform and localized mass loss.

The F(1,1) mode had a strong response around 80 kHz for all five corroded bars. It seemed as though some of the lowest frequencies were affected as the corrosion level increased, especially for the specimen with the localized corrosion. This could be a result of having to couple the transducers separately or the lower frequencies being reflected at discontinuities in the bar profile. The higher frequency flexural waveforms appear to be scattered for all of the specimens.

High frequency guided wave testing was conducted on the same set of bars. A 5.08 MHz single cycle pulse was transmitted through each bar. The results are shown in Figures 6.40-6.44. The highpass and lowpass filters were set at 2 and 10 MHz, respectively. Notice that the lower frequencies lose strength in comparison to higher frequencies. Also notice that as the uniform corrosion level increases the response between the frequency domain peaks starts to increase in strength with respect to the peaks. These frequencies between the frequency domain peaks will be referred to as 'web' frequencies. As the corrosion level increases, the bar profile becomes increasingly non-uniform and heterogeneous. Scattering and shifts in the peak frequencies occur over the entire length of corroded bar, giving rise to the 'web' frequencies. The response was similar to the frequency domain collected for the healthy rebar with an angled rib pattern. As will be shown later, these 'web' frequencies were unique to uniform mass loss specimens (i.e. they did not occur for localized damage). The specimen tested with combined uniform and localized damage had 'web' frequencies with signal strength due to corroding uniformly prior to the localized damage.
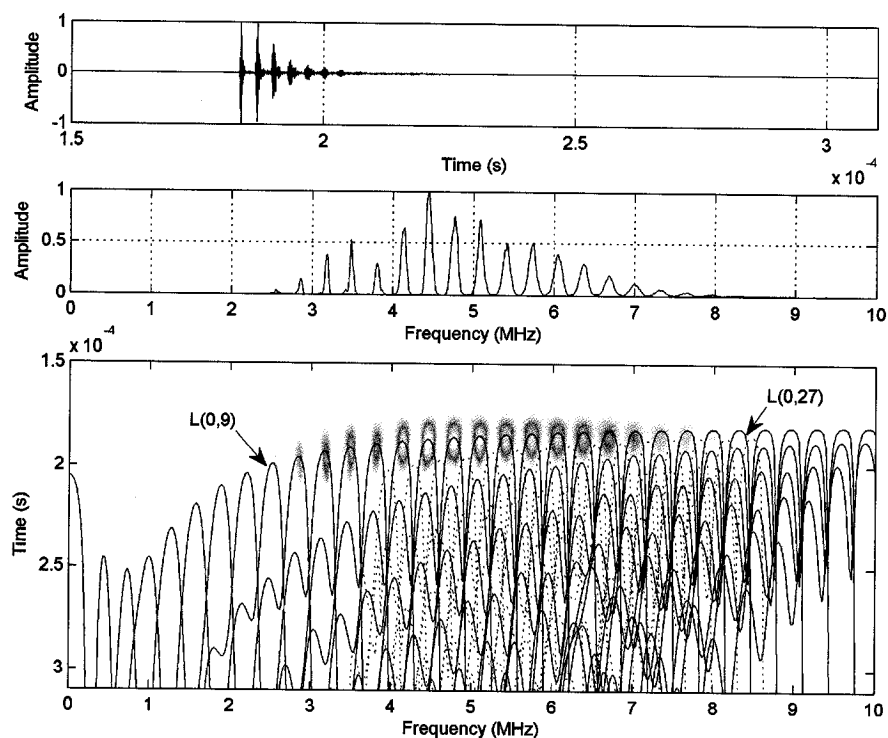
163

Figure 6.40: A 5.08 MHz single cycle pulse transmitted (direct arrangement) through corroded rebar (extracted from accelerated corrosion tests) in air with 1.8% uniform mass loss. The rebar had an orthogonal rib pattern, a 0.472" (11.99 mm) diameter, and was 42" (1.067 m) in length.
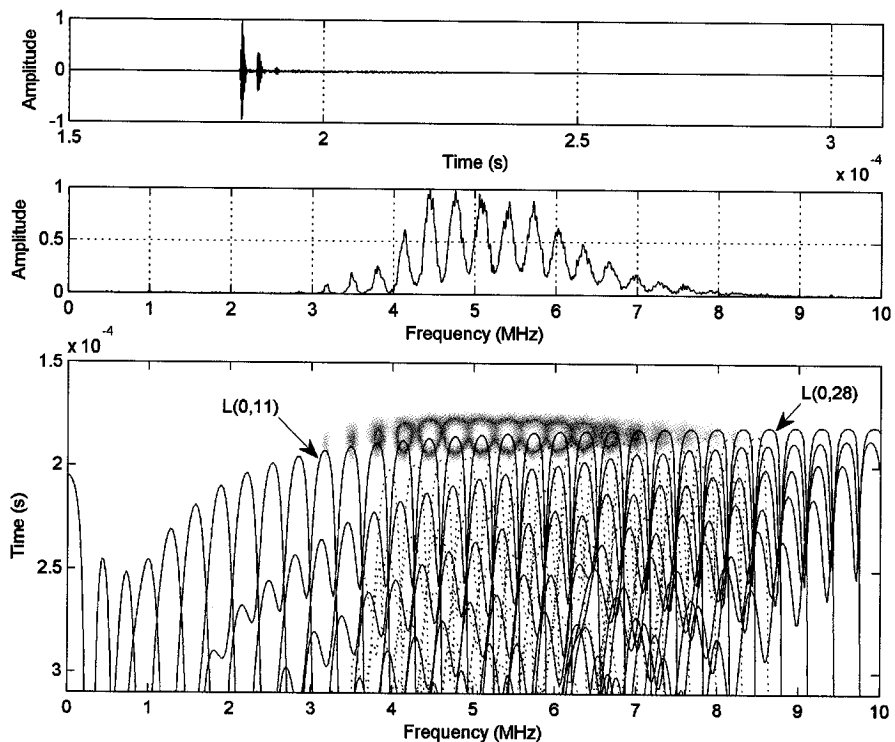

Figure 6.41: A 5.08 MHz single cycle pulse transmitted (direct arrangement) through corroded rebar (extracted from accelerated corrosion tests) in air with 4.2% uniform mass loss. The rebar had an orthogonal rib pattern, a 0.472" (11.99 mm) diameter, and was 42" (1.067 m) in length.
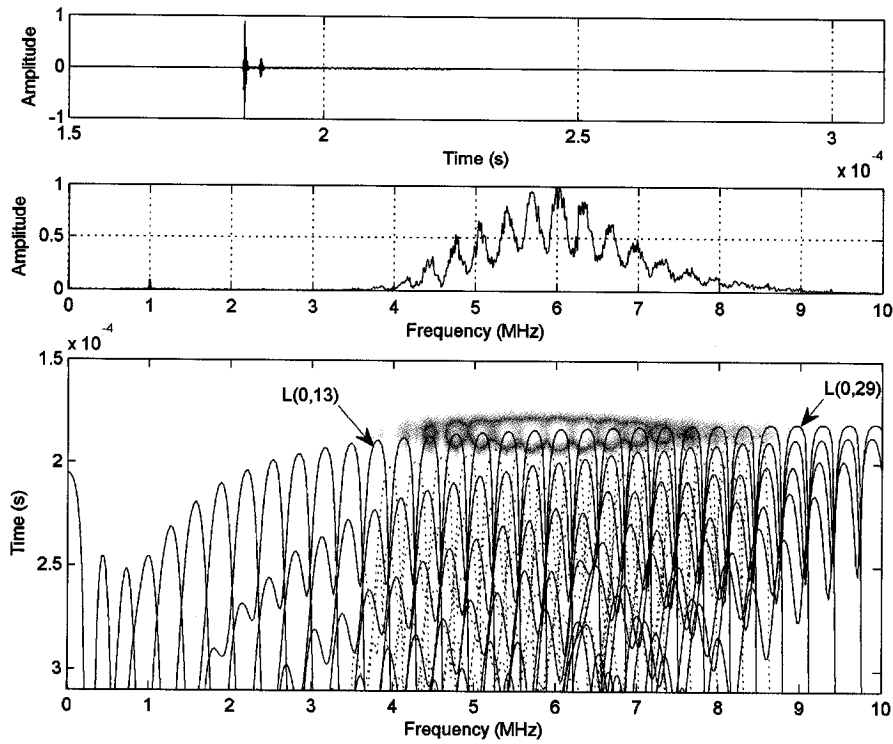
164

Figure 6.42: A 5.08 MHz single cycle pulse transmitted (direct arrangement) through corroded rebar (extracted from accelerated corrosion tests) in air with 9% uniform mass loss. The rebar had an orthogonal rib pattern, a 0.472" (11.99 mm) diameter, and was 42" (1.067 m) in length.

Figure 6.43: A 5.08 MHz single cycle pulse transmitted (direct arrangement) through corroded rebar (extracted from accelerated corrosion tests) in air with 14.1% uniform mass loss. The rebar had an orthogonal rib pattern, a 0.472" (11.99 mm) diameter, and was 42" (1.067 m) in length.
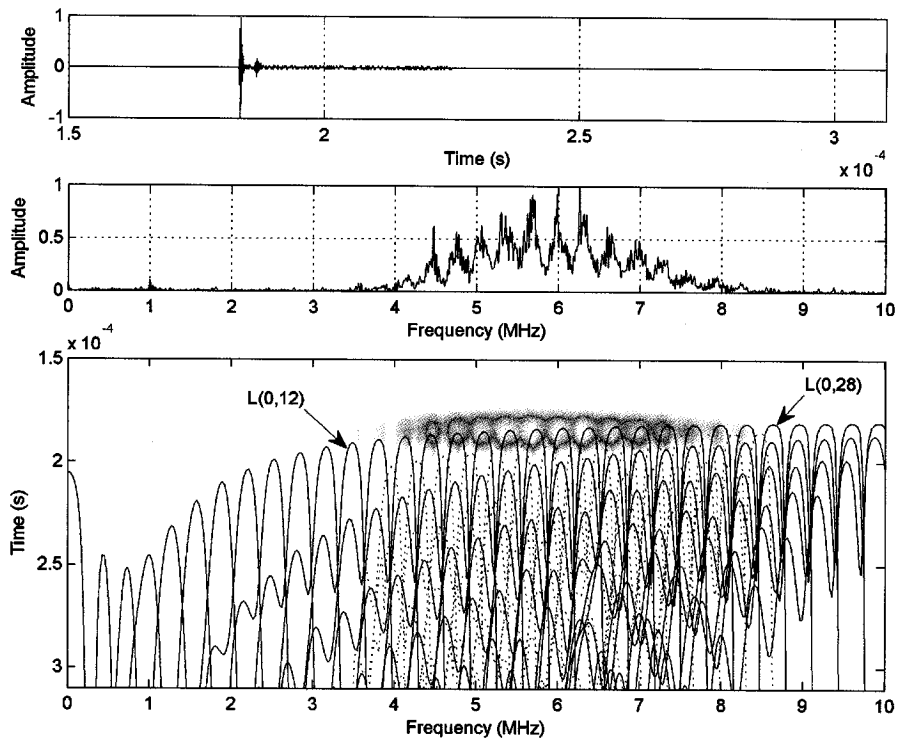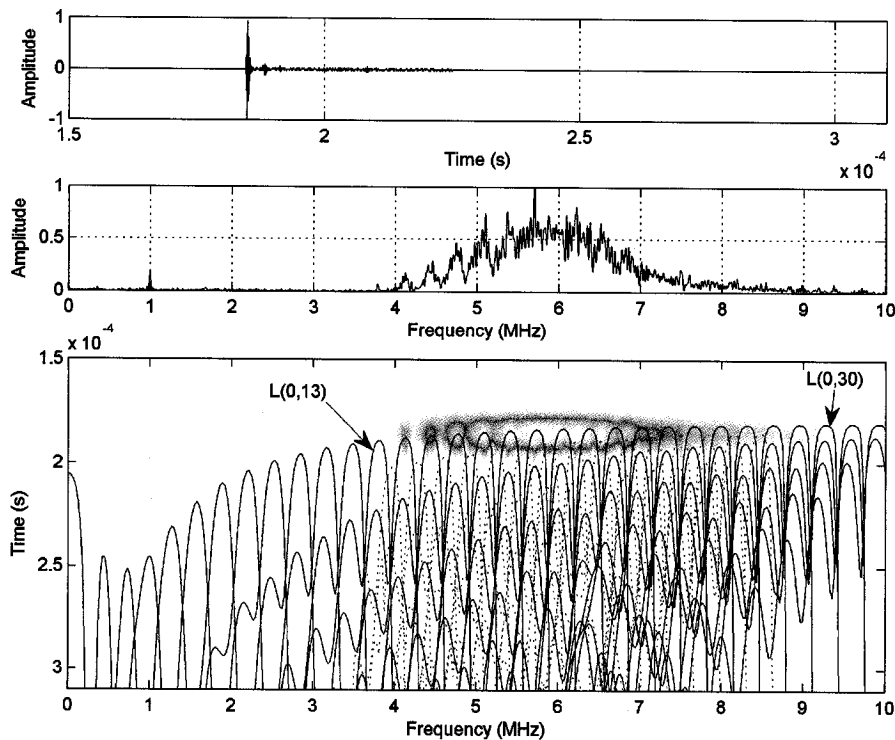
165

Figure 6.44: A 5.08 MHz single cycle pulse transmitted (direct arrangement) through corroded rebar (extracted from accelerated corrosion tests) in air with 13.3% uniform and localized mass loss. The rebar had an orthogonal rib pattern, a 0.472" (11.99 mm) diameter, and was 42" (1.067 m) in length.

6.4.2 EFFECT OF DEBONDING

To better understand the effect of bond loss between the steel and mortar on guided wave behavior, reinforced mortar specimens with simulated debonding were created. A wooden rectangular form was created with inside dimensions of 4" x 4" x 36" (10.2 cm x 10.2 cm x 91.4 cm). Holes were drilled through the form so rebar could span the longest dimension. Rebar was cut to 42" (1.067 m) in length and then centered through the holes. To simulate debonding between the rebar and mortar from uniform corrosion, duct tape was wrapped around the rebar to prevent bond (such as in [123]). Twelve specimens were created with varying amounts of debonding over 36" (91.4 cm) of embedded rebar. The amount of tape started at 3" (7.62 cm, 8.33% debonding), with 3" (7.62 cm) increments up to 36" (91.44 cm, 100% debonding). The tape started at one end of the exposed rebar/mortar interface (same side as sending transducer) and was continuous for the specified length. The rebar extended 3" (76.2 mm) from the inside edge of the formwork on each end to allow for transducer coupling. Mortar batches were mixed, placed, and then consolidated in the formwork around the rebar. Specimens were air cured for 28 days prior to form removal. Figure 6.45 provides an illustration of two simulated defect specimens with varying tape lengths.
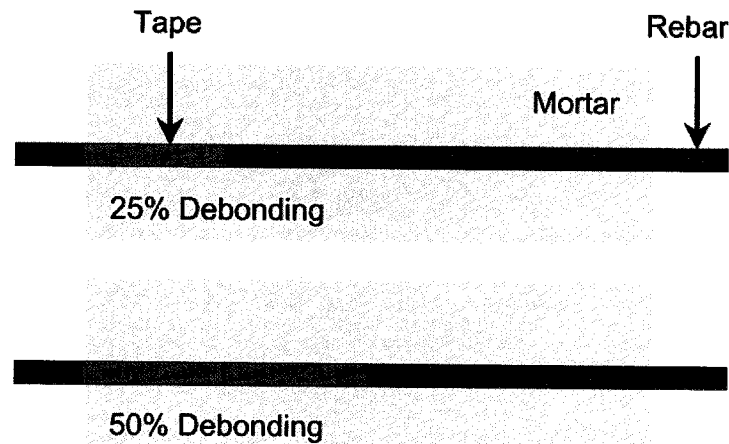
Figure 6.45: Example of simulated tape specimens showing 25% and 50% debonding.

Low frequency testing was first conducted on the simulated debonding specimens using a 125 kHz single cycle pulse transmitted in a direct transducer arrangement. The highpass and lowpass filters were set at 5 kHz and 1 MHz, respectively. Only the test results from the 0%, 25%, 50%, 75%, and 100% debond specimens are shown in Figures 6.46-6.50, respectively. Shown in each Figure is the captured time domain, the frequency domain, and a spectrogram. Also shown are modes of longitudinal (solid line) and flexural (dashed line) propagation that are possible within the frequency range of arriving waveforms. There are three scenarios of possible mode propagation plotted: a steel bar in air (s/a), a steel bar in an infinite surrounding of mortar (s/m), and a steel bar in a cylindrical mortar layer 1.76" (4.48 cm) within in an infinite surrounding of air (s/m/a). While the mortar surrounding the rebar is actually rectangular in shape, a cylindrical shape was assumed based on the capabilities of the theoretical model.

For the specimens in the 0-25% debond range, the signal-to-noise ratio was rather poor and the spectrograms reveal little information about the particular modes of propagation. The spectrogram for the 0-25% debond specimens indicate that the $L(0,1)$ mode has a very weak response. The mode is most likely completely leaking out of the bar. Since the wavelength is rather large compared to the specimen geometry, wave energy may be leaking out, reflecting off of specimen boundaries and entering back into the bar at later arrival times severely scattered. There could also be modes invoked for the bar/mortar/air system. For the specimens at or above 25% debonding, there are modes arriving close to the theoretically predicted $L(0,1)$ mode for a bar in air. The 75-100% debond specimens follow the predicted curve for the $L(0,1)$ mode for the case of a bar in air. Multiple reflections of the $L(0,1)$ mode are visible at later arrival times in the 100% debond spectrogram.

167

Figure 6.46: A 125 kHz single cycle pulse transmitted (direct arrangement) through rebar (orthogonal ribs) in a 0% debond specimen. The gain was set at 50 dB.

Figure 6.47: A 125 kHz single cycle pulse transmitted (direct arrangement) through rebar (orthogonal ribs) in a 25% debond specimen. The gain was set at 50 dB.

168

Figure 6.48: A 125 kHz single cycle pulse transmitted (direct arrangement) through rebar (orthogonal ribs) in a 50% debond specimen. The gain was set at 40 dB.

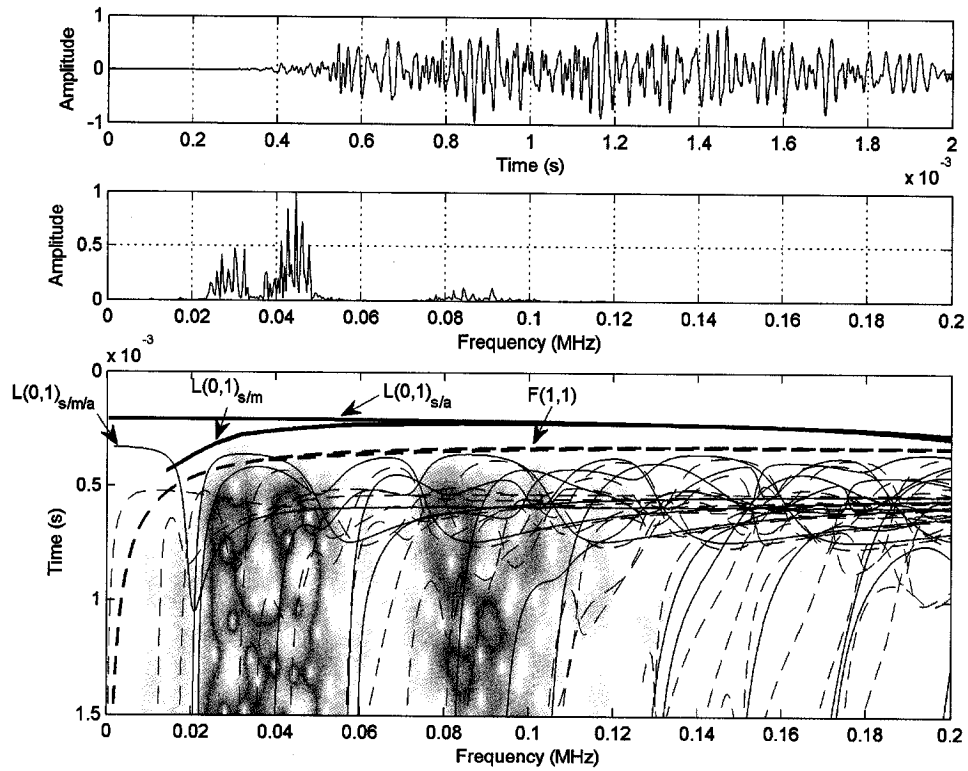**Figure 6.49:** A 125 kHz single cycle pulse transmitted (direct arrangement) through rebar (orthogonal ribs) in a 75% debond specimen. The gain was set at 30 dB.
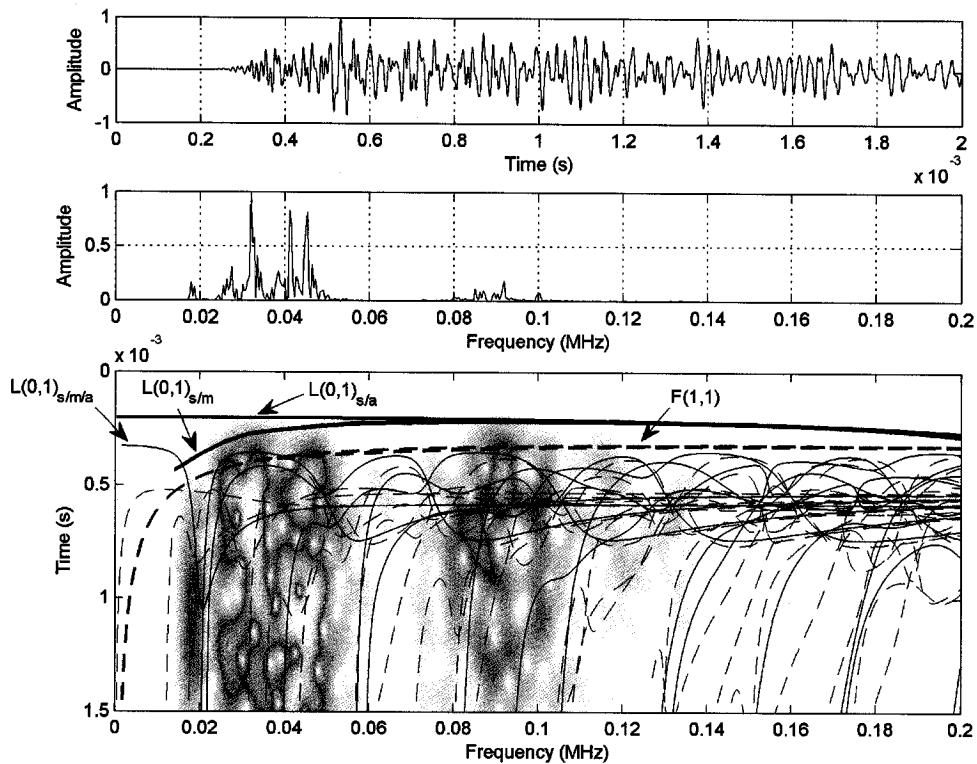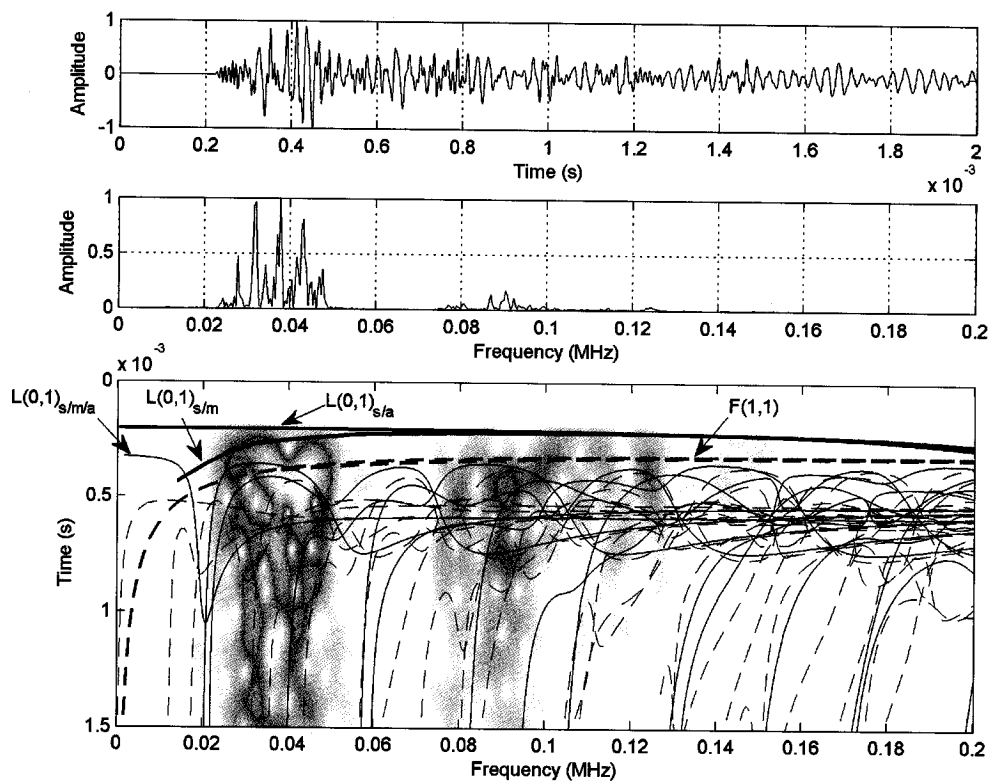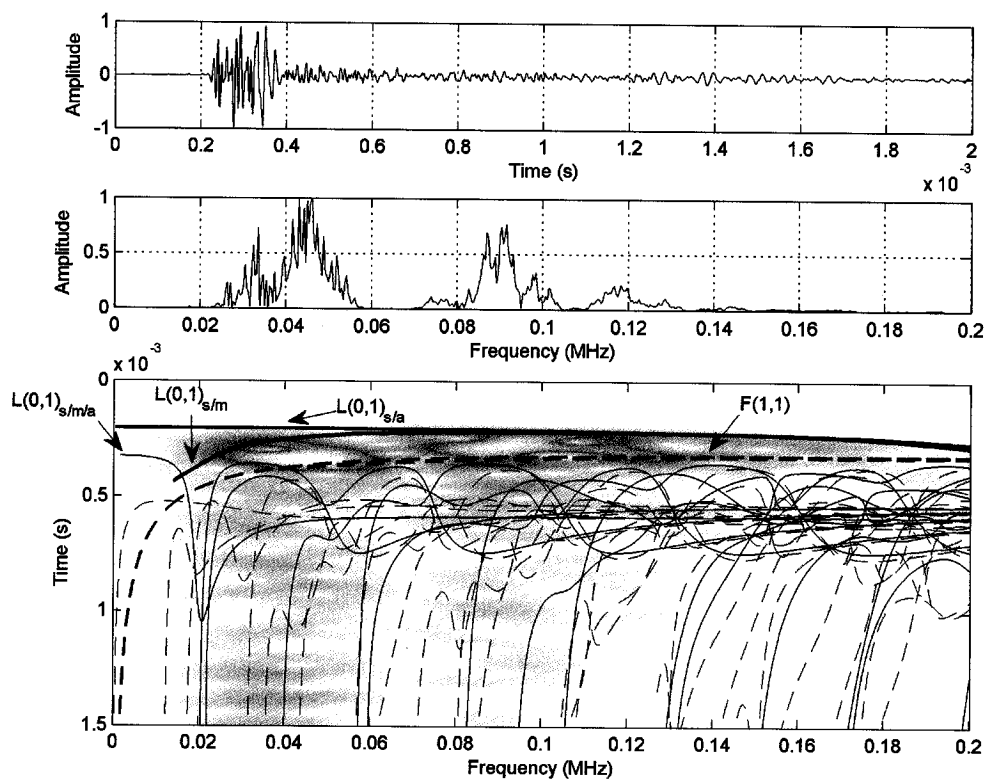
169

Figure 6.50: A 125 kHz single cycle pulse transmitted (direct arrangement) through rebar (orthogonal ribs) in a 100% debond specimen. The gain was set at 20 dB.

In an attempt to compensate for the low signal-to-noise ratio from the single cycle pulse testing, tonebursts were used. A 110 kHz nine-cycle toneburst was transmitted and received. The highpass and lowpass filters were set at 105 kHz and 115 kHz, respectively. The time domain results for the 25%, 50%, 75%, and 100% debond specimens are shown in Figure 6.51. The arrival times of the L(0,1) and F(1,1) modes for a bar in air are shown as the left (red) and right (blue) vertical lines, respectively. As the level of bond decreases between the steel and mortar, the wave behavior approaches the theoretically predicted behavior for the L(0,1) mode in a bar. The signal strength increases as the level of bond decreases. Although the transducers were coupled separately to each individual specimen, the increase in the signal strength was quite evident.

170

Figure 6.51: A 110 kHz nine-cycle pulse transmitted (direct arrangement) through rebar (orthogonal ribs) in a 25%, 50%, 75%, and 100% debond specimen. The theoretical arrival times for the L(0,1) and F(1,1) modes are shown as vertical lines on the left and right, respectively. The signal strengths have been adjusted with respect to the 100% debond specimen gain level.

A 160 kHz fifteen-cycle toneburst was also used on the simulated debonding specimens for reasons that will be illustrated later when accelerated corrosion experiments are presented. Figures 6.52-6.56 show the results of testing conducted on 0%, 25%, 50%, 75%, and 100% debond specimens, respectively. The highpass and lowpass filters were set at 155 and 165 kHz, respectively. The solid and dashed lines are longitudinal and flexural modes, respectively.
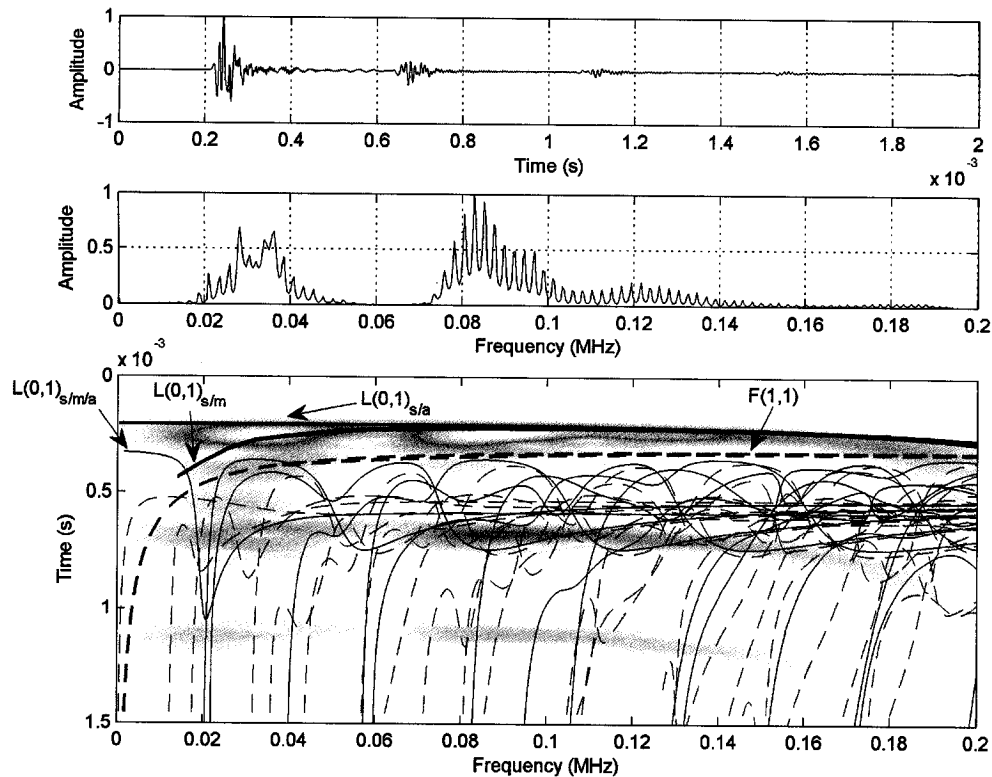
171

Figure 6.52: A 160 kHz fifteen-cycle pulse transmitted (direct arrangement) through rebar (orthogonal ribs) in a 0% debond specimen. The gain was set at 70 dB.
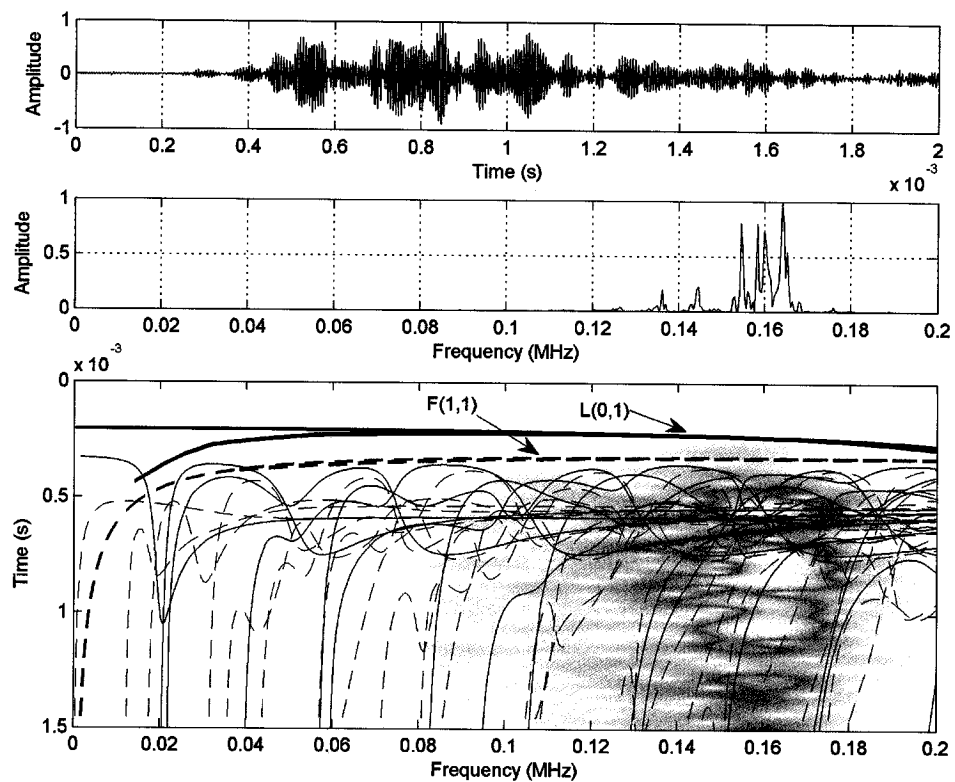
Figure 6.53: A 160 kHz fifteen-cycle pulse transmitted (direct arrangement) through rebar (orthogonal ribs) in a 25% debond specimen. The gain was set at 70 dB.
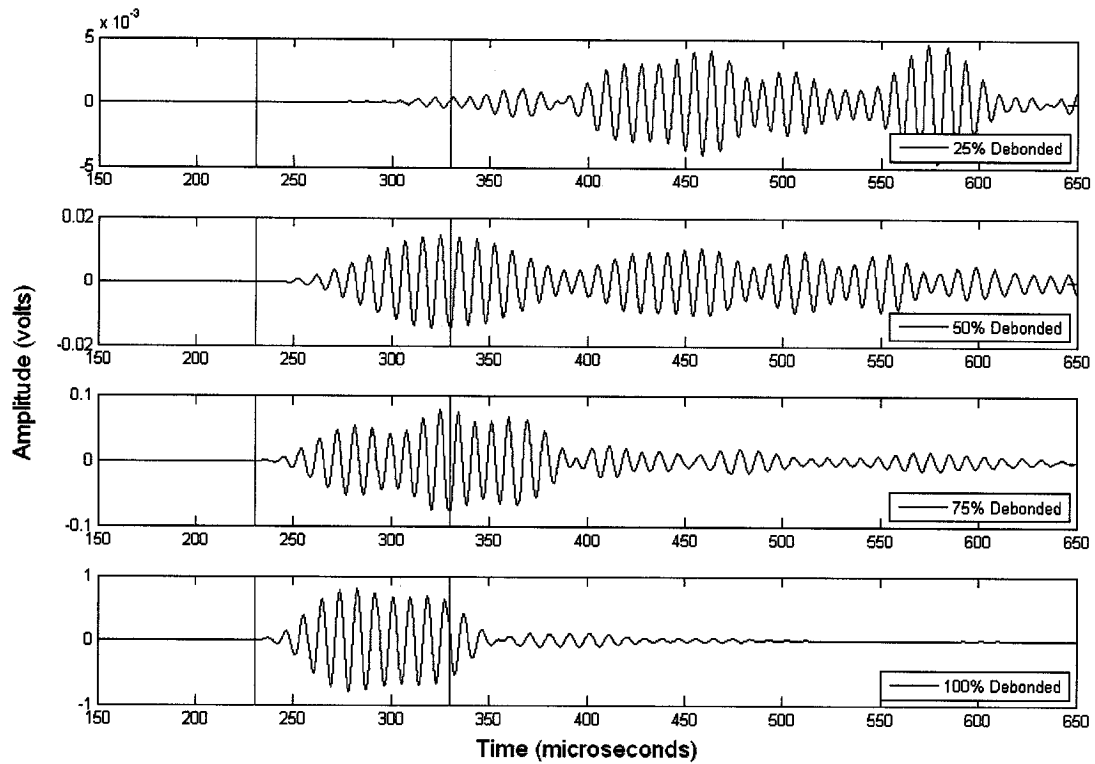
172

Figure 6.54: A 160 kHz fifteen-cycle pulse transmitted (direct arrangement) through rebar (orthogonal ribs) in a 50% debond specimen. The gain was set at 50 dB.

Figure 6.55: A 160 kHz fifteen-cycle pulse transmitted (direct arrangement) through rebar (orthogonal ribs) in a 75% debond specimen. The gain was set at 30 dB.
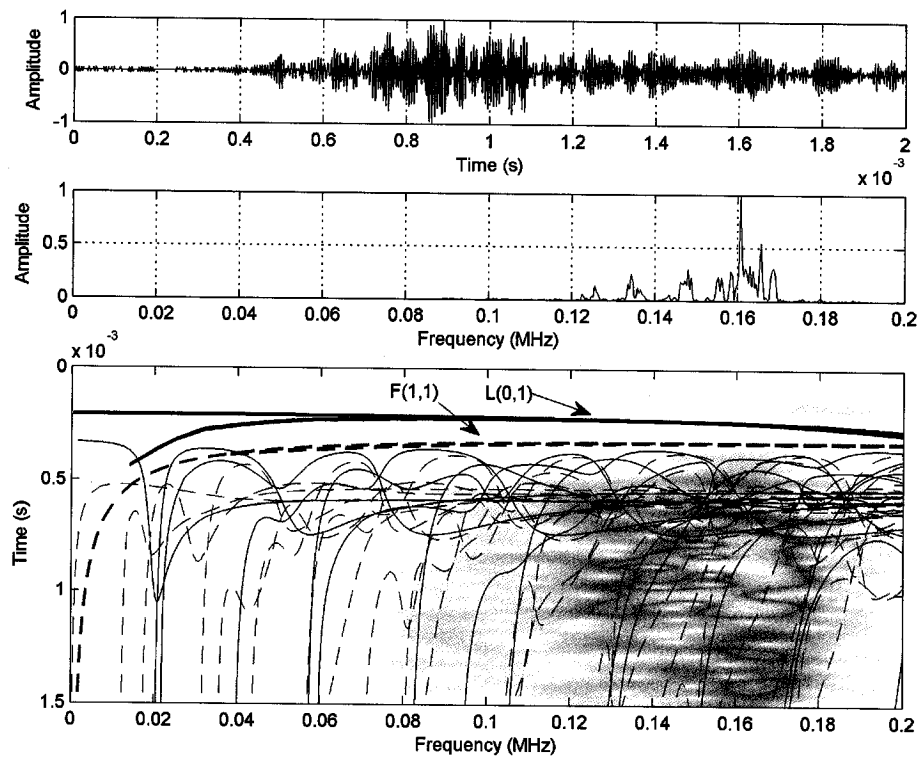
173

Figure 6.56: A 160 kHz fifteen-cycle pulse transmitted (direct arrangement) through rebar (orthogonal ribs) in a 100% debond specimen. The gain was set at 20 dB.
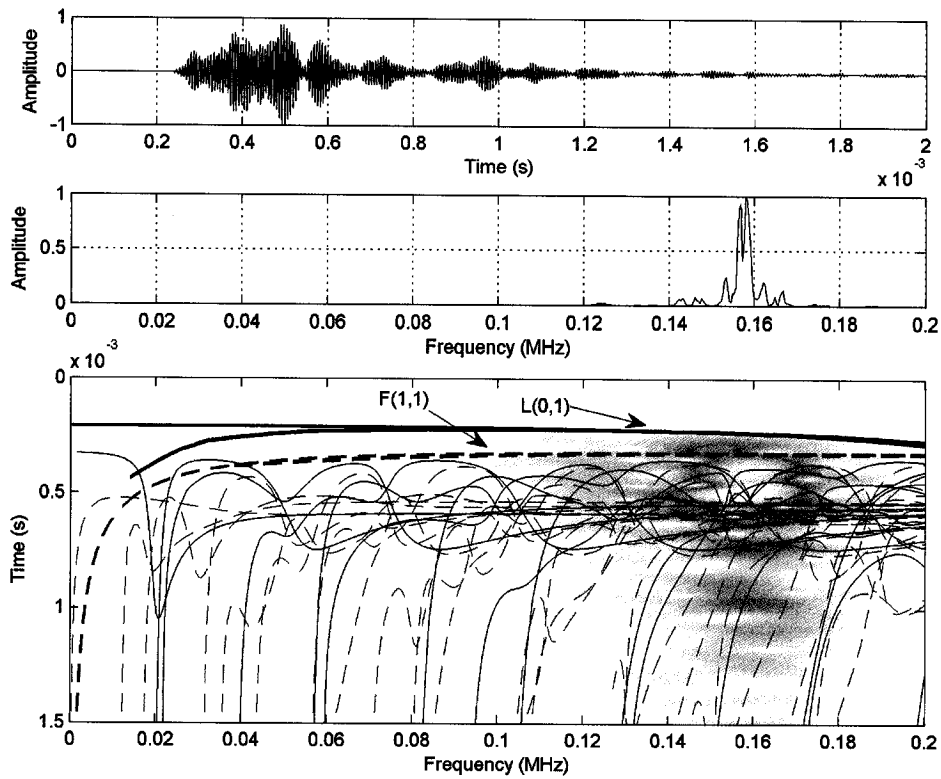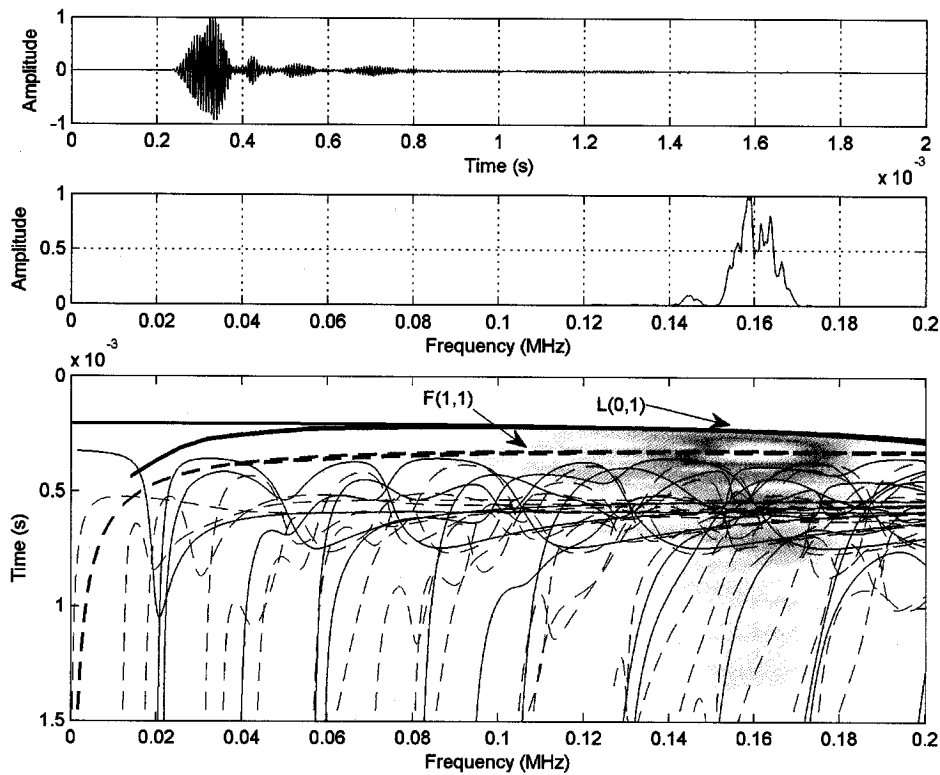
Once again, as the amount of debonding increases the early arriving content increases. It seems that test distances over 27" (0.686 m) did not allow for clear reception of the L(0,1) mode. The signal strength was very low for the 0% specimen, resulting in a poor signal-to-noise ratio. The spectrogram for the 0% debond specimen yielded little information about the invoked modes. Again, the L(0,1) mode is most likely completely leaking out into the surrounding mortar. Some wave energy is being reflected back into the bar by either reflections from the outer mortar/air boundary or from scattering occurring in mortar. The 25% debond specimen has wave energy received from the L(0,1) mode based on the spectrogram. However, most of the wave energy arrives much later. At 50% debond, more wave energy arrives earlier, with a much stronger L(0,1) signal strength. The 75% and 100% debond specimens have signals that behave as predicted for the L(0,1) mode for a bar in air.

In each previous test, quantitative signal strength comparisons were unable to be calculated due to the transducer being coupled to each specimen separately. This coupling will present large amounts of error when comparing between specimens. Therefore, a toneburst test was completed to try and provide a quantitative measure at different frequencies. A frequency sweep was conducted on the debond specimens from 50 kHz to 200 kHz in 3 kHz increments using a direct transducer arrangement. Each frequency was invoked using a 15-cycle toneburst. The highpass and lowpass filters were set at -/+ 5 kHz

174

of the invoked frequency, respectively. The summation of calculated energy for each frequency between 50 and 150 kHz was divided by the summation of energy between 150 and 200 kHz, with the results shown in Figure 6.57 on a decibel scale. Energy is calculated with the following equation:

$$E_t = \int_{t_0}^{t_1} V^2(t)dt \quad \dotfill \quad (6.2)$$

where t is the time, t_0 is the start of the partition, t_1 is the end of the partition, and V(t) is the voltage as a function of time.

There is very little discrepancy between the experimental data points and the linear trendline for simulated debonding below 60%. However, above 60% simulated debonding there is some discrepancy between the data points and the linear trendline. This is thought to occur because the dominant received mode above 60% simulated debonding is the L(0,1) mode (refer to Figures 6.55 and 6.56). However, below 60% simulated debonding the F(1,1) mode and other later arriving waveforms are dominant. The L(0,1) mode does not appear with substantial strength in the time domain until 40% simulated debonding. Under the geometry and frequency range chosen for these specimens, the F(1,1) mode and other later arriving waveforms tracked small length bond changes while the appearance of the L(0,1) mode tracked more severe lengths of bond changes between the rebar mortar interface.
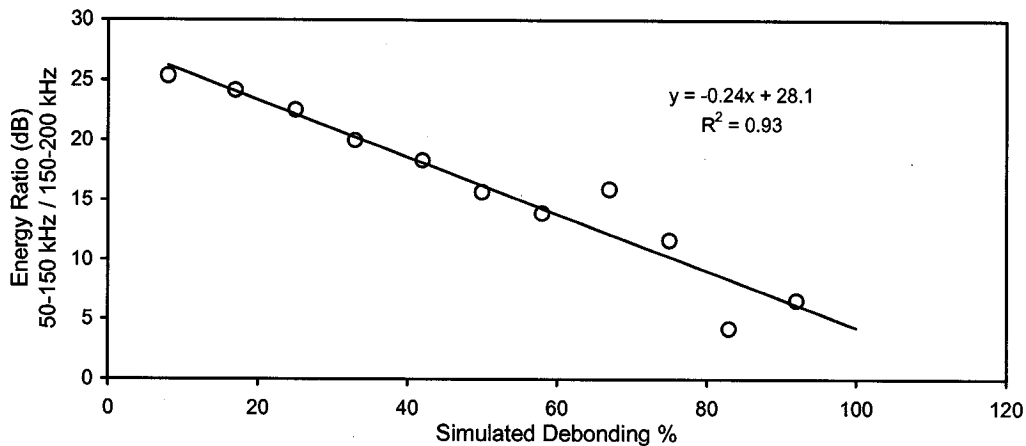
Figure 6.57: Comparison of frequencies between 50-150 kHz and 150-200 kHz captured during a frequency sweep.

An indirect transducer arrangement was used to invoke the F(1,1) mode for evaluation of the simulated debond specimens. An 80 kHz fifteen-cycle pulse was transmitted with the results shown in Figure 6.58-6.62. The highpass and lowpass filters were set at 75 and 85 kHz, respectively. The solid and dashed lines are longitudinal and flexural modes, respectively.
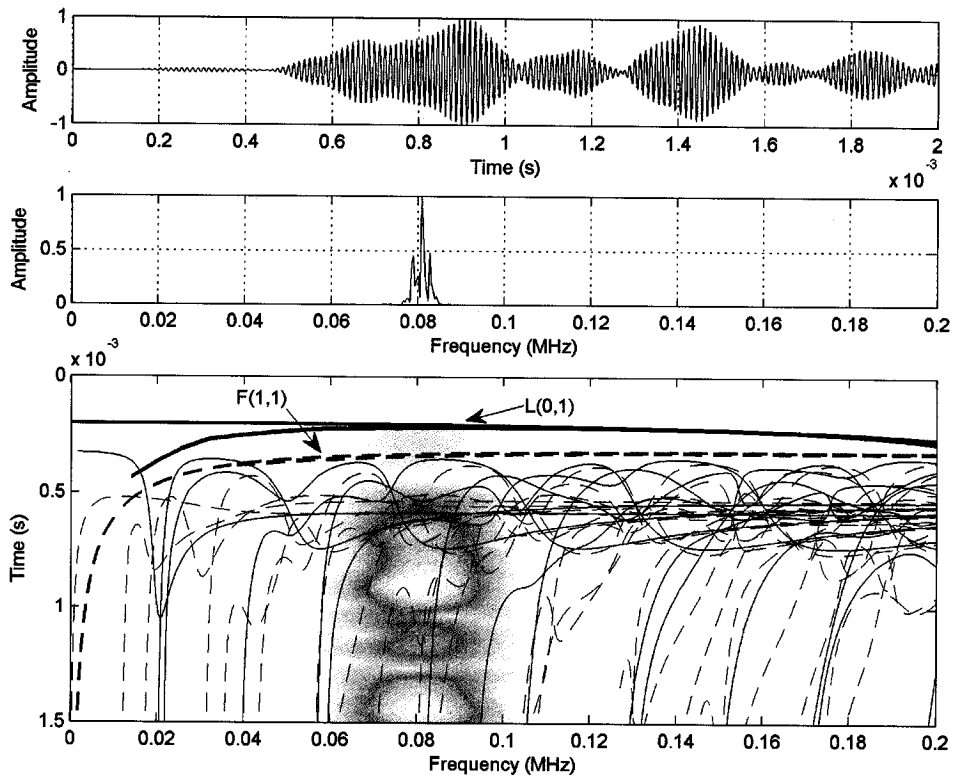
Figure 6.58: An 80 kHz fifteen-cycle pulse transmitted (indirect arrangement) through rebar (orthogonal ribs) in a 0% debond specimen. The gain was set at 60 dB.
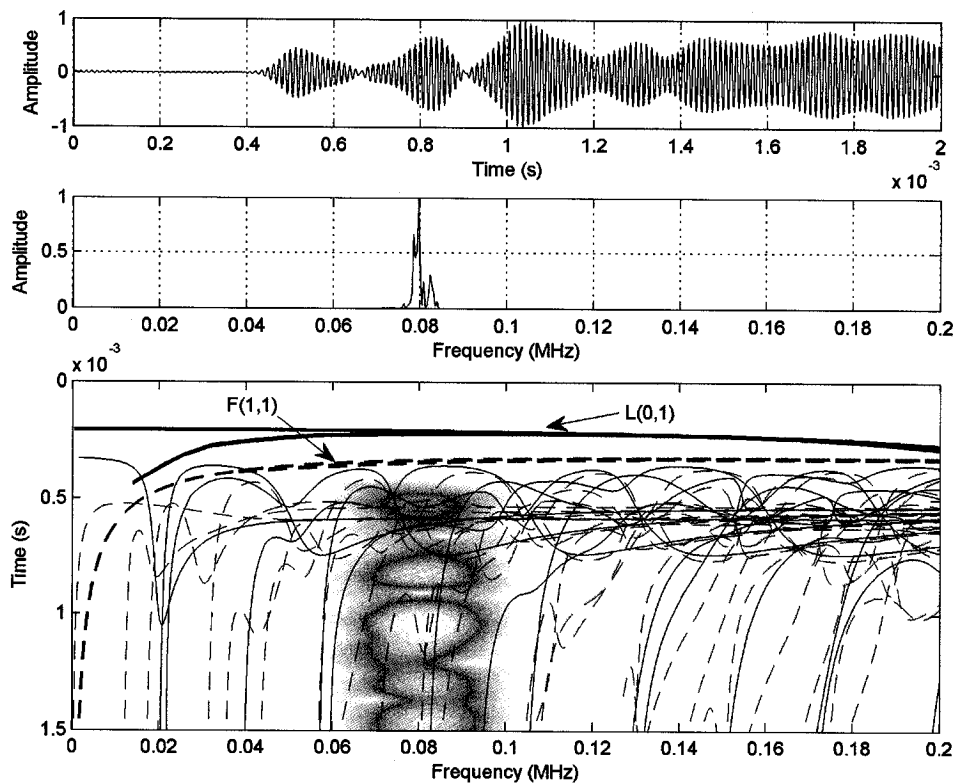
Figure 6.59: An 80 kHz fifteen-cycle pulse transmitted (indirect arrangement) through rebar (orthogonal ribs) in a 25% debond specimen. The gain was set at 60 dB.
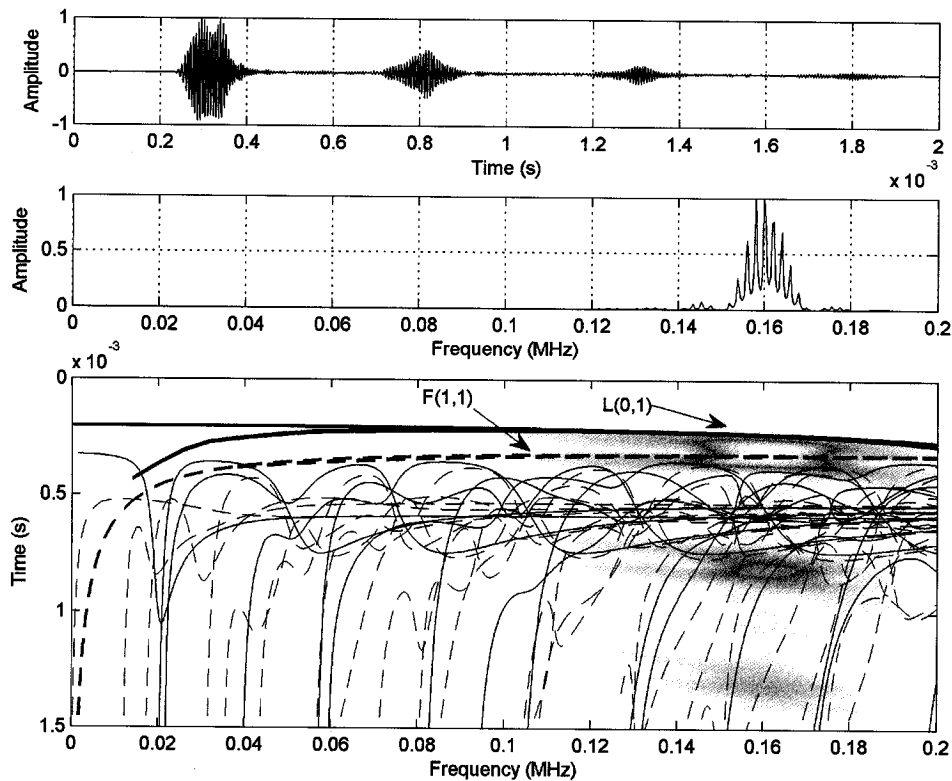
176
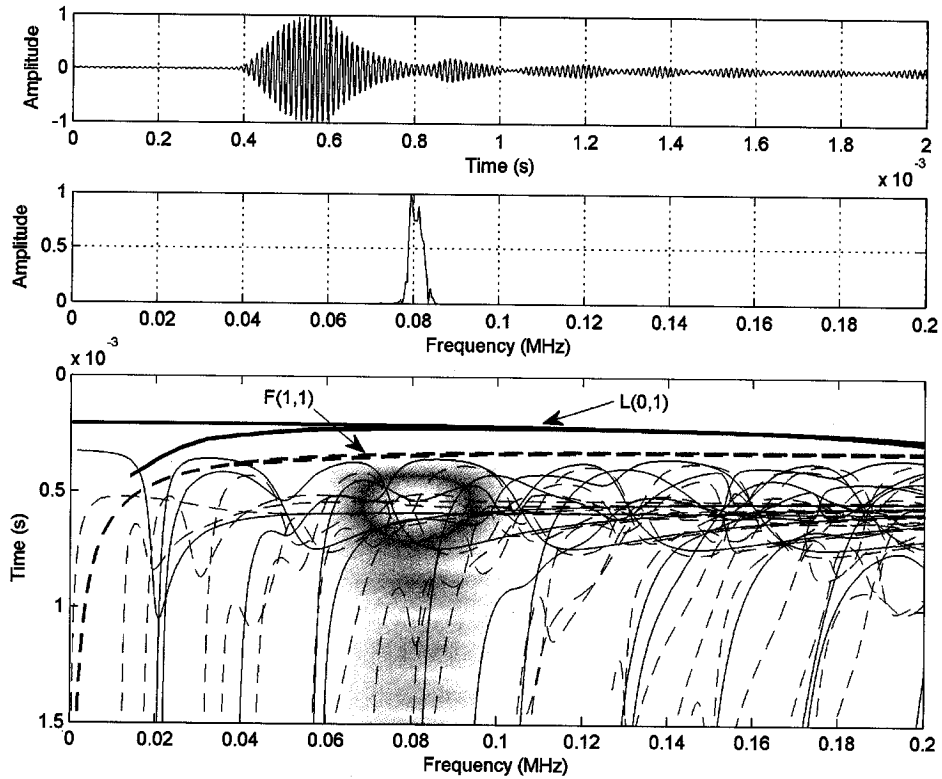
Figure 6.60: An 80 kHz fifteen-cycle pulse transmitted (indirect arrangement) through rebar (orthogonal ribs) in a 50% debond specimen. The gain was set at 40 dB.
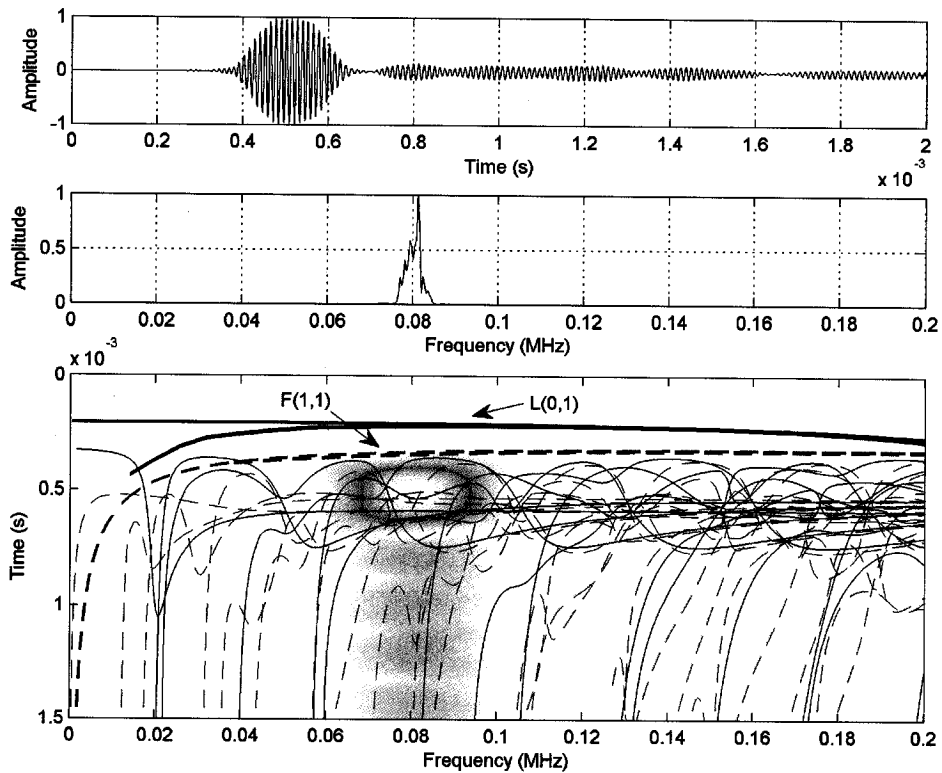
Figure 6.61: An 80 kHz fifteen-cycle pulse transmitted (indirect arrangement) through rebar (orthogonal ribs) in a 75% debond specimen. The gain was set at 30 dB.

177
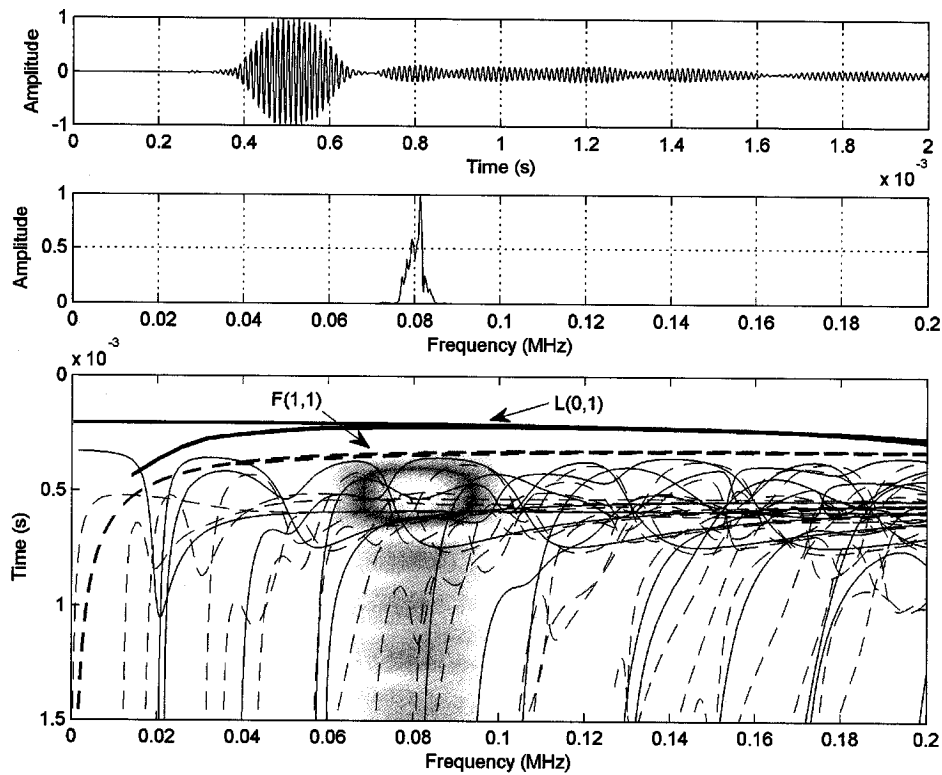
Figure 6.62: An 80 kHz fifteen-cycle pulse transmitted (indirect arrangement) through rebar (orthogonal ribs) in a 100% debond specimen. The gain was set at 30 dB.

For the 0% debond specimen, the majority of the signal strength arrives after the theoretically predicted arrival time of the F(1,1) mode. However, there appears to be some energy that arrives for the L(0,1) mode. As the level of bond diminishes, the arrival time of the mode converges on the F(1,1) arrival time for a bar in air. It seems that the F(1,1) mode for a bar in mortar propagates at a slightly slower velocity than predicted. While quantitative measurements were unable to be calculated due to the separate transducer coupling, notice the gain level differences for the change in bond level. Clearly the signal strength increases as the level of bond decreases.

Mid-range frequencies (1 – 2 MHz) were then invoked in the debond specimens. This is similar to the work done by [115]. Unlike the low frequencies, the mid-range frequencies were much closer to the theoretically predicted behavior. Two longitudinal modes were invoked using 100-cycle tonebursts: the L(0,5) and L(0,8) (refer to Figure 4.5). The Digital Wave transducers (model B-1025) were used, with strong responses found at 1.18 MHz and 2.18 MHz for the respective modes. The highpass and lowpass filters were set at 800 kHz and 2.5 MHz, respectively. The two modes were compared directly for each specimen with respect to their peak amplitudes and area in the frequency domain to give an indication of attenuation. The comparison was made to avoid error associated with transducer coupling. The results of the testing are shown in Figure 6.63.
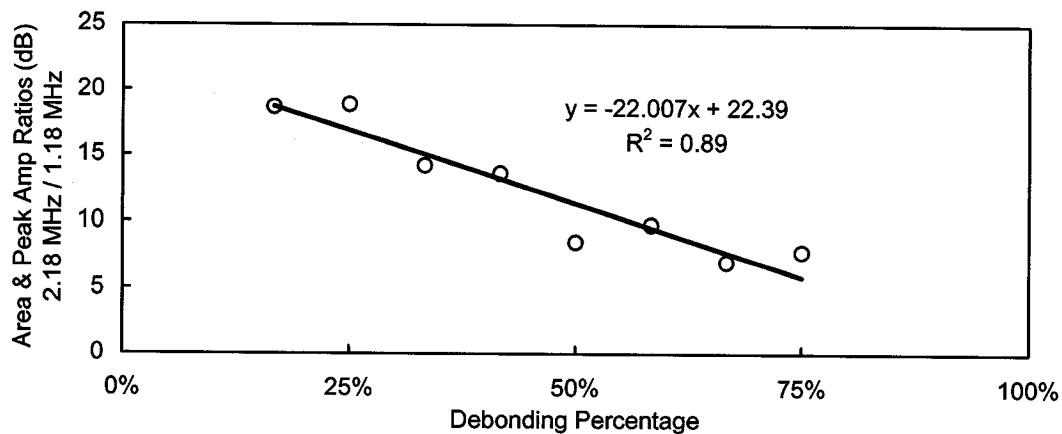
Figure 6.63: Comparison of the peak amplitude and area in the frequency domain for the L(0,5) and L(0,8) modes. The modes were invoked using a 100-cycle toneburst at 1.18 MHz and 2.18 MHz, respectively.

The L(0,5) mode is more attenuated than the L(0,8) by the surrounding mortar (as shown in Chapter 4). As debonding increases, the difference in attenuation decreases. These modes would be more useful for testing interfacial conditions if they were not so sensitive to water and the effects of the rib pattern.

Higher frequency (2 – 8 MHz) testing was conducted on the debond specimens as well. The wave behavior was very similar to the theoretically predicted behavior. The L(0,9) mode was invoked using a 100-cycle toneburst at two separate frequencies where attenuation dips occur: 2.82 MHz and 6.95 MHz. The highpass and lowpass filters were set at 2 MHz and 10 MHz, respectively. The two modes were compared with respect to their peak amplitudes and area in the frequency domain to give an indication of attenuation. The two frequencies were compared to avoid errors associated with transducer coupling. The results of the testing are shown in Figure 6.64. Since the effect of bond loss is less substantial as the frequency is increased, transducer coupling becomes more critical. The test does indicate a trend similar to what was shown with the mid-range frequencies. However, as will be shown later, the change in the bar surface profile is more of an issue with higher frequency testing than the loss of bond due to the displacement structure of the propagating modes.

179
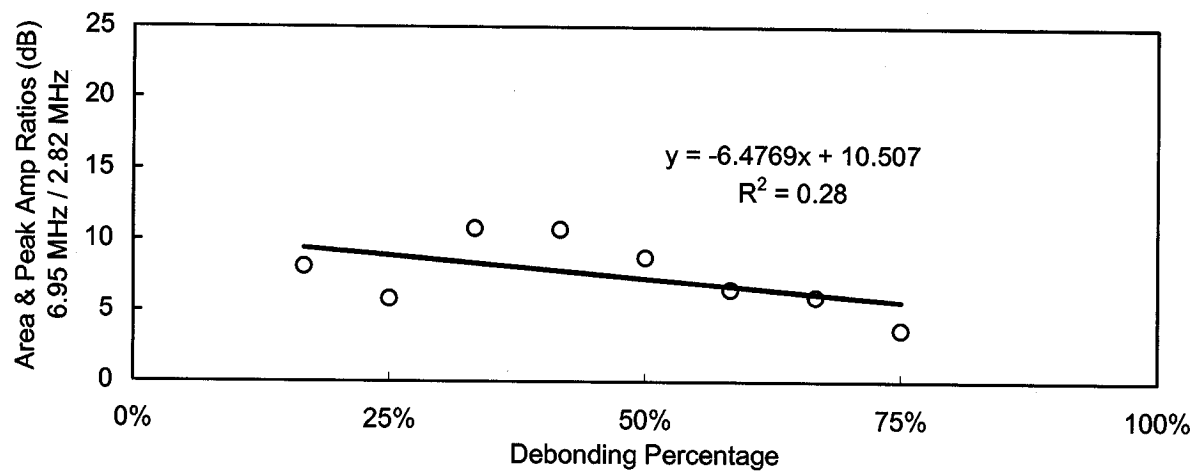
Figure 6.64: Comparison of the peak amplitude and area in the frequency domain for the L(0,9) mode at 2.82 MHz and 6.95 MHz. The modes were invoked using a 100-cycle toneburst.

6.4.3 EFFECT OF LOCALIZED DISCONTINUITIES

Only high frequency testing was investigated with respect to localized corrosion. This frequency range was chosen to start with since the attenuation was the lowest in the rebar/mortar system. First, a 0.472" (11.99 mm) diameter reinforcing bar (orthogonal ribs) 30.38" (77.15 cm) in length was monitored with guided waves while a grinding saw cut through the diameter in one location. The thickness of the grinding saw blade was 0.25" (6.35 mm), with the cut made directly in the center of the rebar. The specimen was monitored in through-transmission mode. A 5.08 MHz single cycle pulse was transmitted. The highpass and lowpass filters were set at 2 and 10 MHz, respectively. Figures 6.65 and 6.66 show the results with the vertical axis scaled for each signal and held constant, respectively. The y-axis label refers to the amplitude of the normalized power spectrum.

180
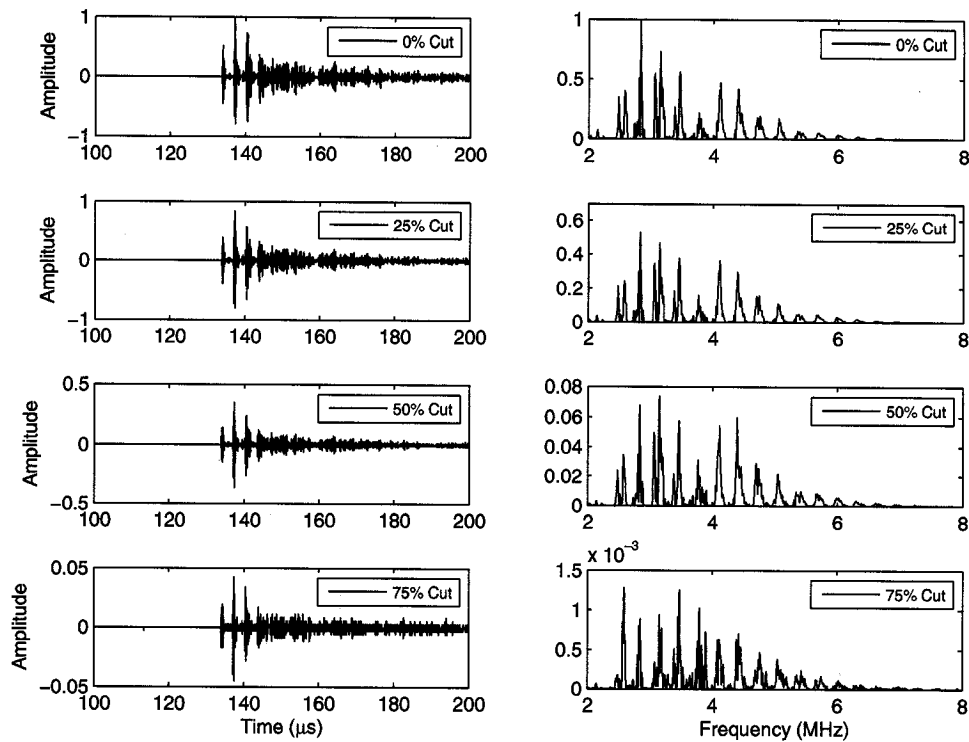
Figure 6.65: A 5.08 MHz single cycle pulse monitoring a bar undergoing a saw cut in a direct transducer arrangement (through-transmission). Signal strengths were adjusted to compensate for the difference in gain levels.
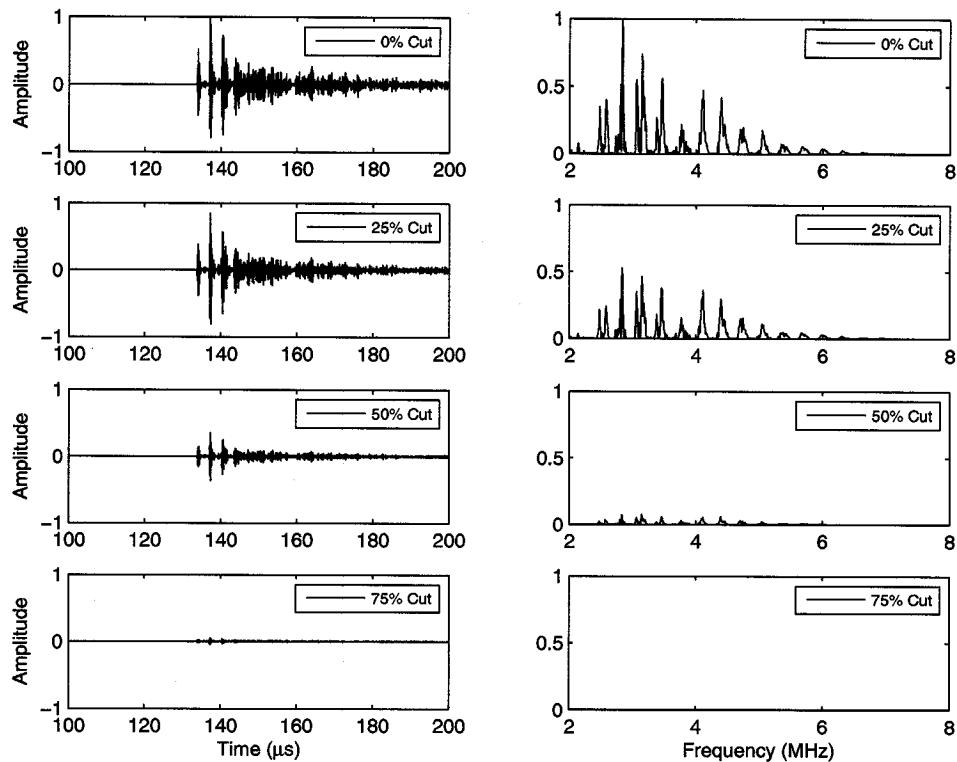
Figure 6.66: A 5.08 MHz single cycle pulse monitoring a bar undergoing a saw cut in a direct transducer arrangement (through-transmission). The y-axis scale is the same for all signals.

181

The results indicate that all of the frequencies are attenuated from the discontinuity. The overall shape of the frequency domain remains relatively the same during testing. Notice that the 'web' frequencies, discussed earlier from the uniformly corroded bar testing and the rebar with an angled rib pattern, do not appear in the frequency domain for any level of localized damage. The attenuation is caused by reflections from the discontinuity. While the localized damage may cause some scattering, it is relatively small in comparison to that caused by uniform damage along the entire length. Also, the base diameter of the rebar only changes at the discontinuity (only ¼" thick), meaning that the location of the attenuation dips should not shift in the frequency domain.

To investigate the feasibility of monitoring discontinuities from pitting corrosion in rebar embedded in mortar, three types of simulated pitting corrosion specimens were created and tested with guided waves. The first specimen was a gap specimen, simulating a complete loss of cross-sectional area over 1" (2.54 cm) of the rebar length. The rebar was simply cut in half, with the weight of the rebar supported by strings. The second specimen was a thin notch specimen, simulating a loss of half the rebar cross-sectional area over a very narrow width. A chop saw was used to create the discontinuity in the small notch specimen. The third specimen was a narrowed specimen, simulating partial loss of cross-sectional area over 2" (5.08 cm) of length. A grinding saw was used to create the discontinuity in the narrowed specimen. Figure 6.67 shows pictures of all three specimens. Notice that both the gap and small notch specimen have cuts that are perpendicular to the axis of the specimen, while the narrowed specimen does not.
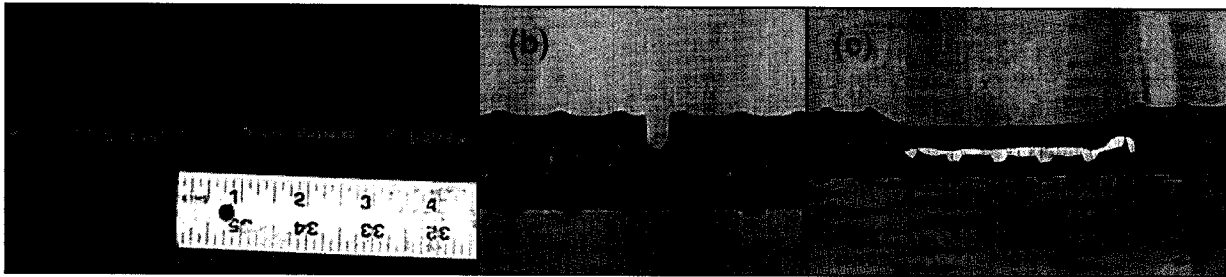
Figure 6.67: Photographs of the **(a)** 1" (2.54 cm) gap specimen, **(b)** small notch specimen, and **(c)** 2" (5.08 cm) notch specimen. The gap is filled with mortar in the 1" (2.54 cm) gap specimen. The small notch is cut through half of the cross-section.

A 5.08 MHz single cycle pulse was transmitted in each specimen and collected in through-transmission and pulse-echo mode. The results of the testing are shown in Figure 6.68. The highpass and lowpass filters were set at 2 and 10 MHz, respectively.

182
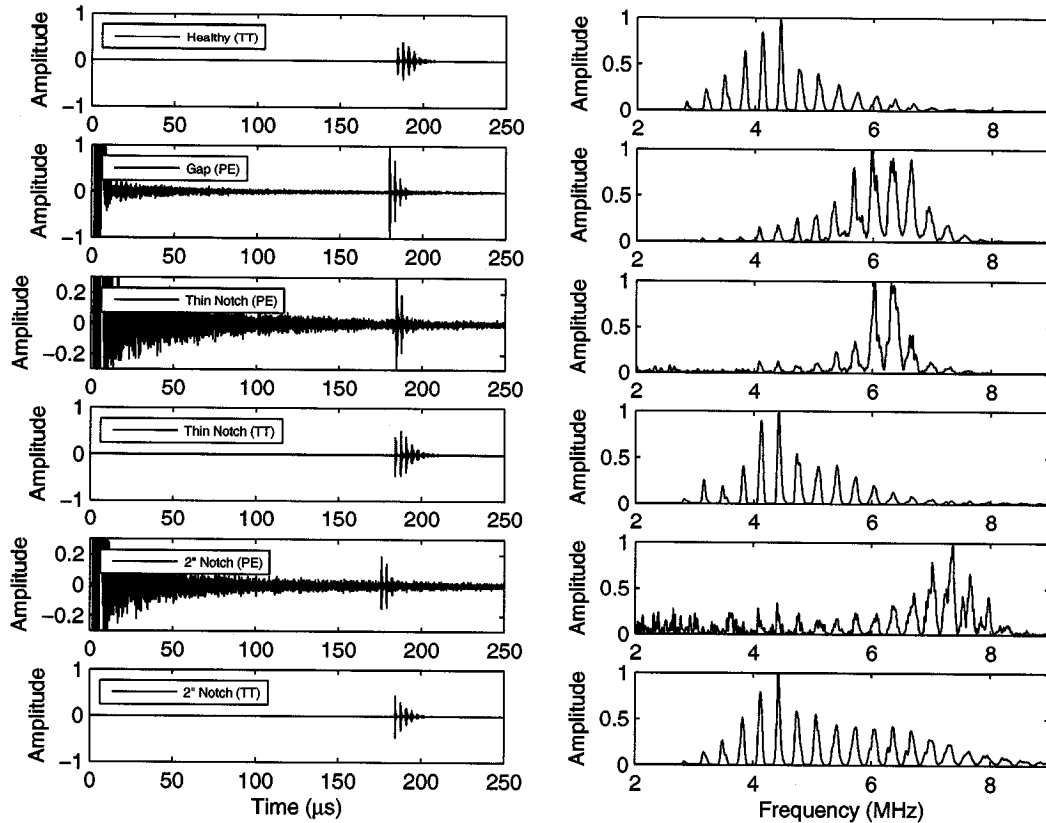
Figure 6.68: Collected time and frequency domains for a healthy specimen, a 1" (2.54 cm) gap specimen in pulse-echo mode, a thin notch specimen in pulse-echo mode, a thin notch specimen in through-transmission mode, a 2" (5.08 cm) notch specimen in pulse-echo mode, and a 2" (5.08 cm) notch specimen tested in through-transmission mode using a 5.08 MHz single cycle pulse.

The through-transmission testing revealed frequency domains similar to what was shown with the saw cut specimen discussed in this section. There are no 'web' frequencies visible, with relatively the same shape for the healthy, thin notch, and 2" notch specimens. The pulse-echo testing was capable of detecting reflections from all three forms of simulated pits. The strongest reflection was from the discontinuity going through the entire cross-section (i.e. gap specimen). The frequency response from the reflections seems shifted heavily towards higher frequencies.

6.5   MODE SENSITIVITY TO ACCELERATED CORROSION

To measure how corrosion affects guided wave behavior, reinforced mortar specimens were designed for use in an accelerated corrosion experiment. The size of the specimens are identical to the size of the simulated debond specimens. A wooden rectangular form was created with inside dimensions of 4" x 4" x 36" (10.2 cm x 10.2 cm x 91.4 cm). Holes were drilled through the form so rebar could span the longest dimension. Rebar was cut, weighed, and then centered through the holes. The rebar extended 3" (76 mm) from the inside edge of the formwork on each end to allow for transducer coupling. Mortar batches

183

were mixed, placed, and then consolidated in the formwork around the rebar. Specimens were air cured for 28 days prior to form removal.

To corrode specimens, an accelerated corrosion test setup was designed. The experimental setup for accelerated corrosion testing, commonly referred to as impressed current or anodic polarization, is shown in Figure 6.69 for both uniform and localized corrosion.
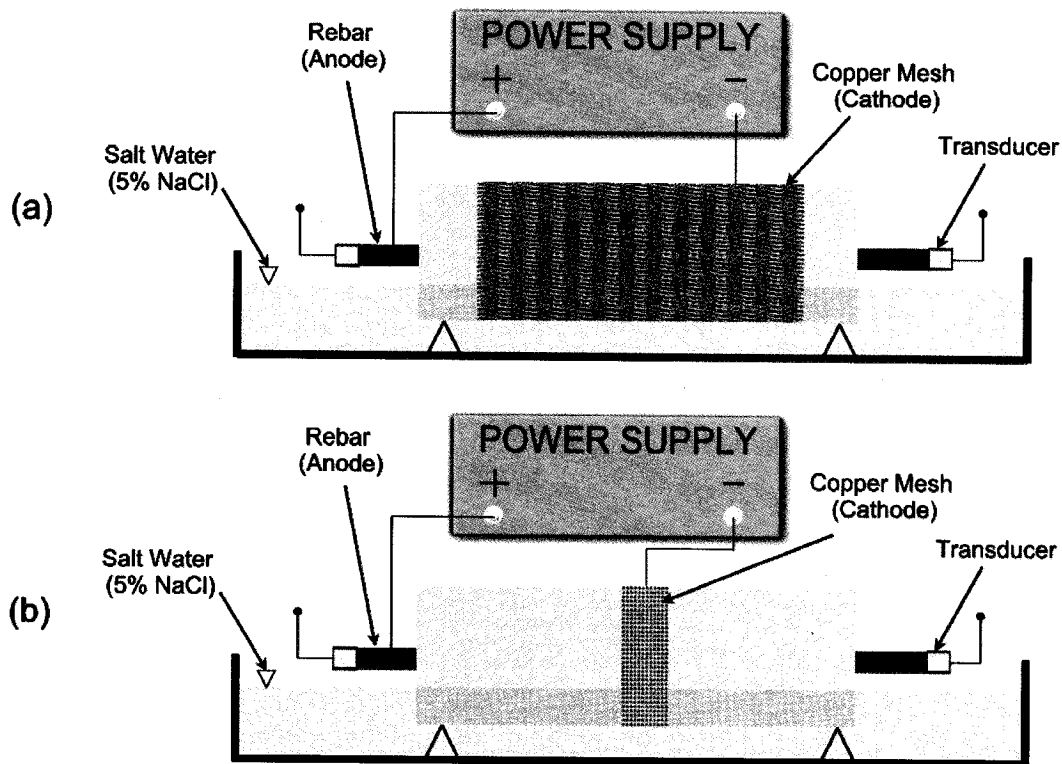
Figure 6.69: Schematic diagram of ultrasonic through-transmission for the accelerated (a) uniform corrosion and (b) localized corrosion experiment.

While others have used slight variations [2,57], the basic premise is to partially submerge the reinforced mortar specimens in a bath of salt water (5% NaCl), as shown in Figure 6.69(a). This allows oxygen, water, and chlorides to reach the rebar. For a faster corrosion rate, the positive lead was attached to the rebar (anode) to attract the negatively charged chlorides. The negative lead was attached to the surrounding copper mesh (cathode) to complete the circuit. To induce a more uniform corrosion around the circumference of the bar, a thin cloth was wrapped around the center of the specimens, while a pump poured salt water onto the top of the specimens. Each specimen had silicone sealant place on the ends to prevent accentuated corrosion at the rebar entry point and to create either uniform or localized corrosion. The type of corrosion (i.e. uniform or localized) determined the length of silicone sealant, copper mesh, and cloth used on the specimen. The middle 30" (76.2 cm) of the uniform corrosion specimens were left entirely exposed, with the rest of the specimen coated with a silicone sealant. The entire localized

184

corrosion specimen was coated with a silicone sealant, except over 3" (7.62 cm) directly in the middle. The copper mesh (cathode) and cloth were wrapped around the length of the specimen where silicone sealant was not applied.

To allow for estimation of the corrosion level during an accelerated test, an empirical study was conducted. Several mortar specimens were corroded to different corrosion levels based on Faraday's law (refer to Chapter 2). A constant potential (i.e. potentiostatic test) of approximately 30 volts was applied while the current level was continuously computer-monitored using an ammeter. Faraday's law provides a relationship between the time of a sustained current level and the associated mass loss. The mass loss is calculated using Equation 2.10 where a is the atomic weight of iron (56 grams), I is the corrosion current (amp), t is the time elapsed (seconds), z is the valency of the reacting electrode (2 for iron), and F is Faraday's constant (96,500 amp-sec). The original bar mass m is measured on a scale before being embedded in mortar. The corrosion level is expressed as a percentage of mass loss:

$$\text{Corrosion Percentage} = 100 \cdot \frac{\Delta m}{m} \quad \text{..(6.3)}$$

After each specimen has undergone accelerated corrosion, the rebar is removed and the mass measured. Figure 6.70 shows the relationship between the measured corrosion levels and the predicted corrosion levels using Faraday's law.

Figure 6.70: Measured mass loss as a function of predicted mass loss using Faraday's law for accelerated corrosion testing of reinforced mortar specimens.

185

The third order polynomial trendline provides a coefficient of determination of 0.94 and is used for the estimation of percentage mass loss for the corroded specimens presented in this report. The nonlinearity of the relationship reflects different stages of the corrosion process. Upon starting accelerated corrosio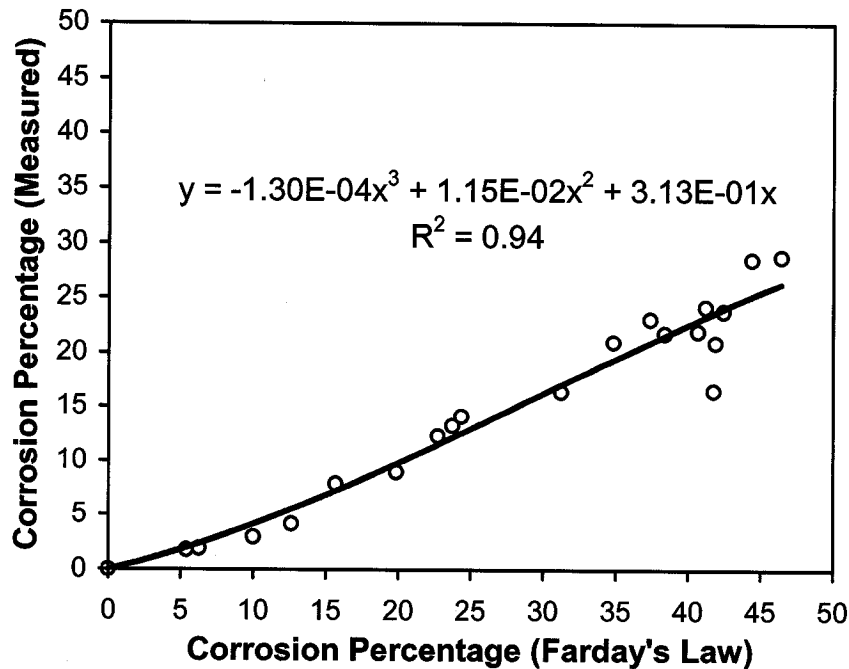n, a protective passive layer exists at the surface of the rebar with healthy mortar surrounding the passive layer. These layers act as resistors between the copper mesh and rebar. Differences between the measured corrosion level and the predicted level by Faraday's law are most likely due to thermal losses from heat generation and the dissolution of water. Other factors influencing the difference are the purity of the steel rebar, electrical properties of the fine aggregates, salt deposits, the overall electrical path between the steel and rebar, mortar permeability, mortar porosity, and mix consolidation [57]. The formation of corrosion products can cause differences as well, as the corrosion product will change forms and react further. As cracking occurs, forming pathways directly to the rebar, the reaction occurs more rapidly. These direct pathways result in less thermal losses and different corrosion products forming. The third order polynomial captures these differences between the measured and predicted values adequately for the purposes of this report.

As stated previously, the specimens were corroded potentiostatically at 30 volts. Current densities reached levels as high as 13 mA/cm^2 (power supply limit), with values typically between $2 - 6$ mA/cm^2. As a point of reference, experiments with natural corrosion (i.e. non-accelerated) yielded a maximum current density of 0.1 mA/cm^2 [124]. Therefore, the current densities used to accelerate corrosion in this report were very high compared with actual corrosion rates in real structures. The current was set this high to allow for rapid ultrasonic testing of the specimens. One drawback to this extreme increase in current density is that previous work has shown that the percentage of steel mass loss necessary to cause the rupture of the concrete cover is sensitive to the current density [124,125]. Saifullah and Clark [125] found that for current densities below 0.25 mA/cm^2, the percentage of mass loss necessary to cause cover cracking increased with increases in the current density. In other words, as the current level goes up, more bar loss is necessary to cause cracking. A similar trend for this current density region was found in [124]. For current densities above 0.25 mA/cm^2, the opposite trend was found. In this region, increases in current density meant that less bar loss was necessary to cause cracking. Figure 6.71 shows the relationship between the percentage of mass loss that occurred at the moment the cover cracked as a function of the current density. Bond strength showed similar sensitivity to the current density. For current densities below 0.25 mA/cm^2, the bond strength of the specimen at the moment of the cover cracking increased with increases in the current density. For current densities above 0.25 mA/cm^2, the bond strength decreased with increases in the current density. Figure 6.72 shows how bond strength is affected for different current densities at cover cracking and at around 20% mass loss. The symbols

$f_{(corroded)}$ and $f_{(control)}$ refer to the maximum load during a pullout test for the corroded specimen and control specimen (0% mass loss), respectively.
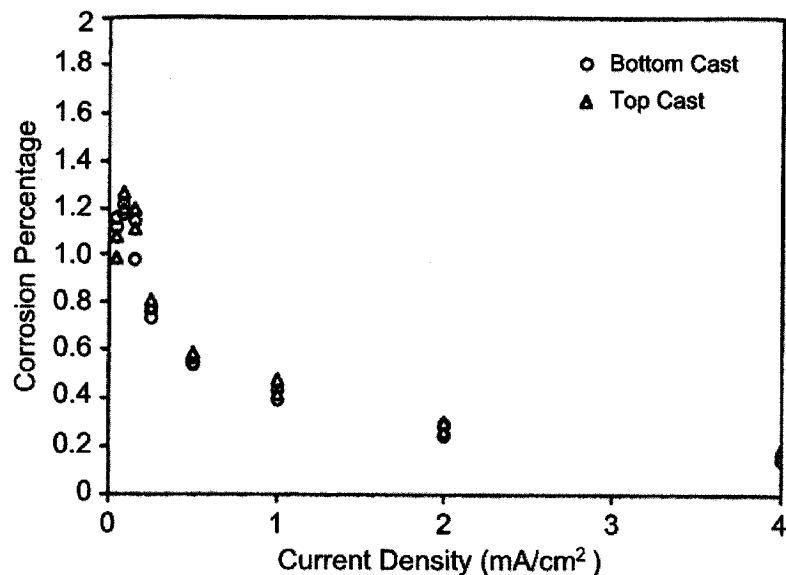
Figure 6.71: Percentage mass loss that occurred for a bar when cracking reached the concrete cover as a function of the current density used to accelerate the corrosion (extracted from [125]).
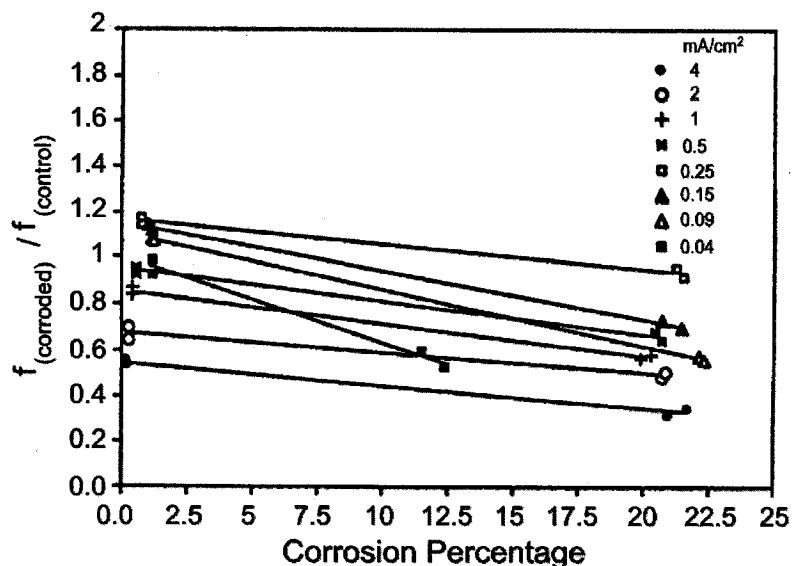
Figure 6.72: Normalized bond strength for different current densities used to accelerate corrosion as a function of percentage mass loss (extracted from [125]).

All specimens showed a decrease in bond strength from the cover cracking to a percentage mass loss of around 20%. However, it is clear that specimens corroded at high current densities experienced a much greater depreciation in bond strength at comparable mass loss percentages than specimens corroded at low current densities. However, the specimens corroded at the lowest current densities showed the largest

187

depreciation in bond strength levels between the cover cracking and 20% mass loss. Saifullah and Clark [125] provided four reasons for the observed behavior:

1. Less creep in concrete occurs at faster strain rates, meaning that at very high current densities the corrosion product forms at a faster rate than the creep rate. Therefore, the beneficial effects of concrete creep to relieve tensile hoop stresses are negated at high corrosion current densities.

2. Pore blocking may occur in the porous layer (i.e. interfacial transition zone) of cement paste immediately adjacent to the rebar for very slow rates of corrosion.

3. Possible detrimental effects to the steel/concrete interface from anodic polarization (similar to observed detrimental effects from cathodic polarization) at high current densities may occur.

4. Changes in the type of corrosion products formed at different current densities may play a role.

Since extremely high current densities were used in this report, the deterioration process will be different than what is observed for natural corrosion. The mortar will most likely not creep substantially from the formation of corrosion products. Cracking of the mortar cover will most likely occur quicker for the same level of mass loss than if the test were accelerated at a slower rate. The bond strength of the specimen at the point that cracking reaches the cover will be more depreciated than at a slower rate. Also, the difference in bond strength between cover cracking and more substantial mass loss (e.g. 20% mass loss) will be less drastic than if natural corrosion occurred. The current level is set high enough that the extrapolation to real structures is not recommended. The purpose of the testing is to assess the feasibility of using the guided wave method for in-situ monitoring of corrosion. If found to be feasible, further testing with a more natural corrosion process is recommended.

The specimen size used was rather small for low frequency guided wave testing. For instance, Beard [95] used a specimen with a square cross section of 3.28' x 3.28' (1 m x 1 m), with notches at the outer surface, to ensure that waves leaked out into the surrounding mortar from the steel reinforcement would not return. A larger specimen size would not allow for corrosion to occur as rapidly using anodic polarization as the specimen size used. The increase in mortar cover would make the ingress of water to the bar depth take much longer and would create more resistance between the anode and cathode. Rebar closest to the cover and at corners is most likely to corrode first due to the ingress of deleterious substances. Therefore, boundaries close to these dimensions would be likely encountered. It also presents a challenge with respect to accelerating the corrosion of the reinforcing bar without causing accentuated corrosion at the exposed ends. Therefore, to allow for relatively quick accelerated corrosion tests, a smaller specimen size for low frequencies was used in this study.

188

Before beginning the accelerated corrosion test presented in this paper, the specimen was wetted with salt water for one week. Wetting the mortar, prior to turning on the power supply to initiate corrosion, is necessary for a few reasons. First, saturation of the specimen lowers the electrical resistance between the anode and cathode, allowing for a faster electrochemical reaction. Second, wetting the mortar helps prevent accentuated corrosion at the exposed rebar ends. Third, the sensitivity of guided waves to corrosion needs to be isolated from the effects of the wetting of the mortar specimen, specifically when in a transient moisture state. By allowing the specimen to become fully saturated with water prior to starting the test, changes in guided wave behavior are more influenced by the corrosion process rather than wetting effects. To elaborate on this point, the mortar specimens were cured in air rather than being moist cured. This was done for a couple of reasons. First, there were capacity limitations for storing the mortar specimens in a humidity-controlled chamber. Second, air-cured concrete is 8-10 times more permeable than moist-cured concrete near the surface. The difference in permeability is insignificant at depths below 1.97" (50 mm). For the specimen size used, the permeability should be high throughout, allowing for a faster corrosion process. However, air curing the specimens has drawbacks. Besides creating mortar with a low compressive strength, the air-cured specimens shrink in size [126]. Shrinkage is reduced by the reinforcing bar, creating tensile stress in the mortar. When the hardened mortar specimen is soaked in water, it swells in size. The swelling strain is generally around 1/3 to 1/2 of the shrinkage strain [127]. Initially, when the surface is wetted, the interior of the specimen remains dry. The interior dry region restrains the free expansion that would take place if the specimen were wetted in its entirety simultaneously [128]. The interior goes into a state of tension while the exterior goes into a state of compression. Adding to this complexity is the creep of the concrete. In a transient moisture state, the creep can be much higher than at constant moisture content. This is explained by the hypothesis that movement of water molecules may facilitate changes in the bonding of the solid microstructure [129].

The filling of pores and voids immediately adjacent to the rebar will facilitate more leakage of waveform energy form the specimen. There could also be further hydration of the specimens, as resaturated concrete (or mortar) will resume its interrupted hydration [24]. Also, wet mortar has slightly different material properties to dry mortar (see Table 4.3). Therefore, caution was exercised to ensure that the effects of wetting the mortar were isolated as much as possible in this report.

6.5.1 MONITORING ACCELERATED UNIFORM CORROSION WITH THE L(0,1) MODE

Several specimens undergoing uniform corrosion were monitored using guided mechanical waves at lower frequencies. The first test presented invoked the fundamental longitudinal mode, i.e. L(0,1). A 15-cycle toneburst was invoked at fifty-one different frequencies in the embedded system. The fifty-one

189

frequencies were from 50 to 200 kHz in 3 kHz increments. This particular bandwidth is the location of the lowest attenuation region of the L(0,1) mode (refer to Figure 4.5). The highpass and lowpass filters were set at -/+ 5 kHz of the invoked frequency. The toneburst excitation and filtering technique were both used to ensure that the frequency content was concentrated in a narrow bandwidth.

The transducers were attached and the specimen was wetted until a level of saturation was reached. Corrosion was then initiated by applying a potential between the copper and rebar. The experiment was repeated several times with the results shown in this report representative of the trials. A three-dimensional plot of the relative attenuation for all frequencies tested over the duration of the accelerated corrosion experiment is shown in Figure 6.73.
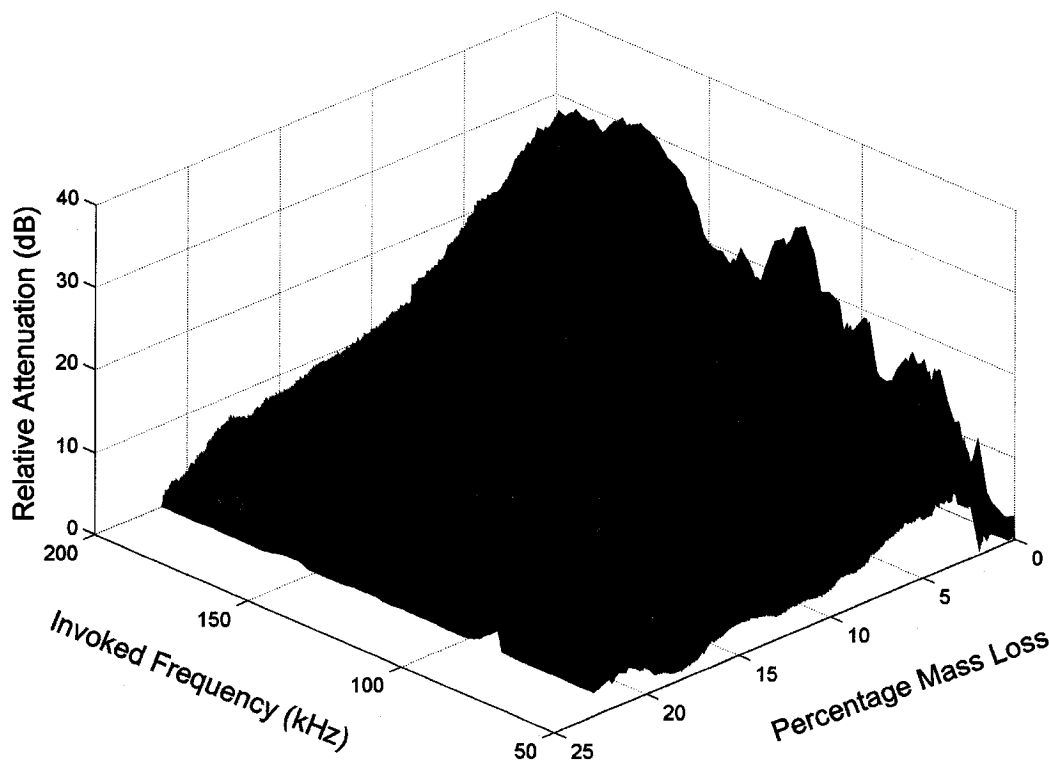
Figure 6.73: Relative attenuation as a function of mass loss during accelerated uniform corrosion. A frequency sweep between 50-200 kHz with 3 kHz increments was invoked using a 15-cycle toneburst.

Figures 6.74 and 6.75 are plots of relative attenuation of the 164 kHz invoked signal as a function of percentage mass loss from uniform corrosion for one trial and three separate trials. The 164 kHz signal was chosen because it displayed the greatest sensitivity to the corrosion process (i.e. greatest decibel change). A plot of the normalized corrosion pressure using the model discussed in Chapter 3 is also shown in Figure 6.75.

190
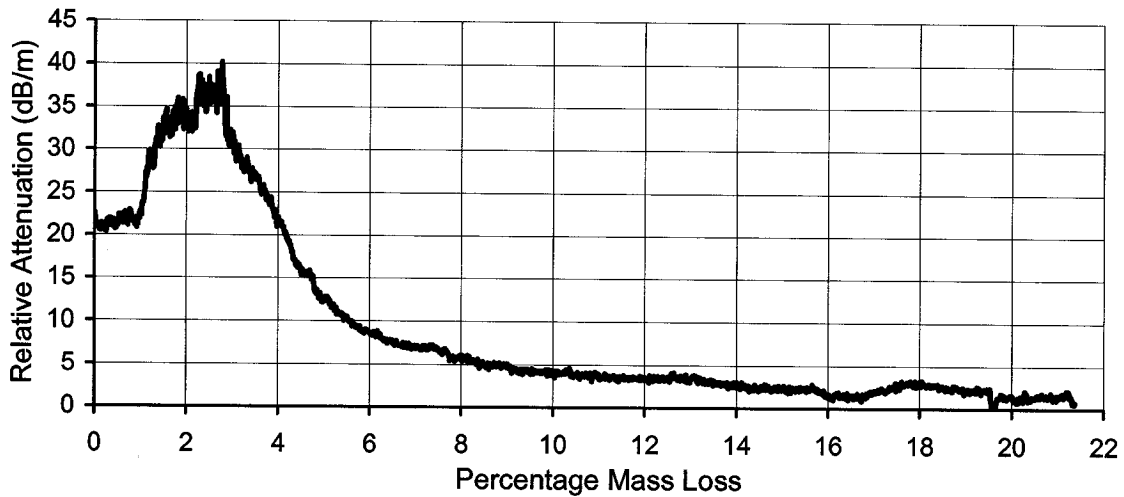
Figure 6.74: Relative attenuation (experimental results) as a function of percentage mass loss during uniform corrosion. The waveform was a 164 kHz fifteen-cycle signal. The highpass and lowpass filters were set at 159 kHz and 169 kHz, respectively.
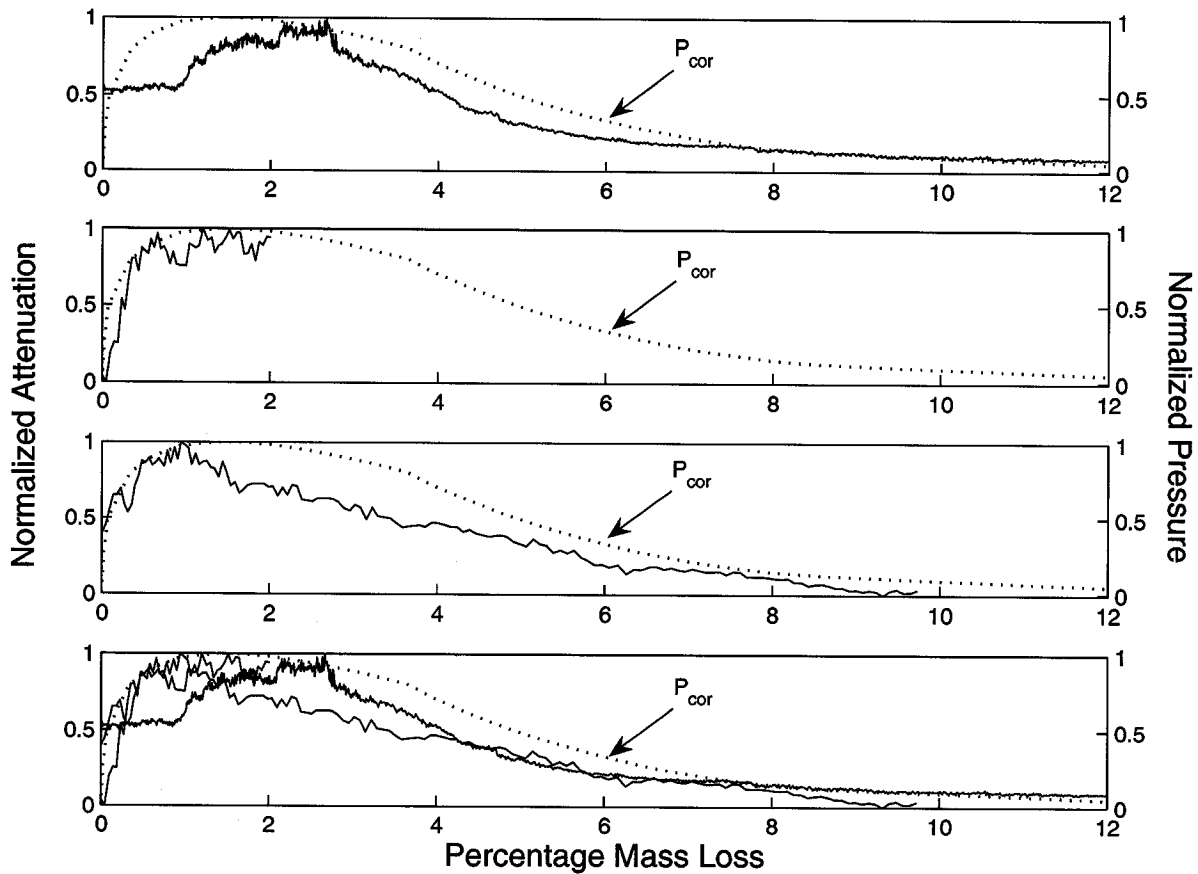
Figure 6.75: Experimental normalized attenuation results (solid line) and theoretical corrosion pressure curve (dashed line) as a function of percentage mass loss during uniform corrosion. The top three plots are separate trials stopped at different percentages of corrosion. The bottom plot has all three trials. The waveform was a 164 kHz fifteen-cycle signal.

191

Notice that the attenuation of the waveform increases from the onset of corrosion to the apex of attenuation (roughly 1-3% mass loss) by approximately 18 dB/m. Corrosion products accumulated between the rebar and mortar, which created pressure. The pressure increased the coupling between the steel and mortar and the stiffness of the corrosion product (refer to Chapter 3). This increase in stiffness created less of an impedance mismatch between the material properties of the steel and corrosion product. The increase in corrosion product stiffness and coupling resulted in more wave energy leaking out into the surrounding mortar. Significant cracking eventually started to occur that reduced the stiffness of the surrounding mortar (i.e. reduction in confinement level) and the corrosion product. This loss of confinement will reduce the amount of wave energy leaked out (i.e. reduction in attenuation). After 3% mass loss, the attenuation dropped in a non-linear fashion and leveled off after significant mass loss had occurred. Captured time domain waveforms for the invoked 164 kHz fifteen-cycle signals are shown in Figures 6.76 and 6.77 with different vertical scaling. The left and right vertical lines are the arrival times for the L(0,1) and F(1,1) modes.
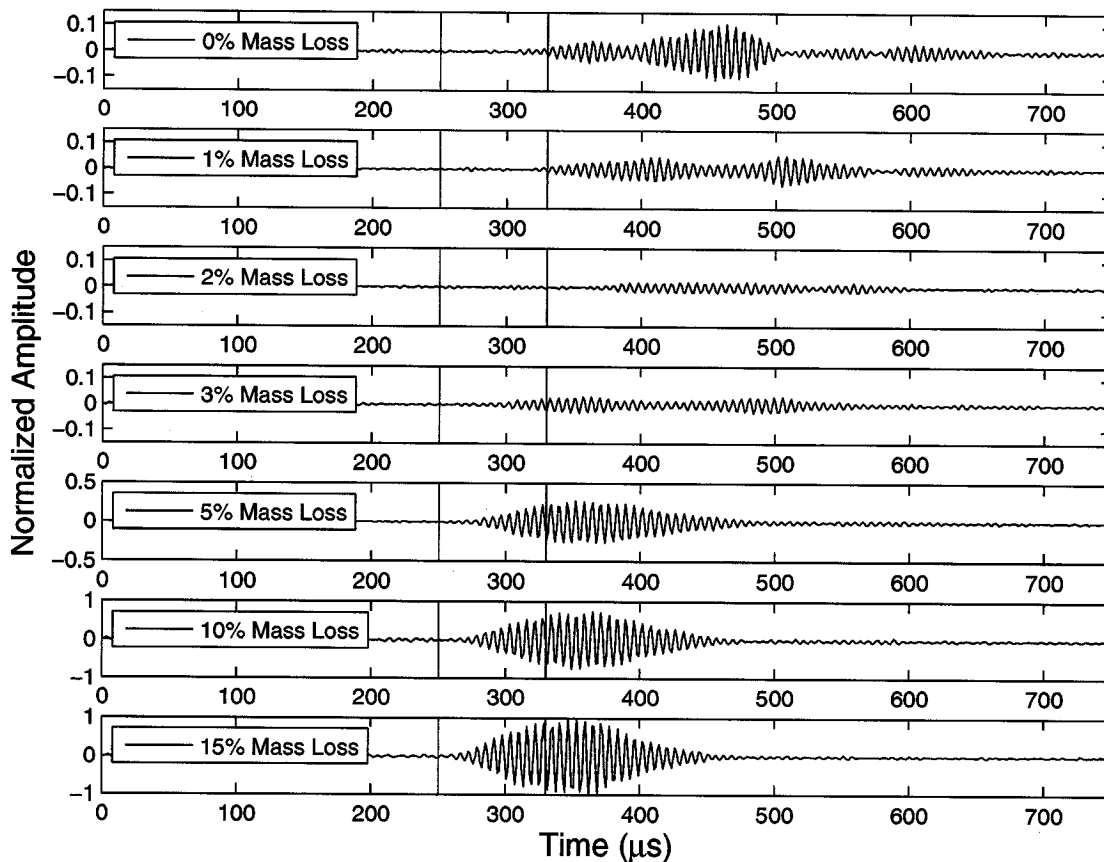
Figure 6.76: Waveforms for 164 kHz collected at 0%, 1%, 2%, 3%, 5%, 10%, and 15% corrosion are shown. Vertical dashed lines have been placed in the time domains indicated the arrival time of the L(0,1) (left) and F(1,1) mode (right) modes. The vertical axis has been scaled for each waveform.

192
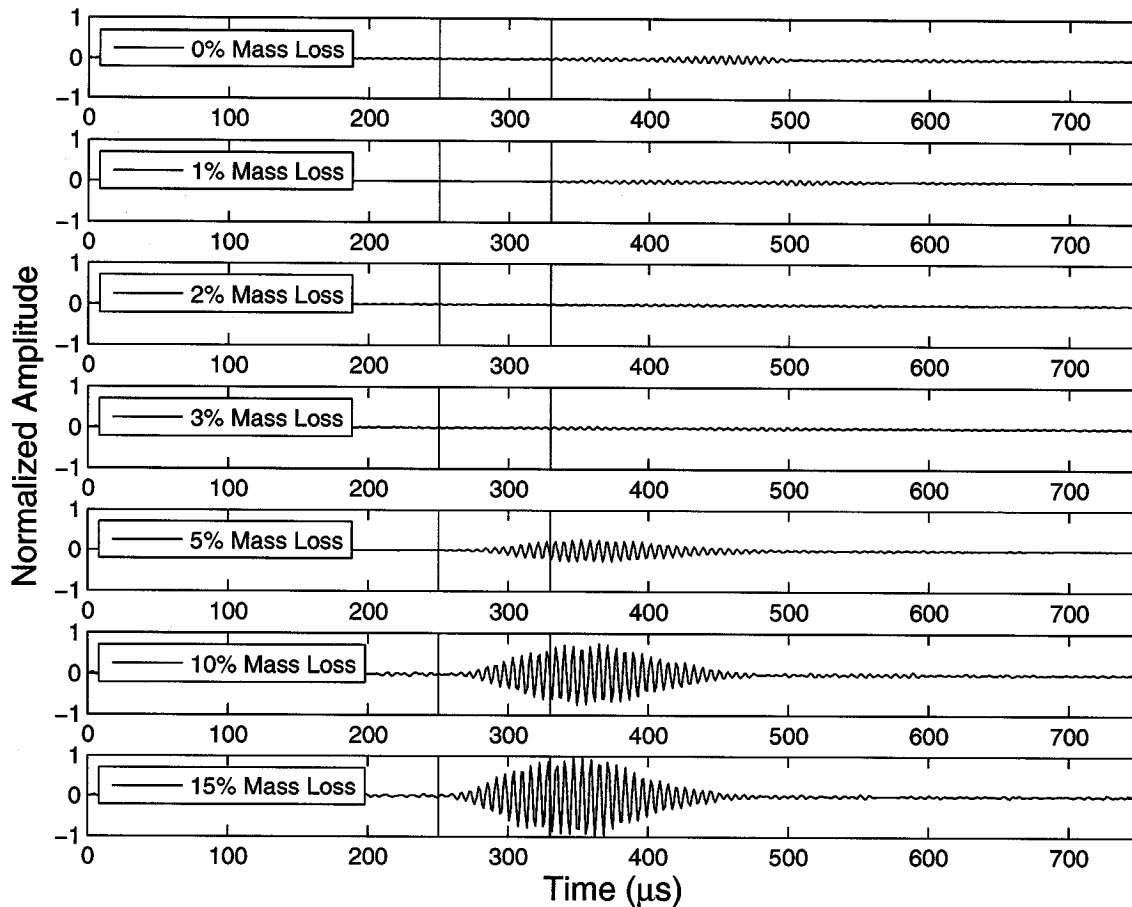
Figure 6.77: Waveforms for 164 kHz collected at 0%, 1%, 2%, 3%, 5%, 10%, and 15% corrosion are shown. Vertical dashed lines have been placed in the time domains indicated the arrival time of the L(0,1) (left) and F(1,1) mode (right) modes. The vertical axis is the same for each waveform to emphasize the increase in signal strength and the change in arrival time.

As mass loss increased from 0% to 1% to 2%, the signal strength (and signal-to-noise ratio) is reduced. From 2% to 3% to 5% mass loss, the signal strength increases significantly and there is a shift in the arrival time of the received waveform. The signal strength continues to increase from 5% to 10% to 15%. It is thought that initially, the F(1,1) and other later arriving waveforms are all that is received. After the mortar begins to crack, causing a reduction in the mortar and corrosion product stiffness and contact conditions, the signal strength increases and the arrival time changes. The arrival time approaches that of the L(0,1) mode. Figures 6.78-6.84 show the time domain, frequency domain, and spectrogram at 0%, 1%, 2%, 5%, 10%, and 15% mass loss, respectively. The highpass and lowpass filters were set at 159 and 169 kHz, respectively. The solid and dashed lines are longitudinal and flexural modes, respectively.

193
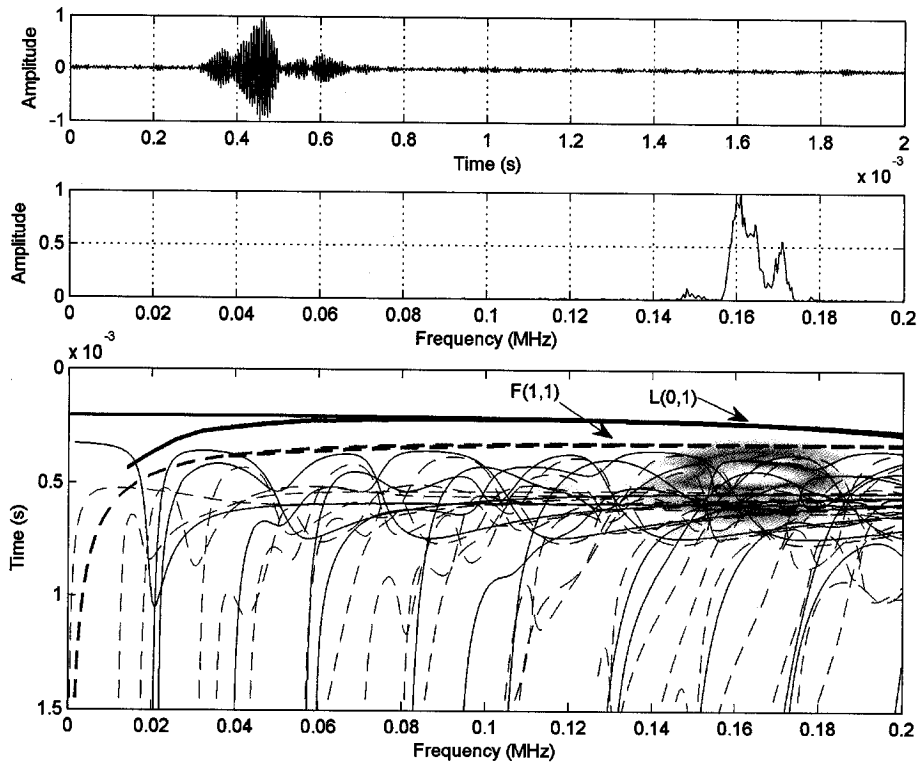
Figure 6.78: A 164 kHz fifteen-cycle pulse transmitted (direct arrangement) through rebar (orthogonal ribs) in a specimen that has undergone 0% mass loss from corrosion. The gain was set at 80 dB.
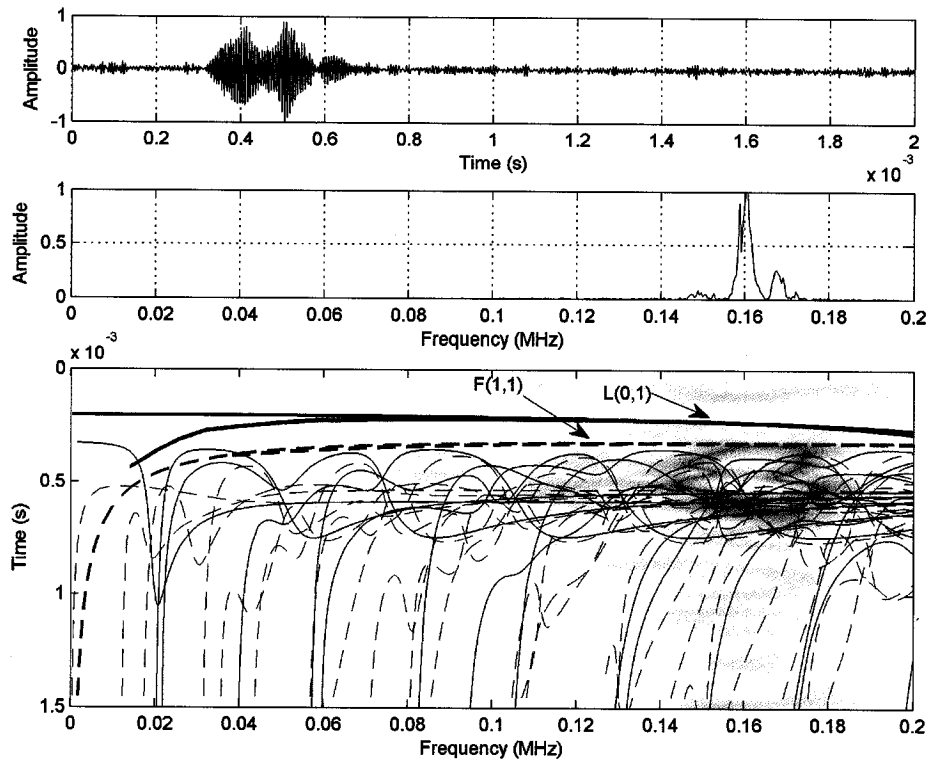
Figure 6.79: A 164 kHz fifteen-cycle pulse transmitted (direct arrangement) through rebar (orthogonal ribs) in a specimen that has undergone 1% mass loss from corrosion. The gain was set at 80 dB.

194
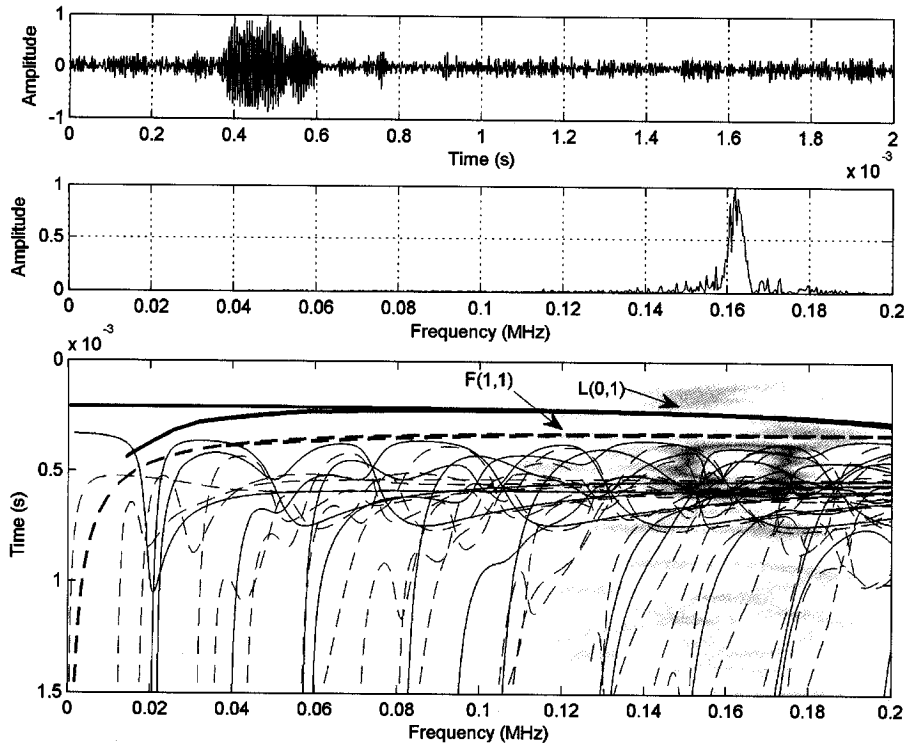
Figure 6.80: A 164 kHz fifteen-cycle pulse transmitted (direct arrangement) through rebar (orthogonal ribs) in a specimen that has undergone 2% mass loss from corrosion. The gain was set at 80 dB.
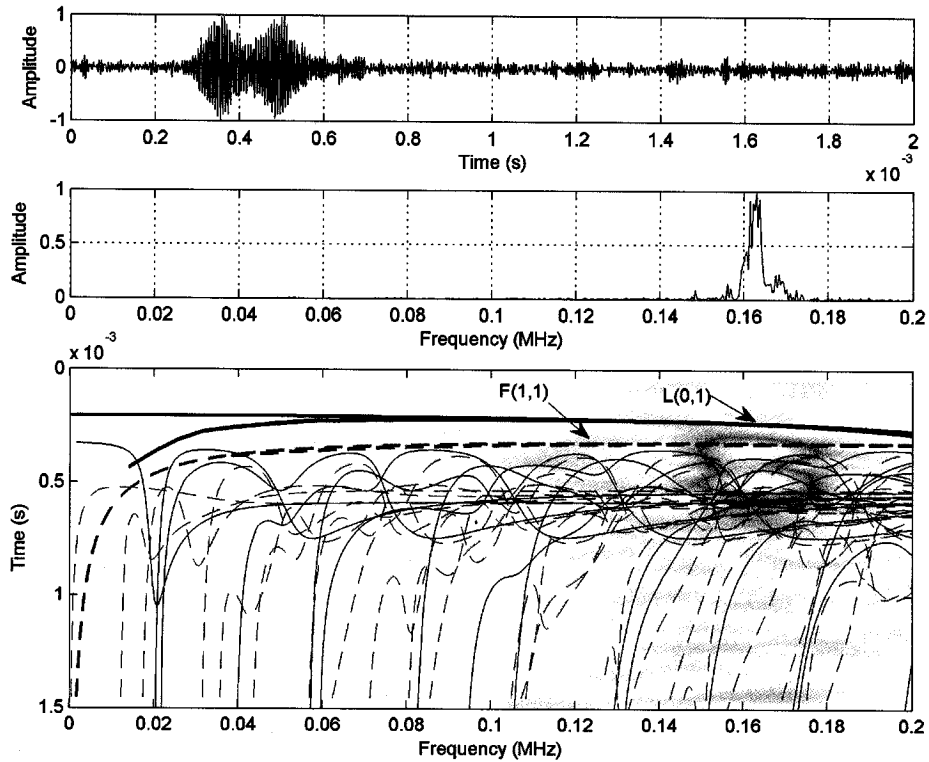
Figure 6.81: A 164 kHz fifteen-cycle pulse transmitted (direct arrangement) through rebar (orthogonal ribs) in a specimen that has undergone 3% mass loss from corrosion. The gain was set at 80 dB.

195
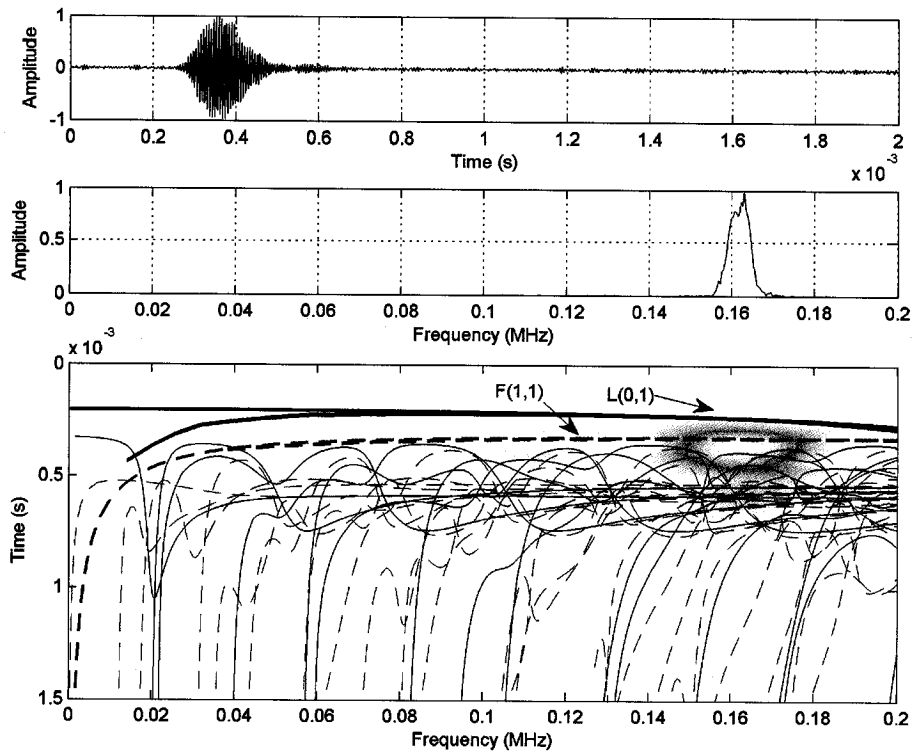
Figure 6.82: A 164 kHz fifteen-cycle pulse transmitted (direct arrangement) through rebar (orthogonal ribs) in a specimen that has undergone 5% mass loss from corrosion. The gain was set at 70 dB.
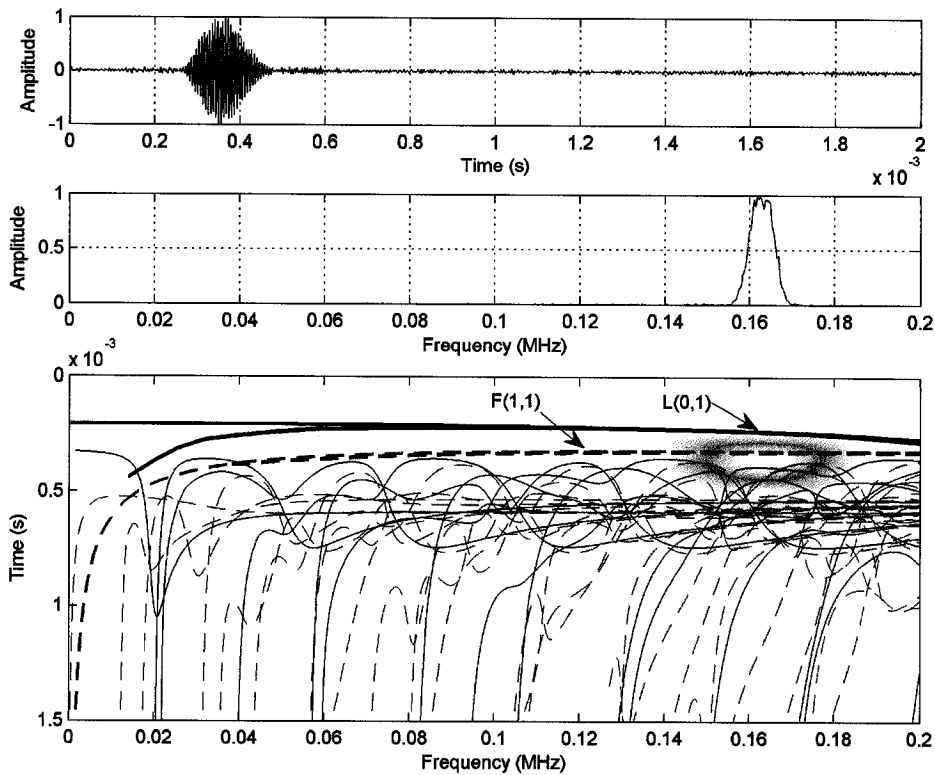
Figure 6.83: A 164 kHz fifteen-cycle pulse transmitted (direct arrangement) through rebar (orthogonal ribs) in a specimen that has undergone 10% mass loss from corrosion. The gain was set at 60 dB.

196
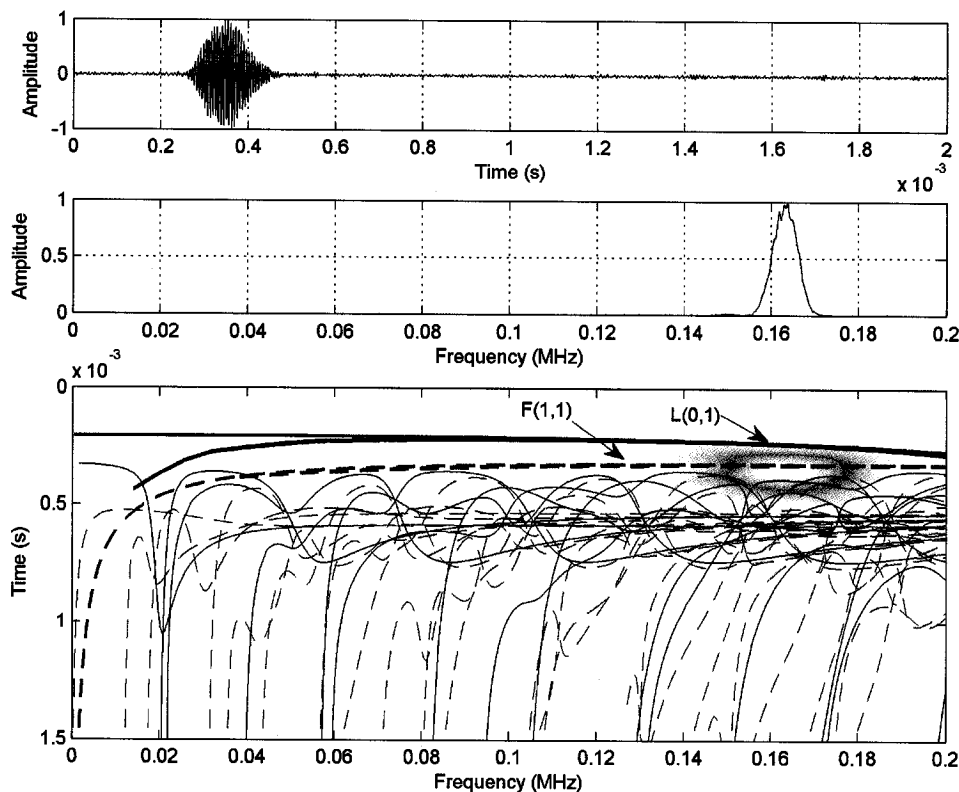
Figure 6.84: A 164 kHz fifteen-cycle pulse transmitted (direct arrangement) through rebar (orthogonal ribs) in a specimen that has undergone 15% mass loss from corrosion. The gain was set at 60 dB.

For early corrosion (0 - 2%), the L(0,1) is attenuated heavily and no longitudinal mode of propagation is recorded. Within the 0 - 2% corrosion range, the F(1,1) mode and other later arriving waveforms are all that is received. As discussed in Section 6.4.2, the later arriving waveforms could be wave energy leaked out into the mortar that reflects off of boundaries and enters back into the bar severely scattered. Modes for the rebar/mortar/air system may also be invoked. However, once the mortar starts to crack and debonding starts to occur (>3% corrosion), the L(0,1) mode starts to appear and gain signal strength. The back edge of the L(0,1) mode overlaps the front edge of the F(1,1) mode. This is expected, since a 15-cycle toneburst excitation was used and the 164 kHz input frequency has a smaller difference in energy velocity (compared to lower frequencies invoked) between the L(0,1) and F(1,1) modes.

From 5 - 15% mass loss, the L(0,1) and F(1,1) modes increase in waveform energy. The energy velocity is very sensitive to the properties of the steel [99] (rather than the mortar) and the leading edge of the waveform is highly attenuated resulting in a small discrepancy between the theoretical prediction of arrival time and the experimental arrival time of the first wave packet. Despite invoking a strong longitudinal waveform with the transducer arrangement, flexural modes of propagation are still created either from imperfections in the sending transducer alignment or from mode conversions. Mode

197

conversions may be caused by the heterogeneous nature of the interface conditions between the steel and mortar. The F(1,1) mode propagates at a lower attenuation in the system (refer to Section 6.3.3) than the L(0,1) mode but at a lower energy velocity. Therefore, the initial increase in attenuation for corrosion product accumulation was monitored by the propagation of the F(1,1) mode and other later arriving waveforms for the testing conducted in this report.

6.5.2 MONITORING ACCELERATED UNIFORM CORROSION WITH THE F(1,1) MODE

Accelerated uniform corrosion specimens were monitored using an indirect transducer arrangement at low frequencies. However, the results varied from test to test once the initial corrosion product accumulation occurred. It is thought that water played a critical role in the results. Signals sent in at frequencies higher than 130 kHz had such a low signal-to-noise ratio that they were not recorded. A frequency of 80 kHz had a strong signal-to-noise ratio for all tests. The wetting of the mortar was monitored with an 80 kHz fifteen-cycle toneburst in an indirect transducer arrangement with Figure 6.85 showing the results.
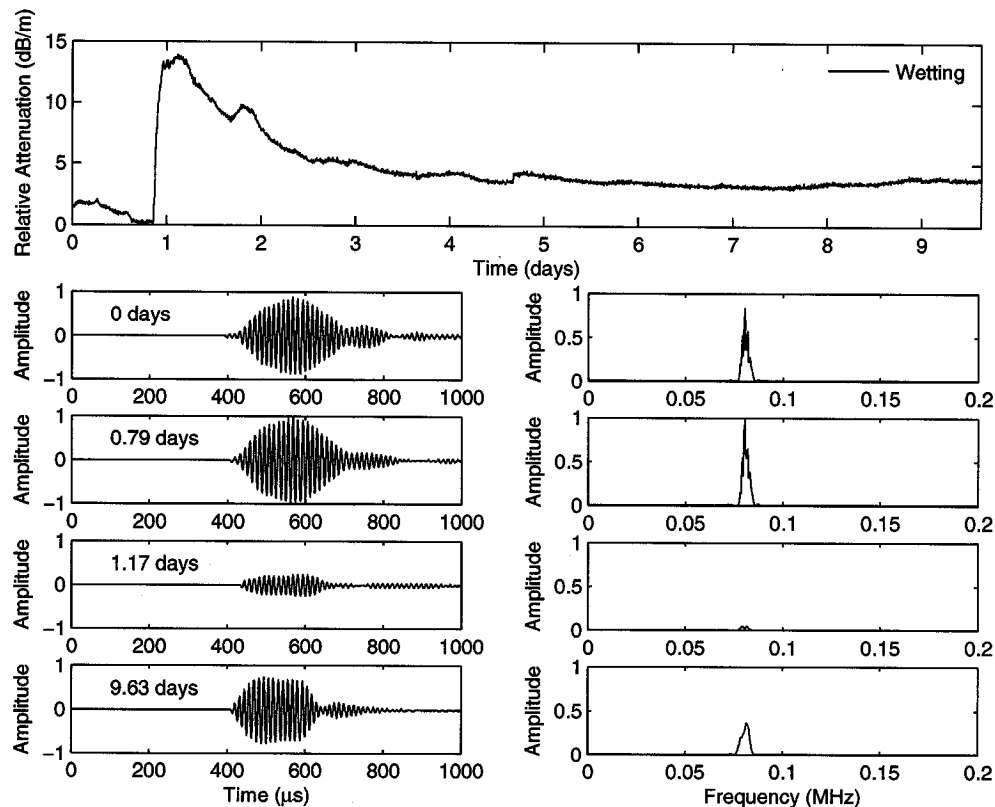
Figure 6.85: Wetting of the mortar prior to corrosion at 80 kHz (indirect transducer arrangement).

The signal strength initially increases slightly (decrease in relative attenuation) and then rapidly decreases. After three days of wetting the specimen reaches a saturation point and the signal strength remains relatively constant. It is thought that the initial increase in signal strength is caused by the

198

interior restraining the free expansion of the surrounding mortar. Once the water reaches the depth of the rebar, the signal strength is quickly reduced due to leakage and the increase in density. As the swelling and material properties of the specimen stabilize, the signal strength remains constant.

Figure 6.86 shows the results for an 80 kHz fifteen-cycle signal transmitted for three different accelerated uniform corrosion experiments using an indirect transducer arrangement. The highpass and lowpass filters were set at 75 and 85 kHz, respectively. Figure 6.87 shows one of the trials compared to the corrosion product model discussed in Chapter 3.
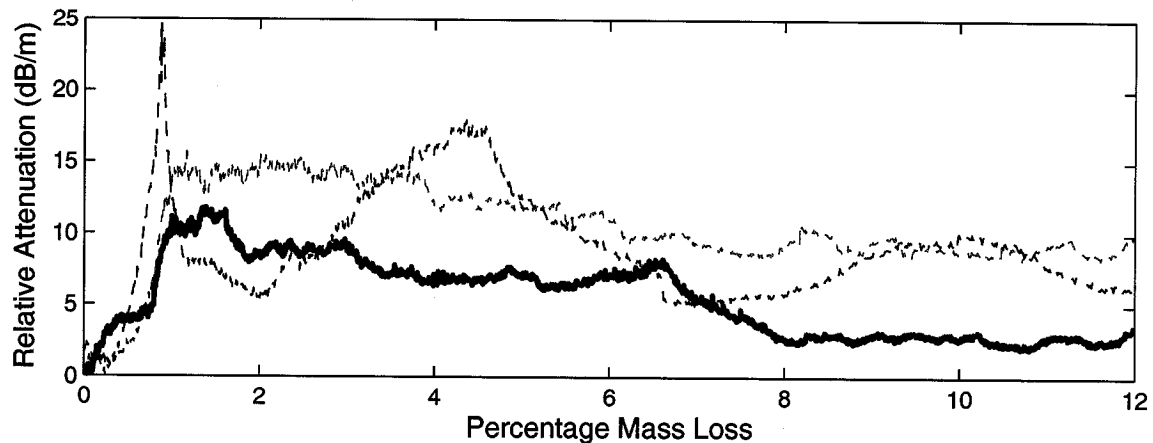
Figure 6.86: Relative Attenuation as a function of percentage mass loss for accelerated uniform corrosion specimens monitored using an indirect transducer arrangement. The input frequency was 80 kHz for all three trials.
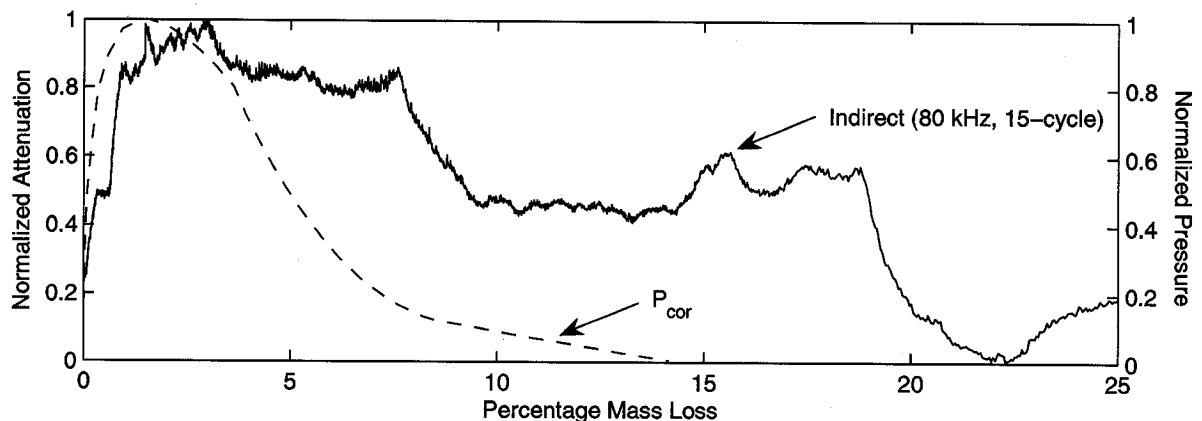
Figure 6.87: Both the experimental attenuation curve (solid line) for the F(1,1) mode and the corrosion pressure theoretical curve (dashed line) are shown as a function of percentage mass loss.

In all three trials the attenuation rises quickly after corrosion is initiated. However, even after substantial corrosion and subsequent cracking the waveform attenuation fluctuates in different directions. While deterioration of bond causes less attenuation, the loss of stiffness of the surrounding mortar can actually cause an increase in attenuation for the F(1,1) mode (refer to Figure 4.16). Cracking will also lead to the

199

ingress of more water, with the F(1,1) mode having more sensitivity to water than the L(0,1) mode. Figure 6.88 shows a cascade of time domains at different percentages of mass loss for an 80 kHz fifteen-cycle signal invoked in one of the indirect transducer arrangement trials.
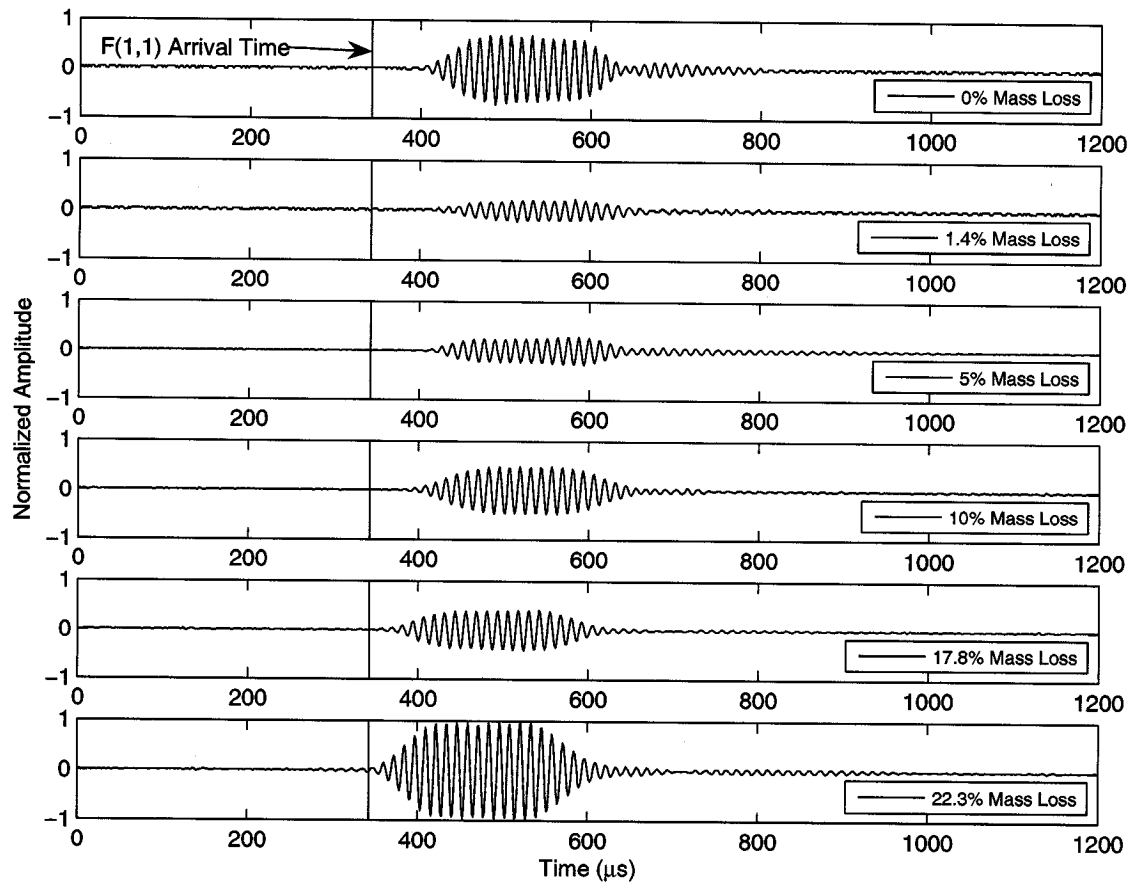
Figure 6.88: Cascade of time domains collected during uniform corrosion test using an indirect transducer arrangement. The vertical line is the theoretical arrival time for the F(1,1) mode. An 80 kHz fifteen-cycle toneburst was used.

Notice that the time of arrival changes from 0 - 22.3% mass loss. While there are slight differences between the velocity of the F(1,1) mode in a bar surrounded by air and a bar surrounded by mortar, the differences are fairly insignificant at 80 kHz. It is not completely known at this time why there was such a difference in velocities. Figures 6.89-6.94 show the time domain, frequency domain, and spectrogram at 0%, 1.4%, 5%, 10%, 17.8%, and 22.3% mass loss, respectively. The F(1,1) curve for a bar in mortar is on top of the curve for a bar in air. After significant corrosion, the waveform coincides with these curves.
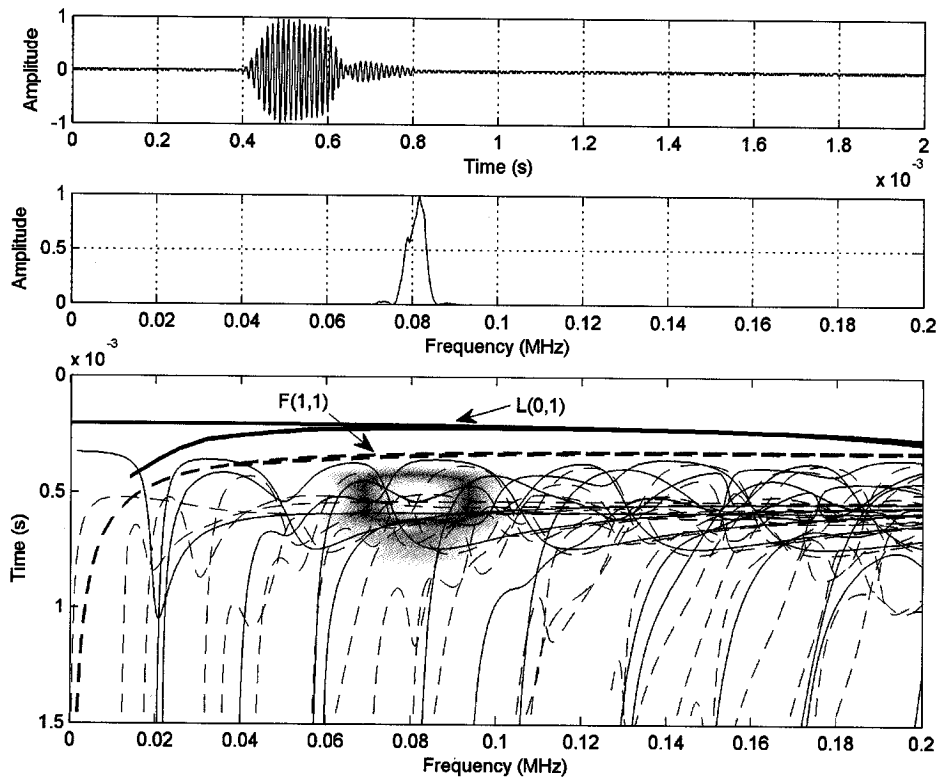
Figure 6.89: An 80 kHz fifteen-cycle pulse transmitted (indirect arrangement) through rebar (orthogonal ribs) in a specimen that has underwent 0% mass loss from corrosion. The gain was set at 40 dB.
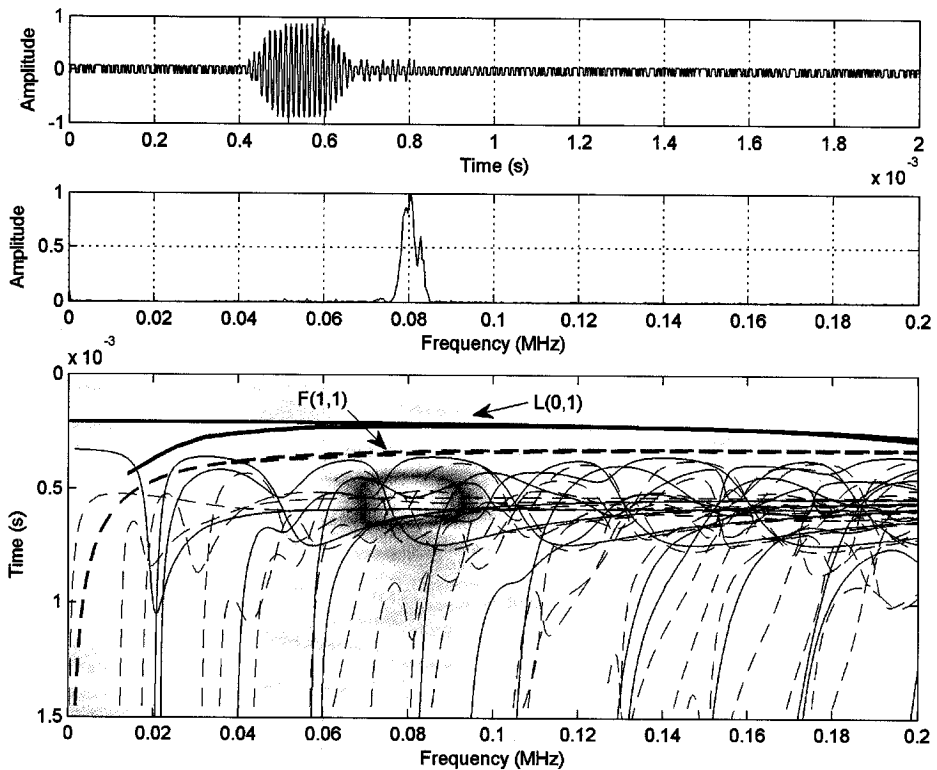
Figure 6.90: An 80 kHz fifteen-cycle pulse transmitted (indirect arrangement) through rebar (orthogonal ribs) in a specimen that has underwent 1.4% mass loss from corrosion. The gain was set at 40 dB.

201
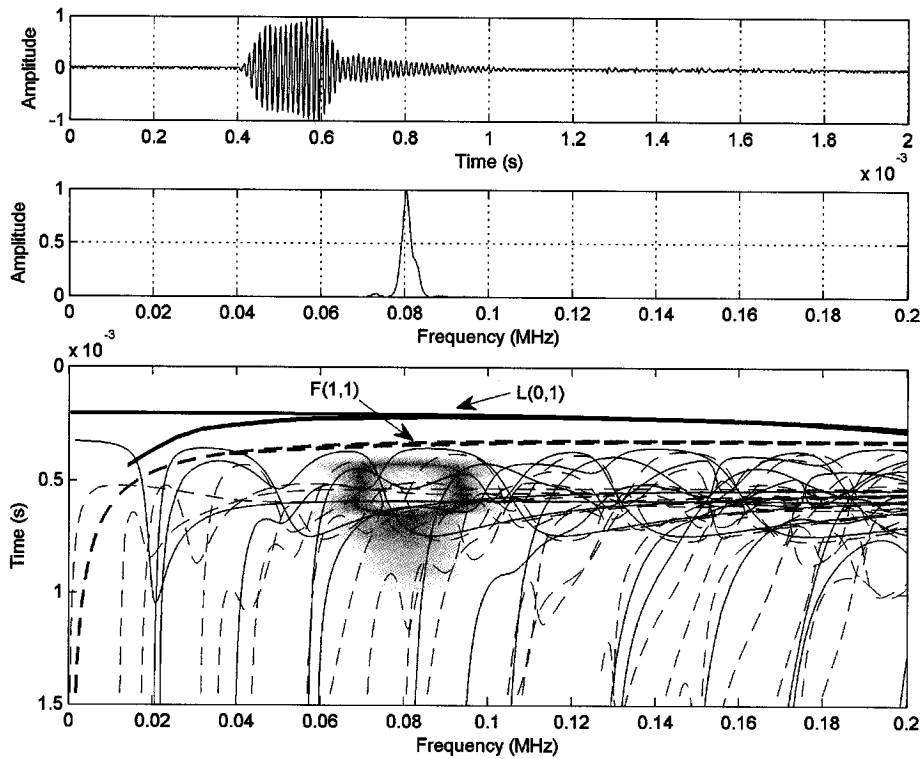
Figure 6.91: An 80 kHz fifteen-cycle pulse transmitted (indirect arrangement) through rebar (orthogonal ribs) in a specimen that has underwent 5% mass loss from corrosion. The gain was set at 50 dB.
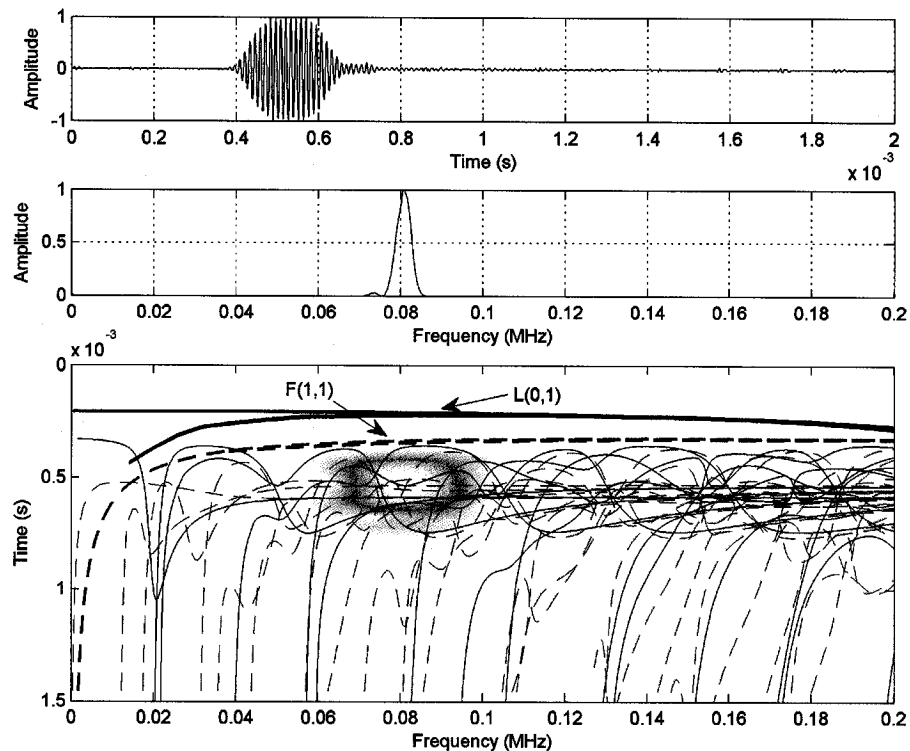
Figure 6.92: An 80 kHz fifteen-cycle pulse transmitted (indirect arrangement) through rebar (orthogonal ribs) in a specimen that has underwent 10% mass loss from corrosion. The gain was set at 50 dB.

202
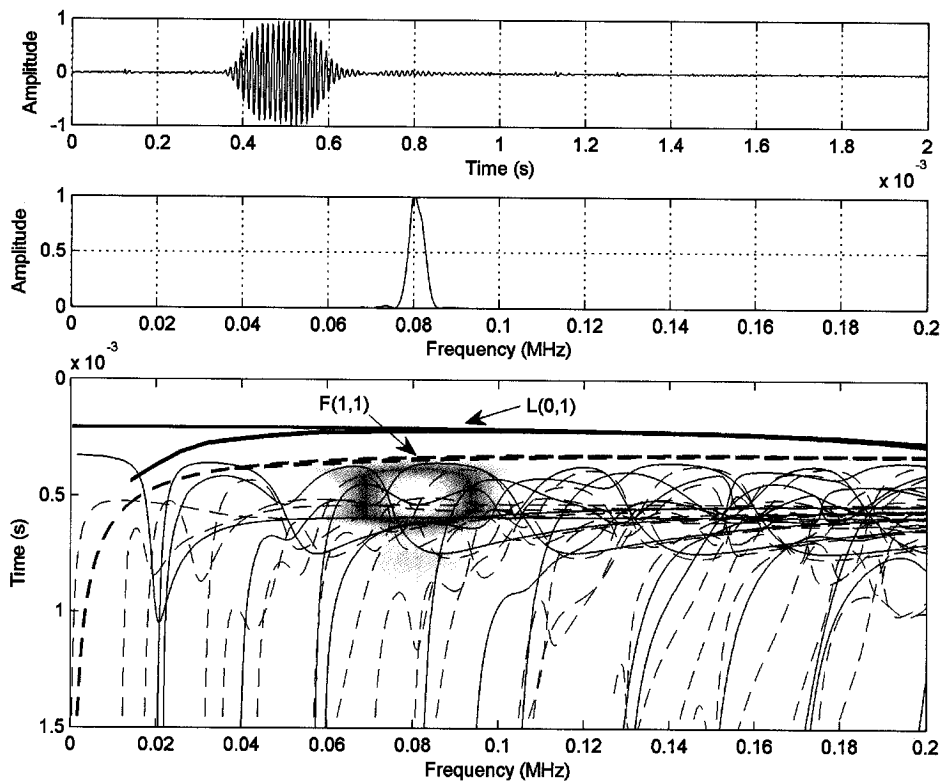
Figure 6.93: An 80 kHz fifteen-cycle pulse transmitted (indirect arrangement) through rebar (orthogonal ribs) in a specimen that has underwent 17.8% mass loss from corrosion. The gain was set at 50 dB.
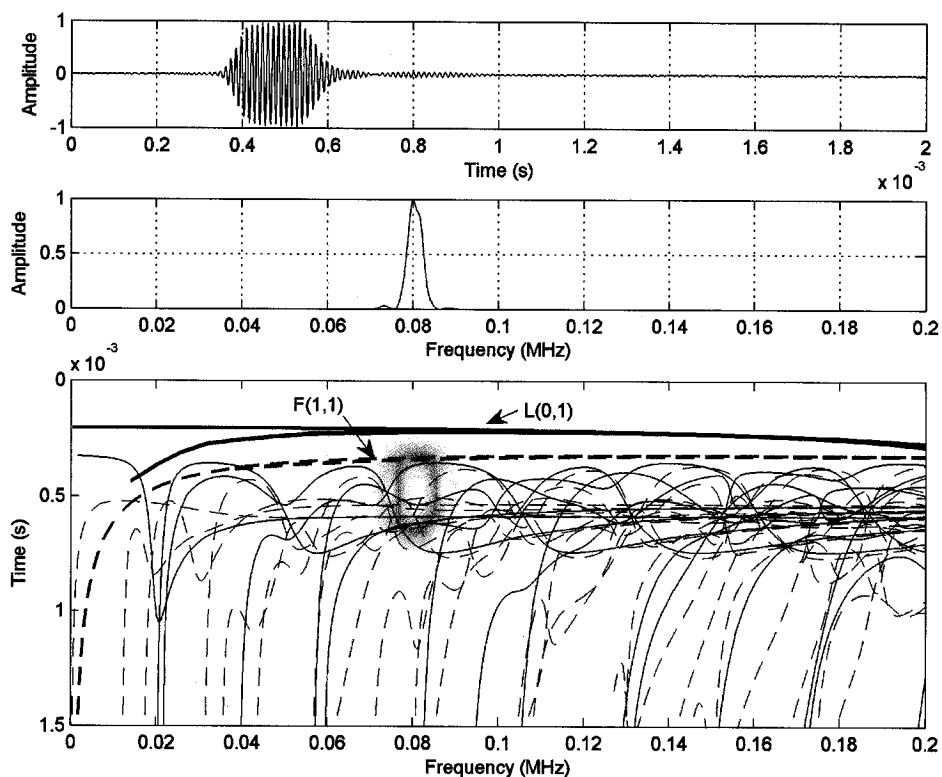
Figure 6.94: An 80 kHz fifteen-cycle pulse transmitted (indirect arrangement) through rebar (orthogonal ribs) in a specimen that has underwent 22.3% mass loss from corrosion. The gain was set at 50 dB.

203

6.5.3 MONITORING ACCELERATED UNIFORM CORROSION WITH THE L(0,9) MODE

Specimens undergoing uniform corrosion were monitored using guided mechanical waves at higher frequencies. The L(0,9) mode was invoked by using 5 MHz Panametrics (model V110) transducers. Single and hundred-cycle toneburst pulses were invoked during testing. Tonebursts were used for this application to ensure that the frequency content was concentrated in a narrow bandwidth and to avoid destructive interference with other modes [99]. For these reasons, the results of the toneburst excitation were used to measure relative attenuation. Figure 6.95 shows a recorded single cycle pulse and hundred-cycle pulse at 5.08 MHz for a healthy mortar specimen with spectrograms. The highpass and lowpass filters were set at 2 and 10 MHz, respectively.
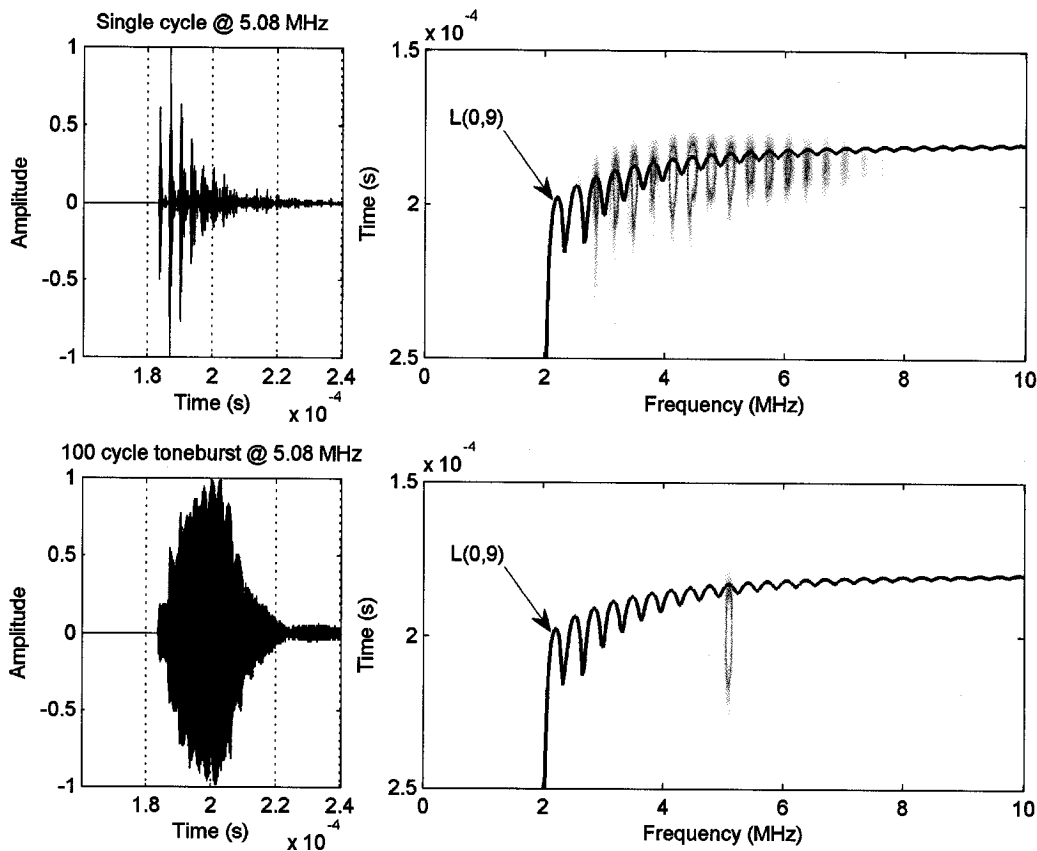
Figure 6.95: Received time domain and spectrogram for a 5.08 MHz single cycle pulse (top) and a 5.08 MHz hundred-cycle pulse (bottom).

The spectrogram of the single cycle pulse verifies that the L(0,9) mode is being invoked in the system. The L(0,9) mode displays mode crossing behavior as discussed in Chapter 4. The frequencies at which toneburst excitations were invoked were chosen by looking at the amplitude peaks in the frequency domain of a 5 MHz single cycle pulse. Figure 6.96 shows the time and frequency domain.
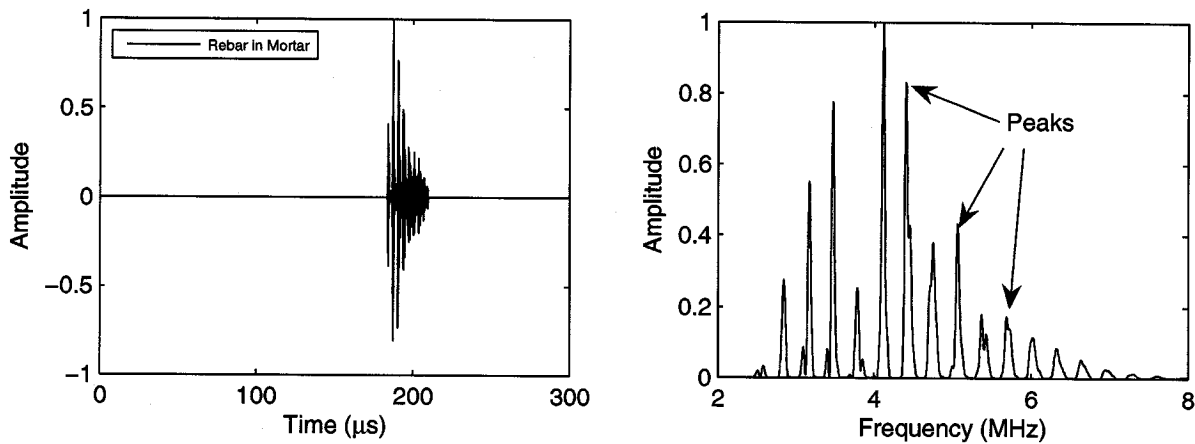
Figure 6.96: Time and frequency domain for a rebar embedded in mortar. The input signal was a 5 MHz single cycle pulse. The specific frequencies used for toneburst excitation were chosen from the frequency domain peaks from the single cycle pulse.

The sixteen peak frequencies (in MHz) found between 2.5 and 7.5 MHz were: 2.59, 2.85, 3.16, 3.47, 3.80, 4.12, 4.41, 4.76, 5.08, 5.39, 5.71, 6.04, 6.34, 6.69, 7.07, and 7.34. Wave propagation at each of these frequencies is considered to be the L(0,9) mode.

The wetting of the mortar was monitored with the hundred-cycle tonebursts. A three-dimensional plot of the relative attenuation of all sixteen frequencies over the wetting period is shown in Figure 6.97. Figure 6.98 shows the time domain for the 2.59 MHz and 7.34 MHz hundred-cycle pulses at three different times during the wetting period. These two frequencies were chosen for comparison because they were the lowest and highest invoked frequencies.

Note that the shaded region between each black line in Figure 6.96 does not imply that there was recorded data in this region or that if there was it would be of that magnitude in attenuation. It simply serves as a graphical tool to help distinguish between the frequency responses. The lowest frequencies invoked show sensitivity to the wetting of the mortar. However, unlike the F(1,1) mode, there is no rapid increase in attenuation but rather a rapid decrease in attenuation. The lower frequencies in the tested range will have an increase in attenuation with immersion in water (refer to Figure 6.19). The change of material properties from dry to wet mortar virtually has no effect on the theoretical attenuation curves for the L(0,9) mode (refer to Figure 4.22). The swelling of the specimen may cause changes in the bond between

205

the steel and mortar. The highest frequencies invoked are not as sensitive to water or bond changes and therefore showed relatively little change. There is, however, a slight increase in attenuation for the highest frequencies tested.
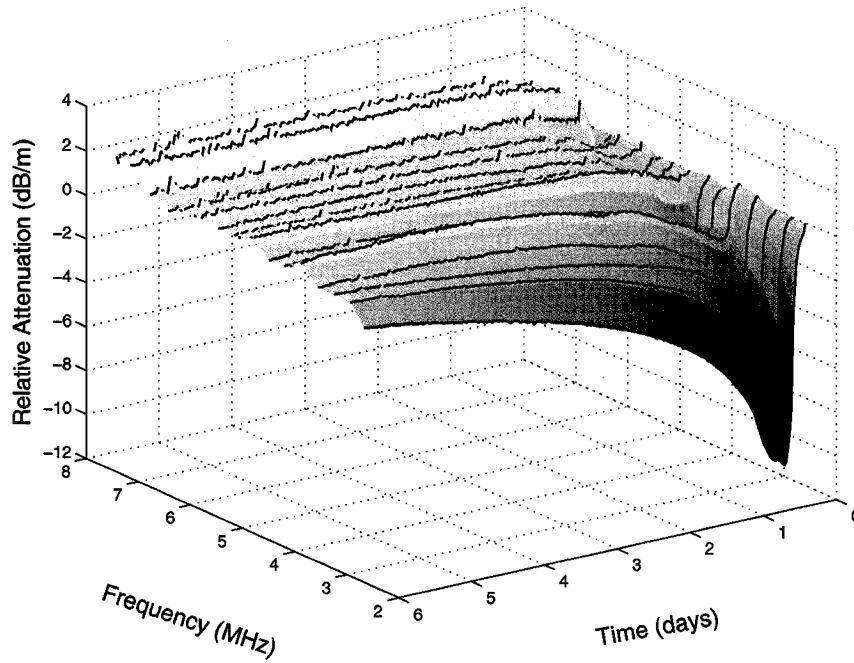
Figure 6.97: Relative attenuation of the L(0,9) mode at different frequencies as a function of time while wetting the mortar.
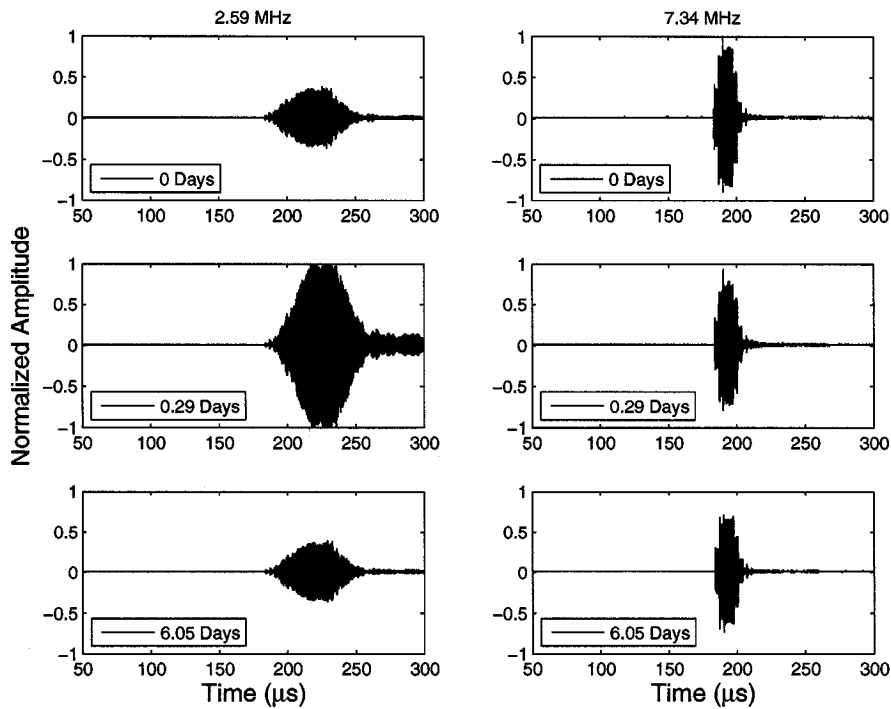
Figure 6.98: Time domains for the L(0,9) mode at two separate frequencies during the wetting of the mortar prior to corrosion.

After saturation levels had been reached from wetting, the corrosion was initiated by applying a potential. Figure 6.99 shows a three-dimensional plot of the frequency domain calculated from a 5.08 MHz single cycle pulse as a function of mass loss.
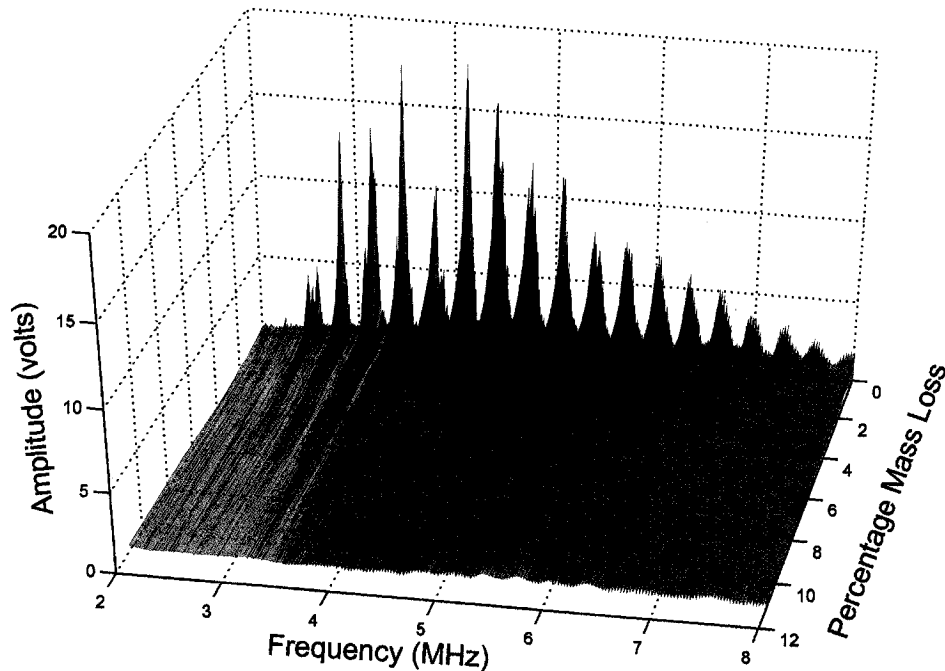
Figure 6.99: Frequency domain as a function of corrosion percentage for a reinforced mortar specimen undergoing accelerated uniform corrosion. The input signal was a single cycle 5.08 MHz pulse.

Figure 6.99 shows that all frequencies are attenuated as the percentage mass loss increases. However, the lower frequencies are more quickly attenuated as compared to the higher frequencies. Figures 6.100 and 6.101 show a three-dimensional and two-dimensional plot of the relative attenuation for all sixteen invoked frequencies as a function of percentage mass loss. Figure 6.101 also has the theoretical corrosion pressure curve (discussed in Chapter 3) added. Monitoring all frequencies after ten percent mass loss was restricted by the amplification capabilities of the pulser/receiver. Note that the shaded region between each black line in Figure 6.100 does not imply that there was recorded data in this region or that if there was it would be of that magnitude in attenuation. It simply serves as a graphical tool to help distinguish between the frequency responses.

Immediately after corrosion is initiated, all of the frequencies invoked begin to attenuate. The lowest frequencies invoked attenuate the most rapidly, while the highest frequencies attenuate much more subtly. Fig. 6.101 shows the change in slope in the attenuation curves in the 2 - 4% range of mass loss. Notice in the same region that the theoretical corrosion pressure curve is close to the apex of pressure and that cracking is predicted to reach the mortar surface. The onset of longitudinal cracking at the bottom of the specimen (partially submerged region) was visually observed to occur in this region. The loss of

207

confinement from the onset of cracking was observed to affect wave energy leakage for low frequency modes due to their displacement profiles at the steel/mortar interface (refer to Sections 6.5.1 and 6.5.2). However, since the higher frequency longitudinal waveforms have most of their energy concentrated in the center of the bar, the effect is minimized. Discontinuities and irregularities of the bar profile are thought to cause scattering, reflections, and mode conversions. The change in slope is most likely due to the crack opening at the bottom of the specimen, which caused corrosion to occur preferentially on the bottom of the rebar. After extraction of the rebar, it was confirmed to have more corrosion on the bottom than on the top, with a photograph provided in Figure 6.102.
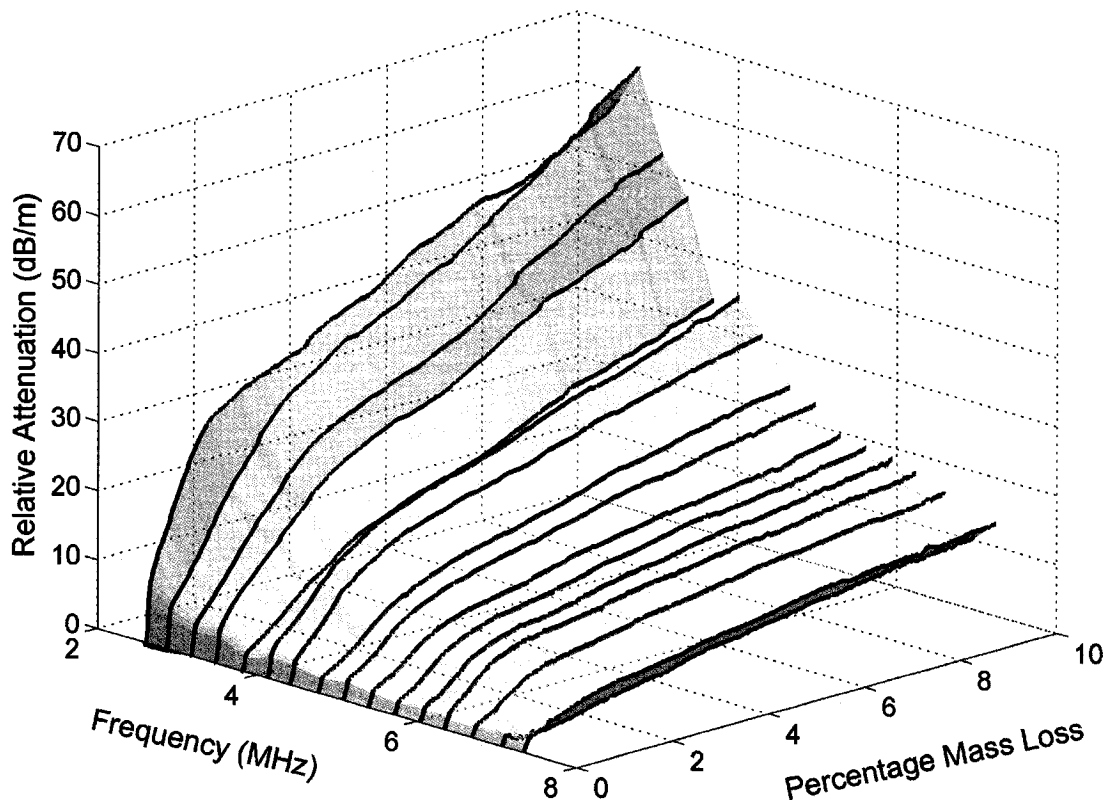
Figure 6.100: A three-dimensional plot of the attenuation for all sixteen invoked frequencies up to 10% mass loss.

208
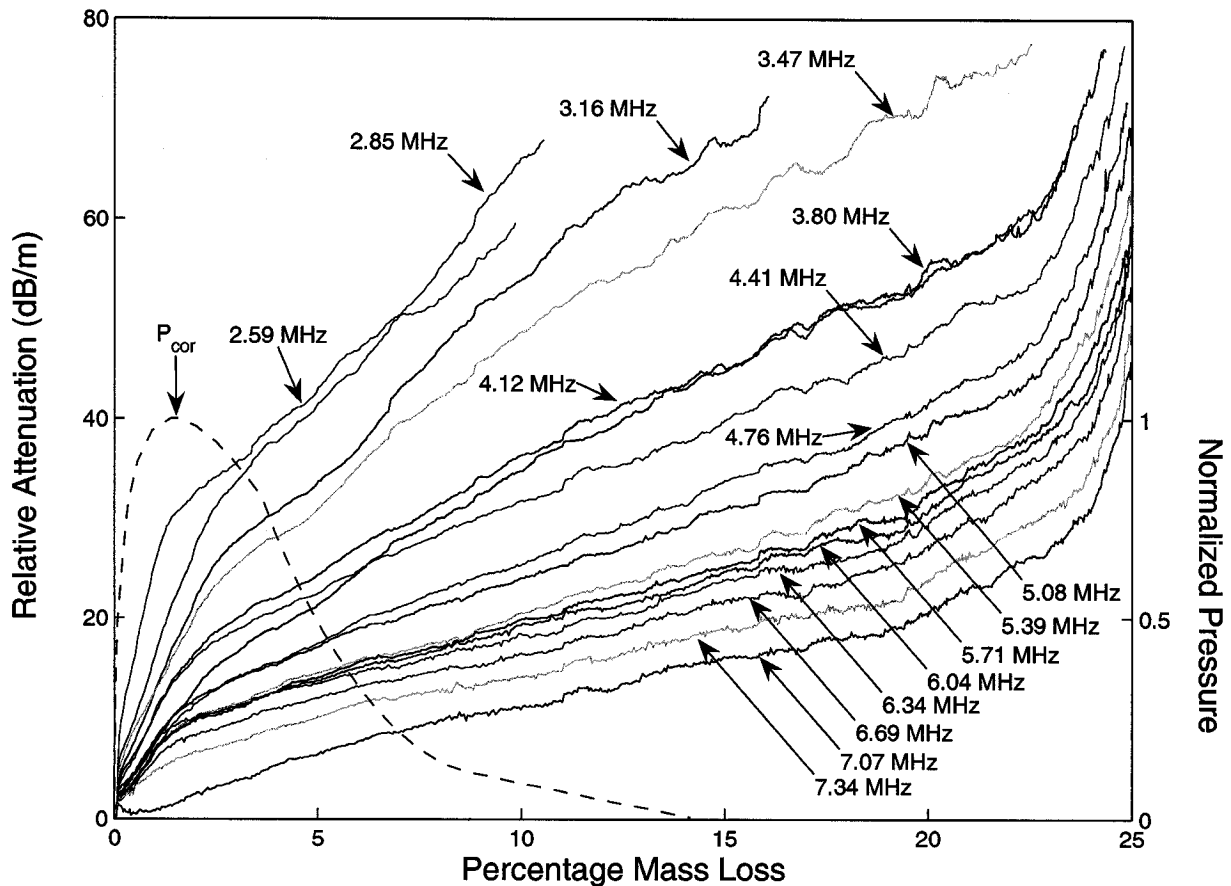
Figure 6.101: Relative attenuation as a function of percentage mass loss for a reinforced mortar specimen undergoing accelerated uniform corrosion. For some low frequencies, the curves end when amplification of the pulser/receiver was taken to the maximum setting and the signal was lost due to noise.

Figure 6.102: (a) Healthy rebar, (b) uniformly corroded rebar (bottom view), and (c) uniformly corroded rebar (side view).

There is a dramatic change in slope in the 20 - 25% range of mass loss. This change in the slope is associated with severe localized corrosion, i.e., pitting, in the rebar (on the entry point into the mortar specimen) on the side where the guided wave was invoked. In other words, the corrosion changed from a relatively uniform corrosion process over the entire length of embedded rebar to a highly localized corrosion process at one location. The attenuation increased dramatically as a result of almost no waveform energy being transmitted past the discontinuity.

209

Relative attenuation obviously requires a baseline measurement for calculation. In the interest of allowing assessment at a later stage of deterioration when a baseline measurement at a healthy stage is impossible, frequencies were compared within the same single cycle pulse over the duration of corrosion. Figure 6.103 shows the calculated amplitude ratio between 5.08 MHz and 6.34 MHz.

Figure 6.103: Calculated amplitude ratio between 5.08 MHz and 6.34 MHz from the same 5.08 MHz single cycle pulse transmitted in a specimen undergoing uniform corrosion.

The higher frequency becomes stronger in amplitude as compared to the lower frequency because more of the energy is centered in the bar. As deterioration occurs, the lower frequency was affected earlier because more of the displacement structure is near the bar surface. While it is unclear whether transducer coupling and/or transducer misalignment will mask this trend on-site, the results are encouraging. Figures 6.104-6.109 provide a time domain, frequency domain, and spectrogram for the specimen at 0%, 1%, 2%, 5%, 10%, and 12% uniform mass loss, respectively. The highpass and lowpass filters were set at 2 and 10 MHz, respectively. The solid and dotted lines are longitudinal and flexural modes, respectively.

210
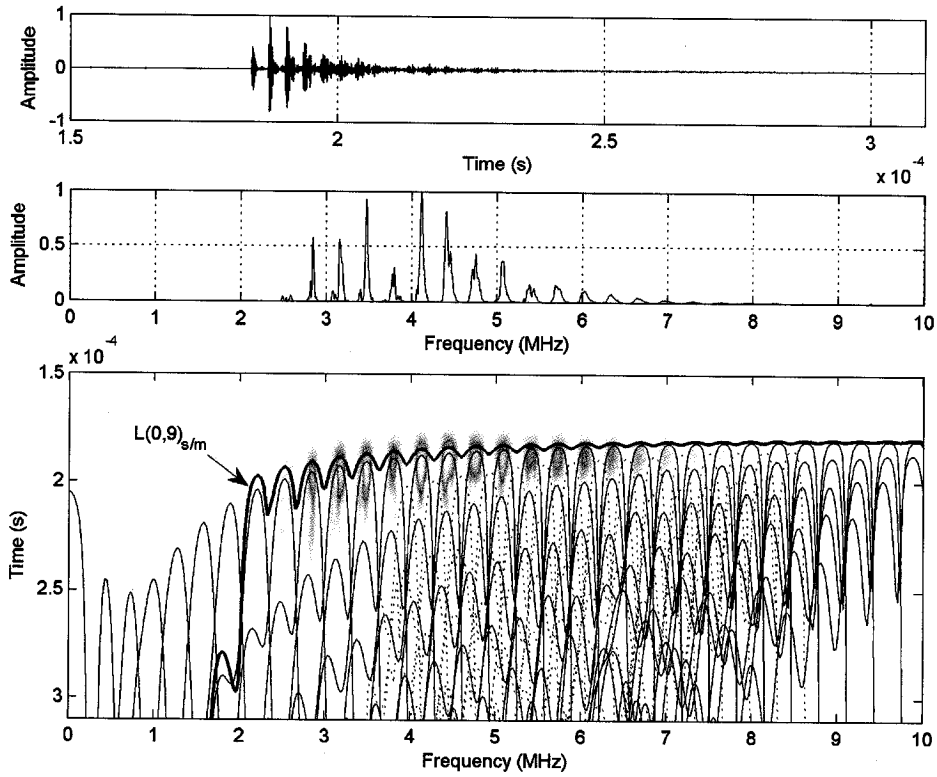
Figure 6.104: A 5 MHz single cycle pulse transmitted (direct arrangement) through rebar (orthogonal ribs) in a specimen that has undergone 0% mass loss from uniform corrosion. The gain was set at 51.8 dB.

Figure 6.105: A 5 MHz single cycle pulse transmitted (direct arrangement) through rebar (orthogonal ribs) in a specimen that has undergone 1% mass loss from uniform corrosion. The gain was set at 54.0 dB.

211

Figure 6.106: A 5 MHz single cycle pulse transmitted (direct arrangement) through rebar (orthogonal ribs) in a specimen that has undergone 2% mass loss from uniform corrosion. The gain was set at 56.8 dB.

Figure 6.107: A 5 MHz single cycle pulse transmitted (direct arrangement) through rebar (orthogonal ribs) in a specimen that has undergone 5% mass loss from uniform corrosion. The gain was set at 61.8 dB.

212

Figure 6.108: A 5 MHz single cycle pulse transmitted (direct arrangement) through rebar (orthogonal ribs) in a specimen that has undergone 10% mass loss from uniform corrosion. The gain was set at 65.8 dB.

Figure 6.109: A 5 MHz single cycle pulse transmitted (direct arrangement) through rebar (orthogonal ribs) in a specimen that has undergone 12% mass loss from uniform corrosion. The gain was set at 69.8 dB.

213

The frequency domain and spectrograms reveal an interesting feature observed in the frequency domain of previous simulated tests (refer to Section 6.4.1) and the rebar with an angled rib pattern. The 'web' frequencies (i.e. those frequencies between the peaks in the frequency domain) increase in signal strength with respect to the peaks again. For uniform mass loss at 2% or greater, these frequencies rise in the normalized frequency domain. Figure 4.21 predicted that there would be no drop off between velocity peaks for a rebar embedded in mortar. However, this behavior was also observed for the corroded bar in air. Figure 6.110 shows a spectrogram for the uniformly corroded rebar tested in air and the uniform corrosion mortar specimen at 8.96% mass loss.
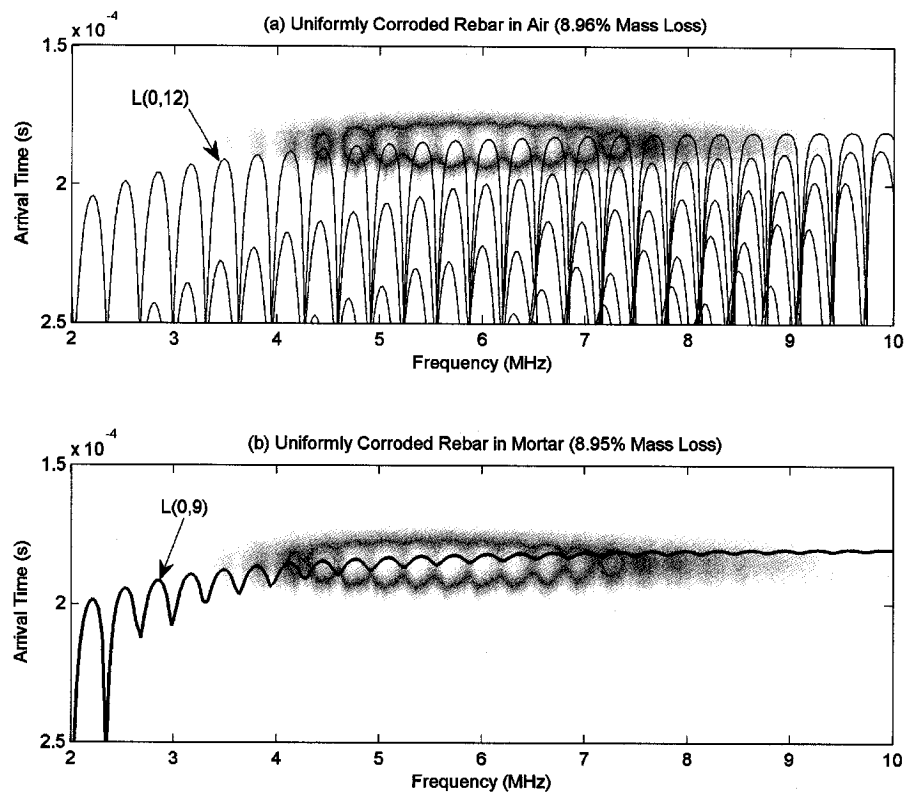
Figure 6.110: Spectrogram for a **(a)** uniformly corroded rebar specimen in air at 8.96% mass loss and **(b)** uniform corrosion mortar specimen at 8.95% mass loss.

The spectral response seems to be the same whether in air or in mortar. Therefore, the 'web' frequencies are not a result of an increase in bond between the steel and mortar. It is thought that as mass loss increases, the bar profile becomes increasingly more non-uniform. As this non-uniformity occurs, scattering, shifts in the peak frequencies, and possible flexural propagation will occur over the entire length of corroded bar giving rise to the 'web' frequencies. This may be a way of distinguishing uniform corrosion damage from localized corrosion damage using a through-transmission setup.

214

6.5.4   MONITORING ACCELERATED LOCALIZED CORROSION WITH THE L(0,9) MODE

Specimens undergoing localized corrosion were monitored using guided mechanical waves at higher frequencies. The same type of specimen and procedure used for uniform corrosion testing was used for testing the effects of localized corrosion on the guided wave behavior, with a few exceptions. The corrosion was focused over the middle 3" (7.62 cm) of the mortar specimen. While this is not the same as pitting corrosion (as simulated in Section 6.4.3), it does provide an example of a more localized corrosion.

The L(0,9) mode was invoked by using 5 MHz Panametrics (model V110) transducers. There were nineteen frequencies (in MHz) invoked between 2.5 and 8.5 MHz (found from system identification described in section 6.5.3): 2.59, 2.85, 3.17, 3.48, 3.78, 4.12, 4.41, 4.76, 5.07, 5.38, 5.70, 6.02, 6.33, 6.64, 6.95, 7.32, 7.64, 7.98, and 8.24. The frequencies were invoked in single and hundred cycle tonebursts and collected in both through-transmission (i.e. pitch-catch) and pulse-echo setups. The results of the toneburst excitations were used to measure relative attenuation. Fig. 6.111 is a three-dimensional graph of the measured relative attenuation as a function of percentage mass loss for all nineteen invoked toneburst frequencies captured in a through-transmission setup. It should be noted that the percentage mass loss in this case is not considered distributed along the entire embedded length as in the previous test. It only serves as an indication of the amount of mass loss that occurs in the localized region of corrosion. Those frequencies that were lost due to a poor signal-to-noise ratio were assumed constant at their last recorded value for this plot. To better illustrate this, a two-dimensional plot of all nineteen frequencies for the entire test is shown in Figure 6.112.

Notice that the signal is only slightly attenuated immediately after corrosion initiation, with the lowest frequencies being the most affected. However, since the corrosion is only occurring over a short length, the response is slight. At approximately 10% mass loss, all of the frequencies begin to rapidly attenuate. Clearly, the localized corrosion affects the waveform signal strength.

215
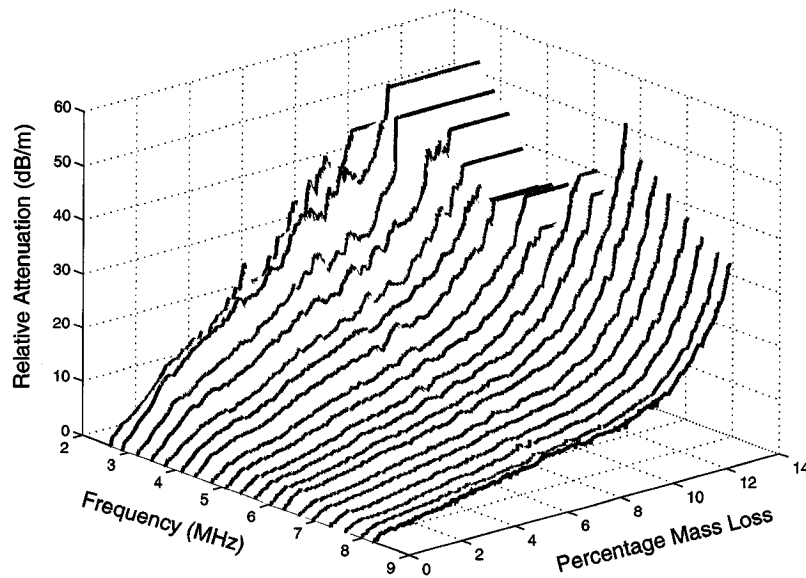
Figure 6.111: Three-dimensional view of relative attenuation as a function of percentage mass loss for all nineteen frequencies invoked using a 100-cycle toneburst while monitoring accelerated localized corrosion.
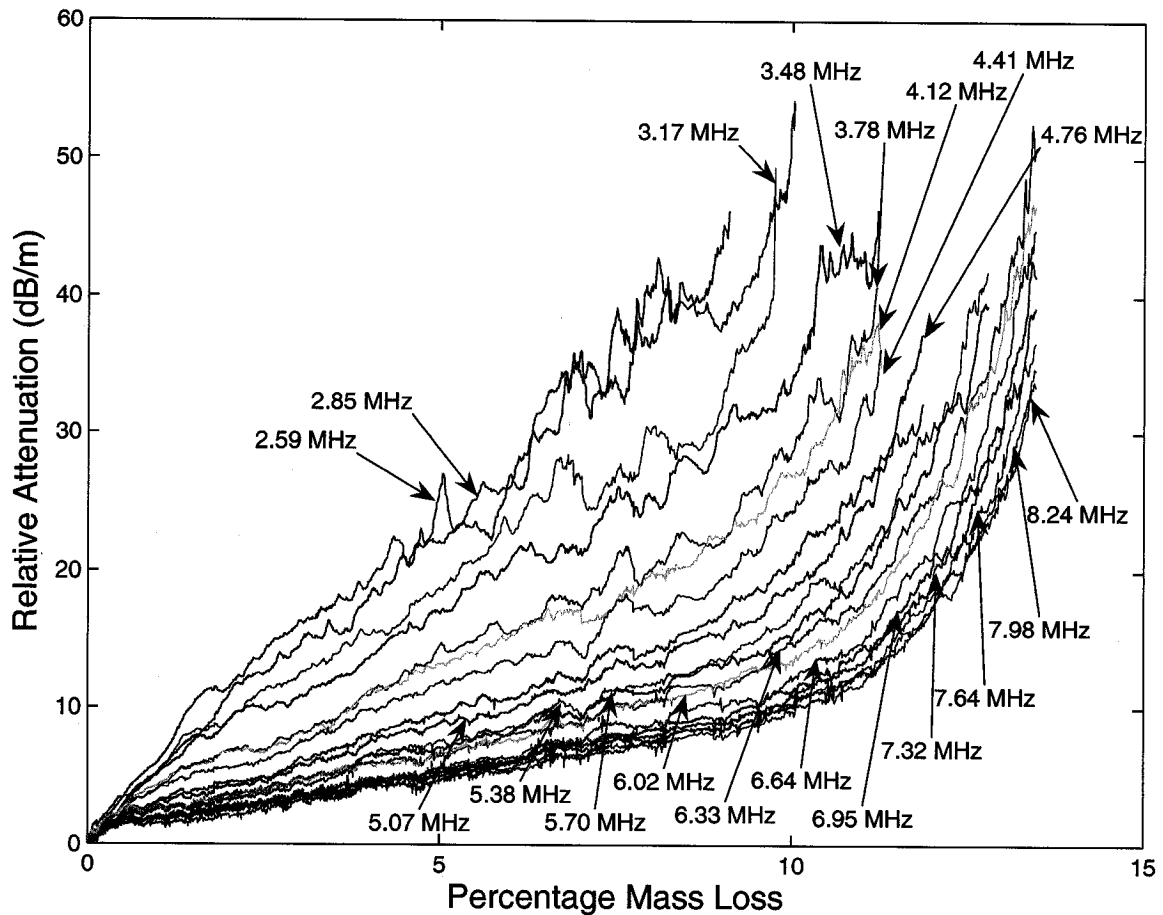
Figure 6.112: Relative attenuation as a function of percentage mass loss for all nineteen frequencies invoked using a 100-cycle toneburst while monitoring accelerated localized corrosion.

The localized corrosion specimen was also monitored in a pulse-echo setup. However, the received pulse-echo waveform remained the same throughout the duration of testing for all nineteen frequencies. As explained previously, when the discontinuity from localized corrosion is 10° or more from being completely perpendicular to the bar axis the waveform reflection is severely attenuated. Fig. 6.113 is a photograph of approximately the middle 7" (17.78 cm) of the localized corrosion bar after extraction from the mortar.

Figure 6.113: **(a)** Healthy rebar and **(b)** localized corrosion rebar (middle section).

There is a distinct tapering effect of the bar diameter, causing mode conversions and scattering of the incident waveform. It seems that through-transmission testing may be the only possible setup for monitoring corrosion in the frequency range tested.

Relative attenuation obviously requires a baseline measurement for calculation. In the interest of allowing assessment at a later stage of deterioration when a baseline measurement at a healthy stage is impossible, frequencies were compared within the same single cycle pulse over the duration of corrosion. Figure 6.114 shows the calculated am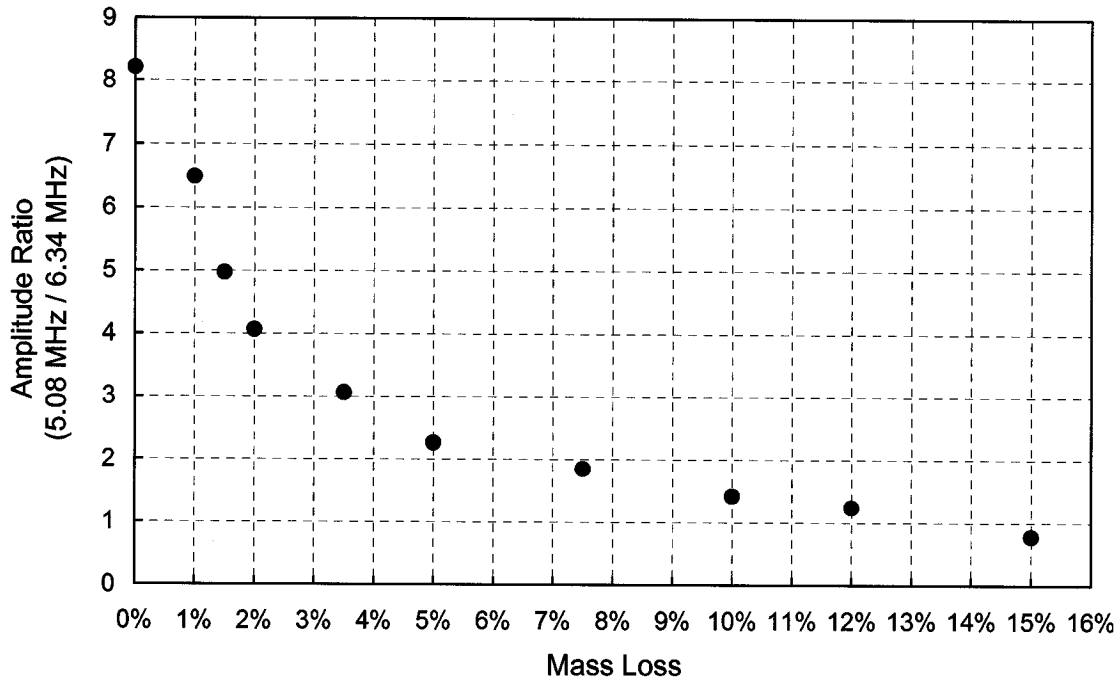plitude ratio between 5.07 MHz and 6.33 MHz. The higher frequency becomes stronger in amplitude as compared to the lower frequency because more of the energy is centered in the bar. As deterioration occurs, the lower frequency is affected more substantially earlier because more of the displacement structure is near the outer surface of the bar. In comparison to Figure 6.103, the ratio for the healthy specimen is less than half. Transducer alignment and coupling most likely leads to this discrepancy. However, for ratios of 2 or lower, both signal significant mass loss. Figures 6.115-6.120 provide a time domain, frequency domain, and spectrogram for the specimen at 0%, 1%, 2%, 5%, 10%, and 12% localized mass loss, respectively. The highpass and lowpass filters were set at 2 and 10 MHz, respectively. The solid and dotted lines are longitudinal and flexural modes, respectively.
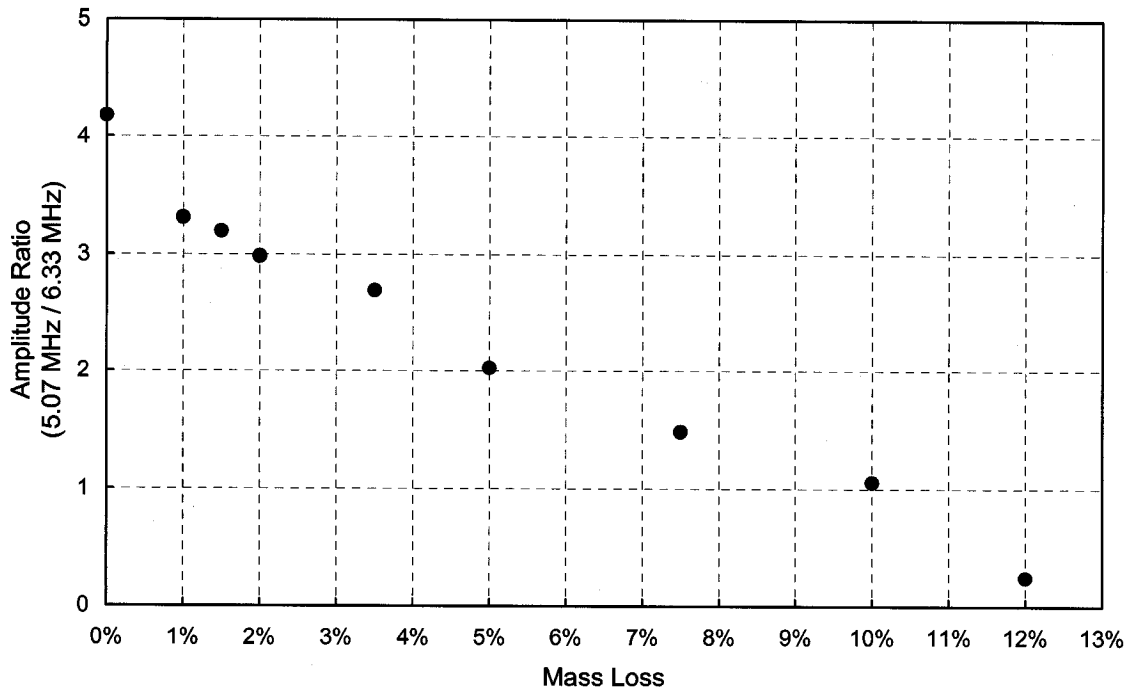
Figure 6.114: Calculated amplitude ratio between 5.07 MHz and 6.33 MHz from the same 5.07 MHz single cycle pulse transmitted in a specimen undergoing localized corrosion.
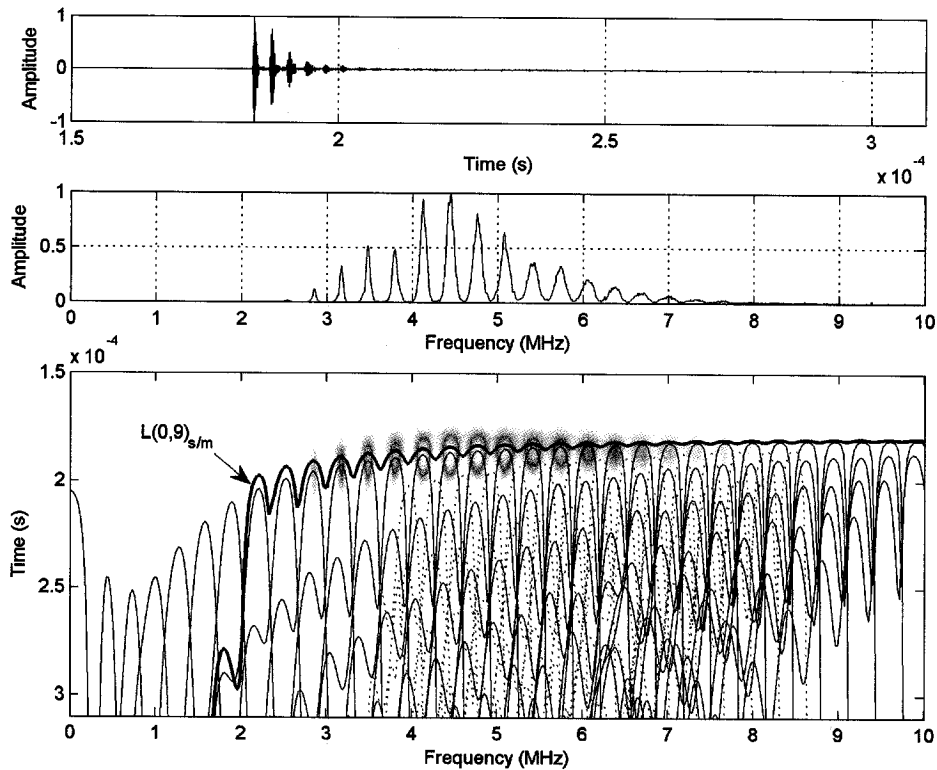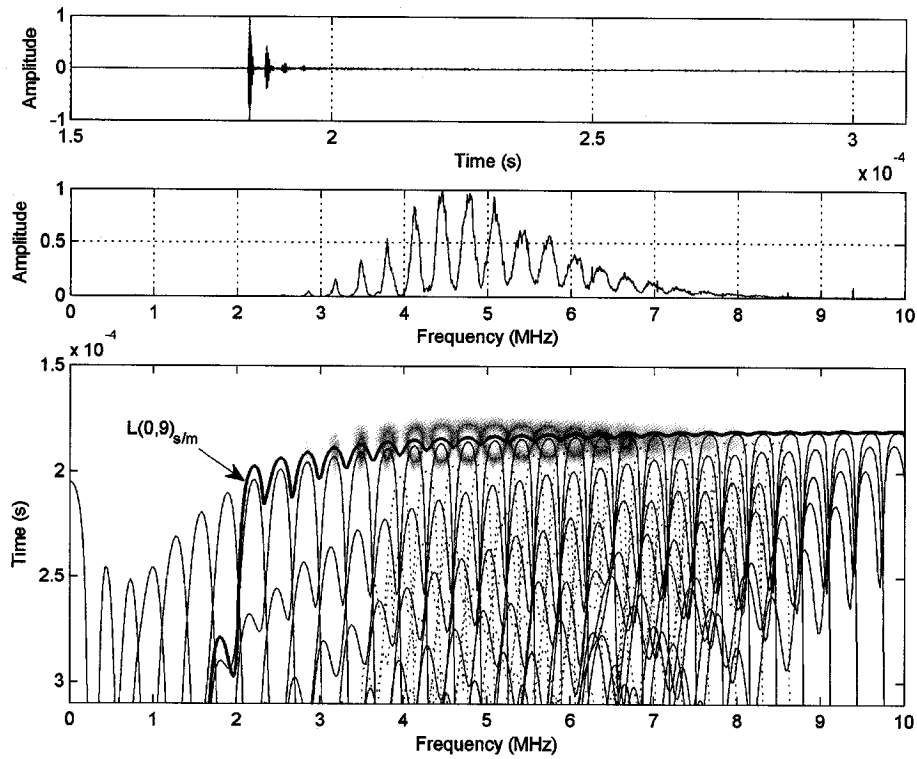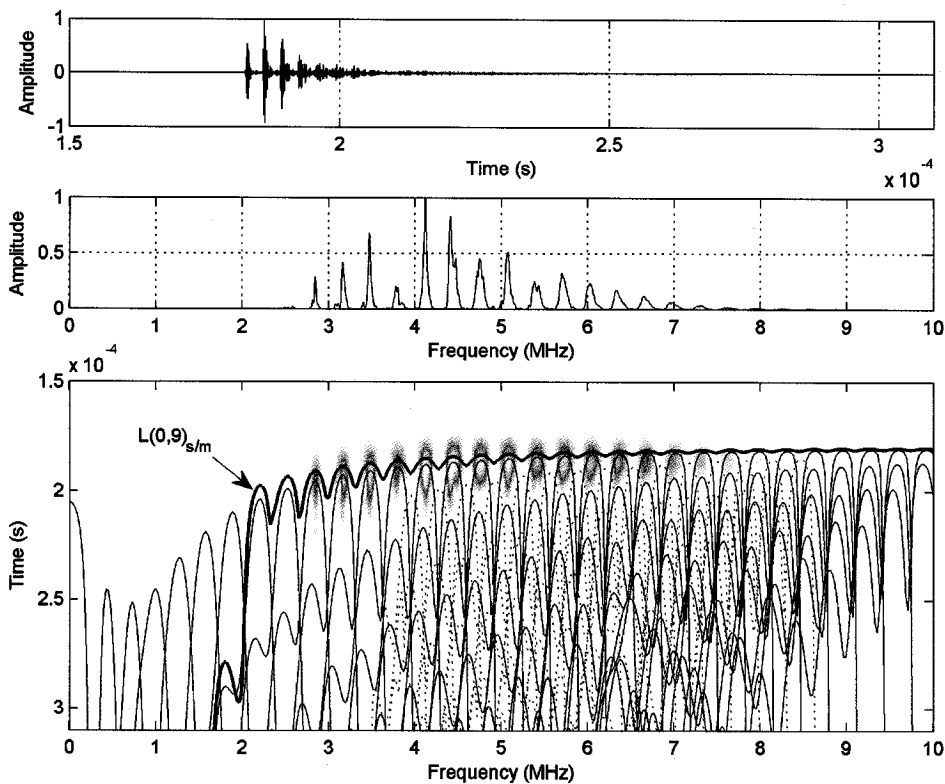

Figure 6.115: A 5.07 MHz single cycle pulse transmitted (direct arrangement) through rebar (orthogonal ribs) in a specimen that has undergone 0% mass loss from localized corrosion. The gain was set at 50.8 dB.
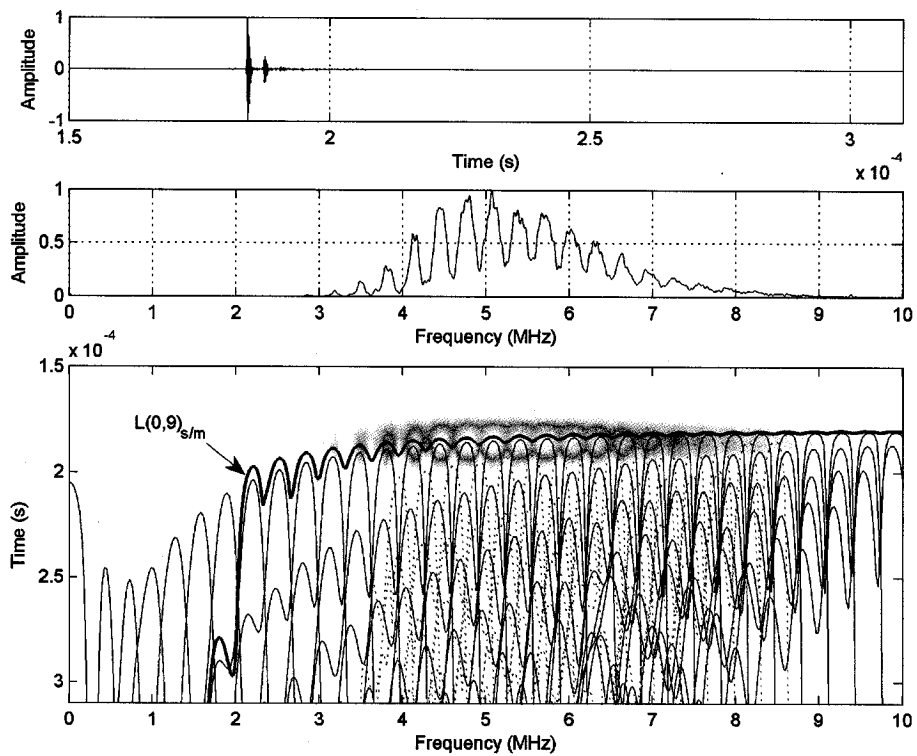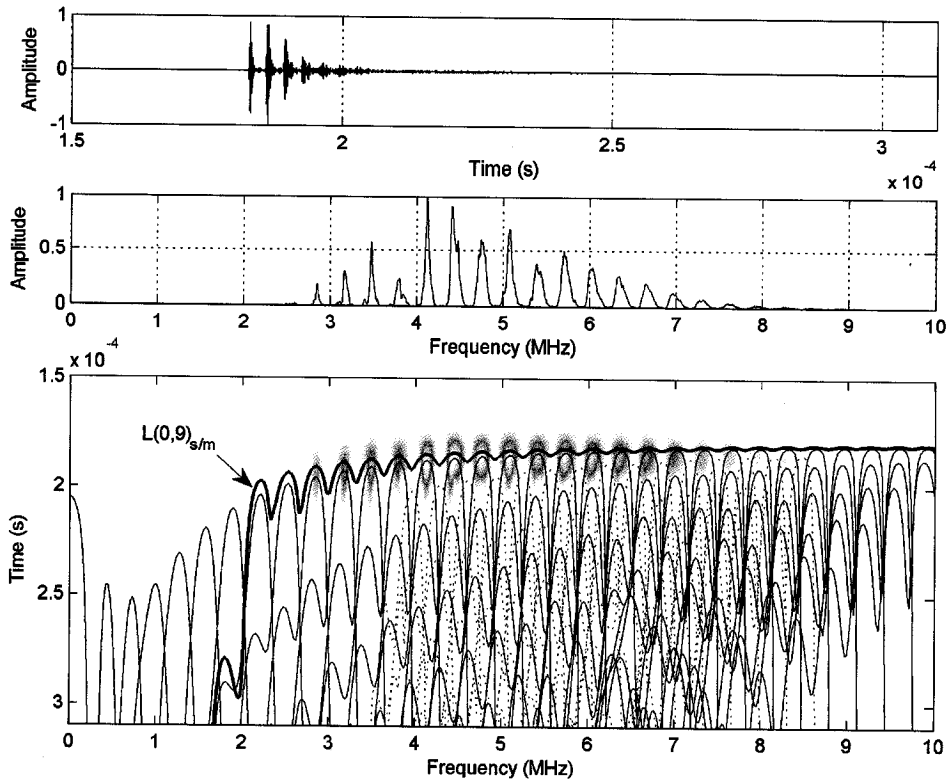
Figure 6.116: A 5.07 MHz single cycle pulse transmitted (direct arrangement) through rebar (orthogonal ribs) in a specimen that has undergone 1% mass loss from localized corrosion. The gain was set at 50.8 dB.
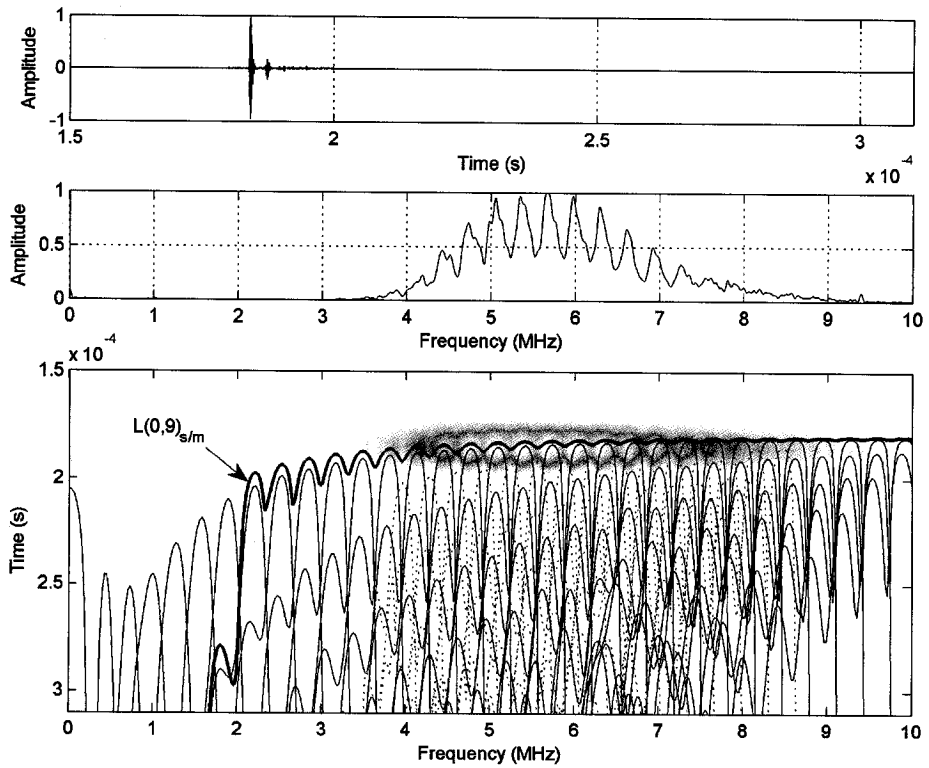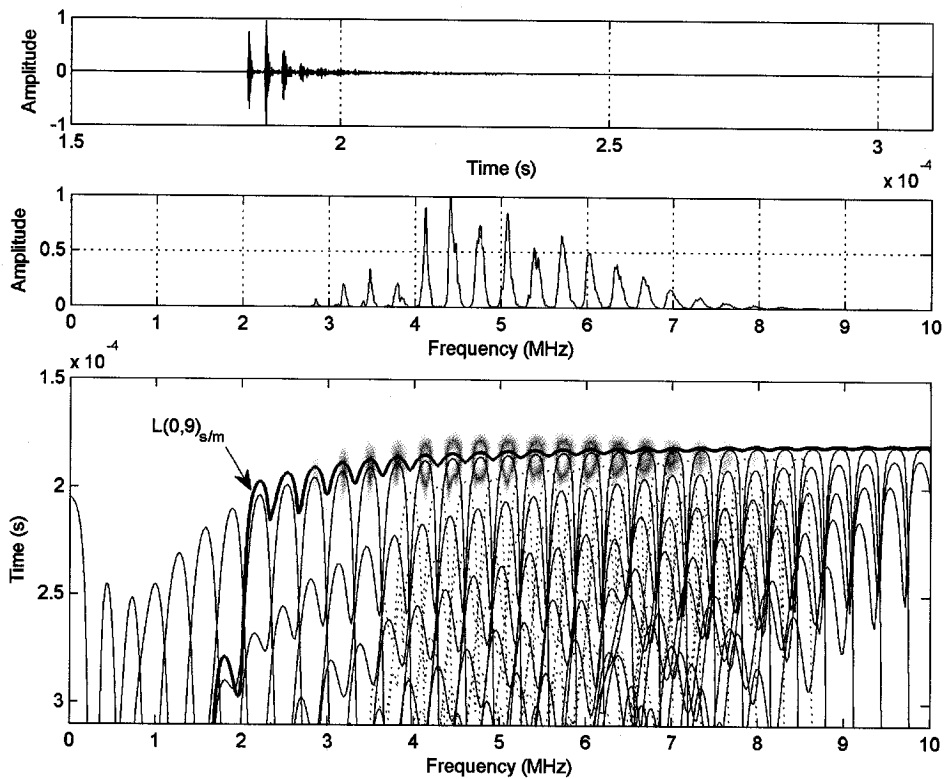

Figure 6.117: A 5.07 MHz single cycle pulse transmitted (direct arrangement) through rebar (orthogonal ribs) in a specimen that has undergone 2% mass loss from localized corrosion. The gain was set at 50.8 dB.
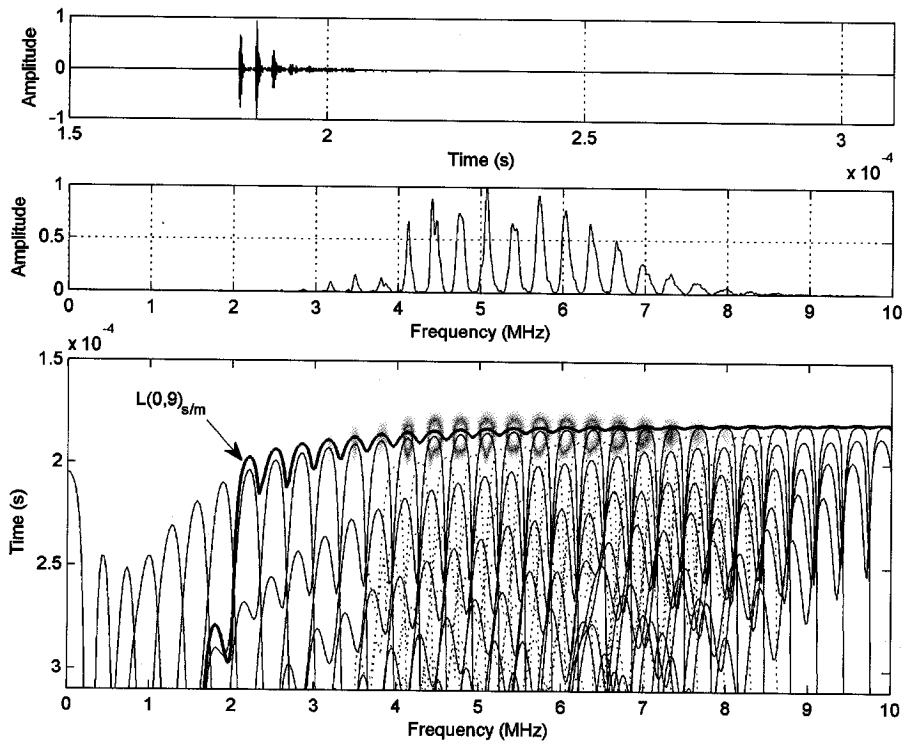
Figure 6.118: A 5.07 MHz single cycle pulse transmitted (direct arrangement) through rebar (orthogonal ribs) in a specimen that has undergone 5% mass loss from localized corrosion. The gain was set at 50.8 dB.
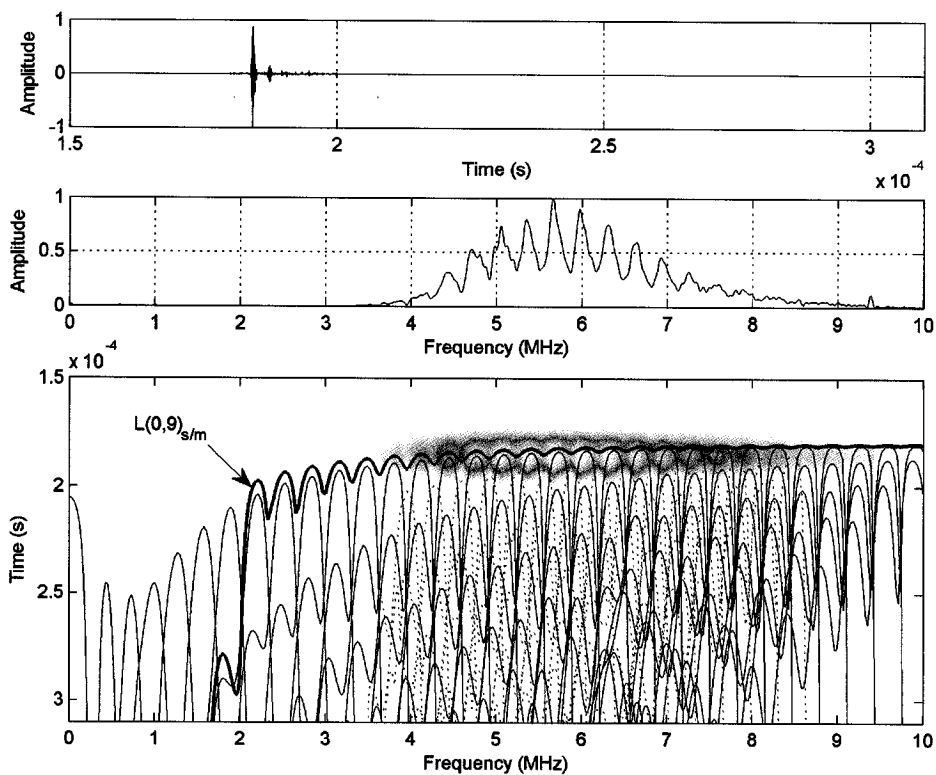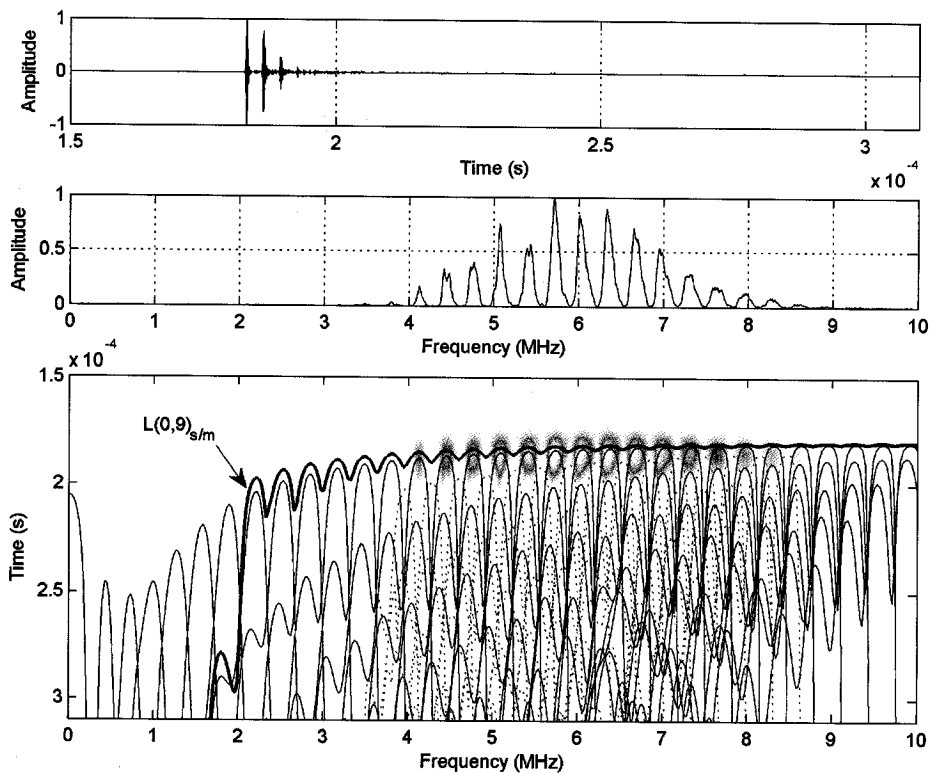

Figure 6.119: A 5.07 MHz single cycle pulse transmitted (direct arrangement) through rebar (orthogonal ribs) in a specimen that has undergone 10% mass loss from localized corrosion. The gain was set at 60.8 dB.
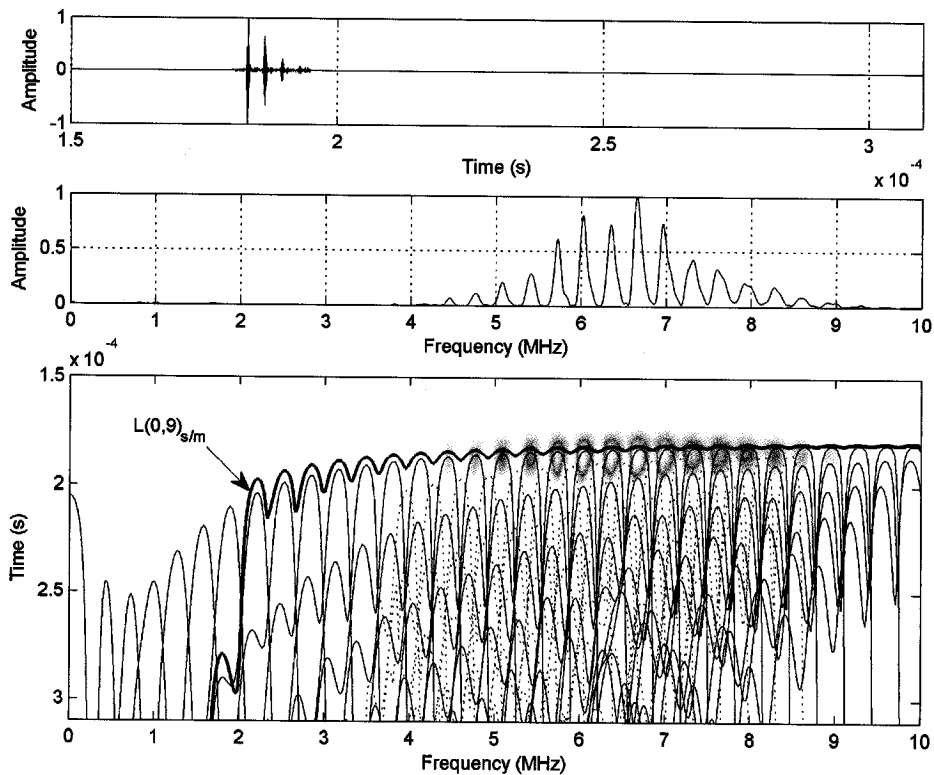
Figure 6.120: A 5.07 MHz single cycle pulse transmitted (direct arrangement) through rebar (orthogonal ribs) in a specimen that has undergone 12% mass loss from localized corrosion. The gain was set at 70.8 dB.

A significant response was not found at the 'web' frequencies for any of the frequency domains, making the results consistent with the simulated pitting experiments.

6.5.5 COMPARISON OF UNIFORM AND LOCALIZED CORROSION RESULTS USING THE L(0,9) MODE

As was shown with toneburst excitations, the relative attenuation levels were comparable for different frequencies invoked for both uniform and localized corrosion. This makes differentiating between uniform or localized corrosion in-situ rather difficult using a through-transmission setup only. A comparison between the uniform and localized corrosion relative attenuation for 7.34 and 7.32 MHz, respectively, is shown in Figure 6.121.

221
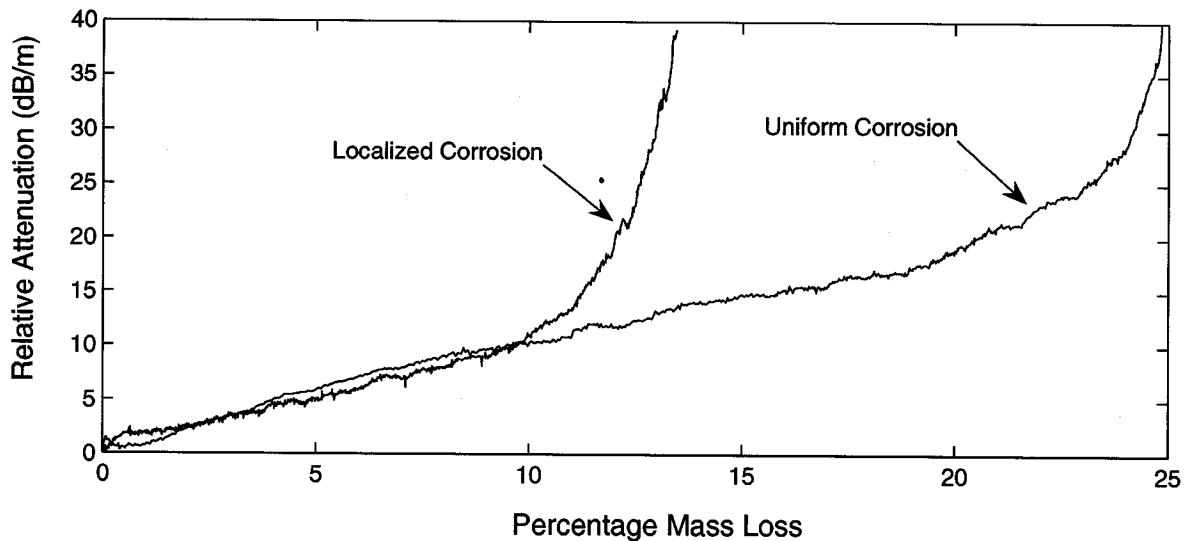
Figure 6.121: Relative attenuation as a function of percentage mass loss for the accelerated localized and uniform corrosion tests. The input signal for the localized and uniform corrosion tests was a 100-cycle toneburst at 7.32 and 7.34 MHz, respectively.

It appears that the relative attenuation for both the localized and uniform corrosion specimens are very close at the highest frequencies. The localized test is essentially a uniform corrosion process over a much shorter duration. The most interesting result is that despite the difference in damage surface area affected by corrosion, the signal strength is affected similarly. The implication is that the minimum diameter between the transducers may be the controlling factor on the relative attenuation. This is a promising result since the minimum bar diameter is a critical design parameter. Notice that for both the uniform and localized tests that there is a rapid increase in relative attenuation at a certain point. Both tests ended when the corrosion process became highly localized (i.e. pitting) to the point of a complete discontinuity. Since the percentage mass loss will not be known for real in-situ measurements, the relative attenuation does not yield enough information to discern whether a uniform or localized corrosion process is occurring. Figure 6.122 shows the frequency domains from a 5.08 and 5.07 MHz single pulse excitation for the uniform and localized corrosion specimens at 0%, 5%, and 10% mass loss, respectively. These points were chosen because the relative attenuation for all three points of mass loss was approximately the same in Figure 6.121. Note that the amplitude, rather than power, is shown in Figure 6.122. The amplitudes have been normalized based on the 0% mass loss specimen for both uniform and localized corrosion damage.

222

Uniform Corrosion Damage

Localized Corrosion Damage
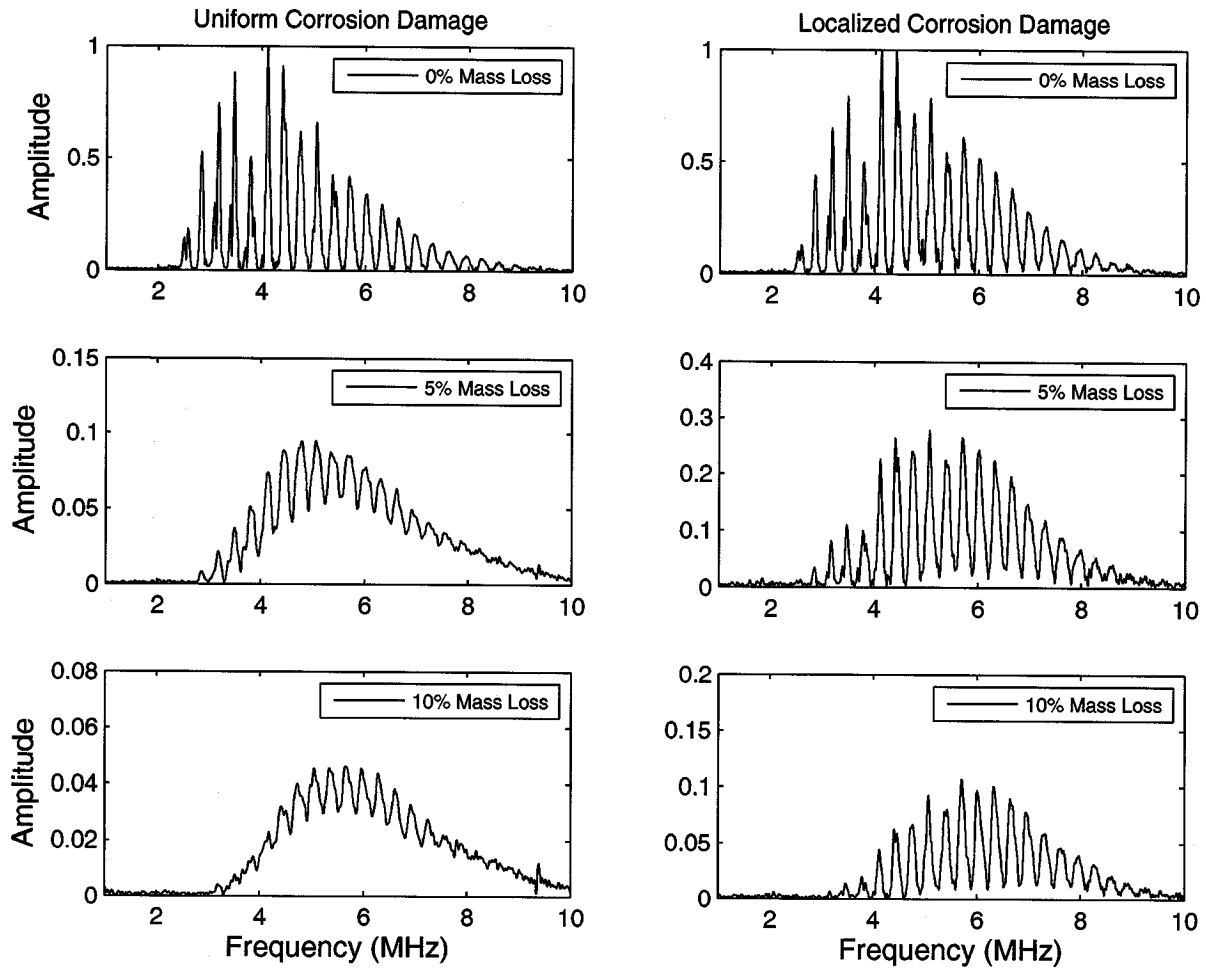
Figure 6.122: Frequency domain for the accelerated uniform corrosion specimen (left) and the accelerated localized corrosion specimen (right) at 0%, 5%, and 10% mass loss. The input signal for the uniform and localized corrosion tests was a single cycle pulse at 5.08 and 5.07 MHz, respectively.

Notice that the response at frequencies between the normalized amplitude peaks start to increase in strength (with respect to the amplitude peaks) as the uniform corrosion level increases. As mass loss increases, the bar profile changes shape significantly. Scattering, shifts in the peak frequencies, and possible mode conversions will occur over the entire length of the corroded bar giving rise to the 'web' frequencies. The same type of frequency response was found for uniformly corroded bars tested in air and embedded in mortar. For localized damage, the 'web' frequencies are only slightly present for 5% and 10% mass loss. Rebar specimens with simulated pits (created from saw cuts) at varying depths were also tested and showed no visible response at the 'web' frequencies. Also notice that the localized corrosion specimen did have a shift to higher frequencies, similar to the uniform corrosion specimen. This shift was not evident in the spectral response of the simulated pitting specimen. The difference is most likely due to the localized corrosion specimen being somewhat of a mixture of uniform corrosion over a limited distance. Figure 6.123 shows a spectrogram for the uniform and localized corrosion tests at

10% mass loss. Notice that 'web' frequencies arrive at approximately the same time as the peak frequencies. This implies that the change in bar surface profile may lead to a shift in the peak frequencies.
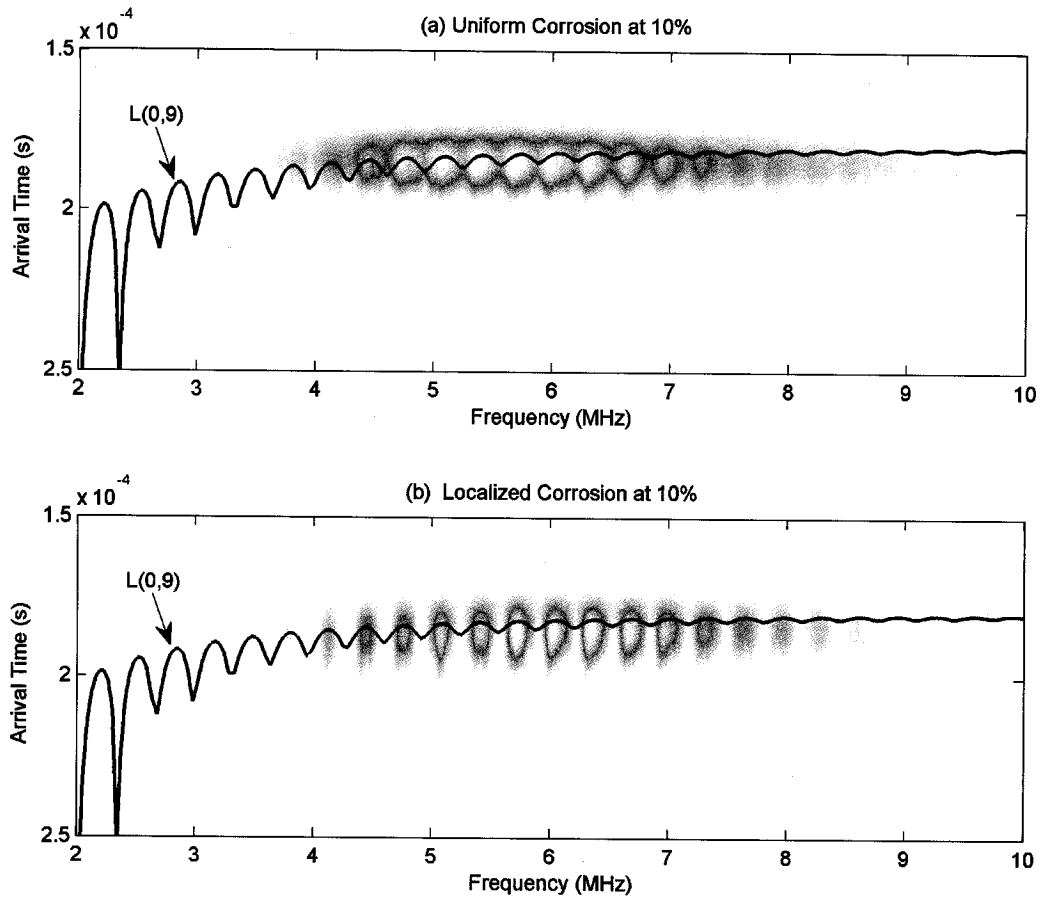
Figure 6.123: Spectrogram for a **(a)** uniform corrosion mortar specimen and **(b)** localized corrosion mortar specimen at 10% mass loss.

224

CHAPTER 7:

CONCLUSIONS

The purpose of this report was to examine guided waves as a viable method for monitoring corrosion in reinforced concrete. Several guided wave experiments have been presented and discussed involving environmental issues, simulated corrosion, and actual corrosion. The results are very promising, but more work needs to be done before a reliable monitoring method is achieved. A summary of the guided wave testing presented in this report is provided in 7.1, while recommendations for future work are provided in Section 7.2.

A general review has been provided in this report on how the corrosion process occurs, structural implications, modeling the corrosion process, alternative nondestructive methods for monitoring corrosion in reinforced concrete, and guided mechanical waves. The purpose of these reviews was to examine the state-of-the-art on providing adequate reliability to reinforced concrete structures with respect to corrosion deterioration and to bring the reader up to speed on the multidisciplinary topics discussed.

7.1 SUMMARY OF GUIDED WAVE TESTING

In Chapter 4, propagation modes for rebar embedded in mortar were chosen for further investigation based on their predicted propagation behavior. The low frequency modes, i.e. $L(0,1)$ and $F(1,1)$, were chosen for a few reasons. First, the modes are more easily distinguishable based on the difference in their energy velocities and the lack of other modes in the frequency range invoked. Second, the modes are sensitive to interface conditions, possibly allowing for the bond level and surrounding mortar deterioration to be monitored. Third, the attenuation is not so high that realistic propagation distances could not be realized. A high frequency mode, i.e. $L(0,9)$, was also selected for investigation. The $L(0,9)$ displays mode-crossing behavior, allowing for this mode to be tracked over a very large frequency range. It is the most easily distinguishable mode because it is the fastest propagating and has the lowest attenuation in the entire system. The $L(0,9)$ mode lacks sensitivity to interface conditions over a large portion of the invoked frequency range, making it desirable for monitoring bar profile deterioration. It was idealized that an in-situ monitoring system would invoke several modes at many different frequencies to monitor many aspects of the deterioration process.

The effect of the reinforcing ribs, water, and mortar need to be better understood in order for the modes to be used. Since rebar is widely used in the construction industry and was recommended for further testing in previous work [23], it was chosen as the waveguide. Deformations, or ribs, are obviously present

225

along the entire length. The effect of the ribs (and different rib patterns) on guided wave behavior needed to be better understood. The effect of water surrounding the bar was examined because of its presence in the corrosion process. Reinforced concrete structures in the marine splash zone have some of the highest corrosion rates. When cracks are present, either from the corrosion product accumulation or other durability issues, water has a quicker pathway to the surface of the rebar. To try and better understand how the presence of water would affect the different modes chosen, water testing was conducted. Finally, the effect of mortar surrounding the bar was examined. While theoretical predictions were calculated as to how the modes would be affected, experiments were needed to better understand the change in mode characteristics.

Testing showed that the reinforcing ribs do affect the guided wave behavior in certain frequency ranges. When the wavelength is much longer than the characteristic dimension of the rib, the guided wave is less affected. At much higher frequencies, where most of the wave displacement structure is concentrated at the center of the bar, the guided wave is less affected. Between these two regions, the reinforcing ribs have a significant effect on guided wave propagation. More theoretical and experimental work is necessary to fully understand the limitations of monitoring cylindrical waveguides with deformation patterns.

Testing confirmed the effect of the rebar being immersed in water was close to the theoretical prediction. The F(1,1) mode was shown to be the most sensitive to water. One interesting feature of the F(1,1) mode is that the phase velocity increases from zero at zero frequency (refer to Figure 4.9). If testing is conducted on the F(1,1) mode below 28.4 kHz (for the particular bar used in this report), the phase velocity is below the bulk compressional velocity of water and wave energy does not leak. The L(0,1) mode has some sensitivity to water over the frequency range tested, with attenuation increasing with frequency. However, as predicted, the L(0,1) mode is not as sensitive as the F(1,1) mode. The lowest frequencies tested for the L(0,9) mode showed sensitivity to water. However, the higher frequencies showed diminished sensitivity.

Testing showed that the low frequency theoretical attenuation prediction for a bar in mortar was a significant overestimation of the attenuation level. The F(1,1) mode has the greatest difference between the theoretical and experimental curves. The F(1,1) mode has attenuation values close in magnitude between being immersed in water and being embedded in mortar over the tested frequency range. This is not a positive feature since water will be present in most structures and could mask deterioration. The difference between the theoretical and experimental curve was found to be less for the L(0,1) mode.

226

However, the attenuation level was still rather high, making monitoring over relatively short distances (e.g. 1 meter) in well-bonded reinforced mortar difficult. The theoretical curve for the L(0,9) mode overestimated attenuation as well. However, the change in attenuation between a bar in air and a bar in mortar is so small that the differences are insignificant at higher frequencies. The attenuation of the L(0,9) mode after the mortar is poured is only significant at the lowest frequencies tested. Even then, the attenuation is much smaller than the L(0,1) or F(1,1) modes for the frequency ranges tested.

Testing was conducted on rebar specimens extracted from accelerated corrosion tests. It was difficult to take away any sort of quantitative information from this testing since transducer coupling created differences in the measured response. However, the tests revealed qualitative information about the modes' sensitivity to bar damage alone. For uniform corrosion, the L(0,1) mode was not substantially affected in frequencies below 200 kHz. However, scattering is observed in the spectrograms as the percentage mass loss increases. The F(1,1) mode showed some sensitivity at very low frequencies to increases in damage, especially with the specimen that underwent both uniform and localized damage. It is thought that the lowest frequencies have a strong reflection from the pit as discussed in Chapter 5. A strong response for the F(1,1) mode around 80 kHz was found for all of the corroded specimens, with some observable scattering. Testing conducted with the L(0,9) mode yielded the most promising results from the corroded bar testing. For low corrosion damage to the rebar, there was no observable spectral response between the frequency domain peaks. The spectral response between the frequency domain peaks, referred to as "web" frequencies, started to increase as the corrosion level increased. It is thought that these frequencies gained signal strength with respect to the peak frequencies from shifts in the peak frequencies caused by the non-uniform heterogeneous bar profile, scattering, and possibly mode conversion. This will be discussed again with uniform corrosion monitoring using the L(0,9) mode, with implications towards differentiating uniform corrosion from localized corrosion.

Testing on reinforced mortar specimens with simulated debonding showed that the low frequencies were sensitive to the level of bond. Bond changes that occur from corrosion can be due to the corrosion product accumulating between the steel and concrete, causing an increased level of bond. The concrete could split from the pressure and cause changes to the bond not only along the length of the rebar, but also along the circumference. While the simulated debonding specimens do not model these issues, they serve as a baseline for comparisons between modes. It seemed that qualitatively the magnitude of the L(0,1) and F(1,1) modes increased as the level of bond decreased. The waveforms took on a completely different shape from a healthy mortar specimen to more substantial debonding. The signal arrives later with substantial scattering for high bond levels. As the bond level decreases, the signal arrives earlier and

takes the shape of the invoked wave packet. However, tracking these modes over the entire range of bond for the specimen size used in this report proved difficult. The results indicated that at higher levels of debonding, the L(0,1) and F(1,1) signals started to appear and increase in strength as the level of contact decreases. This is to be expected from the mortar hydration testing conducted. However, the mortar hydration test was over a shorter distance that would most likely not be feasible for in-situ monitoring. The debonding specimens were one way of assessing the feasibility of these modes over longer distances. The results indicate that the F(1,1) mode may allow monitoring healthy bond and low levels of debonding while the L(0,1) mode can monitor bond later in the deterioration process. This is a result of the F(1,1) mode having less attenuation than the L(0,1) mode for a bar embedded in mortar. However, once debonding does start to occur, the in-flux of water may make the F(1,1) mode a poor choice for further monitoring. This was expected from the theoretical curves shown in Chapter 4. Mid-range frequencies were also tested on the debond specimens. By comparison of the L(0,5) and L(0,8) modes, a correlation was made to the level of bond. Corrosion monitoring was not conducted using these modes for this report due to their high sensitivity to ribs, water, and mortar. However, they may provide information for an in-situ monitoring effort and further testing is recommended.

Higher frequency testing did not provide an adequate measure for the level of bond in the specimen set. While the lowest frequency tested in this range (i.e. 2.59 MHz) showed sensitivity to the mortar in the mortar hydration experiment, it was not as evident for the simulated debonding specimen set. It is thought that the variability from specimen to specimen and the recoupling of the transducers cause the attenuation changes to be masked.

Specimens with localized damage were created and tested using higher frequencies only. A rebar specimen was monitored using guided waves while a grinding saw was used to cut through the middle of the bar. The experiment showed that the signal strength was reduced for all frequencies, with the 'web' frequencies not gaining strength in comparison to the peak frequencies in the spectral response. Guided wave testing on the uniformly corroded bars showed that the signal strength was reduced for all frequencies (with the lowest frequencies more heavily affected), and that the 'web' frequencies gained strength in comparison to the peak frequencies in the spectral response. This finding was important, because it provided an indication that through-transmission testing could possibly differentiate uniform corrosion from localized corrosion.

Reinforced mortar specimens were created with the localized damage in the rebar. The results show that similar guided wave behavior is observed for the bar with localized damage embedded in mortar as for

the bar with localized damage in air. Reflections were observed from the completely cut specimen, the thin notch specimen, and the longer notch specimen with angled cut sides.

The L(0,1) mode was invoked in reinforced mortar specimens undergoing accelerated uniform corrosion. For the specimen size used in this study, the L(0,1) mode was not detectable in the time domain until around 3% mass loss. In the early stage of corrosion (<3% mass loss), it is thought that the F(1,1) mode and other later arriving waveforms were received. The signal is attenuated as the corrosion product initially accumulates between the steel and mortar. The corrosion product created a higher bond level (i.e. increase in coupling), causing wave energy to leak out of the bar into the surrounding mortar at a higher rate. After the pressure reaches an apex and cracking extends towards the cover, the signal begins to gain strength. Once the crack reaches the mortar cover, debonding starts to occur on portions of the bar surface. The reduction in the surrounding mortar stiffness and the decrease in bond results in the L(0,1) becoming clearly detectable and gaining signal strength for more advanced mass loss. The results indicated that the attenuation of the waveform is closely related to the pressure caused by the corrosion product accumulation.

The F(1,1) mode was invoked in reinforced mortar specimens undergoing accelerated uniform corrosion. Unlike the L(0,1) mode, the F(1,1) mode was detectable in the time domain from the outset of testing for the specimen size used. However, the arrival time was slower than the modeling predicted. As with the L(0,1) testing, the F(1,1) mode is attenuated as the corrosion product initially accumulates between the steel and mortar. However, once cracking begins to occur the signal does not rapidly gain strength as did the L(0,1) mode. Chapter 4 sensitivity analysis showed that the F(1,1) mode increases in attenuation with a reduction in stiffness of the surrounding mortar. However, the F(1,1) mode will decrease in attenuation as debonding occurs. The F(1,1) was also shown to be sensitive to water and the wetting of the mortar in the frequency range used for testing. It is thought that the combination of these factors makes the F(1,1) mode in the frequency range tested unreliable for monitoring changes in the bond level between steel and mortar (or concrete).

The L(0,9) mode was invoked in reinforced mortar specimens undergoing accelerated uniform corrosion. The results indicated that the L(0,9) is sensitive to the bar profile deterioration sustained during uniform corrosion. An interesting result was that the lowest frequencies were the most sensitive to the damage, while for almost every higher frequency peak the sensitivity lessened. This is explained by the lower frequencies invoked having more energy at or near the bar surface. As the deterioration ingresses from the bar surface towards the bar center, the frequencies with more mode energy at the corrosion depth were

more sensitive to the deterioration. Another interesting feature of the testing was that the 'web' frequencies increased in the same manner as shown in the spectral response from corroded bars tested in air (discussed earlier).

The L(0,9) mode was invoked in reinforced mortar specimens undergoing accelerated localized corrosion as well. The through-transmission test results show that the L(0,9) is sensitive to the bar profile deterioration sustained during localized corrosion. Again, the lowest frequencies were the most sensitive to the damage, while for almost every higher frequency peak the sensitivity lessened. The pulse-echo testing showed no detectable reflection from the local bar damage. The difficulty is that there are significant drops in signal strength as the angle of discontinuity increases by 10° or more from a perpendicular break. However, the 'web' frequencies were barely observable, similar to the simulated pitting results. Since the attenuation levels for the L(0,9) through uniform and localized corrosion specimens are at comparable rates, the 'web' frequencies show promise to help differentiate uniform corrosion from localized corrosion.

7.2 RECOMMENDATIONS FOR FUTURE WORK

The ultimate goal of this research is an embeddable ultrasonic sensor system capable of monitoring corrosion in reinforced concrete. It is thought that nondestructive monitoring, coupled with service life modeling, may provide a cost-effective solution for ensuring public safety. As discussed in detail, models are available for both the initiation and propagation periods. It is suggested that these models be used from the outset as predictors of service life, with constant updates from the sensor system. There is still a copious amount of work that has yet to be completed before an embeddable ultrasonic monitoring system is realized. A few of the foreseeable steps towards procurement of the sensor system are given below:

- Experimental testing of a beam with stirrups, multiple reinforcing bars, and other local reinforcement.
- Examine the effects of multiple wet/dry cycles, temperature changes, and humidity changes.
- Experimental testing of reinforcement embedded in concrete with varying mix designs.
- Experimental testing of rebar with different diameters and strand specimens.
- Creation of a prototype sensor unit capable of being embedded in concrete. Piezoelectric, magnetostrictive, and electromagnetic acoustic transducers (EMAT) could be tested in order to examine problems associated with transducer coupling, power requirements, and cost.
- Finite element modeling of guided mechanical waves in reinforced concrete undergoing corrosion.

APPENDIX A:

METHODS FOR DETECTION, EVALUATION, AND MONITORING OF CORROSION IN REINFORCED CONCRETE

There are three main parameters of interest for monitoring corrosion in RC structures: the location of corrosion, extent of damage, and the rate of the corrosion reaction. The location of corrosion allows for quick, accurate, and cost effective rehabilitation efforts. The extent of damage can include the amount of mass loss, interfacial damage, or destruction to the surrounding concrete. Quantification of the extent of damage allows for assessment of whether rehabilitation efforts are necessary and if so, what type. Determining the rate of the corrosion reaction allows for an estimation of how much service life a structure has left before rehabilitation and/or intervention using other methods (e.g., cathodic protection systems, and chloride removal) is necessary. One could tear an entire structure apart and ascertain all three parameters in great detail. The interest lies in finding methods that allow for quick, accurate, and cost-effective determination of corrosion parameters in RC structures without hindering their status as viable structures. Figure A.1 is an illustration of a variety of methods used for nondestructive evaluation of corrosion parameters in reinforced concrete.

Nondestructive Methods for Evaluation of Corrosion Parameters in Reinforced Concrete

Human Inspection	Electrochemical	Electromagnetic	Mechanical
Visual Inspection	Corrosion Potential	Electrical Time Domain Reflectometry (ETDR)	Impact Echo (IE)
Crack Width Measurement	Polarization Resistance	Infrared Thermography (IR)	Chain Drag
	AC Impedance Method	Ground Penetrating Radar (GPR)	Acoustic Emission (AE)
	Polarization Curves	Magnetic Flux Leakage (MFL)	Strain Gages (SG)
	Macrocell Techniques	Radiography	Dynamic Testing
	Potentiostatic/Galvanostatic Measurements	Fiber Optics	Ultrasonic Tomography
			Ultrasonic Waveguides

Figure A.1: Nondestructive methods for evaluation of corrosion in reinforced concrete.

The methods listed in Figure A.1 are generally used for evaluation of the propagation period in the corrosion process. While there are several methods also used for evaluation of the initiation period (e.g. conductivity measurements, pH measurements, chloride measurement), they are not reviewed within this text. The review of methods for evaluation of the propagation period is not meant to be exhaustive. It is merely meant to illustrate many of the methods that are currently available or under investigation. Not all methods and/or derivative of methods could be included for length considerations.

A.1   HUMAN INSPECTION

Human inspection is one of the oldest and least expensive forms of corrosion detection in reinforced concrete structures and is the first step to any investigation [130]. A trained and skilled inspector can provide a highly reliable method of structural evaluation. However, many results are obviously prone to human error from fatigue and lack of training. A few types of human inspection methods are discussed.

A.1.1   VISUAL INSPECTION

One uses the human eye to look for surface damage such as rust staining, cracking, and spalling. Spalled concrete is sometimes weighed to have a relative measure of the amount of concrete degradation. Using spalled concrete as a form of measurement for concrete deterioration is not always an option. For instance, concrete should not spall off onto the highway or onto spectators at a stadium. One can also measure the crack width at the surface to quantify the amount of steel cross-section loss [131]. If corrosion areas are suspected hidden beneath the concrete, other methods of assessment can be used to assess the situation more accurately.

One major drawback to visual inspection is that there is a delay between when damage can be seen at the surface of a structure and when it is actually occurring. There is generally a 5-year time lag between corrosion initiation and visible evidence at the surfaces of bridge decks [132]. With pitting corrosion, there may never be visual signs of distress at the surface. In a study comparing nondestructive methods for bridge deck assessment, there were significant delaminations in the bridge chosen for inspection (and confirmed using core samples) but no visible signs at the surface [133].

Visual inspection also relies heavily on the experience of the inspector. Fatigue of the inspector can affect results. Rust staining can be caused by iron aggregates intentionally mixed into the concrete. Cracking and spalling can be attributed to freezing and thawing of the concrete, shrinkage, and overloading. Therefore, visual inspection should almost always be accompanied by more in-depth testing to ensure a thorough structural inspection. Despite the drawbacks, visual inspection is almost always the method that is chosen to start an inspection of a structure or confirm results from other NDT methods. In 1992, the Seattle Kingdome was inspected using impact echo and infrared thermography but visual inspection was used to validate the results [134]. An extensive Colorado bridge survey was undertaken, with visual inspection used to mainly identify corrosion-damaged areas [135]. The Algiers airport, a 20 year old Kuwait structure, and a Bridge in Illinois was inspected using a variety of NDT methods but were first inspected visually [136-138]. These are just a few examples of the wide use of visual inspection in detection of corrosion in RC structures.

232

A.1.2 CRACK WIDTH MEASUREMENT

Cracking occurs from rust product accumulation at the steel/concrete interface, eventually leading to surface cracks. From previous studies, it seems that the concrete cover to bar diameter ratio and the bar diameter itself is a critical factor in determining crack initiation [139]. However, once the crack has initiated the concrete cover to bar diameter ratio and the bar diameter was reported as having no effect on the crack width growth as a function of steel cross-sectional loss [131]. The steel cross-sectional loss seems to have a linear empirical relationship to crack growth. Models to correlate crack width to steel cross-sectional loss have been formulated and were discussed in Section 3.3. Figure A.2 shows the relationship between crack width (w) and steel cross-sectional area loss ($\Delta A_s - \Delta A_o$) for two reinforced concrete beams.
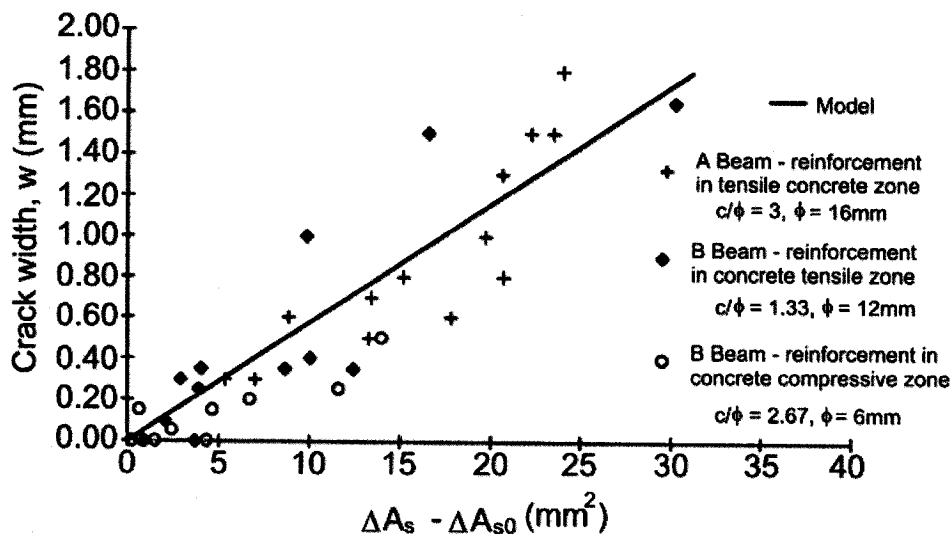
Figure A.2: Crack width as a function of steel cross-sectional area loss for RC beams (extracted from [131]).

The method is advantageous due to its low cost of measurement. However, the method is highly empirical in nature. Surface cracks may not appear until later stages of deterioration or never at all in the case of severely localized corrosion. Cracks from other forms of degradation may be confused with cracks formed from corrosion degradation. Extensive testing is needed to show how a range of rebar diameters, cover depths, porosity, location and concrete mixes affect the empirical model.

A.2 ELECTROCHEMICAL METHODS

Electrochemistry is the study of chemical reactions that involve electrons as reactants and/or products. The corrosion of steel in reinforced concrete is an electrochemical process. The methods discussed in this section deal with measurements of the potential, current, and/or the electrical resistance of the system.

A.2.1 CORROSION POTENTIAL

As the corrosion reaction takes place, electrons are transferred from the anodic location to the cathodic location via the rebar. Ions are transferred through the pore solution at the rebar/concrete interface. From this corrosion reaction, electric fields are created in the concrete that can be measured at the concrete surface. The measurement of this electric field is the basis of the corrosion potential method for RC structures. This is also referred to as open-circuit potential (OCP) or the half-cell potential method. This is one of the most commonly used methods, besides visual inspection, of corrosion detection for field-testing and laboratory testing. Many times the performance of the half-cell potential method is used as a baseline for measuring the performance of other detection methods [140-145], the effectiveness of corrosion inhibiting systems (i.e. admixtures) [146-155], concrete mixes [156,157], rebar coatings [158-162], and the effect of environmental conditions [146,163].

The corrosion potential is representative of the potential at which the rates of the anodic and the cathodic reactions are in equilibrium. It essentially yields a probability of corrosion activity at the time of measurement. The potential is found by measuring the voltage difference between the rebar and a reference electrode. There is a prescribed method for this type of testing under ASTM provisions [164]. For testing in the field, ASTM guidelines recommend using a copper-copper sulfate half-cell (CSE). A plethora of different reference electrodes are used in the laboratory. Figure A.3 illustrates the setup for measuring the corrosion potential.
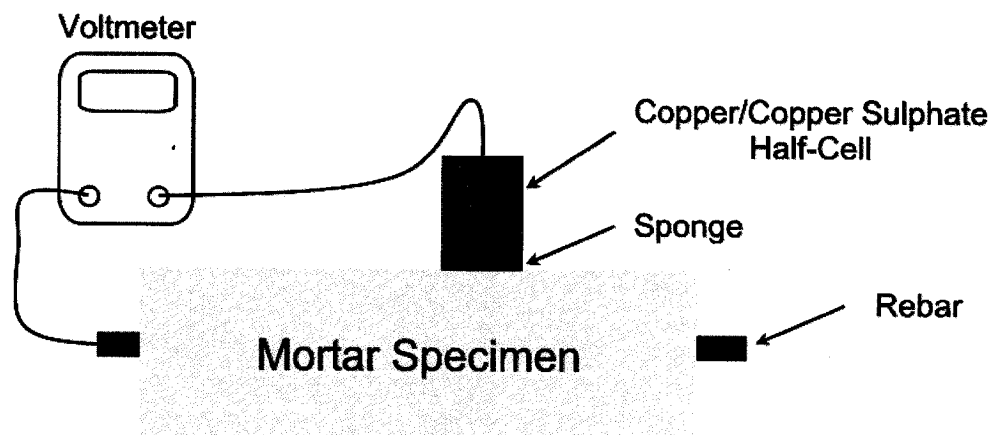
Figure A.3: Corrosion potential measurement using ASTM guidelines.

The rebar is connected to the positive terminal of a high resistance (>10 MΩ) voltmeter. The high impedance of the voltmeter is to prevent current flowing through the electrode. The negative terminal is connected to the copper/copper sulphate half-cell, which is placed at the surface of the concrete. The potential measurement is displayed on the voltmeter.

234

Potential mapping is used in the field where potential measurements are taken at different locations and then an equipotential contour map is created (as shown in Figure A.4).
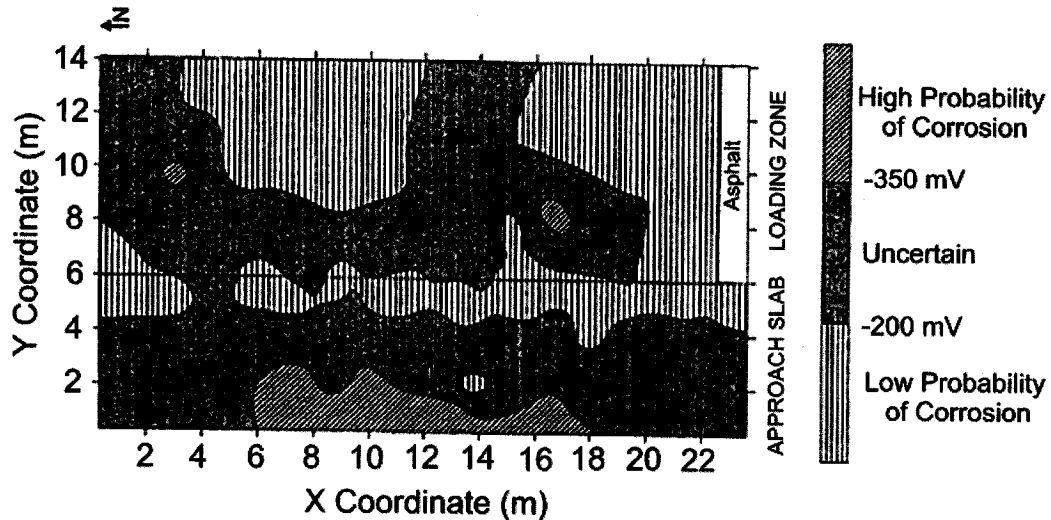
Figure A.4: Equipotential contour map of reinforced concrete pier (extracted from [147]).

Some display results as a cumulative frequency distribution, where potential measurements taken at several locations are displayed on normal probability paper. ASTM provisions (shown in Table 1) provide guidelines for assessing the probability of corrosion based on the potential measurement.

Table A.1: ASTM designation for potential measurements.

Potential, V (CSE)	Probability, %
> -0.20	> 90%, no corrosion
-0.20 < V < -0.35	uncertain
< -0.35	> 90%, corrosion

In simulated corrosion experiments in the laboratory, decreases in the potential are generally a sign of depassivation. Frequently, open circuit potentials (OCP) are presented as plots showing potential as a function of time. Figure A.5 is a plot of the open circuit potential as a function of time for cement mixes with 2g/l NaCl with and without inhibitor (Ferrogard 901®) addition.

235
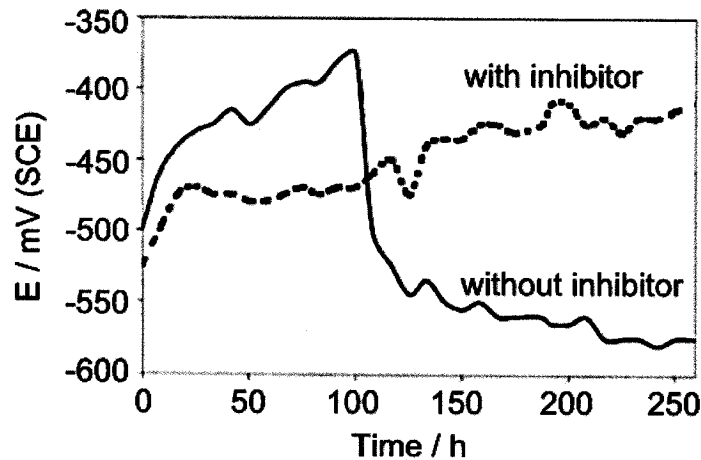
Figure A.5: Open circuit potential as a function of time for different cement mixes (extracted from [150]).

The method, unfortunately, has many drawbacks. The method gives no information regarding actual degradation to the structure or the rate of reaction. There is a rather large range of potentials where corrosion activity is uncertain. The concrete must be sufficiently moist in order to conduct the test. Rebar with coatings are not covered under ASTM guidelines. Electrical connections must be made to rebar that is most likely already embedded into concrete. However, embeddable electrochemical sensors exist and are commercially available [165]. Many corrosion inhibitors, especially surface inhibitors, affect potential measurements and many have ruled out using potential measurements as a viable method for assessing inhibitor system performance [152,166]. Concrete cover cracks can lead to potentials that do not correspond to the real condition of the rebar [167]. Environmental effects play a large role in potential measurements, such as moisture content, resistivity, chloride content, surface coating, temperature, carbonation, pH, oxygen availability, stray currents, rehabilitation history, and cover thickness. Research has been invested in developing compensation procedures for the corrosion potential to account for the spacing between the rebar and the concrete surface, but more testing is needed [168,169]. Ultimately, location of constant corrosion potential differences or gradients between active and passive sites is more important than setting absolute values of potential thresholds [166]. In other words, individual absolute potential values cannot be accepted as a general measure of the condition of steel in field structures [143].

A.2.2 POLARIZATION RESISTANCE

Also referred to as the DC Linear Polarization Resistance (LPR) method, because there is a linear relationship between the change in voltage and the change in applied current per unit area of an electrode that is polarized [42]. The corrosion of steel does not necessarily obey Ohm's Law (V = I*R), but it can be assumed to be in relation if the polarization of the steel is relatively small [170,171]. There are three established variations to this method, but all are used to determine the rate of the corrosion reaction. The

236

corrosion potential, E_{cor}, between the rebar (working electrode) and the reference electrode is first measured. An electrical perturbation is then applied to the rebar (working electrode) [170]. Figure A.6 shows a typical polarization resistance setup.
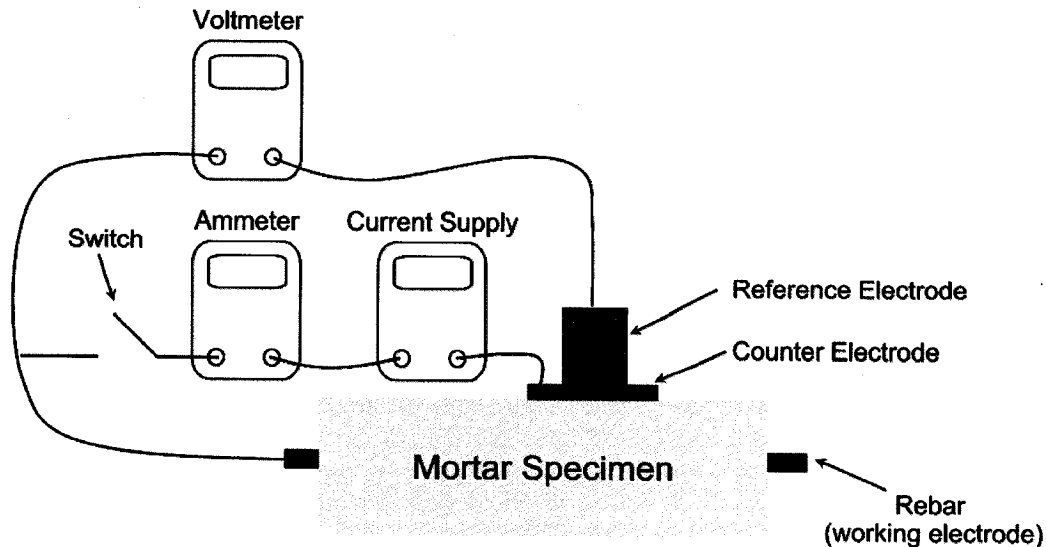
Figure A.6: Typical setup for a polarization resistance measurement.

When the electrical perturbation is a small potential disturbance, ΔE, from the corrosion potential, with the corresponding current flow, ΔI, to the counter electrode measured, the method is termed Potentiostatic Linear Polarization. This has been used on-site for RC structures and in the laboratory to show the effectiveness of corrosion inhibitors, concrete mixes and admixtures, and as a baseline reference for other detection methods [149,172]. The polarization resistance at the steel/concrete interface can be found by:

$$R_p = \frac{\Delta E}{\Delta I} \quad \text{.. (A.1)}$$

and represents the ease at which charged iron ions can leave the metal surface and enter into the solution [173]. Figure A.7 illustrates one version of the equivalent electrical circuit for a corrosion interface. There are many other more detailed circuit diagrams in the literature not shown here. The parameter R_s is the solution (concrete) resistance, R_t is the true polarization resistance and C_{dl} is the double layer capacitance.

237
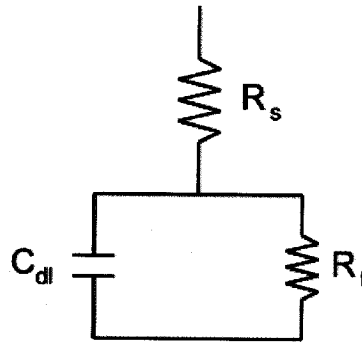
Figure A.7: Circuit diagram representation of steel/concrete interface (extracted from [170]).

The polarization resistance will allow for an estimation of the overall corrosion current between the anode and cathode using the Stearn-Geary equation:

$$I_{corr} = \frac{\beta_a \beta_c}{2.3(\beta_a + \beta_c)} \cdot \frac{1}{R_p} = \frac{B}{R_p} \quad\text{..}\text{(A.2)}$$

where β_a and β_c are the anodic and cathodic Tafel constants and B is the Stearn-Geary constant. Discussion of Tafel plots are out of the scope of the current report, but an excellent review is provided in [31]. B is generally given as 25 mV for corroding rebar in concrete and 50 mV for passive rebar in concrete. Notice that by using R_p, one is assuming that the solution resistance (R_s) is negligible. The true polarization resistance is what is sought after by using the LPR method. The true polarization resistance, R_t, at the concrete and steel interface is equal to:

$$R_t = R_p - R_s \quad\text{...}\text{(A.3)}$$

where R_s is the solution resistance (concrete resistance) between the working electrode (rebar) and the reference electrode. In a highly conductive solution ($R_p \gg R_s$) R_p has negligible error [174]. However, the concrete resistivity is generally not negligible and has to be compensated for in value. If the solution resistance can be found, then R_t can be calculated and substituted for R_p in the equations. A portable LPR meter designed by researchers uses the potentiostatic linear polarization mode to measure R_p and then uses EIS (Section A.2.3) at a frequency of 300 Hz to measure R_s [174]. This allows for an accurate assessment of R_t. The corrosion current density, which is indicative of the corrosion rate, is calculated by the following equation:

$$i_{corr} = \frac{I_{corr}}{A} \quad\text{...}\text{(A.4)}$$

238

where A is the area of the rebar that is perturbed. Generally, a 30 second delay time for potentiostatic measurements is recommended [175].

When the electrical perturbation is a small constant current, ΔI, applied to the rebar (working electrode), with the corresponding change in potential, ΔE, measured, the method is termed galvanostatic linear polarization or the galvanostatic pulse method [143]. One goes about finding the corrosion current in the same manner as the Potentiostatic Linear Polarization method.

The galvanostatic pulse method was used by others to improve the results of the corrosion potential method [143]. The same exact setup is used as shown in Figure A.2.4. By looking at the potential measurement after application of the short constant current pulse of magnitude ΔI, regions of corrosion are more easily identified. Regions of passivity are classified by larger changes in potential, while regions that are corroding are classified by smaller changes in potential. The use of this method for potential mapping is to avoid misinterpretations from aeration conditions, concrete cover, high resistance surface layers, humidity, and pore solution. From previous research, it is less ambiguous because of its added sensitivity to corrosion [143]. The capacitance was estimated by looking at the transient response of the potential, the solution resistance, polarization resistance, and the double layer capacitance [176].

The third variation is a slow linear potential sweep used for the perturbation, with the slope of the current response measured. The method is termed Potentiodynamic Linear Polarization. A potentiostat is used to displace the equilibrium of the rebar by several mV, starting below the corrosion potential and slowly scanning upward to above the corrosion potential. Scan rates vary, with some as high as 1 mV/s [177] and some as low as 0.015 mV/s [154]. Most scan rates fall between those two [145,153,156,157,161-163, 178], with 10 mV/min recommended. The current between the steel and the counter electrode is measured and used to calculate current density, giving an indication of the corrosion rate. One can plot the potential as a function of the current density, with the slope of this curve giving the polarization resistance. Figure A.8 shows the results of concrete blocks reinforced with conventional steel and high-chromium steel immersed in different NaCl concentrations. The slope of the current as a function of potential plot, Figure A.8(a), is then used to calculate the corrosion rate, Figure A.8(b), for the particular time, chloride concentration, and reinforcement. The sweep rate that is used will change the polarization resistance found for the system.

239
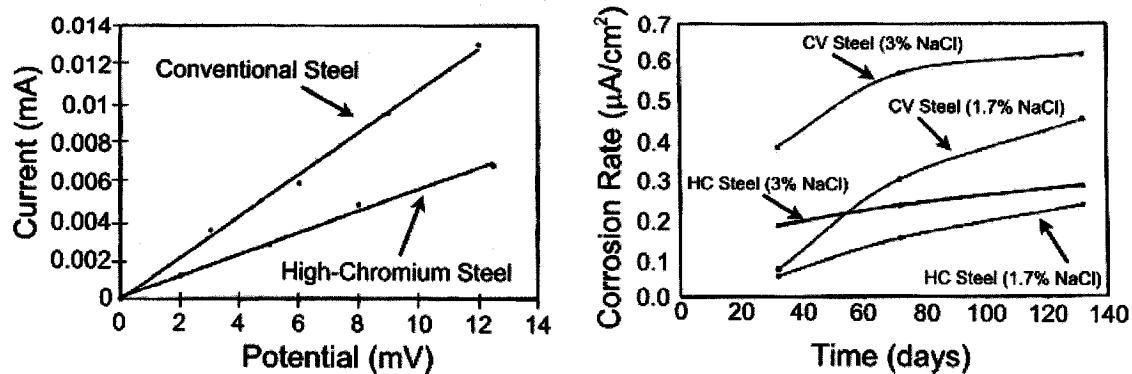
Figure A.8: Concrete blocks reinforced with different steel with **(a)** a plot of current as a function of potential for a particular NaCl concentration and time and **(b)** a plot of corrosion rate as a function of time for different NaCl concentrations (extracted from [172]).

Many times, the LPR method is used in conjunction with OCP measurements. For field inspection, there is commercial equipment sold for the evaluation of the corrosion rate in RC structures using the LPR method [170]. It is used in the field for corrosion rate estimates currently [179]. The LPR method is also used extensively for laboratory testing and field measurements to find the effectiveness of corrosion inhibitors in concretes, concrete mixes, and admixtures [146,147,152-154,156,157,161-163,177,178,180,181]. It is also used as a baseline to compare other NDT methods [142,144].

Many of the same drawbacks that the corrosion potential measurement presented are applicable to the LPR method. Electrical connection must be made to the embedded rebar. The corrosion rate measured is only indicative of the corrosion rate at the time of the test. The method only gives an estimate of the rate of the corrosion; it does not provide information about degradation to the structure or previous corrosion history. Overestimation of corrosion rates from the Tafel slopes is common [149,157]. Evaluation of macrocell corrosion (pitting) using LPR is invalid because the anodic region being polarized is not at its equilibrium potential but is held at a more electropositive potential by the presence of the remote cathode [174]. Environmental effects such as moisture content in the concrete, carbonation of the concrete, chloride ingress, oxygen availability and temperature can affect the measured corrosion rate [173]. Depending on the types of devices used for measuring, different corrosion rates are measured. The method assumes that the area of rebar that is affected by current from the counter electrode is immediately below the counter electrode. This assumption has been shown to be incorrect by researchers [182]. To ensure that the current is flowing only to the rebar lying directly beneath the counter electrode, guard ring devices have been created [183]. Also, steady state data may only be obtained after many hours of initially measuring the perturbation [160].

240

A.2.3 AC IMPEDANCE METHOD

This is commonly referred to as Electrochemical Impedance Spectroscopy (EIS). An alternating potential/current is applied as the perturbation at varying frequencies, with the alternating current/potential measured. The impedance response can be written as:

$$Z = R_s + R_t \left(1 - j\omega C_{dl} R_t \right) / \left[1 + \left(\omega C_{dl} R_t \right)^2 \right] \quad \text{................................ (A.5)}$$

with ω equal to $2\pi f$ (f given in Hz). At very high frequencies the system has no to time to respond to the current and so the impedance is equal to the electrical resistance of the solution (concrete), R_s. At very low frequencies the system comes to equilibrium as fast as the current is changed, with the impedance equal to the electrical resistance of the solution plus the true polarization resistance, R_t. Subtraction of the impedance at a substantially low frequency from the impedance at a substantially high frequency yields the true polarization resistance. The same equations used for the LPR method are applied to EIS to find the corrosion rate. Results are generally given with plots of impedance as a function of frequency (Bode plot) or imaginary impedance components as a function of real impedance components. Figure A.9 is a Bode plot showing the impedance curve as a function of frequency.
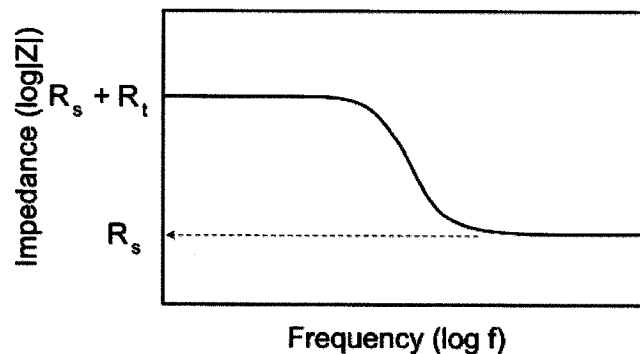
Figure A.9: Bode plot of impedance as a function of frequency for an electrochemical impedance spectroscopy test (extracted from [11]).

The LPR method is basically a single low frequency AC impedance measurement with no information regarding the imaginary component [170]. Since EIS is a transient technique, it can provide information without having to reach a steady state condition [160].

As with OCP and LPR, EIS is used extensively in the laboratory and on-site studies for comparing the corrosion rate for corrosion inhibitors, concrete mixes and admixtures, and as a baseline for other detection methods [141,142,144,149,150,152,160,170,179,184-186]. Drawbacks to this technique are that data interpretation is often difficult [187] and the method can be time consuming [188]. Also, the

simple circuit diagram shown in Figure A.2.5 is a simplification in describing RC structures, with a model transmission line being more applicable [188].

A.2.4 POLARIZATION CURVES

This is also referred to as the Tafel plot technique. A potentiostat is used to lower the potential from the corrosion potential to a much lower potential. The potential is then slowly raised at a rate low enough to form a protective passive film. The potential is raised until there is a sharp increase in current corresponding to either pitting or the transpassive zone. The transpassive zone is where film undergoes an electrical breakdown at high potentials (see Figures 2.3 & 2.4 in region of oxygen evolution). Figure A.10 is a polarization curve for cement mixes with 2 g/l NaCl with and without inhibitor (Ferrogard 901®) addition.
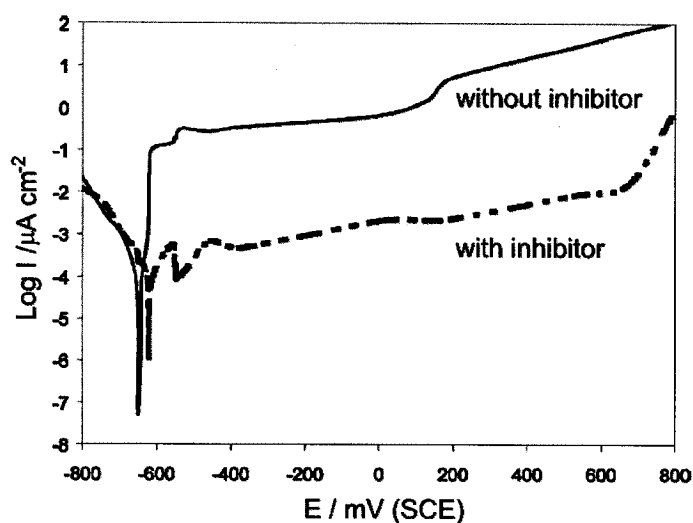
Figure A.10: Potentiodynamic polarization curve for different cement mixes (extracted from [150]).

If the test is stopped at this point, it is considered a polarization curve. If a quick return scan is completed, the method is considered cyclic polarization or cyclic voltammetry. This method is useful for finding out whether a particular metal is pitting in its environment. Also, direct corrosion currents can be measured so there is no need to make assumptions about Tafel constants as with LPR [140]. However, it is generally considered to be destructive in nature due to the large applied potential. Polarization curves [140,145,150,157,158,186] and cyclic polarization curves [148,153,154,159] are used almost exclusively by researchers in the laboratory to test the effectiveness of corrosion inhibitors in concrete.

A.2.5 MACROCELL TECHNIQUES

The current is measured either between two bars at different depths [155,179] or between a rebar and an inert cathode, such as stainless steel or copper. Figure A.11 shows macrocell corrosion current as a function of time for reinforced concrete structures with different protection systems.
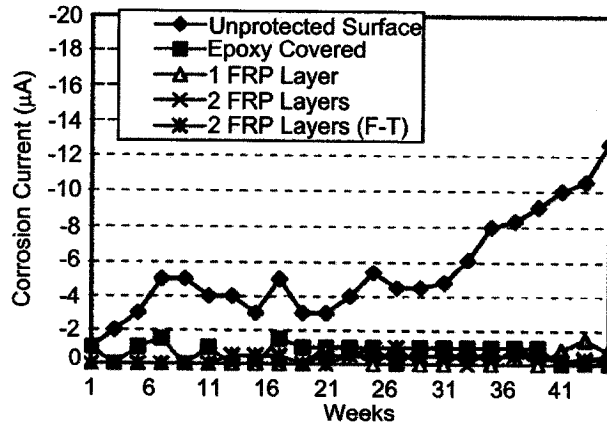
Figure A.11: Macrocell corrosion current as a function of time (weeks) for a reinforced concrete structure (extracted from [155]).

The macrocell corrosion current was measured between the top and bottom steel rebar in the structure. The choice of an inert cathode should allow for a high enough galvanic current to offset the highly resistant environment, but not so high that the life of the sensor system is severely depreciated [145]. Large currents are generally an indication that corrosion has begun. Embeddable macrocell systems for RC structures are commonly referred to as anode-ladder-systems (as shown in Figure A.12(a)). A series of bars are configured in what looks like a ladder to assess the depth of corrosion [189]. An illustration of the time to corrosion model for the anode-ladder system is shown in Figure A.12(b).
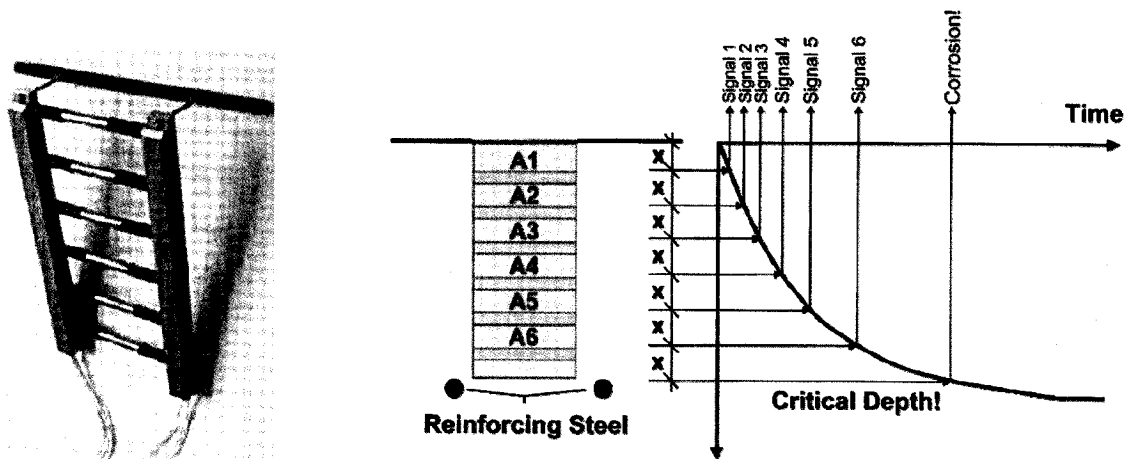
Figure A.12: (a) Anode-ladder-system used in reinforced concrete structures to assess corrosion risk and (b) an illustration of the time to corrosion for the anode-ladder system (extracted from [189]).

A similar technique measures the current between two bars at the same depth, while measuring the potential between one of the bars and a reference electrode [188]. This is referred to as the electrochemical noise technique. Unfortunately, this technique has been shown to be unreliable for testing with reinforced concrete [188].

A.2.6 POTENTIOSTATIC/GALVANOSTATIC MEASUREMENTS

Potentiostatic implies a constant potential, with measurements of the current taken [190]. Large increases in current generally signals corrosion. Galvanostatic implies a constant current, with measurements of the potential at the current. Large decreases in the potential signals corrosion. Much like cyclic polarization, this method can be detrimental to an existing structure and therefore is generally only used to assess corrosion inhibitors and/or admixture agents [148]. Many times this method is used to accelerate corrosion of reinforced concrete in laboratory settings by polarizing the rebar and drawing chloride ions closer.

A.3 ELECTROMAGNETIC METHODS

The methods described in this section either involve inducing a magnetic field or using an electromagnetic wave to inspect reinforced concrete. Electromagnetic waves are the product of changing electric fields that produce a magnetic field. The magnetic field may also be changing, so that each type of field continually produces the other in an electromagnetic structure that propagates through space [191]. The electromagnetic spectrum is shown in Figure A.13.
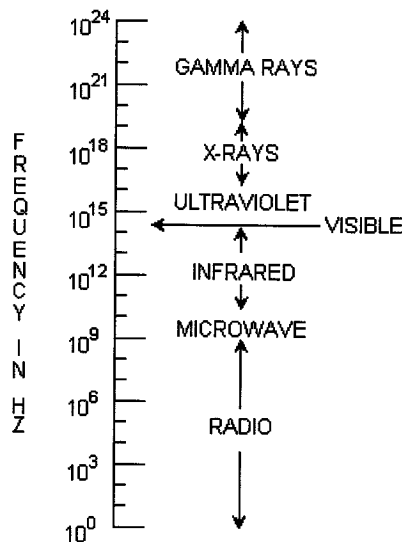
Figure A.13: Electromagnetic spectrum (extracted from [191]).

244

Electromagnetic waves with a frequency range of 1 Hz to 10^9 Hz are considered radio waves with 10^9 Hz to 300×10^9 Hz considered microwaves. Electromagnetic waves from 300×10^9 Hz to 3.7×10^{14} Hz are considered infrared waves, from 3.7×10^{14} Hz to 7.5×10^{14} Hz visible light waves, from 7.5×10^{14} Hz to 1.5×10^{16} Hz ultra-violet waves, from 1.5×10^{16} Hz to 3×10^{19} Hz x-rays, and higher than 3×10^{19} Hz are considered gamma rays.

A.3.1 ELECTRICAL TIME DOMAIN REFLECTOMETRY (ETDR)

Electrical time domain reflectometry has been used traditionally to detect flaws in transmission lines (e.g. telephone lines and television cables). Transmission lines are an electromagnetic waveguide system. Reinforced concrete can be modeled as a twin-conductor transmission line by embedding a sensor wire along the embedded steel (see Figure A.14(a)). External sensors wires (i.e. wires not embedded in concrete) lack sensitivity and are limited by distance.
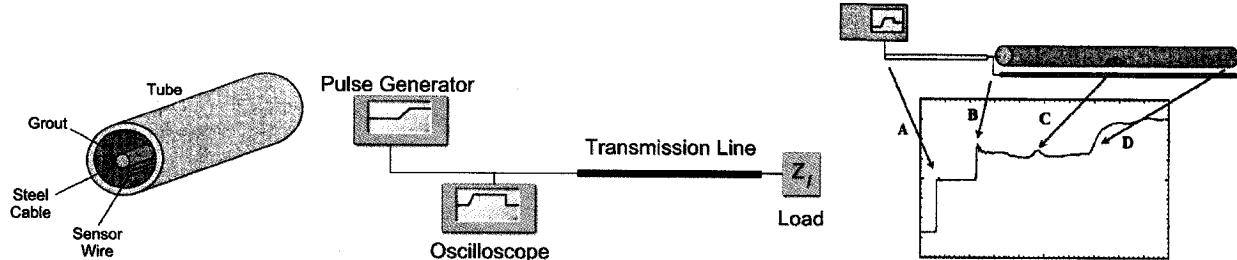
Figure A.14: Illustration of **(a)** a twin conductor transmission line (left), **(b)** electrical time domain reflectometry (ETDR) setup (middle), and **(c)** results for simulated pitting corrosion (extracted from [192]).

An electrical pulse is transmitted along the transmission line from a pulse generator. Discontinuities and defects in the steel create an impedance mismatch, causing a reflection in the sensor wire. An oscilloscope displays the reflection with the setup shown in Figure A.14(b). The characteristic impedance of the transmission line will increase for small decreases in the diameter of the steel. The transit time, magnitude, and polarity of the reflection is inspected to determine the location, severity, and type of corrosion. Researchers have effectively used this embedded sensor wire method in the laboratory to detect pitting corrosion in rebar samples, see Figure A.14(c), and severed cables in seven-wire strand. Other proposals for using ETDR in reinforced concrete structures have been made. A coaxial cable sensor has been proposed to embed in concrete to detect corrosion, cracking, and to be used as a continuous strain gauge [193]. Instead of forming a twin-conductor transmission line with the rebar, the coaxial cable would be independent and relay information regarding degradation to the sensor wire. From cracking and/or corrosion, the cables would incur a change in impedance and cause partial reflection of the electrical pulse transmitted along the cable. Attempts were also made to develop an external sensor wire for existing structures.

245

Although ETDR has been around for quite some time, its use towards detection of corrosion in RC structures is relatively novel. Its sensitivity towards the environment, loading conditions, concrete and rebar properties, etc. has yet to be studied over long term in-field testing. The method is most likely limited to new structures, as embedding sensor wires in pre-existing structures would be difficult. Experiments have shown that the coaxial cable system lacks sensitivity to detection of simple cuts or cracks in the cable due to only small ohmic resistance changes [194].

A.3.2 INFRARED (IR) THERMOGRAPHY

Infrared (IR) thermography involves detection of emitted electromagnetic waves in the infrared range from objects. Cameras sensitive to infrared wavelengths are used to create a map of the surface temperature. Delaminations and cracks from corrosion in reinforced concrete create air voids in the object. When the structure is heated (e.g. sunlight) the air voids will affect heat flow through the structure. The subsurface defects show up as changes in the surface temperature.

This method has been used widely in the past to detect delaminations in bridge decks and pavements [138,195], with ASTM offering provisions for its use [196]. It has been used to inspect the reinforced concrete roof of the Seattle Kingdome [134]. Figure A.15(a) shows how delaminations and/or voids cause temperature gradients along the inside surface of the roof from the outside sunlight.
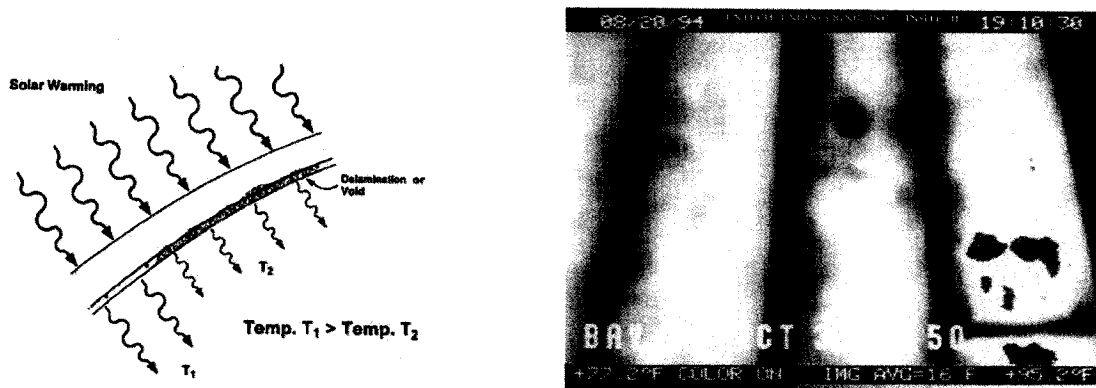
Figure A.15: Seattle Kingdome roof **(a)** illustration of surface temperature changes from delaminations (left) and **(b)** infrared thermogram showing temperature changes along Seattle Kingdome roof (extracted from [134]).

By using an infrared camera, thermograms as shown in Figure A.15(b) can be created to show voids, delaminations, moisture, and surface debris. Safety, fast inspection times, and identification of the horizontal extent of damage to a structure are the main advantages of IR. The disadvantages are the methods sensitivity to temperature effects on the surface from the environment and the lack of information regarding the depth of the damage.

246

A.3.3 GROUND PENETRATING RADAR (GPR)

Ground penetrating radar (GPR) involves transmitting electromagnetic waves in the microwave range into reinforced concrete and capturing the corresponding reflections. The wave sent from the antenna has partial reflections at every interface including air/concrete, concrete/rebar, concrete/air (bottom surface), air voids in concrete, and delaminations that exist between the concrete and steel. Reflections from these interfaces are shown in Figure A.16.
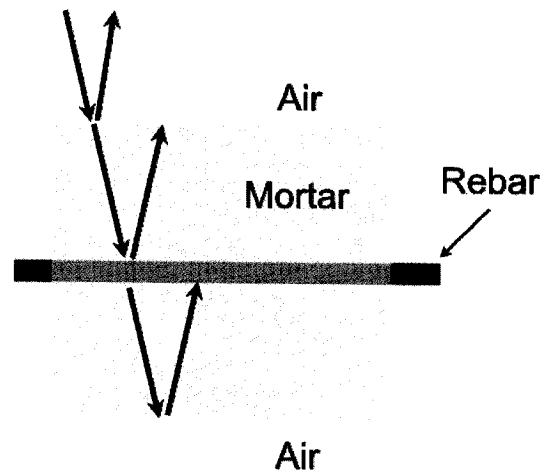
Figure A.16: Reflections from different interfaces in a bridge deck (extracted from [197]).

The reflections from these interfaces are collected by a receiving antenna and processed. Relationships between concrete damage from reinforcement corrosion and the returning electromagnetic wave have been investigated. Researchers have found correlation between the amplitude of the returning waveform and corrosion activity [198]. A decrease in the amplitude was observed for advanced corrosion activity. This is thought to occur due to an increase in the roughness of the rebar/concrete interface, causing scattering and effectively attenuating the electromagnetic wave. The chemical state of the cement was also thought to affect the reflection coefficient at the site. Moisture present in the concrete affected the velocity of the waveform in a subtle fashion. Other researchers who tested multiple GPR systems in the field found that the amplitude and phase of reflected waveforms did not reveal a consistent response that distinguished delaminated concrete from solid concrete [133].

Researchers have developed radar tomography systems where 3D images are created from scans [199]. A synthetic aperture is created by moving the antenna to several new positions and transmitting and receiving a waveform. A high speed, medium resolution system has been created where a physical array of radar elements are used to scan. A low speed, high-resolution system was also created where only one radar element is swept back and forth as the vehicle moves forward. Simulated defects, such as 0.039" (1 mm) air voids and Styrofoam inserts, were created in concrete and identified using GPR in a B-scan

247

image (refer to Figure A.39) [197]. Figure A.17 shows a high-resolution image of embedded Styrofoam in concrete at a depth of 1.97" (5 cm).
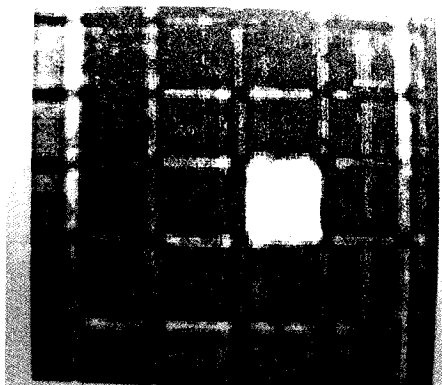
Figure A.17: High-resolution image of Styrofoam insert (extracted from [199]).

GPR has the advantage of a rapid testing speed, with inspection speeds of up to 90 kmh (56 mph) [199]. The main disadvantages are the difficulties with signal processing, interpretation, limited surface access, and cost [197].

A.3.4 MAGNETIC FLUX LEAKAGE (MFL)

Magnetic flux leakage (MFL) generally consists of magnetizing a specimen and scanning its surface with a flux-sensitive sensor (e.g., coils, yokes, solid state magnetic sensors, and particles of finely divided magnetic materials) for leakage fields. One can create the magnetic flux in the specimen by placing it close to a magnetizing agent or electrical current through a conductor (sometimes applying current directly to the specimen) [200]. The effects of induction on flux lines from a discontinuity in a material are shown in Figure A.18(a).
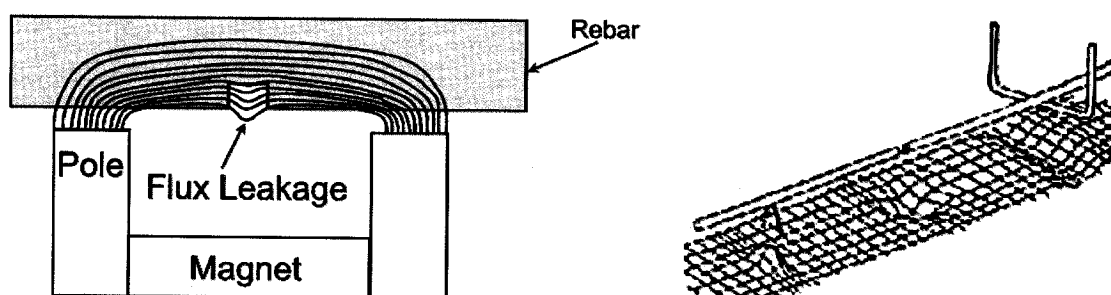
Figure A.18: **(a)** Yoke sensor for detection of flux leakage and a **(b)** three-dimensional plot of the magnetic field variation from a discontinuity (extracted from [201]).

Changes in the cross-sectional area of the rebar will cause flux leakage, meaning the continuous flux lines in the steel are forced into the surrounding concrete. The effect of the concrete is negligible on the

248

magnetic field so a yoke sensor (as seen in Figure A.18(a)) can be used at the concrete surface to measure the field leakage. The amplitude of the field leakage is generally correlated to the defect size.

A scanning device has been created that can be installed on prestressed girders and is capable of scanning the entire length [201,202]. The device is made of a magnet and a series of Hall effect sensors, communicating wirelessly to a remote computer. The variation in the magnetic field that the scanning device detects can be processed as a three-dimensional plot to detect discontinuities as shown in Figure A.18(b).

A phase sensitive inductive sensor has been developed by other researchers to detect and image corrosion products on the surface of steel bars embedded in concrete. A time-varying magnetic field is created by passing AC current through a coil of wire (usually copper). When a metal object is placed in the flux of the magnetic field, a change to the inductance of the coil occurs. The change depends on the permeability (μ) and conductivity (σ) of the metal. For a highly permeable and non-conductive metal (i.e. corrosion product), the inductance of the coil increases based on:

$$L = \frac{\mu N^2 A}{l} \quad\dotfill\text{(A.6)}$$

where N is the number of turns of the coil, A is the coil area, and l is the length of the coil. The coil can be configured as part of a tuned oscillator, whose resonance frequency is related to the inductance:

$$f = \frac{1}{2\pi\sqrt{LC}} \quad\dotfill\text{(A.7)}$$

where C is the capacitance of the tuned system. Therefore, corrosion products should cause an increase in the inductance due to high permeability and lead to a decrease in the resonant frequency of the tuned oscillator. To detect this frequency shift, researches used an off-resonance phase sensitive circuit. This detector sent the output of the sensor oscillator to a comparator that converts the sine wave to a square wave. This square wave and the output of a stable crystal oscillator (reference oscillator) that generates off-resonance square-waves are sent to a phase sensitive detector (PSD). The reference oscillator frequency was shifted off of the resonance frequency of the sensor oscillator so that the system was capable of determining whether the frequency increases or decreases. If the reference and sensor oscillator frequencies were the same, the frequency direction information would be lost. The PSD generates a pulse train, that when integrated, has a frequency equal to the frequency difference between

249

the reference and sensor oscillator frequencies. This information is sent to a frequency-to-voltage converter, then to a computer for graphical display. Photographs of corrosion product, see Figure A.19(a), on the surface of steel have been generated and compared to non-corroded steel surfaces.

(a)

(b)
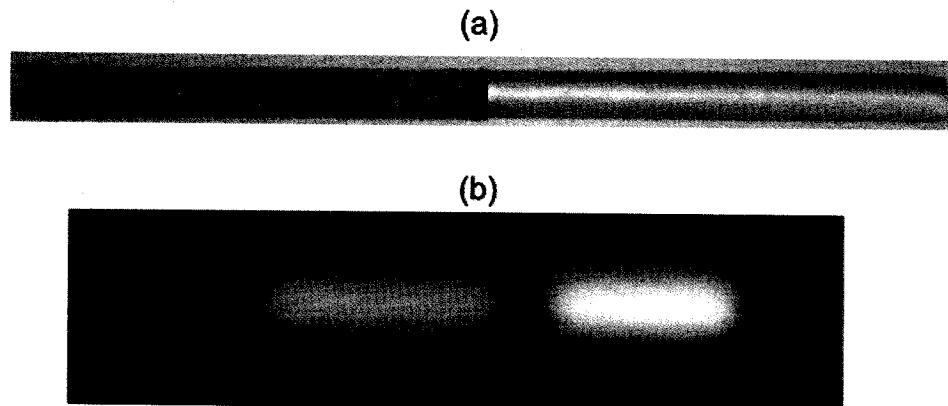
Figure A.19: **(a)** A photograph of a corroded bar (left) and uncorroded bar (right) and **(b)** a phase sensitive sensor image of bar (extracted from [203]).

Different levels of corrosion on steel surfaces have been distinguished in a laboratory setting. The method seems to work when the rebar is placed underneath thick ceramic tile (with similar conductivity and permeability properties as concrete). Moisture changes to the ceramic tile do no seem to affect the results.

Interpretation of signals from MFL is made difficult when other rebar is present. The depth of the rebar also plays a large role in how much leakage can be detected at the concrete surface. The MFL method is rather novel with regards to detection of corrosion in reinforced concrete and further long term in-field testing is needed.

A.3.5 RADIOGRAPHY

Radiography is considered using x-rays and/or gamma rays for inspection. Radiography generally provides high quality 2D images for reinforced concrete because of how different the attenuating characteristics are for concrete, steel, and air [204]. Both x-rays and gamma rays are fairly transparent to concrete [205]. For reinforced concrete structures, a radiation source and film are located on opposite sides of the structure as shown in Figure A.20(a).

250
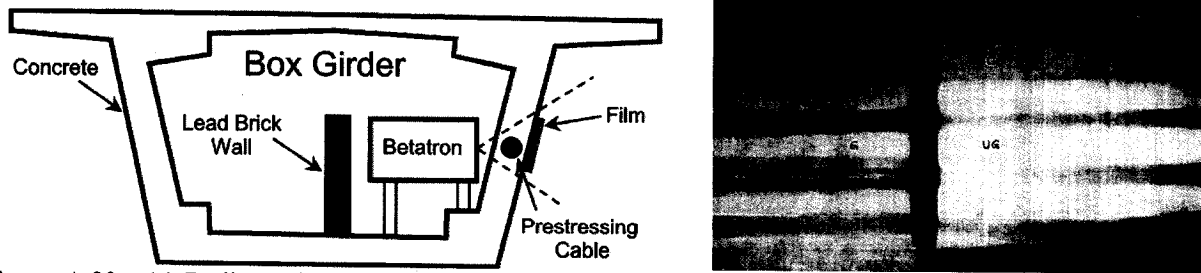
Figure A.20: **(a)** Radiography setup for concrete box girder of bridge with **(b)** grouted (G) and ungrouted (UG) images for prestressed concrete (extracted from [206]).

After exposure to radiation, the film can be processed and images analyzed. Researchers have used these processed images to assess if prestressed concrete bridge girders were properly grouted, to ensure that prestressing strands were intact with good health, and to find the location of strands [206,207]. Figure A.20(b) provides a two-dimensional image of grouted and ungrouted sections of a prestressed concrete section.

Some researchers use characteristics of the film density profile to estimate the corrosion rate [208]. Figure A.21(a) shows film density plotted against scan length.
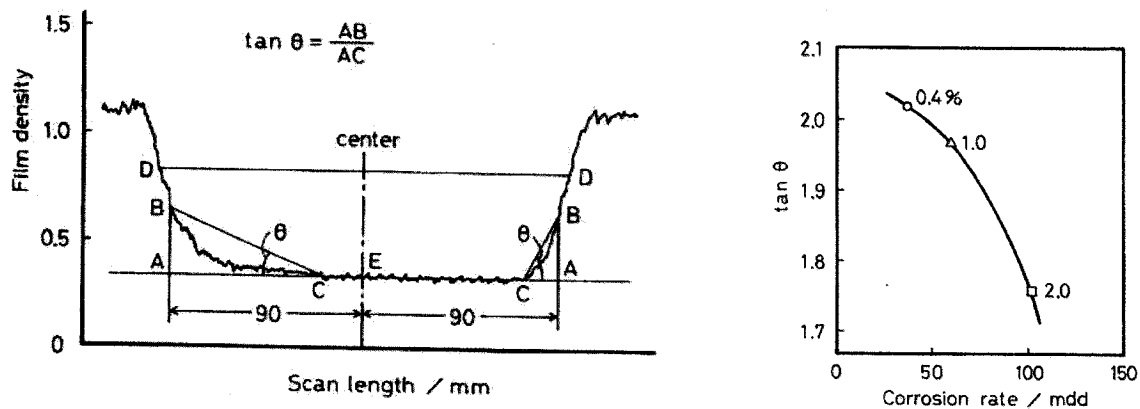
Figure A.21: **(a)** Film density as a function of scan length for a steel bar in 0.394" (1 cm) thick mortar and **(b)** the relationship between tan θ and corrosion rate for varying NaCl concentrations (extracted from [208]).

Point E is considered the middle of the rebar, point A the interface between the rebar and concrete, point C is where the plot deviates from the baseline behavior of the rebar, and point B is where a vertical line through point A intersects the plot. Using tan θ, the corrosion rate can be estimated as shown in Figure A.21(b).

X-rays have been used to examine corrosion products at the surface of reinforcement and to predict concrete cracking from corrosion product buildup [209]. Figure A.22 below shows a 2D image of corrosion product buildup in a reinforced concrete specimen.
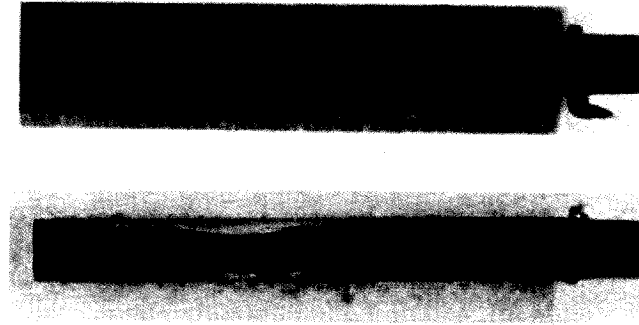
Figure A.22: Two-dimensional image of accelerated corrosion in reinforced concrete at **(a)** 28 days and **(b)** 52 days (extracted from [209]).

Advantages of using radiography towards monitoring corrosion in reinforced concrete is speed, the ability to inspect large surface area in one trial, and the ability to assess tendons near their anchorage points. Disadvantages is that assess is necessary to both sides of a concrete structure, poor resolution of flaws, cost, and safety concerns. Others feel that that it is unlikely that corrosion can be detected using radiography in the field unless it is very severe [205].

A.3.6   FIBER OPTICS

An optical fiber consists of a dielectric material, wrapped in cladding material, that guides light waves over long distances with low attenuation [210,211]. A typical fiber optic cable is shown in Figure A.23.
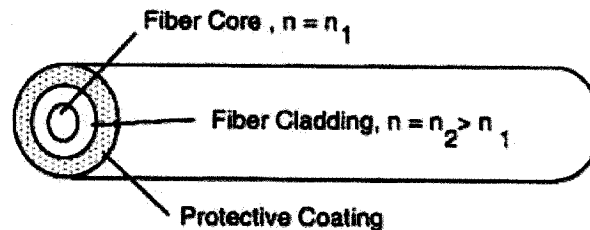
Figure A.23: Representation of a typical fiber optic cable (extracted from [211]).

Every fiber optic sensing system must have the following components: light source, splitter and couplers, sensors, demodulation system, and a processing system [210]. Fiber optic sensors are designed to measure changes in the physical properties of the guided light waves, such as phase, intensity, and wavelength. The way in which they do this varies depending on the type of sensor used. Change to the light produced inside the optical fiber is considered an intrinsic type of sensor, where the light never exits the optical fiber. Change to the light produced outside the optical fiber is considered an extrinsic type of sensor. The light exits the optical fiber, enters another medium and then reenters the optical fiber. There are fiber optic chemical sensors (FOCS), which have four types: absorption/reflection sensor, evanescent sensor, fluorescence sensor, and spectroscopic sensor. An absorption/reflection sensor uses a chemical

reagent that light either passes through or is reflected off of [212]. When this chemical reagent undergoes a color change from interaction with the chemical sought for detection, the amount of light absorbed or reflected will change. An evanescent sensor has the cladding material removed over the length of the sensor. In place of the cladding material, a selective membrane is placed that will interact with the chemical sought to detect. This interaction will affect the light propagating through the core. With a fluorescence sensor, the optical fiber is coated with either a fluorescent or phosphorescent dye over the sensor region. Light that is present in the sensor region illuminates the dye and a change in wavelength is observed. Spectroscopic sensors measure the absorption of light by a chemical species as a function of the wavelength. An example of a spectroscopic sensor is the fiber Bragg grating (FBG) sensor. FBG sensors are created by periodically changing the refractive index of the optical fiber over a short length [210]. The change in refractive index will behave as partially reflecting mirrors, reflecting back a wavelength based on:

$$\lambda = 2n_{eff}\Lambda \dotfill (A.8)$$

where λ is the center wavelength, n_{eff} is the effective refractive index of the fiber core, and Λ is the pitch length of the grating. Figure A.24 shows an illustration of a FBG sensor.
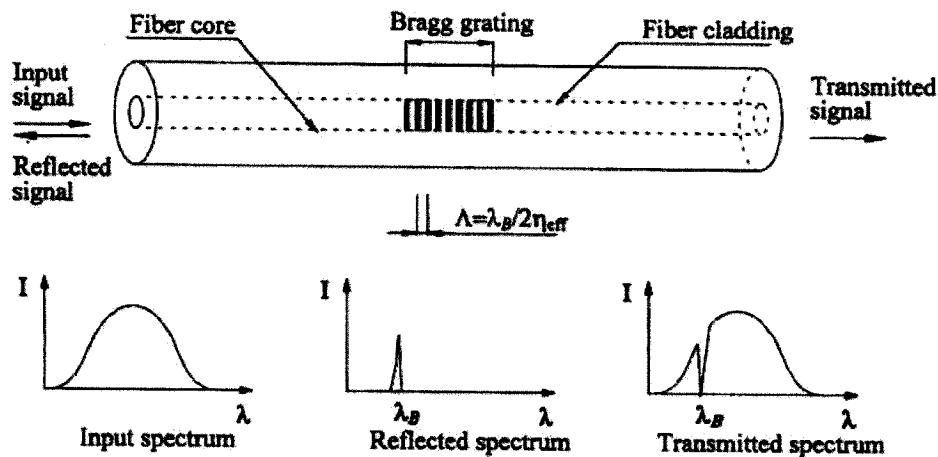
Figure A.24: Illustration of a FBG sensor with corresponding input, reflected, and transmitted spectrum (extracted from [210]).

An abundance of research has been conducted with respect to using fiber optic sensors to detect corrosion in reinforced concrete. Researchers used a Y-shaped fiber optic bundle to try and detect the brown color of rust product accumulation on the surface of reinforcement in concrete [213]. Light is guided to the surface of the steel with the reflected signal varying in proportion to the color of the steel. This is considered a reflection sensor. A reinforced concrete specimen was corroded with small amounts of NaCl

253

added to the mix design. The Y-shaped fiber optic bundle was embedded in the specimen. The results of monitoring the reflected optical power are shown in Figure A.25.
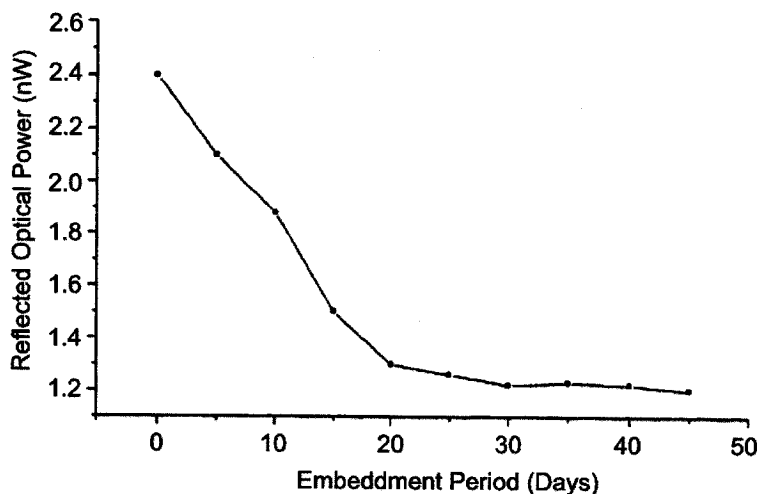
Figure A.25: Reflected optical power as a function of the sensor embedment period in a concrete specimen with corroding reinforcement (extracted from [213]).

The reflected optical power decreases with the progression of corrosion in the specimen. Researchers have used evanescent sensors to try and detect corrosion of reinforced concrete [214]. The glass cladding was removed from fiber optic cable at the sensor location and replaced with metal cladding. The idea is to have a metal cladding that has similar properties to the reinforcement so that it corrodes under the same conditions. Figure A.26(a) shows the metal cladding on the optical fiber and Figure A.26(b) shows the cable after corrosion of the metal cladding.
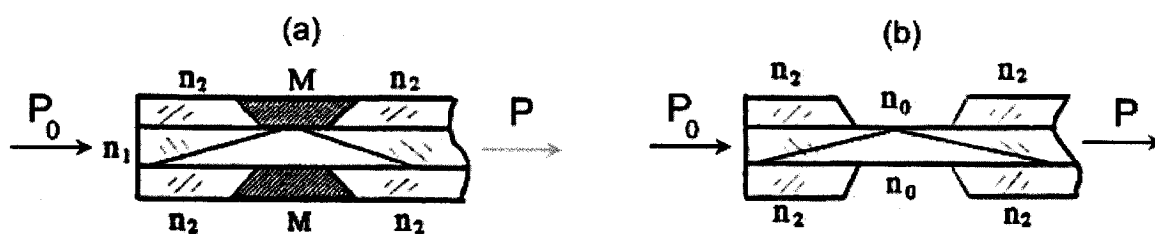
Figure A.26: Evanescent sensor (a) with and (b) without metal cladding (extracted from [214]).

The metal cladding will absorb energy from the guided light. When the metal cladding corrodes, air replaces the corroded metal cladding and the output light signal increases. Experiments were conducted using the sensor in different corrosive environments, with the neutral salt spray test results shown in Figure A.27.

254
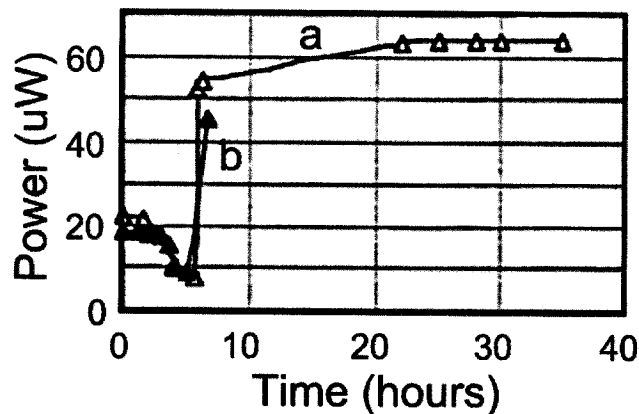
Figure A.27: Optical power as a function of time for evanescent sensor in concrete with corroding reinforcement (extracted from [214]).

The optical power output decreases initially, but after the initiation of corrosion there is a rapid increase in signal strength. A spectroscopic sensor has been designed to detect corrosion in reinforced concrete [215]. An FBG sensor is attached to the reinforcement. When the rebar corrodes, the rust product accumulation will increase the radial strain at the sensor location. The increase in radial strain will cause a shift in the center wavelength detected using the FBG sensor.

Indirectly, there have been many attempts at measuring corrosion in reinforced concrete. Researchers have focused on the design of a fiber optic chloride detector [212,216-219]. One researcher developed several different types of sensors, such as an evanescent sensor using silver nitrate, a reflective sensor using silver chromate, and an absorption mode sensor using silver nitrate and silver chromate [212]. All of the sensors detected a change in the output power of the light signal, but only the absorption mode sensor using silver chromate had a substantial increase in the output power. Most of the other sensors had a decrease in output power that could also be caused by fiber damage. Other researchers focused on sensors for detection of moisture and pH levels [220]. Different types of dyes were embedded into a polymer matrix and coated directly to the side of the fiber optical cable in place of the normal cladding material. Different dyes were used that exhibited color changes when exposed to different moisture and pH levels.

Strain [210,221-223], displacement [224], delaminations [225], and cracking [210,211,223] of structures have been monitored using different fiber optic sensors. Researchers have developed optical fiber sensors to detect strain changes from the cutting of tendon wires [221]. The sensor was produced by winding three optical fibers around each other, creating areas of microbending. Changes in the length of the sensor can be correlated to the change in the intensity of the light propagating through the sensor. The distribution of strain along the length of the sensor can be found using optical time domain reflectometry

255

(OTDR). OTDR transmits light pulses along the core and measures returning reflected light pulses for the transit time and attenuation. Figure A.28 shows the change in strain using the sensor from the cutting of tendon wires.
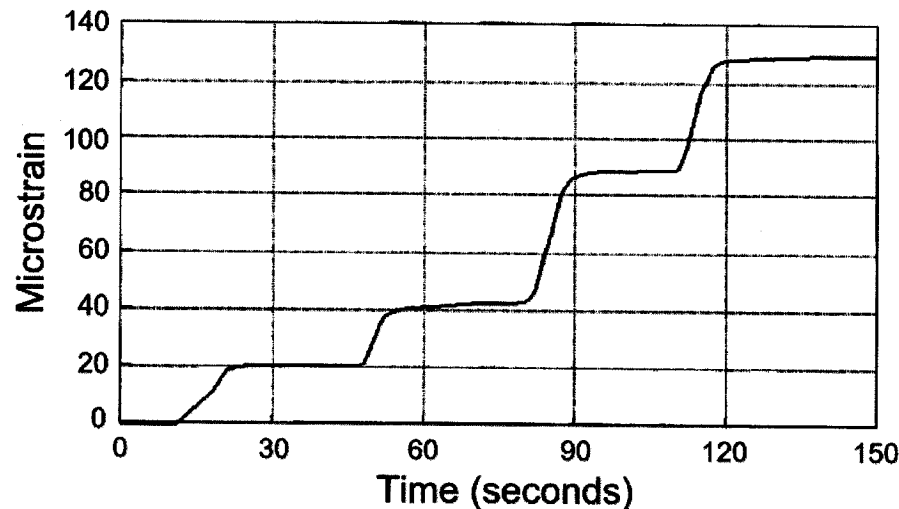
Figure A.28: Microstrain as a function of time from cutting tendon wires (extracted from [221]).

There are many advantages to the use of fiber optics in detection of corrosion in reinforced concrete. Some of the advantages are listed: unaffected by corrosion or electromagnetic interference, low attenuation over long distances, easy to embed, no dependence on the conductivity of concrete, high sensitivity, continuous monitoring capability, flexibility, small size, negligible weight, resistance to harsh environments, and it allows for multiplexing of several sensors along a single fiber. However, many of the sensors discussed in this section have only been used in the laboratory and/or have little actual trials based on corrosion in reinforced concrete. Many of the sensors are sensitive to temperature fluctuations and traffic noise. Even so, the development of fiber optic sensors for detection of corrosion in reinforced concrete is promising.

A.4   MECHANICAL METHODS

Mechanical methods are those that measure the change in mechanical response of a structure while undergoing reinforcement corrosion. Various techniques include either invoking or listening for transient stress waves in the structure and analyzing the received signal, and measuring deflection and/or strain from various loading scenarios.

A.4.1   IMPACT ECHO (IE)

The impact echo (IE) method consists of impacting the surface of a material to create a stress wave and then receiving the stress wave with a transducer after it has been reflected internally. For an excellent

review of the impact echo method, refer to [226]. An impact can be generated by a variety of sources, with the dropping of steel spheres being a common choice. The diameter of the steel sphere dictates the invoked frequency range. At interfaces in the material where there are impedance mismatches (i.e. air/concrete, rebar/concrete), wave reflections will occur. For thick concrete structures, assessment of the arrival time of the reflected pulses in the time domain is generally all that is necessary to find the depth of a flaw, the size of the flaw, or the thickness of the structure. For thin concrete structures, the frequency, velocity of the waveform, and the depth of where the reflection occurred are related by the following:

$$depth = \frac{c}{2f} \dots\dots\dots\dots\dots\dots\dots\dots\dots\dots\dots\dots\dots\dots\dots\dots\dots\dots\dots\dots\dots\dots\dots\dots (A.9)$$

where c is the propagation velocity and f is the frequency. Modes of vibration are invoked in thin concrete structures due to the plate shape. If the velocity of a waveform is known for a particular mix of concrete, the frequency domain can be used to determine the depth of internal flaws, voids, and delaminations in reinforced concrete. The delaminations occurring from corrosion of RC structures have been specifically monitored using IE by researchers in the past [133,138,134,142]. Other researchers analyzed an RC specimen over time using IE and found that the development of microcracking in the concrete matrix could be determined by looking at peak frequency amplitude [142]. IE has been used to confirm the results of other faster inspection methods for in-field measurements such as an inspection of the Seattle Kingdome roof [134]. The method usually provides a more thorough quantitative analysis than many other inspection methods. However, the method takes a measurement point-by-point, meaning that the thorough inspection of large structures is very time consuming and expensive. The method is confined to testing on accessible sides of the structure. The depth of reinforcement, bond between rebar and concrete, size of rebar, impact source, and environmental condition all provide variability to testing.

A.4.2 CHAIN DRAG METHOD

The chain drag method is used to detect delaminations in bridge decks, typically caused by corrosion of the reinforcement. The method is very similar to impact echo (refer to section A.4.1). Both methods use an impactor to invoke mechanical waves in the bridge deck, with the reflected waveforms captured using a reception device. In the case of the chain drag method, an inspector listens for hollow or clear ringing sounds while dragging a chain over the deck. A hollow sound is indicative of delaminated concrete while a clear ringing sound is indicative of well bonded concrete. Figure A.29 illustrates dragging a chain over reinforced concrete, with a human inspector listening for reflected waveforms.

257
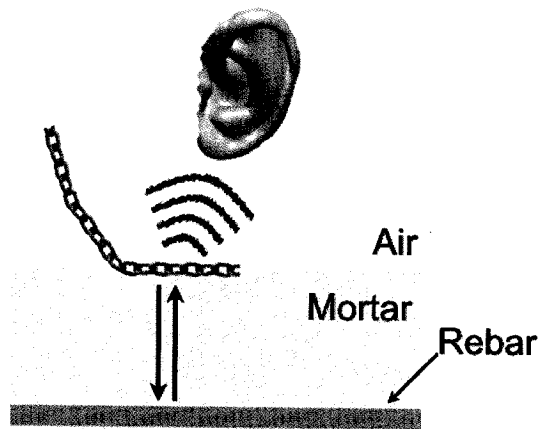
Figure A.29: Chain drag method for detection of delaminations in concrete bridge decks.

ASTM outlines how to measure delaminations in bridge decks using the chain drag method [227]. The ASTM provisions also outline how to use an electro-mechanical sounding device, a hammer, and metal rods to invoke the mechanical waves in the deck. Dragging a chain over the bridge deck is usually the most common choice. The prescribed procedure asks the inspector to lay out a grid system on the bridge deck. The inspector drags the chain over the deck and marks areas as healthy or delaminated. Scaled maps are constructed from the grid system, with the total delaminated area of the bridge deck estimated.

Researchers have used the chain drag method to create scaled maps and to compare with other methods for detection of delaminations in concrete bridge decks [133,138,195]. Figure A.30 shows a scaled map of a bridge deck with delaminated areas identified using the chain drag method [195].
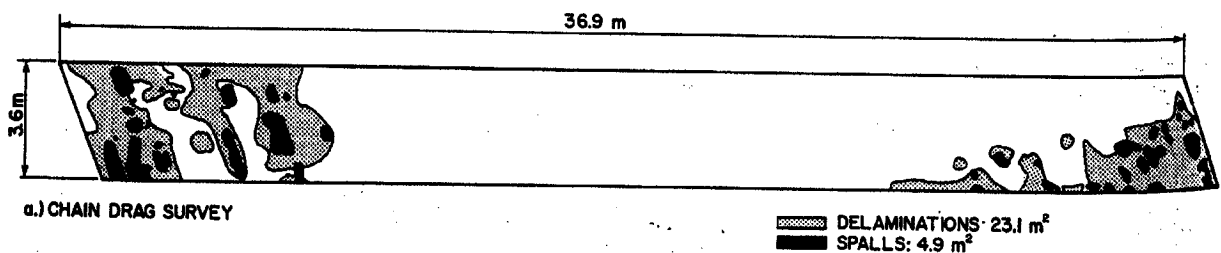
Figure A.30: Scaled map of bridge deck with delaminated areas marked (extracted from [195]).

The method relies heavily on the experience of the inspector. Chain drag surveys are very time-consuming, especially if the grid system has high definition. Traffic noise, concrete moisture content, temperature, the number and training of inspectors, and the sounding device can all play a role in the variation of the results.

258

A.4.3   ACOUSTIC EMISSION (AE)

Acoustic emission (AE) uses a transducer for reception of transient stress waves produced by the material tested. Stress waves are usually the result of material degradation such as cracking, dislocations, debonding, grain boundary sliding, and plastic deformation. The transducer listens for incoming waveforms, causing acoustic emission to generally be labeled as a passive technique. With laboratory testing, one can induce transient stress waves by applying loads and/or deterioration in the material. An AE setup for detection of corrosion in an RC specimen, with the rebar used as a waveguide, is shown in Figure A.31. Many AE systems have been setup with the transducers coupled to the concrete rather than the rebar.
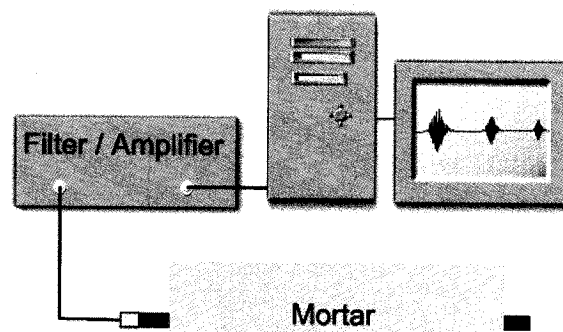
Figure A.31: Acoustic emission setup.

Researchers have investigated AE applicability for detection of corrosion in RC specimens [186,228-230,231-233]. Tests were conducted where impressed current and seawater exposure (wet/dry cycles) were used as two different methods to accelerate corrosion in RC specimens while monitoring using AE [228]. RC specimens exhibited correlation between the threshold counts per day and the exposure time of the specimen to impressed current (see Figure A.32(a)). Threshold counts are acoustic events (i.e. received waveforms) that have signal strength over an arbitrary threshold value. Using the spatial filtering technique, plots of counts per day as a function of the distance along the RC specimen were also constructed. This allows for the use of AE monitoring for detection and location assessment of corrosion in RC specimens. When the RC specimens were exposed to seawater wet/dry cycles and monitored using AE, the results were not as conclusive. Figure A.32(b) shows counts per day as a function of the exposure time to seawater. The only specimen with a noble half-cell potential reading (refer to Section A.2.1) for the entire duration of testing was #45. Figure A.32(b) shows many more counts per day for the specimens that transition from a noble to active potential during testing. However, no correlation is exhibited between counts per day and exposure time subsequent to the half-cell potential transitioning from noble to active [228].

259
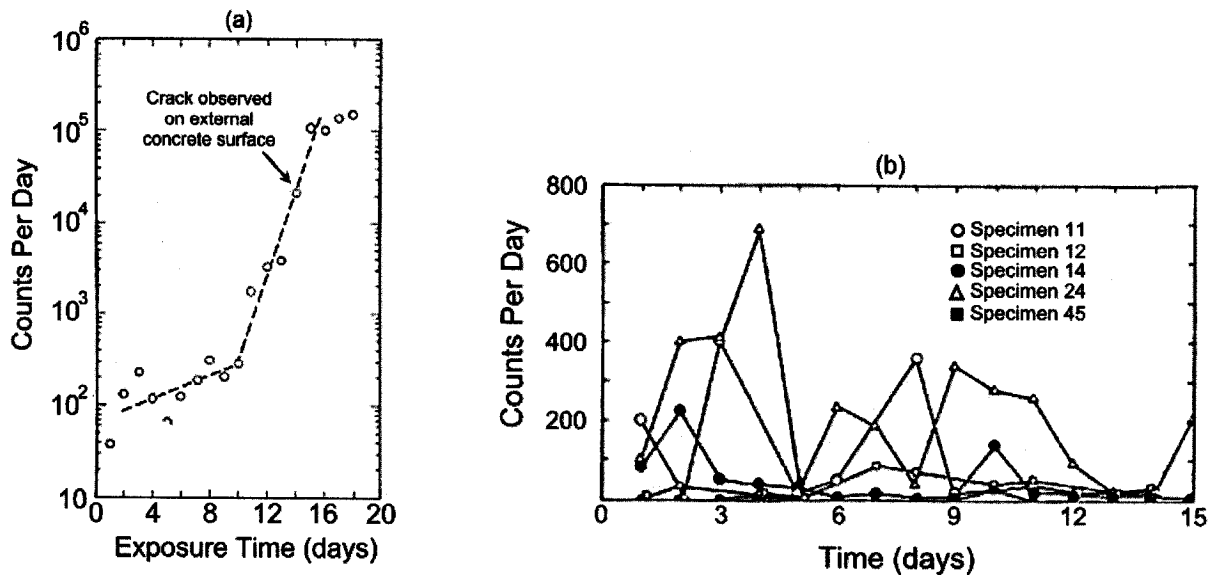
Figure A.32: Threshold counts per day as a function of exposure time of RC specimen to (a) impressed current and (b) sea water (extracted from [228]).

Other researchers using salt electrolyte exposure in wet/dry cycles to accelerate corrosion in laboratory RC specimens found that AE monitoring was able to predict corrosion activity at an earlier stage than galvanic current or half-cell potential measurements [229]. Figure A.33(a) shows acoustic events and galvanic current as a function of specimen exposure time.
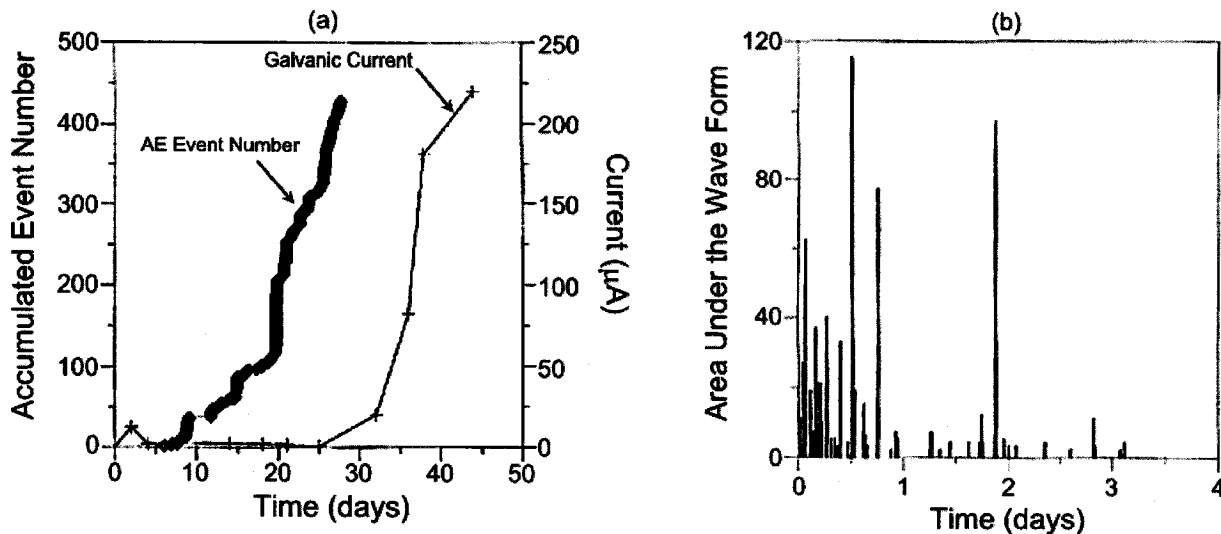
Figure A.33: (a) Acoustic events and current as a function of time for exposure of an RC specimen to wet/dry cycling and (b) AE energy as a function of time for an RC specimen tested during dry cycle after 1 year wet/dry cycling (extracted from [229]).

The number of acoustic events starts to rapidly increase before the galvanic current starts to increase. It is speculated that the corrosion product accumulation starts to cause microcracking in the concrete matrix, with strain energy being converted to acoustic energy. In addition to acoustic events caused by the

260

cracking, researchers have speculated that the friction produced by the corrosion product rubbing against the walls of the cracks, along with the influx of electrolyte into the newly formed cracks leads to even more received acoustic energy [186]. The current most likely is not affected by early microcracking because the resistance of the electrons is largely unaffected until more substantial cracking has occurred.

A specimen was tested at the beginning of a dry cycle (after one year of wet/dry cycles) with a plot of the AE energy as a function of time shown in Figure A.33(b). The amount of energy released is much greater at the beginning of the dry cycle than after 3 days. More crack activity is occurring, with the cracks sharper and larger than later cracks [228]. Most likely the higher corrosion activity is due to water and oxygen being more readily available at the start of the dry cycle than towards the end.

Acoustic emission monitoring was conducted on RC specimens with different levels of corrosion using a cyclical loading experiment. Under the Kaiser effect, a loaded material produces transient stress waves only after a threshold load level has been exceeded. When reloaded, the material should not emit transient stress waves until the previous maximum stress level has been exceeded. Figure A.34 shows AE events as a function of loading for an uncorroded specimen, a corroded specimen with a 0.04" (1 mm) visible crack, and a specimen with a 0.16" (4 mm) visible crack.
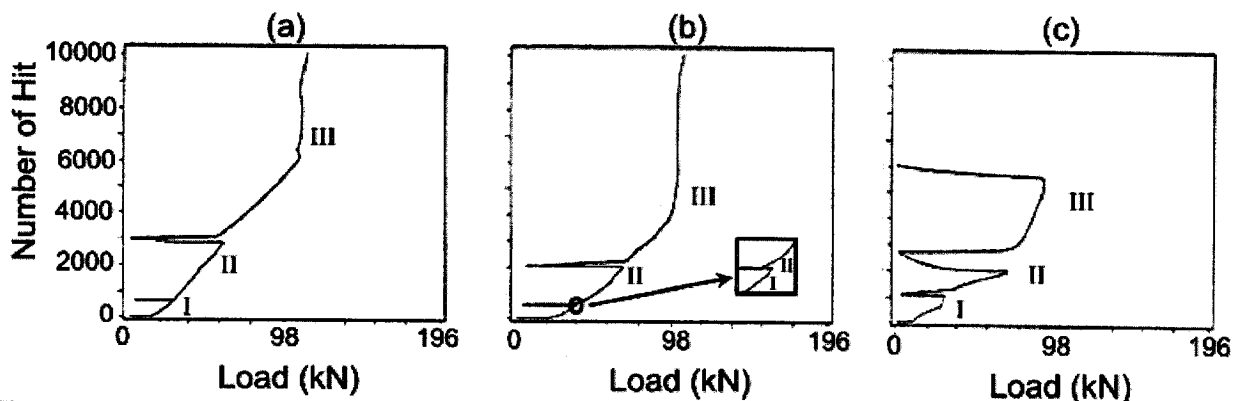
Figure A.34: AE events as a function of loading for RC specimens with (a) no corrosion, (b) corrosion with a crack width of 0.04" (1 mm) and (c) corrosion with a crack width of 0.16" (4 mm) (extracted from [230]).

During the second loading, the uncorroded specimen (Figure A.34(a)) has no AE events until the previous maximum stress level is achieved. The corroded specimens with a 0.04" (1 mm) crack width, see Figure A.34(b), and 0.16" (4 mm) crack width, see Figure A.34(c), reach stress levels of 71% and 28% of the previous maximum stress level previous to AE events occurring, respectively.

Currently an AE monitoring system called SoundPrint® is commercially available. The system uses an array of transducers to try to detect and locate steel wire breaks. Researchers have used the technology to

261

continuously monitor grouted post-tensioned concrete bridges [231]. The system seems to detect and locate fractures in ungrouted and partially grouted tendons with the highest clarity. However, fully grouted tendons seem to present more of a challenge to the system due to the high attenuation of the waveform.

AE monitoring seems to be a very promising passive monitoring method for corrosion in RC structures. Researchers have shown that the influence of seasonal changes has an insignificant effect on the magnitude of AE [233]. The main limitation of the method for detection of corrosion in RC structures seems to be signal attenuation. Concrete is an inherently attenuative material for transient stress waves, whether transducers are coupled to the concrete or on the ends of the rebar (loss through leakage). Corrosion is more easily detected during warm parts of the day than during cold [233]. Also, complexities to signal interpretation can be added when external acoustic events (traffic, impacts, noise) are misidentified.

A.4.4 STRAIN GAGES (SG)

The electrical resistance strain gage is based on the resistance of a conductor changing as a function of the normal strain [234]. Researchers have embedded strain gages (SG) into reinforced mortar specimens subjected to accelerated corrosion to try and detect the change in tension due to rust product formation [235]. Figure A.35 shows the SG measurements from four different types of reinforced mortar specimens. SGO (w/c = 0.50) has no admixtures, SGC (w/c = 0.50) has cement kiln dust added, SGD (w/c = 0.47) has a corrosion inhibitor ($Ca(NO_2)_2$ action), and SGA (w/c = 0.47) has a corrosion inhibitor (aminoalcohol action).
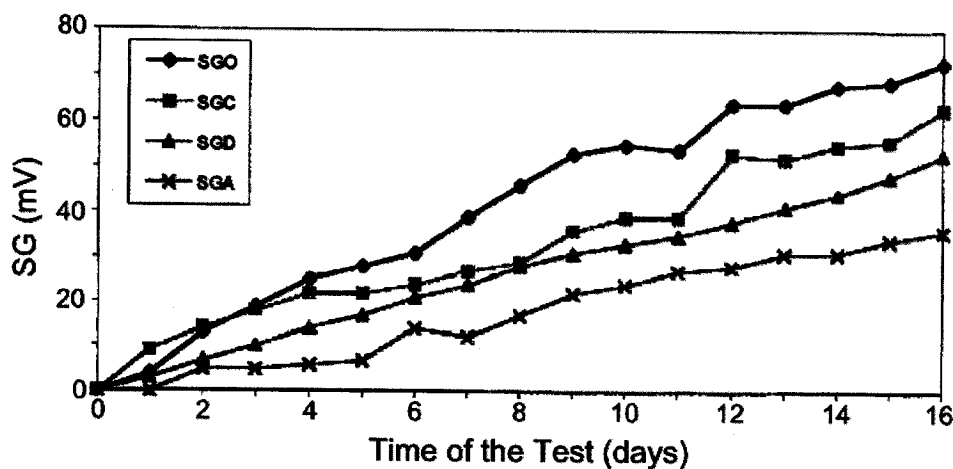
Figure A.35: Strain gage measurement as a function of time during accelerated corrosion (extracted from [235]).

262

The strain gage was able to discern the effectiveness of the admixtures used for inhibiting corrosion. SG measurements used for corrosion detection in reinforced concrete is a relatively novel detection method. It was only prescribed in recent literature to be used for laboratory testing [235]. After mortar cracking, the SG measurements are less affected by corrosion product and more affected by mortar composition. Therefore, the method is only effective for the onset of corrosion in reinforced concrete.

A.4.5 DYNAMIC TESTING

Dynamic testing measures the dynamic response of a structure from a force exerted on it (either from artificial loading or in-service loads) [236]. Structural damage from corrosion will change the stiffness of the structure. The stiffness of a structure is related to the natural frequency of a particular mode of vibration by the relation:

$$f_n = \frac{n^2\pi}{2}\sqrt{\frac{EI}{ML^4}} \quad\quad\quad\quad\quad\quad\quad\quad\quad\quad\quad\quad\quad (A.10)$$

where E is the Young's modulus, I is the second moment of area, n is the mode number, M is the mass per unit length, and L is the span length. Therefore, structural damage from corrosion should be detectable from a shift in the natural frequency of the structure. The magnitude of the change should be an indication of the severity of the damage [237]. Some researchers have measured the natural frequency of damaged RC beams from corrosion and through comparison to a theoretical model of damage were able to predict the strain-stress state of the beam [238]. Structural measurements should be taken at locations where all the modes have relatively high magnitudes.

Modal damping is also used to estimate structural damage from dynamic testing. The modal damping of the structure is quantified by exerting an excitation force to a structure, stopping the force and then measuring the time for the vibration of the structure to cease. The trend for modal damping, with relation to structural damage, is mode dependent [237]. It is thought that since less excitation energy is needed to invoke lower modes, these modes do not disrupt the steel/rust/concrete interface. However, for higher modes, more excitation energy is needed and so disruption of the bond is thought to occur. This effect on the bond during testing strays from the normal definition of NDT methods. Figure A.36 shows the damping ratio for these lower order modes. A drawback to dynamic testing is that it is difficult to test pre-existing structures with no natural frequency and/or modal damping test history. There is no baseline to compare more recent measurements. One way to compensate for this is to compare the dynamic response of the structure under no loading and then when a large load is placed on it. The cost and practicality of using this method becomes prohibitive for larger structures due to the size of the load

263

needed [239]. Others have tried to compensate by creating computer models of the structure and then comparing to the actual response of the structure [240]. For larger structures, the computer model would become highly complex with several uncertainties. Some have concluded that it is much more desirable to rely only on measured data [239]. Other researchers found no significant change in natural frequency and no trend in modal damping before and after structural repairs due to the localized nature of the repairs [241]. Support conditions on structures lead to changes in the dynamic response but do not necessarily indicate structural damage [239]. Another factor leading to erroneous results are environmental factors such as temperature and humidity.
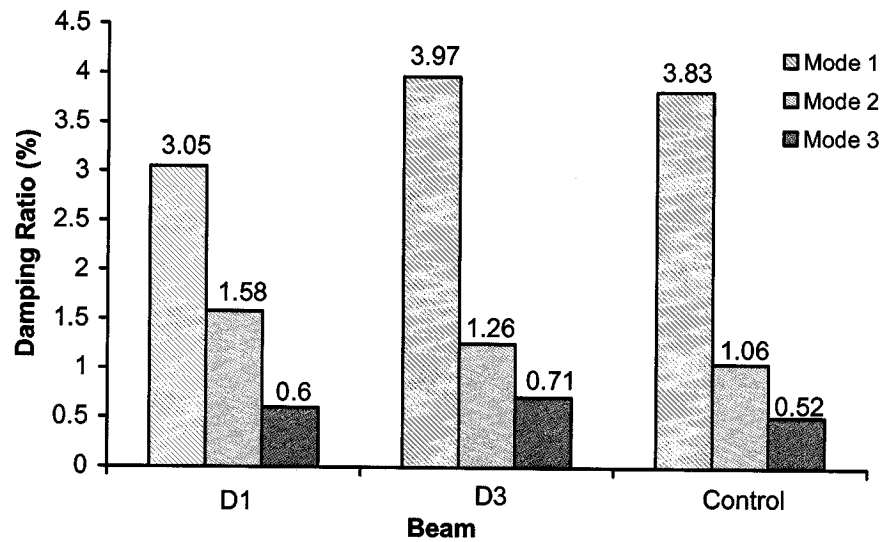
Figure A.36: Comparison of damping ratios for different modes (extracted from [237]).

A.4.6 ULTRASONIC TOMOGRAPHY

An A-scan (through-transmission) was used to inspect RC specimens that underwent accelerated corrosion using impressed current [144]. A total of five different locations for A-scans were chosen to create an average value of waveform amplitude. Other more well-established electrochemical methods (i.e. DC LPR and AC impedance) were used in conjunction with the A-scan to estimate the corrosion rate. Figure A.37 shows the average amplitude attenuation percentage as a function of thickness loss for the RC specimens. The thickness loss was estimated using the AC impedance method (refer to section A.2.3) and the amplitude attenuation percentage was calculated by:

$$\text{Attenuation \%} = \frac{A_1}{A_o} \times 100 \quad \text{...(A.11)}$$

264

where A_1 is the amplitude of the signal at the time of measurement and A_o is the amplitude of the signal prior to any accelerated corrosion.
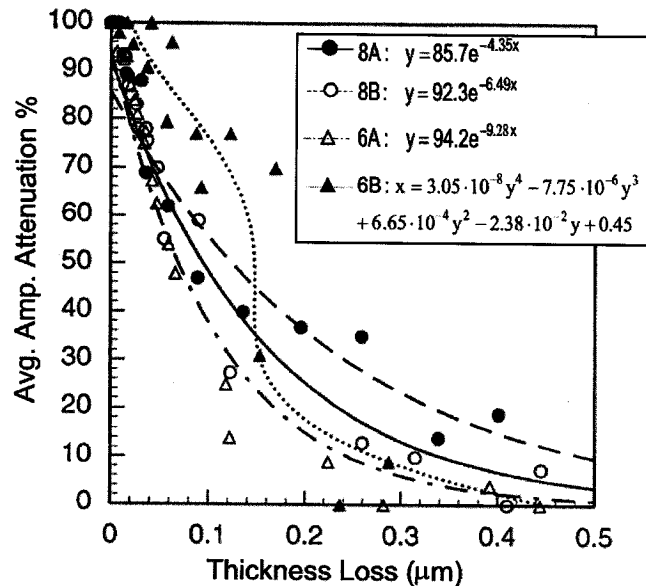
Figure A.37: Average amplitude attenuation percentage for an A-scan as a function of thickness loss for an accelerated corrosion specimen (extracted from [144]).

Specimens are designated as either #6 or #8 at the beginning, with #6 representing 3/4" (1.91 cm) diameter bars and #8 representing 1" (2.54 cm) diameter bars. Specimens are also designated A or B, with A having a w/c = 0.35 and B having a w/c = 0.40. Figure A.37 illustrates that the change in through-transmission signal amplitude has a non-linear relationship with thickness loss. Specimens with a smaller diameter have greater amplitude attenuation, while amplitude attenuation was easier to detect in higher strength concrete due to the brittleness of the microstructure [144].

To detect voids in grouted posttensioned bridges, ultrasonic tomography has been used [242]. Based on the ultrasonic pulse velocity of reflected signals, cross-sections can be constructed. Scans were conducted on both the sides and the top of the specimen, showing that simulated voids were detected by with the use of ultrasonic tomography. To detect corrosion and voids in posttensioned tendons, a C-scan has been used [243,244]. A plain grouted specimen, a partially corroded specimen, and a fully corroded specimen were tested fully submerged in water using a C-scan. A focused transducer was used for the C-scan, with the reflected signal gated so that the peak amplitude and time of flight information could be calculated for different layers of the beam. Figure A.38 shows the image of the layer containing the tendon.

(a) Plain Grouted

(b) Partially Corroded
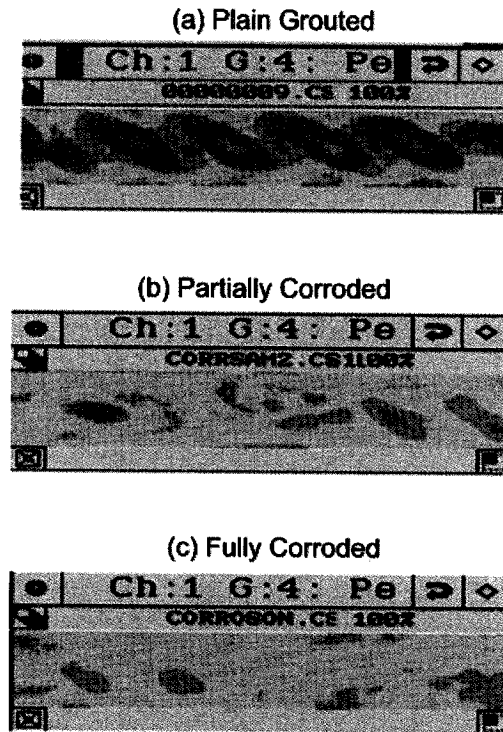
(c) Fully Corroded

Figure A.38: Ultrasonic image of tendon layer for **(a)** plain grouted, **(b)** partially corroded, and **(c)** fully corroded specimen (extracted from [243]).

The plain grouted specimen has many visible strand twists, while the partially and fully corroded specimens have less respectively. The loss of visible twists in the strand is caused by the accumulation of rust product.

Ultrasonic tomography seems to offer promise for corrosion detection in RC structures. It is relatively inexpensive and safe. However, the method is time consuming depending on the necessary resolution. Concrete is a highly attenuative material with respect to ultrasonic waveforms and so the method is constrained by distances and is sensitive to operating frequencies. Signal interpretation is highly complicated in solid materials, especially in a heterogeneous material such as concrete. The presence of shear and Rayleigh waves can complicate matters further. Since ultrasonic tomography is rather new to detection of corrosion in RC structures, further testing is needed.

266

APPENDIX B:

POURBAIX DIAGRAM CONSTRUCTION

The procedure for creation of Pourbaix diagrams is the following [30]:

1. Determine the possible types of ions
2. Formulate the reactions involving the ion types
3. Use the Nernst equation to form a relationship between the potential and ion concentration
4. Draw equilibrium lines where the concentration of each ion type is the same

The fourth step involves the formation of horizontal, vertical, and sloping lines. The horizontal line involves a solid substance, a dissolved substance in water, and free electrons. The horizontal line is independent of pH. The vertical line involves a solid substance, a dissolved substance and hydrogen ions in water. The vertical line is independent of the electrode potential. The sloping line involves a solid substance, a dissolved substance, free electrons, and hydrogen ions. The sloping line is dependent on both the pH and the electrode potential. For more complete numerical examples, the reader is referred to Uhlig's Corrosion Handbook [33].

More explanation will now be provided as to how the diagrams were constructed for iron. However, not all of the reactions are written out explicitly in this text. For more information, consult [33,39]. An equilibrium line in both diagrams is the following:

$$Fe^{+2} + 2e^- = Fe \dotfill (B.1)$$

Using the Nernst equation:

$$E_{eq} = E^\circ - \frac{RT}{ZF} \cdot \ln\frac{[C]^{n_c}[D]^{n_d}}{[A]^{n_a}[B]^{n_b}} - 0.440 - \frac{\left(8.314 \frac{J}{K}\right)\left(298^\circ K\right)}{(2)\left(96,500 \frac{Coulomb}{mole}\right)}(2.303)\log\left(\frac{[Fe]^1}{[Fe^{+2}]^1}\right) = -0.440 + (0.0295)\log[Fe^{+2}] \quad (B.2)$$

The reaction describes a solid substance, a dissolved substance, and free electrons. Therefore, a horizontal line describes it on the Pourbaix diagram, showing it is independent of the pH and dependent on the electrode potential. This line is shown separating the corrosion section from the immunity section. It was assumed for the sake of simplicity that the ferrous ion concentration was 10^{-6} gram atoms of soluble ion per liter. If at equilibrium there are excess electrons (negative electrode potential), then the iron will not breakdown. If at equilibrium free electrons are unavailable, then the reaction above will proceed. An equilibrium line is shown in Figure 2.3 for the following:

$$3Fe + 4H_2O = Fe_3O_4 + 8H^+ + 8e^- \dotfill (B.3)$$

267
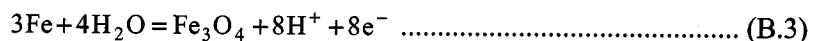
There are two solid substances, free electrons, and hydrogen ions. Therefore a sloping line will describe this reaction on the Pourbaix diagram, meaning it is dependent on both the pH and electrode potential. The sloping line can be seen in the figure above connecting with the horizontal line mentioned before at a pH around 6. The line is bolded heavier than the other lines. This is to indicate that there are two solids involved in the reaction, as opposed to a solid and dissolved ion indicated by the lighter solid line. Again, excess electrons push the reaction in the direction of the iron. Also, excess hydrogen ions drive the pH lower, and since the line is sloping downward, probably create a tendency towards iron. The product Fe_3O_4 is considered part of the oxide layer (i.e. passive layer) that protects steel from corrosion and forms on reinforcing steel when embedded in concrete. Electrons and excess hydrogen ions (lowering of pH) destroy the oxide layer. An equilibrium line is shown in Figure 2.3 for the following:

$$3Fe^{+2} + 4H_2O = Fe_3O_4 + 8H^+ + 2e^- \dotfill (B.4)$$
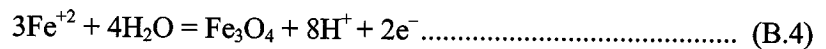
It is the same type of reaction as described previously and is described by a sloping line on the Pourbaix diagram. It connects the Fe^{+2} region to the Fe_3O_4 region. Excess hydrogen ions and electrons drive this towards corrosion. Equilibrium for the Fe_3O_4 product converted to Fe_2O_3 is shown:

$$2Fe_3O_4 + H_2O = 3Fe_2O_3 + 2H^+ + 2e^- \dotfill (B.5)$$
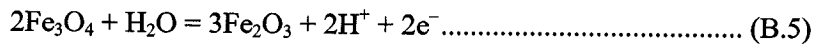
The reaction is a two solid reaction with hydrogen ions and free electrons. This indicates a sloping line on the Pourbaix diagram, with the same slope as the Fe to Fe_3O_4 reaction. The product Fe_2O_3 is the other portion of the oxide layer that protects reinforcing steel embedded in concrete from corrosion. An increase in hydrogen ions and electrons will drive the reaction towards Fe_3O_4.

APPENDIX C:

INITIATION PERIOD MODELING

An accurate model for the ingress of carbon dioxide and chlorides in concrete allows for an estimation of when the deleterious substances will reach the rebar depth and initiate corrosion. Assuming that the concrete has few cracks and is not entrained with deleterious substances, the ingress of chlorides and carbon dioxide occurs through a diffusion process. Descriptions of models for each are outlined in this chapter.

C.1.1 MODELING THE INGRESS OF CARBON DIOXIDE

In order for carbon dioxide to reach the reinforcement depth, it must travel through the concrete pore system. The pore structure of the concrete is determined in large part by the water-to-cement ratio, compaction, curing practices, entrained admixtures, cementitious materials used (e.g., pozzolans and fly ash), and the type of cement. The temperature, relative humidity, and pressure are environmental effects that help determine the rate at which the carbon dioxide travels through the concrete pores. Even the loading conditions affect the rate of carbonation [245]. A generic model for the carbonation depth with respect to time has been described previously and is shown to give the reader an idea of the factors involved with the ingress process [29]:

$$\text{depth} = f(A, B, C, D, C.D, E_1, E_2, C.E_1, C.E_2, F_1, F_2, C.F_1, C.F_2, t_1, t_2) \dots\dots\dots (C.1)$$

where A is the cement composition, B is the cement content, C is the mix proportions of the concrete, D is the compaction of the concrete, E_1 is the relative humidity during curing time, E_2 is the temperature during curing time, F_1 is the relative humidity during exposition time, F_2 is the temperature during exposition time, t_1 is the curing time, t_2 is the exposure time, and all other terms are interaction terms.

Fick's 1st law has been used to model the ingress of carbon dioxide, allowing for a relationship between the depth and the amount of time to be formulated. Fick's 1st law (in one-dimension) can be written:

$$\frac{dq}{dt} = D \cdot A \cdot \left(\frac{\Delta c}{x}\right) \dots\dots\dots\dots\dots\dots\dots (C.2)$$

where q is the amount of diffusing CO_2, t is the time, D is the coefficient of diffusivity, A is the area of the transverse section, Δc is the difference in concentration of CO_2 between air and the carbonation front $(c_1 - c_2)$, and x is the layer thickness. The total amount of CO_2 necessary to neutralize the alkaline substances is the following:

$$dq = a \cdot dV = a \cdot A \cdot dxdq \quad \text{...} \quad (C.3)$$

where a is the density of alkaline substance (calcium hydroxide) and V is the volume of concrete through which the diffusion process is occurring. Substituting this into the previous equation and rearranging:

$$a \cdot x \cdot dx = D \cdot (c_1 - c_2)dt \quad \text{...} \quad (C.4)$$

integrating both sides:

$$\tfrac{1}{2}ax^2 = D(c_1 - c_2)t \quad \text{...} \quad (C.5)$$

arrives at the following solution:

$$x = G\sqrt{t} \quad \text{...} \quad (C.6)$$

where:

$$G = \sqrt{\left(\frac{2D}{a}\right)\Delta c} \quad \text{...} \quad (C.7)$$

Under these assumptions the carbonation depth increases as a function of the square root of time. A drawback to this equation is that it does not take into account the wetting and drying of the concrete. Refer to [29] for further discussion.

Solutions have been provided based off of Fick's 2nd law of diffusion (refer to Appendix D). Many times the closed form solution given as Eqn. D.8 is used for defining the length of the initiation period. However, more involved solutions have been formulated. Please refer to [246] for more discussion regarding mathematical modeling of concrete carbonation. An example of a solution is provided here for the reader. The solution involves using Fick's 2nd law. However, carbon dioxide gas is consumed during the carbonation reaction taking place. This can be accounted for by subtracting the change of carbon dioxide concentration due to carbonation in a unit of time from Fick's one-dimensional equation [247].

$$\frac{\partial C}{\partial t} = \left(\frac{\partial D}{\partial x} \cdot \frac{\partial C}{\partial x}\right) + \left(D \cdot \frac{\partial^2 C}{\partial x^2}\right) - \frac{\partial C_c}{\partial t} \quad \text{...} \quad (C.8)$$

where C_c is the concentration of CO_2 consumed in creating calcium carbonate. The rate at which the carbonation reaction occurs has been modeled previously [247]. The basic rate calculation is dependent

on the particular concrete, relative humidity, the concentrations of carbon dioxide and calcium hydroxide, and the temperature:

$$v = \frac{\partial \left[CaCO_3 \right]}{\partial t} = \alpha_1 \times f_1(h) \times [CO_2] \times [Ca(OH)_2] \times f_4(T) \quad\quad\quad (C.9)$$

where α_1 is a non-dimensional parameter (varies between 0 and 1) dependent on the way the particular concrete affects the rate of reaction. The carbonation rate is typically rewritten in the following form:

$$v = \frac{\partial c}{\partial t} = \alpha_1 \times f_1(h) \times f_2(\phi) \times f_3(c) \times f_4(T) \quad\quad\quad (C.10)$$

where $f_2(\phi)$ describes the concentration of CO_2 and $f_3(c)$ describes the degree of carbonation reaction that has taken place. The functions $f_1(h)$, $f_2(g)$, $f_3(c)$, and $f_4(T)$ can be written:

$$f_1(h) = \begin{cases} 0 & 0 \leq h \leq 0.5 \\ \frac{5}{2}(h - 0.5) & 0.5 \leq h \leq 0.9 \\ 1 & 0.9 \leq h \leq 1 \end{cases} \quad\quad\quad (C.11)$$

$$f_2(g) = \frac{g}{g_{max}} \quad\quad\quad (C.12)$$

$$f_3(c) = 1 - \left(\frac{c}{c_{max}} \right)^m \quad\quad\quad (C.13)$$

$$f_4(T) = k = Ae^{-E_o/RT} \quad\quad\quad (C.14)$$

where h is the relative humidity, g is the carbon dioxide concentration, g_{max} is the maximum carbon dioxide concentration, c is the degree of carbonation, c_{max} is the maximum amount of calcium carbonate, and m is usually equal to one. The Arrhenius equation, represented by k, describes the effect of temperature on the reaction rate where A is a constant, E_o is the activation energy of carbonation, R is the universal gas constant, and T is the temperature (in Kelvins). The reaction slows as the amount of carbonation reaction increases. The reaction rate will increase as the relative humidity, temperature, and concentration of carbon dioxide increase. A non-dimensional parameter α_4, which varies between 0 an 1 and is dependent on the characteristics of the concrete, is multiplied by the reaction rate to calculate how much CO_2 was consumed in the carbonation reaction:

$$\frac{\partial C_c}{\partial t} = \alpha_4 \frac{\partial c}{\partial t} \qu\quad\quad\quad (C.15)$$

271

It is generally assumed that the coefficient of diffusivity for carbon dioxide ingress is dependent on time (degree of hydration), location (curing effect, wall effect), the moisture content and temperature [248]. Temperature not only increases the coefficient of diffusivity naturally but also reduces the moisture content in the pores allowing for faster gas diffusion. Previous literature has reported the dependency of the coefficient of diffusivity to be of the following nature in equation form [40]:

$$D = D_0 F_1(h) F_2(T) F_3(t_e) F_4(\Re) \quad\text{...}\quad (C.16)$$

where D_0 is the diffusivity of carbon dioxide in the standard condition (28 days curing, temperature = 25° C), $F_1(h)$, $F_2(T)$, $F_3(t_e)$, and $F_4(c)$ are functions taking into account the effects of relative humidity, temperature, curing time, and the reduction of diffusivity due to the formation of carbonation, respectively.

$$F_1(h) = (1-h)^{2.5} \quad\text{..}\quad (C.17)$$

$$F_2(T) = e^{\left(\frac{Q}{R}\left(\frac{1}{T_0} - \frac{1}{T}\right)\right)} \quad\text{...}\quad (C.18)$$

$$F_3(t_e) = \chi + (1-\chi)\left(\frac{28}{t_e}\right)^{0.5} \quad\text{.......................................}\quad (C.19)$$

$$F_4(\Re) = 1 - \zeta\Re \quad\text{...}\quad (C.20)$$

where h is the relative humidity, Q is the activation energy of the diffusion process, R is the universal gas constant, T_0 is the reference temperature (usually 298 K), T is the temperature, χ is the ratio between the diffusion coefficient for $t_e \to \infty$ and the diffusion coefficient for $t_e = 28$ days, t_e is the equivalent curing time, ζ is a parameter (between 0 and 1) that measures the slowing of the diffusion phenomenon due to reduction of the porosity, and $\Re$ is the degree of chemical reaction written:

$$\Re = \frac{[CaCO_3]}{[CaCO_3]_{max}} \quad\text{..}\quad (C.21)$$

The flow of the heat and moisture can be modeled as partial differential equations and coupled to these equations for a more accurate estimation of the rate of diffusion [247, 248].

C.1.2 MODELING THE INGRESS OF CHLORIDES

The closed form solution for Fick's 2nd law has often been used to model the depth of chloride penetration after lengths of time. Figure C.1 shows how the chloride concentration depth profile changes over time using Fick's 2nd law of diffusion.

272
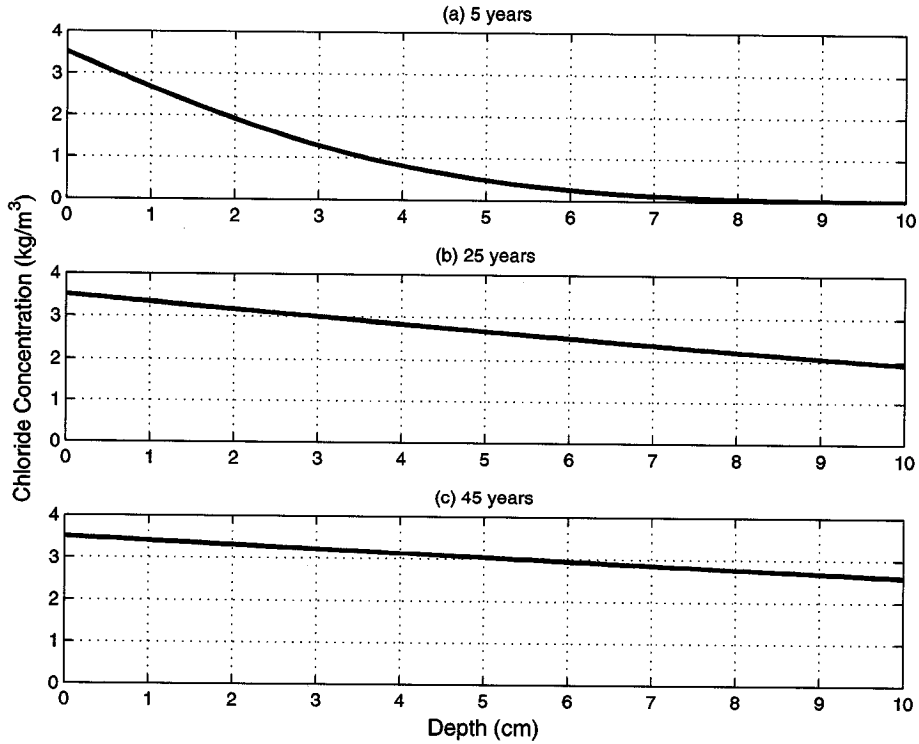
Figures C.1: Chloride concentration as a function of depth using Fick's 2nd Law (assuming constant $D = 1.5 \cdot 10^{-8}$ cm^2/sec, $C_0 = 3.5$ kg/m^3).

Using Fick's 1st law of diffusion, the flux for chloride ions can be written. The flux is dependent on the diffusion of the ions from a concentration gradient and on ions driven by a potential gradient. The flux is written:

$$F = -D_{cl}\nabla C_f - D_{ele}\nabla\phi \quad\quad\quad\quad (C.22)$$

where C_f is the free chloride concentration, D_{cl} is the chloride diffusion coefficient, D_{ele} is the ionic diffusion coefficient, and ϕ is the electric potential. One can balance the mass by using Fick's 2nd law of diffusion. A term is added representing chlorides entering the system through moisture diffusion.

$$\frac{\partial C_t}{\partial t} = \frac{\partial C_t}{\partial C_f}\frac{\partial C_f}{\partial t} = -\mathrm{div}(F) + \mu C_f \frac{\partial w}{\partial t} \quad\quad\quad\quad (C.23)$$

where C_t is the total chloride concentration, w is the moisture content of the concrete, and μ is a unit conversion factor [37] given by the following equation:

$$\mu = \frac{1}{\rho_{sol}\beta_{sol}} \quad\quad\quad\quad (C.24)$$

273

where ρ_{sol} is the density of the pore solution (grams of pore solution per liter) and β_{sol} is the ratio of volume of pore solution to weight of concrete. The diffusion of moisture is written:

$$\frac{\partial w}{\partial t} = \frac{\partial w}{\partial H} \frac{\partial H}{\partial t} = \text{div}\left[D_H \nabla H\right] \quad\quad\quad (C.25)$$

where H is the pore relative humidity, $\partial w/\partial H$ is the moisture capacity, and D_H is the diffusion of humidity coefficient. The binding capacity, $\partial C_f/\partial C_t$, is written:

$$\frac{\partial C_f}{\partial t} = \frac{\partial C_f}{\partial C_t}\left(\text{div}\left[D_{cl}\text{grad}(C_f)\right] + \mu C_f \frac{\partial w}{\partial t} + \text{div}\left[D_{ele}\text{grad}(\phi)\right]\right) \quad\quad (C.26)$$

Unless an external electric potential is impressed on the reinforcement, the third term is usually not taken into account. For the accelerated corrosion testing presented in this report, an electric potential was provided between the copper and steel rebar. These equations would allow for the ingress of chlorides to be modeled for future tests.

The coefficient of diffusivity for chlorides is dependent on many factors. A more advanced model has been proposed based on the effects of the aggregates, water-to-cement ratio, curing time, temperature, humidity, and the free chloride concentration [37]:

$$D_{cl} = f_1(g_i)\cdot f_2(w/c,t_o)\cdot f_3(T)\cdot f_4(H)\cdot f_5(C_f) \quad\quad\quad (C.27)$$

where:

$$f_1(g_i) = D_m\left[1 + \frac{g_i}{\frac{1-g_i}{3} - \frac{D_m}{D_i - D_m}}\right] \quad\quad\quad (C.28)$$

$$f_2(w/c, t_o) = \left[\frac{1}{4} + \frac{28 - t_o}{300}\right](w/c)^{6.55} + \frac{28 - t_o}{62,500} \quad\quad (C.29)$$

$$f_3(T) = e^{\left[\frac{Q}{R}\left(\frac{1}{T_o} - \frac{1}{T}\right)\right]} \quad\quad\quad (C.30)$$

$$f_4(H) = \frac{1}{1 + \left(\frac{1-H}{1-H_c}\right)^4} \quad\quad\quad (C.31)$$

$$f_5(C_f) = 1 - k_{ion}(C_f)^m \quad\quad\quad (C.32)$$

where D_m is the coefficient of diffusivity of the cement paste, g_i is the volume fraction of the inclusions, D_i is the coefficient of diffusivity of the aggregates, t_o is the curing time in days, $H_c = 0.75$ is the critical pore relative humidity, $k_{ion} = \sqrt{70}$, and $m = 0.5$. Most models of the diffusion coefficient make assumptions to reduce the number of terms and make calculations more practical. Many have assumed a constant value for D [249], as it has been observed that the diffusion coefficient slows mainly in the first five years and then approaches a constant value for concrete [250]. Others have used a stochastic value for D. Enright & Frangopol used 5 different mean values for D, each with a lognormal distribution, embedded into the closed form solution to illustrate the sensitivity of the corrosion initiation time to its value [251]. Others have keyed in on a few key design parameters that define the coefficient of diffusivity, such as w/c ratio, degree of hydration, and aggregate volume fraction [252]. Using a least squares regression, the following empirical relationship was formed:

$$D = 10^{\left(-10.22+8.58\left(\frac{w}{c}\right)-4.99\,\alpha_h\,-3.04\,V_{agg}\,+5.09\,\alpha_h\left(\frac{w}{c}\right)-0.91\left(\frac{w}{c}\right)V_{agg}\,+1.6\,\alpha_h\,V_{agg}\,-6.58\left(\frac{w}{c}\right)^2\,-0.92\,\alpha_h^2\,+0.53\,V_{agg}^2\right)}\left(m^2/_s\right) \quad .. \ (C.33)$$

where w/c is the water-to-cement ratio, V_{agg} is the aggregate volume fraction, and α_h is the degree of hydration. Stewart & Rosowsky used this empirical formula to calculate D for a stochastic model [253]. Vu & Stewart assessed several different experimental diffusion coefficients and their relationship to the water-to-cement ratio and constructed Figure C.2 [61].
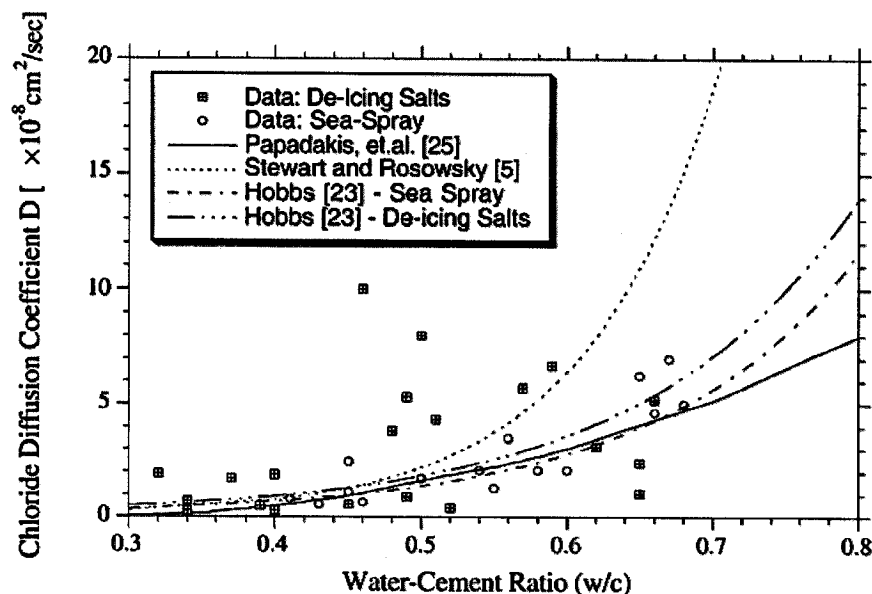
Figure C.2: Chloride diffusion coefficient as a function of water-to-cement ratio (extracted from [61]).

They concluded that the diffusion coefficient used by Papadakis et al. [254] was the best fit for the available data and used the following empirical relationship for stochastic modeling:

275

$$D = D_{H_2O} \cdot 0.15 \cdot \frac{1 + \rho_c \, ^w/_w}{1 + \rho_c \, ^w/_c + \frac{\rho_c}{\rho_a} \, ^a/_c} \left(\frac{\rho_c \, ^w/_c - 0.85}{1 + \rho_c \, ^w/_c} \right)^3 \left(cm^2/_s \right) \dots \text{(C.34)}$$

where a/c is the aggregate-to-cement ratio, w/c is the water-to-cement ratio, ρ_c and ρ_a are the mass densities of cement and aggregates respectively, and D_{H20} is the diffusion coefficient for chloride diffusion coefficient in an infinite solution (=$1.6 \cdot 10^{-5}$ cm²/s for NaCl).

A critical chloride concentration must be reached to destroy the passive layer. The critical threshold chloride concentration has been shown to lie somewhere between 0.6 - 1.2 kg/m³ [253].

Li developed an empirical formula for chloride ingress specifically for RC structures exposed to marine conditions with load-induced cracks [255]. It was shown from experimental testing that when crack widths exceed 0.1 mm, Fick's 2nd law of diffusion is no longer applicable for defining ingress. The proposed empirical formula calculates the mean chloride content at the surface of the reinforcement for load-induced cracks greater than 0.1 mm:

$$\mu_c(t) = C_o e^{at} \dots \text{(C.35)}$$

where C_o is the initial chloride content in concrete at the surface of the reinforcement, a is the coefficient representing the rate of ingress (analogous to the coefficient of diffusion), and t is the time (days). The proposed model is plotted in Figure C.3 with experimental results.
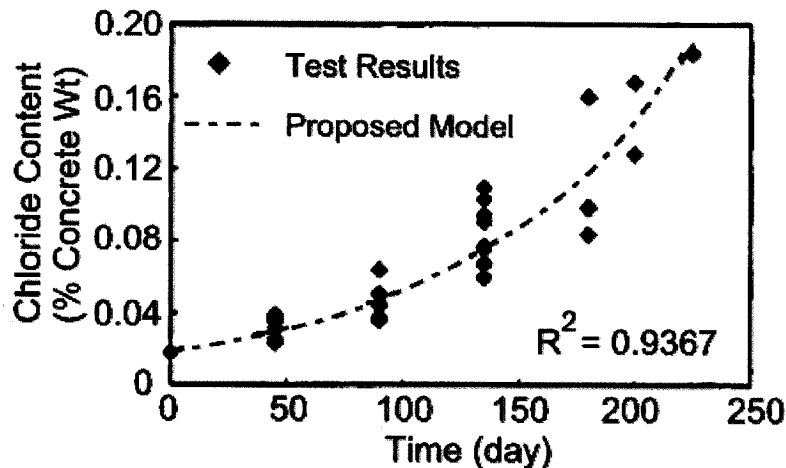
Figure C3: Chloride content as a function of time for chloride ingress model (extracted from [255]).

276

C.1.3 MODELING INTERACTION OF CARBON DIOXIDE AND CHLORIDES

The carbonation reaction slows down the ingress of chlorides. It has been assumed in other models that chloride diffusion is slowed by the factor $F_4(\mathfrak{R})$ given in this Chapter. One can multiply the factor by D_{cl} to reduce the rate of ingress.

APPENDIX D:

FICK'S 2ND LAW OF DIFFUSION

Non-steady state diffusion occurs when the concentration changes within the diffusion volume with respect to time. The differential equation for diffusion is formulated by examining the small volume element shown in Figure D.1:
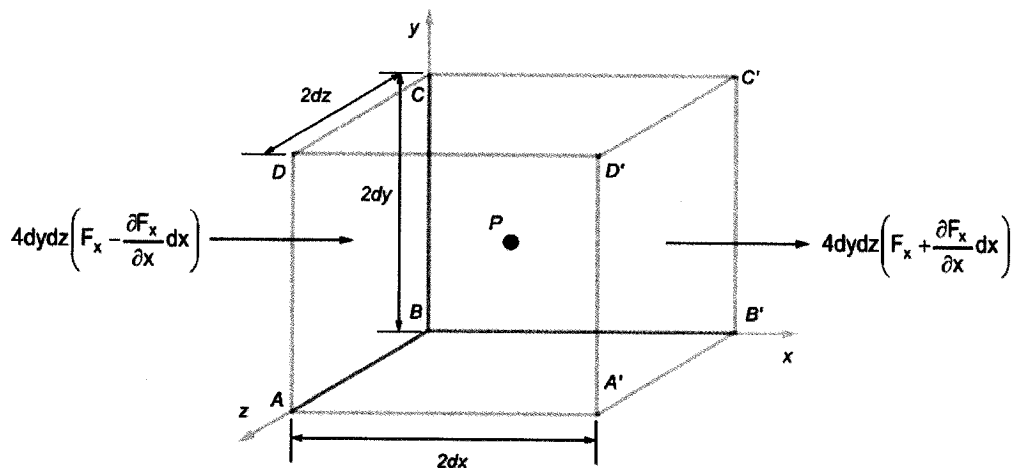
Figure D.1: Rectangular parallelepiped (extracted from [35]).

The center of the small volume element is the point P, with concentration C. Diffusing matter is entering through ABCD and exiting from A'B'C'D'. If the flux of the plane passing through the point P is considered F_x, then the rate of matter passing through ABCD and A'B'C'D' is written as shown in Figure D.1. The rate of increase of the diffusing matter is:

$$-8\,dxdydz\,\frac{\partial F}{\partial x} \quad \text{...} \text{(D.1)}$$

while at the same time the concentration in the element changes by:

$$-8\,dxdydz\,\frac{\partial C}{\partial t} \quad \text{...} \text{(D.2)}$$

Balancing the mass entering and exiting for all three dimensions yields:

$$\frac{\partial C}{\partial t}+\frac{\partial F_x}{\partial x}+\frac{\partial F_y}{\partial y}+\frac{\partial F_z}{\partial z}=0 \quad \text{...} \text{(D.3)}$$

With the use of Fick's 1st law (see Eqns. 2.16 & 2.17) the following can be written:

$$\frac{\partial C}{\partial t} = -\text{div}(F) = \text{div}(D \cdot \nabla C) \quad \text{(three-dimensional)} \dots \text{(D.4)}$$

$$\frac{\partial C}{\partial t} = \left(\frac{\partial D}{\partial x} \cdot \frac{\partial C}{\partial x}\right) + \left(D \cdot \frac{\partial^2 C}{\partial x^2}\right) \quad \text{(one-dimensional)} \dots \text{(D.5)}$$

A closed-form approximation exists for Fick's 2nd law of diffusion. Concrete is modeled as a semi-infinite medium with boundary conditions:

$$C = C_o, \, x = 0, \, t > 0 \dots \text{(D.6)}$$

and initial conditions:

$$C = 0, \, x > 0, \, t = 0 \dots \text{(D.7)}$$

Applying a Laplace transform to Fick's 2nd law of diffusion (see [35]) and using boundary and initial conditions, the following closed form solution is derived:

$$C(x,t) = C_o\left[1 - \text{erf}\left(\frac{x}{2\sqrt{tD}}\right)\right] \dots \text{(D.8)}$$

where:

$$\text{erf}(z) = \frac{2}{\sqrt{\pi}} \int_0^z e^{-t^2} \, dt \dots \text{(D.9)}$$

Tables of calculated erf values exist to allow for quick calculation using this closed form solution. It should be noted that this solution assumes that the coefficient of diffusivity is constant.

279

APPENDIX E:

SERVICE LIFE MODELING

Models have been discussed for both the initiation and propagation periods with respect to corrosion of reinforced concrete. Models from each period, along with a limit state based on an aspect of deterioration, can be chosen and the service life for a particular structure can be estimated. The particular model that one chooses for the initiation and propagation periods will vary.

The general corrosion model shown in Figure 2.5 is one of many that have been proposed by authors. Figure E.1 below is a model set forth by Cady & Weyers that is a slight modification of the Tuutti model.
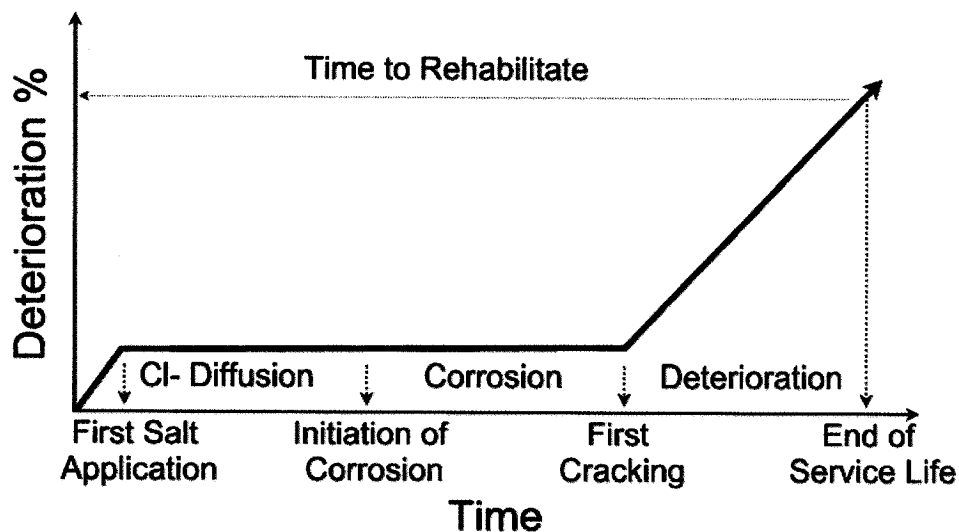
Figure E.1: Cady & Weyers corrosion process model (extracted from [256]).

The model represents the corrosion process in three stages. The first stage is diffusion of the chloride ions into the concrete. It starts immediately after construction of the structure and ends once corrosion of the reinforcement begins. The second stage is the corrosion of the reinforcing steel. Notice that in the model, structural deterioration does not increase between the initiation of corrosion and the first cracking. The third stage is structural deterioration. This begins with the first crack and ends with a predetermined deterioration percentage level. The initial deterioration immediately after the structure is erected is from the construction process and it is generally repaired [11].

The Cady & Weyers corrosion process is just one of many different corrosion models. The corrosion process model looks differently depending on what type of deterioration is considered as critical to the service life of a structure. For instance, [257] proposed using a corrosion process model that displays the propensity for corrosion as a function of time. Figure E.2 shows the model.

280
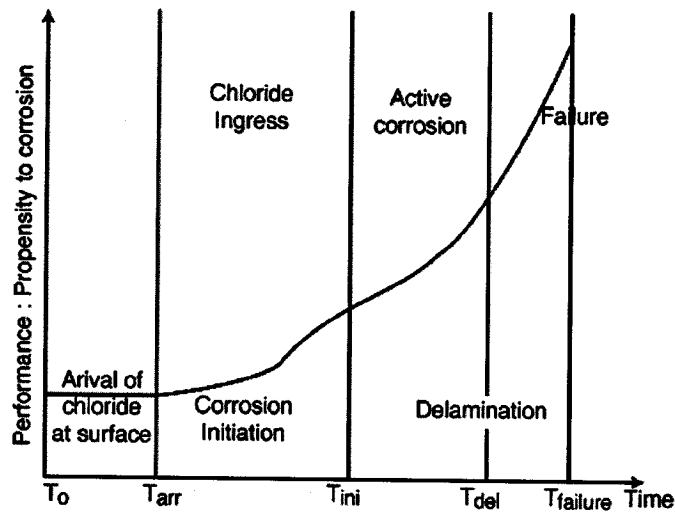
Figure E.2: Propensity for corrosion as a function of time (extracted from [257]).

Ultimately, a corrosion process model could be created that displays any type of deterioration during the service life (e.g. diameter loss, flexural strength, deflection) as a function of time. A service life for a structure is by definition the end of the designed functionality of the structure. The limits states of a functional service life are component and structure dependent [258]. A structure may not meet its credentials for functionality in a variety of ways. For instance, a bridge may be sufficiently strong to hold all loads without collapsing but may deflect excessively at the mid-span. Generally, service life limits are placed in one of two categories: ultimate or serviceability. An ultimate limit is one in which, if reached, results in catastrophic failure of the structure, loss of human life, and/or severe economic damage. The probability of an ultimate limit being reached should be on the order of 1:100000 [9]. A serviceability limit is one in which a repair or rehabilitation effort is needed on the structure. The probability of a serviceability limit being reached should be on the order of 1:100. In many cases RC elements are non-structural in nature (e.g. building facades) and therefore serviceability limits are the only concern [77]. Also, serviceability limits are most likely reached well before any ultimate limits are reached; making serviceability limits a conservative and popular mode of failure. Table E.1 is an incomplete list of ultimate and serviceability limits that have been used in the literature for probabilistic modeling.

Table E.1: Limit states used for service life modeling of RC structures.

	Limit State	Reference
Ultimate	Flexural Resistance	[59],[61],[251],[259-265]
	Shear Resistance	[61],[260],[262],[265]
	Compressive Resistance	[260]
Serviceability	Deflection	[59],[74],[266]
	Crack Width	[72],[74],[260-262],[267]
	Onset of Corrosion	[268]
	Fixed Value after Onset of Corrosion	[60]
	Onset of Cracking	[264],[258],[269]
	Spalling	[264],[270],[271]
	Delamination	[272]
	Combination Index	[273]

For modeling of ultimate parameters, the focus should be on the evolution of the geometry, the material, and the bond properties. The following issues should be addressed specifically [49]:

1) Steel area reduction (main longitudinal bars and stirrups)

2) Changes in the ductility of the rebar from pitting

3) Concrete area reduction from cover cracking and spalling

4) Changes in strength and ductility of concrete in compression (caused by microcracking from corrosion product accumulation)

5) Bond dependence on the corrosion level in rebar

The equations that are used to calculate structural parameters (e.g., flexural resistance and deflection) are case and structure dependent.

A service life model developed by the Strategic Highway Research Program (SHRP) is worth discussion. A methodology on how to assess life-cycle costs for protection and rehabilitation of corroding concrete bridges based on this model was also provided [273]. Life-cycle costs for any of the previously discussed models could be formulated in a similar fashion. The report used a continuous corrosion process curve as shown in Figure E.3.

282
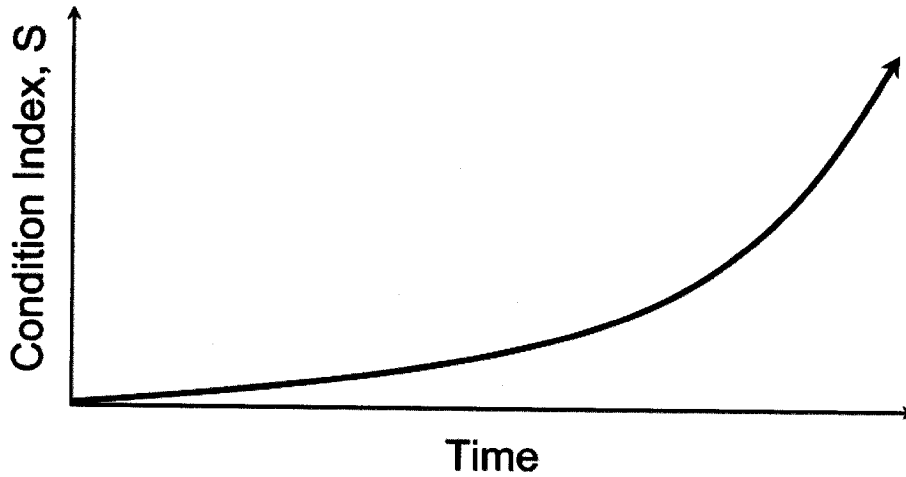
Figure E.3: Continuous corrosion process curve.

The condition index curve was calculated by the following equation:

$$S_t = \frac{100}{[1 + Ae^{-Bt}]} \quad \dots\dots\dots\dots\dots\dots\dots\dots\dots\dots\dots\dots\dots\dots\dots\dots\dots\dots\dots\dots\dots\dots\dots (3.104)$$

where A and B are parameters controlling the rate of deterioration and t is the age of the concrete. Assuming that a structure has never had any repair, rehabilitation, and/or previous protection in the past, the following equations are used in order to calculate A and B:

$$B = \frac{\ln\left\{\dfrac{S_d(100 - S_p)}{S_p(100 - S_d)}\right\}}{t_d - t_p} \quad \dots\dots\dots\dots\dots\dots\dots\dots\dots\dots\dots\dots\dots\dots (3.105)$$

$$A = \frac{\left[\dfrac{100 - S_p}{S_p}\right]}{e^{-Bt_p}} \quad \dots\dots\dots\dots\dots\dots\dots\dots\dots\dots\dots\dots\dots\dots\dots\dots (3.106)$$

where S_d is the condition index at the time of first deterioration, t_d is the age of the concrete at the time of first deterioration, S_p is the condition index at the present time, and t_p is the age of the concrete at the present time. This is assuming that inspections spotted the first signs of deterioration on the structure. If inspections did not locate the first signs of deterioration, then S_d is assumed to be 1.9 and t_d is calculated using the following equation:

$$t_d = \left[\frac{\left(2.695d^{1.22}t^{0.21}\right)}{Z_t^{0.42}P}\right]^{0.8265} \quad \dots\dots\dots\dots\dots\dots\dots\dots\dots\dots (3.107)$$

283

where d is the depth of bar cover, Z_t is the surface chloride concentration, t is the age of the concrete when Z_t is measured, and P is the water-to-cement ratio of the concrete. Assuming that a protective system was built into the structure at the time of initial construction, the t_d value is affected. Examples of special protection are concrete overlays, membranes, sealers, coatings, admixtures, and coated reinforcing steel. In cases of overlays, a weighted average of the water-to-cement ratio is used between the overlay and base concrete. For membranes, sealers, coatings, admixtures and coated reinforcing steel the number of years the protective system delays chloride ingress and/or deterioration is estimated and added to the calculated value of t_d.

There are cases where the present inspection yields a condition index that is lower than 1.9. If the condition index is higher than 1.2, S_d is assumed equal to 1.9 and t_d is equal to the concrete age at present. A condition index of 1.2 is the practical assumption for corrosion initiation. However, to predict future performance another condition index is needed in the future. Therefore, a future condition index of 45 is assumed. A condition index of 45 implies a practical limitation (end of service life) that the report suggests never exceeding. The age of the concrete when a condition index of 45 is reached is calculated based off of a predictive model using the average wet resistivity of the concrete as the input. The parameters A and B are calculated in the same manner as before, only replacing S_p and t_p with S_{45} and t_{45}, respectively.

In cases where the present condition index is less than 1.2, the manner of determination of future performance depends on the present surface chloride content, Z_t. If the present surface chloride content is greater than or equal to 0.10% of the concrete weight, then t_d is calculated using the equation above and S_d is assumed equal to 1.9. The future condition index used is again S_{45} and t_{45}. If the present surface chloride content is less than 0.10% of the concrete weight, then Z_t must be estimated from the level of snowfall and/or exposure to marine environment from a predictive model. Once this estimate is obtained, one proceeds in the same manner as if surface chloride content greater than or equal to 0.10% of the concrete weight had been found. To calculate the condition indices S_d and S_p from on-site inspections, the following equation is used:

$$S = \frac{[CL + 2.5(DELAM) + 7.5(SPALL)]}{8.5} \quad\quad\quad (3.108)$$

where CL is the percent of concrete samples taken from the structure with bar-level chloride content higher than the corrosion threshold value, DELAM is the percentage of concrete area that has delaminated, and SPALL is the percentage of concrete area that has spalled.

284

Up to this point, it has been assumed that the structure has not been repaired, rehabilitated, and/or previously protected. Over the life of a concrete structure, there may be several attempts to repair, rehabilitate, and/or protect the structure from corrosion. If this occurs, the condition index is calculated immediately after the work has been done. This value is referred to as S_r and the t_r value is the age of the concrete at the time of the work. At a later date, the condition index S_p is assessed and t_p is the age of the concrete at present. The parameters A and B are calculated based off of these two sets of points and the future performance is predicted. Using the methodology over the course of the lifetime yields Figure E.4.
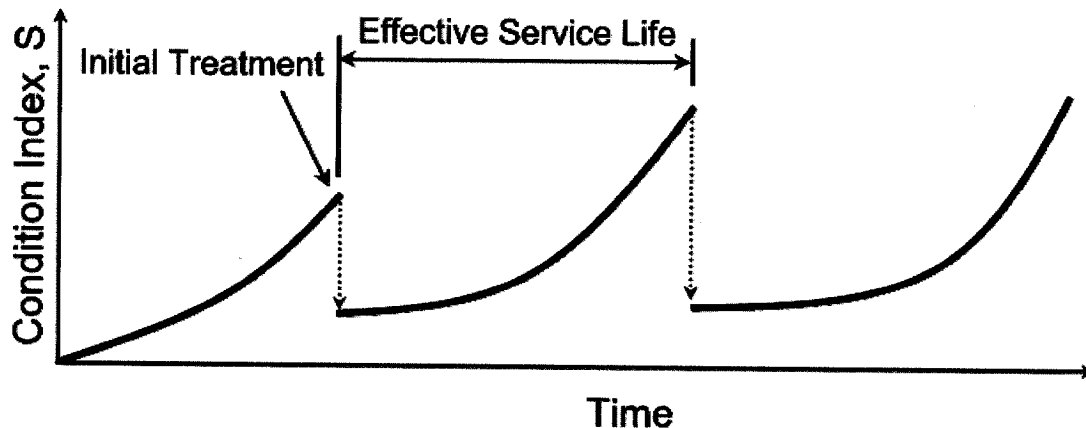
Figure E.4: Condition index over the lifetime of a concrete structure.

This type of adjustment to the corrosion process model over the lifetime from rehabilitation and maintenance is common. In fact the frequency and extent of repairs plays a critical role in choosing a design with corrosion inhibiting systems and embedded sensor networks based on life cycle costs. In most cases, service life modeling is conducted in a probabilistic manner due to the high amount of uncertainty associated with the materials, environment, loading, and structural effects [266]. The key variables defining the initiation and propagation periods are modeled stochastically, allowing for probability density curves to be created for the entire service life. The probabilistic modeling allows for planning and implementation of design changes along with the most cost effective rehabilitation and repair strategies. Due to the relatively limited amount of data for corroding RC structures in real environments, the accuracy of the models is questionable. Adding to the uncertainty is the complexity of the materials, the variable loading, cracking caused by a variety of sources, workmanship, and human error. However, there are quite a few examples in recent literature of probabilistic models being used for service life estimates of corroding RC structures. A few recent representative examples of probabilistic modeling are now presented.

Frangopol, Lin & Estes studied how the reliability depreciates for an RC girder from corrosion [265]. Fick's 2nd law of diffusion, using Eqn. C.33 to calculate the diffusion coefficient, was used to estimate the

285

initiation period. A very conservative initiation period of three years was calculated. By looking at the diameter loss from constant corrosion rates, estimates of the depreciated flexural and shear strength were estimated. The flexural strength was seen as the controlling limit state in the model. Figure E.5 shows the flexural strength reliability index for the structure as a function of time for three different constant corrosion rates.
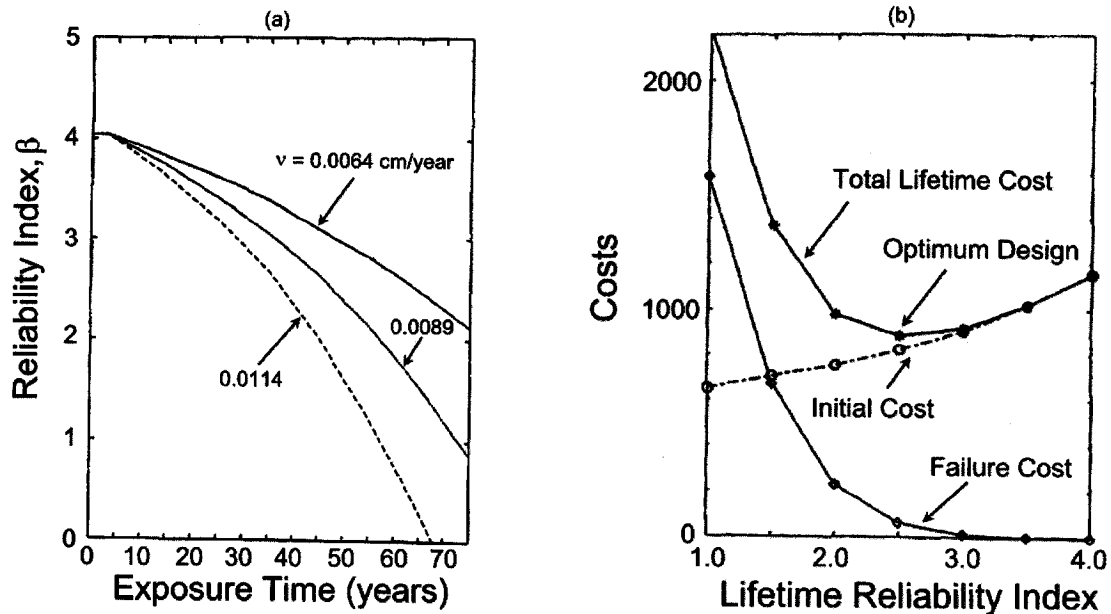
Figure E.5: (a) Flexural strength reliability index as a function of exposure time for three different constant corrosion rates. (b) The cost as a function of the lifetime reliability index is also shown. Both figures were extracted from [265].

As soon as a critical flexural strength reliability index has been reached, the service life of the structure is over. One can use this approach to minimize the expected lifetime costs of the structure. Obviously, using fewer materials will lower the cost. However, by using fewer materials the reliability index is lowered. A lower reliability index increases the probability of failure. Figure E.5 shows a plot of the failure costs, the initial costs of the structure, and the total lifetime costs.

Li [255] used an empirical formula derived from experimental testing (refer to C.3) of chloride-induced corrosion in RC specimens with load-induced cracks exceeding 0.1 mm. The probability of corrosion initiation was calculated by multiplying the probability of a critical chloride concentration being reached at reinforcement level by the probability of corrosion onset for a given critical concentration level. The empirical model for the onset of corrosion is shown in Figure E.6, with the results of visual inspections.
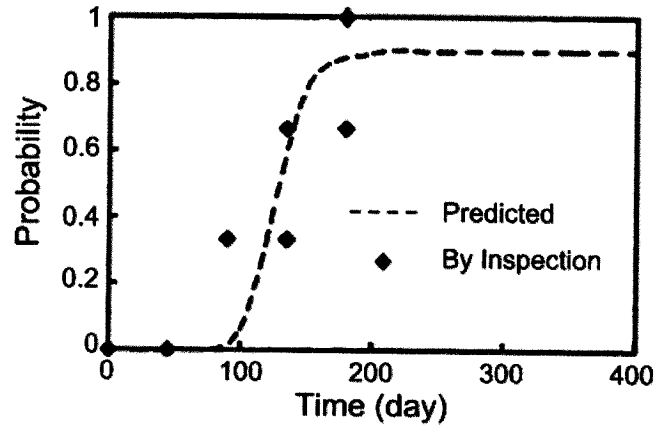
Figure E.6: Probability of the onset of corrosion at certain times (extracted from [255]).

Stewart & Rosowsky compared the onset of corrosion for different levels of chloride exposure (e.g. deicing salts, coastal zone with varying distance to coast) [263]. The ingress of chlorides was modeled using Fick's 2nd law of diffusion. It was assumed that the chloride concentration at the surface is constant with respect to time for deicing salt exposure (based on a previous study [268]) allowing the use of the closed form solution (Eqn. D.8). For coastal zones, it is assumed that the surface chloride concentration accumulates with time and therefore a different closed form solution was used. The critical chloride threshold was a uniformly distributed random variable within the range of 0.6 - 1.2 kg/m³. Figure E.7 shows the probability distributions for the onset of corrosion from chloride ingress for various sources.
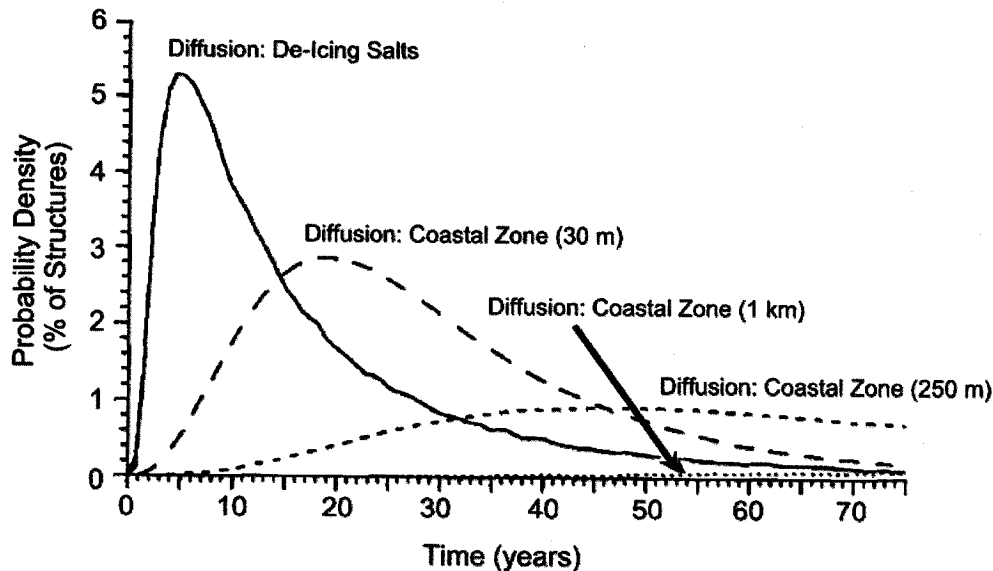
Figure E.7: Probability density for the onset of corrosion as a function of time for different levels of chloride exposure (extracted from [263]).

Notice that deicing salts create a much higher risk for the onset of corrosion than coastal zone exposure. It is also clear that there is a very wide range of time when corrosion can occur from chloride exposure.

Val, Stewart and Melchers used probabilistic modeling and a finite element model to compare the effects of localized (pitting) and general corrosion on the service life of an RC slab bridge [266]. The reduction of cross-sectional area for pitting and general corrosion as a function of time was formulated at a linear rate. A model for bond strength reduction was taken into account with general corrosion. A linear tension-softening curve was used with the finite element model. Two service life limits were compared, with loading effects taken into account. The first was flexural strength (ultimate limit) and the second was deflection (serviceability limit). Figure E.8(a) shows the reliability index (corresponding to the probability of failure) plotted as a function of time (after corrosion initiation) for the ultimate limit state. A constant corrosion current density of 3 $\mu A/cm^2$ was assumed. It was assumed in the analysis that all of the bottom reinforcement was effected by pitting corrosion and that there was no bond for the general corrosion. Therefore, this is a rather conservative estimate of the remaining service life of the structure after corrosion initiation with respect to flexural failure.
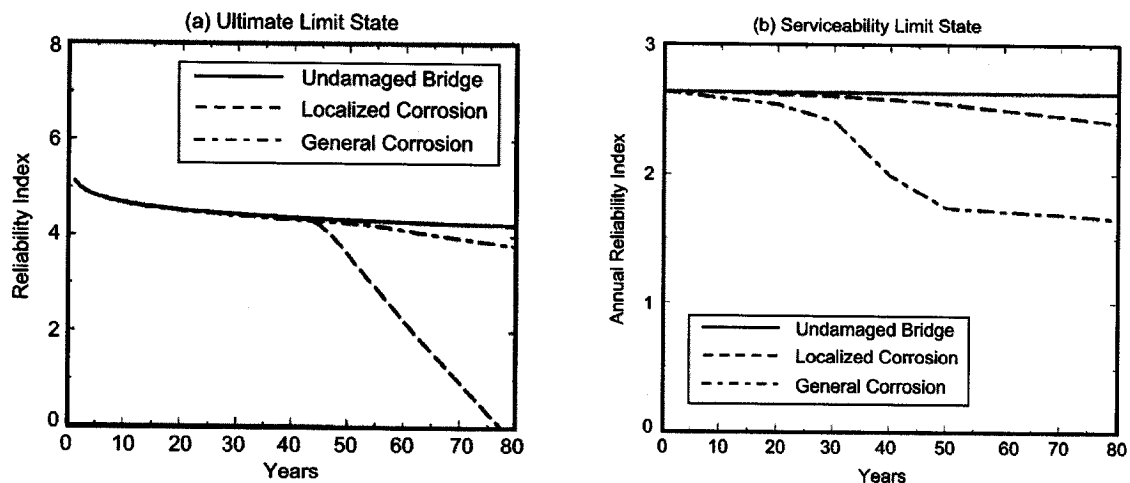
Figure E.8: Reliability index for an RC slab bridge as a function of time for an (a) ultimate (flexural strength) and (b) serviceability (deflection) limit state (extracted from [266]).

Notice that pitting corrosion presents more of a concern for the ultimate limit state than general corrosion. Figure E.8(b) shows the reliability index as a function of time (after corrosion initiation) for the serviceability limit state. A constant corrosion current density of 1 $\mu A/cm^2$ was assumed. The general corrosion was predicted to pose more of a threat to the deflection limit state due to the loss of bond (decrease in stiffness) than the loss of cross-sectional area from pitting corrosion.

Kirkpatrick et al. used a service life model to examine the impact of specification changes (e.g. w/c ratio, cover depth) on RC bridge decks with respect to corrosion [271]. The comparison between older bridges under certain specifications with projected normalized service lives were compared to newer bridges under changed specifications with service lives estimated probabilistically. The propagation period of the

288

newer bridges were assumed constant, while the initiation period was modeled using Fick's 2nd law. The cover depth, surface chloride concentration, diffusion coefficient, and the critical chloride threshold were all stochastic variables. The distribution of the stochastic variables, except for the critical chloride threshold (estimated from literature), was extracted from on-site testing. The bridge deck was sectioned into smaller segments and the time to corrosion initiation was found independently for each segment. The service life of the bridge deck was reached when the amount of segments reaching corrosion initiation was 12%. It was found that the newer bridges, with the change in specifications (lower w/c, greater cover depth), had longer projected service lives than the older bridges. The discrepancy in service life between the sets of bridges was attributed 40% to the change in water-to-cement ratio and 40% to the increase in cover depth. The remainder, not accounted for with the specification changes in the probabilistic model, was attributed to inaccuracies with the projected normalized service life of the older bridges and lack of precision associated with the probabilistic model.

Stewart and Rosowsky updated the probability of an ultimate limit state being reached (flexural) by the known exceedance of a serviceability failure (spalling) in an RC slab bridge [264]. Sagüés created a stochastic service life model using collected on-site inspection information to calibrate certain modeling parameters [60]. Two case examples of inspected bridges were used to compare results and predict future deterioration. Fick's 2nd law of diffusion was used to estimate the initiation period for both cases. A fixed propagation period was used for one case example while the other case example based the propagation period on a distribution of rates. Stewart, Estes and Frangopol used the Liu & Weyers model (refer to Chapter 3) to estimate the time to initiate cracking and then an empirical crack width model to calculate the crack width to probabilistically model the time to reach the critical crack width service limit. Figure E.9 is a comparison between a critical crack width limit of 0.5 and 1.0 mm.
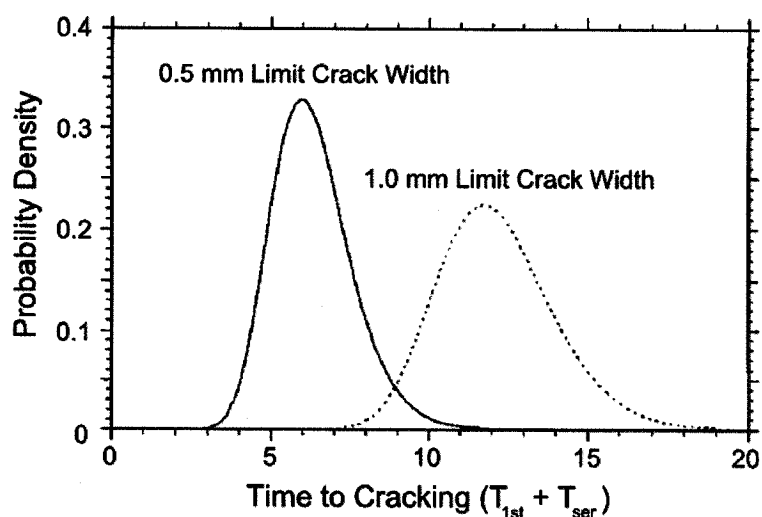
Figure E.9: Probability density to reach a certain crack width as a function of time (extracted from [261]).

Notice that the time to initiate cracking and reach relatively large crack widths is small compared to the time for chlorides to reach a critical chloride threshold at the reinforcement level (Figure E.7).

Vu & Stewart used Fick's 2nd law of diffusion (Papadakis diffusion coefficient) to model the time to corrosion initiation [267]. The Liu & Weyers model (refer to Chapter 3) was used to estimate the time to crack initiation, while the Vu & Stewarts empirical model was used to estimate the time to certain crack widths. The critical parameters were modeled stochastically and a Monte Carlo simulation was conducted. The time to severe cracking takes much longer compared to the time to start cracking based on this stochastic model. The authors also divided the structure up into individual components in order to model the spatial variability. The percentage of a concrete surface that has reached a critical crack width limit is a more useful performance measure for maintenance and repair strategies [267].

Val compared the effect of different limit states on the life cycle cost for an RC structure and found that for short time periods between repairs (up to 5 years) the expected cost of failure due to ultimate limit states (e.g. flexural, shear, compression) were negligible for most elements compared to the serviceability limit states (e.g. severe cracking, spalling) [260]. As the ratio between the expected costs of failure due to the ultimate limit states to the serviceability limit state increased, the time between repairs for the optimum solution decreased.

APPENDIX F:

WAVE PROPAGATION IN AN UNBOUNDED ISOTROPIC MEDIUM

For the context of this report, a wave is a mechanical disturbance moving through a medium. Wave propagation implies the transfer of energy through space [274]. Therefore, this review is provided as a description of how energy is transferred through many different isotropic mediums. The review is concerned primarily with wave motion resulting from mechanical disturbances. The review has been taken from various references, primarily Redwood [87], Kolsky [88], Pavlakovic & Lowe [89], and Love [86]. For a more in-depth review, please consult those references as they provide an excellent background.

F.1 EQUATION OF MOTION

The equations for wave motion in an unbounded isotropic medium are first presented. Isotropic refers to a material being identical in all directions. This background is presented here to give a feel for the equations that, assuming the proper boundary conditions, define wave propagation of various modes in waveguides. To start, imagine a point within an isotropic medium. Assume that the isotropic medium is deformed and the point, which is called 'P', within the infinitesimally small square element PAQB is displaced from its original coordinate location (x, y, z) to the location (x + u, y + v, z + w). Refer to Figure F.1 to see the point 'P'. Although Figure F.1 is only in 2-dimensions, it serves the purpose of illustration adequately. Therefore, the displacement of the point 'P' is written in vector form as:

$$\mathbf{s} = u\mathbf{i} + v\mathbf{j} + w\mathbf{k} \dots\dots\dots\dots\dots\dots\dots\dots\dots\dots\dots\dots\dots\dots\dots\dots (F.1)$$

where $u = u(x,y,z)$, $v = v(x,y,z)$, and $w = w(x,y,z)$. If the medium were not deformed at all, but translated or rotated as a whole, the point 'P' could still move to its displacement location. One must look at a point very close to 'P' in order to study deformation. An adjacent point to 'P', which is called 'Q', starts at (x + δx, y + δy, z + δz) and is displaced to (x + δx + u + δu, y + δy + v + δv, z + δz + w + δw).

291
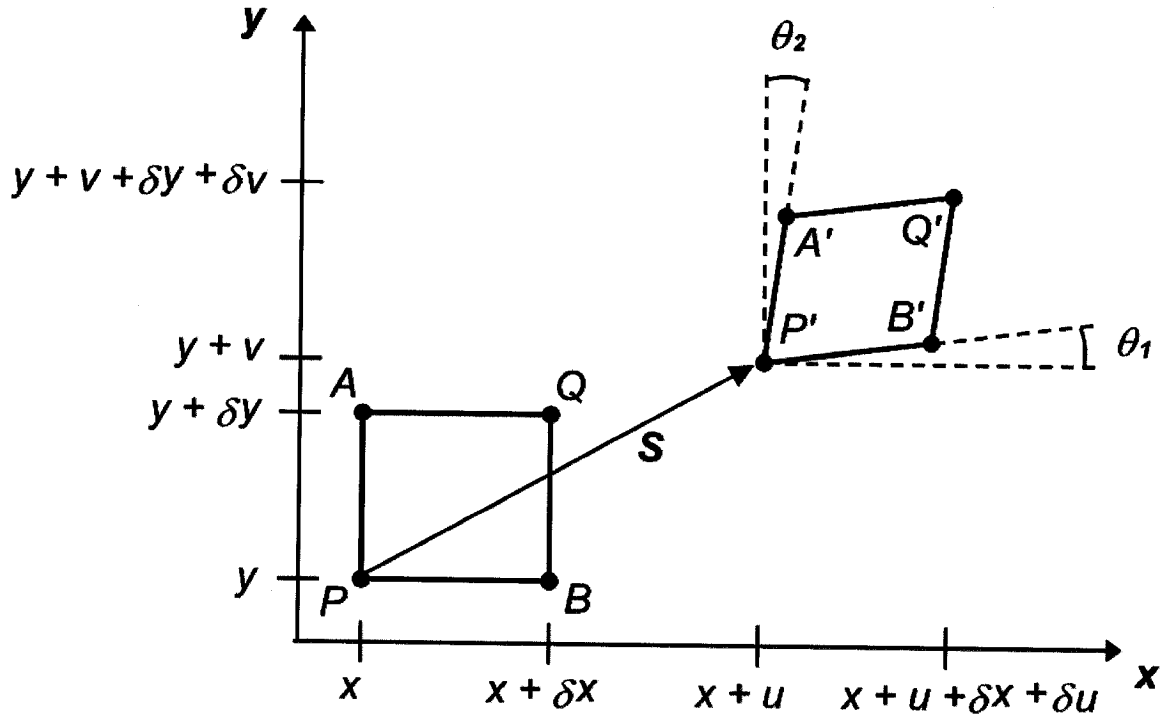
Figure F.1: Displacement of points 'P' and 'Q'.

The displacement terms of point 'Q' (u + δu, v + δv, w + δw) would be the same as 'P' (u, v, w) if the medium were rigid and did not rotate [234]. If one performs a Taylor's series expansion about the point 'P' for the displacement functions u(x,y,z), v(x,y,z) and w(x,y,z), the displacement terms for point 'Q' can be solved for:

$$u + \delta u = u(x_0, y_0, z_0) + \frac{\partial u(x,y,z)}{\partial x}((x + \delta x) - x) + \frac{\partial u(x,y,z)}{\partial y}((y + \delta y) - y) + \frac{\partial u(x,y,z)}{\partial z}((z + \delta z) - z) + \ldots = u + \frac{\partial u}{\partial x}\delta x + \frac{\partial u}{\partial y}\delta y + \frac{\partial u}{\partial z}\delta z + \ldots \cdots (F.2)$$

$$v + \delta v = v(x_0, y_0, z_0) + \frac{\partial v(x,y,z)}{\partial x}((x + \delta x) - x) + \frac{\partial v(x,y,z)}{\partial y}((y + \delta y) - y) + \frac{\partial v(x,y,z)}{\partial z}((z + \delta z) - z) + \ldots = v + \frac{\partial v}{\partial x}\delta x + \frac{\partial v}{\partial y}\delta y + \frac{\partial v}{\partial z}\delta z + \ldots \cdots (F.3)$$

$$w + \delta w = w(x_0, y_0, z_0) + \frac{\partial w(x,y,z)}{\partial x}((x + \delta x) - x) + \frac{\partial w(x,y,z)}{\partial y}((y + \delta y) - y) + \frac{\partial w(x,y,z)}{\partial z}((z + \delta z) - z) + \ldots = w + \frac{\partial w}{\partial x}\delta x + \frac{\partial w}{\partial y}\delta y + \frac{\partial w}{\partial z}\delta z + \ldots \cdots (F.4)$$

If δx, δy, and δz are relatively small, the higher order terms can be neglected. Notice that some of the terms above are strains and can be rewritten as:

$$\varepsilon_{xx} = \frac{\left(\delta x + \frac{\partial u}{\partial x}\delta x\right) - \delta x}{\delta x} = \frac{\partial u}{\partial x} \quad \ldots (F.5)$$

$$\varepsilon_{yy} = \frac{\left(\delta y + \frac{\partial v}{\partial y}\delta y\right) - \delta y}{\delta y} = \frac{\partial v}{\partial y} \quad \ldots (F.6)$$

292

$$\varepsilon_{zz} = \frac{\left(\delta z + \frac{\partial w}{\partial z}\delta z\right) - \delta z}{\delta z} = \frac{\partial w}{\partial z} \quad \text{..(F.7)}$$

These are simple extensions of the medium parallel to the x, y, and z-axis, respectively. The following strain components are shear strains:

$$\gamma_{xy} = \gamma_{yx} = \frac{\partial u}{\partial y} + \frac{\partial v}{\partial x} \quad \text{..(F.8)}$$

$$\gamma_{yz} = \gamma_{zy} = \frac{\partial v}{\partial z} + \frac{\partial w}{\partial y} \quad \text{..(F.9)}$$

$$\gamma_{xz} = \gamma_{zx} = \frac{\partial u}{\partial z} + \frac{\partial w}{\partial x} \quad \text{..(F.10)}$$

These shear strains are equal to the angular motions of an element, with volume, within the isotropic medium. In Figure F.1, the angles θ_1 and θ_2 sum to equal the shear strain γ_{xy}. The cubical dilatation can now be written in terms of the strains, representing the change in volume resulting from a displacement in the medium. It can be found by taking the limit of the increase in volume divided by the original volume as δx, δy, and δz approach zero.

$$\Delta = \varepsilon_{xx} + \varepsilon_{yy} + \varepsilon_{zz} = \frac{\partial u}{\partial x} + \frac{\partial v}{\partial y} + \frac{\partial w}{\partial z} \quad \text{..(F.11)}$$

The cubical dilatation can now be written as:

$$\Delta = \text{div } \mathbf{s} \quad \text{..(F.12)}$$

with 'div' representing the divergence of the field and explained further in Appendix H. The rotation components of the rigid body around the different axes is given by:

$$\overline{\omega}_x = \frac{1}{2}\left(\frac{\partial w}{\partial y} - \frac{\partial v}{\partial z}\right) \quad \text{..(F.13)}$$

$$\overline{\omega}_y = \frac{1}{2}\left(\frac{\partial u}{\partial z} - \frac{\partial w}{\partial x}\right) \quad \text{..(F.14)}$$

$$\overline{\omega}_z = \frac{1}{2}\left(\frac{\partial v}{\partial x} - \frac{\partial u}{\partial y}\right) \quad \text{..(F.15)}$$

where "pure shear" corresponds to all three rotation terms being zero and "simple shear" is the case where one or more terms is not zero. The rotation terms are rewritten in vector form as:

293

$$\overline{\boldsymbol{\omega}} = \frac{1}{2}\left(\frac{\partial w}{\partial y} - \frac{\partial v}{\partial z}\right)\mathbf{i} + \frac{1}{2}\left(\frac{\partial u}{\partial z} - \frac{\partial w}{\partial x}\right)\mathbf{j} + \frac{1}{2}\left(\frac{\partial v}{\partial x} - \frac{\partial u}{\partial y}\right)\mathbf{k} \quad \dots\dots\dots\dots\text{(F.16)}$$

The strain creates stress in a small volume element and that distribution of stress is broken up into the nine stresses as shown in the stress dyadic matrix:

$$\begin{bmatrix} \sigma_{xx} & \tau_{xy} & \tau_{xz} \\ \tau_{yx} & \sigma_{yy} & \tau_{yz} \\ \tau_{zx} & \tau_{zy} & \sigma_{zz} \end{bmatrix} \quad \dots\dots\dots\dots\dots\dots\dots\dots\dots\dots\dots\dots\dots\dots\dots\dots\dots\text{(F.17)}$$

Please note that σ_{xx}, σ_{yy} and σ_{zz} are normal stresses while τ_{xy}, τ_{yx}, τ_{xz}, τ_{zx}, τ_{yz}, τ_{zy} are shear stresses. The first subscript denotes the coordinate axis normal to the plane that the stress acts and the second subscript denotes the direction of the stress. In order for there to be equilibrium in the element $\tau_{xy} = \tau_{yx}$, $\tau_{xz} = \tau_{zx}$ and $\tau_{yz} = \tau_{zy}$. This has been shown explicitly by setting the moment about the center point in the element to zero and solving for the shear stresses [234]. Since the small element has volume, there will be variation in the stress across the faces of the parallelepiped. Shown in Figure F.2 is the value of stress at the center of each face (excluding stresses acting on the yz-plane) [87].
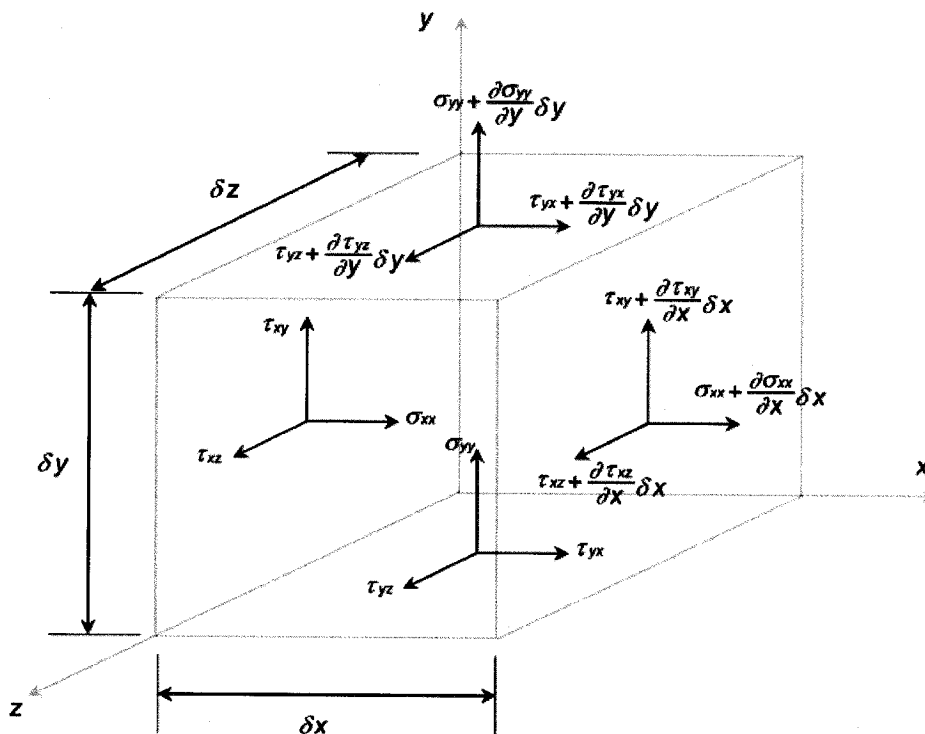
Figure F.2: Small isotropic element under stress (extracted from [87]).

In order to relate the strain components with the stress components in the element, Hooke's Law is used. Hooke's Law is only applicable if the material stays within its elastic range, i.e. the material does not reach plastic deformation. The essentials of this law are best stated by Love [86]:

(1) When the load increases the measured strain increases in the same ratio

(2) When the load diminishes the measured strain diminishes in the same ratio

(3) When the load is reduced to zero no strain can be measured.

Basically, the six components of stress are a linear function of the six components of strain. This is written in matrix form as:

$$
\begin{bmatrix}
\sigma_{xx} \\
\sigma_{yy} \\
\sigma_{zz} \\
\tau_{yz} \\
\tau_{zx} \\
\tau_{xy}
\end{bmatrix}
=
\begin{bmatrix}
c_{11} & c_{12} & c_{13} & c_{14} & c_{15} & c_{16} \\
c_{21} & c_{22} & c_{23} & c_{24} & c_{25} & c_{26} \\
c_{31} & c_{32} & c_{33} & c_{34} & c_{35} & c_{36} \\
c_{41} & c_{42} & c_{43} & c_{44} & c_{45} & c_{46} \\
c_{51} & c_{52} & c_{53} & c_{54} & c_{55} & c_{56} \\
c_{61} & c_{62} & c_{63} & c_{64} & c_{65} & c_{66}
\end{bmatrix}
\begin{bmatrix}
\varepsilon_{xx} \\
\varepsilon_{yy} \\
\varepsilon_{zz} \\
\gamma_{yz} \\
\gamma_{zx} \\
\gamma_{xy}
\end{bmatrix}
\quad\text{.........................(F.18)}
$$

where the 36 different 'c_{ij}' coefficients are the elastic constants of the isotropic material. If $\tau_{xy} = \tau_{yx}$, $\tau_{xz} = \tau_{zx}$, $\tau_{yz} = \tau_{zy}$, $\gamma_{xy} = \gamma_{yx}$, $\gamma_{yz} = \gamma_{zy}$ and $\gamma_{xz} = \gamma_{zx}$ had not been specified, there would be 81 different 'c_{ij}' coefficients (resulting from nine stress and strain components). Love shows that one can reduce the number of coefficients even further when taking into account the strain-energy function [86]. The strain-energy function is a homogeneous quadratic function of the strain-components, where the elastic constants shown above are the coefficients in the function. To ensure the existence of the strain-energy function, $c_{ij} = c_{ji}$ must be true. This reduces the number of coefficients from 36 to 21. Also, since the medium is isotropic, every plane is a plane of symmetry and every axis is an axis of symmetry. Therefore, the following must be true:

$$c_{14} = c_{15} = c_{16} = c_{24} = c_{25} = c_{26} = c_{34} = c_{35} = c_{36} = c_{45} = c_{46} = c_{56} = 0 \quad\text{...........................(F.19)}$$

$$c_{11} = c_{22} = c_{33}; \quad c_{23} = c_{31} = c_{12}; \quad c_{44} = c_{55} = c_{66} = \tfrac{1}{2}(c_{11} - c_{12}) \quad\text{..................................(F.20)}$$

$$
\begin{bmatrix}
\sigma_{xx} \\
\sigma_{yy} \\
\sigma_{zz} \\
\tau_{yz} \\
\tau_{zx} \\
\tau_{xy}
\end{bmatrix}
=
\begin{bmatrix}
c_{11} & c_{12} & c_{12} & 0 & 0 & 0 \\
c_{12} & c_{11} & c_{12} & 0 & 0 & 0 \\
c_{12} & c_{12} & c_{11} & 0 & 0 & 0 \\
0 & 0 & 0 & \tfrac{1}{2}(c_{11}-c_{12}) & 0 & 0 \\
0 & 0 & 0 & 0 & \tfrac{1}{2}(c_{11}-c_{12}) & 0 \\
0 & 0 & 0 & 0 & 0 & \tfrac{1}{2}(c_{11}-c_{12})
\end{bmatrix}
\begin{bmatrix}
\varepsilon_{xx} \\
\varepsilon_{yy} \\
\varepsilon_{zz} \\
\gamma_{yz} \\
\gamma_{zx} \\
\gamma_{xy}
\end{bmatrix}
\quad\text{..........(F.21)}
$$

There are only two elastic constants left. The following notation is used:

$$\lambda = c_{12} \quad \text{...(F.22)}$$

$$\mu = \tfrac{1}{2} (c_{11} - c_{12}) \quad \text{...(F.23)}$$

$$\lambda + 2\mu = c_{11} \quad \text{...(F.24)}$$

where λ and μ are called Lamé's constants. This will leave us with the following matrix and relations:

$$\begin{bmatrix} \sigma_{xx} \\ \sigma_{yy} \\ \sigma_{zz} \\ \tau_{yz} \\ \tau_{zx} \\ \tau_{xy} \end{bmatrix} = \begin{bmatrix} \lambda+2\mu & \lambda & \lambda & 0 & 0 & 0 \\ \lambda & \lambda+2\mu & \lambda & 0 & 0 & 0 \\ \lambda & \lambda & \lambda+2\mu & 0 & 0 & 0 \\ 0 & 0 & 0 & \mu & 0 & 0 \\ 0 & 0 & 0 & 0 & \mu & 0 \\ 0 & 0 & 0 & 0 & 0 & \mu \end{bmatrix} \begin{bmatrix} \varepsilon_{xx} \\ \varepsilon_{yy} \\ \varepsilon_{zz} \\ \gamma_{yz} \\ \gamma_{zx} \\ \gamma_{xy} \end{bmatrix} \quad \text{.....................(F.25)}$$

$$\sigma_{xx} = \lambda\left(\frac{\partial u}{\partial x} + \frac{\partial v}{\partial y} + \frac{\partial w}{\partial z}\right) + 2\mu\left(\frac{\partial u}{\partial x}\right) = \lambda\Delta + 2\mu\varepsilon_{xx} \quad \text{...........................(F.26)}$$

$$\sigma_{yy} = \lambda\left(\frac{\partial u}{\partial x} + \frac{\partial v}{\partial y} + \frac{\partial w}{\partial z}\right) + 2\mu\left(\frac{\partial v}{\partial y}\right) = \lambda\Delta + 2\mu\varepsilon_{yy} \quad \text{...........................(F.27)}$$

$$\sigma_{zz} = \lambda\left(\frac{\partial u}{\partial x} + \frac{\partial v}{\partial y} + \frac{\partial w}{\partial z}\right) + 2\mu\left(\frac{\partial w}{\partial z}\right) = \lambda\Delta + 2\mu\varepsilon_{zz} \quad \text{...........................(F.28)}$$

$$\tau_{xz} = \tau_{zx} = \mu\left(\frac{\partial u}{\partial z} + \frac{\partial w}{\partial x}\right) = \mu\gamma_{zx} \quad \text{..(F.29)}$$

$$\tau_{yz} = \tau_{zy} = \mu\left(\frac{\partial w}{\partial y} + \frac{\partial v}{\partial z}\right) = \mu\gamma_{yz} \quad \text{..(F.30)}$$

Looking at Figure F.2, equilibrium must be achieved among the forces. Gravity is assumed to be negligible for this discussion. The forces in the x, y and z directions are summed:

$$\Sigma F_x = \left(\sigma_{xx} + \frac{\partial \sigma_{xx}}{\partial x} \cdot \delta x - \sigma_{xx}\right)\delta y \delta z + \left(\sigma_{yx} + \frac{\partial \tau_{yx}}{\partial y} \cdot \delta y - \tau_{yx}\right)\delta x \delta z + \left(\tau_{zx} + \frac{\partial \tau_{zx}}{\partial z} \cdot \delta z - \tau_{zx}\right)\delta x \delta y \quad \text{.................(F.31)}$$

$$\Sigma F_y = \left(\tau_{xy} + \frac{\partial \tau_{xy}}{\partial x} \cdot \delta x - \tau_{xy}\right)\delta y \delta z + \left(\sigma_{yy} + \frac{\partial \sigma_{yy}}{\partial y} \cdot \delta y - \sigma_{yy}\right)\delta x \delta z + \left(\tau_{zy} + \frac{\partial \tau_{zy}}{\partial z} \cdot \delta z - \tau_{zy}\right)\delta x \delta y \quad \text{.................(F.32)}$$

$$\Sigma F_z = \left(\tau_{xz} + \frac{\partial \tau_{xz}}{\partial x} \cdot \delta x - \tau_{xz}\right)\delta y \delta z + \left(\tau_{yz} + \frac{\partial \tau_{yz}}{\partial y} \cdot \delta y - \tau_{yz}\right)\delta x \delta z + \left(\sigma_{zz} + \frac{\partial \sigma_{zz}}{\partial z} \cdot \delta z - \sigma_{zz}\right)\delta x \delta y \quad \text{.................(F.33)}$$

This is reduced further to:

$$\Sigma F_x = \left(\frac{\partial \sigma_{xx}}{\partial x} + \frac{\partial \tau_{yx}}{\partial y} + \frac{\partial \tau_{zx}}{\partial z}\right)\delta x \delta y \delta z \quad \text{..(F.34)}$$

$$\sum F_y = \left(\frac{\partial \tau_{xy}}{\partial x} + \frac{\partial \sigma_{yy}}{\partial y} + \frac{\partial \tau_{zy}}{\partial z} \right) \delta x \delta y \delta z \quad \text{...(F.35)}$$

$$\sum F_z = \left(\frac{\partial \tau_{xz}}{\partial x} + \frac{\partial \tau_{yz}}{\partial y} + \frac{\partial \sigma_{zz}}{\partial z} \right) \delta x \delta y \delta z \quad \text{...(F.36)}$$

If the medium is disturbed from its equilibrium position, motion is caused from the excess stresses created from the disturbances [274]. Using Newton's 2nd law, forces can be related to density and acceleration of the particle (assuming no body forces):

$$\rho \cdot \frac{\partial^2 u}{\partial t^2} = \sum F_x = \left(\frac{\partial \sigma_{xx}}{\partial x} + \frac{\partial \tau_{yx}}{\partial y} + \frac{\partial \tau_{zx}}{\partial z} \right) \delta V \quad \text{...................................(F.37)}$$

$$\rho \cdot \frac{\partial^2 v}{\partial t^2} = \sum F_y = \left(\frac{\partial \tau_{xy}}{\partial x} + \frac{\partial \sigma_{yy}}{\partial y} + \frac{\partial \tau_{zy}}{\partial z} \right) \delta V \quad \text{...................................(F.38)}$$

$$\rho \cdot \frac{\partial^2 w}{\partial t^2} = \sum F_z = \left(\frac{\partial \tau_{xz}}{\partial x} + \frac{\partial \tau_{yz}}{\partial y} + \frac{\partial \sigma_{zz}}{\partial z} \right) \delta V \quad \text{...................................(F.39)}$$

Plugging in for the stresses with their respective relations from above:

$$\rho \cdot \frac{\partial^2 u}{\partial t^2} = \left(\frac{\partial}{\partial x} \left(\lambda \left(\frac{\partial u}{\partial x} + \frac{\partial v}{\partial y} + \frac{\partial w}{\partial z} \right) + 2\mu \left(\frac{\partial u}{\partial x} \right) \right) + \frac{\partial}{\partial y} \left(\mu \left(\frac{\partial v}{\partial x} + \frac{\partial u}{\partial y} \right) \right) + \frac{\partial}{\partial z} \left(\mu \left(\frac{\partial u}{\partial z} + \frac{\partial w}{\partial x} \right) \right) \right) \delta V \quad \text{.......................(F.40)}$$

$$\rho \cdot \frac{\partial^2 v}{\partial t^2} = \left(\frac{\partial}{\partial x} \left(\mu \left(\frac{\partial v}{\partial x} + \frac{\partial u}{\partial y} \right) \right) + \frac{\partial}{\partial y} \left(\lambda \left(\frac{\partial u}{\partial x} + \frac{\partial v}{\partial y} + \frac{\partial w}{\partial z} \right) + 2\mu \left(\frac{\partial v}{\partial y} \right) \right) + \frac{\partial}{\partial z} \left(\mu \left(\frac{\partial w}{\partial y} + \frac{\partial v}{\partial z} \right) \right) \right) \delta V \quad \text{.......................(F.41)}$$

$$\rho \cdot \frac{\partial^2 w}{\partial t^2} = \left(\frac{\partial}{\partial x} \left(\mu \left(\frac{\partial u}{\partial z} + \frac{\partial w}{\partial x} \right) \right) + \frac{\partial}{\partial y} \left(\mu \left(\frac{\partial w}{\partial y} + \frac{\partial v}{\partial z} \right) \right) + \frac{\partial}{\partial z} \left(\lambda \left(\frac{\partial u}{\partial x} + \frac{\partial v}{\partial y} + \frac{\partial w}{\partial z} \right) + 2\mu \left(\frac{\partial w}{\partial z} \right) \right) \right) \delta V \quad \text{.......................(F.42)}$$

which can be reduced to:

$$\rho \cdot \frac{\partial^2 u}{\partial t^2} = \left((\lambda + 2\mu) \left(\frac{\partial^2 u}{\partial x^2} \right) + (\lambda + \mu) \left(\frac{\partial^2 v}{\partial x \partial y} + \frac{\partial^2 w}{\partial x \partial z} \right) + \mu \left(\frac{\partial^2 u}{\partial y^2} + \frac{\partial^2 u}{\partial z^2} \right) \right) \delta V \quad \text{......................................(F.43)}$$

$$\rho \cdot \frac{\partial^2 v}{\partial t^2} = \left((\lambda + 2\mu) \left(\frac{\partial^2 v}{\partial y^2} \right) + (\lambda + \mu) \left(\frac{\partial^2 u}{\partial y \partial x} + \frac{\partial^2 w}{\partial y \partial z} \right) + \mu \left(\frac{\partial^2 v}{\partial x^2} + \frac{\partial^2 v}{\partial z^2} \right) \right) \delta V \quad \text{......................................(F.44)}$$

$$\rho \cdot \frac{\partial^2 w}{\partial t^2} = \left((\lambda + 2\mu) \left(\frac{\partial^2 w}{\partial z^2} \right) + (\lambda + \mu) \left(\frac{\partial^2 u}{\partial z \partial x} + \frac{\partial^2 v}{\partial z \partial y} \right) + \mu \left(\frac{\partial^2 w}{\partial x^2} + \frac{\partial^2 w}{\partial y^2} \right) \right) \delta V \quad \text{......................................(F.45)}$$

The equation of motion can be expressed in vector form as [Redwood 1960]:

$$\rho\frac{\partial^2 s}{\partial t^2} = (\lambda + 2\mu)\mathrm{grad}(\Delta) - 2\mu\mathrm{curl}(\varpi) \quad\text{...(F.46)}$$

where 'grad' and 'curl' are explained further in Appendix H. The equation of motion can also be expressed as:

$$\rho\frac{\partial^2 s}{\partial t^2} = (\lambda + 2\mu)\mathrm{grad}(\mathrm{div}(s)) - 2\mu\mathrm{curl}(\tfrac{1}{2}\mathrm{curl}(s)) \quad\text{..........................(F.47)}$$

or [85]:

$$\rho\frac{\partial^2 s}{\partial t^2} = (\lambda + 2\mu)\nabla\nabla\cdot s - \mu\nabla\times\nabla\times s \quad\text{..(F.48)}$$

Writing the equations of motion with use of the vector operators allows for easier transformations to different coordinate systems. Remembering the displacement of point 'P' was the vector (u, v, w), one can decompose the displacement into different components:

$$s = u\mathbf{i} + v\mathbf{j} + w\mathbf{k} = \nabla\Phi + \nabla\times H = \mathrm{grad}(\Phi) + \mathrm{curl}(H) \quad\text{...................(F.49)}$$

where Φ is the scalar potential and $H = H_x\mathbf{i} + H_y\mathbf{j} + H_z\mathbf{k}$ is the vector potential. A scalar potential has only magnitude [274]. A vector field where the curl is zero is termed irrotational and can be assigned a scalar potential. A vector potential has a set of three scalar functions of position and time, which transform the way the rectangular coordinates of a point transform under rotation of axes [274]. A vector field, where the divergence is zero ($\nabla\cdot H = 0$), can be assigned a vector potential and is termed solenoidal [274]. Writing the vector field of the displacements as the gradient of a scalar and the curl of a zero divergence vector is known as the Helmholtz decomposition. By using the potentials, separate wave equations are obtained for compressional (i.e. dilatational) and shear (i.e. transverse) waves [275]. If the direction of particle displacement is always parallel to the direction of wave propagation, then this is a compressional wave. Figure F.3 gives an example of compressional wave motion in a bulk isotropic medium.

298

Figure F.3: Compressional propagation in a bulk medium.

If the direction of particle displacement is always at right angles to the direction of wave propagation, then this is a transverse wave [274]. Figure F.4 below gives an example of transverse motion in a bulk isotropic medium.
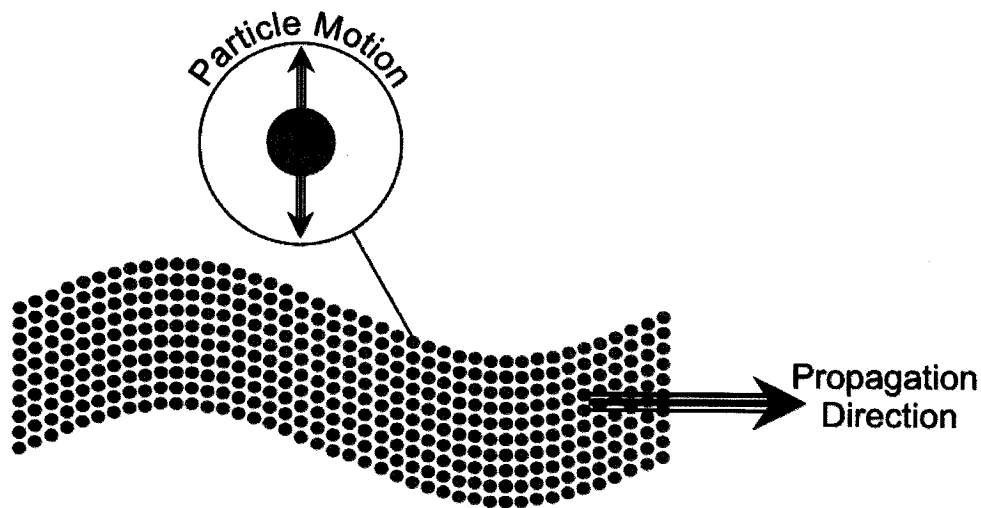
Figure F.4: Shear propagation in a bulk medium.

If the Helmholtz decomposition vector is plugged in for displacement into the equation of motion, the following equation results:

$$\nabla^2 \Phi = \frac{\partial^2 \Phi}{\partial x^2} + \frac{\partial^2 \Phi}{\partial y^2} + \frac{\partial^2 \Phi}{\partial z^2} = \left(\frac{\rho}{\lambda + 2\mu} \right) \frac{\partial^2 \Phi}{\partial t^2} \quad \text{...........................(F.50)}$$

where:

$$\frac{\lambda + 2\mu}{\rho} = \frac{\partial x^2}{\partial t^2} + \frac{\partial y^2}{\partial t^2} + \frac{\partial z^2}{\partial t^2} \quad \text{...(F.51)}$$

$$c_d = \sqrt{\frac{\partial x^2}{\partial t^2} + \frac{\partial y^2}{\partial t^2} + \frac{\partial z^2}{\partial t^2}} = \sqrt{\frac{\lambda + 2\mu}{\rho}} \quad \text{...(F.52)}$$

299

where c_d is the speed of the dilatational waveform. The vector potential will be satisfied by the following equation:

$$\nabla^2 H_i = \frac{\partial^2 H_i}{\partial x^2} + \frac{\partial^2 H_i}{\partial y^2} + \frac{\partial^2 H_i}{\partial z^2} = \left(\frac{\rho}{\mu}\right)\frac{\partial^2 H_i}{\partial t^2} \quad \text{(F.53)}$$

where $i = x,y,z$ and:

$$\frac{\mu}{\rho} = \frac{\partial x^2}{\partial t^2} + \frac{\partial y^2}{\partial t^2} + \frac{\partial z^2}{\partial t^2} \quad \text{(F.54)}$$

$$c_s = \sqrt{\frac{\partial x^2}{\partial t^2} + \frac{\partial y^2}{\partial t^2} + \frac{\partial z^2}{\partial t^2}} = \sqrt{\frac{\mu}{\rho}} \quad \text{(F.55)}$$

where c_s is the speed of the shear waveform. The equations reveal that two, and only two, types of waves propagate in an unbounded infinite medium. For the shear waves, imagine a two-dimensional (x_1x_2)-plane. Shear waves in the (x_1x_2)-plane and normal to the (x_1x_2)-plane are considered "vertically" polarized (SV waves) and "horizontally" polarized (SH waves), respectively [276].

F.2 ATTENUATION IN AN INFINITE MEDIUM

For an unbounded infinite medium, the attenuation is considered dependent only on the material absorption of wave energy in the medium. For a bulk material, material absorption is accounted for in the following manner:

$$\Phi = \text{Amplitude} \cdot e^{i(k_{real}z - \omega t)} e^{-k_{imag}z} \quad \text{(F.56)}$$

The real wavenumber, k_{real}, describes the harmonic propagation of the waveform, while the imaginary wavenumber, k_{imag}, describes the exponential decay of the wave [89]. The complex wavenumber is written:

$$k = k_{real} + i k_{imag} \quad \text{(F.57)}$$

with the potential taking the form:

$$\Phi = \text{Amplitude} * e^{i(kz - \omega t)} \quad \text{(F.58)}$$

When the wavenumber is real, the bulk speeds (i.e. compressional and shear) are equivalent to the following:

300

$$c_d = \frac{\omega}{k_{d\,real}} \quad \text{...(F.59)}$$

$$c_s = \frac{\omega}{k_{s\,real}} \quad \text{...(F.60)}$$

When the wavenumber is complex, bulk velocities are complex as well. The complex bulk velocities are termed c_1 (compressional) and c_2 (shear):

$$c_1 = \frac{\omega}{k_d} = \frac{\omega}{k_{real} + i k_{imag}} = \frac{c_d}{1 + i\frac{k_{imag}}{k_{real}}} = \frac{c_d}{1 + i\frac{\alpha_d}{2\pi}} \quad \text{..............................(F.61)}$$

$$c_2 = \frac{\omega}{k_s} = \frac{\omega}{k_{real} + i k_{imag}} = \frac{c_s}{1 + i\frac{k_{imag}}{k_{real}}} = \frac{c_s}{1 + i\frac{\alpha_s}{2\pi}} \quad \text{..............................(F.62)}$$

where α_d and α_s are the bulk material absorption coefficients for compressional and shear propagation (units of Nepers per wavelength). When there is no material absorption, or it is very low in value, $c_1 = c_d$ and $c_2 = c_s$. The Lamé constants are written:

$$\mu = \rho c_1^2 \quad \text{..(F.63)}$$

$$\lambda = \rho c_2^2 - 2\mu \quad \text{..(F.64)}$$

Plugging in the complex bulk wave speeds yields:

$$\mu = \mu_{real} - i\mu_{imag} \quad \text{..(F.65)}$$

$$\lambda = \lambda_{real} - i\lambda_{imag} \quad \text{..(F.66)}$$

where:

$$\mu_{real} = \frac{\rho(c_s)^2 \left(4\pi^2\right)\left(4\pi^2 - \alpha_s^2\right)}{\left(\alpha_s^2 + 4\pi^2\right)^2} \quad \text{..(F.67)}$$

$$\mu_{imag} = \frac{\rho(c_s)^2 \left(4\pi^2\right)\left(4\alpha_s\pi\right)}{\left(\alpha_s^2 + 4\pi^2\right)^2} \quad \text{..(F.68)}$$

$$\lambda_{real} = \frac{\rho(c_d)^2 \left(4\pi^2\right)\left(4\pi^2 - \alpha_d^2\right)}{\left(\alpha_d^2 + 4\pi^2\right)^2} - 2\mu_{real} \quad \text{.................................(F.69)}$$

$$\lambda_{imag} = \frac{\rho(c_d)^2 \left(4\pi^2\right)\left(4\alpha_d\pi\right)}{\left(\alpha_d^2 + 4\pi^2\right)^2} - 2\mu_{imag} \quad \text{.......................................(F.70)}$$

There were two types of models used to define the material absorption coefficients. The first is referred to as the hysteretic structural damping model. The damping is constant per wavelength traveled. The other model was the Kelvin-Voigt viscous damping model. The damping is no longer constant per wavelength traveled, but increases with the frequency. For more information on these models, refer to [89,100].

APPENDIX G:

CYLINDRICAL COORDINATES

A picture of a cylinder with cylindrical coordinates drawn on is shown in Figure G.1:
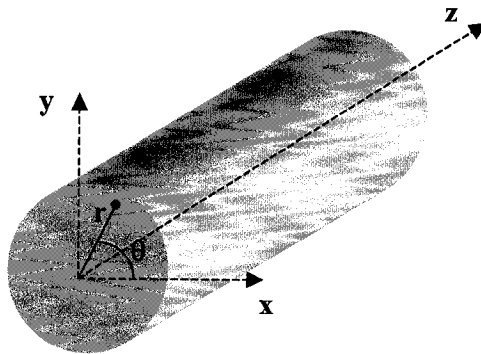
Figure G.1: Cylinder with cylindrical coordinates.

The $r\theta$ plane is dissected below in Figure G.2 to look at the resulting stresses and displacements.
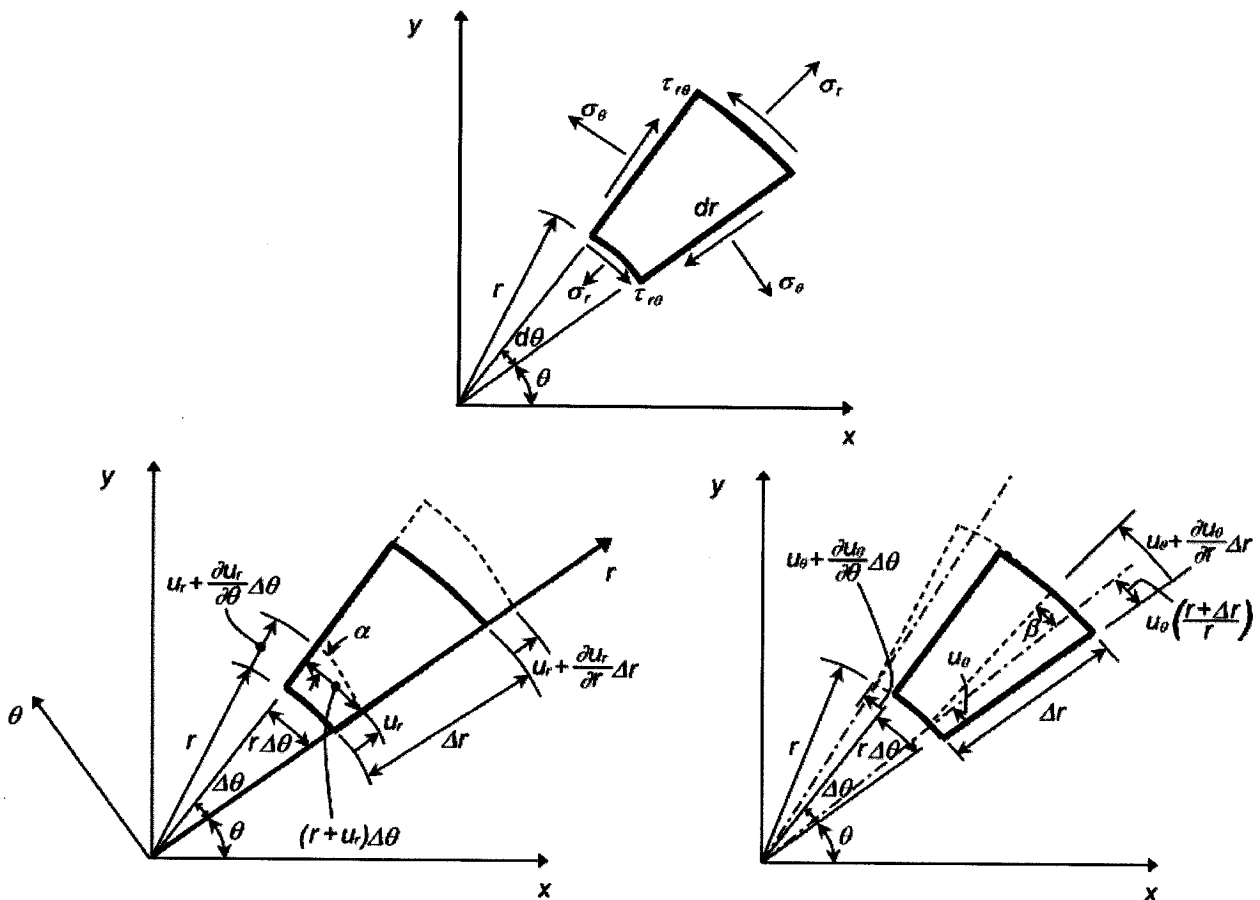
Figures G.2: Resulting stresses (top) and displacements (bottom) in the $r\theta$ plane (extracted from [234]).

The stress dyadic matrix is given below for cylindrical coordinates:

303

$$\begin{bmatrix} \sigma_{rr} & \tau_{r\theta} & \tau_{rz} \\ \tau_{\theta r} & \sigma_{\theta\theta} & \tau_{\theta z} \\ \tau_{zr} & \tau_{z\theta} & \sigma_{zz} \end{bmatrix} \quad \dots\dots\dots\dots\dots\dots\dots\dots\dots\dots\dots\dots\dots\dots\dots\dots\dots\dots \text{(G.1)}$$

where $\tau_{\theta r} = \tau_{r\theta}$, $\tau_{rz} = \tau_{zr}$ and $\tau_{\theta z} = \tau_{z\theta}$. The stress and strain equations are given below for cylindrical coordinates:

$$\varepsilon_{rr} = \frac{u_r + \dfrac{\partial u_r}{\partial r}\Delta r - u_r}{\Delta r} = \frac{\partial u_r}{\partial r} \quad \dots\dots\dots\dots\dots\dots\dots\dots\dots\dots\dots\dots\dots\dots\dots\dots\dots\dots \text{(G.2)}$$

$$\varepsilon_{\theta\theta} = \frac{(r+u_r)\Delta\theta - r\Delta\theta}{r\Delta\theta} + \frac{u_\theta + \left(\dfrac{\partial u_\theta}{\partial \theta}\right)\Delta\theta - u_\theta}{r\Delta\theta} = \frac{u_r}{r} + \frac{1}{r}\frac{\partial u_\theta}{\partial \theta} \quad \dots\dots\dots\dots\dots \text{(G.3)}$$

$$\varepsilon_{zz} = \frac{\partial u_z}{\partial z} \quad \dots\dots\dots\dots\dots\dots\dots\dots\dots\dots\dots\dots\dots\dots\dots\dots\dots\dots\dots\dots\dots\dots\dots\dots\dots \text{(G.4)}$$

$$\gamma_{r\theta} = \alpha + \beta = \frac{u_r + \left(\dfrac{\partial u_r}{\partial \theta}\right)\Delta\theta - u_r}{r\Delta\theta} + \frac{u_\theta + \left(\dfrac{\partial u_\theta}{\partial r}\right)\Delta r - u_\theta \dfrac{(r+\Delta r)}{r}}{\Delta r} = \frac{1}{r}\frac{\partial u_r}{\partial \theta} + \frac{\partial u_\theta}{\partial r} - \frac{u_\theta}{r} \quad \dots \text{(G.5)}$$

$$\gamma_{rz} = \frac{\partial u_z}{\partial r} + \frac{\partial u_r}{\partial z} \quad \dots\dots\dots\dots\dots\dots\dots\dots\dots\dots\dots\dots\dots\dots\dots\dots\dots\dots\dots\dots\dots \text{(G.6)}$$

$$\gamma_{\theta z} = \frac{\partial u_\theta}{\partial z} + \frac{1}{r}\frac{\partial u_z}{\partial \theta} \quad \dots\dots\dots\dots\dots\dots\dots\dots\dots\dots\dots\dots\dots\dots\dots\dots\dots\dots\dots\dots \text{(G.7)}$$

$$\sigma_{rr} = \lambda\Delta + 2\mu\varepsilon_{rr} = \frac{\lambda}{r}\left(u_r + \frac{\partial u_\theta}{\partial \theta} + r\frac{\partial u_z}{\partial z}\right) + (\lambda + 2\mu)\frac{\partial u_r}{\partial r} \quad \dots\dots\dots\dots\dots \text{(G.8)}$$

$$\sigma_{\theta\theta} = \lambda\Delta + 2\mu\varepsilon_{\theta\theta} = \lambda\left(\frac{\partial u_r}{\partial r} + \frac{\partial u_z}{\partial z}\right) + \frac{(\lambda + 2\mu)}{r}\left(u_r + \frac{\partial u_\theta}{\partial \theta}\right) \quad \dots\dots\dots\dots \text{(G.9)}$$

$$\sigma_{zz} = \lambda\Delta + 2\mu\varepsilon_{zz} = \frac{\lambda}{r}\left(u_r + \frac{\partial u_\theta}{\partial \theta} + r\frac{\partial u_r}{\partial r}\right) + (\lambda + 2\mu)\frac{\partial u_z}{\partial z} \quad \dots\dots\dots\dots \text{(G.10)}$$

$$\tau_{r\theta} = \mu\gamma_{r\theta} = \mu\left(\frac{1}{r}\frac{\partial u_r}{\partial \theta} + r\frac{\partial}{\partial r}\left(\frac{u_\theta}{r}\right)\right) \quad \dots\dots\dots\dots\dots\dots\dots\dots\dots\dots\dots \text{(G.11)}$$

$$\tau_{rz} = \mu\gamma_{rz} = \mu\left(\frac{\partial u_r}{\partial z} + \frac{\partial u_z}{\partial r}\right) \quad \dots\dots\dots\dots\dots\dots\dots\dots\dots\dots\dots\dots\dots\dots\dots \text{(G.12)}$$

APPENDIX H:

GRAD, DIV, AND CURL

The vector operator "grad" (called gradient) points in the direction of the greatest change of the scalar field and can be written in general Cartesian coordinates as:

$$\text{grad (F)} = \nabla f = \frac{\partial F}{\partial x}\mathbf{i} + \frac{\partial F}{\partial y}\mathbf{j} + \frac{\partial F}{\partial z}\mathbf{k} \quad \text{..} \quad (\text{H.1})$$

where F is a scalar function. Another well-known vector operator is that of the divergence function, which is called "div". Using the function, a scalar quantity is calculated from a vector field, representing the flux generation per unit volume at each point in the vector field. In other words, it is the rate at which density leaves a region of space. It is shown below in Cartesian coordinates:

$$\text{div (V)} = \nabla \cdot V = \frac{\partial V_x}{\partial x} + \frac{\partial V_y}{\partial y} + \frac{\partial V_z}{\partial z} \quad \text{..} \quad (\text{H.2})$$

where:

$$\nabla = \frac{\partial}{\partial x}\mathbf{i} + \frac{\partial}{\partial y}\mathbf{j} + \frac{\partial}{\partial z}\mathbf{k} \quad \text{...} \quad (\text{H.3})$$

$$\mathbf{V} = V_x\mathbf{i} + V_y\mathbf{j} + V_z\mathbf{k} \quad \text{..} \quad (\text{H.4})$$

Another well-known vector operator is that of the "curl" function. The "curl" of a vector field (in this case the displacement) is a measure of the rate of rotational spin. It is written in general Cartesian coordinates as:

$$\text{curl (V)} = \nabla \times V = \left(\frac{\partial V_z}{\partial y} - \frac{\partial V_y}{\partial z}\right)\mathbf{i} + \left(\frac{\partial V_x}{\partial z} - \frac{\partial V_z}{\partial x}\right)\mathbf{j} + \left(\frac{\partial V_y}{\partial x} - \frac{\partial V_x}{\partial y}\right)\mathbf{k} \quad \text{...............} \quad (\text{H.5})$$

Below are the vector operators shown in cylindrical coordinate form:

$$\text{curl}(V) = \nabla \times V = \left[\frac{1}{r}\frac{\partial V_z}{\partial \theta} - \frac{\partial V_\theta}{\partial z}\right]\mathbf{i}_r + \left[\frac{\partial V_r}{\partial z} - \frac{\partial V_z}{\partial r}\right]\mathbf{i}_\theta + \left[\frac{1}{r}\left\{\frac{\partial}{\partial r}(rV_\theta) - \frac{\partial V_r}{\partial \theta}\right\}\right]\mathbf{i}_z \quad \text{........................} \quad (\text{H.6})$$

$$\text{div}(V) = \nabla \bullet V = \frac{1}{r}\frac{\partial}{\partial r}(rV_r) + \frac{1}{r}\frac{\partial}{\partial \theta}(V_\theta) + \frac{\partial}{\partial z}(V_z) \quad \text{.......................................} \quad (\text{H.7})$$

$$\text{grad}(F) = \nabla F = \frac{\partial F}{\partial r}\mathbf{i}_r + \frac{1}{r}\frac{\partial F}{\partial \theta}\mathbf{i}_\theta + \frac{\partial F}{\partial z}\mathbf{i}_z \quad \text{..} \quad (\text{H.8})$$

where $\mathbf{V} = V_r\mathbf{i}_r + V_\theta\mathbf{i}_\theta + V_z\mathbf{i}_z$; F is a scalar function.

APPENDIX I:

BESSEL FUNCTIONS

The Bessel differential equation can be written in the following form:

$$x^2 \frac{\partial^2 y}{\partial x^2} + x \frac{\partial y}{\partial x} + \left(x^2 - n^2\right) y = 0 \quad \text{..(I.1)}$$

The general solution is the following:

$$y(x) = C_1 J_n(x) + C_2 Y_n(x) \quad \text{...(I.2)}$$

where C_1 and C_2 are constants. The symbol $J_n(x)$ represents a Bessel function of the first kind, also known as a cylinder function [277]. The symbol $Y_n(x)$ represents a Bessel function of the second kind, also referred to as a Neumann or Weber function. Figure I.1 and I.2 show $J_n(x)$ and $Y_n(x)$ for n = 0, 1 and 2, respectively.
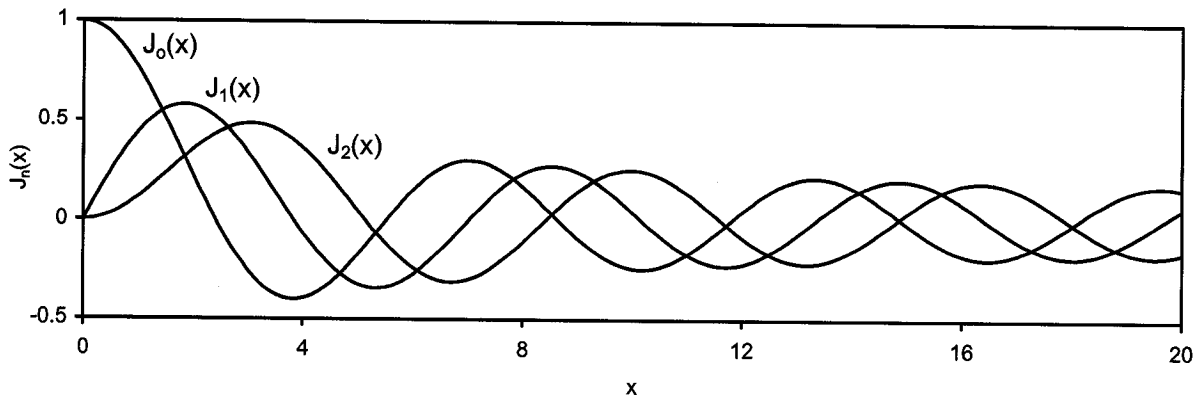
Figure I.1: Bessel functions of the first kind.
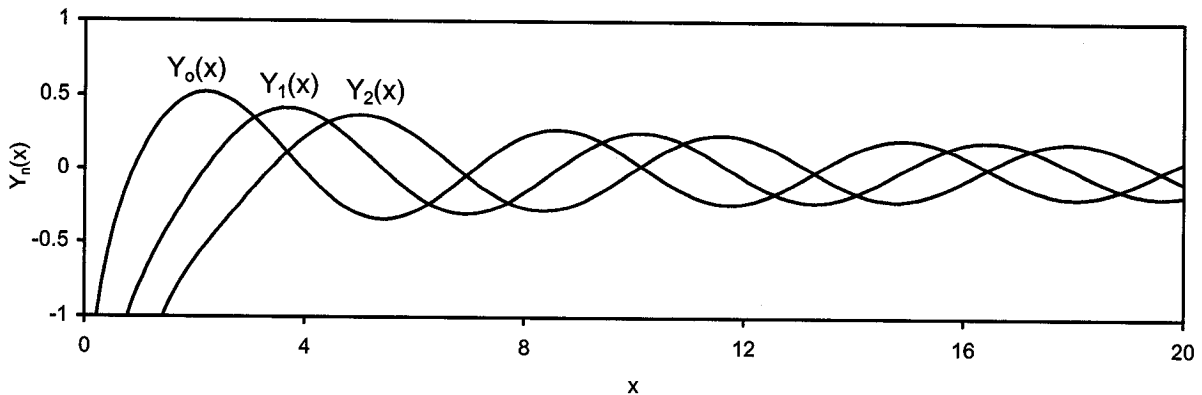
Figure I.2: Bessel functions of the second kind.

306

From Chapter 4, when the phase velocity of the guided wave is larger than the compressional velocity of the bulk material ($c_p > c_d$) the argument 'α' is real. The differential equation involving the scalar potential is written:

$$\frac{\partial^2 f}{\partial r^2} + \frac{1}{r}\frac{\partial f}{\partial r} + \left(\alpha^2 - \frac{n^2}{r^2}\right)f = 0 \dots\dots\dots\dots\dots\dots\dots\dots\dots\dots\dots\dots\dots\dots\text{(I.3)}$$

which has the following solution:

$$f(r) = A \cdot J_n(\alpha r) + B \cdot Y_n(\alpha r)\dots\dots\dots\dots\dots\dots\dots\dots\dots\dots\dots\dots\dots\text{(I.4)}$$

When a physical solution is necessary at $x = 0$, the constant B is set to zero because $Y_n(x)$ does not converge on a solution at zero.

When the argument 'x' is purely imaginary, the Modified Bessel functions $I_n(x)$ and $K_n(x)$ are used. The symbol $I_n(x)$ represents a Modified Bessel function of the first kind. The symbol $K_n(x)$ represents a Bessel function of the second kind, also referred to as a Basset or Macdonald function. Figures I.3 and I.4 show $I_n(x)$ and $K_n(x)$ for $n = 0$, 1 and 2, respectively.
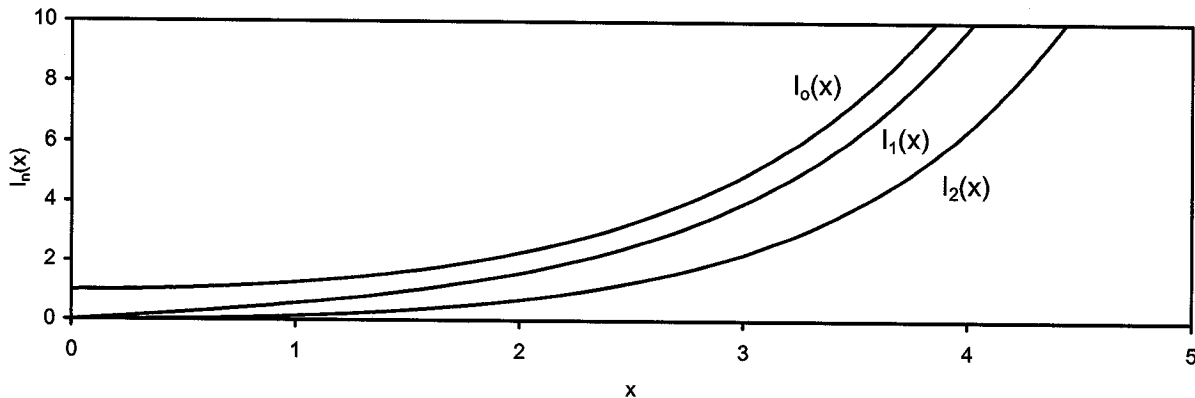
Figure I.3: Modified Bessel functions of the first kind.
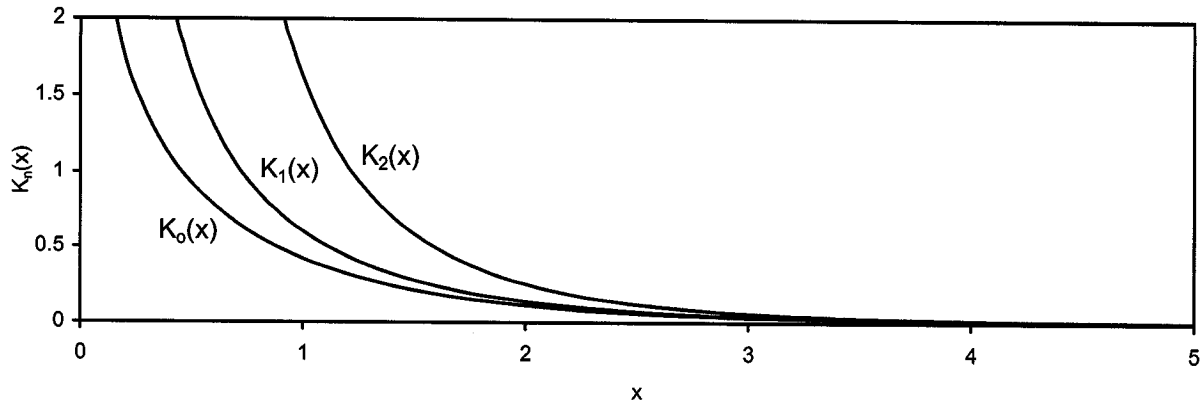
Figure I.4: Modified Bessel functions of the second kind.

From Chapter 4, when the phase velocity of the guided wave is less than the compressional velocity of the bulk material ($c_d > c_p$) the argument 'α' is imaginary. The differential equation involving the scalar potential is written:

$$\frac{\partial^2 f}{\partial r^2} + \frac{1}{r}\frac{\partial f}{\partial r} - \left(\alpha^2 + \frac{n^2}{r^2}\right)f = 0 \quad\text{...(I.5)}$$

which has the following solution:

$$f(r) = A{\cdot}I_n(\alpha r) + B{\cdot}K_n(\alpha r) \quad\text{...(I.6)}$$

When a physical solution is necessary at $x = 0$, the constant B is set to zero because $K_n(x)$ does not converge on a solution at zero.

The Hankel function of the first kind is a combination of Bessel functions of the first and second kind and decreases as its argument becomes larger:

$$H_n^1(x) = J_n(x) + iY_n(x) \quad\text{..(I.7)}$$

It is generally used to solve for outwardly propagating waveforms. The Hankel function of the second kind *increases* as its argument becomes larger. It too is a combination of the Bessel functions of the first and second kind:

$$H_n^2(x) = J_n(x) - iY_n(x) \quad\text{..(I.8)}$$

It is generally used to solve for inwardly propagating waveforms. However, this cannot be used for incoming waves because it would imply that at an infinite distance away from the center of the cylinder,

the wave has infinite energy. Therefore, the inward propagating waveform is set to zero, thus explaining why Figure 4.1 shows only outward propagating waves in the outermost layer.

The recurrence relationships for the Bessel functions are different. Using the same terminology as [Pavlakovic & Lowe 2001], recurrence parameters γ_1 and γ_2 are introduced. In Table 4.1, the values for the recurrence parameters were given subject to whether α and β are real or imaginary. The recurrence parameters have been utilized in the general recurrence relationships found below:

$$Z_n{}'(\alpha r) = \frac{n}{r} Z_n(\alpha r) - \alpha\gamma_1 Z_{n+1}(\alpha r) \quad\quad\quad\quad\quad\quad\text{(I.9)}$$

$$Z_n{}'(\beta r) = \frac{n}{r} Z_n(\beta r) - \beta\gamma_2 Z_{n+1}(\beta r) \quad\quad\quad\quad\quad\quad\text{(I.10)}$$

$$Z_{n+1}{}'(\alpha r) = \alpha Z_n(\alpha r) - \frac{(n+1)}{r} Z_{n+1}(\alpha r) \quad\quad\quad\quad\quad\text{(I.11)}$$

$$Z_{n+1}{}'(\beta r) = \beta Z_n(\beta r) - \frac{(n+1)}{r} Z_{n+1}(\beta r) \quad\quad\quad\quad\quad\text{(I.11)}$$

$$W_n{}'(\alpha r) = \frac{n}{r} W_n(\alpha r) - \alpha W_{n+1}(\alpha r) \quad\quad\quad\quad\quad\quad\text{(I.13)}$$

$$W_n{}'(\beta r) = \frac{n}{r} W_n(\beta r) - \beta W_{n+1}(\beta r) \quad\quad\quad\quad\quad\quad\text{(I.14)}$$

$$W_{n+1}{}'(\alpha r) = \gamma_1 \alpha W_n(\alpha r) - \frac{(n+1)}{r} W_{n+1}(\alpha r) \quad\quad\quad\quad\text{(I.15)}$$

$$W_{n+1}{}'(\beta r) = \gamma_2 \beta W_n(\beta r) - \frac{(n+1)}{r} W_{n+1}(\beta r) \quad\quad\quad\quad\text{(I.16)}$$

Please note the following substitutions whenever a second derivative appears.

$$\frac{\partial^2 f}{\partial r^2} = -\frac{1}{r}\frac{\partial f}{\partial r} + \left(\frac{n^2}{r^2} - \alpha^2\right) f \quad\quad\quad\quad\quad\quad\quad\text{(I.17)}$$

$$\frac{\partial^2 h_r}{\partial r^2} = -\frac{1}{r}\frac{\partial h_r}{\partial r} + \left(\frac{(n+1)^2}{r^2} - \beta^2\right) h_r \quad\quad\quad\quad\quad\text{(I.18)}$$

$$\frac{\partial^2 h_z}{\partial r^2} = -\frac{1}{r}\frac{\partial h_z}{\partial r} + \left(\frac{n^2}{r^2} - \beta^2\right) h_z \quad\quad\quad\quad\quad\quad\text{(I.19)}$$

309

APPENDIX J:

TRANSDUCERS

The transducer type used to send and receive lower frequency guided waves was a piezoelectric compressional transducer (Digital Wave model B-1025), with a 0.365" (9.3 mm) diameter face. To test the response of the transducer over the lower frequency region, two transducers were coupled face to face with the response of several invoked frequencies recorded. A 50-cycle (toneburst) pulse was sent in at frequencies between 20 and 250 kHz in 5 kHz increments with the signal amplitude at 200 volts peak-to-peak. The highpass filter was set at 1 kHz and the lowpass filter was set at 300 kHz.
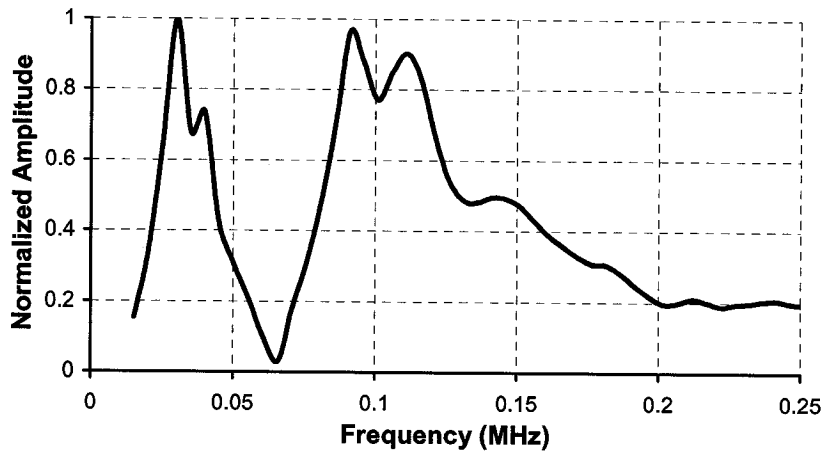
Figure J.1: Frequency response of transducer set (Digital Wave model B-1025) used for low frequency testing.

The transducers used to generate Figure J.1 show that the response is not completely flat over the frequency range used for testing. This distribution of invoked response can be seen in the results. Tonebursts are used in this report to try and isolate certain frequencies. Figure J.2 shows four frequency domains for the same set of Digital Wave transducers coupled face to face with single, five, fifteen, and thirty-cycle pulses at 250 kHz invoked.

310
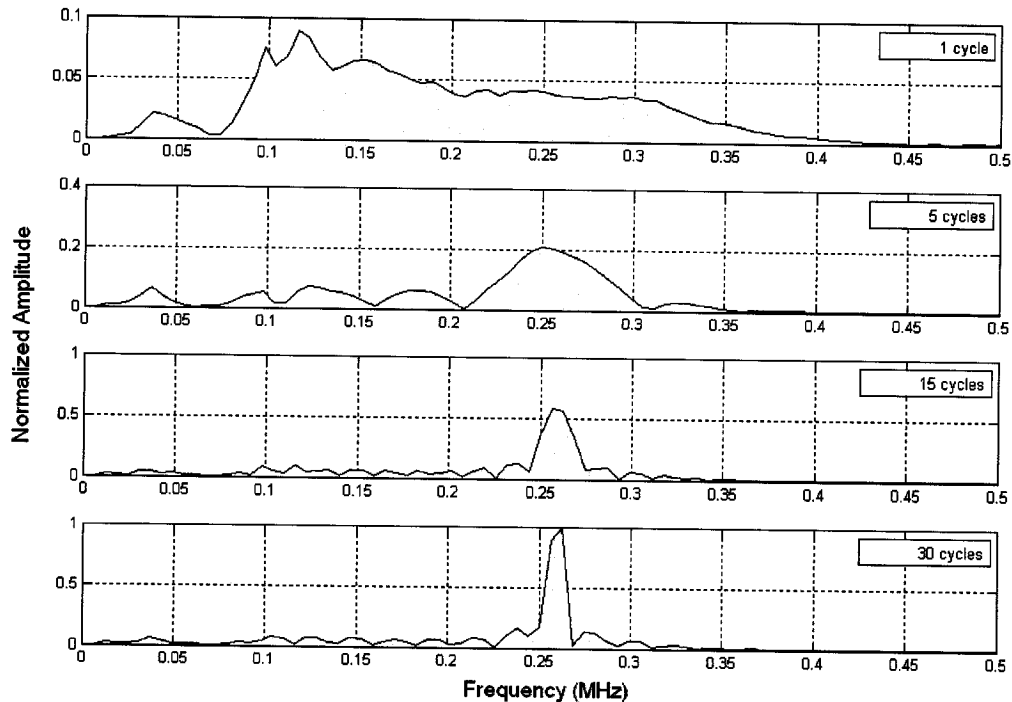
Figure J.2: Frequency domain for transducers coupled face to face with a single, five, fifteen, and 30-cycle toneburst signal at 250 kHz invoked.

The transducer type used to send higher frequency guided waves was a piezoelectric contact compressional transducer (Panametrics model V110), with a 0.25" (6.35 mm) diameter face and a center frequency of 5.21 MHz. The transducer type used to receive higher frequency guided waves in through-transmission mode is the same model transducer but with a center frequency of 5.1 MHz. Figure J.3 shows the response of the two Panametrics transducers used to generate higher frequency waveforms.
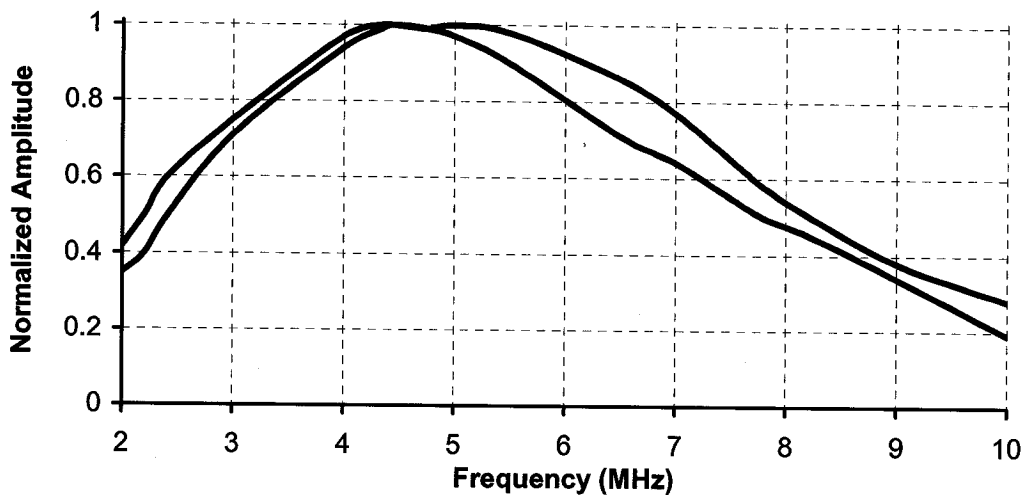
Figure J.3: Frequency response of transducers (Panametrics model V110) used for high frequency testing.

APPENDIX K:

SPECTROGRAM

For a collected signal it is useful to view the frequency content based on the time-of-arrival. This can be accomplished by the use of a spectrogram. A spectrogram is of primary importance to identify multiple guided wave modes within the same signal. A time-dependent Fourier transform can be used to see how a spectral distribution of a nonstationary process evolves with time [278]. To calculate the time-dependent Fourier transform, a discrete-time Fourier transform is performed within a finite windowed segment of the time domain signal. The window is then slid further down the time axis, overlapping the previous window, and again calculating the time-dependent Fourier transform. The process is continued until the entire signal has been processed. The time-dependent Fourier transform can be interpreted as a smoothed version of the Fourier transform of the part of the signal within the window [279]. The results can be viewed as a two-dimensional plot of frequency content as a function of time, with the magnitude of the signal shown as color. This is referred to as a spectrogram. Figure K.1(a) shows a time domain signal. The signal is comprised of 8,192 points, collected at a sampling rate of 25 MHz. A spectrogram has been computed for this signal using a Hamming window of 400 points. Each consecutive window will overlap the previous for 390 points. The spectrogram is shown in Figure K.1(b).
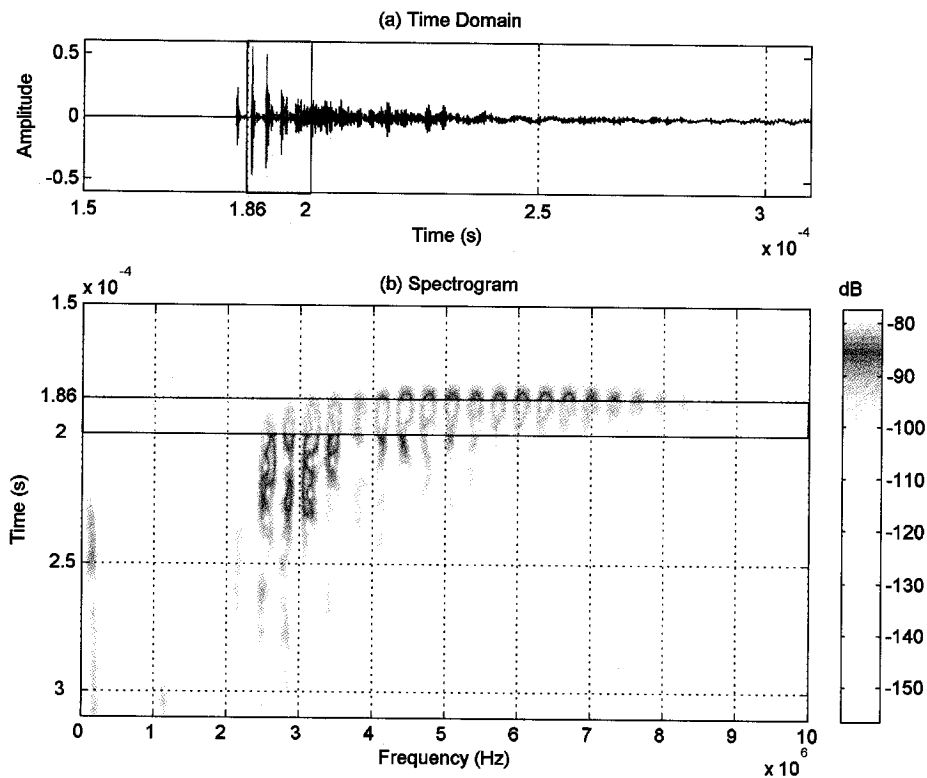
Figure K.1: **(a)** Time domain signal and **(b)** spectrogram.

312

Matlab was used to generate all spectrograms shown in this report. The specific command for generating the spectrogram shown in Figure K.1(b) was spectrogram(data,400,390,8192,25000000), where 'data' is an array containing the collected signal. A colorbar has been added to the right side of the spectrogram to show how color indicates the magnitude (in decibels) of the signal. Notice that a shaded region has been added from 186 µs to 200 µs for both the time domain and spectrogram. This is mean to illustrate the effectiveness of the spectrogram, allowing the frequency content to be viewed based on the time-of-arrival. For closely spaced dispersion curves, the reassigned spectrogram can be used and is discussed elsewhere [280].

313

REFERENCES

1. W.H. Hartt, R.G. Powers, V. Leroux, and D.K. Lysogorski, "Critical Literature Review of High-Performance Corrosion Reinforcements in Concrete Bridge Applications," FHWA-RD-04-093, 2004.

2. G.K. Al-Sulaimani, M. Kaleemullah, I.A. Busanbul, and F. Rasheeduzzafar, "Influence of Corrosion and Cracking on Bond Behavior and Strength of Reinforced Concrete Members," *ACI Structural Journal*, Vol. 87, No. 2, pp. 220-231, 1990.

3. K. Tuutti, *Corrosion of Steel in Concrete*, Swedish Cement and Concrete Research Institute, 1982.

4. S. Rostam, "Reinforced Concrete Structures – Shall Concrete Remain the Dominating Means of Corrosion Prevention?," *Materials and Corrosion*, Vol. 54, pp. 369-378, 2003.

5. G. Morcous and Z. Lounis, "Prediction of Onset of Corrosion in Concrete Bridge Decks Using Neural Networks and Case-Based Reasoning," *Computer-Aided Civil and Infrastructure Engineering*, Vol. 20, pp. 108-117, 2005.

6. K. Zhou, B. Martin-Perez, and Z. Lounis, "Finite Element Analysis of Corrosion-Induced Cracking, Spalling and Delamination of RC bridge decks," 1st Canadian Conference on Effective Design of Structures, Ontario, Canada, pp. 187-196, 2005.

7. Z.P. Bazant, "Physical Model for Steel Corrosion in Concrete Sea Structures—Theory," *ASCE Journal of the Structural Division*, Vol. 105, No. 6, pp. 1137-1153, 1979.

8. R. Baboian, "Synergistic Effects of Acid Deposition and Road Salts on Corrosion," *Corrosion Forms and Control for Infrastructure*, ASTM STP 1137, Ed. Victor Chaker, American Society for Testing and Materials, Philadelphia, 1992.

9. L. Bertolini, B. Elsener, P. Pedeferri, and R. Polder, *Corrosion of Steel in Concrete: Prevention, Diagnosis, Repair*, Weinheim: WILEY-VCH, 2004.

10. *Corrosion in reinforced concrete structures*, Ed: H. Böhni, Boca Raton: CRC Press, 2005.

11. A. Bentur, S. Diamond, and N.S. Berke, *Steel Corrosion in Concrete: Fundamental and Civil Engineering Practice*, London: E & FN Spon, 1997.

12. I.A. Wootton, L.K. Spainhour, and N. Yazdani, "Corrosion of Steel Reinforcement in Carbon Fiber-Reinforced Polymer Wrapped Concrete Cylinders," *Journal of Composites for Construction*, Vol. 7, No. 4, pp. 339-347, 2003.

13. J. Bennett, T.J. Schue, K.C. Clear, D.L. Lankard, W.H. Hartt, and W.J. Swiat, "Electrochemical Chloride Removal and Protection of Concrete Bridge Components: Laboratory Studies," SHRP-S-657, Strategic Highway Research Program, 1993.

14. A. Sanjurjo, S. Hettiarachchi, K. Lau, B. Wood, and P. Cox, "Development of Metallic Coatings for Corrosion Protection of Steel Rebars," SHRP-I-622, Strategic Highway Research Program, 1993.

15. J.P. Broomfield and J.S. Tinnear, "Cathodic Protection of Reinforced Concrete Bridge Components," SHRP-92-618, Strategic Highway Research Program, 1992.

16. H. Mutsuyoshi, "Present Situation of Durability of Post-Tensioned PC Bridges in Japan" *Durability of Post-Tensioning Tendons*, Ed: L. Taerwe, Fédération Internationale du Béton, Sausanne, Switzerland, 2001.

17. J. Grata, "Road salt, hits from trucks likely led to bridge collapse," *Pittsburgh Post-Gazette*, December 29, 2005.

18. R.W. Poston and J.S. West, "Investigation of the Charlotte Motor Speedway Bridge Collapse," *Proceedings of the Structures Congress and Exposition, Metropolis and Beyond - Proceedings of the 2005 Structures Congress and the 2005 Forensic Engineering Symposium*, pp. 2469-2479, 2005.

19. NASA Corrosion Technology Laboratory Homepage, http://corrosion.ksc.nasa.gov.

20. G.H. Koch, M.P.H. Brongers, N.G. Thompson, Y.P. Virmani, and J.H. Payer, "Corrosion Cost and Preventive Strategies in the United States," FHWA-RD-01-156, Federal Highway Administration, 2001.

21. E.J. Fasullo, "Infrastructure: The Battlefield of Corrosion," *Corrosion Forms and Control for Infrastructure*, ASTM STP 1137, Ed. Victor Chaker, American Society for Testing and Materials, Philadelphia, 1992.

22. J.L. Borgerson and H. Reis, "Monitoring the setting times and strength gain of mortar using ultrasonic guided waves," *Insight*, Vol. 48, No. 11, pp. 670-676, 2006.

23. M.D. Beard, M.J.S. Lowe, and P. Cawley, "Ultrasonic Guided Waves for Inspection of Grouted Tendons and Bolts," *Journal of Materials in Civil Engineering*, Vol. 15, No. 3, pp. 212-218, 2003.

24. S. Mindess and J.F. Young, *Concrete*, Upper Saddle River: Prentice-Hall, Inc., 1981.

25. T.C. Powers, "Structure and physical properties of hardened Portland cement past," *Journal of American Ceramic Society*, Vol. 41, pp. 1-6, 1958.

26. G. Fagerlund, "Influence of slag cement on the frost resistance of concrete – a theoretical analysis," *CBI Forskning (Cement – och Betonginstitutet)*, No. 1, 1980.

27. T.A. Söylev and R. François, "Corrosion of Reinforcement in Relation to Presence of Defects at the Interface between Steel and Concrete," *Journal of Materials in Civil Engineering*, Vol. 17, No. 4, pp. 447-455, 2005.

28. W. Zhu, M. Sonebi, and P.J.M. Bartos, "Bond and interfacial properties of reinforcement in self-compacting concrete," *Materials and Structures*, Vol. 37, pp. 442-448, 2004.

29. *Corrosion of Steel in Concrete: Report of the Technical Committee 60-CSC RILEM*, Ed. P. Schiessl, New York: Chapman and Hall, 1988.

30. C. Altstetter, Unpublished Manuscript, University of Illinois, 2005.

31. D. Jones, *Principles and Prevention of Corrosion*, New York: Macmillan Publishing Company, 1992.

32. E.J. Hansen and V.E. Saouma, "Numerical Simulation of Reinforced Concrete Deterioration: Part II—Steel Corrosion and Concrete Cracking," *ACI Materials Journal*, Vol. 96, No. 3, pp. 331-338, 1999.

33. *Uhlig's Corrosion Handbook*, 2nd Edition, Ed. R.W. Revie, New York: John Wiley & Sons Inc., 2000.

34. K. Bhargava, A.K. Ghosh, Y. Mori, and S. Ramanujam, "Modeling of time to corrosion-induced cover cracking in reinforced concrete structures," *Cement and Concrete Research*, Vol. 35, pp. 2203-2218, 2005.

35. J. Crank, *The Mathematics of Diffusion*, 2nd Edition, Oxford: Clarendon Press, 1975.

36. O.B. Isgor and A.G. Razaqpur, "Finite element modeling of coupled heat transfer, moisture transport and carbonation processes in concrete structures," *Cement & Concrete Composites*, Vol. 26, pp. 57-73, 2004.

37. A. Ababneh, F. Benboudjema, and Y. Xi, "Chloride Penetration in Nonsaturated Concrete," *Journal of Materials in Civil Engineering*, Vol. 15, No. 2, pp. 183-191, 2003.

38. K. Thangavel and N.S. Rengaswamy, "Relationship between Chloride/Hydroxide Ratio and Corrosion Rate of Steel in Concrete," *Cement and Concrete Composites*, Vol. 20, pp. 283-292, 1998.

39. M. Pourbaix, *Lectures on Electrochemical Corrosion*, New York: Plenum Press, 1973.

40. W. Puatatsananon and V.E. Saouma, "Nonlinear Coupling of Carbonation and Chloride Diffusion in Concrete," *Journal of Materials in Civil Engineering*, Vol. 17, No. 3, pp. 264-275, 2005.

41. N. Ihekwaba, B. Hope, and C. Hansson, "Carbonation and electrochemical chloride extraction from concrete," *Cement and Concrete Research*, Vol. 26, No. 7, pp. 1095-1107, 1996.

42. N.J. Carino, "Nondestructive Techniques to Investigate Corrosion Status in Concrete Structures," *Journal of Performance of Constructed Facilities*, Vol. 13, No. 3, pp. 96-106, 1999.

43. B.H. Hertlein, "Assessing the Role of Steel Corrosion in the Deterioration of Concrete in the National Infrastructure: A Review of the Causes of Corrosion and Current Diagnostic Techniques," *Corrosion Forms and Control for Infrastructure*, ASTM STP 1137, Ed. Victor Chaker, American Society for Testing and Materials, Philadelphia, 1992.

44. B. Elsener, "Macrocell corrosion of steel in concrete – implications for corrosion monitoring," *Cement & Concrete Composites*, Vol. 24, pp. 65-72, 2002.

45. *Stainless Steel in Concrete: State of the Art Report*, Ed. Ulf Nurnberger, EFC Publications Number 18, 1996.

46. M.G. Fontana, *Corrosion Engineering*, 3rd Ed., New York: McGraw-Hill, 1986.

47. J.Cairns, G. A. Plizzari, Y. Du, D.W. Law, and C. Franzoni, "Mechanical Properties of Corrosion-Damaged Reinforcement," *ACI Materials Journal*, Vol. 102, No. 4, pp. 256-264, 2005.

48. J.A. Gonzalez, C. Andrade, C. Alonso, and S. Feliu, "Comparison of rates of general corrosion and maximum pitting penetration on concrete embedded steel reinforcement," *Cement and Concrete Research*, Vol. 25, No. 2, pp. 257-264, 1995.

49. D. Coronelli and P. Gambarova, "Structural Assessment of Corroded Reinforced Concrete Beams: Modeling Guidelines," *Journal of Structural Engineering*, Vol. 130, No. 8, pp. 1214-1223, 2004.

50. W. Aquino, *Long Term Performance of Seismically Rehabilitated Corrosion-Damaged Columns*, PhD Thesis, University of Illinois, 2002.

51. J.G. Cabrera, "Deterioration of Concrete Due to Reinforcement Steel Corrosion," *Cement & Composites*, Vol. 18, pp. 47-59, 1996.

52. A.A. Almusallam, A.S. Al-Gahtani, A.R. Aziz, and Rasheeduzzafar, "Effect of Reinforcement Corrosion on Bond Strength," *Construction and Building Materials*, Vol. 10, No. 2, pp. 123-129, 1996.

53. P.S. Mangat and M.S. Elgarf, "Bond characteristics of corroding reinforcement in concrete beams," *Materials and Structures*, Vol. 32, pp. 89-97, 1999.

54. L. Amleh and S. Mirza, "Corrosion Influence on Bond between Steel and Concrete," *ACI Structural Journal*, Vol. 96, No. 3, pp. 415-423, 1999.

55. Y. Takagishi, H. Ichikawa, H. Tabuchi, and A. Moriwake, "An Experimental Study on Deterioration and Repairing of a Marine Concrete Structure," *Concrete in Marine Environments*, ACI SP-109, American Concrete Institute, Detroit, pp. 253-276, 1988.

56. K. Leet and D. Bernal, *Reinforced Concrete Design*, Boston: McGraw-Hill, 1997.

57. Y. Auyeung, P. Balaguru, and L. Chung, "Bond Behavior of Corroded Reinforcement Bars," *ACI Materials Journal*, Vol. 97, No. 2, pp. 214-220, 2000.

58. M.-T. Liang, L.-H. Lin, and C.-H. Liang, "Service Life Prediction of Existing Reinforced Concrete Bridges to Chloride Environment," *Journal of Infrastructure Systems*, Vol. 8, No. 3, pp. 76-85, 2002.

59. C.Q. Li, "Life-Cycle Modeling of Corrosion-Affected Concrete Structures: Propagation," *Journal of Structural Engineering*, Vol. 129, No. 6, pp. 753-761, 2003.

60. A.A. Sagüés, "Modeling the Effects of Corrosion on the Lifetime of Extended Reinforced Concrete Structures," *Corrosion*, Vol. 59, No. 10, pp. 854-866, 2003.

61. K.A.T. Vu and M.G. Stewart, "Structural Reliability of Concrete Bridges including improved Chloride-Induced Corrosion Models," *Structural Safety*, Vol. 22, pp. 313-333, 2000.

62. Y. Liu and R.E. Weyers, "Modeling the Time-to-Corrosion Cracking in Chloride Contaminated Reinforced Concrete Structures," *ACI Materials Journal*, Vol. 95, pp. 675-681, 1998.

63. Z.P. Bazant, "Physical Model for Steel Corrosion in Concrete Sea Structures—Application," *ASCE Journal of the Structural Division*, Vol. 105, No. 6, pp. 1155-1166, 1979.

64. Y. Liu, *Modeling the Time-to-Corrosion Cracking of the Cover Concrete in Chloride Contaminated Reinforced Concrete Structures*, PhD Thesis, Virginia Polytechnic Institute and State University, 1996.

65. S.J. Pantazopoulou and K.D. Papoulia, "Modeling Cover-Cracking due to Reinforcement Corrosion in RC Structures," *Journal of Engineering Mechanics*, Vol. 127, No. 4, pp. 342-351, 2001.

66. *Corrosion, Vol. 1: Metal/Environment Reactions*, 2nd Ed., Ed. L.L. Shreir, Boston: Newnes-Butterworths, 1978.

67. W.C. Young and R.G. Budynas, *Roark's Formulas for Stress and Strain*, 7th Ed., New York: McGraw-Hill, 2002.

68. I. Petre-Lazar, "Aging Assessment of Concrete Structures Submitted to Steel Corrosion," PhD Thesis, Laval University, 2000.

69. R. de Borst, J.J.C. Remmers, A. Needleman, and M.-A. Abellan, "Discrete vs. Smeared Crack Models for Concrete Fracture: Bridging the Gap," *International Journal for Numerical and Analytical Methods in Geomechanics*, Vol. 28, pp. 583-607, 2004.

70. C.V. Nielsen and N. Bicanic, "Radial fictitious cracking of thick-walled cylinder due to bar pull-out," *Magazine of Concrete Research*, Vol. 54, No. 3, pp. 215-221, 2002.

71. X. Wang and X. Liu, "Bond strength modeling for corroded reinforcements," *Construction and Building Materials*, Vol. 20, pp. 177-186, 2006.

72. A. Suwito and Y. Xi, "Service Life of Reinforced Concrete Structures with Corrosion Damage due to Chloride Attack," *Life-Cycle Performance of Deteriorating Structures: Assessment, Design and Management*, pp. 207-218, 2003.

73. C.K.Y. Leung, "Modeling of Concrete Cracking Induced by Steel Expansion," *Journal of Materials in Civil Engineering*, Vol. 13, No. 3, pp. 169-175, 2001.

74. C.Q. Li, W. Lawanwisut, and J.J. Zheng, "Time-Dependent Reliability Method to Assess the Serviceability of Corrosion-Affected Concrete Structures," *Journal of Structural Engineering*, Vol. 131, No. 11, pp. 1674-1680, 2005.

75. C. Andrade, C. Alonso, and F.J. Molina, "Cover Cracking as a Function of Bar Corrosion: Part I—Experimental Test," *Materials and Structures*, Vol. 26, pp. 453-464, 1993.

76. C.Q. Li and R.E. Melchers, "Time-Dependent Reliability Analysis of Corrosion-Induced Concrete Cracking," *ACI Structural Journal*, Vol. 102, No. 4, pp. 543-549, 2005.

77. K. Vu, M.G. Stewart, and J. Mullard, "Corrosion-Induced Cracking: Experimental Data and Predictive Models," *ACI Structural Journal*, Vol. 102, No. 5, pp. 719-726, 2005.

78. M. Ohtsu and S. Yosimura, "Analysis of Crack Propagation and Crack Initiation due to Corrosion of Reinforcement," *Construction and Building Materials*, Vol. 11, No. 7-8, pp. 437-442, 1997.

79. J. Padovan and J. Jae, "FE Modeling of Expansive Oxide Induced Fracture of Rebar Reinforced Concrete," *Engineering Fracture Mechanics*, Vol. 56, No. 6, pp. 797-812, 1997.

80. K. Lundgren, "Bond between Ribbed Bars and Concrete. Part 2: The Effect of Corrosion," *Magazine of Concrete Research*, Vol. 57, No. 7, pp. 383-395, 2005.

81. F.J. Molina, C. Alonso, and C. Andrade, "Cover Cracking as a Function of Rebar Corrosion: Part 2—Numerical Model," *Materials and Structures*, Vol. 26, pp. 532-548, 1993.

82. A. Ouglova, Y. Berthaud, M. François, and F. Foct, "Mechanical properties of an iron oxide formed by corrosion in reinforced concrete structures," *Corrosion Science*, Vol. 48, pp. 3988-4000, 2006.

83. D.C. Gazis, "Three-Dimensional Investigation of the Propagation of Waves in Hollow Circular Cylinders: Analytical Foundation," *Journal of the Acoustical Society of America*, Vol. 31, No. 5, pp. 568-573, 1959.

84. K.F. Graff, *Wave Motion in Elastic Solids*, Ohio State University Press, 1975.

85. J.L. Rose, *Ultrasonic Waves in Solid Media*, New York: Cambridge University Press, 1999.

86. A.E. H. Love, *A Treatise on the Mathematical Theory of Elasticity*, 4th Ed., Cambridge: University Press, 1927.

87. M. Redwood, *Mechanical Waveguides*, New York: Pergamon Press Ltd., 1960.

88. H. Kolsky, *Stress Waves in Solids*, New York: Dover Publications, Inc., 1963.

89. B. Pavlakovic and M. Lowe, *Disperse User's Manual: Version 2.0.11*, 2001.

90. T. Kundu, *Ultrasonic Nondestructive Evaluation: Engineering and Biological Material Characterization*, Boca Raton: CRC Press LLC, 2004.

91. J.L. Rose, "A Baseline and Vision of Ultrasonic Guided Wave Inspection Potential," *Journal of Pressure Vessel Technology*, Vol. 124, pp. 273-282, 2002.

92. D.S. Hughes, W.L. Pondrom, and R.L. Mims, "Transmission of Elastic Pulses in Metal Rods," *Physical Review*, Vol. 75, pp. 1552-1556, 1949.

317

93. L.Y. Tu, J.N. Brennan, and J.A. Sauer, "Dispersion of Ultrasonic Pulse Velocity in Cylindrical Rods," *Journal of the Acoustical Society of America*, Vol. 27, pp. 550-555, 1955.

94. J. Oliver, "Elastic Wave Dispersion in a Cylindrical Rod by a Wide-Band Short-Duration Pulse Technique," *Journal of the Acoustical Society of America*, Vol. 29, pp. 189-194, 1957.

95. M.D. Beard, *Guided Wave Inspection of Embedded Cylindrical Structures*, Ph.D. Thesis, Univ. of London, 2002.

96. B. Pavlakovic, M. Lowe, and P. Cawley, "The Inspection of Tendons in Post-Tensioned Concrete Using Guided Ultrasonic Waves," *INSIGHT*, Vol. 41, No. 7, pp. 446-452, 1999.

97. W. Na, T. Kundu, and M.R. Ehsani, "Ultrasonic Guided Waves for Steel Bar Concrete Interface Testing," *Materials Evaluation*, Vol. 60, No. 3, pp. 437-444, 2002.

98. W. Na, T. Kundu, and M.R. Ehsani, "A Comparison of Steel/Concrete and Glass Fiber Reinforced Polymers/Concrete Interface Testing by Guided Waves," *Materials Evaluation*, Vol. 61, No. 2, pp. 155-161, 2003.

99. B.N. Pavlakovic, M.J.S. Lowe, and P. Cawley, "High-Frequency Low-Loss Ultrasonic Modes in Imbedded Bars," *Journal of Applied Mechanics*, Vol. 68, pp. 67-75, 2001.

100. B.N. Pavlakovic, *Leaky Guided Ultrasonic Waves in NDT*, PhD Thesis, University of London, 1998.

101. D. Bancroft, "The Velocity of Longitudinal Waves in Cylindrical Bars," *Physical Review*, Vol. 59, pp. 588-593, 1941.

102. T. Miller, C.J. Hauser, and T. Kundu, "Nondestructive Inspection of Corrosion and Delamination at the Concrete-Steel Reinforcement Interface," *American Society of Mechanical Engineers (Publication) NDE*, Vol. 23, Proceedings of the ASME Nondestructive Evaluation Engineering Division – 2002, pp. 121-128, 2002.

103. B.A. Auld, *Acoustic Fields and Waves in Solids: Volume II*, New York: John Wiley & Sons, 1973.

104. P.M. Morse and H. Feshbach, *Methods of Theoretical Physics*, New York: McGraw-Hill, 1953.

105. J.D.N. Cheeke, *Fundamentals and applications of ultrasonic waves*, Boca Raton: CRC Press, 2002.

106. E.P. Papadakis, "Revised Grain-Scattering Formulas and Tables," *Journal of the Acoustical Society of America*, Vol. 37, No. 4, pp. 703-710, 1965.

107. E.P. Papadakis, "Ultrasonic Attenuation Caused by Scattering in Polycrystalline Metals," *Journal of the Acoustical Society of America*, Vol. 37, No. 4, pp. 711-717, 1965.

108. E.P. Papadakis, "Influence of Preferred Orientation on Ultrasonic Grain Scattering," *Journal of Applied Physics*, Vol. 36, No. 5, pp. 1738-1740, 1965.

109. L.E. Kinsler, A.R. Frey, A.B. Coppens, and J.V. Sanders, *Fundamentals of Acoustics*, 4th Ed., New York: John Wiley & Sons, Inc., 2000.

110. J.M. Gere and S.P. Timoshenko, *Mechanics of Materials*, 4th Ed., New York: PWS Publishing Company, 1997.

111. C. Lanczos, *Applied Analysis*, Englewood Cliffs: Prentice Hall, Inc, 1956.

112. L. Pochhammer, "Uber die Fortpflanzungsgeschwindigkeiten kleiner Schwingungen in einem Unbegrenzten Isotropen Kreiszylinder," *J.f.d reine u. angew. Math*, Vol. 81, pp. 324-336, 1876.

113. C. Chree, "The Equations of an Isotropic Elastic Solid in Polar and Cylindrical Co-ords., their Solutions and Applications," *Transactions of the Cambridge Philosophical Society*, Vol. 14, pp. 250-369, 1889.

114. F. Wu and F.-K. Chang, "Debond Detection using Embedded Piezoelectric Elements in Reinforced Concrete Structures – Part I: Experiment," *Structural Health Monitoring*, Vol. 5, No. 1, pp. 5-15, 2006.

115. C. He, J.K. Van Velsor, C.M. Lee, and J.L. Rose, "Health Monitoring of Rock Bolts using Ultrasonic Guided Waves," *Review of Quantitative Nondestructive Evaluation*, Vol. 25, Ed. D.O. Thompson & D.E. Chimenti, pp. 195-201, 2006.

116. P.A. Gaydecki, F.M. Burdekin, W. Damaj, D.G. John, and P.A. Payne, "Digital Deconvolution Analysis of Ultrasonic Signals influenced by the presence of Longitudinally aligned steel cables in pre-stressed concrete," *Measurement Science and Technology*, Vol. 3, pp. 909-917, 1992.

117. P. Rizzo and F.L. di Scalea, "Monitoring Steel Strands via Ultrasonic Measurements," *Proceedings of SPIE*, Vol. 4696, pp. 62-73, 2002.

118. F.L. di Scalea, P. Rizzo, and F. Seible, "Stress Measurement and Defect Detection in Steel Strands by Guided Stress Waves," *Journal of Materials in Civil Engineering*, Vol. 15, No. 3, pp. 219-227, 2003.

119. G.B. Niles, "In Situ Method of Inspecting Anchor Rods for Section Loss using the Cylindrically Guided Wave Technique," *IEEE Transactions on Power Delivery*, Vol. 11, No. 3, pp. 1601-1605, 1996.

120. T. Kundu, S. Banerjee, and K.V. Jata, "An experimental investigation of guided wave propagation in corrugated plates showing stop bands and pass bands," *Journal of the Acoustical Society of America*, Vol. 120, No. 3, pp. 1217-1226, 2006.

121. "Standard Test Method for Static Modulus of Elasticity and Poisson's Ratio of Concrete in Compression," *Annual Book of ASTM Standards*, ASTM C 469-94, 1999.

122. T. Vogt, M. Lowe, and P. Cawley, "The scattering of guided waves in partly embedded cylindrical structures," *Journal of the Acoustical Society of America*, Vol. 113, No. 3, pp. 1258-1272, 2003.

123. K.A. Bartels, C. Dynes, and H. Kwun, "Nondestructive evaluation of prestressing strands with magnetostrictive sensors," *Proceedings of SPIE*, Vol. 3400, pp. 326-337, 1998.

124. C. Andrade, C. Alonso, J. Rodriquez, and M. Garcia, "Cover Cracking and Amount of Rebar Corrosion: Importance of the Current Applied Accelerated Tests," *Concrete Repair, Rehabilitation and Protection*, Ed. R.K. Dhir & M.R. Jones, pp. 263-272, 1996.

125. M. Saifullah and L.A. Clark, "Effect of Corrosion Rate on the Bond Strength of Corroded Reinforcement," *Proceedings of the International Conference on Corrosion and Corrosion Protection of Steel in Concrete*, Ed. R.N. Swamy, pp. 591-602, 1994.

126. R.E. Davis, "A summary of investigations of volume changes in cements, mortars and concretes produced by causes other than stress," *American Society for Testing Materials – Proceedings*, Vol. 30, No. 1, pp. 668-685, 1930.

127. A.M. Neville, *Properties of Concrete*, 3rd Edition, London: Pittman Publishing Ltd, 1981.

128. M.J. McGinnis and S. Pessiki, "Water-Induced Swelling Displacements in Core Drilling Method," *ACI Materials Journal*, Vol. 104, No. 1, pp. 13-22, 2007.

129. Zdeněk P. Bažant, "Mathematical model for creep and thermal shrinkage of concrete at high temperature," *Nuclear Engineering and Design*, Vol. 76, pp. 183-191, 1983.

130. J.P. Broomfield, *Corrosion of Steel in Concrete: Understanding, Investigation and Repair*, London: E & FN Spon, 1997.

131. T. Vidal, A. Castel, and R. Francois, "Analyzing Crack Width to Predict Corrosion in Reinforced Concrete," *Cement and Concrete Research*, Vol. 34, pp. 165-174, 2004.

132. C.A. Ballinger, "Methodology for the Protection and Rehabilitation of Existing Reinforced Concrete Bridges," Quarterly Report No. 3, Wilbur Smith Associates, BTML Division, Report to the Strategic Highway Research Program, SHRP-89-C104, 1991.

133. M. Scott, A. Rezaizadeh, A. Delahaza, C.G. Santos, M. Moore, B. Graybeal, and G. Washer, "A comparison of Nondestructive Evaluation Methods for Bridge Deck Assessment," *NDT & E International*, Vol. 36, pp. 245-255, 2003.

134. G.J. Weil and T.J. Rowe, "Nondestructive Testing and Repair of the Concrete Roof Shell at the Seattle Kingdome," *NDT & E International*, Vol. 31, No. 6, pp. 389-400, 1998.

135. M.P. Enright and D.M. Frangopol, "Survey and Evaluation of Damaged Concrete Bridges," *Journal of Bridge Engineering*, Vol. 5, No. 1, pp. 31-38, 2000.

136. S. Kenai and R. Bahar, "Evaluation and Repair of Algiers new airport building," *Cement & Concrete Composites*, Vol. 25, pp. 633-641, 2003.

137. J.A. Qazweeni and O.K. Daoud, "Concrete Deterioration in a 20-Year-Old Structure in Kuwait," *Cement and Concrete Research*, Vol. 21, pp. 1155-1164, 1991.

138. H.L.M. Reis and M.D. Baright, "Evaluation of Bridge Deck Delamination Investigation Methods," Final Report, Project IC-H1, 95/96, Report No. ITRC FR 95/96-1, Illinois Transportation Research Center, 1998.

139. C. Alonso, C. Andrade, J. Rodriguez, and J.M. Diez, "Factors Controlling Cracking of Concrete Affected by Reinforcement Corrosion," *Materials and Structures*, Vol. 31, No. 211, pp. 435-44, 1998.

140. D. Baweja, H. Roper, and V. Sirivivatnanon, "Relationships between Anodic Polarisation and Corrosion of Steel in Concrete," *Cement and Concrete Research*, Vol. 23, pp. 1418-1430, 1993.

141. J.J. Chang, W. Yeih, R. Huang, and C.T. Chen, "Suitability of Several Current used Concrete Durability Indices on Evaluating the Corrosion Hazard for Carbonated Concrete," *Materials Chemistry and Physics*, Vol. 84, pp. 71-78, 2004.

142. M-T. Liang and P-J. Su, "Detection of the Corrosion Damage of Rebar in Concrete using Impact-Echo Method," *Cement and Concrete Research*, Vol. 31, pp. 1427-1436, 2001.

143. J. Mietz and B. Isecke, "Monitoring of Concrete Structures with respect to Rebar Corrosion," *Construction and Building Materials*, Vol. 10, No. 5, pp. 367-373, 1996.

144. W. Yeih and R. Huang, "Detection of the Corrosion Damage in Reinforced Concrete Members by Ultrasonic Testing," *Cement and Concrete Research*, Vol. 28, No. 7, pp. 1071-1083, 1998.

145. J-H. Yoo, Z-T. Park, J-G. Kim, and L. Chung, "Development of a Galvanic Sensor System for Detecting the Corrosion Damage of the Steel Embedded in Concrete Structures: Part I. Laboratory Tests to Correlate Galvanic Current with Actual Damage," *Cement and Concrete Research*, Vol. 33, pp. 2057-2062, 2003.

146. L.G. Andión, P. Garcés, F. Cases, C.G. Andreu, and J.L. Vazquez, "Metallic Corrosion of Steels Embedded in Calcium Aluminate Cement Mortars," *Cement and Concrete Research*, Vol. 31, pp. 1263-1269, 2001.

147. M.M.B. Bola and C.M. Newtson, "Field Evaluation of Marine Structures Containing Calcium Nitrite," *Journal of Performance of Constructed Facilities*, Vol. 19, No. 1, pp. 28-35, 2005.

148. L. Dhouibi, E. Triki, A. Raharinaivo, G. Trabanelli, and F. Zucchi, "Electrochemical Methods for Evaluating Inhibitors of Steel Corrosion in Concrete," *British Corrosion Journal*, Vol. 35, No. 2, pp. 145-149, 2000.

149. B.B. Hope and A.K.C. Ip, "Chloride Corrosion Threshold in Concrete," *ACI Materials Journal*, Vol. 84, No. 4, pp. 306-314, 1987.

150. H.E. Jamil, M.F. Montemor, R. Boulif, A. Shriri, and M.G.S. Ferreira, "An Electrochemical and Analytical Approach to the Inhibition Mechanism of an Amino-Alcohol-Based Corrosion Inhibitor for Reinforced Concrete," *Electrochimica Acta*, Vol. 48, pp. 3509-3518, 2003.

151. R.W. Poston, R.L. Carrasquillo, and J.E. Breen, "Durability of Post-Tensioned Bridge Decks," *ACI Materials Journal*, Vol. 84, No. 4, pp. 315-326, 1987.

152. S. Qian and D. Cusson, "Electrochemical Evaluation of the Performance of Corrosion-Inhibiting Systems in Concrete Bridges," *Cement & Concrete Composites*, Vol. 26, pp. 217-233, 2004.

153. O.T. de Rincón, O. Pérez, E. Paredes, Y. Caldera, C. Urdaneta, and I. Sandoval, "Long-Term Performance of ZnO as a Rebar Corrosion Inhibitor," *Cement & Concrete Composites*, Vol. 24, pp. 79-87, 2002.

154. D.D.N. Singh, R. Ghosh, and B.K. Singh, "Fluoride Induced Corrosion of Steel Rebars in Contact with Alkaline Solutions, Cement Slurry and Concrete Mortars," *Corrosion Science*, Vol. 44, pp. 1713-1735, 2002.

155. M-H. Teng, E.D. Sotelino, and W-F. Chen, "Performance Evaluation of Reinforced Concrete Bridge Columns Wrapped with Fiber Reinforced Polymers," *Journal of Composites for Construction*, Vol. 7, No. 2, pp. 83-92, 2003.

156. K.M.A. Hossain, "Chloride Induced Corrosion of Reinforcement in Volcanic Ash and Pumice based Blended Concrete," *Cement & Concrete Composites*, Vol. 27, pp. 381-390, 2005.

157. H.R. Soleymani and M.E. Ismail, "Comparing Corrosion Measurement Methods to Assess the Corrosion Activity of Laboratory OPC and HPC Concrete Specimens," *Cement and Concrete Research*, Vol. 34, pp. 2037-2044, 2004.

158. A. Cheng, R. Huang, J.K. Wu, and C.H. Chen, "Effect of Rebar Coating on Corrosion Resistance and Bond Strength of Reinforced Concrete," *Construction and Building Materials*, Vol. 19, pp. 404-412, 2005.

159. C. Dehghanian, "Study of Surface Irregularity on Corrosion of Steel in Alkaline Media," *Cement and Concrete Research*, Vol. 33, pp. 1963-1966, 2003.

160. D.G. John, P.C. Searson, and J.L. Dawson, "Use of AC Impedance Technique in Studies on Steel in Concrete in Immersed Conditions," *British Corrosion Journal*, Vol. 16, No. 2, pp.102-106, 1981.

161. A. Macias and C. Andrade, "Corrosion of Galvanized Steel Reinforcements in Alkaline Solutions," *British Corrosion Journal*, Vol. 22, No. 2, pp. 119-129, 1987.

162. A. Macias and C. Andrade, "Corrosion of Galvanized Steel in Dilute $Ca(OH)_2$ Solutions (pH 11.1 – 12.6)," *British Corrosion Journal*, Vol. 22, No. 3, pp. 162-171, 1987.

163. M.A. Sanjuán, "Effect of Curing Temperature on Corrosion of Steel Bars Embedded in Calcium Aluminate Mortars Exposed to Chloride Solutions," *Corrosion Science*, Vol. 41, pp. 335-350, 1999.

164. ASTM C876, "Standards Test Method for Half-Cell Potentials of Reinforcing Steel in Concrete," 1991.

165. R. Davies, "Remote Monitoring of Reinforced Concrete Structures," *Concrete (London)*, Vol. 38, No. 5, pp. 14-15, 2004.

166. B. Elsener, "Half-Cell Potential Mapping to Assess Repair Work on RC Structures," *Construction and Building Materials*, Vol. 15, pp. 133-139, 2001.

167. A. Raharinaivo, P. Brevet, G. Pannier, and G. Grimaldi, "The Influence of Concrete Deterioration on Reinforcement Rusting," *Corrosion Prevention & Control*, Vol. 33, No. 4, pp. 83-87, 1986.

168. V. Leelalerkiet, J-W. Kyung, M. Ohtsu, and M. Yokota, "Analysis of Half-Cell Potential Measurement for Corrosion of Reinforced Concrete," *Construction and Building Materials*, Vol. 18, pp. 155-162, 2004.

169. M. Ohtsu and T. Yamamoto, "Compensation Procedure for Half-Cell Potential Measurement," *Construction and Building Materials*, Vol. 11, pp. 395-402, 1997.

170. S.G. Millard, K.R. Gowers, and R.P. Gill, "Practical Field Measurement of Reinforced Corrosion in Concrete using Linear Polarisation Methods," *British Journal of NDT*, Vol. 34, No. 9, pp. 444-452, 1992.

171. M. Stearn and A.L. Geary, "Electrochemical Polarisation: A Theoretical Analysis of the Shape of Polarisation Curves," *Journal of the Electrochemical Society*, Vol. 104, pp. 56-63, 1957.

172. V. Nachiappan and E.H. Cho, "Corrosion of High Chromium and Conventional Steels Embedded in Concrete," *Journal of Performance of Constructed Facilities*, Vol. 19, No. 1, pp. 56-61, 2005.

173. S.G. Millard, D. Law, J.H. Bungey, and J. Cairns, "Environmental Influences on Linear Polarisation Corrosion Rate Measurement in Reinforced Concrete," *NDT & E International*, Vol. 34, pp. 409-417, 2001.

174. K.R. Gowers, S.G. Millard, J.S. Gill, and R.P. Gill, "Programmable Linear Polarisation Meter for Determination of Corrosion Rate of Reinforcement in Concrete Structures," *British Corrosion Journal*, Vol. 29, No. 1, pp. 25-32, 1994.

175. J.A. Gonzalez, A. Molina, M.L. Escudero, and C. Andrade, "Errors in the Electrochemical Evaluation of very small Corrosion Rates: I. Polarization Resistance Method Applied to Corrosion of Steel in Concrete," *Corrosion Science*, Vol. 25, pp. 917-930, 1985.

176. D.W. Law, S.G. Millard, and J.H. Bungey, "Use of Galvanostatic Pulse Measurements on Active Reinforcing Steel in Concrete to Assess Corrosion Rates," *British Corrosion Journal*, Vol. 36, No. 1, pp. 75-80, 2001.

321

177. N. Kouloumbi and G. Batis, "Chloride Corrosion of Steel Rebars in Mortars with Fly Ash Admixtures," *Cement & Concrete Composites*, Vol. 14, pp. 199-207, 1992.

178. G. Baronio, M. Berra, L. Bertolini, and T. Pastore, "Steel Corrosion Monitoring in Normal and Total-Lightweight Concretes Exposed to Chloride and Sulphate Solutions, Part II: Polarisation Resistance Measurements," *Cement and Concrete Research*, Vol. 26, No. 5, pp. 691-696, 1996.

179. A.A. Sagües, "Corrosion of Epoxy Coated Rebar in Florida Bridges," Final Report to Florida D.O.T. No. 0510603, 1994.

180. P. Garcés, J. Fraile, E. Vilaplana-Ortego, D. Cazorla-Amorós, E.G. Alcocel, and L.G. Andión, "Effect of Carbon Fibres on the Mechanical Properties and Corrosion Levels of Reinforced Portland Cement Mortars," *Cement and Concrete Research*, Vol. 35, pp. 324-331, 2005.

181. P. Montes, T.W. Bremner, and D.H. Lister, "Influence of Calcium Nitrite Inhibitor and Crack Width on Corrosion of Steel in High Performance Concrete subjected to a Simulated Marine Environment," *Cement & Concrete Composites*, Vol. 26, pp. 243-253, 2004.

182. S. Feliu, J.A. González, V. Feliu, and M.C. Andrade, "Confinement of the Electrical Signal for In Situ Measurement of Polarization Resistance in Reinforced Concrete," *ACI Materials Journal*, Vol. 87, No. 5, pp. 457-460, 1990.

183. D.W. Law, S.G. Millard, and J.H. Bungey, "Linear Polarisation Resistance Measurements using a Potentiostatically Controlled Guard Ring," *NDT & E International*, Vol. 33, pp. 15-21, 2000.

184. P. Gu, Y. Fu, P. Xie, and J.J. Beaudoin, "Characterization of Surface Corrosion of Reinforcing Steel in Cement Paste by Low Frequency Impedance Spectroscopy," *Cement and Concrete Research*, Vol. 24, No. 2, pp. 231-242, 1994.

185. A. Carnot, I. Frateur, S. Zanna, B. Tribollet, I. Dubois-Brugger, and P. Marcus, "Corrosion Mechanisms of Steel Concrete Moulds in Contact with a Demoulding Agent Studied by EIS and XPS," *Corrosion Science*, Vol. 45, pp. 2513-2524, 2003.

186. H. Idrissi and A. Limam, "Study and Characterization by Acoustic Emission and Electrochemical Measurements of Concrete Deterioration caused by Reinforcement Steel Corrosion," *NDT&E International*, Vol. 36, pp. 563-569, 2003.

187. G.K. Glass, "An Assessment of the Coulostatic Method Applied to the Corrosion of Steel in Concrete," *Corrosion Science*, Vol. 37, No. 4, pp. 597-605, 1995.

188. K.R. Gowers and S.G. Millard, "Electrochemical Techniques for Corrosion Assessment of Reinforced Concrete Structures," *Proceedings of the Institution of Civil Engineers, Structures and Buildings*, Vol. 134, No. 2, pp. 129-137, 1999.

189. M. Raupach and P. Scheißl, "Macrocell Sensor Systems for Monitoring of the Corrosion Risk of the Reinforcement in Concrete Structures," *NDT & E International*, Vol. 34, pp. 435-442, 2001.

190. P.L. Fuhr and D.R. Huston, "Corrosion Detection in Reinforced Concrete Roadways and Bridges via Embedded Fiber Optic Sensors," *Smart Materials and Structures*, Vol. 7, pp. 217-228, 1998.

191. R. Wolfson and J.M. Pasachoff, *Physics*, Boston: Little Brown, 1987.

192. W. Liu, R.G. Hunsperger, M.J. Chajes, K.J. Folliard, and E. Kunz, "Corrosion Detection of Steel Cables using Time Domain Reflectometry," *Journal of Materials in Civil Engineering*, Vol. 14, No. 3, pp. 217-223, 2002.

193. J.A. Stastny, C.A. Rogers, and C. Liang, "Distributed Electrical Time Domain Reflectometry (ETDR) Structural Sensors: Design Models and Proof-of-Concept Experiments," *SPIE Proceedings 1919*, pp. 366-376, 1993.

194. E.I. Okanla, P.A. Gaydecki, and F.M. Burdekin, "Detecting Faults in Posttensioning Ducts by Electrical Time-Domain Reflectometry," *Journal of Structural Engineering*, Vol. 123, No. 5, pp. 567-574, 1997.

195. D.G. Manning and F.B. Holt, "Detecting Delamination in Concrete Bridge Decks," *Concrete International: Design and Construction*, Vol. 2, No. 11, pp. 34-41, 1980.

196. ASTM D4788, "Standard Test Method for Detecting Delaminations in Bridge Decks using Infrared Thermography," 1993.

322

197. D. Huston, N. Pelczarski, B. Esser, K. Maser, and W. Weedon, "Damage Assessment in Roadways with Ground Penetrating Radar," *Proceedings of SPIE*, Vol. 3995, pp. 483-491, 2000.

198. S.S. Hubbard, J. Zhang, P.J.M. Monteiro, J.E. Peterson, and Y. Rubin, "Experimental Detection of Reinforcing Bar Corrosion using Nondestructive Geophysical Techniques," *ACI Materials Journal*, Vol. 100, No. 6, pp. 501-510, 2003.

199. S.B. Chase, "Tomographic Imaging of Bridge Decks using Radar," *Structures Congress – Proceedings*, pp. 280-283, 1999.

200. D.E. Bray and R.K. Stanley, *Nondestructive Evaluation: A Tool in Design, Manufacturing, and Service*, Revised Edition, New York: CRC Press, 1997.

201. A. Ghorbanpoor, "Evaluation of Prestressed Concrete Girders Using Magnetic Flux Leakage," *Structures Congress – Proceedings*, pp. 284-287, 1999.

202. H. Scheel and B. Hillemeier, "Location of Prestressing Steel Fractures in Concrete," *Journal of Materials in Civil Engineering*, Vol. 15, No. 3, pp. 228-234, 2003.

203. G. Miller, P. Gaydecki, S. Quek, B.T. Fernandes, and M.A.M. Zaid, "Detection and imaging of surface corrosion on steel reinforcing bars using a phase-sensitive inductive sensor intended for use with concrete," *NDT & E International*, Vol. 36, pp. 19-26, 2003.

204. A.T. Ciolko and H. Tabatabai, "Nondestructive Methods for Condition Evaluation of Prestressing Steel Strands in Concrete Bridges, Phase I: Technology Review," NCHRP Project 10-53, 1999.

205. P. Kear and M. Leeming, "Radiographic Inspection of Post-Tensioned Concrete Bridges," *Insight*, Vol. 36, No. 7, pp. 507-510, 1994.

206. S. Srinivasan, K. Saravanan, V. Kapali, N.U. Nayak, R.H. Suresh, R.M. Kalyanasundaram, A. Madhavamayandi, Y. Mahadeva Yier, and N.S. Rengaswamy, "Radiographic Examination of Prestressed Concrete Box Girder Bridges," *Materials Performance*, Vol. 35, No. 10, pp. 61-65, 1996.

207. H. Thielsch, "Radiography of Concrete Stacks," *Materials Evaluation*, Vol. 22, No. 9, pp. 425-427,432, 1964.

208. I. Sekine and M. Fujinawa, "Exploratory Tests of Corrosion of Reinforcing Steel in Concrete by X-radiography," *Materials Evaluation*, Vol. 42, No. 1, pp. 121-126, 1984.

209. T. Skoulikidis, D. Marinakis, and G. Batis, "X-Ray Permeability of Corrosion Products as a Measure of the Rate of Corrosion of Rebars and Prediction of Concrete Cracking," *ASTM STP 906*, pp. 108-117, 1985.

210. J.R. Casas and P.J.S. Cruz, "Fiber Optic Sensors for Bridge Monitoring," *Journal of Bridge Engineering*, Vol. 8, No. 6, pp. 362-373, 2003.

211. C.K.Y. Leung, "Fiber Optic Sensors in Concrete: The Future?," *NDT&E International*, Vol. 34, pp. 85-94, 2001.

212. P. Cosentino, B. Grossman, C. Shieh, S. Doi, H. Xi, and P. Erbland, "Fiber-Optic Chloride Sensor Development," *Journal of Geotechnical Engineering*, Vol. 121, No. 8, pp. 610-617, 1995.

213. N. Singh, S.C. Jain, A.K. Aggarwal, M.L. Singla, and M. Singh, "A Simple Fiber Optic Technique for In-Situ Corrosion Sensing in Structures," *Proceedings of SPIE*, Vol. 3993, pp. 201-205, 2000.

214. X.M. Li, W.M. Chen, Y. Zhu, S.L. Huang, and K.D. Bennett, "Monitoring the Corrosion of Steel in Reinforced Concrete using Optical Waveguide Methods," *Proceedings of SPIE*, Vol. 3986, pp. 172-179, 2000.

215. J.R. Casas and D.M. Frangopol, "Monitoring and Reliability Management of Deteriorating Concrete Bridges," Proceedings of the 2nd International Workshop on Life-cycle Cost Analysis and Design of Civil Infrastructure Systems, pp. 127-141, 2001.

216. P.L. Fuhr, D.R. Huston, and B. MacCraith, "Embedded Fiber Optic Sensors for Bridge Deck Chloride Penetration Measurement," *Optical Engineering*, Vol. 37, No. 4, pp. 1221-1228, 1998.

217. D.R. Huston and P.L. Fuhr, "Fiber Optic Bridge Deck Chloride Detection," *Proceedings of Structures Congress XV*, Vol. 2, pp. 974-978, 1997.

218. P.L. Fuhr, D.R. Huston, A.J. McPadden, and R.F. Cauley, "Embedded Chloride Detectors for Roadways and Bridges," *Proceedings of SPIE*, Vol. 2719, pp. 229-237, 1996.

219. P.L. Fuhr, D.R. Huston, M. Nelson, O. Nelson, J. Hu, and E. Mowat, "Fiber Optic Sensing of a Bridge in Waterbury, Vermont," *Journal of Intelligent Material Systems and Structures*, Vol. 10, pp. 293-303, 1999.

220. W. Grahn, P. Makedonski, J. Wichern, W. Kowalsky, and S. Wiese, "FIBEROPTICAL Sensors for In-Situ Monitoring of Moisture and pH-value in Reinforced Concrete," *Proceedings of SPIE*, Vol. 4480, pp. 395-403, 2002.

221. G.P. Hammersley and M.J. Dill, "The Long-Term Monitoring of Civil Engineering and Building Structures –Developments in Techniques for Monitoring Corrosion in Reinforced and Post-Tensioned Concrete," *Journal of Systems and Control Engineering*, Vol. 212, No. 13, pp. 175-188, 1998.

222. B. Culshaw, C. Michie, P. Gardiner, and A. McGown, "Smart Structures and Applications in Civil Engineering," *Proceedings of the IEEE*, Vol. 84, No. 1, pp. 78-86, 1996.

223. C.K.Y. Leung, N. Elvin, N. Olson, T.F. Morse, and Y-F. He, "A Novel Distributed Optical Crack Sensor for Concrete Structures," *Engineering Fracture Mechanics*, Vol. 65, pp. 133-148, 2000.

224. D. Inaudi and S. Vurpillot, "Monitoring of Concrete Bridges with Long-Gage Fiber Optic Sensors," *Journal of Intelligent Material Systems and Structures*, Vol. 10, pp. 280-292, 1999.

225. N. Elvin, C.K.Y. Leung, V.S. Sudarshanam, and S. Ezekiel, "A Novel Fiber Optic Delamination Detection Scheme: Theoretical and Experimental Feasibility Studies," *Journal of Intelligent Systems and Structures*, Vol. 10, pp. 314-321, 1999.

226. *CRC Handbook on Nondestructive Testing of Concrete*, Eds. V.M. Malhotra & N.J. Carino, Boca Raton: CRC Press, 1991.

227. ASTM D4580, "Standard Practice for Measuring Delaminations in Concrete Bridge Decks by Sounding," 2003.

228. M.S. Weng, S.E. Dunn, W.H. Hartt, and R.P. Brown, "Application of Acoustic Emission to Detection of Reinforcing Steel Corrosion in Concrete," *Corrosion*, Vol. 38, No. 1, pp. 9-14, 1982.

229. Z. Li, F. Li, A. Zdunek, E. Landis, and S.P. Shah, "Application of Acoustic Emission Technique to Detection of Reinforcing Steel Corrosion in Concrete," *ACI Materials Journal*, Vol. 95, No. 1, pp. 68-76, 1998.

230. S. Yuyama, T. Okamoto, M. Shigeishi, M. Ohtsu, and T. Kishi, "A Proposed Standard for Evaluating Structural Integrity of Reinforced Concrete Beams by Acoustic Emission," *Acoustic Emission: Standards and Technology Update*, ASTM STP 1353, Ed. S.J. Vahaviolos, West Conshohocken: ASTM, 1999.

231. D.W. Cullington, D. MacNeil, P. Paulson, and J. Elliot, "Continuous acoustic monitoring of grouted post-tensioned concrete bridges," *NDT & E International*, Vol. 34, pp. 95-105, 2001.

232. M. Ing, S. Austin, and R. Lyons, "Cover zone properties influencing acoustic emission due to corrosion," *Cement and Concrete Research*, Vol. 35, pp. 284-295, 2005.

233. R. Lyons, M. Ing, and S. Austin, "Influence of diurnal and seasonal temperature variations on the detection of corrosion in reinforced concrete by acoustic emission," *Corrosion Science*, Vol. 47, pp. 413-433, 2005.

234. R.G. Budynas, *Advanced Strength and Applied Stress Analysis*, 2nd Edition, Boston: McGraw-Hill, 1999.

235. G. Batis and Th. Routoulas, "Steel Rebars Corrosion Investigation with Strain Gages," *Cement & Concrete Composites*, Vol. 21, pp. 163-171, 1999.

236. O.S. Salawu and C. Williams, "Review of Full-Scale Dynamic Testing of Bridge Structures," *Engineering Structures*, Vol. 17, No. 2, pp. 113-121, 1995.

237. H.A. Razak and R.C. Choi, "The Effect of Corrosion on the Natural Frequency and Modal Damping of Reinforced Concrete Beams," *Engineering Structures*, Vol. 23, pp. 1126-1133, 2001.

238. R. Capozucca and M.N. Cerri, "Identification of Damage in Reinforced Concrete Beams Subjected to Corrosion," *ACI Structural Journal*, Vol. 97, No. 6, pp. 902-909, 2000.

239. O.S. Salawu, "Detection of Structural Damage through Changes in Frequency: A Review," *Engineering Structures*, Vol. 19, No. 9, pp. 718-723, 1997.

240. G.E. Warren and L.J. Malvar, "Structural Assessment of Reinforced Concrete Piers using the Impact Load Method," *Experimental Techniques*, Vol. 18, No. 3, pp. 15-21, 1994.

241. O.S. Salawu and C. Williams, "Bridge Assessment using Forced-Vibration Testing," *Journal of Structural Engineering*, Vol. 121, No. 2, pp. 161-173, 1995.

242. J. Martin, K.J. Broughton, A. Giannopolous, M.S.A. Hardy, and M.C. Forde, "Ultrasonic tomography of grouted duct post-tensioned reinforced concrete bridge beams," *NDT & E International*, Vol. 34, pp. 107-113, 2001.

243. S. R. Iyer, S.K. Sinha, and A.J. Schokker, "Ultrasonic C-Scan Imaging of Post-Tensioned Concrete Bridge Structures for Detection of Corrosion and Voids," *Computer-Aided Civil and Infrastructure Engineering*, Vol. 20, pp. 79-94, 2005.

244. S.K. Sinha, A.J. Schokker, and S.R. Iyer, "Non-Contact Ultrasonic Imaging of Post-Tensioned Bridges to Investigate Corrosion and Void Status," *Proceedings of IEEE Sensors*, Vol. 2, No. 1, pp. 487-492, 2003.

245. A. Castel, R. François, and G. Arliguie, "Effect of loading on carbonation penetration in reinforced concrete elements," *Cement and Concrete Research*, Vol. 29, pp. 561-565, 1999.

246. M.-T. Liang and S.-H. Lin, "Mathematical Modeling and Applications for Concrete Carbonation," *Journal of Marine Science Technology*, Vol. 11, No. 1, pp. 20-33, 2003.

247. A.V. Saetta, B.A. Schrefler, and R.V. Vitaliani, "The Carbonation of Concrete and the Mechanism of Moisture, Heat and Carbon Dioxide Flow through Porous Materials," *Cement and Concrete Research*, Vol. 23, pp. 761-772, 1993.

248. Y.F. Houst and F.H. Wittmann, "Depth Profiles of Carbonates formed during Natural Carbonation," *Cement and Concrete Research*, Vol. 32, pp. 1923-1930, 2002.

249. M.A. Sanjuán, C. Andrade, and M. Cheyrezy, "Concrete carbonation tests in natural and accelerated conditions," *Advances in Cement Research*, Vol. 15, No. 4, pp. 171-180, 2003.

250. P.B. Bamforth and W.F. Price, "An international review of chloride ingress into structural concrete," Report No. 1303/96/9092, Taywood Engineering Ltd Technology Division, 1997.

251. M.P. Enright and D.M. Frangopol, "Probabilistic Analysis of Resistance Degradation of Reinforced Concrete Bridge Beams under Corrosion," *Engineering Structures*, Vol. 20, No. 11, pp. 960-971, 1998.

252. D.P. Bentz, E.J. Garboczi, and E.S. Lagergren, "Multi-Scale Microstructural Modeling of Concrete Diffusivity: Identification of Significant Variables," Cement, Concrete and Aggregates, Vol. 20, No. 1, pp 129-139, 1998.

253. M.G. Stewart and D.V. Rosowsky, "Time-Dependent Reliability of Deteriorating Reinforced Concrete Bridge Decks," *Structural Safety*, Vol. 20, pp. 91-109, 1998.

254. V.G. Papadakis, A.P. Roumeliotis, M.N. Fardis, and C.G. Vagenas, "Mathematical Modelling of Chloride Effect on Concrete Durability and Protection Measures," *Concrete Repair, Rehabiliation and Protection*, Ed. R.K Dhir & M.R. Jones, London: E&FN Spon, pp. 165-174, 1996.

255. C.Q. Li, "Initiation of Chloride-Induced Reinforcement Corrosion in Concrete Structural Members—Prediction," *ACI Structural Journal*, Vol. 99, No. 2, pp. 133-141, 2002.

256. J. Zemajtis, *Modeling the Time to Corrosion Initiation for Concretes with Mineral Admixtures and/or Corrosion Inhibitors in Chloride-Laden Environments*, PhD Thesis, Virginia Polytechnic Institute and State University, 1998.

257. M.I. Rafiq, M.K. Chryssanthopoulos, and T. Onoufriou, "Performance Updating of Concrete Bridges using Proactive Health Monitoring Methods," *Reliability Engineering & System Safety*, Vol. 86, pp. 247-256, 2004.

258. R.E. Weyers, "Service Life Model for Concrete Structures in Chloride Laden Environments," *ACI Materials Journal*, Vol. 95, No. 4, pp. 445-453, 1998.

259. D.V. Val, M.G. Stewart, and R.E. Melchers, "Effect of reinforcement corrosion on reliability of highway bridges," *Engineering Structures*, Vol. 20, No. 11, pp. 1010-1019, 1998.

260. D.V. Val, "Effect of Different Limit States on Life-Cycle Cost of RC Structures in Corrosive Environment," *Journal of Infrastructure Systems*, Vol. 11, No. 4, pp. 231-240, 2005.

261. M.G. Stewart, A.C. Estes, and D.M. Frangopol, "Bridge Deck Replacement for Minimum Expected Cost Under Multiple Reliability Constraints," *Journal of Structural Engineering*, Vol. 130, No. 9, pp. 1414-1419, 2004.

262. M.G. Stewart and D.V. Val, "Multiple Limit States and Expected Failure Costs for Deteriorating Reinforced Concrete Bridges," *Journal of Bridge Engineering*, Vol. 8, No. 6, pp. 405-415, 2003.

263. M.G. Stewart and D.V. Rosowsky, "Time-Dependent Reliability of Deteriorating Reinforced Concrete Bridge Decks," *Structural Safety*, Vol. 20, pp. 91-109, 1998.

264. M.G. Stewart and D.V. Rosowsky, "Structural Safety and Serviceability of Concrete Bridges Subject to Corrosion," Journal of Infrastructure Systems, Vol.4, No. 4, pp. 146-155, 1998.

265. D.M. Frangopol, K.-Y. Lin, and A.C. Estes, "Reliability of Reinforced Concrete Girders under Corrosion Attack," *Journal of Structural Engineering*, Vol. 123, No. 3, pp. 286-297, 1997.

266. D.V. Val, M.G. Stewart, and R.E. Melchers, "Effect of reinforcement corrosion on reliability of highway bridges," *Engineering Structures*, Vol. 20, No. 11, pp. 1010-1019, 1998.

267. K.A.T. Vu and M.G. Stewart, "Predicting the Likelihood and Extent of Reinforced Concrete Corrosion-Induced Cracking," *Journal of Structural Engineering*, Vol. 131, No. 11, pp. 1681-1689, 2005.

268. P.C. Hoffman and R.E. Weyers, "Predicting critical chloride levels in concrete bridge decks," *Proceedings of ICOSSAR 93*, Eds. G.I. Schueller, M. Shinozuka, and J.T.P. Yao, Balkema, Rotterdam, pp. 957-959, 1993.

269. S. Ahmad, B. Bhattacharjee, and R. Wason, "Experimental Service Life Prediction of Rebar-Corroded Reinforced Concrete Structure," *ACI Materials Journal*, Vol. 94, No. 4, pp. 311-316, 1997.

270. A. van Beek, G.C.M. Gaal, J.M. van Noortwijk, and J.D. Bakker, "Validation model for service life prediction of concrete structures," 2nd *International RILEM Workshop on Life Prediction and Aging Management of Concrete Structures*, Ed. D.G. Naus, May 5-6, Paris, France, pp. 257-267, 2003.

271. T.J. Kirkpatrick, R.E. Weyers, M.M. Sprinkel, and C.M. Anderson-Cook, "Impact of specification changes on chloride-induced corrosion service life of bridge decks," *Cement and Concrete Research*, Vol. 32, pp. 1189-1197, 2002.

272. "Recording and coding guide for the structure inventory and appraisal of the nation's bridges," Report No. FHWA-PD-96-001, Federal Highway Administration, 1995.

273. R.L. Purvis, K. Babaei, K.C. Clear, and M.J. Markow, "Life-Cycle Cost Analysis for Protection and Rehabilitation of Concrete Bridges Relative to Reinforcement Corrosion," Report No. SHRP-S-377, Strategic Highway Research Program, National Research Council, 1994.

274. R.B. Lindsay, *Mechanical Radiation*, New York: McGraw-Hill, 1960.

275. W.M. Ewing, W.S. Jardetzky, and F. Press, *Elastic Waves in Layered Media*, New York: McGraw-Hill, 1957.

276. J.D. Achenbach, *Wave Propagation in Elastic Solids*, New York: American Elsevier Publishing Company, 1973.

277. G.N. Watson, *Theory of Bessel Functions*, 2nd Ed., Cambridge: University Press, 1966.

278. T. Lahti, *Analysis of methods for acoustical systems based on the FFT and intensity techniques*, Technical Research Centre of Finland, Publications 67, 1990.

279. L.R. Rabiner and R.W. Schafer, *Digital Processing of Speech Signals*, London: Prentice-Hall International, Inc., 1978.

280. M. Niethammer, L.J. Jacobs, J. Qu, and J. Jarzynski, "Time-frequency representation of Lamb waves using the reassigned spectrogram," *Journal of the Acoustical Society of America*, Vol. 107, No. 5, pp. 19-24, 2000.

CURRICULUM VITAE

Benjamin L. Ervin
Nondestructive Testing and Evaluation Laboratory
Department of Industrial & Enterprise Systems Engineering
University of Illinois at Urbana-Champaign
117 Transportation Building
104 South Mathews Avenue
Urbana, IL 61801
(217) 244-9015, bervin@uiuc.edu

EMPLOYMENT

MIT Lincoln Laboratory, September 2007
Technical Staff - Biodefense Systems Group

EDUCATION

Candidate to Ph.D. in Systems and Entrepreneurial Engineering, October 2007
University of Illinois at Urbana-Champaign
Department of Industrial & Enterprise Systems Engineering
Tentative Thesis Title: *"Monitoring Corrosion of Rebar Embedded in Mortar using Guided Ultrasonic Waves"*
Dissertation Adviser: *Professor Henrique Reis*

M.S. in General Engineering, 2003
University of Illinois at Urbana-Champaign
Department of General Engineering
Thesis Title: *"Detection of Corrosion in Reinforced Concrete Structures using an Ultrasonic Approach"*
Thesis Adviser: *Professor Henrique Reis*

B.S. in General Engineering with Honors, 2001
University of Illinois at Urbana-Champaign
Department of General Engineering
Secondary Field: Business Systems Integration and Consulting
Project Title: *"Redesign of a Gearbox"*
Project Adviser: *James Leake*

TEACHING EXPERIENCE

All experience was acquired at the University of Illinois at Urbana-Champaign.

Department of General Engineering

1. Teaching Assistant for *GE 312 -- Instrumentation and Test Laboratory*, 2001-2002, 2005-Present
   - Developed and presented all laboratory lectures, materials, and solutions
   - Demonstrated proper instrumentation and guided students through experimentation

2. Course Grader for *GE 311 -- Engineering Design Analysis*, 2000-2002
   - Lectured on finite element software and organized balsa wood structural design competition
   - Graded all homework, quizzes, projects, and exams

3. Teaching Assistant for *GE 320 -- Introductory Control Systems*, 2001
   - Presented all laboratory lectures and guided students through experimentation
   - Graded homework assignments and all laboratory reports

327

4. Course Grader for *GE 410 -- Component Design*, 2001
   - Graded all homework, quizzes, projects, and exams

Department of Mathematics

1. Course Grader for *Calculus I*, 1998-1999
   - Graded all homework assignments

2. Course Grader for *Calculus II*, 1998-1999
   - Graded all homework assignments

3. Course Grader for *Calculus of Several Variables*, 1998-1999
   - Graded all homework assignments

HONORS AND ACHIEVEMENT

- Excellent Teaching Assistant Award for Industrial and Enterprise Systems Engineering Department, 2007
- Award for Excellence in Teaching at the University of Illinois at Urbana-Champaign, *Instrumentation and Test Laboratory*, 2001-2002, 2005-2006
- Gamma Epsilon Graduate Adviser, University of Illinois at Urbana-Champaign, 2003-2005
- General Engineering Graduate Service Award, University of Illinois at Urbana-Champaign, 2003
- University of Illinois at Urbana-Champaign Dean's List, Fall 1997, Spring 2000, Fall 2000, Spring 2001
- Illinois Department of Professional Regulation Registered Engineering Intern, 2001
- Kenneth W. Hamming Scholarship, University of Illinois at Urbana-Champaign, 2000
- Gamma Epsilon Honor Society Member, University of Illinois at Urbana-Champaign, 1999-Present

RESEARCH EXPERIENCE AND PUBLICATIONS

Research Assistant for Nondestructive Testing and Evaluation Laboratory in the Department of General Engineering at the University of Illinois at Urbana-Champaign, 2002-2007
- Designed an accelerated corrosion experiment for use with reinforced mortar beam specimens
- Designed experimental setup utilizing guided ultrasonic waves for monitoring corrosion in reinforced mortar
- Designed reinforced mortar pullout specimens and conducted pullout testing to measure bond strength from corrosion deterioration

Journal Publications

1. B.L. Ervin, D.A. Kuchma, J.T. Bernhard, and H. Reis, "Monitoring corrosion of rebar embedded in mortar using high-frequency guided ultrasonic waves," Submitted for Publication in ASCE Journal of Engineering Mechanics.

2. B.L. Ervin, J.T. Bernhard, D.A. Kuchma, and H. Reis, "Estimation of general corrosion damage to steel reinforced mortar using frequency sweeps of guided mechanical waves," *INSIGHT - The Journal of the British Institute for Non-Destructive Testing*, Vol. 48, No. 11, pp. 682-692, 2006.

3. H. Reis, B.L. Ervin, D.A. Kuchma, and J.T. Bernhard, "Estimation of Corrosion Damage in Steel Reinforced Mortar Using Guided Waves," *ASME Journal of Pressure Vessel Technology*, Vol. 127, No. 3, pp. 255-261, 2005.

4. K. Hietpas, B. Ervin, J. Banasiak, D. Pointer, D.A. Kuchma, H. Reis, and J.T. Bernhard, "Ultrasonics and Electromagnetics for a Wireless Corrosion Sensing System Embedded in Structural Concrete," *Smart Structures and Systems*, Vol. 1, No. 3, pp. 267-282, 2005.

Conference Publications

1. B.L. Ervin, H. Reis, J.T. Bernhard, and D.A. Kuchma, "Monitoring Uniform and Localized Corrosion in Reinforced Mortar using High-Frequency Guided Longitudinal Waves," Submitted to the Proceedings of the SPIE, Sensors and Smart Structures Technologies for Civil, Mechanical, and Aerospace Systems, San Diego, CA, March 9 – 13, 2008.

2. B.L. Ervin, H. Reis, J. Bernhard, and D.A. Kuchma, "Monitoring Localized Corrosion of Rebar Embedded in Mortar using High-Frequency Guided Ultrasonic Waves," Submitted to the 6th International Workshop on Structural Health Monitoring, Stanford, CA, September 11 – 13, 2007.

3. B.L. Ervin, J.T. Bernhard, D.A. Kuchma, and H. Reis, "Monitoring General Corrosion of Rebar Embedded in Mortar using High-Frequency Guided Mechanical Waves," *Proceedings of the SPIE*, Sensors and Smart Structures Technologies for Civil, Mechanical, and Aerospace Systems, San Diego, CA, March 18 – 22, Vol. 6529, 2007.

4. W.M. Kriven, M. Gordon, B. Ervin, and H. Reis, "Corrosion Protection of Concrete Reinforcing Bars using Geopolymers," *Proceedings of the 31st International Conference on Advanced Ceramics and Composites*, Cocoa Beach, FL, January 21 – 26, 2007.

5. B.L. Ervin, J.T. Bernhard, D.A. Kuchma, and H. Reis, "Estimation of Corrosion Damage to Steel Reinforced Mortar using Frequency Sweeps of Guided Mechanical Waves," *Proceedings of the SPIE*, Sensors and Smart Structures Technologies for Civil, Mechanical, and Aerospace Systems, San Diego, CA, February 26 - March 2, Vol. 6174, pp. 141-152, 2006.

6. H. Reis, B.L. Ervin, D.A. Kuchma and J.T. Bernhard, "Estimation of Corrosion Damage in Steel Mortar using Waveguides," *Proceedings of the SPIE*, Nondestructive Evaluation and Health Monitoring of Aerospace Materials, Composites, and Civil Infrastructure IV, San Diego, CA, March 16 – 19, Vol. 5767, pp. 105-114, 2005.

7. K. Hietpas, B. Ervin, D.A. Kuchma, H. Reis, and J.T. Bernhard, "Wireless Embedded Rust Monitoring Systems," *Proceedings of the 2004 Antenna Applications Symposium*, Monticello, IL, September 15 – 17, pp. 27-44, 2004.

8. H. Reis, B. Ervin, D.A. Kuchma, and J. Bernhard, "Evaluation of Corrosion Damage in Steel Reinforced Concrete," *Proceedings of the 4th International Workshop on Structural Health Monitoring*, Stanford University, Stanford, CA, September 15 – 17, pp. 139-146, 2003.

Technical Reports

1. H.L.M. dos Reis and B.L. Ervin, "Detection of Corrosion in Reinforced Concrete Structures Using an Acoustic Approach," Technical Report UILU ENG 03-3001, University of Illinois, Urbana, IL (*Extracted from M.S. Thesis*), 2003.

Reviewer

- Journal of Physics D: Applied Physics
- IEEE Transactions on Ultrasonics, Ferroelectrics, and Frequency Control
- Journal of Composite Materials
- Measurement Science & Technology
- Smart Materials and Structures
- ASCE Journal of Materials in Civil Engineering

LEADERSHIP AND VOLUNTEER EFFORTS

- The Nondestructive Testing and Evaluation Laboratory regularly participates in the IMPRINT Program (C/O Dean Parker). In this program under-represented high school graduates admitted to the College of Engineering are invited to spend a summer working in an engineering laboratory in order to facilitate their immersion in an academic research environment. I have had the privilege of hosting and guiding the following students:
  - Mr. Frederick Jackson   (Summer 2006)
  - Mr. Norberto Rivera   (Summer 2004)
  - Mr. Todd Baxter   (Summer 2003)
- Volunteer Kiwanis Little League ® baseball coach in Champaign-Urbana area, 2002-2004
- Created and coached traveling youth baseball team in Central Illinois area, 2005-2006